The emission, storage and dispersion of CO2 within and above the urban canopy layer in central London

Bjorkegren, Alex

Awarding institution:
King's College London

The emission, storage and dispersion of CO_2 within and above the urban canopy layer in central London

PhD Thesis

Alex Björkegren

Department of Geography

King's College London

University of London

Submitted:03/03/2016

Defended: 10/06/2016

Finalised: 10/06/2016

Acknowledgements

I would like to thank my supervisor, Professor Sue Grimmond, for her constant guidance, assistance and support throughout this study. I would also like to thank Professor Bruce Malamud for his invaluable advice on statistical methods and graphical presentation. The comments and proofreading of both have vastly improved the contents and form of this thesis.

This thesis was written as part of the micrometeorological group at King's College London (KCL), now relocated to the University of Reading (UoR). It was funded as part of the NERC grant NE/H003231/1 ClearfLo project. Additional funding which contributed to the collection of ancillary measurements was provided by EU emBRACE (282672), EU BRIDGE (211345) and co-financed by "HORIZON 2020" EU Framework Programme.

Additional thanks go to Associate Professor Andreas Christen for the provision of software implementing the flux footprint model, to Dr Fredrik Lindberg for his advice and script to calculate morphometric parameters, Dr Mario Iamerino and Dr Helen Ward for their advice regarding the GreaterQF model, Giulia Zazzeri and Dr Rebecca Fisher for the use of data measured by Picarro along a transect throughout Greater London and two measurement campaigns at KCL, and Dr Simone Kotthaus for her assistance on numerous topics and provision of CO_2 flux and boundary layer height data sets. I would also like to thank the KCL Directorate of Estates and Facilities, in particular Duncan Ede, for their assistance with access to the Strand building roof, and the IT services at both KCL and UoR for their support in the management and storage of our data.

I would like to thank Ms. Sue Björkegren and Dr Caiti Lundberg for their advice and proofreading of the manuscript. The comments from Ms. Claire Best and the reviewers aided the development of parts of chapters 2, 3 and 5 and are greatly appreciated. Collective reviewing of figures by members of the micromet team during weekly meetings also improved the presentation and interpretation of the data, and collective maintenance of instruments made the data collection possible. The people who contributed to this include, but are not limited to, Dr Ben Crawford, Dr Veronica Bellucco, Dr Cris Castillo, Mr Jon Durrans, Mr Oscar Finnemore, Ms Grace Healy, Dr Andrew Gabey, Ms Mariana Lina Gouvea, Ms Jinda Sea-Jung, Mr Cristoph Kent, Mr Tino Kretschmer, Dr Thomas Loridan, Dr Lucía López Martínez, Mr Will Morrison, Mr John Mustchin, Mr Lukas Pauscher, Mr Elliott Warren, and Mr Duick Young. Technical support was provided by Dr Jiangping He, Dr Trevor Blackall, Dr Bruce Main, Dr Paul Smith, and Mr Kjell zum Berge. Additional thanks to Professor Euan Nisbet and Dr David Lowry of Royal Holloway, University of London, for their assistance with the calibration of equipment. I would also like to thank Mr Nigel Best for his assistance with transport and logistics, and Ms Samantha Best for her help during the photosynthesis measurements and the tree survey, as without her assistance neither would have been possible.

Abstract

Human activity in urban areas is responsible for the majority of total (direct and indirect) emissions of carbon dioxide. Accurate assessment of these emissions is necessary for understanding the underlying processes and to assess compliance with environmental legislation. Several urban studies have assessed net emissions at the local scale (10^2–10^4 m) using the eddy covariance method, however in practice this is often approximated as the vertical turbulent exchange – carbon dioxide stored within the canopy or advected horizontally is neglected. The main objective of this study is to characterise the carbon dioxide (CO_2) exchanges and emissions in urban areas at the micro to local scale. This involves assessing exchanges using a profile system and eddy covariance flux systems located at a height representative of the local scale. The profile system, designed as part of the PhD, allows the microscale and local scale influences to be separated. Horizontal movement of CO_2 is investigated using both horizontal profile and transect measurements of CO_2 made by mobile sensors at multiple spatial scales, and by field measurements of CO_2 exchange by vegetation, soil and Thames river water. Taken together these components enable the final chapter of this thesis which compares inventory and EC/profile estimates of net emissions. Sources of error and uncertainty in these estimates are explored.

The centre of London is shown to be a major and increasingly large source of CO_2. The effects of individual processes or factors on the atmospheric CO_2 concentration are evaluated through comparison of CO_2 concentrations measured over different time periods. In this way it is found that CO_2 concentrations at a site in central London vary primarily with anthropogenic factors such as traffic density and combustion of fuel for space heating, and secondarily with meteorological factors such as mixing layer depth. Evidence for variation of CO_2 concentrations due to non-human biological factors such as photosynthetic uptake by vegetation is almost entirely absent.

Methods used to calculate the change in the CO_2 in the air volume below an eddy covariance flux system (CO_2 storage) are assessed. CO_2 storage (ΔC_S) calculated from measurements made solely at the eddy covariance flux system height are found to be an inadequate measure of the change in CO_2 stored below; measurements of CO_2 concentration need to be made at least at one other site, preferably at or below the mean height of the local roughness elements (e.g., buildings, trees). On an annual basis ΔC_S is found to contribute a negligible amount to the calculated net emissions and, if net emissions are not required to be calculated on a sub-diurnal timescale, may be neglected.

The effects of the advective terms of the micrometeorological method of estimating net emissions are found to be more substantial, with vertical advection tending to reduce the estimate of net emissions and horizontal advection tending to increase estimates at this site. Good agreement was found between net annual CO_2 emissions calculated using the micrometeorological method and those calculated via the inventory method. From the latter it was clear that the majority of CO_2 emissions in central London are due to traffic, following by

combustion for building heating and human respiration. Natural sources or sinks of CO_2, such as soil respiration and photosynthetic uptake of CO_2 by vegetation, had a negligible effect.

Despite the complexity of the urban environment this work enables policymakers to identify key targets for CO_2 emissions reduction. It also informs researchers of the main components which must be measured for accurate estimation of net emissions and provides suggestions for the most efficient means of doing so. It contributes not only to our understanding of CO_2 emissions in the urban environment, a subject of global importance given the impact of urban CO_2 emissions on global atmospheric CO_2 levels and hence on climate change, but also to our ability to further that understanding with more accurate and cost-effective measurement methods.

Contents

List of Figures

List of Tables

List of Symbols

This section provides a summary of all symbols used in the thesis, including the units where applicable. Variables are listed in alphabetical order, with Greek symbols followed by roman. NA = not applicable, which may mean the quantity is unit less, that units are not appropriate, or that the units will depend on another variable to the one listed (e.g., standard deviation, root mean squared error). Symbols are italicised but abbreviations (e.g., 'RH' for 'Relative Humidity') are not. All units are standard international (base or derived) except for Veh, which is the number of vehicles which have passed a set point. Equations reproduced in text are referenced by number only, whereas those reproduced elsewhere are denoted by 'Equation' and the appropriate reference.

Variable	Description	Units
$\Delta[CO_2]$	Difference in CO_2 concentration between two locations or time periods.	ppm
$\Delta[CO_2]/\Delta t$	Change in carbon dioxide concentration with time.	μmol m^{-3} s^{-1}, mmol m^{-3} s^{-1}
$\Delta[CO_2]/\Delta x$	Change in carbon dioxide concentration with horizontal separation.	μmol m^{-4} s^{-1}, mmol m^{-4} s^{-1}, ppb m^{-1}
$\Delta[CO_2]/\Delta z$	Change in carbon dioxide concentration with vertical separation.	μmol m^{-4} s^{-1}, mmol m^{-4} s^{-1}
ΔC_S	Carbon dioxide storage: the change in the total amount of carbon dioxide within a notional volume of air over a given time period.	μmol m^{-2} s^{-1}, mmol m^{-2} s^{-1}
ΔC_{SBP}	A carbon dioxide storage time series calculated from a particular configuration of sample inlets defined as 'best practice'.	μmol m^{-2} s^{-1},
ΔC_{SP}	Carbon dioxide storage calculated from a set of carbon dioxide measurements made at multiple (usually vertically offset) locations – i.e., from a carbon dioxide concentration profile.	μmol m^{-2} s^{-1}, mmol m^{-2} s^{-1}
ΔC_{SS}	Carbon dioxide storage calculated from a set of carbon dioxide measurements made at a single location.	μmol m^{-2} s^{-1}, mmol m^{-2} s^{-1}
ΔV	Difference in traffic intensity between two locations or time periods.	Veh h^{-1}
Δz_i	The span over which a measurement made at location *i* is considered to be representative.	m
λ	Time scale	s
σ	Standard deviation, the positive square root of the variance.	NA
$\sum \Delta C_S$	Cumulative sum of ΔC_S.	μmol m^{-2}
τ	Time constant of a gas analyser's response to a step change in scalar concentration.	s
ψ	Wavelet function.	NA
Ψ^*	Complex conjugate of the wavelet function.	NA
$\hat{\psi}$	Fourier transform of the wavelet function	NA
ω	Angular frequency	rad s^{-1}
a	Empirically derived, instrument specific constant.	NA*
A_{xy}	Advection of CO_2 in the horizontal plane.	μmol m^{-2} s^{-1}
$A_{x,\,Zs}$	Horizontal advection calculated parallel to the Strand street canyon and up to the height of the Strand building.	μmol m^{-2} s^{-1}
A_z	Advection of CO_2 vertically.	μmol m^{-2} s^{-1}
b	Empirically derived, instrument specific constant.	NA*
B	Bell taper function for windowed Fourier transform.	NA
C_δ	Empirically derived constant used to reconstruct a time series from a wavelet power spectrum	NA
$[CO_2]$	Carbon dioxide concentration.	ppm, mmol m^{-3}
$[CO_2]_h$	Carbon dioxide concentration at height z_h.	ppm, mmol m^{-3}
$[CO_2]_i$	Carbon dioxide concentration at height z_i.	ppm, mmol m^{-3}

Variable	Description	Units
d	Bins for u, v, w values, based on the concurrent CO_2 storage values.	NA
E_A	CO_2 emissions from animal respiration/decomposition.	µmol m^{-2} s^{-1}
E_B	CO_2 emissions from space heating.	µmol m^{-2} s^{-1}
E_k	Spectral energy in the frequency domain	Square of the variable analysed
E_P	The net effect of vegetation	gCO_2 m^{-2} yr^{-1}
$E_{P, leaf}$	Net effect of leaves of vegetation, i.e., respiration less photosynthetic uptake of CO_2	gCO_2 m^{-2} yr^{-1}
E_{PR}	CO_2 emissions from plant respiration.	gCO_2 m^{-2} yr^{-1}
E_R	CO_2 emissions from human respiration.	gCO_2 m^{-2} yr^{-1}
E_S	CO_2 emissions from respiration of organisms in bare soil.	gCO_2 m^{-2} yr^{-1}
E_V	CO_2 emissions from vehicles.	gCO_2 m^{-2} yr^{-1}
E_W	CO_2 emissions from the Thames river water.	gCO_2 m^{-2} yr^{-1}
f	Frequency. May be in Hz or non-dimensional ($f=nz'/U$)	Hz, NA
F_A	CO_2 flux from animal respiration/decomposition.	µmol m^{-2} s^{-1}
F_B	CO_2 flux from space heating.	µmol m^{-2} s^{-1}
$F\{g\}$, $F\{h\}$	Fourier transform of the hypothetical time series, g and h.	NA
F_{CO2}	Vertical CO_2 flux.	µmol m^{-2} s^{-1}
F_P	CO_2 flux from vegetation.	µmol m^{-2} s^{-1}
$F_{P, leaf}$	CO_2 flux from leaves of vegetation, i.e., respiration less photosynthetic uptake of CO_2 by leaves.	µmol m^{-2} s^{-1}
F_{PR}	CO_2 flux from plant respiration.	µmol m^{-2} s^{-1}
F_R	CO_2 flux from human respiration.	µmol m^{-2} s^{-1}
F_S	CO_2 flux from respiration of organisms in bare soil.	µmol m^{-2} s^{-1}
F_{Soil}	CO_2 flux from respiration of organisms in soil.	µmol m^{-2} s^{-1}
$F_{Soil, 10}$	CO_2 flux from respiration of organisms in soil when the soil temperature is 10 ºC.	µmol m^{-2} s^{-1}
F_V	CO_2 flux from vehicles.	µmol m^{-2} s^{-1}
F_W	CO_2 flux from Thames river water.	µmol m^{-2} s^{-1}
g, h	Hypothetical time series	NA
H	'Hole constant', defines the wind speeds defined as 'calm' and therefore removed from quadrant analysis.	NA
$[H_2O]$	Water vapour concentration	mmol m^{-2} s^{-1}
i	Measurement location. In this study i = Heights A to J (Figure 2.1d).	NA
ITT	Integral Timescale of Turbulence	s, Hz
j	Index of scales of wavelet analysis	NA
k	Frequency index.	NA
$K\downarrow$	Incoming shortwave radiation	W m^{-2}
$K\uparrow$	Outgoing shortwave radiation	W m^{-2}
L	Obukhov length	m
$L\downarrow$	Incoming longwave radiation	W m^{-2}
$L\uparrow$	Outgoing longwave radiation	W m^{-2}
M_i	i^{th} iteration of a model	NA
n	Natural frequency	number of cycles per 30 minutes
n_i	Total number of measurement locations in a profile.	NA
n_v	Number of data points or values in a particular set or class.	NA
N	Length of data series x_t	NA
NEE	Net Ecosystem Exchange: the sum of all emissions to the atmosphere, less any CO_2 removed by photosynthesis (Kirschbaum and Mueller, 2001)	µmol m^{-2} s^{-1}, mmol m^{-2} s^{-1}
p	p-value	NA
PAR	Photosynthetically Active Radiation	µmol m^{-2} s^{-1}
P(FP>1)	Probability of results containing at least one false positive	NA

Variable	Description	Units
q	Quadrant number.	NA
Q^*	Net radiation	W m^{-2}
Q_{10}	The increase in soil respiration rate per 10 ºC increase in soil temperature, see (7.4).	NA
Q_E	Latent heat flux	W m^{-2}
$Q_{F,\ R/B}$	Heat flux from human respiration/space heating of buildings	W m^{-2}
Q_H	Sensible heat flux	W m^{-2}
R^2	Coefficient of determination	NA
RH	Relative Humidity	%
RMSE	Root Mean Squared Error	NA
s_j	j^{th} scale of the wavelet analysis	s
S_q	Stress fraction for quadrant, q.	NA
S_y	Spectral power of time series y	mmol^2 m^{-4} s^{-2}
t	Time	s, h, days, yr
T	Calculation period of the carbon dioxide storage.	s, min
T_A	Air Temperature	°C
TKE	Turbulent Kinetic Energy	m^{-2} s^{-2}
T_P	Time for a gas sample to travel from a sample point to the analyser	s
T_R	Response time of a gas analyser	s
t_s	Sampling interval of an instrument measuring carbon dioxide concentration	s
T_S	Response time of a system	s
T_{Soil}	Soil temperature	ºC
u	Zonal wind component	m s^{-1}
u^*	Friction velocity	m s^{-1}
u'	Instantaneous deviation from the mean of the zonal wind component u	m s^{-1}
$\overline{(u'w')}_{\Delta t,d}$	Mean of the covariance of the instantaneous deviation from the mean of the zonal and vertical wind components for time period Δt and CO_2 storage class d.	m^2 s^{-2}
U	Mean horizontal wind speed	m s^{-1}
v	Meridonal wind component	m s^{-1}
V	Traffic intensity i.e., number of vehicles passing a set point in a specified time period. Subscripts denote time period, location, direction or vehicle class of traffic.	Veh h^{-1}
w	Vertical wind component	m s^{-1}
w'	Instantaneous deviation from the mean of the vertical wind component w	m s^{-1}
$W_t(s)$	Wavelet transform at time, t, and scale, s	NA
x	Primary horizontal direction	NA
X_{max}	Horizontal distance of the maximum of the flux footprint function from the flux tower.	m
$\overline{x_t}$	Mean of x_t	NA
x_t	Value of a notional series at time, t.	NA
x_t'	Instantaneous deviation from the mean of x_t.	NA
x_k	x_t transformed to the frequency domain.	NA
y	Secondary horizontal direction	m
y_1, y_2	Notional CO_2 storage time series	
z	Vertical distance or direction. If subscripted with a capital letter, indicates one of z_i.	m
z'	Height of a measurement above ground less the zero plane displacement height	m
z_b	Mean building element height	m
z_h	Height of Eddy Covariance equipment and the highest point of the measured carbon dioxide profile	m
z_i	Heights above ground of measurement locations of a carbon dioxide concentration profile	m
z_s	Height of the Strand building	m

* As logarithms are unit-less, no units are appropriate.

List of Acronyms

AADF	Annual Average Daily Flows (Veh day^{-1})
a.g.l.	Height above ground level.
ATC	Automated Traffic Count.
BBC	British Broadcasting Corporation
BM	'Benchmark' A data set consisting of data measured on Sundays for which Sunday trading laws do apply and there are no Olympic or Paralympic activities.
BST	British Summer Time, in effect from the last Sunday of March to the first Sunday of October and equal to GMT +1.
C1, C2, …	Configurations of the *[CO_2]* profile.
CAZ	Central Activity Zone, London.
CC	City Centre
CH_4	Methane.
CO_2	Carbon dioxide.
D1, D2, …	Days of interest or note, Figure 4.13.
DBH	Diameter at breast height
DC	Direct Current
DECC	Department of Energy and Climate Change
DEFRA	Department for Environment, Food and Rural Affairs
DEM	Digital Elevation Model
DfT	Department for Transport.
d.p.	Number of decimal places to which a value is given.
DoN	Days of Note
DoY	Day of Year
E1, E2, …	Configurations of eddy covariance equipment
EC	Eddy Covariance.
EMB	Embankment gardens
FoI	Freedom of Information request.
GBL	Global Background Level of CO_2 concentration as measured at the Mauna Loa Observatory.
GLA	Greater London Authority.
GMT	Greenwich Mean Time. Equivalent to Coordinated Universal Time (UTC).
H_2O	Water
$HO_{(W/S)}$	High Occupancy period in (Winter /Summer).
H/W	Height:width ratio of a street canyon
IC	Intercomparison point
IDL	Interactive Data Language
IMAS	Identification of Micro-scale Anthropogenic Sources
IPCC	Intergovernmental Panel on Climate Change
IN	Institutional
IQR	Interquartile range
KCL	King's College London
KS	King's College London, Strand campus
KSB	King's College London, Strand campus, Balcony
KSK	King's College London, Strand Campus, King's building
KSK15S	King's College London, Strand Campus, King's building, 15m to the south of KSK
KSLH	King's College London, Strand Campus, Lower Horizontal profile
KSN	King's College London, Strand Campus, Norfolk building
KSNW	King's College London, Strand campus, North Wing building
KSS	King's College London, Strand campus, Strand building

KSS45W	King's College London, Strand campus, Strand building, 45 m to the west of KSS
KSSW	King's College London, Strand campus, Strand building, West
KSUH	King's College London, Upper Horizontal profile
LAEI	London Atmospheric Emissions Inventory
LC	Land cover
LU	Land use
LCS	Land categorisation scheme, a means of categorising the surface based on land cover and/or use.
LCUN	In-house land categorisation scheme providing details on land cover, use and neighbourhood factors.
LES	Large eddy simulation model
$LO_{(W/S)}$	Low Occupancy period in (Winter/Summer)
LSPD	Lagrangian stochastic particle dispersion model
MM7C	Multimap, 7 classes. A land categorisation scheme derived from Multimap data with the original categories aggregated to 7 classes.
MT	Middle Temple gardens
NAEI	National Atmospheric Emissions Inventory
NF	Neighbourhood factors
NGVA	Natural and bio gas vehicle association
NOAA	National Oceanic and Atmospheric Administration
ONS	Office for National Statistics, UK
OP	'Olympic/Paralympic' A data set consisting of data measured on Sundays for which Sunday trading laws do not apply and there are Olympic or Paralympic activities.
QEMX	Queen Eleanor Memorial Cross, a point of reference for comparing maps.
RCJ	Royal Courts of Justice
RMSE	Root Mean Squared Error
s.f.	Number of significant figures to which a value is given
SO	'Sunday Only' A data set consisting of data measured on Sundays for which Sunday trading laws do not apply and there are no Olympic or Paralympic activities.
SR	Suburban/Residential
T1, T2, …	Configurations of the vertical temperature profile.
TEM	Temple gardens
TfL	Transport for London
THR	Thermal comfort range
TLI	Thames Royal National Lifeboat Institution Tower Lifeboat station
UA	Urban Atlas. A land categorisation scheme developed by the European Environment Agency (European Union 2011a, b).
UK	United Kingdom of Great Britain and Northern Ireland
UN	United Nations
USA	United States of America

Chapter 1. Context and Objectives

1.1 Introduction

Carbon dioxide (CO_2) is the largest component of the radiative forcing of climate change (IPCC, 2014). It acts as an insulator, absorbing outgoing infra-red radiation from the earth's surface and re-emitting isotropically such that a portion of the radiation is returned to earth. The calculated global effect is an increase of 1.82 W m^{-2} or 64% of the net change in downward radiation at the tropopause (IPCC, 2014). Human activity in urban areas is responsible for 30-40% directly emitted anthropogenic greenhouse gases (Satterthwaite, 2008) and 70% total emissions of CO_2 (Canadell *et al.,* 2009). In spite of their low land surface cover (2%, Satterthwaite 2008) urban areas are therefore important when attempting to understand the processes governing the global carbon cycle. The main sources of CO_2 in an urban environment are anthropogenic in origin, predominantly comprising of emissions from vehicles and building heating (Velasco and Roth, 2010).

In this chapter the different measurement techniques and some of the essential concepts which underlie this thesis are introduced (Section 1.2). Methods and results from previous studies are discussed (Sections 1.3 and 1.4), and the objectives for this thesis are detailed in Section 1.5.

Urban areas are rapidly expanding and are therefore gaining importance as a source of greenhouse gases and impact of urban air quality on human health. The limitations of current attempts to measure direct emissions from cities via micrometeorological techniques include a poor connection between measurement height and street level under stable conditions (Helfter *et al.,* 2011); hence there is a need for measurements right down into the urban canyon. In addition, the high urban heterogeneity (Grimmond *et al.,* 2002) means there is a need for measurements covering a greater range of land surface types than is usually possible with one flux tower. As a relatively non-reactive gas for which there exists reliable, high accuracy measuring equipment, CO_2 also has value as a tracer for within canyon atmospheric transport processes. This is important due to the greater number of people affected by street canyon air quality. The main objectives for this thesis are to:

- Describe and predict the storage and transport of carbon dioxide within and above an urban canyon.
- Compare and evaluate current methods to calculate CO_2 storage. Provide a recommended protocol for future urban studies.
- Assess methods to gap fill CO_2 storage data.
- Identify and examine CO_2 venting events in an urban environment.
- Evaluate total CO_2 emissions from a central London area via inventory and micrometeorological methods

1.2 Carbon balance of the urban environment: measurement techniques and questions of scale

Atmospheric processes and the techniques to measure them are classified by their spatial and/or temporal scale. In order of increasing size these are referred to as (Figure 1.1, Oke, 1987) micro (10 mm to 1 km), local (100 m to ca. 80 km), meso (10 km to 200 km) and macro (100 km to 100,000 km) and the associated timescales range from seconds to years.

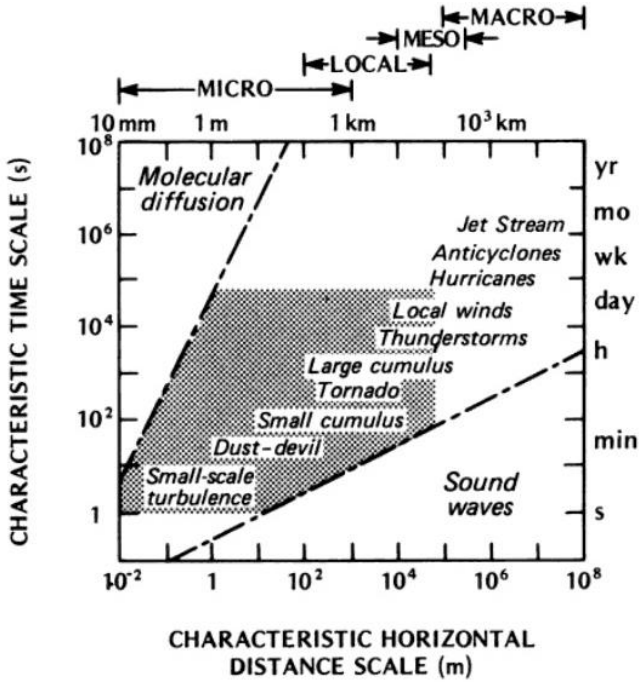

Figure 1.1: The extent of atmospheric phenomena in time and space. The planetary boundary layer (Table 1.A.1) is shaded (source: Oke, 1987). This study will focus on processes which occur on a micro (city street to district) scale i.e., about 1 km².

Satellite measurements are one of three main ways to determine ecosystem CO_2 exchange and the controlling processes. They have the lowest or coarsest spatial resolution of the methods discussed in this section (e.g., 30 km x 60 km, SCIAMACHY, Sotis, 2007). This method provides information about a whole city (meso scale) but little information within the city, which is of interest as urban areas are variable at much smaller spatial scales (ca. 1 km², Grimmond *et al.,* 2002).

A second method, the inventory approach, involves accounting for the known sources and sinks within a particular area (Figure 1.2b). This typically combines an emissions inventory (database(s) of all known sources of the gas of interest, usually focussing on those of anthropogenic origin) and an ecological inventory (database(s) of all organisms such as trees, animals, etc., which absorb or emit the gas of interest e.g., Velasco *et al.* (2014)). Analysis may be limited spatially if (e.g., gas and electricity usage) data are not available on a sub-borough scale (Velasco and Roth, 2010), and temporally if measurements are not frequent, e.g., tree diameter at breast height (DBH) growth once per fortnight. Even when data are available, several assumptions may need to be made e.g., the use of an 'average' car for traffic emissions. The emissions from combustion are usually estimated as the product of the amount of fuel burned and the mass of CO_2 per unit of fuel consumed (e.g., IPCC 1997), but this may

vary with, for example, engine temperature and age and the data available may not be representative of the study area characteristics. Emissions data for spatially delocalised sources or sinks, such as parks or landfill are often not well constrained and the effect of land use changes or management is often not included. The inventory method has been used successfully to assess anthropogenic heat emissions at the local to whole city scales (Iamarino *et al.*, 2012), but propagation of errors can result in large uncertainties (Marland, 2008 cited in Velasco and Roth, 2010).

The third method, referred to here as the micrometeorological approach, is to designate a volume of air over the surface of interest (Figure 1.2a) and sum the movements of CO_2 through the volume's facets as well as any change in the amount stored within the volume. A net movement of CO_2 into the volume would suggest that the ecosystem is a CO_2 sink. Conversely, a net movement out of the volume indicates the ecosystem is a CO_2 source. This is known as the Net Ecosystem Exchange (NEE) and it is defined (Aubinet *et al.,* 2005) as the sum of the net vertical flux (F_{CO2}) into or out of the top of the volume of interest, the horizontal exchange or advection (A_{xy}), the non-turbulent vertical exchange or advection (A_z) and net accumulation or depletion in CO_2 in the volume (ΔC_S, also called CO_2 storage):

$$NEE = F_{CO_2} + A_{xy} + A_z + \Delta C_S \tag{1.1}$$

In practice, many monitoring sites (Grimmond *et al.,* 2002; Baldocchi, 2003; Velasco and Roth, 2010) approximate NEE as the net flux into or out of the top of the volume of interest. This requires the assumptions of horizontal homogeneity (horizontal advection into the volume is equal to transport out of the volume) and fully turbulent conditions with negligible storage or vertical advection, but considerably reduces the equipment required (measurements are only required at one point, rather than along a vertical and/or horizontal profile).

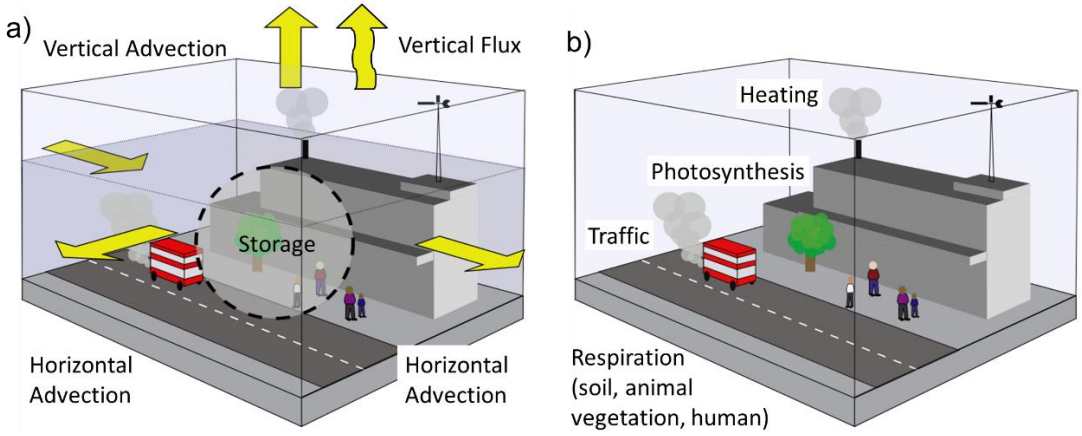

Figure 1.2: (a) Micrometeorological and (b) inventory methods of determining the net emissions for a set area.

In urban environments during stable atmospheric conditions the ΔC_S term will be non-negligible (Helfter *et al.*, 2011); for example, ΔC_S was found to be five times the magnitude of the turbulent vertical flux term (F_{CO2}) close to dawn and dusk in suburban Vancouver, Canada (Crawford and Christen, 2014). Other urban studies found ΔC_S to be smaller, but still

significant, with maximum ΔC_S values 11% and 22% of the magnitude of F_{CO2} in Edinburgh, Scotland (Nemitz *et al.,* 2002) and Basel, Switzerland (Feigenwinter *et al.,* 2012) respectively. Similarly, rural studies have found both vertical and horizontal advection to be of the same magnitude as CO_2 storage (Aubinet *et al.*, 2005), suggesting that the contribution of these components to the net exchange may be significant. Urban CO_2 flux studies are discussed further in Section 1.3 and CO_2 profile studies in Section 1.4.

1.3 Urban CO_2 studies

The majority (54%) of the 24 studies listed in Table 1.1 were performed in European cities. North American (21%) and East Asian (17%) were the next most common, followed by North African and Oceanic with only one study (4%) each. This broadly reflects the distribution of tower sites as part of the FLUXNET global monitoring network (FLUXNET, 2015), but unfortunately does not mean that the current understanding and measurement of net emissions by European cities is exhaustive. Comparison of measured fluxes for different sites within the same city (e.g., Mexico City, Velasco *et al.,* 2005 and Velasco *et al.,* 2009; London, Helfter *et al.*, 2011, Ward *et al.*, 2015) shows differences of equal magnitude to those observed between cities (Table 1.1).

As noted by Grimmond *et al.* (2002), urban areas are heterogeneous at spatial scales ranging from the micro (street) to the local (neighbourhood) and can contain a greater diversity of surface types and land uses than is typically found in rural areas. This makes applying emission measurement techniques developed in rural areas to urban environments challenging. Although there are some similarities in canopy structure between forest and urban sites, the sources and sinks of CO_2 are different. In the urban area, even in highly vegetated suburbs (Crawford and Christen 2014) there are reduced sinks and enhanced emissions (Ward *et al.,* 2015). As well as micro-scale, mobile traffic (Henninger and Kuttler, 2007) and human sources (respiration, Moriwaki and Kanda, 2004), there are a preponderance of high level sources due to space heating (Kotthaus and Grimmond, 2012) at close to mean canopy height (e.g., chimneys and air vents on the rooves of buildings). The sealed urban surface also reduces soil respiration as a source and urban areas typically have minimal coarse wood debris and other decaying vegetation.

Despite some studies in urban areas registering CO_2 concentrations below global background levels (Tans, 2009) and, in some highly vegetated suburbs, negative daytime fluxes during the leaf-on period, all studies which have reported annual emissions have found urban areas to be net producers of CO_2. In a review of measured CO_2 emissions from urban areas using the micrometeorological method, Grimmond and Christen (2012) show a strong, positive correlation between the rate of CO_2 emissions (taken as the vertical flux, 1.1) and building density; however, Lietzke and Vogt (2013) found vertical CO_2 fluxes to be 'directly connected to traffic density'. In terms of total emissions, Crawford and Christen (2015) attributed 70% and 26% of total annual CO_2 emissions to vehicles and buildings (combustion for space heating)

respectively in a low-rise, low density suburb of Vancouver, Canada. Velasco *et al.* (2014) reported similar (72%, 24%) values for Escandón, a compact midrise, densely populated residential and commercial neighbourhood of Mexico City. At the study site discussed in this thesis (high density institutional, commercial and office buildings), Ward *et al.* (2015) calculated the contributions from buildings and vehicle emissions as 70% and 19% respectively, i.e., almost the inverse of those reported for Vancouver and Mexico City. Helfter *et al.* (2011) measured CO_2 emissions 1.9 km to the north-west of the Ward *et al.* (2015) study site and reported similar values for winter, but very different average annual contributions of 59% and 38% for building heating and traffic respectively. Vegetation, bare soil and human respiration typically contribute less than 5% to the total flux, but this is highly dependent on land cover and use. The spatial variation of CO_2 emissions and the relation to stationary measurements are topics that will be explored in this thesis through both transect and profile measurements. The latter is the topic of the following section.

*Table 1.1: Selection of urban CO_2 flux and concentration studies since 2002. For an overview of urban CO_2 concentration studies prior to 2002, see Grimmond et al. (2002). Urban CO_2 concentration ($[CO_2]$) is normalised by concurrent annual mean measured at Mauna Loa observatory (Tans, 2009). Mean and range of F_{CO2} are given where available. Estimates of annual emissions have been given where appropriate (data were collected for ≥ 1 year) with a * indicating that the value was calculated from data reported in the referenced paper, rather than reported by the paper. Sites are classified by land use as follows: CC: city centre, SR: suburban/residential, IN: institutional. Normalised $[CO_2]$ are given to two d.p.; all other values are given with the precision of the publication cited.*

Reference	*City*	*Site type*	*Population (1000s)*	*Measurement height (canopy height)*	*Period*	*Normalised $[CO_2]$ range*	*F_{CO2} (µmol m^{-2} s^{-1})*	*Annual Emissions ($kgCO_2$ m^{-2} yr^{-1})*
Grimmond *et al*. (2002)[a, b]	Chicago, USA	SR	7 839 [c]	27 m (6.3 – 11.4 m)	1995/165-222	1.04 to 1.15	-2 to 10	
Nemitz *et al*. (2002)	Edinburgh, Scotland	CC	449 [d]	69.5 m	2000/301-334 1999/Oct-Nov 1999/May-Jun	0.96 to 1.13	22 (-12 to 135)	36.1 [e]
Soegaard and Moller-Jensen (2003)	Copenhagen, Denmark	CC	1,077 [f]	40 m (20 – 25 m)	2001-2002		6 to 32	12.8 * (flux) 13.9 * (inventory)
Christen and Vogt (2004)[g, h]	Basel, Switzerland [i]	CC/IN	259 [j]	31 m (14.6 m)	2002/161-191	0.97 to 1.13	9.90 (3 to 15)	13.7 *
Grimmond *et al*. (2004)	Marseille, France	CC	1,357 [f]	34.6 and 43.9 m (15.6 m)	2001/155-197		5 to 30	
Moriwaki and Kanda (2004)	Tokyo, Japan	SR	34,450 [f]	29 m (7.3 m)	2001/May to 2002/Apr	0.91 to 1.21	7.98 (4.5 to 25.0) *	12.3 [k]
Velasco *et al*. (2005)	Mexico City, Mexico	CC	18,735 [l]	37 m (12 m)	2003/097-119	1.06 to 1.18	-5 to 36.4	12.8 [k]
Coutts *et al*. (2007)	Melbourne, Australia [i]	SR	3,641[l]	38 and 40 m (16 and 12 m)	2004/Feb -2005/Jun	0.94 to 1.00	2 to 11.5	8.5 [k]
Schmidt *et al*. (2008)	Münster, Germany	CC	1,254 [l]	65 m (25 m)	2006/Aug to 2006/Sep		-9 to 29	
Vesala *et al*. (2008)[m]	Helsinki, Finland	IN	1,094 [l]	31 m (20 m)	2005/Dec – 2006/Aug		-10 to 17	6.4 [n]
Burri *et al.* (2009)	Cairo, Egypt	IN	11,894 [o]	35 m (not given)	2007/Nov to 2008/Feb	1.01 to 1.07	6.18 (1.19 to 9.86)	
Velasco *et al*. (2009)	Mexico City, Mexico	CC	19,028 [o]	42 m (12 m)	2006/Mar to 2009/Feb	1.04 to 1.12	2 to 25	17.6 [k]
Sparks and Toumi (2010)	London, UK	CC	8,567 [o]	50 m (25 m)	2008/156-195, 2008/354-2009/288	1.00 to 1.13	18.6 (8 to 35)	25.8 *
Christen *et al*. (2011)	Vancouver, Canada [i]	SR	2,146 [l]	24.8 m (5.1 – 7.7 m) [p]	2008/May to 2010/Apr		17.7	24.6
Crawford *et al.* (2011)	Baltimore, USA	SR	2,207 [l]	41.2 m (5.6 – 11.4 m)	2002-2006		-6 to 11	1.3
Pawlak *et al*. (2011)	Łódź, Poland	CC	758 [o]	37 m (11 m)	2006/Jul-		0 to 30	10.8
Helfter *et al.* (2011)	London, UK	CC	8,567 [q]	190 m (8.8 m)	2006/Oct-2008/May	0.96-1.03	7 to 47	35.5
Gioli *et al.* (2012)	Florence/Firenze, Italy	CC	358 [r]	36 m (19 m)	2005/Sep -	1.03 to 1.12 [s]	26.2 (9.7 to 39.4)	30.3 *
Liu *et al*. (2012)	Beijing, China	SR	> 22,000	47 m (16.7 m)	2006 – 2009		15.8 (8.86 to 31.82)	18.0
Lietzke and Vogt (2013)	Basel, Switzerland	CC/IN	259 [j]	39 m (17 m)	Oct/2009 – Mar/2011	0.99 to 1.08	8.2	15.6 *
Velasco *et al.* (2013)	Telok Kurao, Singapore	SR	5,535 [t]	20.7 m (9.29 m)	2010/Oct – 2012/Jun		0.3 to 7.4	6.5
Hirano *et al.* (2015)	Tokyo, Japan	SR	13,216	52 m (9 m)	2012/Nov – 2013/Oct		2.3 to 21.6	15.8
Ward *et al*. (2015)	London, UK	CC	8,567 [q]	48.6 m (21.2 m) [v]	2011/Jan – 2013/Apr		0 to 125	46.6

	Swindon, UK	SR	209 [u]	12.5 m (4.5 – 6 m) [w]		-7 to 19	6.4

a) Information obtained from listed study reference and additional information from Grimmond and Oke (1999a; 1999b; 2002).
b) CO_2 results in Grimmond *et al.* (2002)
c) UN (2007) data for 1995
d) Edinburgh Council, (2003)
e) Helfter *et al.* (2011)
f) UN (2007) data for 2000
g) Study overview in Rotach *et al.* (2005)
h) CO_2 results in Vogt *et al.* (2006)
i) Multiple sites in same city.
j) CityPopulation.de (2009a) data for Basel from 2000
k) Velasco and Roth (2010)
l) UN (2007) data for 2005
m) Further information in Jarvi *et al.* (2009)
n) Jarvi *et al.* (2012)
o) UN (2007) data for 2007
p) Crawford and Christen (2014)
q) UN (2007) data for 2010
r) CityPopulation.de (2009b) data for Florence from 2011
s) Matese *et al.* (2009)
t) Singapore Department of Statistics (2015)
u) ONS (2015a)
v) Kotthaus and Grimmond (2012)
w) Ward *et al*. (2013)

1.4 CO_2 Profile studies

Most CO_2 profiles (systems measuring CO_2 at two or more levels either concurrently or in a regular sequence) that have been installed to date have been in forests; including Douglas fir (Price and Black, 1990; Vermetten *et al.,* 1994), spruce (Jarvis *et al.*,1997; Siebicke *et al.,* 2010), deciduous (Goulden *et al.,* 1996; Baldocchi, 1997; Simpson *et al*., 1998), tropical (Iwata *et al.,* 2005; Hutyra *et al.,* 2008; Araujo *et al.,* 2010), and mixed (Molder *et al.,* 2000; Aubinet *et al.,* 2003) (Table 1.2). Other sites include those with crops and forests (Zhao *et al.*, 1997; Haszpra *et al*., 2001), pasture, with and without livestock (Denmead *et al.,* 1998), cotton and maize crops (Xu *et al.,* 1999) and urban (Vogt *et al*., 2006). The profiles have had 2 to 12 levels which varying between 0.001 (Iwata *et al.,* 2005) and 4.11 (Molder *et al.,* 2000) times the mean canopy height. A few studies have made constant measurements using multiple gas analysers (Simpson *et al.,* 1998; Siebicke *et al.,* 2010); however, the majority use a valve array to switch between measurement heights. The impact of this and other aspects of CO_2 profile design on calculated CO_2 storage is discussed in Section 3.1.1 and evaluated using data collected as part of this project in Section 5.3.

In rural environments the primary source of CO_2 is decomposition of leaf litter and respiration of micro-organisms in the soil, i.e., CO_2 is primarily released to the atmosphere at ground level. Over short vegetation this results in an exponential decrease in concentration with increasing height above ground level (e.g., Bakwin *et al.*, 1995) as emissions are mixed from the roughness sublayer through to the planetary boundary layer (Table 1.A.1 in Appendix 1.A). In areas with taller vegetation, such as forests, the vertical concentration profile may be more linear (e.g., Hutyra *et al*., 2008) or even constant with height (Aubinet *et al*., 2005, daytime conditions). Measurement of vertical CO_2 concentration profiles in urban areas are less common; however, results from Basel (Lietzke and Vogt, 2013) show strong wind dependence for CO_2 concentrations adjacent to a building and in the centre of the road. The road and the buildings lining it (hereafter referred to as a ‘street canyon’) was not symmetrical; the eastern side was lower than the western side. When the wind was from the east, i.e., when it passed over the shorter side first, the vertical profiles were reasonably similar in shape to rural ones. When the wind was from the west, the vertical CO_2 profiles in the centre of the street were almost vertical, except for the lowest level. The CO_2 profiles adjacent to the building (in the lee of the wind) were elevated, particularly at the roof height of the east wall of the street canyon. This suggests that the vertical distribution of the CO_2 in urban areas is likely to be more complex than in rural environments.

Table 1.2: Selection of studies since 1990 which have measured CO_2 concentrations at multiple fixed locations (i.e., sufficiently close together to measure processes on the microscale and not as part of a mobile transect). If the following quantities were calculated from the CO_2 concentration ($[CO_2]$) data, this has been noted under 'Analysis' as: vertical CO_2 gradient: $\Delta[CO_2]/\Delta z$, horizontal CO_2 gradient: $\Delta[CO_2]/\Delta x$, change in CO_2 stored within the airspace: ΔC_S, vertical CO_2 flux (if calculated from the profile): F_{CO2}, horizontal advection along one (A_x) or two dimensions: A_{xy}, vertical advection: A_z.

Reference	Location	Latitude and Longitude	Profile heights (m a.g.l.)	Mean canopy height (m)	Profile heights relative to canopy height	Data sampled (archived)	Dates data collected	Environment	Analysis
Price and Black (1990)	Vancouver Island, British Columbia	49 02' N, 124 12' W	7.8, 10.8	7.5	1.04, 1.44	15 minute (8 minute)	205/1987 – 218/1987	Douglas fir forest	F_{CO2}
Wofsy *et al.* (1993)	Harvard Forest, Massachusetts	42.54°N, 72.18°W	0.05, 1, 3, 6, 12, 18, 24, 29	24	0.0021, 0.042, 0.125, 0.25, 0.5, 0.75, 1, 1.21	3.75 minute	Apr/1990 – Dec/1991	50 – 70 yr old mixed deciduous forest.	ΔC_S
Vermetten *et al.* (1994)	Speuld site, Netherlands	52.1 ºN, 5.4 ºE	5, 10, 15, 20, 30	18	0.28, 0.56, 0.83, 0.11, 1.67	5.5 minute (4 minute)	1989	Douglas fir forest	F_{CO2}
Goulden *et al.* (1996)	Harvard Forest, Massachusetts	42º32' N, 72º11' W	0.05, 0.85, 2.8, 6.2, 9.5, 18.2, 30.8	20-24 (22)	0.0023, 0.039, 0.13, 0.28, 0.43, 0.83, 1.4	3.75 minute	Oct/1990 – Oct/1994	50 – 70 yr old mixed deciduous forest.	ΔC_S
Baldocchi (1997)	Oak ridge, Tennessee	35 57' 30'' N, 84 17' 15'' W	0.75, 10, 18, 36	26	0.029, 0.385, 0.692, 1.385	30 s (20 s)	141/1995 – 252/1995	Temperate broadleaf deciduous forest.	ΔC_S
Jarvis *et al.* (1997)	Saskatchewan, Canada	53° 59' N, 105° 7' W	1.5, 3, 6, 12, 27	10-11 (10.5)	0.14, 0.29, 0.57, 1.14, 2.57	2 minute (1 minute)	143/1994 – 264/1994	Boreal black spruce forest	ΔC_S
Simpson *et al.* (1998)	Camp Borden, Ontario	49 19' 33'' N, 76 56' 12'' W	33.4, 46.5	20	1.67, 2.325	Constant, multiple GAs	212/1995 – 236/1995	Mixed deciduous forest.	F_{CO2}
			24.5, 33.4	20	1.225, 1.67	Constant, multiple GAs	236/1995 – 284/1995		
			24.5, 28, 32.4, 38.4, 44.9	20	1.225, 1.4, 1.62, 1.92, 2.245	4 s (3.2 s)	198/1995 – 317/1995		
Zhao *et al.* (1997)	North Carolina	35 21' 55'' N, 77 23' 38'' W	51, 123, 496	20 - 30	2.04, 4.92, 19.84 (assuming canopy height of 25 m)	Constant, multiple GAs	Jun/1992 – Jun/1994	Mostly mixed forest and crops.	$\Delta[CO_2]/\Delta z$
Denmead *et al.* (1998)	-	-	0.5, 1, 2, 3.5	Grass		100 s		Pasture, with and without livestock.	
Xu *et al.* (1999)	Davis, California	38 31', -121 46' (inferred)	2.5, 6.6	1.7 (cotton) 3.3 (corn)	1.47, 3.88 0.76, 2	10 s (8 s)	261-262/1996	Cotton, maize fields	$[CO_2]$
Molder *et al.* (2000)	Norunda, Sweden	60 5' N, 17 29' E	8.5, 13.5, 19, 24.5, 28, 31.7, 36.9, 43.8,	24.5	0.35, 0.55, 0.78, 1, 1.14, 1.29, 1.51, 1.79,	12 s	Jun/1994-	Forest	$\Delta[CO_2]/\Delta z$

			58.5, 73, 87.5, 100.6		2.39, 2.98, 3.57, 4.11				
Hazpra *et al.* (2001)	Hegyhátsál, Hungary	46 57'N, 16 39' E	10, 48, 82, 115	Not given	Not given	2 minute (1 minute)	Sep/1994 -	60% arable, 30% woodland, 10% other	ΔC_S, F_{CO2}
Aubinet *et al.* (2003)	Vielsam, Belgium	50 18' N, 6 00' E	9, 22, 36	27-35 (31)	0.29, 0.71, 1.16	-	Summer 1997	Mixed forest	$\Delta[CO_2]/\Delta z$, A_z, A_{xy}, ΔC_S
Iwata *et al.* (2005)	Caxiuana, Brazil	1 43' S, 51 27' W	0.2, 2, 8, 16, 32, 55.5	35	0.0057, 0.057, 0.23, 16, 0.91, 1.59	5 minute	16/04/1999 - 11/06/1999, 24/06/1999 - 08/08/1999, 06/09/1999 - 09/09/1999, 07/10/1999 - 19/10/1999	Tropical rainforest	ΔC_S
	Jaru, Brazil	10 5' S, 61 56' W	0.05, 2.7, 25, 35, 45, 62.7	35	0.0014, 0.077, 0.71, 1, 1.29, 1.79	5 minute	19/04/1999 – 24/05/1999	Tropical rainforest	
Vogt *et al.* (2006)	Basel, Switzerland	47 33' 57'' N, 7 35' 49'' E	0.1, 1.5, 3.1, 6.8, 10.8, 13.2, 17.2, 21.2, 25.2, 31.0	14.6	0.00685, 0.103, 0.212, 0.466, 0.740, 0.904, 1.18, 1.45, 1.73, 2.12	30 s (20 s)	Dec/2001 – Jul/2002	Urban	$\Delta[CO_2]/\Delta z$, ΔC_S [a]
Hutyra *et al.* (2008)	Tapajos, Brazil	2 51' S, 54 58' W	0.91, 10.4, 19.6, 28.7, 39.4, 50, 62.2	40-45 (42.5)	0.021, 0.24, 0.46, 0.68, 0.93, 1.18, 1.46	2 minute	Jan/2002- Jan/2006	Tropical forest	ΔC_S
Araujo *et al.* (2010)	60 km NW of Manaus, Brazil	2 35' 21.08'' S, 60 06' 53.63'' W	0.5, 3, 7, 11, 20, 30 (x 5 identical profiles)	> 30	N/A	2.5 minute (30 s)	Apr/2006 – Oct/2006	Tropical rainforest	ΔC_S
Siebicke *et al.* (2010)	South Germany	50° 08' 31'' N, 11° 52' 01'' E	2.25 (horizontal profile)	25	0.09	Constant, multiple GAs	152/2008 – 227/2008	Spruce wood.	$\Delta[CO_2]/\Delta x$
Lietzke and Vogt (2013)	Basel, Switzerland	7.5805 E/47.5617 N	6, 9 14, 21, 39 and 3, 6, 9, 14, 19	17	0.353, 0.529, 0.824, 1.24, 2.29 and 0.176, 0.353, 0.529, 0.824, 1.12	30 s (23 s)	Oct/2009 – Mar/2011	Urban	ΔC_S
Crawford and Christen (2014)	Vancouver, Canada	49.2261 N, 123.0784 W	2.1, 24.8	5.1 (buildings) 7.7 (trees)	0.412, 4.86	Constant, multiple GAs	7th Sep/2011 – 8th Sep/2011	Suburban	ΔC_S

a) Feigenwinter *et al.* (2012)

Both the CO_2 stored in an airspace (ΔC_S, 1.1) and CO_2 advected by non-turbulent motion through the top of the volume of air of interest (A_Z, 1.1) depend on the vertical distribution of CO_2 and may be calculated from it (see Sections 3.1.1 and 3.1.4). Several rural studies (Aubinet *et al.,* 2005; Papale *et al.,* 2006; van Gorsel *et al.,* 2007; Feigenwinter *et al.,* 2008) found ΔC_S to be at its most negative just after dawn and most positive just after dusk, with slightly (ΔC_S < 0.5 µmol m^{-2} s^{-1}) positive values for the rest of the day. The magnitude of the cycle varied; Aubinet *et al.* (2005) reported ranges of -5 to +3 µmol m^{-2} s^{-1} for two sites in France and Belgium, but -1 to +2 µmol m^{-2} s^{-1} for similarly forested sites in Italy, Germany, France and the Czech Republic. The storage term has been found to have greater importance relative to the vertical flux term during periods of weak turbulence (Aubinet *et al*., 2005; van Gorsel *et al.,* 2007). Although there is good agreement regarding the form of the mean diurnal cycle between sites, individual ΔC_S values tend to show large scatter (Feigenwinter *et al*., 2008). Reported urban CO_2 storage values range from -3.4 to 2.6 µmol m^{-2} s^{-1} in two high density city centres (Basel, Feigenwinter *et al.,* 2012 and Edinburgh, Nemitz *et al.,* 2002). Crawford and Christen (2014) recorded a smaller range of -0.82 to +1.1 µmol m^{-2} s^{-1} in a lower density, more vegetated residential suburb of Vancouver. These results should be treated with caution as the Vancouver values were calculated based on the assumption of a constant relation between carbon dioxide concentration measured above the blending height (i.e., within the inertial sublayer, Table 1.A.1 in Appendix 1.A) and the concentration at street level. In contrast, for Basel, Feigenwinter *et al.* (2012) did not make this assumption and reported ΔC_S calculated from $[CO_2]$ at ten levels; however, the results are only for one month (15th June to 15th July 2002). One of the contributions of this study is the calculation of CO_2 storage over a greater range of meteorological and anthropogenic conditions, enabling a more accurate assessment of its contribution to the overall net emissions budget (1.1) and of the processes affecting it.

Vertical CO_2 advection was calculated for multiple forested sites in Western Europe by Aubinet *et al*., (2005) following Lee (1998). Average values ranged from 0.1 to 10 µmol m^{-2} s^{-1} and were strictly positive (CO_2 was always emitted to the atmosphere). By contrast, net vertical advection calculated by Hong *et al*. (2008) using the same method and data from a Korean forest was negative, but equal and opposite to horizontal advection. Both positive and negative horizontal advection was observed by Aubinet *et al.* (2005) with values ranging from -1 to +5 µmol m^{-2} s^{-1} across all sites for which values were reported. At the time of writing, no study reporting vertical or horizontal advection in an urban environment at the micro scale was known to the author and calculation of these quantities is one of the contributions of this thesis.

1.5 Structure of this thesis

This section outlines the topics covered in each chapter of the thesis. This is summarised with respect to the two methods used to calculate the carbon balance in this thesis (Figure 1.2) in Figure 1.3.

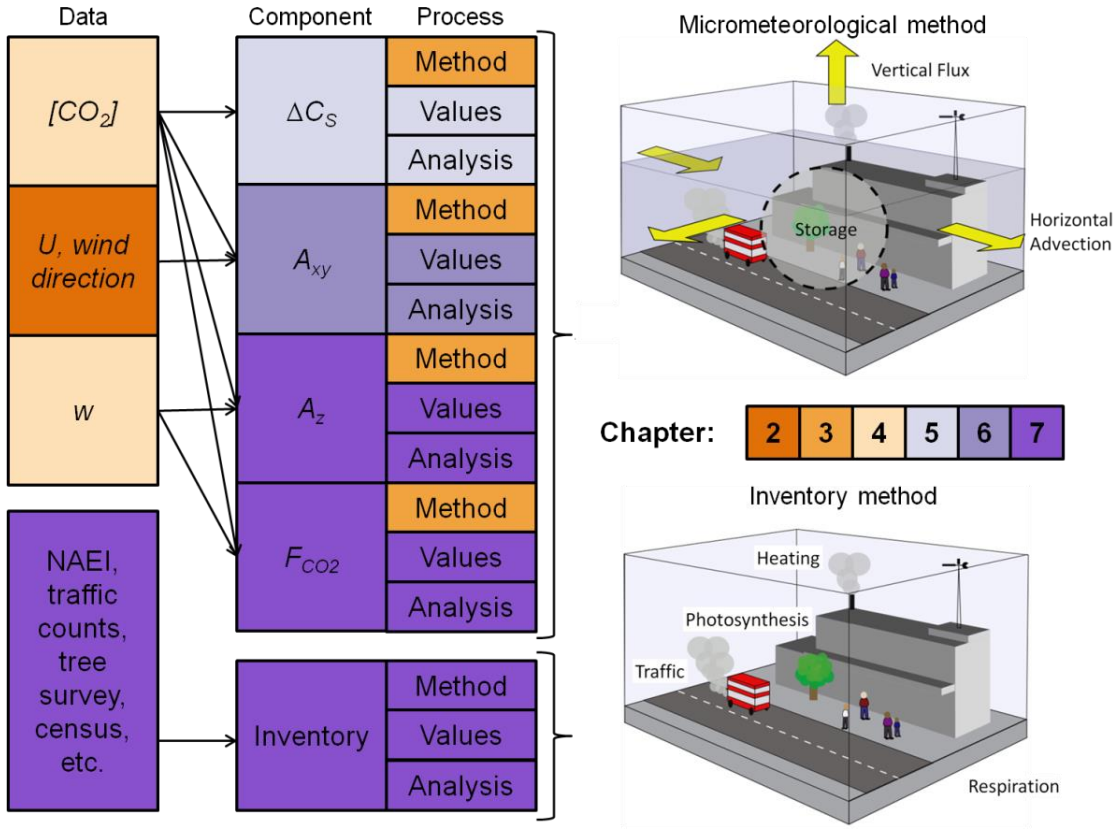

Figure 1.3: The components of the carbon dioxide exchange as calculated by the (top) micrometeorological and (bottom) inventory methods. Data required to calculate each component are given on the left and include CO_2 concentration ($[CO_2]$), mean horizontal wind speed (U), wind direction, the vertical wind component (w), and data from the National Atmospheric Emissions Inventory (NAEI). Each component, along with its method of calculation, values, analysis, and data required to calculate it, is shaded according to the chapter of the thesis in which it appears (legend, right).

Chapter 2 is concerned with the location, instrumentation and general meteorological characteristics of the site during the study period. Chapter 3 contains more detail on the methods of calculating the micrometeorological components of the CO_2 exchange. Outlines of the specific objectives for each of the subsequent chapters are as follows:

Chapter 4:

- Assess the temporal variation of CO_2 concentrations above and within the street canyon and put these variations in the context of other urban CO_2 studies.
- Describe the impact of microscale roof-top sources on local scale measurements
- Evaluate the effect of public events such as the Olympics and bank holidays on city centre CO_2 concentrations.
- Relate measured CO_2 concentrations to natural (e.g., atmospheric stability) and anthropogenic (e.g., number of vehicles) factors.

Chapter 5:

- Report and compare CO_2 storage calculated by two different instruments and methods for at least one full seasonal cycle.
- Develop a method to automatically detect venting of CO_2 stored within the canyon, relate it to other variables and investigate the underlying processes.
- Quantify the impact of the spatial and temporal resolution of CO_2 concentration measurements on calculated CO_2 storage.
- Build a statistical model to gap fill CO_2 storage time series.

Chapter 6:

- Investigate the impact of land cover and use on CO_2 concentrations across central and Greater London using transect measurements.
- Characterise the spatial scale of CO_2 variation in an urban environment.
- Calculate horizontal CO_2 gradients within and between land use/cover classes, and horizontal advection within the study street airspace.

Chapter 7:

- Determine and compare net CO_2 emissions from Central London via the inventory and micrometeorological methods.
- Gauge the relative importance of each component of the net emissions for both methods and suggest which should be prioritised as part of future urban environment research.

The final chapter (Chapter 8) addresses the contributions and conclusions drawn from this work.

Appendix 1.A: Structure of the atmosphere within 10 km of the earth's surface

Table 1.A.1: Summary of the atmospheric layers below 10 km, their scale and their characteristics. z_b is defined as the height of the local roughness elements, in the vicinity of this study, predominantly buildings.

Atmospheric Layer	Depth	Characteristics
Urban Canopy Layer	Average building height (z_b)	- Roughness length generally defined by the characteristics of the urban canyon or generic city street, except where vegetation is taller than the buildings. - Individual roughness elements e.g., buildings and trees, variety of surface properties (albedo, emissivity, degree of insolation, etc.) and the large number of heat and trace gas sources which are not constant in time nor space lead to very complex flow structure (Roth, 2000) with a high spatial variability of both wind velocity and trace gases in three dimensions (AMS, 2012).
Roughness Sublayer (Transition Layer) (Interfacial Layer) (Wake Layer)	$2z_b$, varies with spacing of roughness elements (Raupach *et al.,* 1991)	- Roughness elements at the base of this layer render the flow three dimensional (Raupach and Thom, 1981 *in* Schmid *et al.,* 1991). - Fluxes may be dominated by local sources and sinks. - Point measurements may not be representative of mean surface layer fluxes on a local scale. - Intense turbulence blends the spatial and temporal variations in atmospheric variables towards the lower boundary of the inertial sublayer.
Inertial Sublayer (Constant-Flux Layer) (Turbulent Surface Layer)	10% height PBL	- Lies above the roughness sublayer. - Base corresponds to the urban equivalent of the blending height (Rotach *et al.,* 2002) - Turbulence is well developed, logarithmic wind speed profile (AMS, 2012) - Monin-Obukhov Similarity Theory (MOST) applies under ideal conditions (large fetch, stationarity) - Vertical turbulent fluxes of variables such as momentum, heat and concentration of trace gases are considered to be constant (vary by less than 10% with height) both vertically and horizontally provided that the flux source area is homogeneous (Schmid *et al.*1991) - Measurements taken within this layer may be considered representative at the local scale - Layer may not exist in urban areas, due to the longer roughness length and associated increased turbulence (Schmid *et al.,* 1991).
Mixing Later (Convective Boundary Layer)	Variable with conditions and diurnal cycle	Present during the daytime, growth driven by solar heating of the surface. Well mixed on an hourly timescale. (Stull, 1988).
Planetary Boundary Layer (Atmospheric Boundary Layer)	Variable with conditions and diurnal cycle	- well mixed on a daily timescale (Figure 1.1) due to turbulence generated by frictional drag on the atmosphere by roughness elements (trees, buildings, etc.) on the earth's surface and by convection due to heating by the earth's surface (Oke, 1987) - layer has a clear diurnal cycle with the depth varying with the strength of the mixing. (Oke, 1987).

Chapter 2. Methods: Study area and observations[1]

2.1 Study area

The focus of this study was observations conducted in the vicinity of the Strand Campus of King's College London (KCL), on the north bank of the River Thames in central London. London is the capital city of the United Kingdom (UK), a collection of islands in northern Europe with a temperate, maritime climate. The population of the UK is highly urbanised (in 2011 81.5% of the usually resident population of England and Wales resided in urban areas, Office of National Statistics, 2013) and there are thirteen cities with over 500,000 residents. Of these, the London conurbation (known as Greater London) is by far the largest, with 8.1 million inhabitants or 12.1% of the UK resident population (Nomis, 2011) and extends approximately 25 km in all directions from the Strand campus.

The campus is located near the centre of the London Central Activity Zone (CAZ) (Figure 2.1 a), a region containing the primary political, cultural and business institutions of the UK. The main boroughs of the heavily developed CAZ (Camden, City of London, and Westminster) account for nearly 30% (1.4 million in 2011) of London's jobs (Greater London Authority (GLA) Economics, 2014a) and have a large difference between day and night time population (2.1 million and 0.4 million respectively, GLA Opinion Research and Statistics, 2013). The smaller nocturnal population results in lower demands for heating compared to residential areas (Velasco and Roth, 2010, Iamarino *et al.,* 2012). This area is heavily influenced by commuter traffic: 1.1 million people passed through the Central London cordon (Figure 2.1a) during the 7 am to 10 am peak on an average weekday in 2009, with 20% of the journeys made via a motorised vehicle (Transport for London, 2010). Institutions located in the immediate vicinity of the Strand campus are predominantly cultural (Somerset House, Aldwych Theatre and Bush House – home of the BBC world service until 2012), political (High Commission of India, Australian High Commission) and governmental (Inland Revenue Service).

Measurements have been made at 10 locations on the Strand campus (Table 2.1) and at 5 more in the surrounding area (Appendix 2.A, Figure 2.1) to examine the CO_2 balance and exchanges of central London, with a focus on the relation between the urban canyon (microscale) and above (local scale) (Figure 1.1).

2.1.1 Strand Campus

The campus itself consists of approximately a dozen buildings, ranging in age from the early 1800s to the mid-1900s arranged around two courtyards and a private access road. It extends from The Strand, a 4 lane road divided in two by the St Mary-le-Strand church, in the north, to Victoria Embankment, bordering the Thames, to the south. KSNW is situated near two mature London Plane (*Platanus acerifolia*) trees and others line the additional westbound single carriageway (A4) to the north, and a dual carriageway (Victoria Embankment, A3211) to the south. Land cover characteristics for the EC source areas of the KSS tower (40 m to the east of

[1] Sections 2.1, 2.2, and Appendix 2.B contain some content published as part of Bjorkegren *et al.* (2015).

KSSW) are (% plan area): roads: 43%, buildings: 38%, water: 14%, vegetation (trees): 5% (2%) (Ward *et al.,* 2015). The trees were predominantly mature London Plane trees that line the Strand street canyon and other major roads nearby. This vegetation density is typical for the central London area (Lindberg and Grimmond, 2011). Whilst photosynthetic uptake of CO_2 does occur, it is likely to be an insignificant control on the CO_2 flux or the CO_2 storage within the monitored street canyon. Ward *et al.* (2015) found the role of vegetation to be negligible.

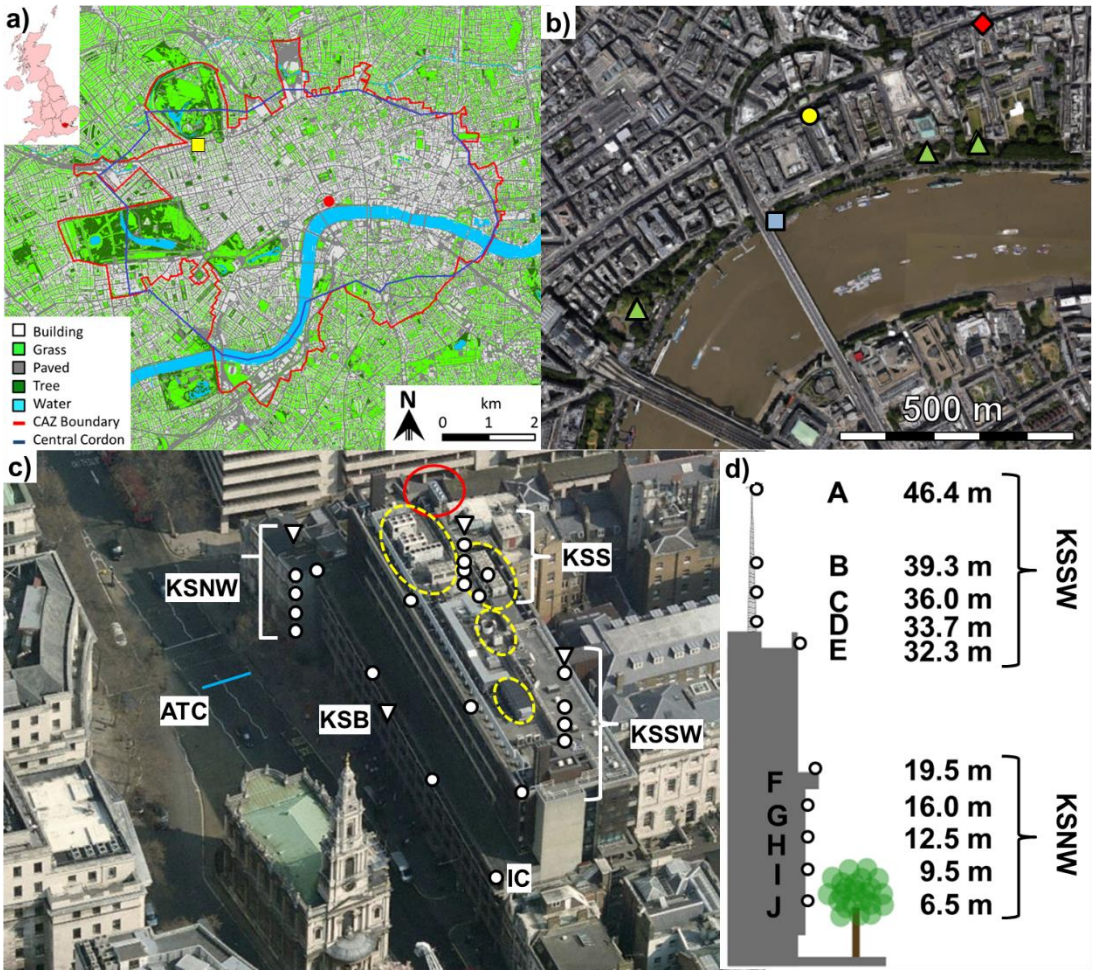

Figure 2.1: Sample sites at King's College London, Strand campus (KS), UK (a) Land cover map (Lindberg and Grimmond, 2011) centred on the Strand campus (red dot) with the Central Activity Zone (CAZ, red line), Transport for London (TfL) Central London Cordon (blue line) and Marylebone Road (MR) monitoring station (yellow square). Location of Greater London within the UK is shown in red (top right inset). (b) Past and current measurement sites (see Table 2.1) in the vicinity of KS (yellow dot): Thames Royal National Lifeboat Institution (blue square), Royal Courts of Justice automated traffic count (red diamond), and (left to right) Embankment gardens, Temple gardens and Middle Temple gardens (green triangles). (c) Measurement sites at KS include traffic count [undertaken week starting 8th July 2013 (blue line, 'ATC')], switched [CO_2] profile (white circles: KSSW, KSNW and comparison point, IC) and EC (white triangles). Rooftop sources are circled: chillers (yellow, dotted), boiler chimneys (red, solid). Not labelled: KSLH: four hollow points running from IC to KSNW; KSUH: three hollow points along roof edge parallel and above KSLH. (d) Vertical [CO_2] profile locations z_i viewed from the ATC location in (c) with height above ground level. (b) and (c) Map data: Google, Bluesky (2014).

Sources of CO_2 in the vicinity of KS include rooftop emissions due to burning of natural gas for heating and venting of high-CO_2 air from air conditioning ducts (Figure 2.1c, Kotthaus and Grimmond, 2012). At the micro-scale, the close to roof-level based observations are affected by boiler and chiller vents (Figure 2.1c). The output of the air vents and boiler chimneys vary

with space heating demand – which itself is a function of building occupancy and air temperature. Demand, and hence emissions, is highest for weekdays during term time in cold months. The human activities within the building are dominated by the academic year, so when classes are in session there is a much greater occupancy of the building (Section 4.2). Wind direction analysis suggests the river is not a significant source of CO_2 (not shown) and there are no major power stations or other industrial activity nearby.

Table 2.1: Naming convention for measurement locations at the Strand campus

University	Campus	Building	Acronym
King's College London (K)	Strand campus (S)	Balcony of Strand building	KSB
		King's building	KSK
		15 m south of KSK	KSK15S
		Lower profile (Horizontal)	KSLH
		Norfolk building	KSN
		North Wing	KSNW
		Strand building	KSS
		45 m west of KSS	KSS45W
		West end of Strand building	KSSW
		Upper profile (Horizontal)	KSUH

The street canyon's height: width ratio varies from 0.74 at KSNW to 1.28 at KSSW. The road (called A4 or the Strand) has four one-way lanes along which vehicles are permitted to travel from east north east to west south west. These split around the St Mary-le-Strand church in front of KS, with two running either side (Figure 2.1c). Typically 16,000-19,000 vehicles per day, of which the majority (71%) are cars (Automated Traffic Count (ATC) 8th to 15th July 2013, Section 4.6.1) use the southern two lanes. Traffic speed is slow, reaching a minimum average speed of 26 km h^{-1} (16 mph) at the beginning of the rush hour peak in traffic volume (18:00 BST) (ATC 8th to 15th July 2013, Section 4.6.1). Considerable congestion, particularly in the vicinity of the two bus stops is observed at this time.

2.1.2 Additional sites

Other measurement sites in the vicinity of the Strand campus include the Thames Royal National Lifeboat Institution (TLI) Tower Lifeboat station on the south side of Victoria Embankment (water samples for CO_2 flux measurements, water temperature), Victoria Embankment opposite Bankside pier (CO_2 uptake by London Plane tree measurements), Victoria Embankment, Temple and Middle Temple gardens (soil moisture and CO_2 flux measurements) and the road outside the Royal Courts of Justice (RCJ, automated traffic count) (Figure 2.1b, Figure 2.8).

2.2 Observations

A complete table of measurements made at or in the vicinity of the Strand campus is available in Appendix 2.A and a summary of the meteorological observations made at KS is provided in

Appendix 2.B. The instrument location, sampling interval and time period for which the data are available are indicated. In the following section the details of the measurements and the processing prior to analysis are provided.

2.2.1 CO_2 H_2O, and temperature profile

CO_2, water and temperature were measured using profiles (Figure 2.2) that were established in multiple configurations (Table 2.2). The CO_2 and H_2O profile involved pulling air from various locations to the gas analyser where the concentration measurement was made, whereas the temperature measurements (Table 2.3) were *in situ* fine wire observations.

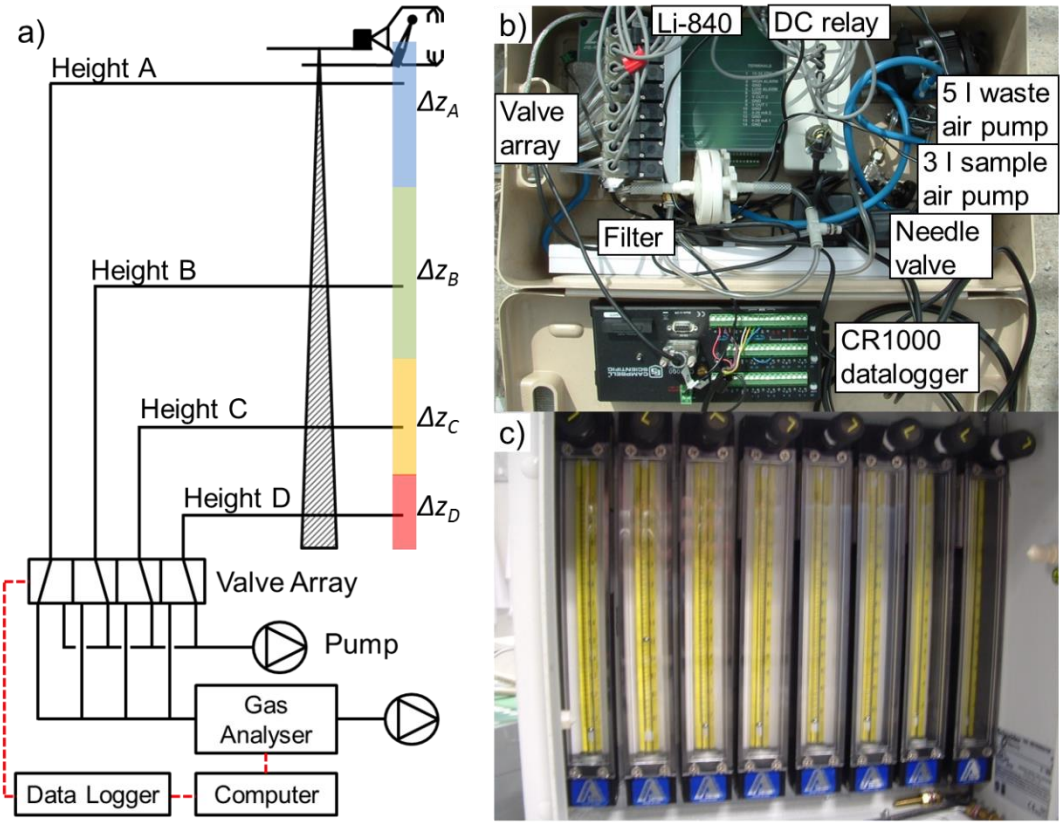

Figure 2.2: Design and instrumentation of the switched vertical profile. (a) KSSW (Figure 2.1c) tower colour shaded areas: vertical span over which measurements are considered to be relevant ($\Delta z_{A\text{-}D}$), black lines: tubing, red dashed lines: wires. Valve array shown with gas analyser measuring height A (far left valve). (b) Labelled view of CO_2 profile measurement system. (c) Rotameters.

As CO_2 storage and vertical fluxes involve processes at the micro- to local-scales, the air sampling heights (z_i) are chosen to span from within the urban canyon to 13.3 m above the Strand building height, so within the roughness sublayer and inertial sublayer. The base of the inertial sublayer is 2-3 times the mean roughness element height (z_b) (Grimmond and Oke 1999b, Roth 2000, Grimmond *et al.,* 2004). As z_b in the vicinity of the KSS is 21 m (Kotthaus and Grimmond, 2012) the sampling heights span z_i/z_b 0.24 –2.21.

The KSSW and KSS support structure is a guyed tower (11.36 m with 1.95 m steel pole attached to the top for total height of 13.31 m, T -145, Aluma Tower Company Inc., USA). A pneumatic mast (< 9 m, CSQT9-6/HP, Clark Masts systems Ltd, UK) was installed at KSK and later at KSNW.

Table 2.2: CO_2/H_2O profile configurations for the measurements made at KS site. Height above ground level, z_i, is given relative to mean building height (z_b, 21 m, Kotthaus and Grimmond, 2012).

Config.	Period of operation (year/day)	Location	Instrument (serial number)	Levels (m a.g.l.)	Levels (z_i/z_b)	Data Availability
C1	2009/351 – 2011/024	KSS	LI840-016, LI840-018	33.60, 43.18	1.60, 2.06	85.2%, 82.9%
C2	2011/020 - 2011/285	KSS	LI840-016	31.82, 33.60, 35.50, 38.07, 43.18	1.52, 1.60, 1.69, 1.81, 2.06	54.7%
		KSS: Vent sites	LI840-016	31.80, 33.50	1.51, 1.60	80.9%
C3	2011/285 - 2012/085	KSS	LI840-018	31.82, 33.60, 35.50, 38.07, 43.18	1.52, 1.60, 1.69, 1.81, 2.06	95.3%
		KSS: Vent sites	LI840-018	31.80, 33.50	1.51, 1.60	
		KSNW	LI840-016	16	0.76	68.8%
C4	2012/085 - 2012/102	KSNW	LI840-016	16	0.76	42.7%
C5	2012/102 - 2012/150	KSNW	LI840-016	6.5, 9.5, 12.5, 16	0.31, 0.45, 0.60, 0.76	83.5%
		KSLH	LI840-016	19.5 *	0.93 *	
C6	2012/150 - 2013/055	KSSW	LI840-018	33.7, 36.0, 39.3, 46.4	1.60, 1.71, 1.87, 2.21	90.7%
		KSUH	LI840-018	32.3 **	1.54 **	
		KSNW	LI840-016	6.5, 9.5, 12.5, 16	0.31, 0.45, 0.60, 0.76	94.1%
		KSLH	LI840-016	19.5 *	0.93 *	
C7	2013/056 - 2013/127 2013/133 - 2013/154	KSSW	LI840-016	33.7, 36.0, 39.3, 46.4	1.60, 1.71, 1.87, 2.21	83.2%, 83.9%
		KSUH	LI840-016	32.3 **	1.54 **	
		KSNW	LI840-018	6.5, 9.5, 12.5, 16	0.31, 0.45, 0.60, 0.76	93.7%, 97.2%
		KSLH	LI840-018	19.5 *	0.93 *	
C8	2013/128 - 2013/132 2013/155 – 2013/216 2013/266 2014/160	KSSW	LI840-016	46.4	2.21	98.9%, 96.8%, 97.0%
		KSNW	LI840-018	16	0.76	99.4%, 98.0%, 98.2%
C9	2013/217 – 2013/265	KSSW	LI840-016	46.4	2.21	96.6%
C10	2014/160 - 2015/124 2015/209 – 2015/365	KSSW	LI840-016	33.7, 36.0, 39.3, 46.4	1.60, 1.71, 1.87, 2.21	94.0% 84.9%
		KSUH	LI840-016	32.3 **	1.54 **	
		KSNW	LI840-018	6.5, 9.5, 12.5, 16	0.31, 0.45, 0.60, 0.76	96.8% 84.7%
		KSLH	LI840-018	19.5 *	0.93 *	
C11	2015/125 – 2015/209	KSNW	LI840-018	6.5, 9.5, 12.5, 16	0.31, 0.45, 0.60, 0.76	96.2%
		KSLH	LI840-018	19.5 *	0.93 *	

** : Four sampling sites along the KS Strand building balcony, one of which is an intercomparison site with the KSSW LI840.*

***: Three sampling sites along the KS Strand building roof, located vertically above the three western-most KSLH sites.*

When operated as a profile (configurations C2, C3, C6 and C8), two systems allow air to be sampled from 16 points. Air is drawn continuously through 4 mm internal diameter polyurethane tubing with a TH060N-20 pump (Brammer Stratford, UK). Flow rates are set to 1.3×10^{-5} m^3 s^{-1} (2 s.f.) by a P11A6- BDOA / 112-19-CA rotameter array (Aalborg, USA) and a SS-1RS6MM a needle valve (Swagelok, UK). Spare tubing located prior to the rotameter array is rolled to provide a condensation loop to prevent liquid water entering the valve array and the

air sample is filtered (1 µm filter, FALP04700, Millipore) before entering the measurement cell to remove aerosol and improve performance between calibration and cleaning. A VKF333-5DZ-M5-Q valve array (SMC Pneumatics, UK) (Figure 2.2) is used to select each consecutively for 75 s via a DC relay, controlled by a datalogger (CR1000/CR5000 with a CRBasic program, Campbell Scientific Ltd, USA). The valves are normally set to direct airflow towards a 'waste' pump (D5, Charles Austen pumps, UK) via the R port. When activated, a valve directs airflow to the LI840 gas analyser (LI-COR Biosciences, USA) (Figure 2.2). When configured for single height measurement (C1, C4, C7), the valve array is bypassed and the air is drawn through the system solely by the sample pump.

Table 2.3: Temperature profile configurations for the measurements made at KS site. z_b= mean building height, 21 m (Kotthaus and Grimmond, 2012).

Con-fig.	Period of operation (year/day)	Site	Instru-ment	Levels (m a.g.l.)	Levels (z_i/z_b)	Data availability (%)
T1	2009/351-2012/083	KSS	Omega	31.8, 33.4, 35.3, 37.1, 37.8, 40.4, 43.0, 44.8	1.51, 1.59, 1.68, 1.77, 1.80, 1.92, 2.05, 2.13	47.5%
T2	2012/095-2012/234	KSSW	Omega	33.7, 35.0, 35.5, 36.0, 39.3, 42.0, 44.5, 46.4	1.60, 1.67, 1.69, 1.71, 1.87, 2.00, 2.12, 2.21	91.5%
T3	2012/235-	KSSW	Omega	33.7, 35.0, 35.5, 36.0, 39.3, 42.0, 44.5, 46.4	1.60, 1.67, 1.69, 1.71, 1.87, 2.00, 2.12, 2.21	88.0%
		KSNW		6.5, 12.5, 16	0.31, 0.60, 0.76	68.0%
		KSLH		19.5 *	0.93 *	

**: Three sampling sites along the KS Strand building balcony*

The data collected from the system consists of the variables from the LI840 gas analyser and, separately, the valve status. The former are collected at 2 Hz, by an in-house program (Li840.py) that writes hourly files with the native XML format directly to a laptop co-located within a waterproof box (Zarges, Germany) at each site. The latter, sampled at 1 Hz via the datalogger, are also split into hourly files within the same directory. The two files are transferred to a central data store every hour and if there are missing files an automated email system notifies the research group that attention is needed.

The environmental controls for the interior of the LI840 are robust: external variation in pressure of 6 hPa and temperature of 11 °C resulted in internal variation of less than 1 hPa and 0.1 °C respectively. Correcting for pressure and temperature fluctuations is therefore unnecessary. Raw data also do not need to be corrected for water vapour density as this is handled by the LI840 internal software. Data processing prior to analysis is therefore limited to valve assignment, removal of data points potentially contaminated by a previous sample, and averaging in time (as the data are collected by a closed path gas analyser, the suggestions for averaging by Kowalski (2012) do not apply). This is completed using in-house software, written in R. The time taken for a sample to clear from the system was determined to be 6 s by supplying high CO_2 air across one of the inlets (Appendix 2.C). The first 10 s and last 1 s of the time series recorded at each height were therefore discarded prior to averaging to prevent contamination of the signal with air from a previous sample point. The 10 s 'buffer' is quick enough to justify a 75 s 'run time' at each sample site. This allows the profile to cycle through 8

air intakes in 10 minutes, which is appropriate to characterise processes on the micro scale (Oke, 1987).

As data are collected by multiple gas analysers, two collocated sampling points are used to remove systematic bias between instruments (Table 2.2, Figure 2.1c). LI840 gas analysers are located at KSNW and KSSW, and at KSSW there is also a LI7500. The collocated sampling points are: (1) valve 5 (v5) of both KSSW and KSNW, which is 19.5 m a.g.l. (z_i/z_b = 0.93); and (2) KSSW v1 and LI7500 at 46.4 m a.g.l. (z_i/z_b = 2.21). Although the systems are designed to sample the comparison points at the same time, there are occasions when the timing was not exact. Hourly median values are used to determine the linear regression relation and remove any systematic errors between systems. All data are corrected for these errors prior to detailed analysis. As the LI840 systems are more accessible than the LI7500, and therefore easier to calibrate on a regular basis, the relation between the *[CO_2]* measured by each instrument is used to adjust the LI7500 values and extend the time required between calibrations of the LI7500, minimising data loss and the disruption entailed by having to take the tower down.

A linear model fitted to mean *[CO_2]* values at 1 minute resolution for KSSW v1 and KSSW LI7500 had slope 0.92 ± 0.0046 (2 s.f.), intercept -50 ± 1.9 ppm (2 s.f.), with *p*-value < 2.2 x 10^{-16} (2 s.f.). The high correlation (R^2=0.98, 2 s.f.) between the two data series and the results from the linear model confirm that the response of the two gas analysers at different *[CO_2]* is predictable and can be accounted for when making comparisons between data series measured by each instrument.

2.2.1.1 CO_2 Profile Maintenance and data availability

The LI840 gas analysers are regularly calibrated for CO_2 concentration against two standard gases. These are 0 ppm CO_2 (99.998% N_2, BOC, UK) and 805 ppm CO_2 (Synthetic air with 805 ppm CO_2, Air Liquide, UK). A Li610 dew point hygrometer (LI-COR, USA) is used to provide air with a precise water content to calibrate the LI840 gas analysers for water vapour concentration. The instruments were compared to those at Nesbit/Lowry Lab Royal Holloway University of London on 5th January 2008. Comparison of the LI840 data to collocated measurements found the drift in measured CO_2 concentration to be linear with time. Post processing of the LI840 CO_2 concentration data therefore includes an empirically derived linear correction for drift.

Data availability for each configuration is reported in Table 2.2. Reasons for data gaps include physical component failure (e.g., burnt out of air pumps), theft or failure of on-site computers, electricity supply failure, extensive building works, instrument removed for calibration, software problems and instrument failure.

2.2.2 Eddy covariance Measurements

Eddy covariance (EC) observations have been undertaken at several sites and using a range of instruments (Table 2.4).

EC measurements of CO_2 flux require a sonic anemometer and a fast response gas analyser. Two of the gas analysers used in this study are open path (LI7500 and LI7500A, LI-COR, USA) (Figure 2.3a) and the third is closed path (LI6262, LI-COR, USA) (Figure 2.3c). Sites with open path gas analysers also had CSAT3 anemometers, whereas KSB, the King's College Strand building Balcony site, had a Gill 3D anemometer (KSB, Gill Instruments Ltd, UK, Figure 2.3d) installed. All EC data were collected at 10 Hz, apart from a case study period (2014/013-2014/043, E7, Table 2.4) where measurements at KSSW and KSNW were made at 20 Hz. Details of ancillary measurements, including variables such as rain rate, used in quality assessment and control of the calculated fluxes are presented in Section 2.2.3.

Table 2.4: Eddy covariance instrumentation configurations for the measurements made at KS site. The height of the instrument in m above ground level, z_i, is given as well as the ratio to the mean building height, z_b (21 m, Kotthaus and Grimmond, 2012).

Con-fig.	Dates Active	Site	Instrument (serial number)	z_i	z_i/z_b	Data Availability (%)
E1	2008/273 - 2009/279	KSK	CSAT3 (0192-2), LI7500 (75H-0995)	33.6	1.6	87.8%
E2	2009/305 – 2010/021	KSS	CSAT3 (0192-2), LI7500 (75H-0995)	45.1	2.1	84.9%
E3	2010/022 – 2011/233	KSK	CSAT3 (1188-1)	33.6	1.6	91.8%
		KSS	CSAT3 (0192-2), LI7500 (75H-0995)	45.1	2.1	91.7%
E4	2011/234 – 2012/085	KSK	CSAT3 (1188-1), LI7500A (75H-1973)	33.6	1.6	91.6%
		KSS	CSAT3 (0192-2), LI7500 (75H-0995)	45.1	2.1	90.9%
E5	2012/086 – 2013/062	KSK	CSAT3 (1188-1), LI7500A (75H-1973)	33.6	1.6	85.7%
		KSSW	CSAT3 (0192-2), LI7500 (75H-0995)	46.4	2.2	81.7%
E6	2013/063 – 2013/072	KSB	Gill R3-50 (307)	19.9	0.95	0%
		KSSW	CSAT3 (0192-2), LI7500 (75H-0995)	46.4	2.2	100%
E7	2013/073 – 2014/141 2015/012 – 2015/260	KSB	Gill R3-50 (307)	19.9	0.95	66.6%, 79.7%
		KSNW	CSAT3 (1188-1), LI7500A (75H-1973)	20.5	0.98	87.8%, 82.2%
		KSSW	CSAT3 (0192-2), LI7500 (75H-0995)	46.4	2.2	97.2%, 90.5%
E8	2014/142 – 2015/011	KSB	Gill R3-50 (307), LI6262 (478)	19.9	0.95	66.6%
		KSNW	CSAT3 (1188-1), LI7500A (75H-1973)	20.5	0.98	87.8%
		KSSW	CSAT3 (0192-2), LI7500 (75H-0995)	46.4	2.2	97.2%
E9	2015/261 – 2015/365	KSB	CSAT3 (1188-1), LI7500A (75H-1973)	19.9	0.95	91.1%
		KSNW	Gill R3-50 (307)	20.5	0.98	0%
		KSSW	CSAT3 (0192-2), LI7500 (75H-0995)	46.4	2.2	6.0%

Full details of the eddy covariance data processing and flux calculation are given in Kotthaus (2014). They may be summarised as follows:

Prior to calculation of the fluxes, the data must be pre-processed; this is done by an in-house program called LondonFlux. The 10 Hz CSAT and LI7500 data are cross-correlated to allow for time lag between the IRGA and the sonic anemometer. An initial quality assessment and control removes values from the raw data if the diagnostics for the instrument indicates problems such as path obstruction, or if the observed data are not physically reasonable in either absolute value or variation within a 30 minute time period. An in-house de-spiking procedure (Identification of Micro-scale Anthropogenic Sources (IMAS), Kotthaus and Grimmond, 2012) removes periods affected by rooftop emissions that are insufficiently distant from the tower to be well mixed before they reach the sensor height. Outputs consist of 30 minute averaged LI7500 data, 30 minute averaged CSAT data and a gap filled time series of

meteorological data at half hourly resolution. These form the inputs for the flux calculation stage, which is done in a Linux environment using ECpack. Instrument information is provided in three calibration files; however, as the LI7500 has already implemented any calibration factors and the CSAT3 does not require any, these are not used. Processing by ECpack includes a planar fit co-ordinate transformation of the wind vectors over a 24 hour window. This is followed by a yaw rotation to align the wind speed results with the mean wind field. The sonic temperature is corrected for humidity effects and the scalar concentrations for changes in air density.

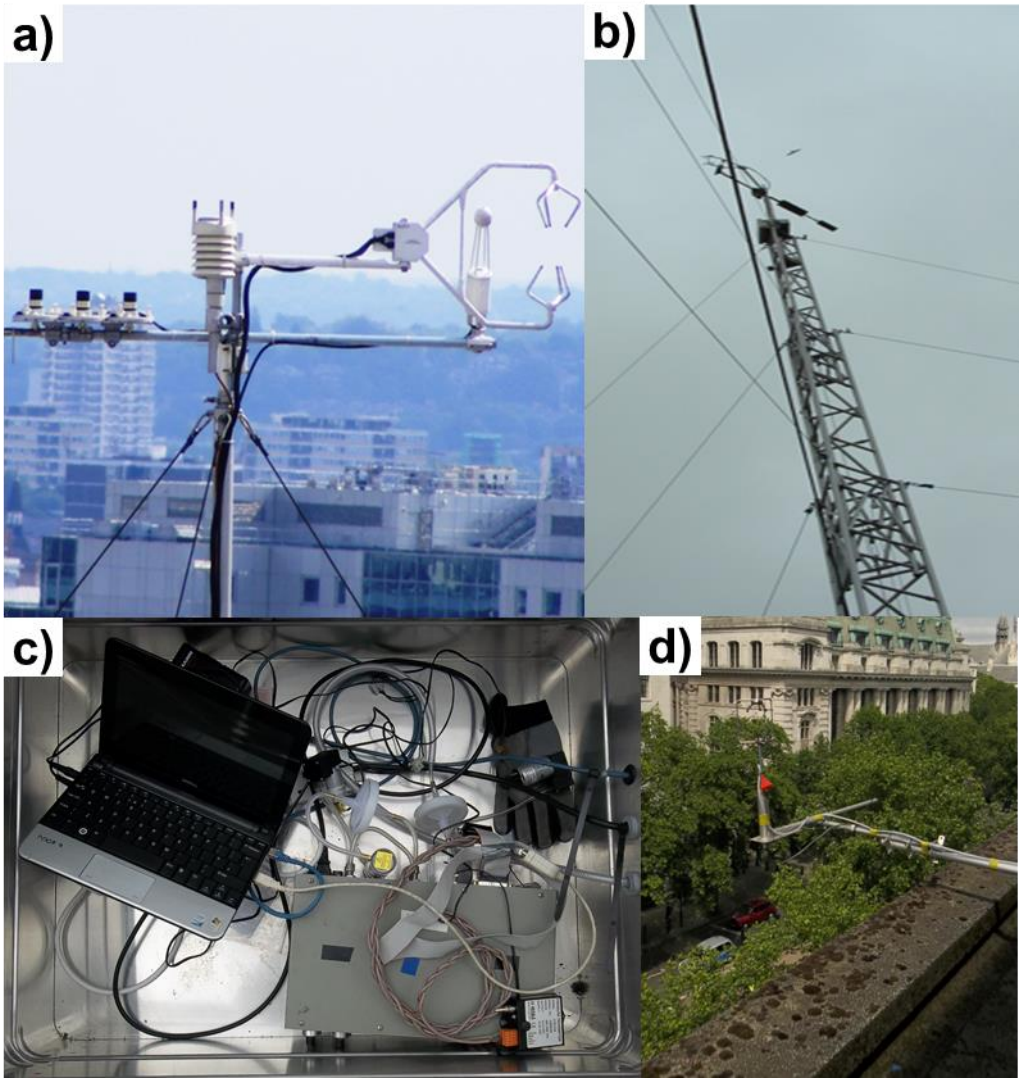

Figure 2.3: Photographs of eddy covariance equipment. (a) LI7500 and CSAT3 at KSK, (b) KSSW tower with (left) CSAT3 and LI7500, (c) LI6262 and laptop in a Zarges box at KSB, (d) Gill 3D sonic anemometer with LI6262 air intake (red funnel) viewed from balcony.

Post processing of the data involves identifying and removing outliers. The first stage relates the daily standard deviation to the difference between the calculated flux for a half hourly period and the daily mean. If the difference is greater than three times the deviation and (in the case of scalar quantities), path obstruction is reported for greater than 1% of the time period, the data point is removed. The latter criterion is relaxed to allow values where the path is obstructed for less than or equal to 90% of the time period for values calculated solely from

sonic anemometer data. The 30 minute flux and stability data are written to different files depending on the level of quality control applied to the input data.

2.2.3 Ancillary meteorological measurements

Additional meteorological measurements made concurrently to the CO_2 profile at the Strand campus can be divided into weather, radiation and mixing layer height observations.

The weather group consists primarily of measurements made by WXT510 and/or WXT520 (Vaisala Ltd, Finland), but also includes observations of rain rate made by tipping bucket raingauges (ARG100, Campbell Scientific, UK). Gaps in the WXT data which are shorter than 2 hours are filled by linear interpolation. For gaps longer than 2 hours, the gap is filled with data from another site which has been corrected for site differences using corrections derived from linear regression of the data for the previous and following day. Gaps in rain rate present at all sites are filled with data from the nearest World Meteorological Organisation site (St James' Park, WMO 3770). The diurnal cycle of other variables such as wind speed and relative humidity is preserved when no data is available using a cubic smoothing spline that covers the two days either side of the gap.

Measurements of long and short wave radiation are obtained above and within the canyon using CNR1 and CNR4 (Kipp and Zonen, The Netherlands) net radiometers. Other variables, such as ultraviolet light and photosynthetically active radiation are also measured at KSS45W (see Appendix 2.A for details). Processing of radiation data consists of time averaging to the common interval of 30 minutes.

2.2.4 River CO_2 flux

To measure the CO_2 flux from the River Thames samples were taken from the Royal National Lifeboat Association pier adjacent to Waterloo. Ambient $[CO_2]$ 1 m above the surface was recorded using a mobile handheld CO_2 sensor (Green Eye, Global Sensors, USA; CO200, Extech Instruments, USA) sensor and adjusted to lab values using a correction factor developed in house. The airflow from a modified LI6400 (LI-COR, USA) system (Figure 2.4, Figure 2.5) was set to this value and allowed to stabilise for five minutes before river water (40 ml) was injected into a sample cell with known basal area. Reference and sample $[CO_2]$ were recorded at 1 Hz for approximately 40 minutes after injection to compare uptake or release of CO_2 by the water sample to that of an inert reference material (Perspex). The CO_2 flux was calculated as the change in CO_2 concentration per unit time and unit surface area of the sample.

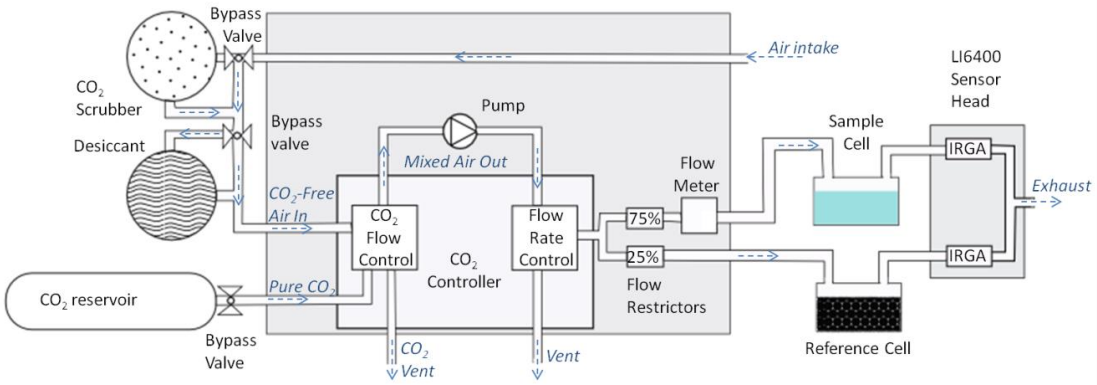

Figure 2.4: LI6400 system (grey shading) modified to measure CO_2 flux of a water sample.

Samples were taken at hourly intervals on two days for flow (25th July 2013) and ebb (31st July 2013) tides. The sample was collected using a valve attached to a water and air tight sample bag from which all air and water had previously been extruded. This was to prevent loss of CO_2 from the water sample.

Figure 2.5: Equipment used for measurement of CO_2 fluxes from river water.

2.2.5 Soil CO_2 flux

Emission of CO_2 from soil was measured in Embankment gardens (westernmost point, Figure 2.1b) using the traditional method of air injection. This was followed by measurement of the soil's response (Figure 2.6c) by a LI6400 gas analyser and soil chamber (6400-09, LI-COR, USA). Measurements were made over three surface types: bare soil (undisturbed, native London clay), bare soil (disturbed and fertilised with high-carbon compost), and lawn grass on 23rd July and 2nd September, 2014.

2.2.6 Spatial variations of CO_2 Concentration

The spatial variation of *[CO_2]* in the area surrounding the Strand campus was surveyed on foot and by bicycle at 10 s resolution using the aforementioned mobile handheld CO_2 sensors contained within a perforated box and mounted on the front of a bicycle at approximately 1 m above street level. A GPS (Foretrex 301, Garmin, USA) logged the location several times per

minute at irregular intervals. Location and CO_2 concentration data were linearly interpolated to 1 s. Mobile sensors were compared to LI840 (KSSW) data prior and post foot surveys and sensor data adjusted accordingly. Full details are available in Chapter 6.

2.2.7 Photosynthetic uptake

The net photosynthetic uptake of CO_2 by grass (Figure 2.6a) and London Plane tree (Figure 2.6b) leaves ($F_{P,\,leaf}$) was measured using a standard LI6400 (LI-COR, USA) set up. London Plane tree samples were limited to those within reach at street level; however, this included leaves from mature trees, not just saplings. Measurements of photosynthetic uptake by grass were made in Embankment gardens (furthest point west, Figure 2.1b) and all three plane trees selected for measurement were planted on the north side of Victoria Embankment.

Measurements were made on four days (29th May, 5th June, 27th August and 9th September) during the summer of 2014. Due to the proximity of the trees to the river, and irrigation of the adjacent park, soil moisture was not expected to be a limiting factor. Response curves for light and CO_2 were recorded using the inbuilt light-response software of the LI6400. Target CO_2 concentrations were adjusted manually. In this study, the convention is that release of CO_2 to the atmosphere is denoted by a positive term, whilst uptake of CO_2 from the atmosphere is denoted by a negative term; however, when calculating response curves it is more convenient to work with predominantly positive values. Measurements of $F_{P,\,leaf}$ were therefore multiplied by -1 prior to plotting (Figure 2.7) and analysis (Section 7.3.1.2).

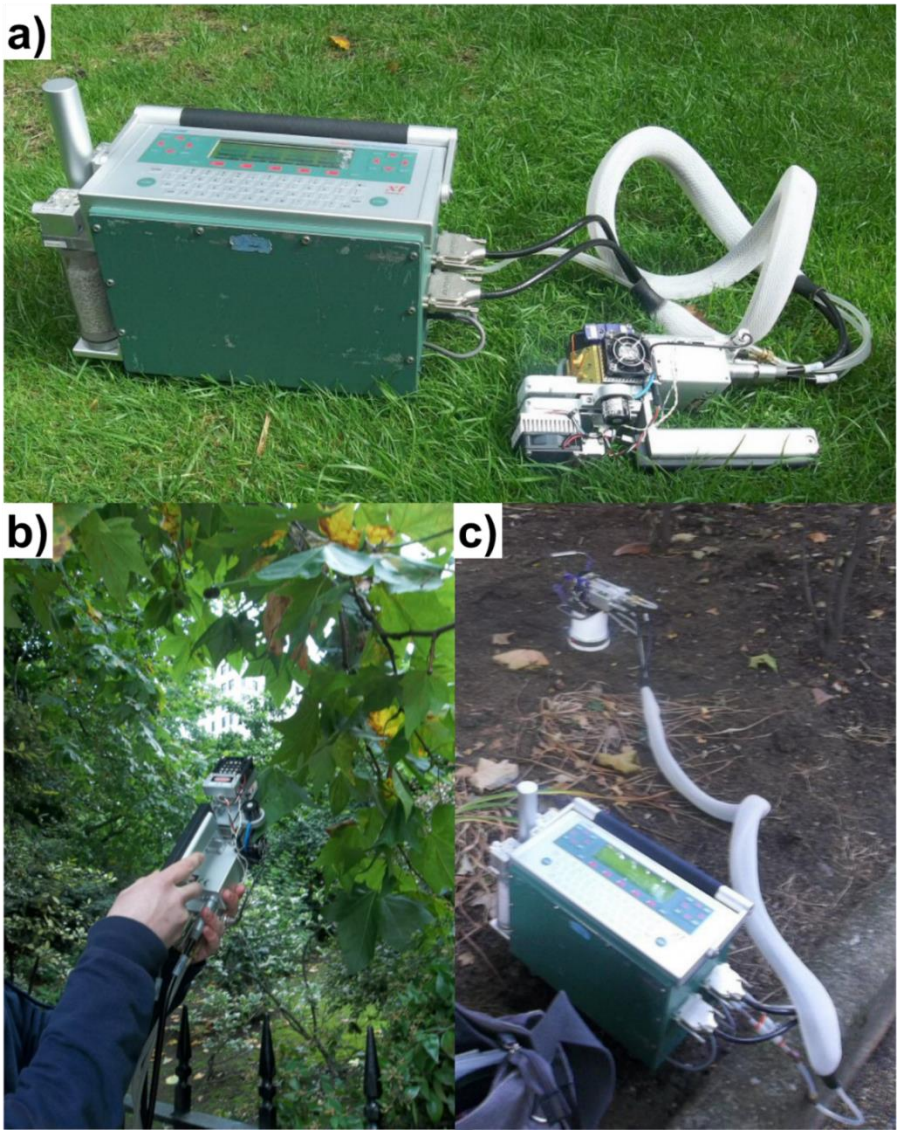

Figure 2.6: (a) LI6400 taking a light response curve of grass in Embankment gardens, 27th August 2014. (b) LI6400 IRGA head taking a light response curve of a London Plane leaf on Victoria Embankment 27th August 2014. (c) Soil CO_2 flux measurements (no light response), Embankment gardens, 23rd July 2014.

The measured net photosynthetic uptake of CO_2 for London Plane trees and lawn grass shows no clear relation between the examined variables (air temperature, leaf temperature, and atmospheric CO_2 concentration) and photosynthetic flux (rate of transfer of CO_2 from the atmosphere to the leaf) over the range examined (Figure 2.7). For this reason only the intensity of photosynthetically active radiation (PAR) was used to estimate the uptake of CO_2 by photosynthesis. The range of PAR and atmospheric CO_2 concentration values examined included all values that the plants were likely to experience (Figure 2.B.4 in Appendix 2.B and Figure 4.1 in Section 4.2, respectively). The ranges of air and leaf temperatures were more limited as measurements were only made between 29th May, 2014 and 9th September, 2014 inclusive, that is, during the warmer months due to the limited availability of personnel and equipment. It is possible that the photosynthetic flux rates measured with air temperatures between 15 ºC and 35 ºC (23.6% of all half hourly periods 2012/153 – 2013/151, 40.9% of the leaf-on period, i.e., mid-April to mid-November for 2012/153 – 2013/151) respond differently to changes in PAR to those measured at lower temperature. However, given the low land cover

fraction of grass in central London, it is assumed that any difference in response to PAR due to differences in air temperature will have a negligible impact on the total estimated emissions.

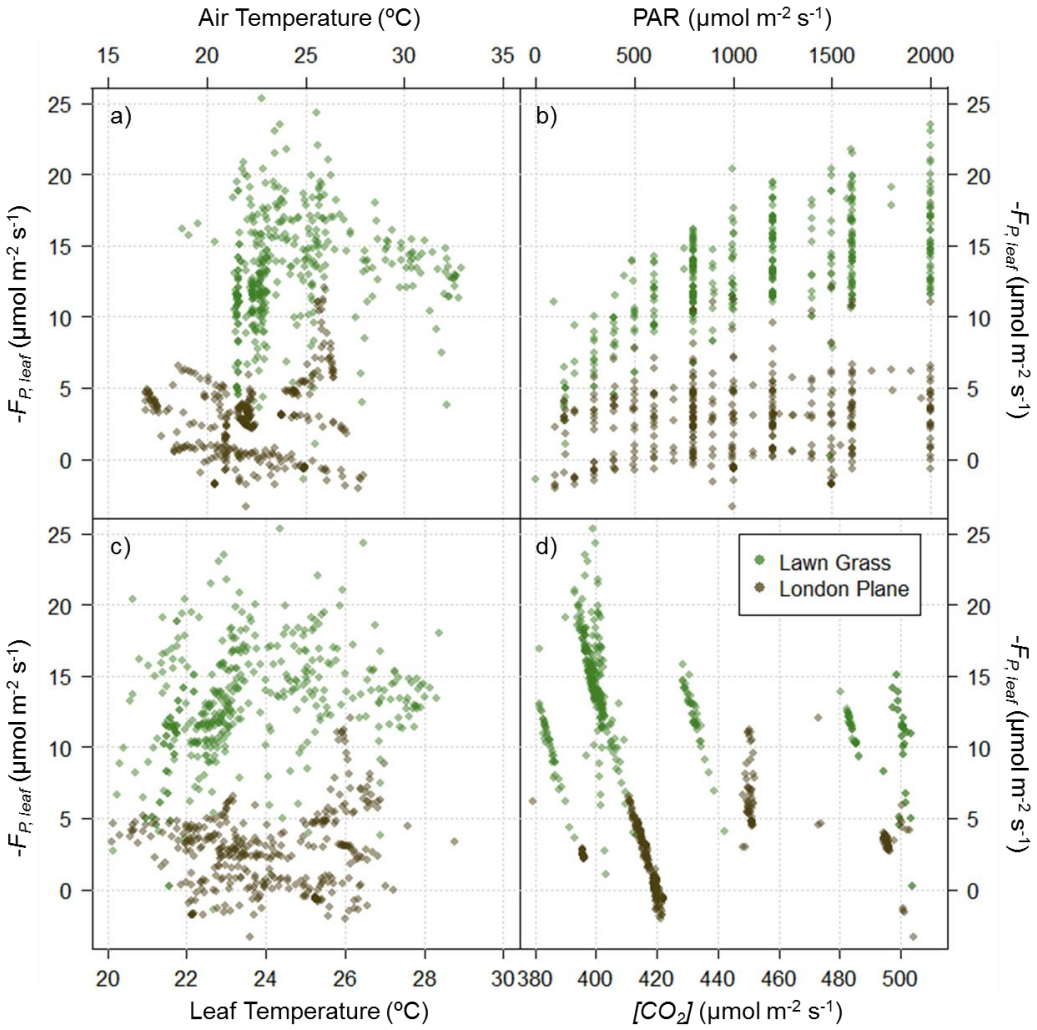

Figure 2.7: Variation of net photosynthetic flux from the leaves of vegetation ($-F_{P,leaf}$, µmol m^{-2} s^{-1}) with a) air temperature (°C), b) photosynthetically active radiation (PAR, µmol m^{-2} s^{-1}), c) leaf temperature (°C), and d) CO_2 concentration ($[CO_2]$, ppm) measured for grass and London Plane trees in and adjacent to Victoria Embankment gardens, summer 2014.

2.2.8 Traffic counts

Traffic adjacent to KSNW (Figure 2.1c) was counted for the week starting 8th July, 2013, by Advanced Transport Research Ltd using an Automatic Traffic Counter (pneumatic tubing) to monitor speed, volume and type of traffic. Results for the week were given at five minute intervals for ten classes (Table 2.5).

Longer term traffic counts were available from a Transport for London (TfL, 2013a) maintained automatic traffic counter (induction loop) located at the junction of the Strand with Fleet Street, opposite the Royal Courts of Justice (RCJ, Figure 2.1b, Figure 2.8). Hourly vehicle totals (but not type or speed) were available for each lane from 1 December, 2010, when the site was installed, until 16 May, 2013 when the site was removed for major works taking place in the area.

Table 2.5: Vehicle classifications used by automated traffic counter (Advanced Transport Research Ltd, UK).

Length	Axles	Groups	Description	Vehicles	Class
Short: up to 5.5m	2	1 or 2	Very short	Bicycles or Motorcycle	1
	2	1 or 2	Short	Saloon, Hatchback, Estate, 4 wheel drive, Pick-up, Light Van, Bicycle, Motorcycle, etc.	2
Medium: 5.5 to 14.5 m	3, 4 or 5	3	Short - Towing	Trailer, Caravan, Boat, etc.	3
	2	2	Two axle Truck or bus		4
	3	2	Three Axle Truck or Bus		5
	>3	2	Four Axle Truck		6
Long: 11.5 to 19.0 m	3	3	Three Axle Articulated	Three axle articulated or rigid vehicle and trailer	7
	4	>2	Four Axle Articulated	Four axle articulated or rigid vehicle and trailer	8
	5	>2	Five Axle Articulated	Five axle articulated or rigid vehicle and trailer	9
	>5	>2	Six Axle Articulated	Six (or more) axle articulated or rigid vehicle and trailer	10

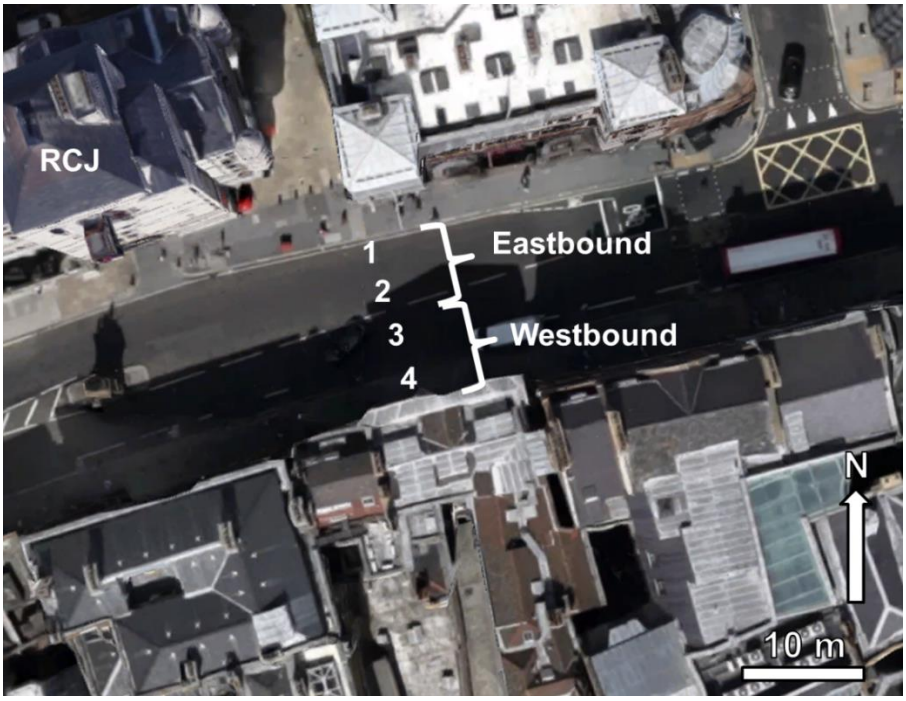

Figure 2.8: Approximate location of the traffic count site relative to the south east corner of the Royal Courts of Justice (RCJ). Lanes are number 1:4 with lanes 1 and 2 carrying eastbound traffic, and lanes 3 and 4 carrying westbound traffic. Lanes 1 and 4 are nearside (adjacent to the kerb) and lanes 2 and 3 are offside (non-adjacent to the kerb).

Appendix 2.A Instrumentation used at or near KS

This appendix contains details of each instrument installed at the sites on or close to the King's College Strand campus for which data is held by the micromet group. Instruments installed temporarily for e.g., intercomparison, are not listed. This thesis does not use data from all of the instruments listed, however all instruments installed have been listed for completeness. A site acronym beginning with 'KS' indicates the site was located on the Strand campus. An end date of 'publication' indicates that the instrument was still installed when the thesis was sent for publication.

Table 2.A.1: Equipment present at relevant Micromet sites 2009-2015. Headers record long site name, latitude, longitude, and site acronym. Table body records equipment installed at each site (model, manufacturer and number if more than one), sampling rate and period of observations (year, day of year).

Embankment gardens	**0.1217 W, 51.5081 N**	**EMB**
SM300, Delta T (x16)	30 min	2010211-2010286 x4, 2010211-2010265 x 4, 2010211-2010316 x 2, 2010211-2010004 x2, 2012075-2012306, 2012307-2013063, 2011040–2015105 x2
ML2, Delta T	30 min	2010254-2010342
ML2x, Delta T	30 min	2010173-2015105
KCL Strand campus, Strand building balcony, boom	**0.1164 W, 51.5120 N**	**KSB**
R3-50, Gill	10 Hz	2013063-2015260
LI6262, LI-COR	3 Hz	2014141-2015011
CSAT3, Campbell Scientific	10 Hz	2015261-2016048
LI7500, LI-COR	10 Hz	2015261-2016048
KCL Strand campus, King's Building roof, pole tower	**0.1161 W, 51.5115 N**	**KSK (Discontinued)**
CSAT3, Campbell Scientific	10 Hz	2008273-2009279; 2010022-2013063
LI7500, LI-COR	10 Hz	2008273-2009279
LI7500A, LI-COR	10 Hz	2011131-2013058
KH2O, Campbell Scientific	10 Hz	2010238-2010294
CNR1, Kipp and Zonen	15 min	2008273-2009273
CNR4, Kipp and Zonen	15 min	2010264-2013063
SKL2620/5, Skye Instruments	1 min	2008273-2009273
SKU420/5, Skye Instruments	1 min	2008273-2009273
SKU430, Skye Instruments	1 min	2008273-2009273
WXT510, Vaisala	5 s	2008273-2013063
ARG100, Campbell Scientific	15 min	2008231-2013063
Apogee_K, Apogee	10 min	2009323-2010150 (x1), 2010150-2011127 (x3), 2011136-2013063 (x2)
Raytek_J, Raytek	10 min	2009323-2010150 (x4), 2010150-2011127 (x3), 2011136-2013063 (x1)
KCL Strand campus, King's Building roof, 15 m south of pole tower	**0.1169 W, 51.5118 N**	**KSK15S**
CL31, Vaisala (x2)	15 s	2006333-2009112, 2007338-2008233
Apogee_K, Apogee (x4)	10 min	2010234-2011127 (x3), 2011136-2013139 (x4), 2013140-publication (x3)
CNR1	15 min	2007051-2008224
KCL Strand Campus, Norfolk Building	**0.1158 W, 51.5116 N**	**KSN**
Type 2 Thermocouple, Omega (x5)	10 min	2010193-2010290
KCL, Strand Campus, North Wing building	**0.1159 W, 51.5122 N**	**KSNW**
LI840, LI-COR	2 Hz	2012102-2016048

WXT520, Vaisala	5 s	2012137-2016048
CSAT3, Campbell Scientific	10 Hz	2013073-2015251
LI7500, LI-COR	10 Hz	2013073-2015261
ARG100, Campbell Scientific	15 min	2013073-2016048
R3-50, Gill	10 Hz	2015261-2016048
KCL Strand campus, Strand building roof, lattice tower.	**0.1164 W, 51.5120 N**	**KSS**
WXT510, Vaisala	5 s	2009286-2012084
CSAT 3, Campbell Scientific	10 Hz	2009305-2012084
LI7500, LI-COR	10 Hz	2009305-2012084
LI840, LI-COR	2 Hz	2010025-2012084
CNR1, Kipp and Zonen	15 min	2009282-2012084
SKL2620/5, Skye instruments	1 min	2009282-2012084
SKU420/5, Skye Instruments	1 min	2009282-2012084
SKU430, Skye Instruments	1 min	2009282-2012084
Raytek_K, Raytek	10 min	2010082-2012084
Type 2 Thermocouple, Omega (x8)	10 min	2009351-2012084 (x8)
KCL Strand campus roof, Strand Building, 45 m west of lattice tower	**0.1161 W, 51.5113 N**	**KSS45W**
CL31, Vaisala	15 s	2009112-publication
Vantage Pro Plus, Davis (x2)	2.5 s	2011111-2011136
LAS, Kipp and Zonen	10 Hz	2010001-2011265
PIR, Eppley	15 min	2009351-publication
PSP, Eppley	15 min	2009351-publication
ARG100, Campbell Scientific	15 min	2009351-publication
SKL2620/5, Skye Instruments	1 min	2009351-publication
SKU420/5, Skye Instruments	1 min	2009351-publication
SKU430, Skye Instruments	1 min	2009351-publication
BLS900, Scintec	1 min	2010295-2011136
SPN1, Delta-T	15 min	2011014-publication
KCL Strand campus, Strand building roof, lattice tower.	**0.1164 W, 51.5120 N**	**KSSW**
WXT520, Vaisala	5s	2012086-publication
CSAT 3, Campbell Scientific	10 Hz	2012086-publication
LI7500, LI-COR	10 Hz	2012086-publication
LI840, LI-COR	2 Hz	2012109-publication
CNR4, Kipp and Zonen	1 min	2012086-publication
SKL2620/5, Skye instruments	1 min	2012086-publication
SKU420/5, Skye Instruments	1 min	2012086-publication
SKU430, Skye Instruments	1 min	2012086-publication
Raytek_K, Raytek	1 min	2012086-2013339
Type 2 Thermocouple, Omega (x8)	10 min	2012086-publication
Middle Temple gardens	**0.1113 W, 51.5116 N**	**MT**
SM300, Delta T (x8)	30 min	2011163-2012116 (x2), 2011163- (x2), 2012135-2012316 (x2), 2012331-2013140 (x2), 2013155-,2013186-2015265
Royal Courts of Justice	**0.1125 W, 51.5136 N**	**RCJ**
Automated Traffic Count	1 hour	2010335- 2013136
Temple Gardens	**0.1130W, 51.5112 N**	**TEM**
ML2, Delta T	30 min	2010245-2010342
Thames Royal national Lifeboat Institution	**0.1177 W, 51.5098 N**	**TLI**
TG-4100, Tinytag (x2)	1 min	2010094-2011120, 2011137-2015265
LI6400, LI-COR	1 Hz	2013206, 2013212

Appendix 2.B Meteorological and other characteristics of the KS site

This section was adapted from the supplementary material of Björkegren *et al.* (2015) with major alterations and provides an overview of the meteorological conditions and other variables measured at the Strand campus for the study period of this thesis. It does not contain any carbon dioxide concentration measurements or any derived variables (e.g., vertical turbulent flux); these are reported in chapters 3 to 7. Note, whilst eddy flux equipment was installed within the Strand street canyon, fluxes calculated from this equipment are not reported here, as discussed in Section 3.1.2.

Time of dawn and dusk are seasonally variant (Figure 2.B.1). The canyon is shadowed by the 30.5 m high Strand building at noon and measured insolation ($K\downarrow$, Figure 2.B.1c) is accordingly reduced. A much smaller difference is observed between the incoming ($L\downarrow$) and outgoing ($L\uparrow$) longwave radiation above and within the Strand street canyon (Figure 2.B.2a vs. c and b vs. d, respectively). Net radiation may be negative overnight (Figure 2.B.3a) as heat stored within the fabric of buildings is re-emitted and reaches peaks of ca. 500 W m^{-2} during the day in summer.

The sensible heat flux (Q_H) reaches peak values approximately twice that of the latent heat flux (Q_E) (Figure 2.B.3), in other words, a Bowen ratio of 2. If individual Bowen ratio values are constrained to be within ± 50 (>95% of available data), then the majority of individual and hourly/monthly mean values (87.0% and 89.9% respectively) have a magnitude greater than one, in other words, Q_H tends to be larger than Q_E, as expected for such an area with a predominantly sealed surface and low vegetation fraction (81% and 5%, respectively, Ward *et al.,* 2015).

The diurnal cycles of photosynthetically active radiation (PAR), soil temperature and relative humidity all vary seasonally and are highest in summer (Figure 2.B.4a, b, d, June to August). The time elapsed since the last rainfall shows no such variation, with rain falling approximately every 2 to 3 days (Figure 2.B.4c). The aggregated air pressure (Figure 2.B.5b) data also show no seasonal or diurnal variation; however, the air temperature, friction velocity and mixing layer height (mixing layer height calculated using a modified gradient method from vertical backscatter profiles, see Section 4.5.3 for details) do, and reach their respective maxima during the summer. Whilst the shortwave radiative components ($K\downarrow$, $K\uparrow$, PAR) peak at ca. 12:00 GMT, all other variables with a diurnal and seasonal variation discussed thus far peak 2 to 4 hours later in the day. This suggests that the majority of the variation in the variables observed is driven by changes in insolation with a lag time of approximately 3 hours.

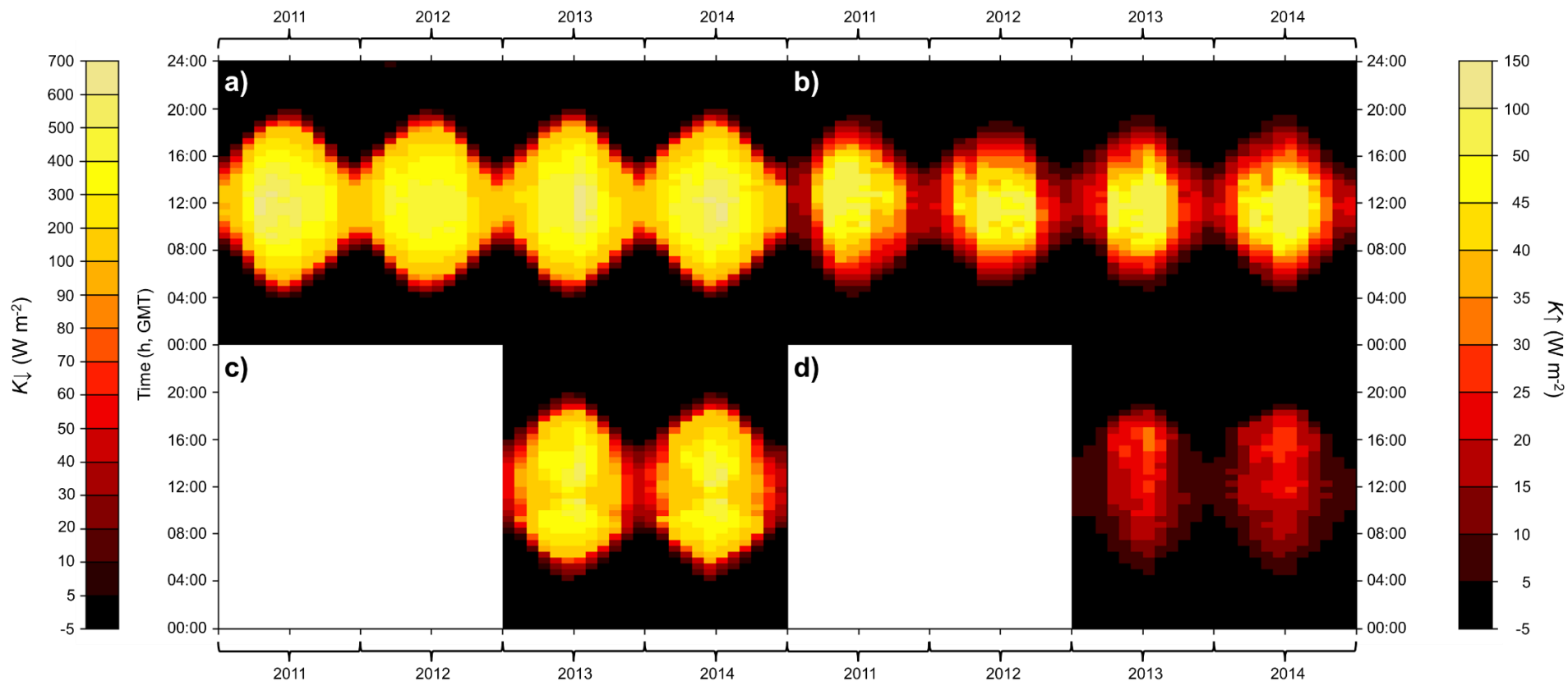

Figure 2.B.1: Mean (a, c) incoming shortwave radiation (K↓), (b, d) outgoing shortwave radiation (K↑) aggregated by hour of day and month of year measured by (a, b) CNR1 and CNR4 at KSS and KSSW respectively and (c, d) CNR1 at KSNW for years 2011 to 2014. Measurement site changed from KSS to KSSW on 2012/085. See legends (vertical outside edge of each plot) for units.

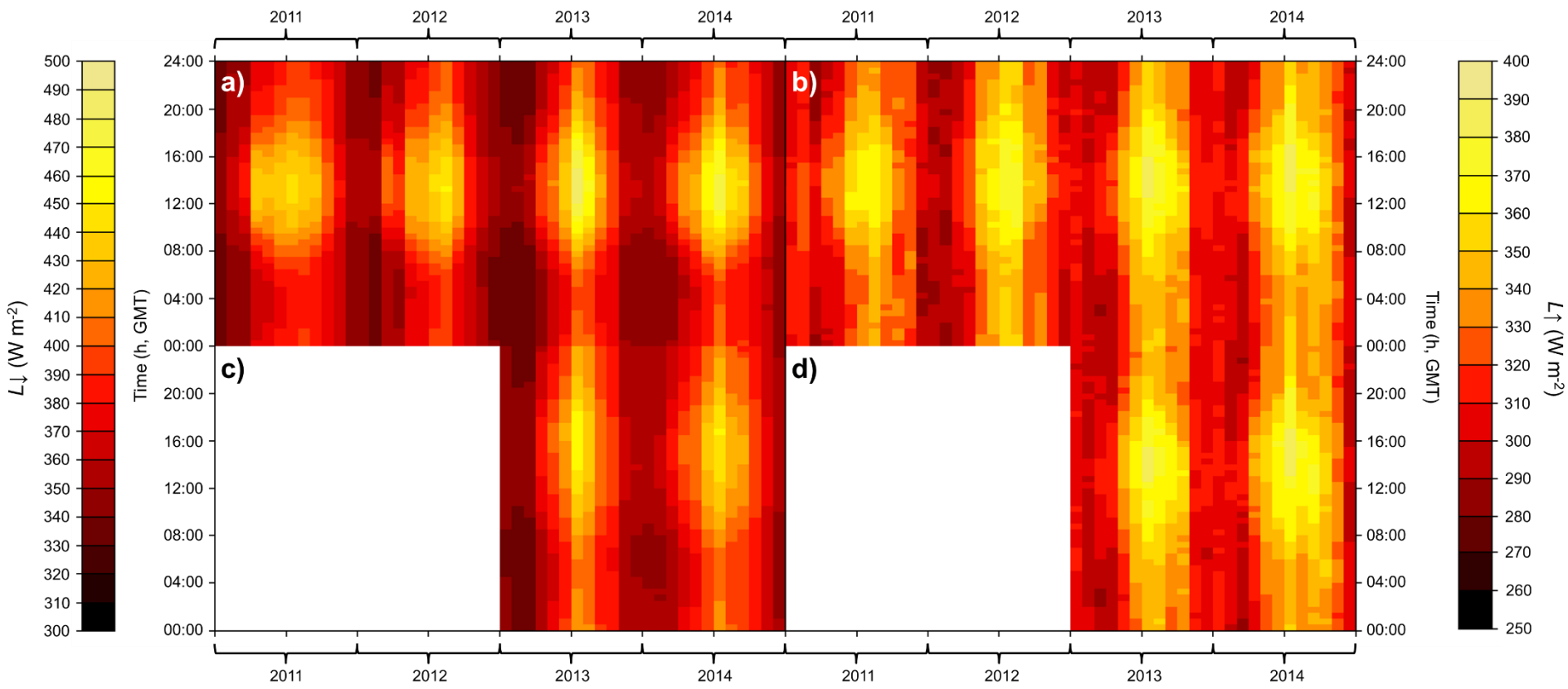

Figure 2.B.2: Mean (a, c) incoming longwave radiation (L↓), (b, d) outgoing longwave radiation (L↑) aggregated by hour of day and month of year measured by (a, b) CNR1 and CNR4 at KSS and KSSW respectively and (c, d) CNR1 at KSNW for years 2011 to 2014. Measurement site changed from KSS to KSSW on 2012/085. See legends (vertical outside edge of each plot) for units.

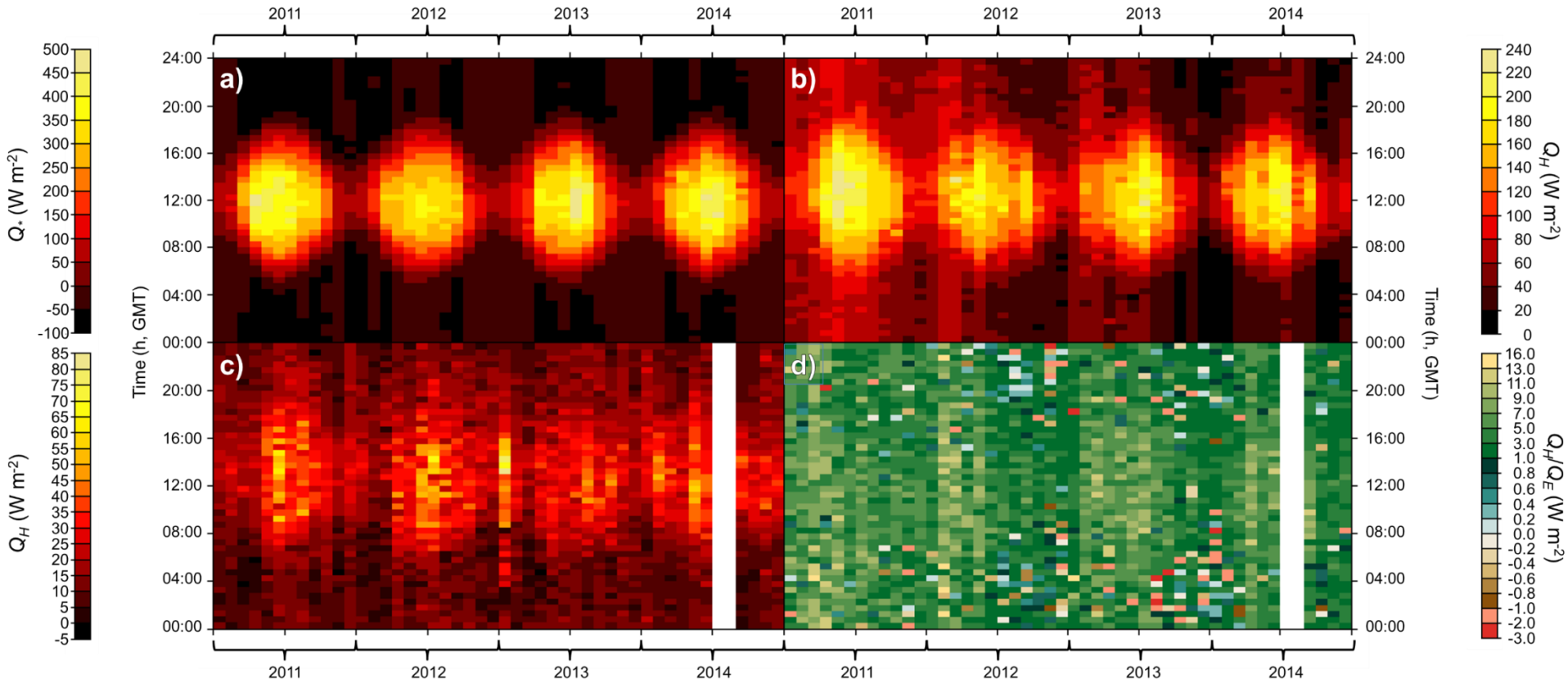

Figure 2.B.3: Mean (a) net all wave radiation (Q_*, CNR1, CNR4), (b) sensible heat flux (Q_H, CSAT3), (c) latent heat flux (Q_E, LI7500), and (d) Bowen ratio (Q_H/Q_E, CSAT3, LI7500) aggregated by hour of day and month of year at KSS and KSSW for years 2011 to 2014. Measurement site changed from KSS to KSSW on 2012/085. See legends (vertical outside edge of each plot) for units.

The prevailing wind direction at KSSW was from the south west except for February, March and November 2013, and July and September 2014, when wind tended to come from the north (Figure 2.B.6a). Wind speeds above the street canyon were typically highest between 12:00 and 16:00 GMT, with maximum hourly/monthly mean values recorded in June 2012 (Figure 2.B.6b). Despite this, wind speeds in winter (December to February) tended to be greater than those in summer (June to August). Low wind speeds (< 3 m s^{-1}) were predominantly between 02:00 and 06:00 GMT (Figure 2.B.6a). Neither above (Figure 2.B.6a) nor within-canyon (Figure 2.B.6c) wind direction showed any consistent seasonal variation, although as above the canyon, within canyon wind speeds tended to be higher in winter (Figure 2.B.6d).

A measure of atmospheric stability, z'/L (the ratio of the height above ground level less the zero plane displacement height, z', to the Obukhov length, L), was calculated (Kotthaus and Grimmond, 2014a) at half hourly resolution from data measured by a CSAT3 at KSSW, height A (Figure 2.1c, d) for April 2012 to December 2014 (Figure 2.B.7). The percentage of 30 minute periods per month classified as stable ($z'/L > 0.01$, see Section 4.5.3 for discussion of z'/L classification) ranged from 0-41% over the 33 months, April 2012 to December 2014. The maximum frequency was during the period 23:30 and 00:00 GMT in January 2014.

Stable periods occur during 5% or more of the available data in 7 of the 33 months analysed. These were December 2012, October and December 2013, and January, March, October and November 2014. Stable periods were most common in winter (December to February, 42% of all stable periods), followed by autumn (September to November, 39%), spring (March to May, 14%) and summer (June to August, 6%) (Figure 2.B.7) (season percentages do not sum to 100 due to rounding). Of the 16 half hourly periods between 22:00 and 06:00 GMT, 14 had an incidence of stable periods of 5% or greater, in other words, stable periods were more common between dusk and dawn. In 2013 and 2014 the average percentage of stable periods per day was 3.08% and 4.03% respectively. For the same periods 0.62% and 0.73% were classed as very stable ($z'/L>0.1$). These occurred predominantly overnight (20:00 to 06:00 GMT, Figure 2.B.8) and were least common in summer (6%), followed by spring (29%), winter (30%) and autumn (36%) (Figure 2.B.8). These values are slightly higher than those observed at a site nearby by Kotthaus and Grimmond (2014a). This may be due to the higher elevation of the measurements reported in this study (50.3 m above mean street level vs. 49.0 m).

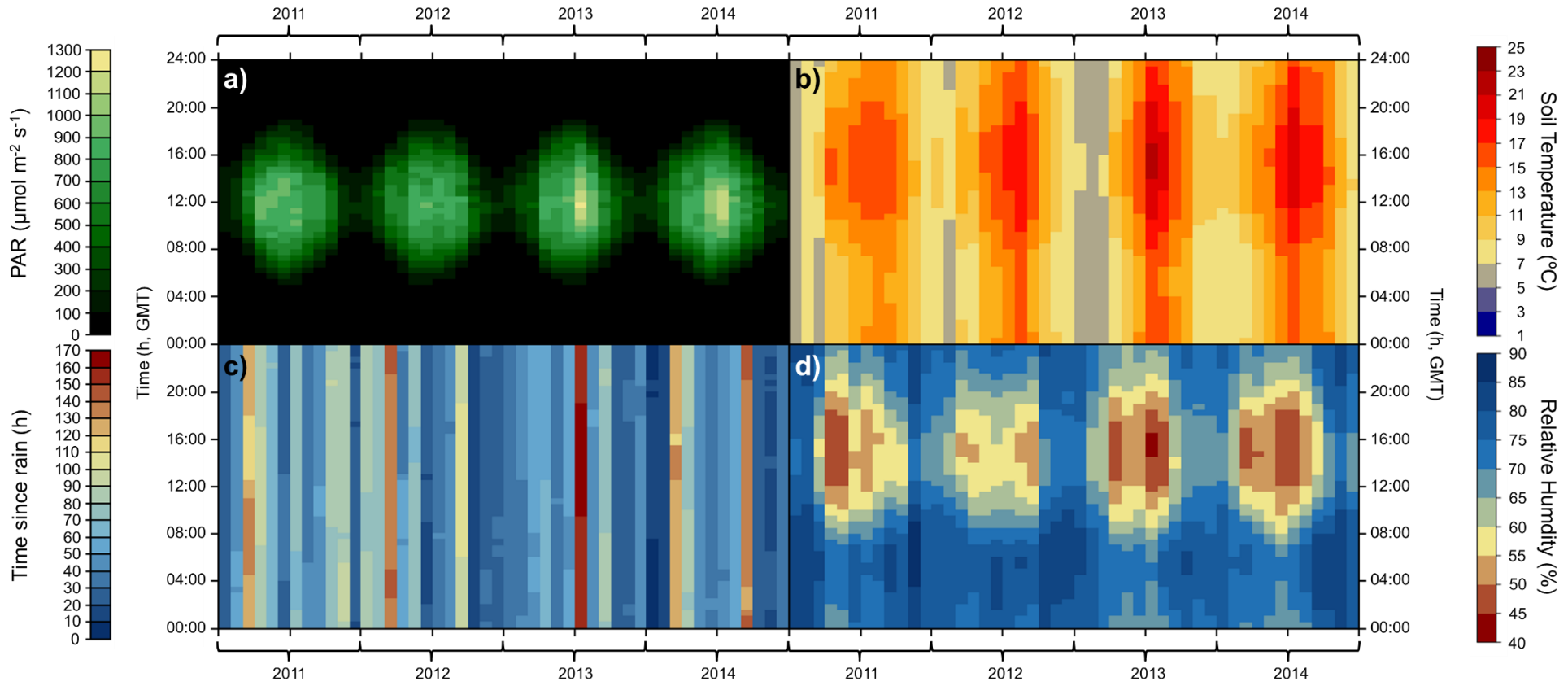

Figure 2.B.4: Mean (a) photosynthetically active radiation (PAR, SKYE), (b) soil temperature (T_{Soil}, SM300), (c) time since last rainfall (ARG100, KSS45W), and (d) relative humidity (WXT520, KSS(W)). Variables in (a) and (b) measured across multiple sites. Data aggregated by hour of day and month of year for years 2011 to 2014. See legends (vertical outside edge of each plot) for units.

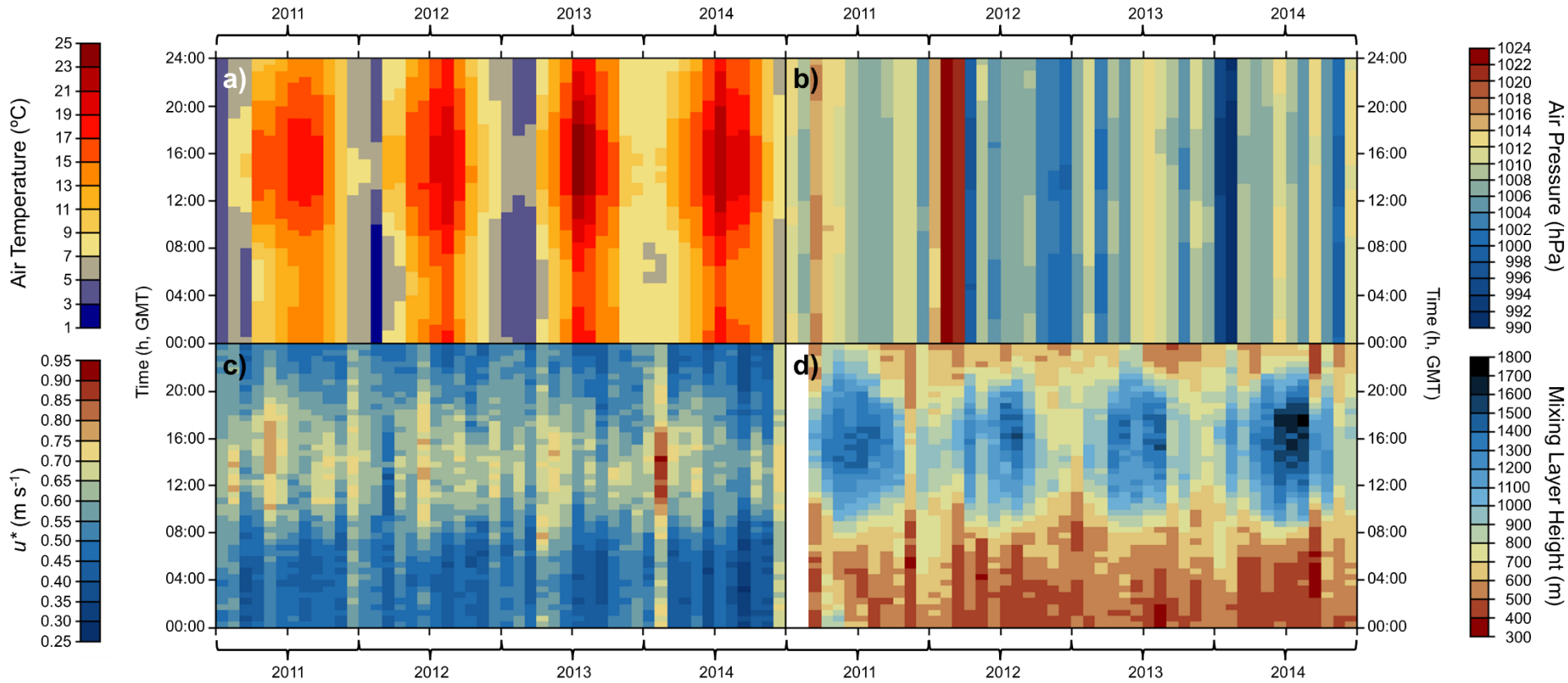

Figure 2.B.5: Mean (a) air temperature (WXT520), (b) air pressure (WXT520), (c) friction velocity (u, CSAT3), and (d) mixing layer height (CL31). (a to c) measured at height A, KSS(W), (d) calculated from vertical backscatter profile data measured at Maryleborne Road for 2011 to 2014. Data aggregated by hour of day and month of year for years 2011 to 2014. Measurement site for (a to c) changed from KSS to KSSW on 2012/085. See outside vertical edge of each plot for scale and units.*

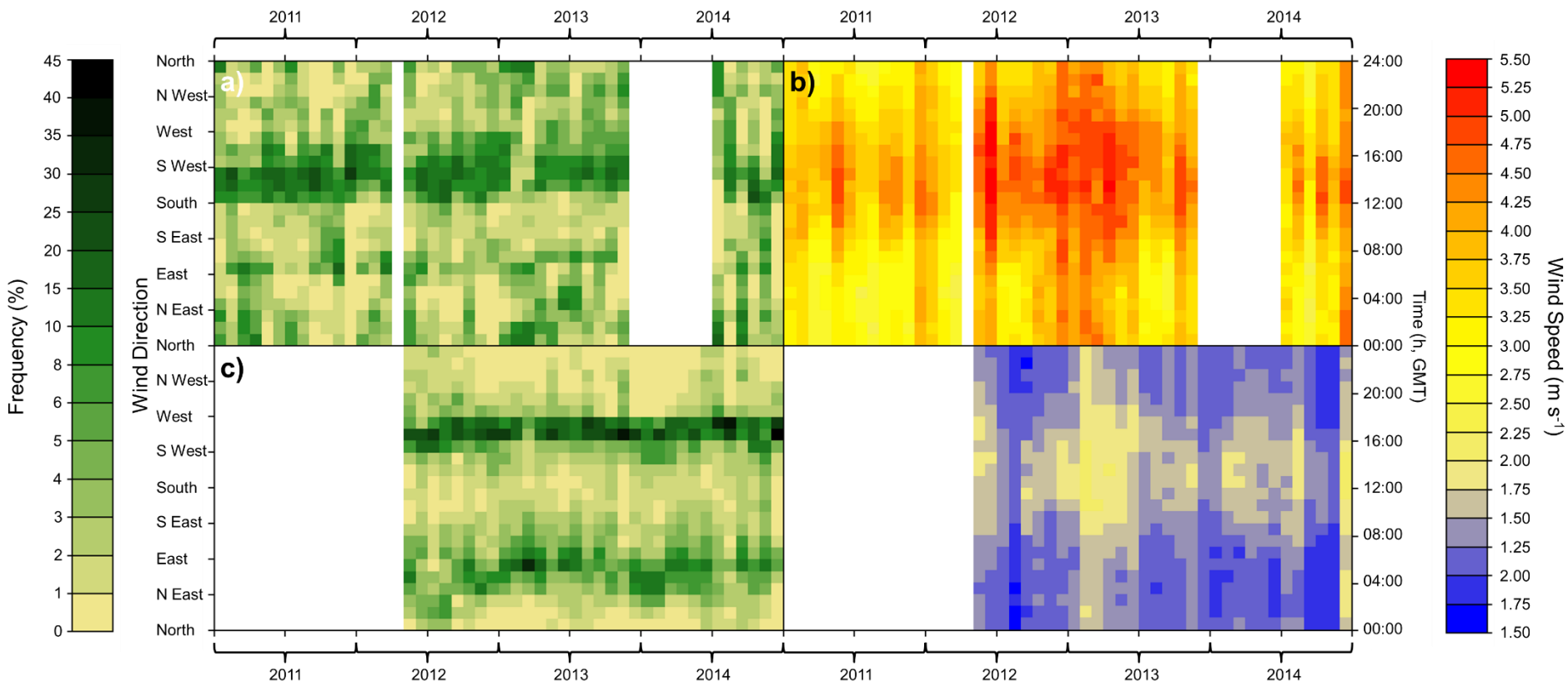

Figure 2.B.6: (a, c) Frequency of wind direction (WXT520) and (b, d) mean wind speed (WXT520) measured at (a, b) height A KSS(W) and (c, d) height F KSNW for 2011 to 2014. Measurement site changed from KSS to KSSW on 2012/085. See outside vertical edge of each plot for scale and units.

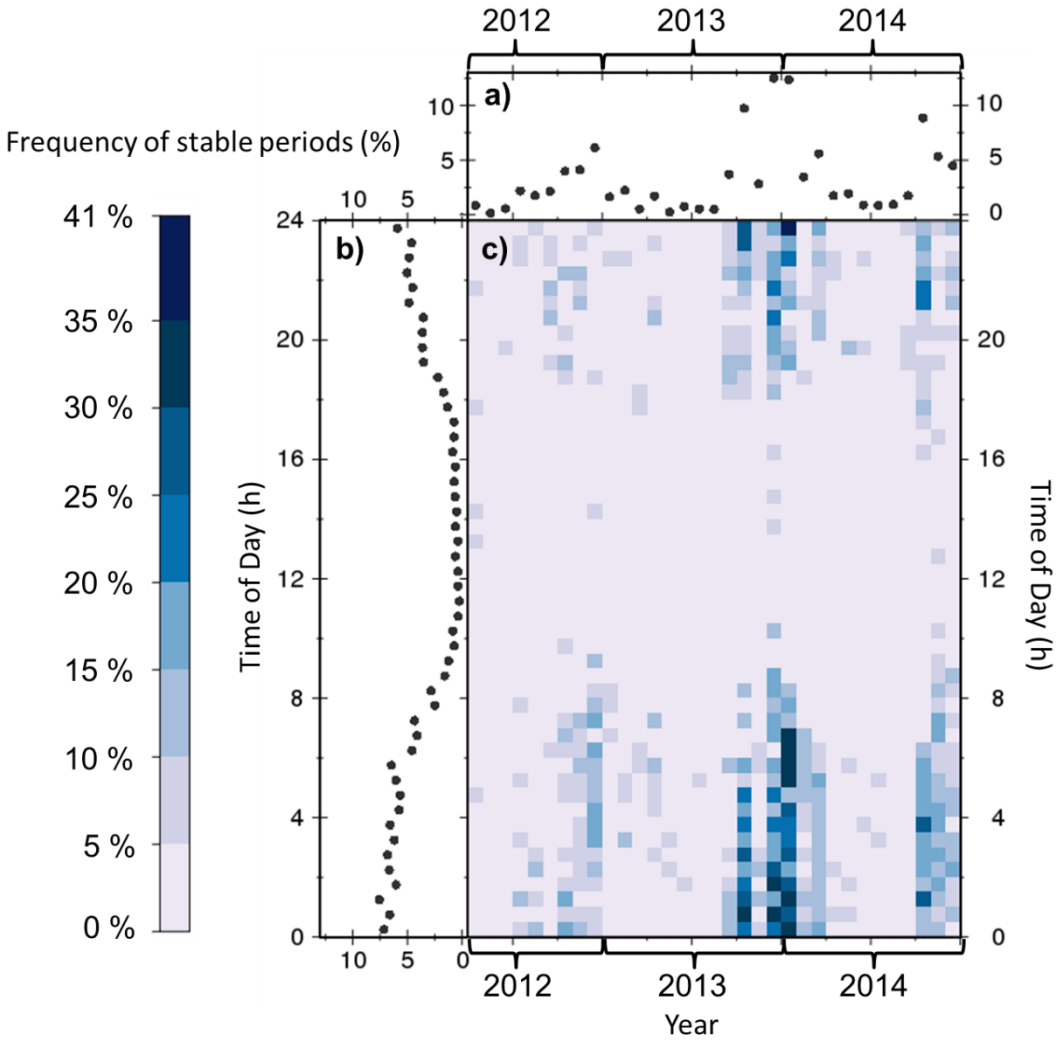

Figure 2.B.7: Frequency of half hourly periods with z'/L > 0.01 (stable atmospheric conditions) at KSSW for April 2012 to December 2014 as a percentage of total periods for which values are available (key, far left). (a) Frequency of stable periods for each month, (b) frequency of stable periods for each half hour of day (GMT), (c) frequency of stable periods by month of year (x-axis) and time of day (y-axis).

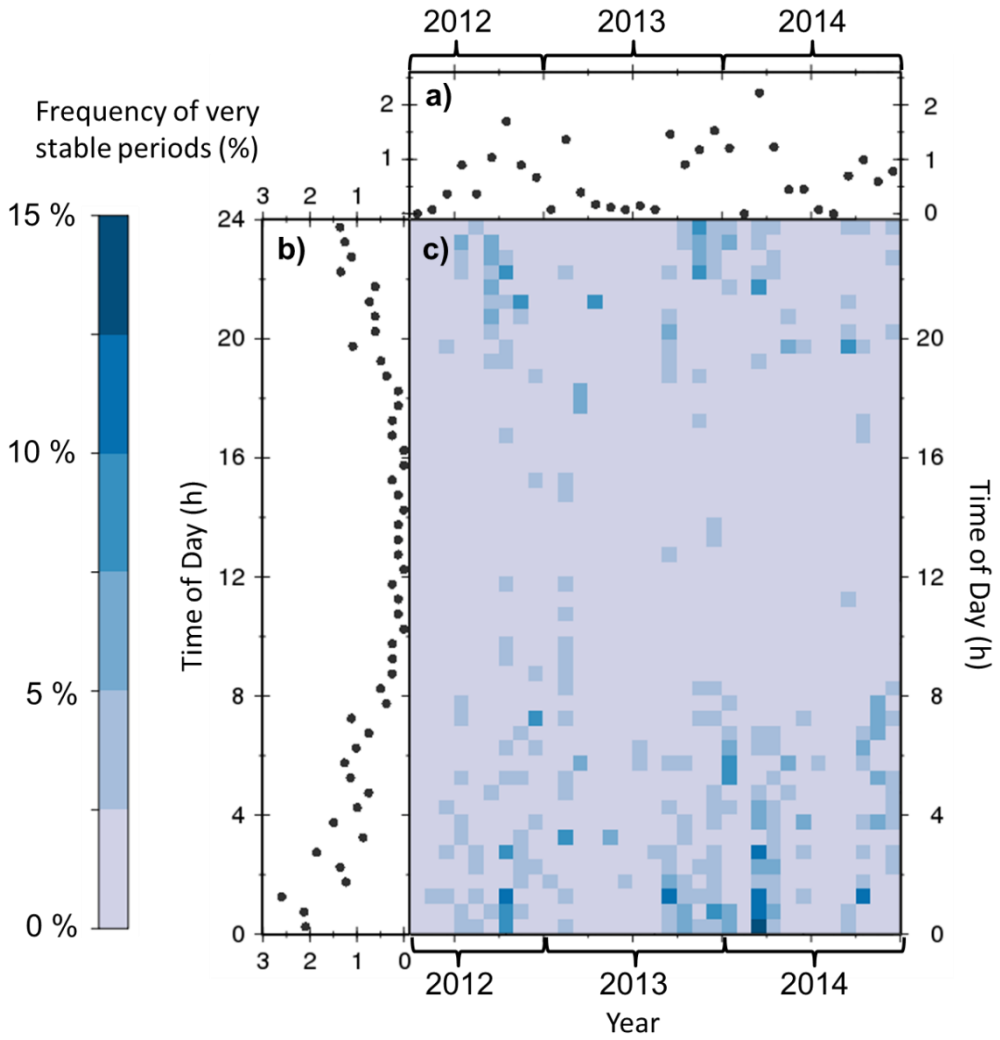

Figure 2.B.8: Frequency of half hourly periods with z'/L > 0.1 (very stable atmospheric conditions) at KSSW for April 2012 to December 2014 as a percentage of total periods for which values are available (key, far left). (a) Frequency of very stable periods for each month, (b) frequency of very stable periods for each half hour of day (GMT), (c) frequency of very stable periods by month of year (x-axis) and time of day (y-axis).

The final set of data summarised in this section are the traffic count data recorded at the Royal Courts of Justice (RCJ) as described in Section 2.2.8. Unlike the majority of variables discussed previously, no major seasonal variation is observed in total traffic volumes (Figure 2.B.9). Total traffic volumes instead vary according to diurnal and hebdomadal cycles, with weekday (Monday to Friday, Figure 2.B.9a) values much higher than weekend (Figure 2.B.9b) values and less seasonally variant. The temporal pattern of total number of vehicles at RCJ (Figure 2.1b) for 2010 to 2013 were approximately equal for both eastbound lanes (Figure 2.B.10a, b) and midway between those in the two westbound lanes (Figure 2.B.10c, d). It is likely that this is due to the crossroads just east of the traffic count location (Figure 2.8); lane 3 (westbound, offside, i.e., away from the kerb) is the lane for traffic to turn right at the crossroads, whilst lane 4 is the one for traffic headed straight over the crossroads, towards the traffic count location and, further west, the Strand. All lanes have low traffic volumes between 01:00 and 06:00 GMT on weekdays, with higher overnight traffic volumes persisting until approximately 02:00 GMT on weekends. The number of vehicles is high and sustained

throughout the day from 08:00 to 23:00 GMT and traffic patterns for individual lanes are similar between years. The features of the RCJ traffic data are discussed further in Section 4.5.1.

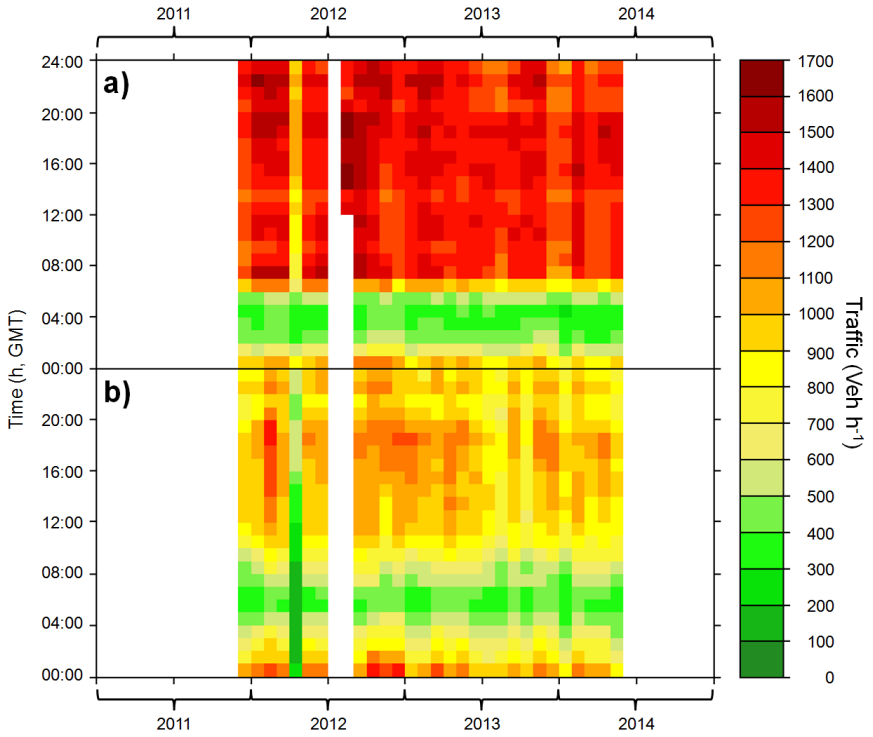

Figure 2.B.9: Mean traffic volume by hour of day and month of year at RCJ on (a) weekdays and (b) weekends for 2011 to 2014. See far right for scale.

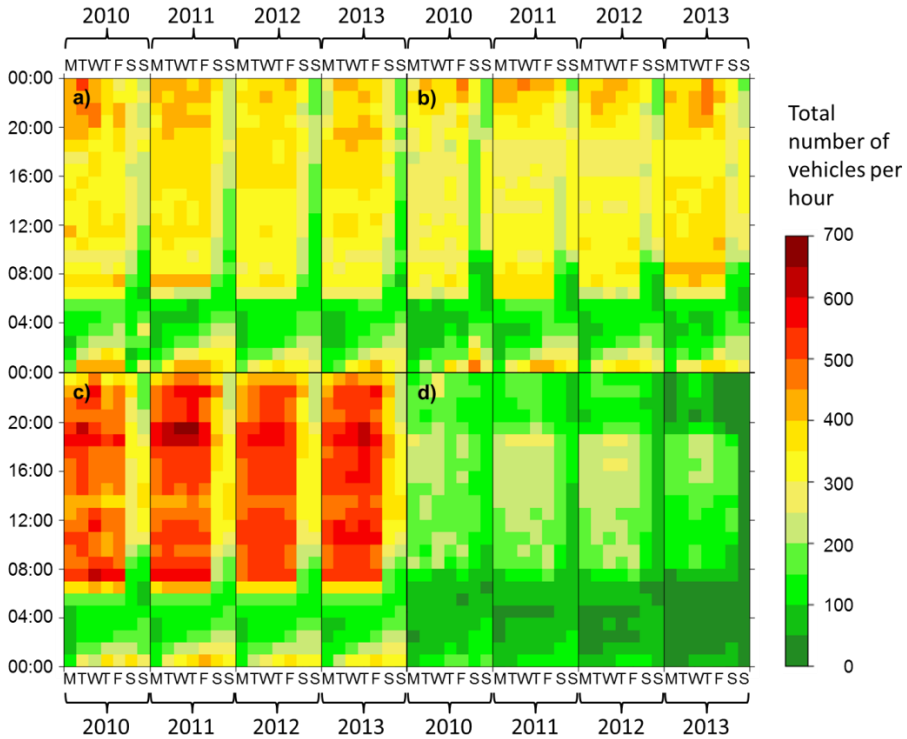

Figure 2.B.10: Hourly traffic flows (key, right) at the Royal Courts of Justice (RCJ) (TfL, 2013a) by time of day, day of week, year, and lane: (a) lane 1, eastbound nearside, (b) lane 2, eastbound offside, (c) lane 3, westbound offside, (d) lane 4, westbound nearside (Figure 2.8).

Appendix 2.C Response time of the CO_2 profiling system

This appendix discusses the response time of the air profiling system and how this is factored into data processing.

The response time of the system (T_S) can be defined as the total time taken for a sample of air to travel from the sampling point to the gas analyser (T_P) and the time for the gas analyser to respond to the change in concentration (T_R). To determine T_R, air of a known CO_2 concentrations (0 ppm, 805 ppm) were supplied directly to a valve for the 30 s before the valve was due to be deactivated. This was repeated three times, switching from 0 to 805 ppm, and three times from 805 to 0 ppm with 3 minute between step changes. Using this data both the time constant (τ) for the gas analyser's response to the step change in concentration and the amount of data that must be discarded to avoid contamination by the previous sample can be calculated.

T_S was estimated by supplying high CO_2 air across one of the sample inlets of the KSSW profile for 30 s. Three minutes were allowed for the system to restore to background concentrations and the perturbation was repeated ten times. Background $[CO_2]$ was taken to be the mean of measured $[CO_2]$ for air sampled continuously from the tested inlet for the half hour prior to testing T_S (433.72 ± 0.69 ppm (2 d.p.)). T_S was defined as the delay between when air was first supplied to the inlet and when measured $[CO_2]$ rose above background + 10%.

Subtracting T_R from T_S gives T_P, the time difference between when the sampled air parcel is present at the sampling site and when the sample is measured at the gas analyser. This value is used to correct the time stamp of the profile data.

τ was less than 3 s and the measured value reached within 10% and 1% of the final value within 4.5 and 6 s respectively. The total response time (T_S) was predicted to be 23.6 s (theoretical T_P of 19.1 s calculated from the volume of the tube and average flow rate and T_R of 4.5 s). This agrees well with the measured value of 23.12 ± 0.38 s (2 d.p.). There is some smoothing of the signal; the mean time for $[CO_2]$ > background + 10% was 32.0 s, 2 s longer than the forcing, hence only average profiles are reported in this study.

Chapter 3. Micrometeorological Theory, Data Processing and Statistical Methods[2]

This chapter outlines the theoretical background of the methods used to calculate and analyse components of the net ecosystem exchange (NEE) in this thesis (Section 3.1). It also describes some the processing of the data sets for each component (Section 3.2), and the statistical methods (Section 3.3) applied to them as part of the analysis reported in chapters 4 to 7.

NEE can be defined as "the net carbon movement between an ecosystem and the atmosphere" (Aber and Melillo, 2001). In a rural environment it is the difference between the total carbon uptake from the atmosphere by photosynthesis and the release to the atmosphere by autotrophic and heterotrophic respiration (Kirschbaum and Mueller, 2001). By analogy, in an urban environment it can be defined as the difference between the sum of all CO_2 sources within a given volume and the sum of the CO_2 sinks. This thesis will discuss NEE from an atmospheric perspective, i.e., uptake of CO_2 from the atmosphere due to photosynthesis is a loss and release to the atmosphere by respiration or combustion is a gain:

$$\text{NEE} = \Sigma(\text{Sources}) - \Sigma(\text{Sinks}) \tag{3.1}$$

As discussed (Section 1.2), NEE can be calculated using either inventory or micrometeorological methods. The majority of this thesis analyses data obtained by the latter method, though ancillary inventory approach measurements are described in Chapter 2, reported in Chapter 7, and used for interpretation of results. This chapter will therefore begin with a description of the derivation and calculation of each term in the NEE equation as derived from mass conservation and the continuity equations (Aubinet, 2003).

$$NEE = \Delta C_S + F_{CO_2} + A_z + A_{xy}$$

$$= \int_0^{z_h} \frac{\partial \overline{[CO_2]}}{\partial t} dz + \left(\overline{w'[CO_2]'}\right)_{z_h} + \int_0^{z_h} \bar{w}(z) \frac{\partial \overline{[CO_2]}}{\partial z} dz + \int_0^{z_h} \left(\bar{u}(z) \frac{\partial \overline{[CO_2]}}{\partial x} + \bar{v}(z) \frac{\partial \overline{[CO_2]}}{\partial y}\right) dz \tag{3.2}$$

These are (left to right) CO_2 storage (ΔC_S), vertical CO_2 flux (F_{CO2}), and CO_2 advection (A_{xy} and A_z), which are calculated from time (t) average (overbar) and instantaneous deviation from the mean ($'$) of atmospheric CO_2 concentration ($[CO_2]$), and the zonal (u), meridional (v) and vertical (w) wind components measured over height (z) up to a position z_h. As these quantities are observed in a predominantly turbulent boundary layer, deterministic analysis is computationally intensive. The third section of this chapter therefore provides the statistical methods used to analyse the data, including power spectra, wavelet analysis and quadrant analysis.

[2] Parts of section 3.1.1, and Appendix 3.A, were published as part of Bjorkegren *et al.* (2015).

3.1 Components of Net Ecosystem Exchange

3.1.1 CO_2 Storage

CO_2 storage is ideally evaluated as the change in average concentration ($\overline{[CO_2]}$) with time (*t*), integrated over the vertical extent (z_h) of the air volume of interest (modified from Aubinet *et al.,* 2005):

$$\Delta C_S = \int_0^{z_h} \left(\frac{\partial \overline{[CO_2]}}{\partial t} \right) dz \tag{3.3}$$

Formal manipulation of the mass balance equation allows the calculation of the storage term as the difference between two instantaneous CO_2 profiles divided by the length of the period, *T*, between the two and integrated over the vertical extent of the profile (Finnigan, 2006):

$$\int_0^{z_h} \frac{\overline{\partial [CO_2]}}{\partial t} dz = \int_0^{z_h} \left(\frac{1}{T} \int_{-T/2}^{T/2} \frac{\partial [CO_2]}{\partial t} dt \right) dz = \int_0^{z_h} \frac{1}{T} \left([CO_2]_{z,t=\frac{T}{2}} - [CO_2]_{z,t=-\frac{T}{2}} \right) dz$$

$$\cong \frac{1}{T} \sum_i \left(\overline{[CO_2]}_{i,t=\frac{T}{2}} - \overline{[CO_2]}_{i,t=-\frac{T}{2}} \right) \Delta z_i \tag{3.4}$$

This requires simultaneous and continuous measurements at all heights of the profile. In practice it is easier to make continuous measurements in time rather than in space, and the exact form is often replaced by the difference between two time averaged profiles at the start and end of the vertical flux averaging period (Aubinet *et al., 2*005; Araujo *et al., 2*010, 3.4 RHS) evaluated over a finite number of measurement points (z_i). This also avoid a second problem; as noted in the literature (Finnigan, 2006; Yang *et al., 2*007), instantaneous measurements may be easily biased by errant gusts.

The approach to calculate CO_2 storage depends upon the number of locations at which CO_2 concentration data are collected. 'Single height' CO_2 storage (ΔC_{SS}) is calculated from $[CO_2]$ data at one location, usually by eddy covariance equipment in the inertial sub-layer (Nemitz *et al.,* 2002; Crawford and Christen, 2014). Alternatively, in the second approach, the 'profile' method, ΔC_S can be calculated from data collected at multiple heights (ΔC_{SP}). The profile method uses a vertical $[CO_2]$ profile at heights z_i, which is generally measured by cycling through all the heights within a set time period with a data-logger controlled valve array (Xu *et al.,* 1999; Molder *et al.,* 2000; Vogt *et al.,* 2006; Hutyra *et al.,* 2008). This cycle period may not be the same as the averaging period used in the ΔC_{SP} calculation, for example, measurements collected with a sampling interval, t_s, of 2 Hz for 75 s at 8 heights, giving a full profile cycle every 10 minutes, may be used to calculate ΔC_{SP} with an averaging period (*T*) of 30 minutes. The storage is calculated as the sum of the changes in time averaged concentration ($\overline{\overline{[CO_2]}}$) between time $t=-T/2$ and $t=T/2$ for each location (*i*) in the profile, weighted by the vertical span, Δz_i, over which each profile measurement is considered to be representative and divided by the averaging period, which can be expressed as (modified from Aubinet *et al.,* 2005):

$$\Delta C_{SP} = \frac{1}{T} \sum_i \left(\overline{[CO_2]}_{i,t=\frac{T}{2}} - \overline{[CO_2]}_{i,t=-\frac{T}{2}} \right) \Delta z_i \tag{3.5}$$

If the measurements at each height are not made concurrently, $[CO_2]$ at each height may first be interpolated in time to generate instantaneous profiles from which ΔC_{SP} can be calculated, though this is neglected in some cases (Iwata *et al.,* 2005). The impact of interpolation on calculated ΔC_{SP} is evaluated in Appendix 3.A.

The single height method is a simplification of the profile method to one height, which is usually the height of the eddy covariance equipment (z_h). The change in $[CO_2]$ with time at z_h is weighted by the vertical distance from the ground to the measurement point. The single height CO_2 storage (ΔC_{SS}) is given by (modified from Nemitz *et al.*, 2002):

$$\Delta C_{SS} = \frac{\Delta[CO_2]}{\Delta t} z_h \quad (3.6)$$

As the data are continuous the change in the instantaneous CO_2 concentration with time ($\Delta[CO_2]/\Delta t$) can be used instead of the change in the time averaged CO_2 concentration with time ($\overline{[CO_2]}/\Delta t$), though it may still be advisable to average in time to reduce measurement noise (Finnigan, 2006).

The ΔC_{SS} calculation assumes any change in $[CO_2]$ below the measurement height results in a change of equivalent magnitude at the measurement height. This assumption appears not to be supported by any evidence in the literature; reported diurnal cycles of CO_2 mixing ratios in the roughness sub-layer over both rural (e.g., Xu *et al.,* 1999) and urban (e.g., Lietzke and Vogt, 2013) surfaces are known to vary with height. This problem is particularly acute during periods of low turbulence, such as at night or during cold weather, where measurements above the surface layer may become decoupled from processes near ground level (Helfter *et al.,* 2011).

If temporal variability is large compared to the spatial variability, the single height method may provide a more accurate measure of storage than the profile method as the maximum data availability at each sample location for the latter may be $1/n_i$ of the total time series, where n_i is the number of heights. Data availability may be improved by installation of multiple gas analysers (Simpson *et al.,* 1998; Siebicke *et al.,* 2010); however, this introduces the problem of ensuring that measurements are comparable between heights. In this project this issue was addressed by installation of co-located air sampling points to allow inter-comparison of instruments.

It has been proposed that using time-averaged $[CO_2]$ to calculate CO_2 storage under-estimates the magnitude of the change in CO_2 stored within a volume by at least a factor of two (Finnigan, 2006). In other words, although both ΔC_{SP} and ΔC_{SS} have, in previous work, been assumed to represent (with some degree of uncertainty) the true ΔC_S signal, neither can strictly be said to do so. Theoretical calculations (Finnigan, 2006) demonstrate that the magnitude of the error varies with the ratio of the integral timescale of the turbulent time series (ITT, Section 3.3.2) to the averaging period of the CO_2 profile or resolution of the point measurement (Finnigan, 2006). This hypothesis is tested in Section 5.3.2.4.

3.1.2 Vertical Flux

The measured CO_2 concentration time series results from a superposition of several processes at different temporal and spatial scales. The signals of interest to this thesis are generated by turbulence in the urban boundary layer and as such have characteristic time scales on the order of an hour or less. These instantaneous or turbulent deviations (x_t') in the measured signal (x_t) can therefore be separated from the longer-term 'mean' ($\bar{x}_t$) or synoptic signal, which in this study is taken over 30 minutes (Stull, 1988).

$$x'_t = x_t - \bar{x}_t \tag{3.7}$$

The process of separating turbulent deviations from longer term means is called Reynolds decomposition. Reynolds decomposition requires certain postulates, specifically that the mean of all perturbations is zero, the mean of a mean is equal to a mean, and that a mean operator is commutative unless both variables are perturbations. In practice this requires the signal be stationary over the time period averaged (Stull, 1988). If the data to be averaged are not stationary, then a block average is meaningless. For data sets where non-stationarity is rare, it may be viable to simply reject any periods for which the block-averages for sub-intervals differ by more than a set amount from each other or from the overall average. Data sets which have a large volume of non-stationary data may require shorter averaging intervals or the fitting and removal of a trend by a linear or higher order model.

The turbulent component of the vertical flux of CO_2 is calculated as the covariance between the instantaneous deviations from the mean values of the vertical wind velocity (w') and trace gas concentration ($[CO_2]'$) (e.g., Grimmond *et al., 2*002; Baldocchi, 2003; Burba and Anderson, 2005; Velasco and Roth, 2010).

$$F_{CO2} = \overline{[CO_2]'w'} = \frac{1}{N}\sum_{i=1}^{N} w'_i [CO_2]'_i \tag{3.8}$$

High temporal resolution (10-20 Hz) measurements of the wind velocity in three dimensions and the CO_2 concentration are required. The equipment described in Section 2.2.2 is typical, consisting of a sonic anemometer and a rapid response gas analyser.

One of the major assumptions of this method is that the flux is fully turbulent, i.e., that the majority of the net vertical transport of scalar quantities is via eddies (Burba and Anderson, 2005). Observations at KSS(W) support this assumption and suggest this method of flux calculation is generally viable as over 90% of the half hourly periods observed were unstable (z'/L < -0.01) (Section 4.5.3). The tendency towards unstable conditions, even at night, is due to enhanced mechanical mixing over urban areas (roughness length) and enhanced convective mixing (e.g., urban heat island effect).

The vertical flux equation (3.8) is an approximation, made possible by the acceptance of certain assumptions. In addition to the assumptions of stationarity and turbulence (discussed above, Section 3.1.2) are two others (Lee, 1998; Burba and Anderson, 2005): any fluctuations in air density are negligible, and there is no convergence or divergence of flow (i.e., horizontal

advection is negligible, and the mean vertical wind component is equal to zero). Other assumptions concern the relation of the measurement point to the signal of interest: namely it is assumed that a point measurement can represent an area of interest, and that the measurement is influenced only by the area or processes of interest. These assumptions and their validity are summarised in Table 3.1.

Even if the equipment is sited such that all required assumptions are reasonable, there are still a number of potential sources of error which must be addressed during processing (Table 3.2, Section 2.2.2). The assumptions in Table 3.1 were not considered reasonable for the KSNW or KSB sites due to the relatively low sensor height ($z_i/z_b < 1$) and turbulent vertical CO_2 fluxes from these sites are not reported in this study.

Table 3.1: Summary of assumptions required for eddy covariance, derived from Burba and Anderson (2005).

Assumption	Validity
A point measurement can be representative of an upwind area.	Comparison of aggregation with EC, comparison of lower EC stations with higher towers.
Flux is fully turbulent	A reasonable assumption given the high roughness length and associated degree of mechanical mixing, verified by observations.
Average of fluctuations is zero	Use the Ogive test to select the most appropriate averaging interval (Sun *et al., 2*006).
Air density fluctuations negligible	Correct with Webb-Pearman-Leuning (WPL) function (Webb *et al.*, 1980; Leuning, 2007).
Flow convergence and divergence negligible	Primarily a problem over sloping terrain. London is built upon a floodplain but some correction for flow divergence will still be necessary.

Table 3.2: Potential sources of error for measurement by Eddy Covariance. Modified from Burba and Anderson (2005).

Source of Error	Approximate Range	Remedy
Frequency response	5-30%	Minimise necessity by using open path sensors sampling at a frequency > 2 times that of eddies measured, and placed in close proximity to each other. Frequency Response corrections (Burba and Anderson, 2005).
Time Delay	5-15%	Insert time offset into data processing program
Spikes, noise	0-15%	Spike removal
Unlevelled instrument/flow	0-25%	Coordinate rotation
Density fluctuation	0-50%	WPL correction (Webb *et al.*, 1980; Leuning, 2007)
Band Broadening for Non-Dispersive Infra-Red gas analyser.	0-5%	Band-broadening correction, LI7500 internal software (LI-COR, 2003).
Spectroscopic effect for LASER	0-30%	No standard correction available
Missing data filling	0-20%	Methodology/tests. Spare sensors/data loggers kept on hand in case of instrument breakdown.

3.1.3 Horizontal Advection

The advection component of the net ecosystem exchange (3.2) in the horizontal *x* direction, A_x, can be calculated as the product of the mean horizontal concentration gradient and the mean wind speed along *x*. For the Strand street canyon, *x* is defined as parallel to the street canyon axis, running negative to positive west to east.

$$A_x = \int_0^{z_h} \left(\bar{u}(z) \frac{\partial \overline{[CO_2]}}{\partial x} \right) dz \tag{3.9}$$

The advection term can be calculated from horizontal CO_2 profiles (Aubinet *et al.*, 2005) or from single tower measurements (Hong *et al.*, 2008). Where multiple horizontal profiles at different levels exist, as at KS with KSLH and KSUH (Configurations C5, C6, C8, Table 2.2) the advection term can be vertically integrated over the height of the notional volume of air for which the measurements are considered representative.

In this thesis advection was calculated from switched horizontal profiles with data recorded at 2 Hz for 75 s at each sample point. The data were processed as described in Section 2.2.1. Run averages were linearly interpolated to a regular one minute time series (*approx*, R Development Core Team, 2013) (see Appendix 3.A for the impact of interpolation on results). Interpolated data were discarded (set to NA) if the gap between two samples was greater than 15 minute (1.5 times the cycle time) i.e., if data were missing. The 30 minute average CO_2 concentrations were calculated from time periods with greater than 50% data availability. Values from western sampling points were subtracted from those from eastern sampling points for the same time period and divided by the spatial separation to give $\partial \overline{[CO_2]} / \partial x$. Half hourly wind speed and direction data from the CSAT and WXT instruments at KSSW and KSNW was used to calculate the along and across canyon wind components. $\partial \overline{[CO_2]} / \partial x$ was multiplied by the along-canyon wind component, weighted by the vertical span over which the measurements were deemed relevant and summed over the vertical extent of the two profiles to give the overall along-canyon advection term.

3.1.4 Vertical Advection

The vertical advection of CO_2, A_z, can be calculated as the product of the mean vertical velocity at z_h, $\overline{w}$, and the difference between the mean CO_2 concentration across the vertical span of the air volume of interest ($\langle \overline{[CO_2]} \rangle$) and the average CO_2 concentration at z_h ($\overline{[CO_2]_h}$) following Lee (1998):

$$A_z = \overline{w} \left(\overline{[CO_2]_h} - \langle \overline{[CO_2]} \rangle \right) \tag{3.10}$$

As the CO_2 concentrations required are time-averaged rather than instantaneous, A_z can be calculated from a switched vertical profile provided the average concentrations for the samples taken at each height are considered to be representative for the entire cycle period. In this thesis vertical advection was calculated from data collected at 2 Hz for 75s at each sample point in the vertical profile and processed as described in Section 2.2.1. As CO_2 concentrations at each measurement location were averaged over 30 minutes (the same period as the vertical

flux) prior to calculation of the difference from the CO_2 concentration at z_h, no explicit interpolation in time was performed. Mean vertical wind velocity was derived from 10Hz measurements made by CSAT3 at z_h, KSSW (Section 2.2.2).

3.2 Filling gaps in the measurement time series

As noted in Sections 2.2.1 and 2.2.2, the data sets from which the micrometeorological components of NEE are calculated are not complete but have periods of missing data. If these gaps are not addressed they may result in a systematic error when calculating e.g., annual net emissions. In this section the methods used to fill data gaps with appropriate values is reported.

3.2.1 CO_2 storage measurements

Although attempts to model CO_2 concentrations and calculated CO_2 storage values from other data were unsuccessful (Section 5.4), the seasonal and diurnal cycles observed in the aggregated CO_2 storage data (Section 5.1, Appendix 5.A) enable the use of mean diurnal cycles from appropriately stratified (hour of day, weekday vs. weekend, month) data to substitute for missing data. This reduced gaps from 81.9% to 100% for the 2012/153-2013/151 (1st June 2012 to 31st May 2013) period. Gaps were distributed evenly across all hours of day but not month of the year. The percentage of data that was missing was highest in March (58.1% missing), May (32.3%) and June (30.0%) and lowest in August (0.0%).

3.2.2 Vertical flux measurements

The EC vertical CO_2 flux measurements at KSSW had initial data availability (Table 3.3) of 64.5% to 79.7%. Whilst data availability were reasonably consistent by time of day (66.2% to 71.0%), the monthly availability were very different (24.9% to 84.9%) (Figure 3.1). The gaps were filled with averages derived from the same month, time of day and day of week (weekday vs. weekend) for (round 1) the same year and (round 2) 2012 to 2014.

Given that the vertical CO_2 flux varies with time of day, month of year and with whether the day is a working day (weekdays, Monday to Friday) or a rest day (weekend, Saturday to Sunday) (Figure 3.2a, b), filling data gaps with a simple annual average would lead to unrealistic 30 minute estimates of net emissions and (due to the unequal distribution of data gaps across the year) bias the estimation of net annual emissions. Monthly mean diurnal cycles for April to September showed relatively little inter-annual variation (Figure 3.2a, b); however, differences between the years were more pronounced for the other months. Missing data were therefore first filled by the appropriate half hourly/day of week/monthly mean value derived from data collected that same year (round 1, Table 3.3). Any gaps still present after this round were filled with the appropriate half hourly/day of week/monthly mean value derived from all data collected 2012/095 to 2014/365 (round 2, Table 3.3). The first round was capable of filling at least half of all data gaps, with the second filling all that remained. Vertical flux data were not stratified or gap-filled by wind direction as comparison of vertical CO_2 flux with wind direction measured at height A, KSSW (WXT520) for 2012 to 2014 suggested that the latter had little predictive value (Figure 3.3) due to low variation with wind direction from the median value. The sector with the

greatest variation from the median value (240 - 360º, Figure 3.3) also had the greatest range of CO_2 flux values and therefore the most uncertainty if the wind direction was used as a predictive factor for filling data gaps.

Table 3.3: Data availability for KSSW EC fluxes (30 minute) initially and after gap filling round 1. No gaps existed after round 2.

Time Period	Total number (30 min)	Missing data number (%)	Missing after round 1 number (%)
2012/095 – 2012/366	13056	2650 (20.3)	0 (0.0)
2013	17520	6213 (35.5)	384 (2.2)
2014	17520	6035 (34.4)	2976 (17.0)
2012/153 – 2013/151	17520	5774 (33.0)	384 (2.2)

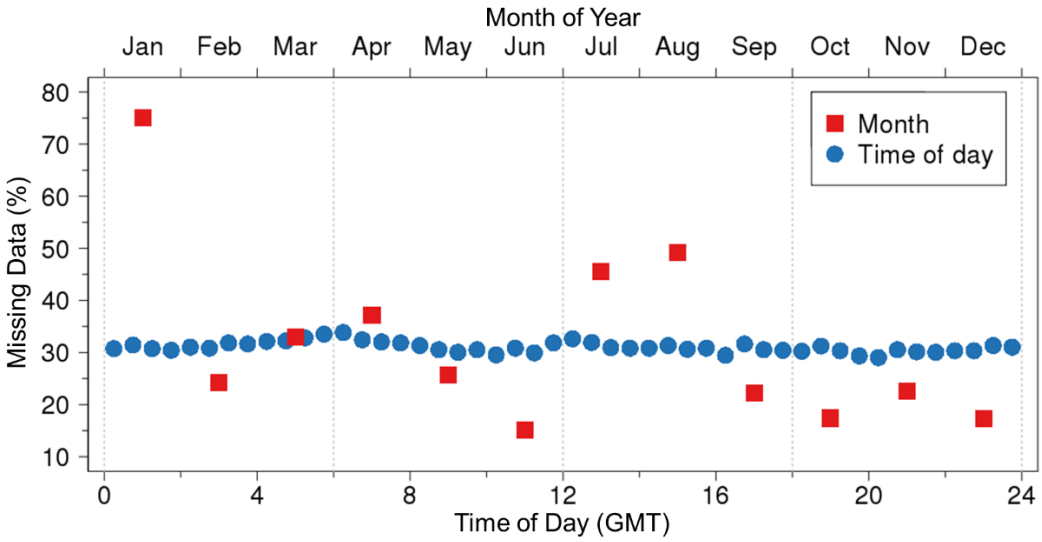

Figure 3.1: Missing EC data (height A, Figure 2.1d; KSSW, %) 2012/095 to 2014/365 by month of year (red, square) and time of day (half hourly periods, blue, circles).

The effect of the gap filling on monthly total emissions calculated from the vertical flux only was investigated as follows. Two months, one in summer (June 2013) and one in winter (December 2014), were selected as base data sets. These were chosen from all vertical flux data measured at height A, KSSW for 2012 to 2014 as having the best data availability (8.5% and 10.8% for June 2013 and December 2014 respectively). 'Gappy' data sets were then constructed by removing data to generate overall data availabilities at 10% intervals from 90% to 0%. This was done 100 times for all data availabilities except 0% (only 1 possible configuration) and 90% for the December 2014 data set (data availability initially lower that 90%). The 'gappy' data sets were then gap filled using the methods described previously. Good agreement between the gap filled and base or best estimates of the monthly total emissions were found for data availabilities of 90% to 30% (missing data 10% to 70%, Figure 3.4), suggesting that the method is appropriate for the data availabilities of the study period (Table 3.3).

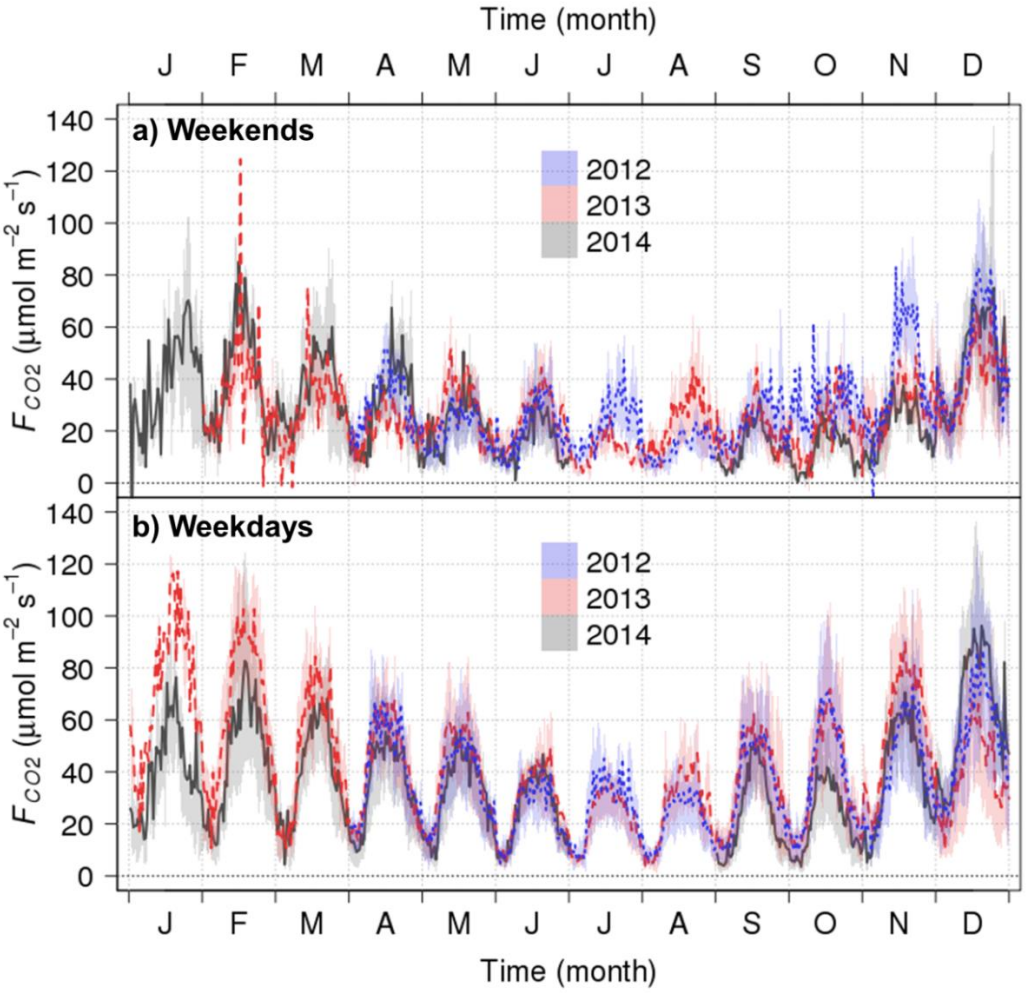

Figure 3.2: Mean monthly (a) weekend and (b) weekday diurnal cycles of vertical CO_2 flux (F_{CO2}) measured at height A, KSSW (Figure 2.1d) in 2012 to 2014 inclusive. Line denotes mean, shaded region denotes interquartile range.

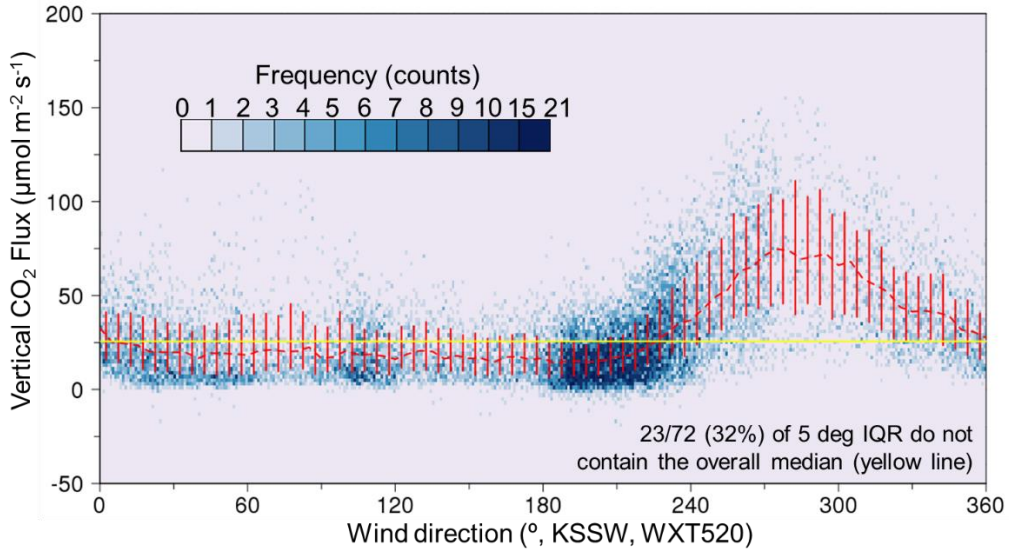

Figure 3.3: Vertical CO_2 flux with horizontal wind direction at height A, KSSW (Figure 2.1d) for 2012 to 2014. Vertical lines: interquartile range (IQR) of vertical flux for each 5° wind sector, horizontal dash line: median of vertical flux for each 5° wind sector, horizontal solid line: overall median vertical flux.

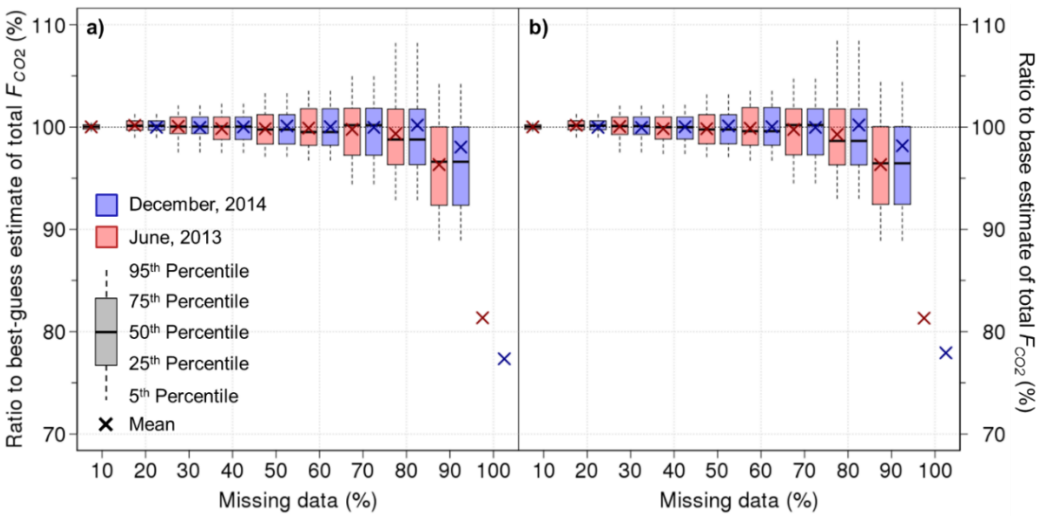

Figure 3.4: Ratio of total monthly emissions calculated from vertical flux data (F_{CO2}) for (red) June 2013 and (blue) December 2014 by percentage of data missing. (a) Compares completely gap-filled data sets to a 'best guess' estimate i.e., the gap-filled base data set, (b) compares datasets with only the additional missing data gap filled (i.e., retaining the gaps from the base data set) to the base (non-gap filled) data set.

3.2.3 Horizontal advection measurements

The calculated horizontal advection showed some seasonal variation (Figure 6.15). The data gaps were not evenly distributed across the year (Figure 3.5). Examination of the components of the horizontal advection calculation (horizontal $[CO_2]$ gradient at KSLH, horizontal $[CO_2]$ gradient at KSUH, along-canyon wind velocity) found this to be mostly due to the horizontal CO_2 concentration gradient ($\Delta[CO_2]/\Delta x$) along the KS building balcony (KSLH, Figure 6.12a). There was no evidence for similar seasonal patterns at KSUH, ca. 10 m above (Figure 6.12b). Nevertheless, $\Delta[CO_2]/\Delta x$ for both horizontal profiles was gap filled with monthly mean diurnal cycles on the basis of the characteristics of $\Delta[CO_2]/\Delta x$ at KSLH and consistency of method for both sites.

The along-road wind component was gap filled by fitting a loess line to the mean of the within-canyon along road wind component (WXT520, KSNW) to the above canyon wind direction (WXT520, KSSW) (Figure 3.6). Comparison of the residuals from the loess line with wind speed showed increasing magnitude with wind speed; however, as the direction of the wind relative to the CO_2 concentration gradient is crucial for the calculation of horizontal advection and this could not be reasonably determined from the data, the along-canyon wind velocity was gap filled only by the loess values with no adjustment for wind speed.

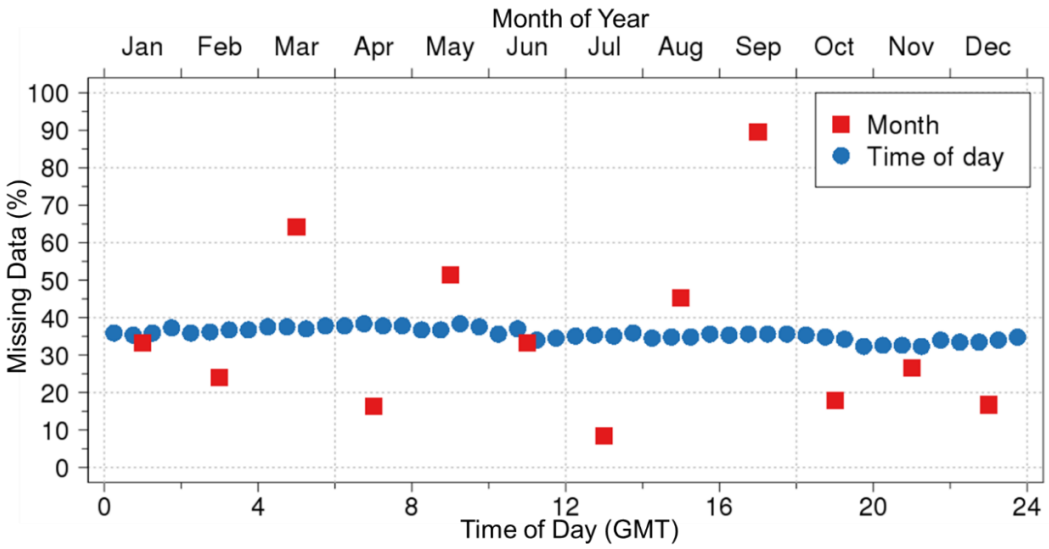

Figure 3.5: Missing horizontal advection data (2012/153 - 2013/151) by month of year (red, square) and time of day (half hourly periods, blue, circles).

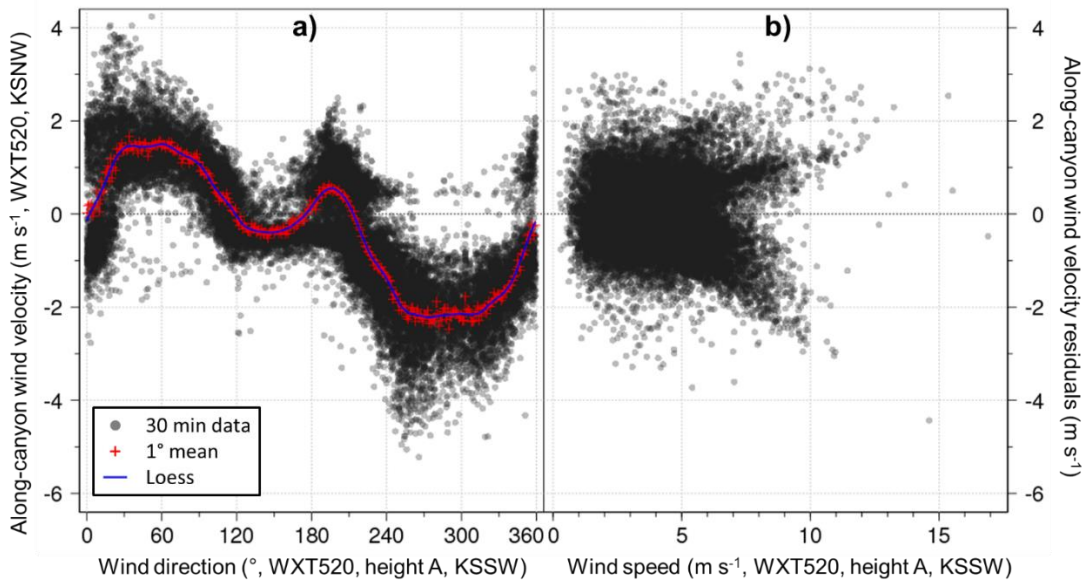

Figure 3.6: (a) Along-canyon wind velocity (positive: east to west, negative: west to east) and horizontal wind direction measured at KSNW height F and KSSW height A (Figure 2.1d) respectively by WXT520 for 2012/153 – 2013/151. (b) residuals (points - loess line) with horizontal wind speed measured at height A by WXT520. Circular points: 30 minute averages, crosses: one degree means, solid line: loess.

3.2.4 Vertical advection measurements

Unlike the vertical flux and the CO_2 storage, vertical advection does not have an obvious variation with time at any temporal scale. Values are controlled by the magnitude of the vertical CO_2 concentration gradient and the mean vertical wind speed (Section 3.1.4). As the main control on the vertical CO_2 concentration gradient in central London is human activities, this component of the vertical advection was gap filled in the same manner as the CO_2 storage and the vertical turbulent CO_2 flux – with mean values taken from data with the same time of day, day of week (weekday or weekend) and month of year. The vertical wind speed was not found

to vary consistently with time of day or season; however, results discussed in Section 4.5.2 and Björkegren *et al.* (2015) showed that the vertical wind speed varied predictably with wind direction. The general trend was extracted by local regression of the vertical wind speed (CSAT3, height A, KSSW) on wind direction (WXT520, height A, KSSW) using the *loess* R function (Figure 3.7). The residuals for the loess line for each degree and 0.1 increment in wind speed were averaged to generate a wind direction and speed specific value of the vertical wind speed which could be used for gap filling. The gap filled vertical wind speed and vertical CO_2 concentration gradient datasets were used to calculate the gap filled vertical advection data. This method was successful at improving the data availability of vertical advection from 62.1% for 2012/152-2013/151 to 100%. The proportion of missing data is high as the vertical advection requires data from both the switched vertical profile and the sonic anemometer, and the latter is sensitive to rain.

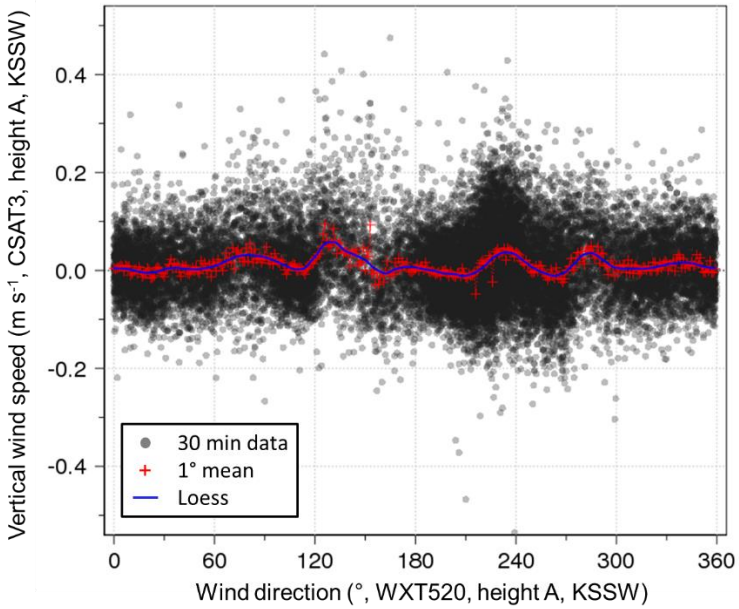

Figure 3.7: Vertical wind speed and horizontal wind direction measured at KSSW height A for 2012/153 – 2013/151. Circular points: 30 minute averages, crosses: one degree means, solid line: loess.

3.3 Statistical Analysis

3.3.1 Fourier transform

The Fourier transform is a common method used to identify periodic signals in data by converting from the time domain to the frequency domain (Press *et al., 2*009). It is an extension of Fourier series, where a time series can be represented as the sum of sine and cosine waves of varying wavelength. As sine and cosine functions do not decay i.e., they repeat infinitely, Fourier analysis is not effective at locating a signal in time (Farge, 1992). This can be mitigated somewhat by using a windowed or short-time Fourier transform, in which the time series to be analysed is first multiplied by a function that is non-zero only for a short, defined period. The transform is then computed, the window shifted, and the process repeated again (Kaiser, 2011). Once the transform has been calculated, whether windowed or otherwise, it can be used

to calculate a power or energy spectrum from which frequencies which contribute heavily to the signal can be identified (Stull, 1988).

The energy spectrum is the sum of the squared real and imaginary components of the Fourier transform at each frequency, up to the Nyquist frequency or half the frequency of the original time series (Stull, 1988). The spectral energy density is calculated as the energy spectrum divided by the difference between neighbouring frequencies, plotted over the natural frequency, the number of cycles per time period. In micrometeorology, particularly when plotting wind components, the spectral energy density is often plotted either over radians per second or over a frequency that has been normalised by the period, mean wind speed and effective height above ground level. The spectral energy density may also be normalised by multiplication with the frequency. When plotted as linear/linear, or with a log abscissa, the area under the curve is proportional to the variance of the signal explained by that range of frequencies. When plotted as log/log, any power law relationships appear as straight lines. The latter is the most common presentation in the meteorological literature (Stull, 1988).

Problems with the Fourier transform include the difficulty of localising a signal in time as well as frequency, and high frequency noise when transforming time series with sudden transitions. For calculation of the Fourier transform of discrete data (rather than of a continuous function) there is the further constraint of a complete, regularly sampled, data set as any errors or missing data become delocalised throughout the entire spectrum (Press *et al., 2*009). Nevertheless, it is a useful tool and is the basis for assessing the Integral Timescale of Turbulence (ITT) as described in the next section.

3.3.2 Integral Timescale of Turbulence (ITT)

The ITT, that is, "a characteristic time scale for the dynamics of measured quantities in a turbulent flow" (de Waele *et al.*, 2002) may be calculated as the inverse of the peak natural frequency of the normalised energy spectrum (Hanna, 1981; Oikawa and Meng, 1995). Previous work (Kaimal *et al.,* 1976) found the timescales for vertical and horizontal wind speeds to be equivalent only at heights greater than 100 m above flat, rural ground of uniform roughness (Readings *et al.,* 1974). Due to the inhomogeneity and greater roughness length of the urban surface, it is likely that the height at which the timescales for the different wind components equalise above the KS site is far above all the sampling points. This hypothesis is supported, though not confirmed, by Christen *et al.* (2007) who found the length scales of the horizontal and vertical wind components in central Basel, Switzerland, to be significantly different at 6 sample points with z_i/z_b ranging from 0.25 to 2.25. In this thesis, the timescales for each wind component are therefore evaluated separately.

For the analysis here data, x_t, of length N were de-trended (x'_t) using a fitted linear model (lm, R Development Core Team, 2013), conditioned by applying a bell taper, B, (calculated as 8.4.3, Stull, 1988) and transferred to the frequency domain (x_k) using a fast Fourier transform (*fft*, R

Development Core Team, 2013) where *k*, the frequency index, ranges from 0 to N-1, and *i* denotes the square root of -1.

$$B = \begin{cases} sin^2(5\pi t/N): 0 \leq t \leq 0.1N \\ 1: 0.1N < t < 0.9N \\ sin^2(5\pi t/N): 0.9N \leq t \leq N \end{cases} \quad (3.9)$$

The output from the fast Fourier transform function was compared to that from the discrete Fourier transform (in-house code, 3.10) (Equation 3 in Torrence and Compo, 1998) for 30 minutes of vertical wind speed data measured at 10 Hz at height A, KSSW, 00:30 – 01:00, 2013/193. Agreement was good: adjusted R^2 for a linear regression of the *fft* output onto the discrete Fourier transform output was 1.0, as was the slope ($p < 0.001$). The *fft* function was then chosen in preference to the in-house coding of the discrete Fourier transform due to its greater computational efficiency.

$$x_k = \frac{1}{N}\sum_{t=0}^{N-1} x'_t e^{-2\pi itk/N} \quad (3.10)$$

x_k is symmetric about the Nyquist frequency, *k=N/2*, apart from a sign change for the imaginary component (Stull, 1998). As frequencies greater than the Nyquist frequency cannot be resolved, these are 'folded back' and added to the lower frequencies when calculating the spectral energy, E_k.

$$E_k = \left|x_{k,Real}\right|^2 + \left|x_{k,Imag}\right|^2 + \left|x_{(N-k),Real}\right|^2 + \left|x_{(N-k),Imag}\right|^2 \quad (3.11)$$

The resultant energy spectrum was normalised by the variance and natural frequency (Oikawa and Meng, 1995). Spectra for each stability class were collated and binned into 100 equally spaced non dimensional frequencies and the peak frequency selected by visual inspection (Hanna, 1981).

3.3.3 Wavelet Analysis

Wavelet analysis decomposes time series data into time and frequency space (Graps, 1995). Like a Fourier transform, a wavelet transform can be reported as a power spectrum, which is the squared modulus of the transform, plotted against a measure of frequency and, for the wavelet transform, time. The spectrum may then be normalised by timescale to allow comparison between spectra (Equation 8 in Torrence and Compo, 1998). Wavelet analysis has three major advantages compared to other spectral methods such as the Fourier transform and Lomb-Scargle periodogram:

1. It can locate signals in both the time and the frequency domain without the inaccuracies introduced by windowing (Kaiser, 1994 *via* Torrence and Compo, 1998).
2. There are potentially infinite wavelet bases, allowing emphasis to be placed on different 'forms' of signal, e.g., asymmetric.
3. It is reasonably efficient to calculate.

The wavelet transform has been successfully used for the identification of coherent motions or transfer of scalars in the urban boundary layer (Feigenwinter and Vogt, 2005; Salmond *et al.,* 2005; Moriwaki and Kanda, 2006; Christen *et al.,* 2007). As a method of analysis for atmospheric time series, particularly those recorded within urban areas, wavelet analysis has the further advantage of not requiring the time series be stationary (Daubechies, 1990), a condition that, whilst technically necessary for the eddy covariance method to be theoretically valid, is often violated over complex terrain (Velasco *et al., 2*005, Reba *et al., 2*009).

In this section the methods used in this thesis for calculation and benchmarking of the continuous wavelet transform are presented (the discrete wavelet transform is not discussed). Both 'slow'/'manual' (scale and translate) and 'fast' (discrete Fourier transform) methods are illustrated.

3.3.3.1 Manual Calculation

Manual calculation of the continuous wavelet transform ($W_t(s)$) requires the convolution of a wavelet function with the time series (Figure 3.8, 3.12). The first step is multiplication of a portion of the time series (x_t) by the complex conjugate (*) of a wavelet function, ψ, that has been translated in time, t, and normalised by scale, s, ($\psi(t/s)$) (Figure 3.1a and b). This is followed by summation of the product, translation of the wavelet function by a set number of data points and repetition of the previous three steps for all N time series data points (Figure 3.1c) and multiple widths or scale factors, of the wavelet function (Torrence and Compo, 1998).

$$W_t(s) = \sum_{t'=0}^{N-1} x_{t'} \psi * \left[\frac{(t'-t)\delta t}{s}\right] \quad (3.12)$$

The exact product of the wavelet and time series will vary with the form of the wavelet function, any pre-processing of the data (all time series shown below have had the mean removed and been scaled by their standard deviation unless stated otherwise) and whether the wavelet function has been 'stretched' or compressed to allow analysis at different periodicities (Torrence and Compo, 1998). A wavelet function can take any form provided it has a mean of zero, (i.e., when convolved with a flat signal it must return a series with no amplitude at any frequency) and is localised in both the time and the frequency domains (i.e., it is only convolved with a finite number of points and the results of the convolution can be attributed to a defined time and frequency) (Farge, 1992).

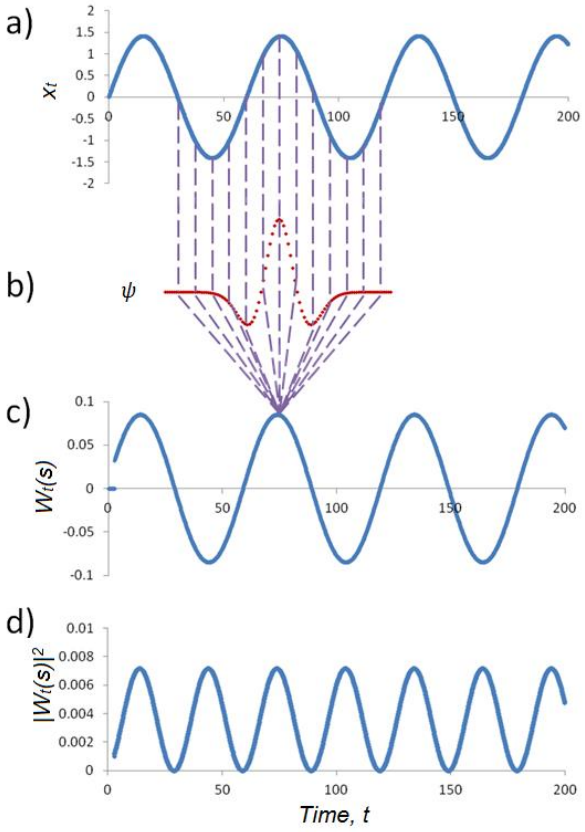

Figure 3.8: Manual process of wavelet transform, all x-axes given in arbitrary time units, all y-axes arbitrary amplitude. a) Sine wave; b) scaled 'Mexican hat' wavelet equivalent to a Fourier wavelength of 31.8; c) sum of the convolution of a) (the original signal) and b) (the wavelet), resulting in the wavelet transform at wavelength 31.8; d) square of the amplitude of the wavelet transform, i.e., the power spectrum corresponding to wavelength 31.8.

Factors to consider when selecting a wavelet function include whether the wavelet basis is orthogonal or non-orthogonal, whether it is real or complex, the width of the function and its shape (Salmond *et al., 2*005). As the wavelet transform was used here for time series analysis, not signal processing, it was not necessary to have as compact a representation of the signal as possible. A non-orthogonal wavelet was therefore deemed preferable, as the spectrum produced is more easily interpretable and will not vary if the time series is offset (Torrence and Compo, 1998). This is helpful when comparing spectra from two different sites where an event may be 'seen' at one site before the other.

Complex valued wavelets, which return both amplitude and phase information, are better suited to highlighting periodic signals than abrupt changes (Torrence and Compo, 1998). The complex valued Paul wavelet has the advantage of being progressive, and unlike the symmetrical, real valued Mexican Hat, can distinguish between different directions in the signal due to having Fourier coefficients of zero for negative wavenumbers (Farge, 1990). This makes it ideal for analysis of signals in which there is a causal or time component. Despite this the Mexican Hat, or second derivative of a Gaussian, wavelet is a popular choice for analysing atmospheric time series (e.g., Feigenwinter and Vogt, 2005), particularly as abrupt changes or 'spikes' in the time series show up as zero crossing points in the wavelet coefficients (Salmond *et al., 2*005). It is

this quality which makes the Mexican Hat wavelet particularly suited for the automated venting detection method described in Section 5.2.2.

3.3.3.2 'Fast' method

The second method of performing wavelet analysis is less intuitive but considerably quicker, particularly for large datasets (Torrence and Compo, 1998). The 'fast' method involves transforming both the wavelet function and the data set into Fourier space and taking the pointwise product (convolution theorem: *F{g*h}=F{g}.F{h}*, where *F{g}* is the Fourier transform of the time series *g*) as this enables calculation of the convolution at all data points in one operation.

In the continuous limit the Fourier transform (3.10) of a wavelet function, $\psi(t/s)$, is $\hat{\psi}(s\omega)$, where the value of the angular frequency, ω, relates to the frequency index.

$$\omega = \begin{cases} \frac{2\pi k}{N\delta t} : \ k \leq \frac{N}{2} \\ -\frac{2\pi k}{N\delta t} : \ k > \frac{N}{2} \end{cases} \tag{3.13}$$

The wavelet transform (via the convolution theorem) is obtained by multiplying the Fourier transforms of the time series, $\hat{x}_k$, and the complex conjugate of the wavelet function, $\hat{\psi}^*(s\omega)$. The inverse Fourier transform is used to bring the result back into the time domain, where again *i* denotes the square root of -1 (Torrence and Compo, 1998):

$$W_t(s) = \sum_{k=0}^{N-1} \hat{x}_k \hat{\psi} * (s\omega) e^{i\omega t \delta t} \tag{3.14}$$

This is calculated in an in-house R (R Development Core Team, 2013) adaptation of the Torrence and Compo (1998) software (Appendix 3.B: schematic, Appendices 3.C-D software). The wavelet function is normalised at each time scale, such that the integral of the squared modulus of the wave function is equal to 1.

$$\hat{\psi}(s\omega) = \left(\frac{2\pi s}{\delta t}\right)^{1/2} \hat{\psi}_0(s\omega) \tag{3.15}$$

At each scale the sum over the frequency index from 0 to N-1 is therefore equal to N:

$$\sum_{k=0}^{N-1} \left|\hat{\psi}(s\omega)\right|^2 = N \tag{3.16}$$

This ensures that results from each scale are directly comparable as the wavelet transform varies only with the amplitude of the Fourier transform of the time series.

The wavelet power spectrum ($|W_t(s)|^2$) is defined as the square of the amplitude of the wavelet transform. In the examples below, the wavelet function is entirely real valued and hence the power spectrum is simply the square of the real part of the wavelet transform. Due to the large volumes of data, it was desirable to be able to detect significant features automatically. This is not facile, as even random signals give areas of correlation in a continuous, non-orthogonal wavelet transform (Farge, 1990). In general, assessing the significance of features in the wavelet power spectrum is done by comparison to an appropriate background spectrum, about

which it is assumed the wavelet background spectrum will be distributed in a predictable fashion, e.g., if it is normally distributed, then values in the wavelet power spectrum more than two standard deviations away from the background spectrum may be said to be significant at the 5% level (Torrence and Compo, 1988).

Typical choices for background spectra are a Gaussian (white) noise, a red noise generated from the lag-1 autocorrelation of the time series, or the time averaged (global) wavelet spectrum (Torrence and Compo, 1988). Previous studies (Torrence and Compo, 1988; Galmarini and Attie, 2000; Attie and Durand 2003; Salmond *et al., 2*005) have assumed the wavelet transform coefficients are Chi square distributed, and generated scale specific confidence levels for the wavelet transform. As neither the original data, nor the wavelet transform are normally distributed (the time series data and wavelet coefficients were negatively skewed compared to a white noise at the 5% significance level), this assumption cannot be considered valid. Therefore, whilst the experience of previous researchers suggests that confidence levels obtained by this method successfully highlight signals of interest when the final peak detection is done by eye, it is not thought to be a sufficient in and of itself when detection is entirely automated.

Other tests are applicable only for certain wavelets. For complex wavelets, Farge (1990) reports that singularities in the time series may be detected as lines of constant phase, whereas Salmond *et al.* (2005) demonstrate that discontinuities can be identified when using the Mexican hat (second derivative of a Gaussian or Marr's) wavelet as zero crossing points in the wavelet coefficients.

In order to test the wavelet program's ability to identify signals of differing shape, period, and amplitude relative to white noise, the program was benchmarked using artificially generated data containing signals of known periodicity (pseudo-random normally distributed numbers generated in Matlab, 2011b).

The first data set was designed to test the wavelet's ability to reliably identify peaks at different background concentrations. Atmospheric CO_2 concentration is known to be non-stationary on the hourly and even half hourly scale during certain times of day, such as the transition periods around dawn and dusk, where the boundary layer is (respectively) expanding and diluting or contracting and concentrating the trace gases therein. In an urban setting, the ability of the morning and evening rush hours to rapidly raise CO_2 concentrations cannot be ignored. It is desirable that the amplitude of the wavelet transform for a signal be invariant to the 'background' concentration, i.e., a jump of 2 ppm over 2 s when the 5 minute average is 420 ppm should give the same signal as jump of 2 ppm over 2 s when the 5 minute average is 450 ppm. The software should fulfil this condition according to 3.15. The power spectrum for a ramped signal (Figure 3.9) shows no increase in amplitude with increasing 'baseline' input.

It is also desirable to be able to identify signals of different periodicity- both when overlaid and when they occur separately (Figure 3.10). Whilst the wavelet power spectrum clearly identifies the signals at both periodicities (6 and 60), it also introduces 'significant' peaks at high

frequencies, particularly at periodicities less than 2. This effect is not observed when analysing time series synthesised from sine waves (Figure 3.11), rather than step functions (Figure 3.10). This highlights the importance of matching the form of the wavelet to the signal analysed in order to avoid spurious results.

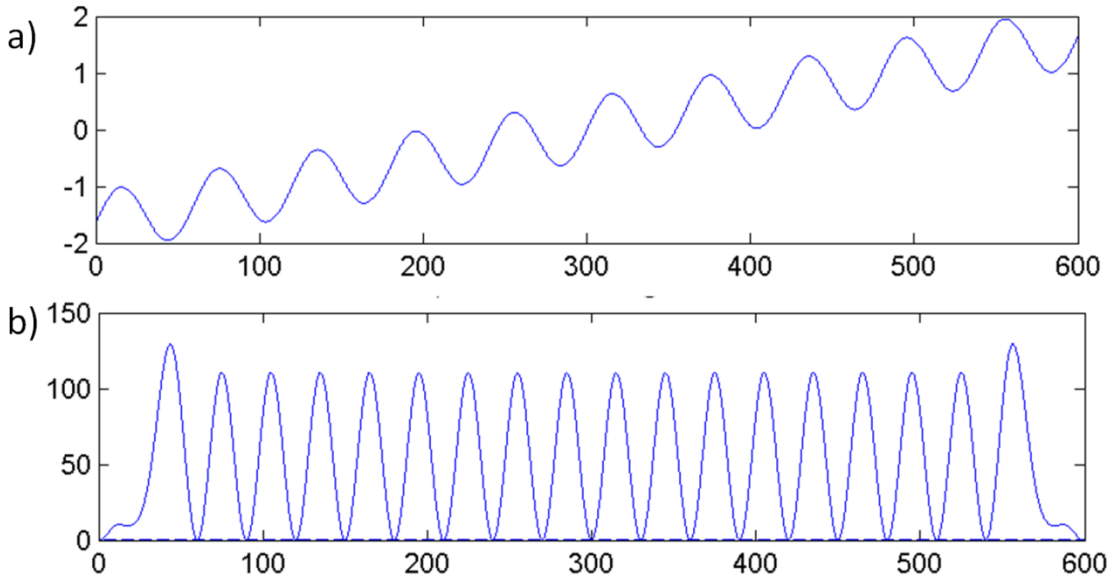

Figure 3.9: a) Time series data input: sine wave (wavelength 60) imposed on a ramp. b) Wavelet power spectrum at Fourier wavelength 60.5. All times and amplitudes are given in arbitrary units. First and last peaks are within the cone of influence (affected by the edge of the data) and should be disregarded.

It is expected that due to the numerous microscale emissions and eddies a time series of atmospheric *[CO_2]* will be noisy. Figure 3.12 illustrates the ability of the wavelet transform to identify a periodic signal at different signal to noise ratios. At an amplitude ratio of approximately 0.7:1 (signal: noise), the signal is identifiable, both by eye and by the wavelet transform. The ability to pick the signal out by eye is lost as the ratio approaches 0.7:10, but it is still detected by the wavelet transform (not shown). By the time the ratio reaches 0.7:100, neither method is capable of detecting the signal.

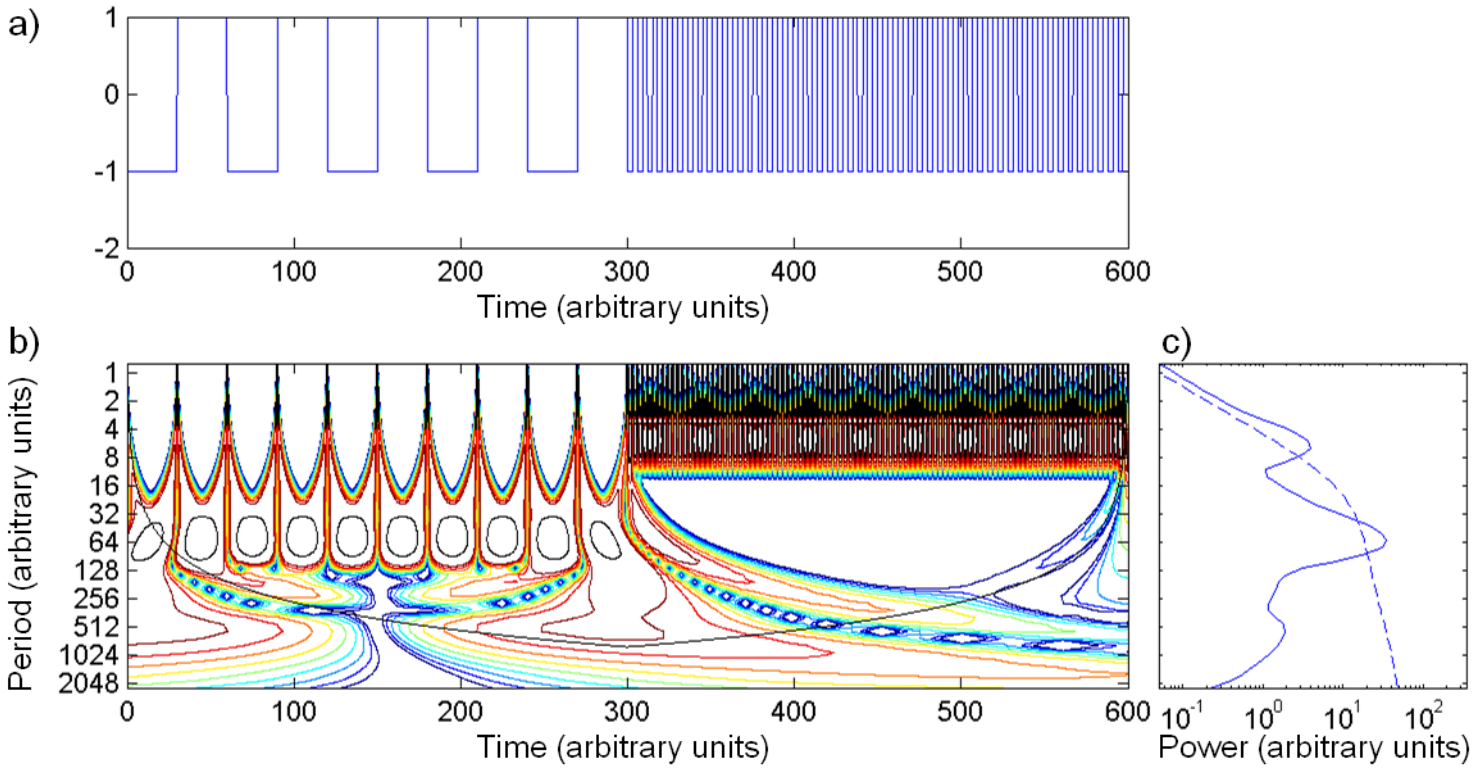

Figure 3.10, see next page for caption

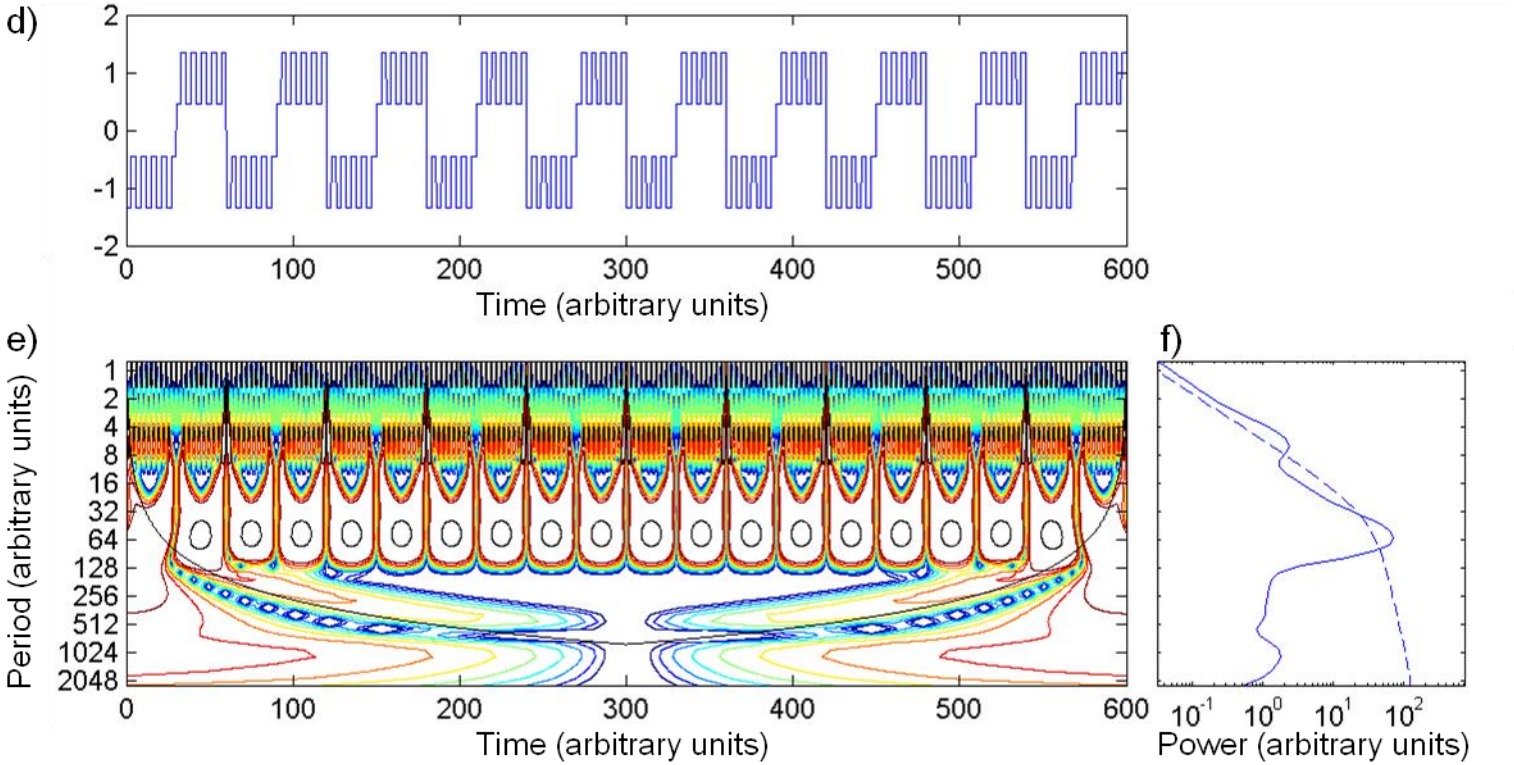

Figure 3.10: Synthesised time series (a and d), their wavelet power spectra (b and e) and their global wavelet spectra (c and f). Black curve along the base of (b) and (e) denotes cone of influence and black outlines near the middle and top of each plot indicate the signal is significant at the 95% level. Signals have wavelengths of 6 and 60.

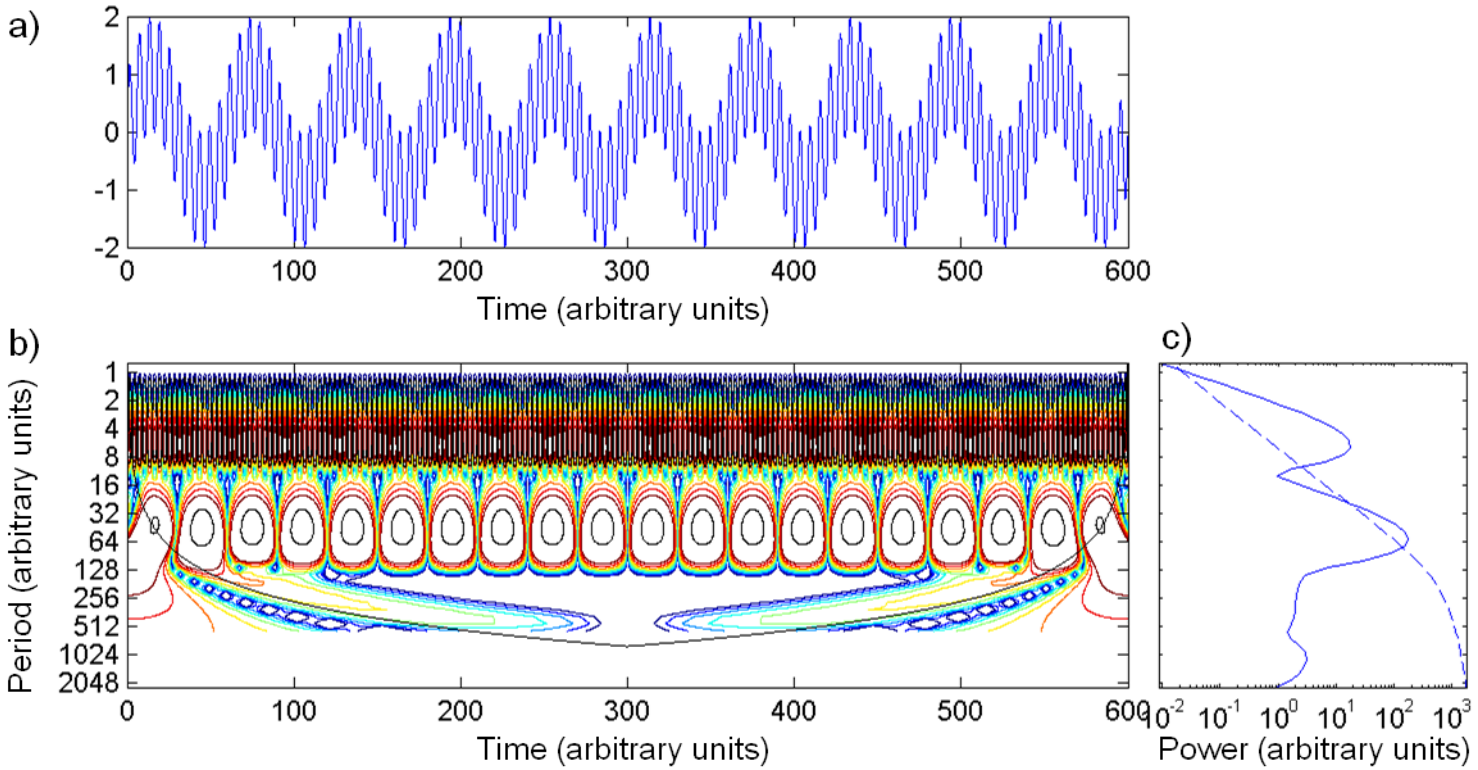

Figure 3.11: Synthesised time series of sine waves, wavelength 6 and 60 (a), the associated wavelet power spectrum (b) and global wavelet spectrum (c). Black curve along the base of (b) denotes cone of influence and black outlines indicate the signal is significant at the 95% level.

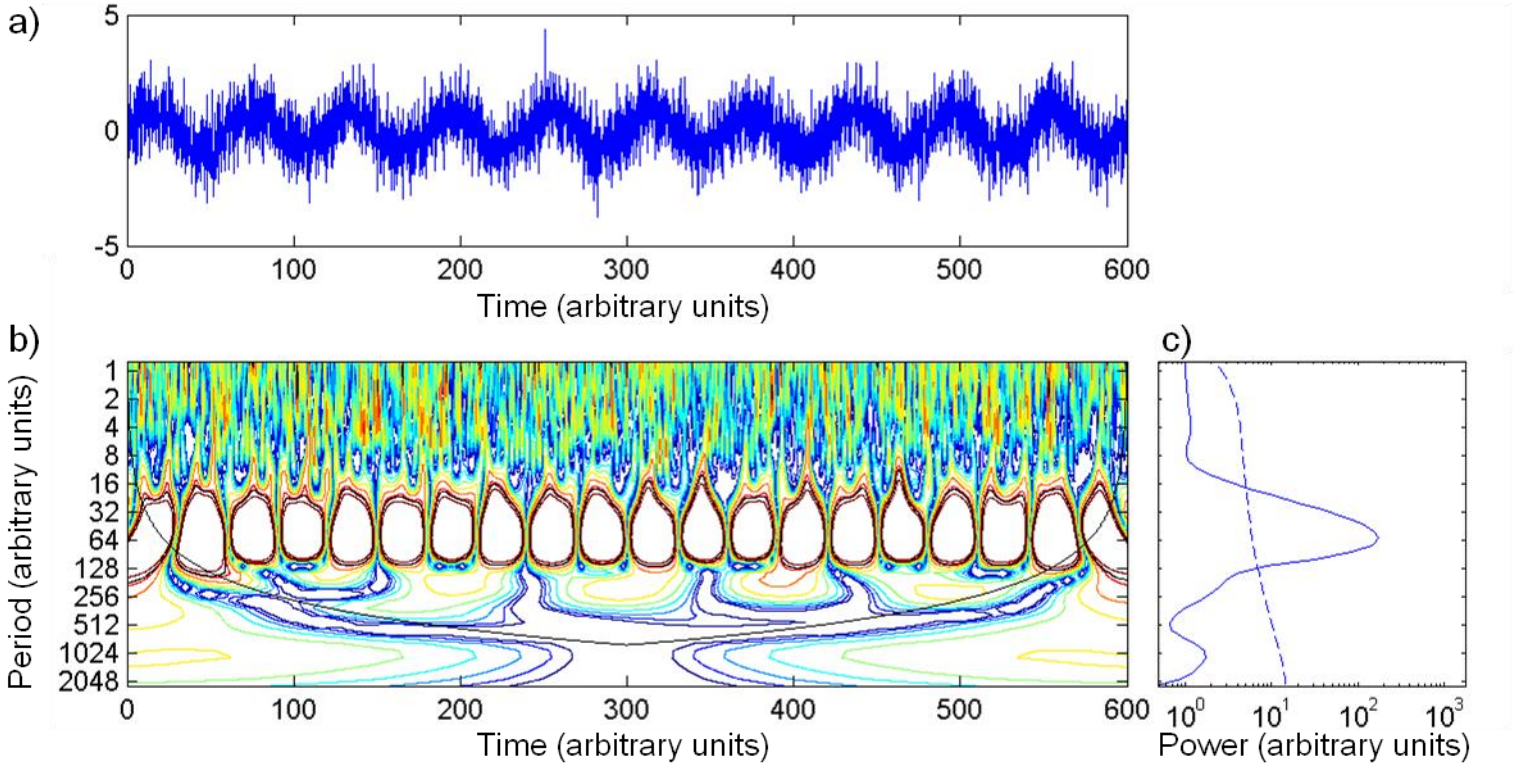

Figure 3.12, see next page for caption

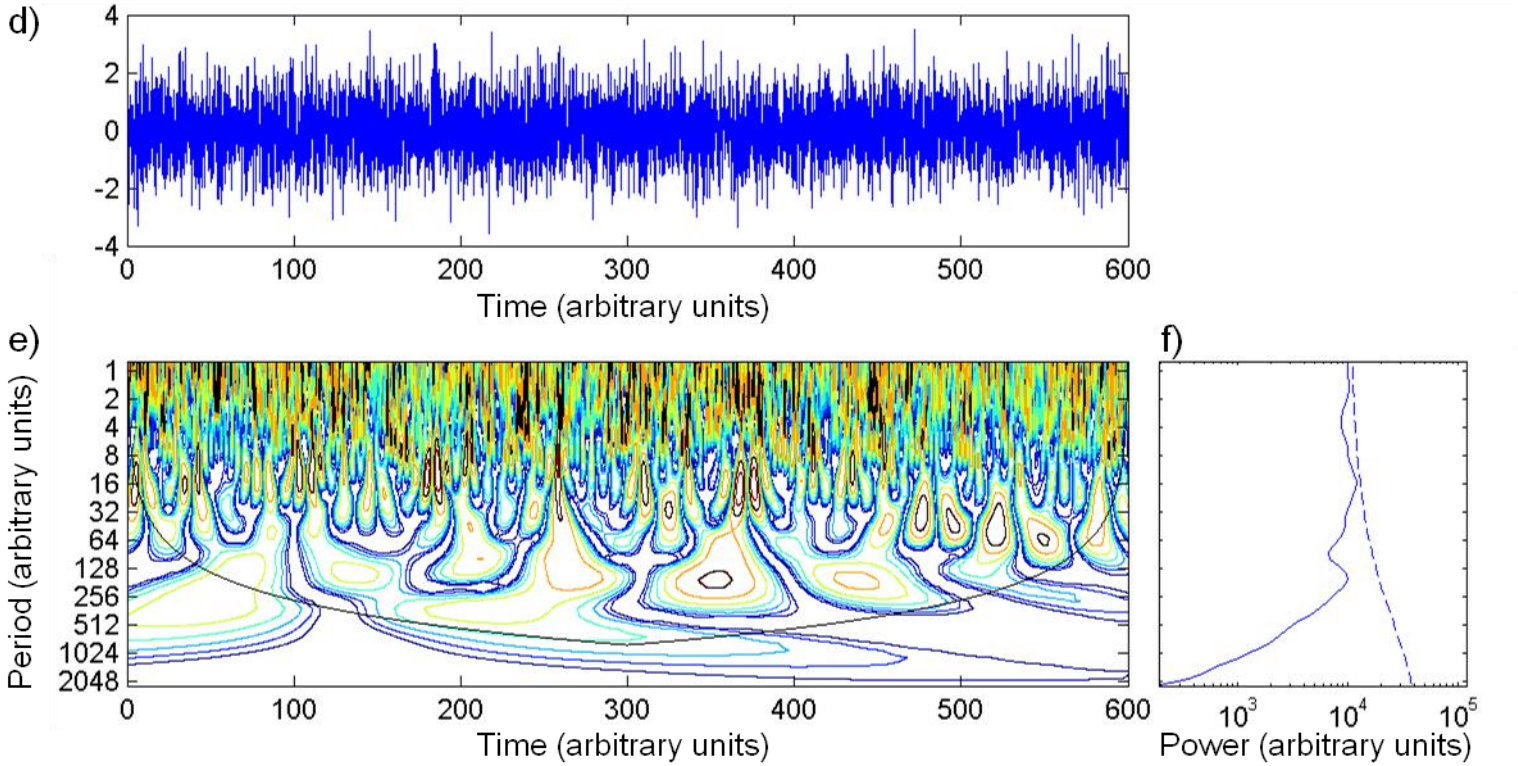

Figure 3.12: Synthesised time series (a and d), their wavelet power spectra (b and e) and their global wavelet spectra (c and f). Black curve along the base of (b) and (e) denotes cone of influence and black outlines indicate the signal is significant at the 95% level. (a)-(c) have a ratio for signal to noise standard deviation of 0.7:1.0, for (d)-(f) the ratio is 0.7:100.9, all values given to 1 d.p.

To check the accuracy of the software's wavelet transform routine, the original time series was reconstructed from the wavelet transform (Figure 3.13). This is done using a delta function (Farge, 1992, cited in Torrence and Compo, 1998) and involves summing the real component of the wavelet transform over all scales, s_j, normalised by the scale (Equation 11 in Torrence and Compo, 1998):

$$x_t = \frac{\delta j \delta t^{1/2}}{C_\delta \psi_0(0)} \sum_{j=0}^{J} \frac{\Re\{W_t(s_j)\}}{s_j^{1/2}} \qquad (3.17)$$

where C_δ is an empirically derived constant. The small-scale structure of the time series is preserved throughout the time series (Figure 3.13) and the absolute values agree well (R^2 of 0.98). Previous iterations of the processing which did not include longer time scales only had good agreement in absolute magnitude within the central third of the data set (not shown). Towards the edges, the absolute values of the two series were less similar; the reconstructed data remained closer to zero, whilst the measured series was generally positive in the first third and negative in the last. This can be interpreted either as a failure to capture the largest scale/lowest frequency variations, or an intrinsic detrending/insensitivity to non-stationarity. As the processing of the data was considerably quicker in R than in the original Matlab, the extra time required to process data at the longer timescales was negligible and these were included for accuracy.

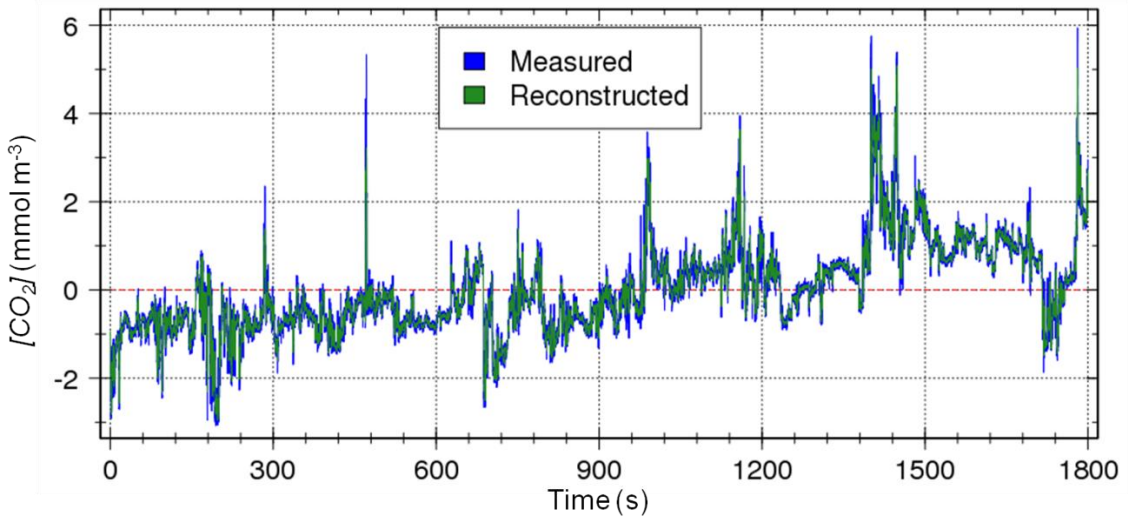

Figure 3.13: Comparison of measured (blue) and reconstructed (green) 10 Hz [CO_2] (LI7500, 10Hz) time series data for 2013/193 00:00-00:30 GMT, KSSW (height A). Measured data had the mean removed and was scaled to a standard deviation of 1 prior to analysis and plotting.

3.3.4 Quadrant Analysis

One method of identifying coherent structures in boundary layer turbulence is quadrant analysis (Wallace *et al.,* 1972, Lu and Willmarth, 1973 via Oikawa and Meng, 1995), where the covariance of the instantaneous deviations from the mean of the longitudinal (*u*) and vertical (*w*) wind speed (*u'w'*) is split into four combinations of positive and negative *u'* and *w'*, with abscissa *u'* and ordinate *w'*. Quadrants are labelled 1 to 4 anticlockwise from *+u'+w'* and represent

outward interactions, ejections, inward interactions and sweeps respectively. ‘Interactions’ make negative contributions to the Reynolds stress, the others, positive. The relative contributions of each quadrant (S_q) to the transfer of momentum (or, if other quantities are plotted, transfer of scalars, heat, etc.) may be calculated following Katul *et al.* (2006) as the average covariance of the instantaneous deviations from the mean of the longitudinal and vertical wind velocity for that quadrant (denoted by the subscript *q*), divided by the overall mean:

$$S_q = \frac{\overline{u'_q w'_q}}{\overline{u'w'}} \tag{3.18}$$

This calculation was performed for half hourly time series of *u* and *w* data to enable interpretation of the results of the wavelet transform.

Appendix 3.A Interpolation in time and space

This section was originally published as part of Björkegren *et al.* (2015) and has been reproduced with some minor changes to Table 3.A.2.

In this section the non-concurrent, spatially irregular CO_2 concentration time series is interpolated onto a regular time/space grid using three different interpolation methods. The interpolated concentration time series and derived CO_2 storage time series are compared to benchmarks and the necessity of interpolating CO_2 concentration time series prior to the CO_2 storage calculation is evaluated.

Appendix 3.A.1 Theory

The exact form of the CO_2 storage calculation requires continuous measurements of the $[CO_2]$ profile in time and space (Aubinet *et al.,* 2005). As switched profile measurements are obtained by sampling from several heights sequentially (Molder *et al.,* 2000), the resulting data are discontinuous at each height. As calculation of the CO_2 storage requires a complete instantaneous profile, further processing can include interpolation of the 'missing' data to provide a continuous concentration time series from which complete profiles can be drawn. Alternatively, the average of the values observed throughout a cycle may be taken as representative of that cycle time period.

Calculation of CO_2 storage also requires integration of the change in $[CO_2]$ over the vertical extent of the profile (Aubinet *et al.,* 2005). This can either be accomplished by weighting the change in concentration at each height by the vertical span over which it is deemed relevant or interpolating to a metre grid and summing over the vertical extent without weighting. The former is mathematically equivalent to taking the average of adjacent heights (e.g., Yang *et al.,* 2007).

Appendix 3.A.2 Interpolation in time

The effectiveness of different methods of interpolating $[CO_2]$ in time are evaluated using continuous 2 Hz LI840 $[CO_2]$ measurements (KSSW, z_i = 46.4 m). Data covering half a seasonal cycle (2013/160 – 365) were split into 75 s 'runs' and processed as described in Sections 2.2.1 and 2.2.2 to provide a benchmark time series with 8 data points per ten minutes. A switched profile time series was simulated by extracting every 8th data point (method illustrated in Figure 3.A.1), which was used as input data for three different interpolation functions.

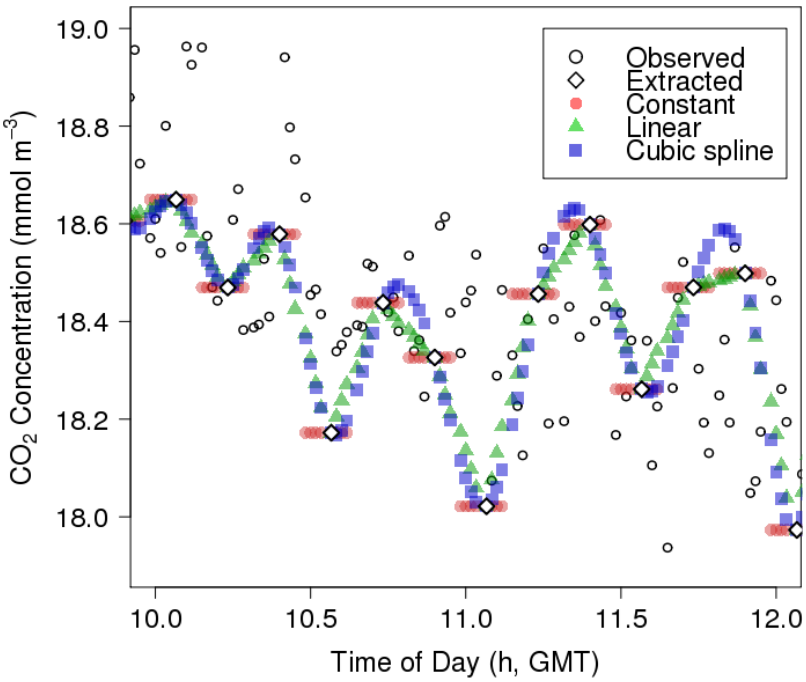

Figure 3.A.1: CO_2 concentration time series observed (key) at KSSW, height A (Figure 2.1d); an 'extracted' (key) time series consisting of every 8th point of the 'observed' series, and three time series interpolated (Constant, Linear and Cubic spline; key) from the extracted data for day 2014/038 10:00-12:00 GMT. For details of interpolation see Section *3A.2.*

The first function, termed 'constant' interpolation, assumes all concentrations within 5 minutes either side of an extracted data point are equal to the extracted value (Figure 3.A.1). This is equivalent to undertaking no interpolation in time but constructing *[CO_2]* profiles from the measurements closest to a particular time point. The other two functions, 'linear' and 'cubic spline' interpolation were performed using the *approx* and *spline* R functions (R Development Core Team, 2013) respectively (Figure 3.A.1 'Linear', 'Cubic'). Leading or trailing missing values were not interpolated.

Interpolated *[CO_2]* time series regressed on to the benchmark had coefficients of determination greater than 0.98 (Table 3.A.1). The linear interpolation performed the best in terms of R^2 and root mean squared error (RMSE), but the constant value method had values for the slope and intercept of the regression that more closely approached 1 and 0 respectively. The cubic interpolation was the least effective but the difference was small.

Table 3.A.1: Coefficient of determination (R^2), Slope, Intercept, Root Mean Squared Error (RMSE) and Degrees of Freedom (DoF) for a linear regression of an interpolation in time of an extracted (Figure 3.A.1) [CO_2] time series on to the benchmark time series (Figure 3.A.1). CO_2 storage time series were calculated from interpolated [CO_2] time series. All values given to 3 s.f.

	Interpolation Method	R^2	Slope	Intercept	RMSE	DoF x10^3
CO_2 Concentration (mmol m^{-3})	None	0.987	0.993	0.131	0.151	181
	Linear	0.989	0.992	0.146	0.140	210
	Cubic	0.987	0.992	0.136	0.151	210
CO_2 Storage (mmol m^{-2} s^{-1})	None	0.000	0.000	0.022	7.73	26
	Linear	0.030	0.945	-0.002	5.34	209
	Cubic	0.011	0.601	-0.001	5.39	209

The high, positive correlation between interpolated and measured time series for $[CO_2]$ does not hold as well for ΔC_S. None of the R^2 values exceeded 0.05. The ΔC_S calculated from the linearly interpolated time series was closest to the measured values – despite low R^2, the slope and intercept for the regression were 0.95 and 0.00 respectively and it had the lowest RMSE.

The lack of strong agreement between the ΔC_S time series calculated from interpolated data and the benchmark suggests that wherever possible measurements should be made continuously, rather than using a switched profile. Interpolation can adequately reproduce $[CO_2]$; however, as measured CO_2 storage values for a switched profile are typically on the order of 1 μmol m^{-2} s^{-1}, the actual CO_2 storage signal is likely to be smaller than the interpolation error.

Appendix 3.A.3 Interpolation in space

Given a 'true profile' with continuous measurements in space and time is unavailable, the full ten height profile was taken as a 'benchmark'. Data from the four heights (A, E, F, J) identified (Section 5.3.1) as the 'best' configuration for that number of sample points were divided into 10 minute profiles time-centred on the z_i = 46.4 m a.g.l. (height A, KSSW) observation and were not interpolated in time. Each 10 minute vertical profile (composed of measurements at 4 heights) was interpolated to the remaining six sample points (B, C, D, G, H, I). The interpolation between observations included: linear, cubic and none (i.e., $[CO_2]$ at the interpolated heights were assumed to be the same as $[CO_2]$ at A, E, F or J).

Linear regression was performed between the interpolated and the measured time series for each interpolated height and interpolation method. When summed over all interpolated heights for each interpolation method, the lowest RMSE (51.7, 58.3, 58.6 ppm) was when linear interpolation was used, followed by no interpolation and cubic interpolation, respectively (Table 3.A.2). The linear interpolation was poorest for the sample points C, D and G (R^2 = 0.86–0.87). Both the 'none' and cubic interpolation improve with decreasing height; however, this may be due to the choice of sample points. Due to the larger vertical separation between A and B-D than E and B-D, the latter had a much greater impact upon the 'none' (concentrations taken to be equal to the closest extracted sample point) and cubic interpolations at B-D than the former, despite concentrations measured at B-D often being more similar to A (Section 5.3.1). If B-D are considered to be 'closer' to A for the purposes of the 'no' interpolation ('vertical zone', Figure 3.A.2), the RMSE for the profile drops to below that of the linear interpolation. Whilst the linear interpolation still performs best in the canyon, simple span weighting is more effective above. All methods perform acceptably (R^2 > 0.8) for all heights and could be applied without prior knowledge of the profile shape. If the typical profile shape is known and there are obvious physically induced 'break points' in the vertical profile, span weighting to the breakpoints and not to the midpoints between sample locations is the preferred method of spatial interpolation.

Figure 3.A.2 (Left): As Table 3.A.1 for [CO_2] time series measured at four heights and interpolated in space. Sample locations (A, E, F, J, Figure 2.1d) in brackets indicate the data source for the 'none' interpolation method. The correlation coefficient (R^2) are shaded red (poor fit, lower values) to green (better fit, higher values). The root mean squared (RMSE) are shaded green (lower values) to red (higher values). Both R^2 and slope given to 2 d.p., RMSE and intercept to 1 d.p. Also given are the degrees of freedom (DoF).

Table 3.A.2 (Right): Measurement locations extracted (filled points) and interpolated (hollow points) grouped by the nearest extracted point (proximity) or the nearest extracted point within the same vertical 'zone'.

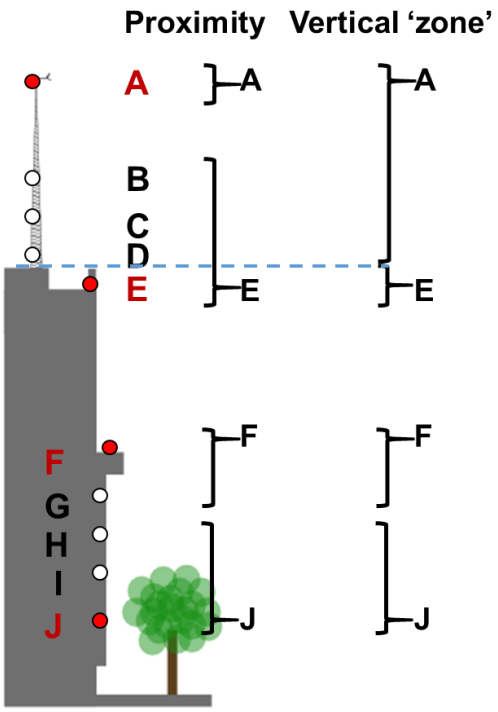

Interpolation Method	Sample Location	R^2	Intercept (ppm)	Slope	RMSE (ppm)	DoF x10^3
None (Proximity)	B (E)	0.82	64.3	0.84	10.4	41
	C (E)	0.82	50.9	0.87	10.9	41
	D (E)	0.85	50.3	0.87	10.0	41
	G (F)	0.86	3.2	1.00	10.7	38
	H (J)	0.91	28.9	0.93	7.9	38
	I (J)	0.90	30.0	0.93	8.4	38
None (Vertical zone)	B (A)	0.90	24.0	0.95	7.7	41
	C (A)	0.89	10.5	0.98	8.5	41
	D (A)	0.90	12.5	0.97	7.9	41
	G (F)	0.86	3.2	1.00	10.7	38
	H (J)	0.91	28.9	0.93	7.9	38
	I (J)	0.90	30.0	0.93	8.4	38
Linear	B	0.89	35.2	0.91	8.4	37
	C	0.86	32.2	0.92	9.9	37
	D	0.86	43.9	0.89	9.6	37
	G	0.87	-0.8	1.01	9.9	37
	H	0.94	12.4	0.97	6.2	37
	I	0.91	21.1	0.95	7.8	37
Cubic	B	0.81	76.1	0.81	11.0	37
	C	0.81	61.8	0.84	11.5	37
	D	0.84	57.3	0.86	10.4	37
	G	0.86	10.5	0.98	10.5	37
	H	0.92	25.2	0.95	7.2	37
	I	0.90	26.4	0.94	8.1	37

Appendix 3.B: Wavelet analysis software, overview

This section consists of a schematic (Figure 3.B.1) of the software for performing wavelet analysis on a time series, here denoted by *Y*. The R code for the main program is given in Appendix 3.C, other functions are provided in Appendix 3.D

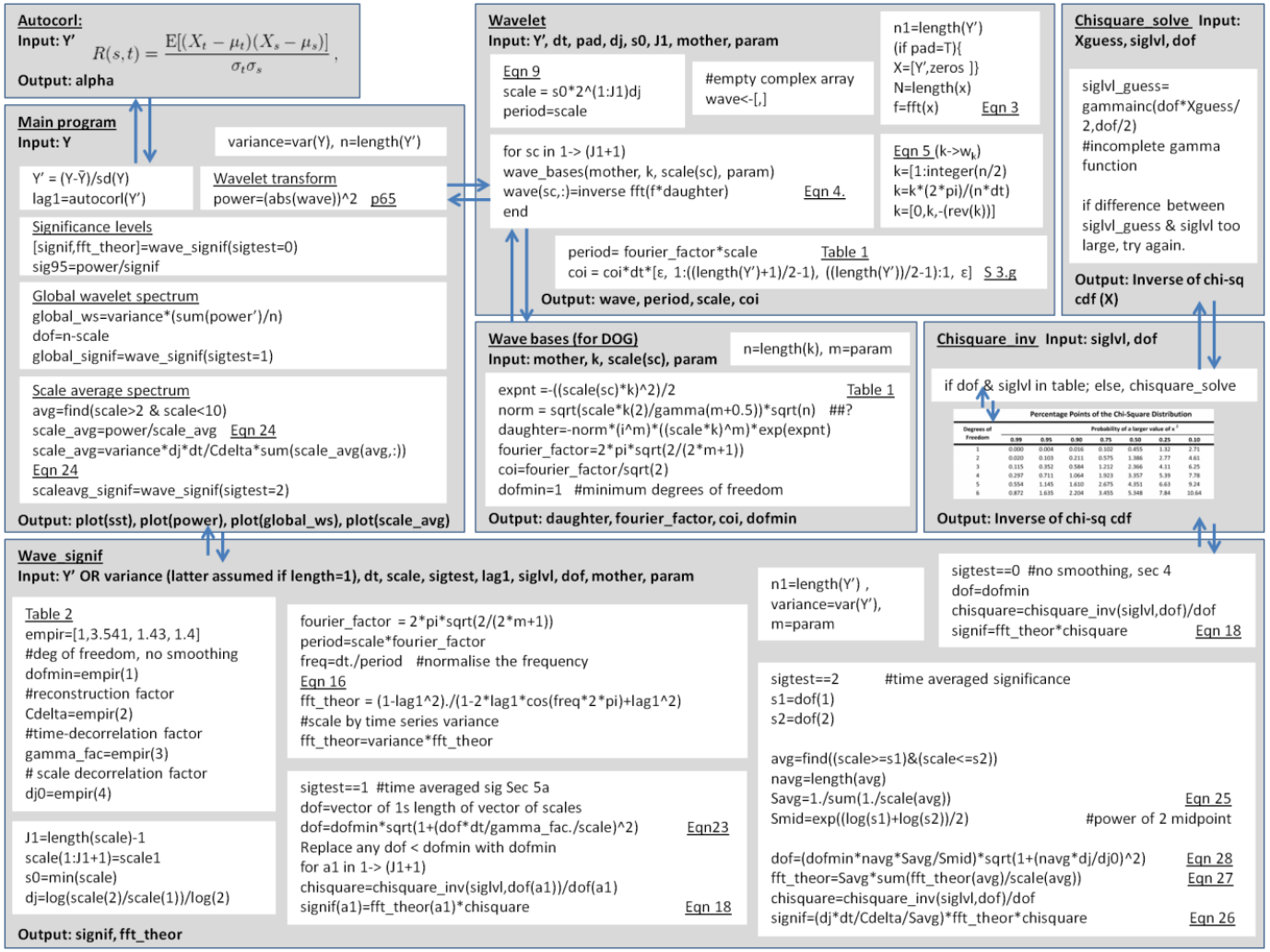

Figure 3.B.1: Schematic of the software used to calculate the wavelet transform and power spectra. Software modified from Torrence and Compo (1998). Equation numbers are correct for Torrence and Compo (1998).

Appendix 3.C: Main wavelet analysis program

This section consists of the R code for the main wavelet analysis program.

```
rm(list=ls())

# Path to the main directory where scripts are:
SP_PATH <- "/home/micromet/Roofprograms/" # Data02 - script path
DB_PATH <- "/data/its-tier2/micromet/" # Data02 - dataBridge01
OT_PATH <- "/net/glusterfs_micromet/micromet/users/micromet/works/" # Data02 - raw data

## load libraries and functions
library(ncdf);library(plotrix);library(hexbin);library(scales)
source(paste(SP_PATH,"LUMA/LUMAfunctions_C.R", sep=""))
source(paste(SP_PATH,"Alex_Analysis/Wavelet/Wavelet_functions.R", sep=""))
source(paste(SP_PATH,"Alex_Analysis/Alex_functions_V4.R", sep=""))

##Define days
DSTART <- "13298";DSTOP <- "13298"
DATE_STR <- as.Date(DSTART,"%y%j")
DATE_STP <- as.Date(DSTOP, "%y%j")
DATE_LIST<- seq(DATE_STR,DATE_STP,1)

delta_t <- 0.05 ##resolution of measurements
Cdelta<-3.541 ##for DOG. For Morlet Cdelta is 0.776

##define sites and instruments
name.CST<-c("KSSW","KSNW"); name.LI7<-c("KSSW","KSNW")
inst.CST<-c("CSAT3","CSAT3") ; inst.LI7<-c("Li7500","Li7500","Storage")

###define variables and units
y_short <-c("dCss","dCsp") #c("w","T","CD","HO")
y_vals <-c("Single height CO2 storage", "Profile CO2 storage")#c("Vertical
velocity","Temperature","[CO2]","H2O")
y_units <-c("mmol.m^-2.s^-1","mmol.m^-2.s^-1") #c("(m.s^-1)","(C)","(mmol.m^-3)","(mmol.m^-
3)")
p_units <-c("mmol.m^-4.s^-2","mmol.m^-4.s^-2") #c("m^2.s^-2)","(C^2)","(mmol^2.m^-
6)","(mmol^2.m^-6)")

##define time series
set_start <-seq(0,23.5,0.5)*3600
set_end <-seq(0.5,24,0.5)*3600

CST<-array(list(NA),length(name.CST));CSTT<-array(list(NA),length(name.CST));
LI7<-array(list(NA),length(name.LI7));LI7T<-array(list(NA),length(name.LI7));

for (idate in 1:length(DATE_LIST)) ##start loop over dates
{ Tinfo <- lf_Tinfo(DATE_LIST[idate]); print(paste(Tinfo["tD",]))

 In <- paste(DB_PATH,"data/",Tinfo["tD","YEAR"],"/London/",sep="")
 Out <- paste(OT_PATH,"Wavelet/",sep="")

 for (site in 1:length(name.CST)) ##read in CSAT data
 {var.cst<-c("u", "v", "w","Tsonic")
 CST[[site]]<-Af_ncdf(DB_PATH,Tinfo,name.CST[site],inst.CST[site],"10Hz",var.cst,1)
 CSTT[[site]]<-CST[[site]][,1]; CST[[site]]<-CST[[site]][,(-1)]}

 for (site in 1:length(name.LI7)) ##Read in LI7500 data
 {var.cst<-c("C_CO2","C_H2O","CS_T_1","CS_T_2")
 LI7[[site]]<-Af_ncdf(DB_PATH,Tinfo,name.LI7[site],inst.LI7[site],"10Hz",var.cst,1)
 LI7T[[site]]<-LI7[[site]][,1]; LI7[[site]]<-LI7[[site]][,(-1)]}
```

```
for (inst in 1:2) ##cycle over instruments
{group_dat<-cbind(CST[[inst]],LI7[[inst]]) ##select data
for (ToD in 1:length(set_start)) ##cut down to specific time of day
{list_time<-which(CSTT[[inst]]>set_start[ToD] & CSTT[[inst]]<=set_end[ToD])
for (vr in 1:ncol(group_dat)) ###cycle over variables
{sst<-group_dat[list_time,vr]
list_na<-!is.na(sst)
times<-CSTT[[inst]][list_time]
sst<-sst[list_na]
times<-times[list_na]

variance_dat<-var(sst) ####normalise the data
sst<-(sst - mean(sst))/sqrt(variance_dat)

n <-length(sst)
if(n%%2==1){sst<-sst[-n] ##make data of even length
times<-times[-n]
n<-length(sst)}
pad<-1
dj <-0.25; # this will do 4 sub-octaves per octave
s0 <-2*delta_t; # this says start at a scale equal to nyquist frequency
j1 <-45; # this sets maximum number of scales
#lag1 <-0.72; # lag-1 autocorrelation for red noise background
lag1<-autocorl(sst); ##automatically calculates lag1

mother<-"DOG" ##define mother wavelet

wave_out<-wavelet(sst,delta_t,pad,dj,s0,j1,mother,2)
wave<-wave_out[[1]]; period<-wave_out[[2]];
scales<-wave_out[[3]]; coi<-wave_out[[4]]
powers<-(abs(wave))^2; rm(wave_out)

sig_out<-wave_signif(1.0,delta_t,scales,0,lag1,-1,-1,mother,-1) ###significance levels
signifs<-sig_out[[1]]; fft_theor<-sig_out[[2]]; rm(sig_out)
sig95<-matrix(signifs,nrow=length(signifs),ncol=n) ##expand to a matrix (J+1) by n
sig95<-powers/sig95

global_ws<-variance_dat*rowSums(powers)/n
dof<-n-scales
global_signif<-wave_signif(variance_dat,delta_t,scales,1,lag1,-1,dof,mother,-1)[[1]]

avg<-which(scales>=0 & scales<10)
scale_avg<-matrix(scales,nrow=length(scales),ncol=n)
scale_avg<-powers/scale_avg #Equation 24
scale_avg<-variance_dat*dj*delta_t/Cdelta*apply(scale_avg[avg,],2,sum) ##Equation 24
bound<-c(scales[avg[1]],scales[avg[length(avg)]])
signif_out<-wave_signif(variance_dat,delta_t,scales,2,lag1,-1,bound,mother,-1)
scaleavg_signif<-signif_out[[1]]; rm(signif_out)

####write the data out
t_dat<-times
t_dat<-cbind(t_dat,scale_avg)
t_dat<-cbind(t_dat,wave[16,])
fname<-paste(Out,"Data/Sca_av_",name.CST[inst],"_",Tinfo["tD","YEAR"]
,Tinfo["tD","DOY"],"_",set_end[ToD]/60,"_",y_short[vr]
,"_",mother,"_R.csv",sep="")
write(t(t_dat), file=fname, ncolumns=ncol(t_dat),sep=",")

out1<-rbind(c(0,times),cbind(period,powers))
out2<-rbind(c(-999,times),c(-999,coi),cbind(period,sig95))
out3<-rbind(period,global_ws) #,global_signif)
```

```
fname<-paste(Out,"Power/Power_",name.CST[inst],"_",Tinfo["tD","YEAR"],Tinfo["tD","DOY"]
,"_",set_end[ToD]/60,"_",y_short[vr],"_",mother,'_R.csv',sep="")
write(t(out1), file=fname, ncolumns=ncol(out1),sep=",")

fname<-paste(Out,"Signif/Signif_",name.CST[inst],"_",Tinfo["tD","YEAR"],Tinfo["tD","DOY"]
,"_",set_end[ToD]/60,"_",y_short[vr],"_",mother,'_R.csv',sep="")
write(t(out2), file=fname, ncolumns=ncol(out2),sep=",")

fname<-paste(Out,"Spectra/Spectrum_",name.CST[inst],"_",Tinfo["tD","YEAR"]
,Tinfo["tD","DOY"],"_",set_end[ToD]/60,"_",y_short[vr]
,"_",mother,'_R.csv',sep="")
write(t(out3), file=fname, ncolumns=ncol(out3),sep=",")
}}}} ###variable, time of day, instrument, date
```

Appendix 3.D: Wavelet analysis functions

This section includes the R code for all the wavelet specific functions listed in Appendices 3.C and 3.D. Note inclusion of incomplete gamma function from pracma package (Borchers, 2015).

```
####functions used for wavelet analysis
##
## autocorl
## wavelet
## wave_bases
## wave_signif
## chisquare_inv

autocorl<-function(DATA){
 alpha<-rep(NA,2); N<-length(DATA)
 for (lg in 1:2)
 {y_dat <- DATA[(lg+1):N]
 y_lag <- DATA[1:(N-lg)]
 y_dat_mean <- mean(y_dat)
 y_lag_mean <- mean(y_lag)
 y_dat <- y_dat - y_dat_mean # remove mean
 y_lag <- y_lag - y_lag_mean # remove mean
 y_dat_sq <- y_dat*y_dat
 y_lag_sq <- y_lag*y_lag
 y_lag_dat <- y_lag*y_dat
 nom <- sum(y_lag_dat) #get nominator
 var_lag <- sum(y_lag_sq)
 var_dat <- sum(y_dat_sq)
 denom <- (sqrt(var_lag)*sqrt(var_dat)) # get denominator
 alpha[lg] = (nom/denom); # get autocorrelation for each lag
 } calc_alpha = ((alpha[1] + sqrt(alpha[2]))/2) # get coeff for series background spectrum
 return(calc_alpha)
 }

wavelet<-function(DATA,delta_t,pad,dj,s0,J1,mother,param){
 n1<-length(DATA)
 if(s0==(-1)){s0<-2*delta_t}
 if(dj==(-1)){dj<-(1/4)}
 if(J1==(-1)){J1<-floor((log(n1)/log(2))+0.4999)}#floor can't do complex #s, log->inverse exp
 if(mother==(-1)){mother<-"MORLET"}

 x<-DATA-mean(DATA)
 if(pad==1)
 {base2<-floor((log(n1)/log(2))+0.4999) #power of 2 closest to N
 x<-c(x,rep(0,((2^(base2+1))-n1)))}

 n<-length(x)

 k<-1:floor(n/2) #wavenumber array used in transform (Equation 5)
 k<-k*((2*pi)/(n*delta_t))
 k<-c(0,k,-k[rev(1:floor((n-1)/2))])

 f<-fft(x) ##Equation 3

 scales<-s0*(2^((0:J1)*dj))
 period<-scale
 wave <-matrix(complex(real=0,imaginary=0),nrow=(J1+1), ncol=n) ###tes if this is necessary

 for (a1 in 1:(J1+1))
 {bases<-wave_bases(mother,k,scales[a1],param)
 daughter<-bases[[1]];fourier_factor<-bases[[2]];coi<-bases[[3]];dofmin<-bases[[4]]
```

```
 mult<-f*daughter ##split this in 2 from original
 wave[a1,]<-fft(mult, inverse=T)/length(f)} #wavelet transform Equation 4

 period<-fourier_factor*scales
 coi<-coi*delta_t*c(1E-5,1:(((n1+1)/2)-1),rev(1:(((n1+1)/2)-1)),1E-5) #COI Sec.3g
 wave<-wave[,1:n1] ##remove padding
 wave_out<-array(list(NA),4)
 wave_out[[1]]<-wave;wave_out[[2]]<-period;wave_out[[3]]<-scales;wave_out[[4]]<-coi
 return(wave_out)
 }

wave_bases<-function(mother,k,sca1,param)
{ mother<-toupper(mother); i<-complex(real=0, imaginary=1)
 bases<-array(list(NA),4); n<-length(k)
 if(mother=="MORLET")
 {if(param==(-1)){param<-6}
 k0<-param
 expnt <-(-1)*(sca1*k - k0)^2/2*(k[which(k > 0)])
            norm <-sqrt(sca1*k[2])*(pi^(-0.25))*sqrt(n) # total energy=N (Equation 7)
            daughter <- norm*exp(expnt)
            daughter <- daughter*(k[which(k > 0)]) # Heaviside step function
            fourier_factor <- (4*pi)/(k0 + sqrt(2 + k0^2)) # Scale-->Fourier [Sec.3h]
            coi <- fourier_factor/sqrt(2) # Cone-of-influence [Sec.3g]
            dofmin <- 2 # Degrees of freedom
 }else if (mother=="PAUL") #--------------------------------- Paul
           {if (param==(-1)){param = 4}
            m <- param
            expnt <-(-1)*(sca1*k)*(k[which(k > 0)])
            norm <- sqrt(scale*k[2])*(2^m/sqrt(m*prod(2:(2*m-1))))*sqrt(n)
            daughter <- norm*((sca1*k)^m)*exp(expnt)
            daughter <- daughter*(k[which(k > 0)]) # Heaviside step function
            fourier_factor <- 4*pi/(2*m+1)
            coi <- fourier_factor*sqrt(2)
            dofmin <- 2
 }else if (mother=="DOG") #---------------------------------- DOG
           {if (param==(-1)){param <- 2}
            m <- param
            expnt <- (-1)*((sca1*k)^2)/2
            norm <- sqrt(sca1*k[2]/gamma(m+0.5))*sqrt(n);
            daughter <- (-1)*norm*(i^m)*((sca1*k)^m)*exp(expnt)
            fourier_factor <- 2*pi*sqrt(2/(2*m+1))
            coi <- fourier_factor/sqrt(2)
            dofmin <- 1
 }else{
           print('Mother must be one of MORLET,PAUL,DOG')
           daughter<-NA; fourier_factor<-NA; coi<-NA; dofmin<-NA}

 bases[[1]]<-daughter;bases[[2]]<-fourier_factor;bases[[3]]<-coi;bases[[4]]<-dofmin
 return(bases)
}

wave_signif<-function(DATA,delta_t,sca1,sigtest,lag1,siglvl,dof,mother,param)
{ n1<-length(DATA)
 J1<-length(sca1)-1
 scales<-sca1 #scales[1:(J1+1)]<-sca1
 s0<-min(scales)
 dj<-log(scales[2]/scales[1])/log(2)

 if(n1==1){variance<-DATA
 }else{variance<-var(DATA)}

 if(sigtest==(-1)){sigtest<-0}
```

```
 if(lag1==(-1)){lag1<-0}
 if(siglvl==(-1)){siglvl<-0.95}
 if(mother==(-1)){mother<-"MORLET"}
 mother<-toupper(mother)

if(mother=="MORLET") #------------------morlet
 {if(param==(-1)){param<-6}
 k0<-param
 fourier_factor<-(4*pi)/(k0+sqrt(2+k0^2)) #scale -> fourier Sec .3h
 empir<-c(2,-1,-1,-1)
 if(k0==6){empir[2:4]<-c(0.776,2.32,0.60)}
 }else if(mother=="PAUL") #------------------paul
 {if(param==(-1)){param<-4}
 m<-param
 fourier_factor<-(4*pi)/(2*m+1) #scale -> fourier Sec .3h
 empir<-c(2,-1,-1,-1)
 if(m==4){empir[2:4]<-c(1.132,1.17,1.5)}
 }else if(mother=="DOG") #----------------dog
 {if(param==(-1)){param<-2}
 m<-param
 fourier_factor<-(2*pi*sqrt(2/(2*m+1))) #scale -> fourier Sec .3h
 empir<-c(1,-1,-1,-1)
 if(m==2){empir[2:4]<-c(3.541,1.43,1.4)}
 if(m==6){empir[2:4]<-c(1.966,1.37,0.97)}
 }else{
          print('Mother must be one of MORLET,PAUL,DOG')
          fourier_factor<-NA; empir<-rep(NA,4)}


 period <- scales*fourier_factor;
 dofmin <- empir[1] # Degrees of freedom with no smoothing
 Cdelta <- empir[2] # reconstruction factor
 gamma_fac <- empir[3] # time-decorrelation factor
 dj0 <- empir[4] # scale-decorrelation factor

 freqs <- delta_t / period # normalized frequency
 fft_theor <- (1-lag1^2) / (1-2*lag1*cos(freqs*2*pi)+lag1^2) # (Equation 16)
 fft_theor <- variance*fft_theor # include time-series variance
 signifs <- fft_theor
 if (dof[1]==(-1)){dof <- dofmin}

 if(sigtest==0) #-------no smoothing, DOF=dofmin sec.4
 {dof<-dofmin
 chisquare<-chisquare_inv(siglvl,dof)/dof
 signifs<-fft_theor*chisquare ##Equation 18
 }else if(sigtest==1) #------time averaged signif
 {if(length(dof)==1){dof<-rep(0,(J1+1))+dof}
 truncated<-which(dof<1)
 dof[truncated]<-1
 dof<-dofmin*sqrt(1+(dof*delta_t/(gamma_fac*scales))^2) ##Equation 23
 truncated<-which(dof<dofmin)
 dof[truncated]<-dofmin #set min of dof to dofmin
 for (a1 in 1:(J1+1))
 { chisquare<-chisquare_inv(siglvl,dof[a1])/dof[a1]
 signifs[a1]<-fft_theor[a1]*chisquare}
 }else if(sigtest==2) #---scale averaged signif
 {if(length(dof)!=2)
 {print("DOF must be set to [S1,S2], the range of scale-averages")}
 if(Cdelta==(-1))
 {print(paste("Cdelta and dj0 not defined for ",mother," with param = ",param,sep=""))}
 s1<-dof[1];s2<-dof[2]
 avg<-which(scales>=s1 & scales<=s2) #scales between s1 and s2
```

```
 navg<-length(avg)
 if(navg==0){print(paste("Error no valid scales between",s1,"and",s2))}
 Savg<-1/sum(1/scales(avg)) #Equation 25
 Smid<-exp((log(s1)+log(s2))/2) #power of 2 midpoint
 dof<-(dofmin*navg*Savg/Smid)*sqrt(1+(navg*dj/dj0)^2) #Equation 28
 fft_theor<-Savg*sum(fft_theor[avg]/scales[avg]) #Equation 27
 chisquare<-chisquare_inv(siglvl,dof)/dof
 signifs<-(dj*delta_t/Cdelta/Savg)*fft_theor*chisquare #Equation 26
 }else{print("Sigtest must be 0, 1 or 2")}

 out<-list(signifs, fft_theor)
 return(out)
}

chisquare_inv<-function(P,V)
{
 Chi_tab=[0.0000393,0.000157,0.000982,0.00393,3.841,5.024,6.635,7.879,10.828;...
 0.010003,0.02010,0.05064,0.1026,5.991,7.378,9.210,10.597,13.816];
 Pvals=[0.005,0.01,0.025,0.05,0.95,0.975,0.99,0.995,0.999];
 Deg_fre=[1,2];

          if ((1-P) < 1E-4){print("P must be < 0.9999")}
# if (P<10)
# Pindex= Pvals==P;
# Degidx= Deg_fre==V;
# X=Chi_tab(Degidx,Pindex);
# else
 MINN <- 0.01
          MAXX <- 10
 TOLERANCE = 1E-4
 out<-seq(MINN,MAXX,by=TOLERANCE); out<-cbind(out,rep(NA,length(out)))
 for(ot in 1:nrow(out)){out[ot,2]<-gammainc(V*out[ot,1]/2,V/2)[[3]]}
           PDIFF <- abs(out[,2] - P) # error in calculated P
 lowest <- which(PDIFF==min(PDIFF))
 X<-out[lowest,1]
          return(X)
          }

## g a m m a i n c . R Incomplete Gamma Function
## from pracma package
gammainc <- function(x, a) {
 if (!is.numeric(a) || !is.numeric(x))
 stop("All arguments must be real numbers.")
 if (length(a) > 1 || length(x) > 1)
 stop("Arguments must be of length 1; function is not vectorized.")
 if (x == 0 && a == 0) return(1)
 if (a < 0)
 stop("Argument 'a' must be real and nonnegative.")

 if (x > 0) xam <- -x + a*log(x)
 else xam <- -x + a*log(x + 0i)
 if (abs(xam) > 700.0 ){ #|| abs(a) > 170.0) {
 warning("Arguments 'x' and/or 'a' are too large.")
 return(NA)
 }

 # Computation of the incomplete gamma function
 gin <- gim <- gip <- 0

 if (x == 0.0) {
 ga <- gamma(a)
 gim <- ga
```

```
 gip <- 0.0
 } else if (x <= 1.0 + a) {
 s <- 1/a
 r <- s
 for (k in 1:60) {
 r <- r * x/(a+k);
 s <- s+r;
 if (abs(r/s) < 1e-15) break
 }
 gin <- exp(xam) * s
 ga <- gamma(a)
 gip <- gin/ga
 gim <- ga - gin
 } else if (x > 1.0 + a) {
 t0 <- 0
 for (k in 60:1) {
 t0 <- (k-a)/(1 + k/(x+t0))
 }
 gim <- exp(xam)/(x+t0)
 ga <- gamma(a)
 gin <- ga - gim
 gip <- 1 - gim/ga
 }
 return(c(lowinc = Re(gin), uppinc = Re(gim), reginc = Re(gip)))
}
```

Chapter 4 Controls on CO_2 concentrations in central London

4.1 Introduction

As discussed in Section 1.3 and 1.4, some of the factors affecting the atmospheric carbon dioxide concentration (*[CO_2]*) in urban environments are very different to those found in rural environments. Even those sources or sinks which are similar, such as uptake of CO_2 by vegetation, may be modified (longer growing seasons due to the urban heat island effect (Imhoff *et al*., 2000), reduced impact due to lower land surface cover) and not directly comparable to rural counterparts. In this chapter the factors or processes controlling CO_2 concentrations in central London are assessed. As these operate at many different timescales (Table 4.1) this chapter begins by reporting annual, diurnal and seasonal patterns of the *[CO_2]* profile and discussing the impact of human activities at different time scales (Section 4.2). The effect of space heating on *[CO_2]* is evaluated using 1 h median *[CO_2]* measured directly above two types of rooftop sources when the building is minimally (e.g., vacation) and heavily (e.g., term time) occupied using periods with similar air temperatures (Section 4.3). This analysis is extended to cover events of interest, including the Olympics and bank holidays in Section 4.4. An assessment is made of the impact of traffic (Section 4.5.1), the urban surface and its interaction with synoptic wind conditions (Section 4.5.2), and local scale atmospheric stability (Section 4.5.3) on the concentration profile.

As expected, the influence of human activities can be seen in the variations in *[CO_2]* at different heights. Seasonal differences change not only the meteorological conditions (e.g., changing atmospheric stability and mixing layer height) but also the usage of buildings (e.g., need for heating, number of people within the building). Within seasons there are strong hebdomadal variations in human behaviour between weekdays and weekends. These include large differences in building usage and traffic patterns but without strong meteorological variations. At the diurnal time-scale both human activities and atmospheric conditions vary. The latter determines the source area of the measurement and the extent to which emissions from land use types in the measurement footprint are blended before reaching the sample point. The impacts of source area and land use type are explored in greater depth in chapters 6 and 7.

Table 4.1: Factors affecting CO_2 concentrations ($[CO_2]$), the timescales at which they tend to vary, including days of note (DoN) such as public holidays or heavy rainfall, sub-factors which control or are linked to each primary factor and whether these sub-factors are measured at or in the vicinity of KS.

Factor	Timescales	Sub-factors	Measured?
Anthropogenic factors (all vary with daylight savings time)			
Vehicle Emissions	Daily, weekly, DoN	Fleet characteristics (age, fuel type)	Averages available
		Vehicle speed	Averages available
		Number of vehicles	At discrete locations
		Cold/hot start	No
Building Emissions for space heating	Daily, weekly, seasonal, DoN	Air temperature	Yes
		Building occupancy	No
		Fuel type	Yes, in aggregate
Human respiration	Daily, weekly, seasonal, DoN	Population	Day and night time populations of boroughs from census data (does not include tourists)
		Activity	No
		Physical characteristics: age, weight, etc.	No
Other combustion: cooking, industry	Daily, weekly, DoN	Activity type	No
		Fuel type	Yes, in aggregate
Natural factors			
River efflux	Daily (tidal), seasonal, DoN	Carbon content	No
		Water temperature	Yes
		Recent rainfall (sewer overflow)	Yes
Mixing layer height	Daily, seasonal	Calculated from backscatter profiles of ceilometers	Yes
Boundary layer stability	Daily, seasonal	Calculated from high temporal resolution 3D wind measurements above the blending height.	Yes
Vegetation	Daily, seasonal	Incident radiation	Yes
		Soil moisture	Yes
		Soil temperature	Yes
		Air temperature	Yes
		$[CO_2]$	Yes
		Species	Surveyed
		Damage (insects, etc.)	No
		Age	Calculated from survey (woody vegetation)
Soil	Daily, seasonal	Soil moisture	Yes
		Soil temperature	Yes
		Soil carbon content	No
Animals	Daily, seasonal	Population	No
		Activity	No
		Species	No
		Physical characteristics: age, weight, etc.	No

4.2 Temporal variation

The 2 Hz *[CO_2]* data (LI840, Section 2.2.1) enable analysis of the temporal variation of *[CO_2]* at time scales ranging from the sub-hourly (one cycle through all measurement heights takes 10 minutes) to the interannual.

4.2.1 Annual and Seasonal cycle

Monthly mean *[CO_2]* measured at KSS or KSSW tower top (height A, Figure 2.1d) tend to increase at a rate equivalent to or greater than the Global Background Level (GBL) observed at the Mauna Loa Observatory (NOAA, 2014) (Table 4.2). Monthly mean *[CO_2]* increase each year for 71% of months (Table 4.2). Most of the months in which concentrations are lower compared to the previous year occur in 2014 and only two are below the GBL. On an annual scale the city centre can be considered a CO_2 source.

Table 4.2: Monthly mean CO_2 concentrations measured at KSS and KSSW by LI840 in ppm and relative to monthly mean Global Background Levels (GBL) at Mauna Loa (NOAA, 2014). Sites changed from KSS to KSSW 2012/085 (see Figure 2.1 for locations). Monthly [CO_2] colour coded according to whether they are greater (red) or lesser (green) for that month year on year. Ratios to GBL colour coded as greater (red) and lesser (green) than 1.

	$[CO_2]_{KSS(W)}$ (ppm)				$[CO_2]_{KSS(W)}/[CO_2]_{GBL}$			
Month\Year	2011	2012	2013	2014	2011	2012	2013	2014
January		420	436	444		1.07	1.1	1.12
February		415	435	420		1.06	1.1	1.06
March		405	429	412		1.03	1.08	1.03
April	401		413	414	1.03		1.04	1.04
May	395		406	411	1.01		1.02	1.03
June	404	399	404	397	1.03	1.01	1.02	0.99
July	396	402	405	393	1.01	1.02	1.02	0.99
August	396	398	403	408	1.01	1.01	1.01	1.02
September	404	403	412	426	1.03	1.02	1.04	1.07
October	417	418	424	428	1.06	1.06	1.07	1.07
November	436	433	449	444	1.11	1.1	1.13	1.11
December	421	441	460	440	1.07	1.12	1.16	1.1

Nearly all hourly median *[CO_2]* values are also above GBL throughout the year (Figure 4.1), GBL of 391.62, 393.82, 396.48, and 398.61 ppm for 2011 to 2014 respectively (NOAA, 2014)). Within-canyon *[CO_2]* matches or exceeds that recorded at the tower top at all times of year. Annual mean *[CO_2]* measured at KSSW in 2013 was 423 ppm, 27 ppm above GBL (NOAA, 2014); however, much higher concentrations were recorded, particularly when the weather was cold and during term time. The lowest *[CO_2]* values occur in a broad minimum over the summer holidays (the impact of the building occupancy, notably the presence of students can be seen in the rise in *[CO_2]* after the start of term, (Figure 4.1), with a second, shorter minimum during the Christmas-New Year period when the campus is shut and extended holidays reduce the number of workers present. The impact of the working week is explored further in the next section.

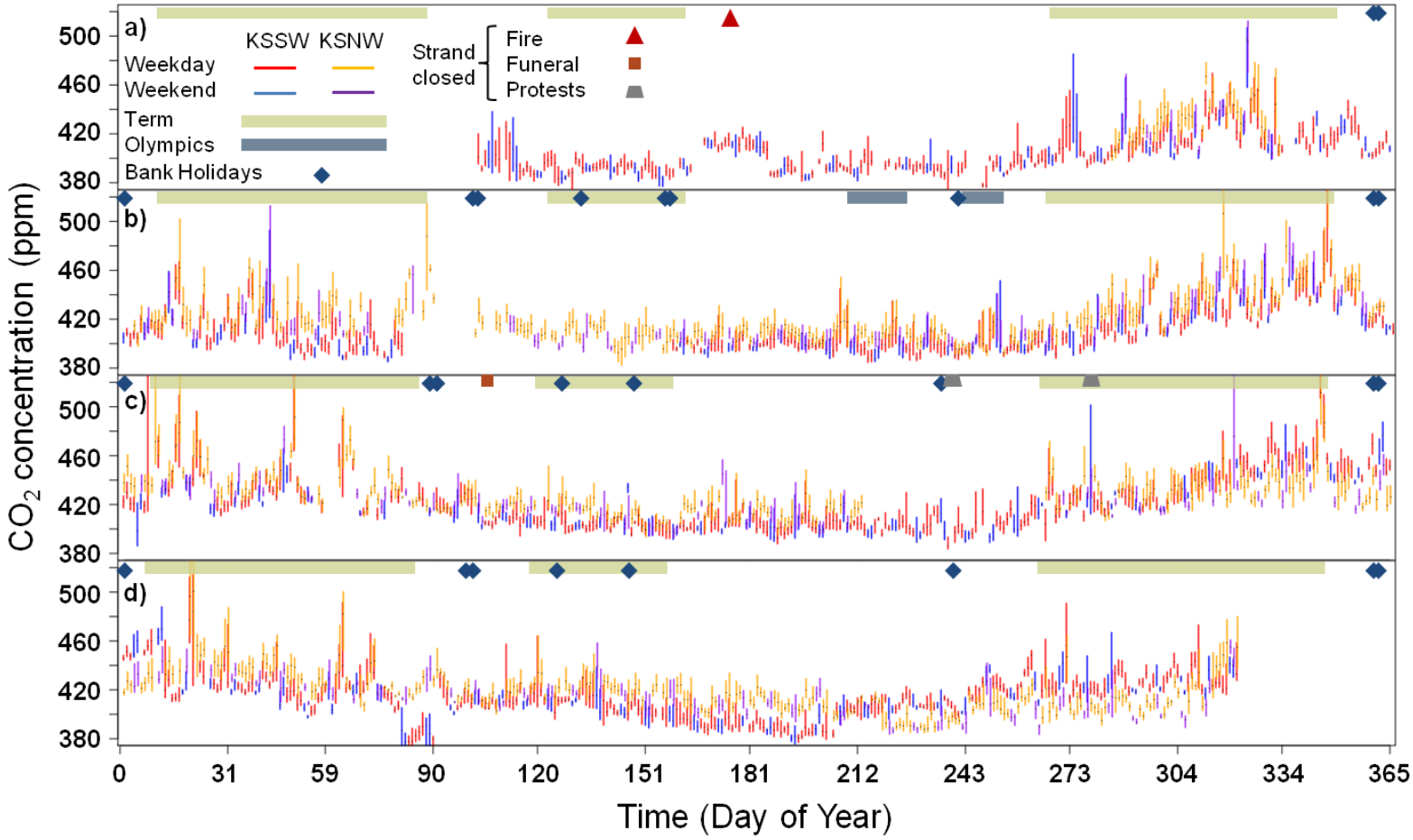

Figure 4.1: CO_2 concentrations (ppm, 1 minute averages) measured above and within the Strand street canyon (2011/111-2012/084; 2012/156-2013/266) for (a) 2011, (b) 2012, (c) 2013, (d) 2014. Vertical bar: interquartile range for data collected over one day. Red: weekday at height A; orange: weekday at height G; blue: weekend at height A; purple: weekend at height F (see Figure 2.1d for heights). Days of note include: term time days (pale horizontal bar), bank holidays (blue diamond), fires (red triangle), Olympics (dark bar) and Strand road closures (Lady Thatcher's funeral, red square; protests, grey trapezoid) are indicated on the top of each annual plot.

The potential of the summer minimum to be caused by photosynthetic uptake was explored by taking the linear regression of *[CO_2]* measured at height A (Figure 2.1d) by LI840 for 2012 to 2015 on multiple variables associated with plant productivity, namely Bowen ratio, time since rainfall, and photosynthetically active radiation (PAR). Both the Bowen ratio and the time since rainfall were associated with small (<6 ppm) variation in *[CO_2]* across the entire range of values observed (Bowen ratio: -1 to 50, time since rainfall: 0 to 29 days). The variation with PAR was much greater, but was almost identical to the magnitude of the variation with mixing layer depth (Section 4.5.3), which also varies with incoming shortwave radiation. In other words, due to the low vegetated land fraction (Section 2.1), the decrease in *[CO_2]* is likely to be due to the increase in mixing layer depth, with which the PAR co-varies, rather than photosynthetic uptake by vegetation. The effect of vegetation on urban CO_2 emissions is explored further in Section 7.3.1.

The seasonal cycle of *[CO_2]* observed in this study agrees reasonably well with previous observations in London (Sparks and Toumi, 2010), insofar as *[CO_2]* tends to vary according to demand for space heating, with lowest concentrations measured June to September and highest December to February (with the aforementioned exception of the Christmas – New Year period). In contrast, Haiduc and Beldean-Galea (2011) found the *[CO_2]* measured in three small to medium sized Romanian cities peaked during the autumn, as plant die-off reduced uptake via photosynthesis, but soil temperatures remained high enough for significant release of CO_2 by respiration. Their results should, however, be interpreted with caution as measurements were made only from 8:30 am to 5:30 pm.

As a project initially designed to investigate the metabolism of natural vegetation on Long Island, measurements made by Woodwell *et al*. (1973) in a 2000-ha oak-pine forest, 97 km east of New York City, could be considered semi-rural and would be expected to agree well with results from the smallest (population ca.10,000) of the three Romanian towns studied by Haiduc and Beldean-Galea (2011). Instead, a peak of about 15 ppm above the late summer minimum was observed December-January. The 'signal' from mega-cities can therefore be seen to have a greater impact on the measured seasonal cycle of *[CO_2]* than photosynthetic uptake and respirative release of CO_2 by flora and fauna in the vicinity of the measurement site, even for stations of the order of 100 km away from an urban area. Whilst the processes investigated in this study are micro to local in scale, their cumulative impact is meso to macro scale. Overall *[CO_2]* is greater within the city centre than global background levels and higher concentrations are associated with heating demand and building occupancy. The latter is explored further in Section 4.3.

4.2.2 Hebdomadal cycle

The working week in the UK is Monday to Friday. The Strand campus is closed to undergraduates on Saturday and Sunday, and traffic volume on the Strand is reduced

(Figure 4.14a). This section provides a qualitative overview of the importance and impact of traffic, human respiration and atmospheric stability on *[CO_2]* by comparing *[CO_2]* with height above the street for three days: a Sunday (low traffic, low population, Figure 4.2a), a day on which there were timed restrictions on traffic for the Strand (Lady Thatcher's funeral, no traffic, normal population, Figure 4.2b), and a weekday (normal traffic, normal population, Figure 4.2c).

The main features of the weekend plot (Figure 4.2a) are lower *[CO_2]* values throughout the day compared to the weekday plot and a broad peak in *[CO_2]* at low elevations between 3 and 9 pm. Weekday concentrations are much higher (Figure 4.2c), particularly at street level, and the main peak occurs between 4 and 8 am, with the highest *[CO_2]* at street level measured between 7 am and 8 am. Much of this peak can be assigned to traffic emissions, as a similar peak begins on day 2013/107 (Figure 4.2b), but ceases growing at 06:00 GMT (07:00 BST) when road closures began (buses had begun to be diverted an hour prior). Vertical mixing and dilution of the emissions are observed (Figure 4.2b) as measured *[CO_2]* at 08:00 GMT were approximately 10 ppm lower at street level than at the highest measurement point.

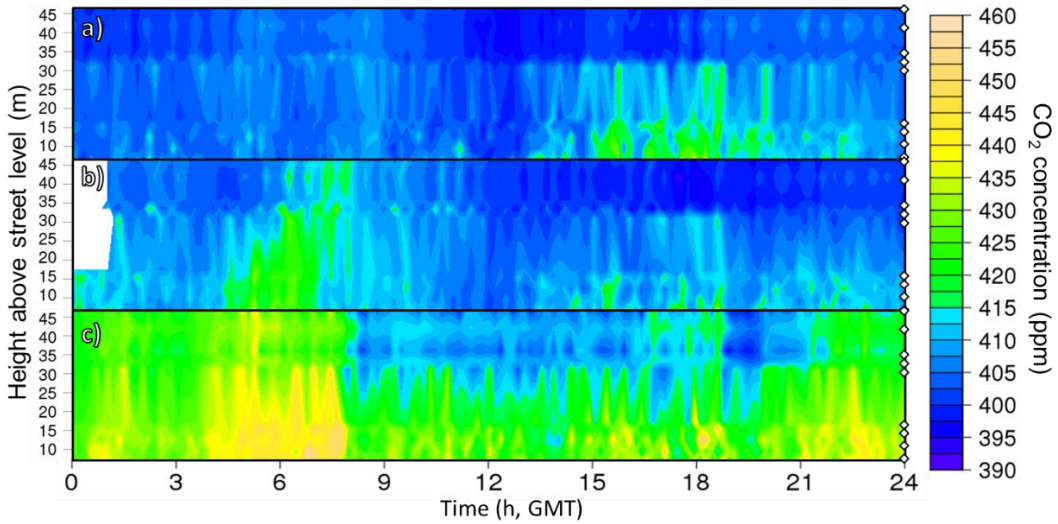

Figure 4.2: 1 minute CO_2 (ppm) average concentrations (key, far right) by time of day (x-axis, h) and height above the Strand (m) for (a) Sunday 2013/104, (b) Wednesday 2013/107, Lady Thatcher's funeral and (c) Wednesday 2013/114. White diamonds (right) denote measurement locations (Table 2.2), Figure 2.1d heights A-E, G-J).

Once the mixing out of earlier emissions is complete (ca. 08:30 GMT) the vertical *[CO_2]* profile reverts to decreasing concentrations with increasing height, albeit with a much smaller difference between height A and height J (5.10 ppm) than is typically observed on normal weekdays (e.g., Figure 4.2c). Given that the funeral was held on a weekday, it is assumed that the population density of the borough of Westminster was not greatly dissimilar to the average daytime population (including tourists) of 41,760 km^{-2} (GLA, 2014b; ONS, 2011). Given the very low fraction of permeable land cover (Section 2.1.1), this difference is unlikely to be due to emissions from soil respiration and is instead ascribed to

respiration by people lining the streets at that time. This suggests an increase in *[CO_2]* at street level in the vicinity of KS on the order of 1 ppm for every 8200 people per km^2, but due to the assumptions discussed above, should be treated with caution and taken as a broad estimate only.

4.2.3 Diurnal cycle

The diurnal pattern of measured *[CO_2]* is characterised by a peak in both absolute concentration and variance at 9:00, UTC, coinciding with the rush hour (Figure 4.3, Figure 4.14a). There is a similar, smaller, peak in the evening, though as traffic remains high throughout the day (Figure 4.14a), this increase is likely to be at least partially due to reduced mixing in the urban boundary layer.

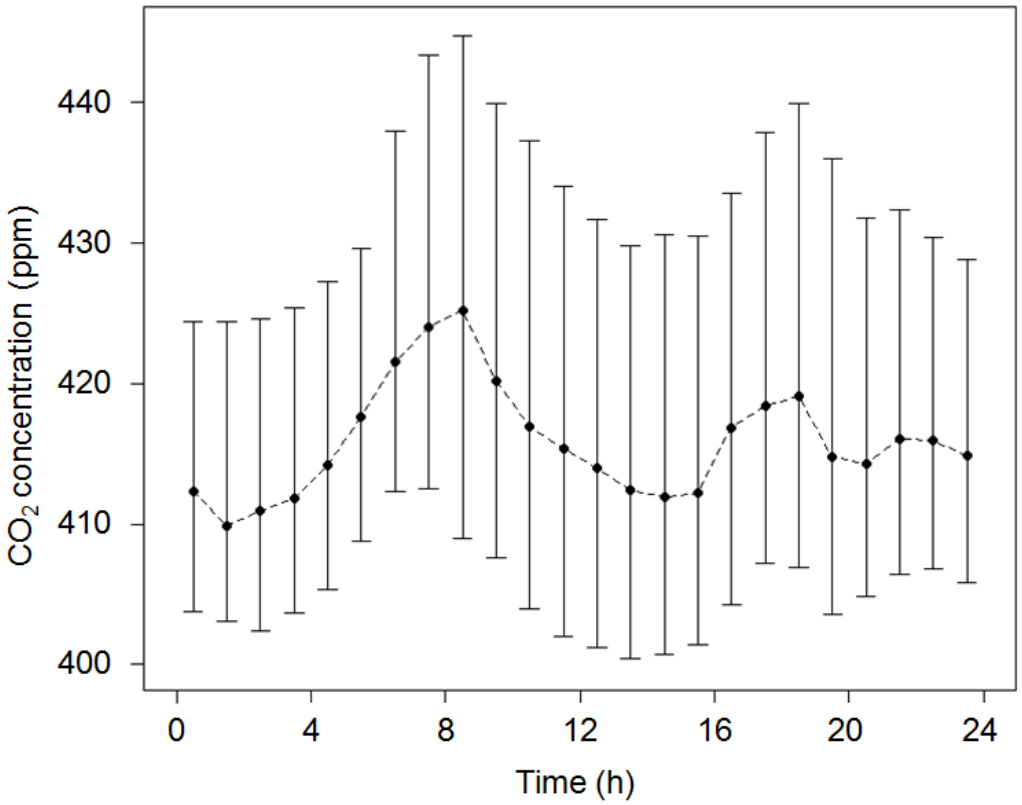

Figure 4.3: Diurnal cycle of hourly (GMT) median CO_2 concentration, 2012/001-366, Height G (Figure 2.1d, z_i/z_b = 0.76), C3-C6. Vertical bars denote interquartile range.

Annual hourly median *[CO_2]* ranges from 409.9 to 425.2 ppm (1.04 – 1.08, normalised by GBL, Figure 4.3), whilst daily median *[CO_2]* ranges from 392.7 to 525.7 ppm (1.00 – 1.33, normalised by GBL) at half canyon height (Figure 4.1), indicating that there are large CO_2 sources in the vicinity of the measurement site. These are significantly higher than the range of 0.96-1.03 recorded by Helfter *et al.* (2011); however, at least part of this difference may be due to the difference in measurement height (190 vs. 46.4 m above street level and below in this study) as measurements reported by Sparks and Toumi (2010) at $2z_b$ gave

mean half-hourly *[CO_2]* of 410 ± 21 ppm, which agrees well with the values reported in this study.

The diurnal range (15 ppm) is relatively low compared to previous studies, such as Reid and Steyn (1997), who recorded a peak to peak difference of 27 ppm (averaged over 11 days) in Vancouver, and Vogt *et al.* (2006) who reported 61 ppm (averaged over 28 days) in Basel. Both the range and the diurnal cycle are similar to that measured in Edinburgh by Nemitz *et al.* (2002), with a main peak in the morning (07:00-10:00) about 15 ppm above midnight levels and a lower, broader one later in the day. This cycle is unlike that observed in Mexico City (Velasco *et al., 2*009), which did not contain a second peak in the afternoon, though concentrations did rise steadily overnight. Velasco *et al.* (*2*009) attributed the overnight peak to the formation of a stable nocturnal boundary layer and subsequent accumulation of CO_2 emitted by vehicles during the evening rush hour. Due to the similarity in traffic patterns and working hours between Mexico City and central London, the difference in the median diurnal cycle of CO_2 concentration is thought to be due to greater insolation and a deeper, more sustained daytime boundary layer in Mexico City relative to temperate N European cities. The impact of the boundary layer on the *[CO_2]* profile is discussed further in Section 4.5.3.

4.3 Microscale sources

Combustion for space heating can be a major source of CO_2 in urban areas (Helfter *et al*., 2011) and varies depending upon building occupancy and air temperature (T_A). At the Strand campus heating is provided by a central gas-fired boiler (McIntyre, 2013), the chimneys of which were situated to the east of the KSS and KSSW measurement sites. As the primary study site is an academic building, there are periods in both winter and summer when the occupancy is quite different. This is expected to influence the micro-scale vertical *[CO_2]* profile. Direct measurements of *[CO_2]* made near roof vents and chillers for the period 2011/025-2012/085 (Configurations C2andC3, Table 2.2) are analysed.

Low (LO) and high (HO) occupancy periods of a fortnight are compared for seasons with mean working day T_A below and within the UK thermal comfort range (THR, range defined as 16 – 24 °C; Workplace (Health, Safety and Welfare) Regulations (1992), Hartley (2006)). The micro-scale variability of rooftop sources ($[CO_2]_i$) are reported relative to top of tower ($[CO_2]_h$) or local- scale variability ($\Delta[CO_2] = [CO_2]_i - [CO_2]_h$).

The periods chosen have similar temperature distributions (Figure 4.4, insert), with a slight bias towards lower T_A during the low occupancy (LO) period in both seasons. It is therefore assumed that within-season differences in measured $\Delta[CO_2]$ are due to the presence or absence of people (students during term time). As access to the Strand and King's buildings are not monitored on weekdays, it is not possible to calculate the building occupancy (postgraduate students and staff) population during vacation periods; however, during the

Christmas to New Year period it is expected to be limited to a very small number of staff as the University is closed.

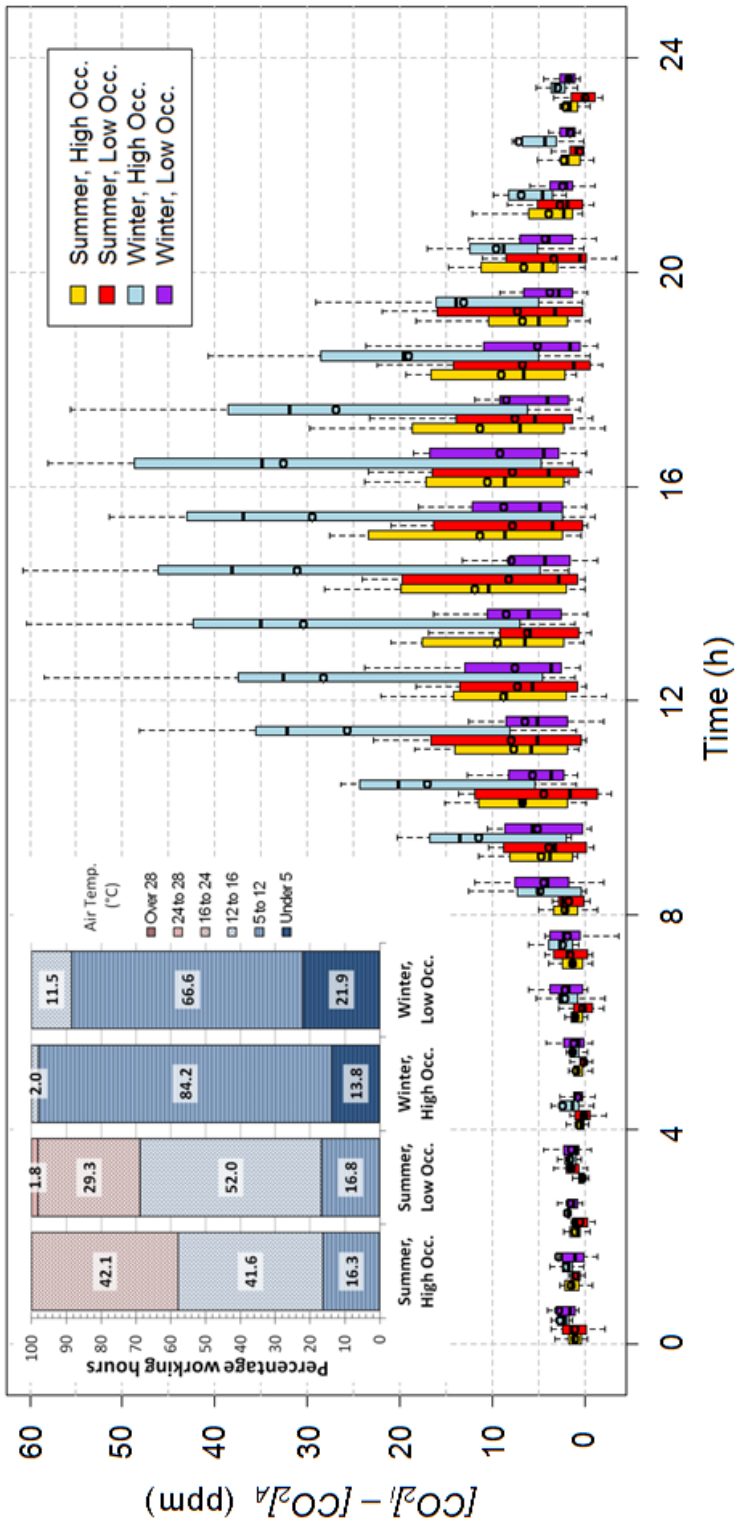

Figure 4.4: CO_2 concentration measured over an air conditioning vent ($[CO_2]_i$, 2 m to south west of KSS) relative to background ($[CO_2]_h$, KSS, z_i=43.18) for two periods of high occupancy (Summer: 2011/141 – 2011/154 & Winter: 2011/336 – 2011/349) and two of low occupancy (Summer: 2011/155 – 2011/168 & Winter: 2011/350 – 2011/363)(key, right inset). Bar: median, circle: mean, box: interquartile range, whiskers: 95% confidence limits. Left inset: Temperature distribution measured at KSK (WXT510) for each period.

In summer (S), median $[CO_2]$ above the air conditioning vents reaches a maximum of 10.5 ppm above local background levels (14:00 – 15:00 local time, HO), with the latter defined as measurements made at the top of the KSS tower. It rises above 5 ppm for 8 out of 10 working hours (working hours defined as 08:00 to 18:00 GMT) during the HO_S period, and 4 out of 10 working hours of the LO_S period (working hours with T_A below THR are 57.9 and 68.9% for HO_S and LO_S respectively) (Figure 4.4).

Hourly $\Delta[CO_2]$ distributions are similarly skewed for summer HO_S and LO_S, rising from skew of approximately 0 at 09:00 local time to 0.5 at 20:00, with LO_S skew generally higher than HO_S by 0.1. This indicates a slightly higher frequency of high $\Delta[CO_2]$ periods on HO summer days.

In winter (W), all working hour T_A values are below the THR (Figure 4.4, insert). Whilst median LO_W $\Delta[CO_2]$ remains below 5 ppm for all but one hour, and within 2.5 ppm of summer LO_S values throughout the day, median HO_W $\Delta[CO_2]$ rises from approximately equal to summer values (23:00 – 08:00) to a peak of 38 ppm (15:00 – 16:00).

Unlike summer values, in winter the hourly LO_W data are highly positively skewed (skew > 1) between 11:00 and 19:00. This may be due to intermittent venting from above roof air conditioning. It cannot have been due to emissions from the central boiler as this was turned off (Olive Byrne, personal communication, 2014) during the holiday. In contrast, the skew of the binned hourly HO_W data ranges from 0 overnight to -0.6 during the afternoon. Air temperatures well below the THR and high building occupancy result in a large proportion of time periods with high building emissions from space heating and hence high $\Delta[CO_2]$. Similar trends were observed for measurements made over a chiller to the south of the KSS tower (Appendix 4.A).

Attempts to quantify the impact of these emissions using the flux-gradient method were unsuccessful. Stability conditions for which the flux-gradient method would be appropriate ($|z'/L| < 1$, Kaimal and Finnigan, 1994; see Section 4.5.3 for details of z'/L) occurred for only 1400 half hourly periods or 29 days out of a 348 day observation period (C2 and C2, Section 2.2.1) for which span corrected LI840 data were available. This was deemed insufficient to quantify the contribution of space heating at KS to the overall flux on an annual timescale.

An alternative method was to relate the $[CO_2]$ measurements to ambient T_A for different temporal subsets of the overall $[CO_2]$ time series. The subsets chosen were weekday vs. weekend (differences ascribed to commuter population of surrounding buildings), and term vs. holiday (differences ascribed to student population of the Strand building). Data were split into day (09:00 to 17:00 GMT) and night (09:00 to 05:00 GMT) cohorts to avoid direct comparisons between observations with different mixing layer depths and traffic emissions. The $[CO_2]$ decreased with increasing T_A until approximately 20 °C, at which both night-time and daytime $[CO_2]$ values increased with T_A, with the increase more pronounced during the night than the day. Work days (weekdays and/or term time days) tended to have higher concentrations than non-work (weekends and/or holidays), except above ca. 20 °C. The difference between work and non-work day concentrations was most positive at lower T_A. For the comparison between term time and holidays the difference decreased from ca. 25 ppm at 2 °C to ca. 5 ppm between

6 and 16 °C. Above 16 °C the difference decreased further to below 0 by 20 °C. The difference between weekday and weekend $[CO_2]$ decreased linearly with increasing T_A from ca. 12 ppm and 2 ppm at 0 °C to 0 ppm and -6 ppm at 25 °C for day and night time respectively; however, the correlation between $[CO_2]$ and T_A was very low (R^2 of 0.1). In summary, the effect of the space heating on $[CO_2]$ at height A for buildings around KS increases by 0.6 ppm for every degree decrease in T_A for all air temperatures between -2 and 30 °C, whereas the space heating at the Strand building increases $[CO_2]$ by 5 ppm between 6 and 16 °C and has an increasing effect with decreasing T_A (-0.6 ppm $°C^{-1}$) either side of this range. The impact of space heating on CO_2 concentrations is therefore both building use and air temperature dependent.

4.4 Olympics and other unusual events

This section assesses the impact of certain days of interest such as national holidays or strikes on $[CO_2]$ measured in central London. It will begin with a discussion of the effect of the Olympics on the micro and local scale $[CO_2]$ measured at the Strand campus, including the change to Sunday Trading laws. It will then describe the effect of bank holidays on the CO_2 profile, and will finish by comparing the vertical and spatial variation of measured $[CO_2]$ during the week around Christmas with the one immediately prior.

4.4.1 Olympic Lane restrictions

Lane restrictions for the London 2012 Olympics came into force on Wednesday the 25th July, with the games officially starting the following Friday. Although no traffic data for the relevant period in 2010, 2011 or 2013 were available to directly compare the impact of the Olympics on traffic flow, comparison of counts at the Royal Court of Justice (RCJ, 250 m to the east north east of KS) for the Olympic period ($V_{Olympic}$) with those made 4 months prior (V_{April}) suggest a slight reduction in peak daytime vehicle counts (typical weekday counts range from 400 per hour between 00:00 and 03:00, GMT, to 1500 per hour between 09:00 and 20:00, GMT) and a small overnight increase (Figure 4.5).

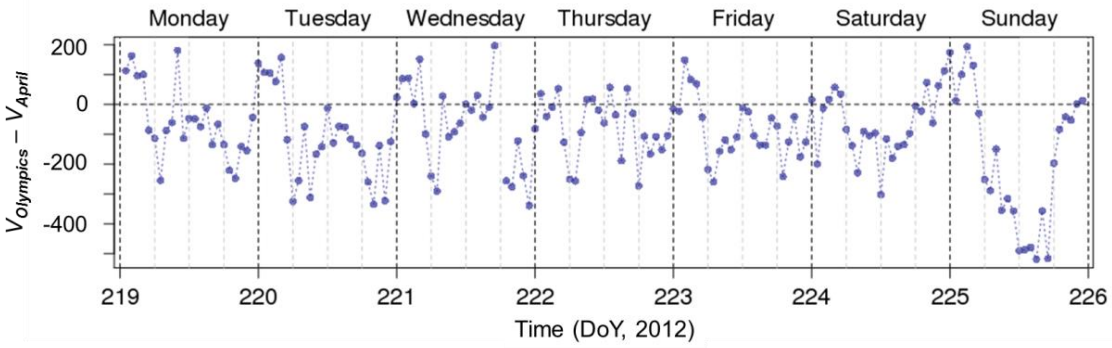

Figure 4.5: Difference between vehicle numbers counted automatically at the Royal Courts of Justice for a week during the Olympics ($V_{Olympics}$, 2012/219-225) and one 4 months prior (V_{April}, 2012/107-113) (FoI, TfL, 2013a). No events (e.g., marathon) took place within Central London during either week.

In this section, *[CO_2]* profile data for the first week following the lane restrictions are compared with an equivalent period in 2013 in order to assess the impact of the Olympics on *[CO_2]* within the street canyon (KSNW) and at the local scale (KSSW). This is done by comparing the diurnal cycles measured at height A (KSSW, Figure 2.1d) during the following year (2013) with those at height A in 2012 (during the London Olympic games) and at height G ($z_i/z_b \approx 3/4$) for both years (Figure 4.6). A positive difference indicates that *[CO_2]* was lower at height A in 2013 than the data compared and vice versa for a negative difference.

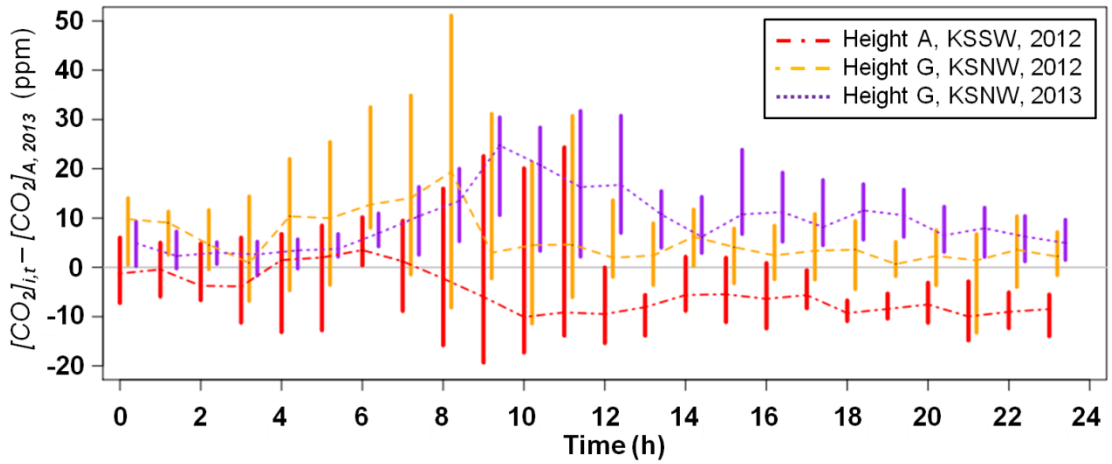

Figure 4.6: Effect of the London 2012 Olympics on the diurnal cycle of hourly median CO_2 concentrations plotted as the difference of [CO_2] measured at location i, time t, ($[CO_2]_{i,t}$) from [CO_2] measured at Height A (z_A) in 2013 ($[CO_2]_{A,\,2013}$) with time of day. Data collected 2012/207-213 and 2013/205-211. Dotted lines denote median and vertical bars the interquartile range.

The Olympics had little impact on the observed *[CO_2]* at the local scale between 00:00 and 07:00 GMT (Figure 4.6). It was not until the onset of the morning rush hour that *[CO_2]* above the canyon during 2012 dipped significantly (greater than the accuracy limit of the LI840, i.e., 1% of reading, LI-COR, 2003) below that measured in 2013, with the maximum difference occurring at 10:00-12:00 GMT and remaining greater than 5 ppm for the rest of the day. This is in accordance with news reports at the time (Smale, 2012) which suggested traffic in the city centre was lower as tourists tended to avoid the centre in favour of the Olympic park in Stratford, and residents postponed trips until after the Olympics were over.

Within the canyon, measured *[CO_2]* were higher during the small hours and peaked earlier in the day (04:00 to 08:00 GMT) during the Olympics than in 2013. This was potentially due to an initiative by TfL (TfL, 2013b) which aimed to reduce daytime congestion by rescheduling road freight to deliver out-of-hours (00:00 to 06:00). A reduction in CO_2 emissions was also observed in Beijing during the 2008 Olympics (Worden *et al., 2*012), predominantly due to traffic controls.

4.4.2 Impact of the Sunday Trading (London Olympic Games and Paralympic Games) Act 2012.

UK retailers may open for business on all days of the week; however, there are restrictions on Sunday opening hours for retailers with a shop area of greater than 280 m^2 and which are not otherwise exempt (Sunday Trading Act, 1994). Sunday trading laws were suspended for the duration of the Olympics and Paralympics (22nd July 2012 to 8th September 2012, Sunday

Trading (London Olympic Games and Paralympic Games) Act, 2012). This section examines whether the suspension of the Sunday trading laws had any measurable effect on *[CO_2]* in central London.

Data for three sets of days were extracted for analysis. The first set was named 'Sunday Only' (SO) and consisted of days for which the usual Sunday trading laws were suspended and there were no Olympic or Paralympic activities (22nd of July and 2nd and 9th of August, 2012). The second set consisted of days for which Sunday trading laws were suspended and Olympic or Paralympic activities took place (27th July, 5th and 12th August, 2nd September, 2012. 9th September excluded from analysis due to poor data quality) and was called the Olympic/Paralympic (OP) set. The third set was selected after visual inspection of hourly/monthly plots (Appendix 2.B) of factors which could affect the *[CO_2]* profile in order to find a number of days with similar conditions but without the Sunday Trading laws suspension to act as a benchmark (BM). These days were the 17th and 24th June, and the 1st, 8th and 15th July, 2012. Comparison of mean and median diurnal cycles of atmospheric conditions for these sets showed predominantly similar values for radiation, but higher midday latent heat flux and friction velocity for the benchmark days (Appendix 4.B).

Relaxing Sunday trading laws did not appear to increase traffic relative to the benchmark (Figure 4.7); however, this result cannot be extended to suggest that traffic volumes would not increase were Sunday trading laws to be suspended again or abolished entirely as the suspension period coincided with traffic controls (TfL, 2013b) and a public information campaign advising people to postpone trips to the city centre if possible.

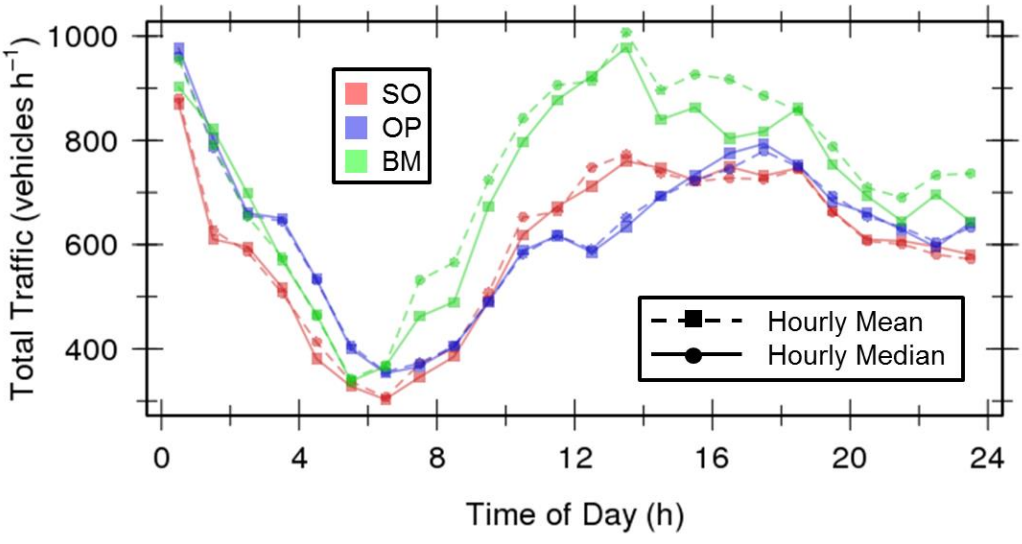

Figure 4.7: Hourly mean and median traffic count at RCJ (Figure 2.1b) for three sets of days: 'Sunday Only' (SO), 2012/204, 232, 239; 'Olympic/Paralympic' (OP), 2012/211, 218, 225, 246; 'Benchmark' (BM), 2012/169, 176, 183,190, 197.

When hourly mean *[CO_2]* profiles for the SO and OP periods are plotted as the difference from the BM, there are clear differences in diurnal cycle (Figure 4.8). The SO period has much higher (5 to 19 ppm) *[CO_2]* at all heights between midnight and 8 am GMT (01:00 – 09:00 BST). Concentrations close to the road after 08:00 GMT are about 7 ppm below the benchmark and

are equal or below BM *[CO_2]* at all heights after 17:00 GMT (18:00 BST). Concentrations in the morning decrease close to the road first with upward mixing seemingly paused around midday. It is suggested that this is due to radiative shadowing of the street canyon by the Strand building, and that the overall cycle of *[CO_2]* in the SO period is primarily controlled by boundary layer stability. The latter half of the overnight peak in concentrations (Figure 4.8a) coincides with a minimum in traffic volume (Figure 4.7) and is therefore likely to be due to the collapse of the boundary layer rather than street level emissions.

During the games, the diurnal cycle is more muted with all hourly values differing from the benchmark by no more than 7 ppm. Street level *[CO_2]* values are higher throughout the day than the benchmark (Figure 4.8b), despite fewer vehicles passing RCJ (Figure 2.1b) per hour (Figure 4.7). It is possible that this is either due to slower traffic speed due to lane restrictions, or to higher emissions from human respiration due to the greater number of tourists during the games period. The former is more likely as the latter would require the population density to more than double compared to the average (Section 4.2.2). Above canyon *[CO_2]* tended to be equal or less than BM except between 04:00 and 07:00 GMT.

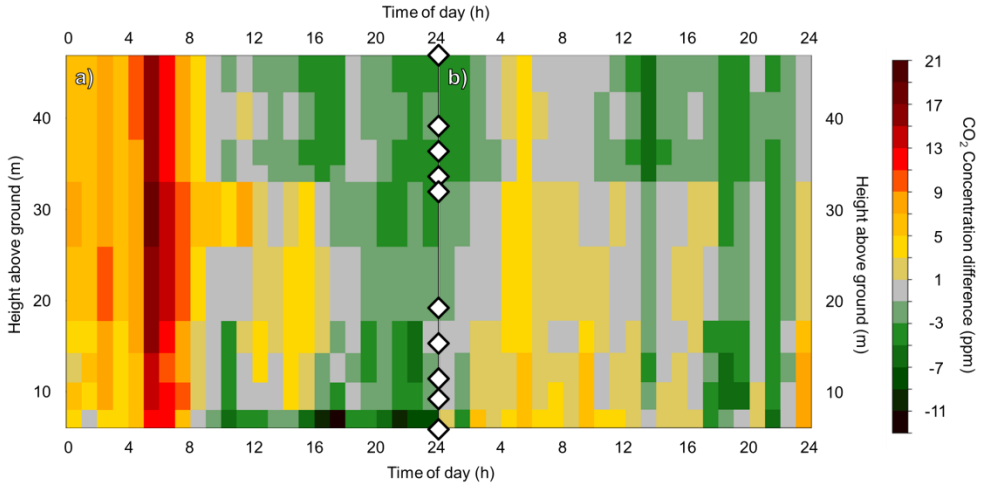

Figure 4.8: Hourly mean CO_2 concentration profiles for the (a) Sunday Only and (b) Olympic/Paralympic periods plotted as the difference from the benchmark with height above ground (y-axis) and time of day (x-axis) in ppm. White diamonds denote measurement locations.

Despite measured *[CO_2]* in the BM period often exceeding the SO and OP equivalents, the mean enhancement for the SO and OP periods relative to BM across the entire profile and all times of day were 2.0 and 0.1 ppm, respectively. This suggests that the impact of suspending Sunday trading laws on central London would have been to slightly increase *[CO_2]* were it not for the reductions in trips to the city centre due to the Olympics and the traffic controls for the Olympics implemented by TfL (2013b).

4.4.3 Bank Holidays

Unlike the London Olympics, bank holidays occur in the UK every year. England has 8 bank holidays, 3 in the Christmas to New Year period (discussed later), two associated with Easter, and three non-religious, the latter occurring in the spring and summer. It is these last three that

are the focus of this section and Figure 4.9 as emissions due to space heating are likely to be minimal during the warmer months.

A similar cycle of morning and evening peaks is observed for both working days and bank holidays, albeit with a much greater range on working days. All days were in spring or summer, hence the collapse of the boundary layer and subsequent peak in measured $[CO_2]$ occurs later in the day (9 pm to 11 pm, Appendix 2.B) than diurnal cycles composed from year-round measurements (Figure 4.9, Figure 4.3). It is expected that commuter traffic would be higher for working days, so it is unsurprising that the morning peak concentration is greater. Despite similar $[CO_2]$ in the afternoon, weekday values after 8 pm were approximately 10 ppm higher than on bank holidays (Figure 4.9a).

At lower elevations (Figure 4.9b) the 'party effect' as described by Velasco *et al*. (2009) is observed. This can be defined as higher CO_2 emissions at street level in the small hours on non-work days as people travel home from evening-night time recreational activities. Within the street canyon, $[CO_2]$ on bank holidays begins to drop relative to weekdays between 6 am and 9 am, as expected due to rush hour traffic and lack thereof on non-workdays. $[CO_2]$ at z_i/z_s= 0.6 (z_s is the height of the Strand building, 30.5 m) is unlike the trend of equal or decreasing $[CO_2]$ with height, suggesting recirculation of street level emissions to half canyon height. This is explored further in Section 5.5.2. Weekday $[CO_2]$ within the canyon remains elevated above the background to a greater extent than on bank holidays by approximately 10 ppm until the evening, when it is somewhat reduced. The effect is much smaller above the canyon. This is to be expected as there is a reasonably well defined transition in behaviour of measured $[CO_2]$ at the roof level of the Strand building from within-canyon signal to local-scale signal on days with low demand for space heating (e.g., Figure 4.17 and Section 5.5.1).

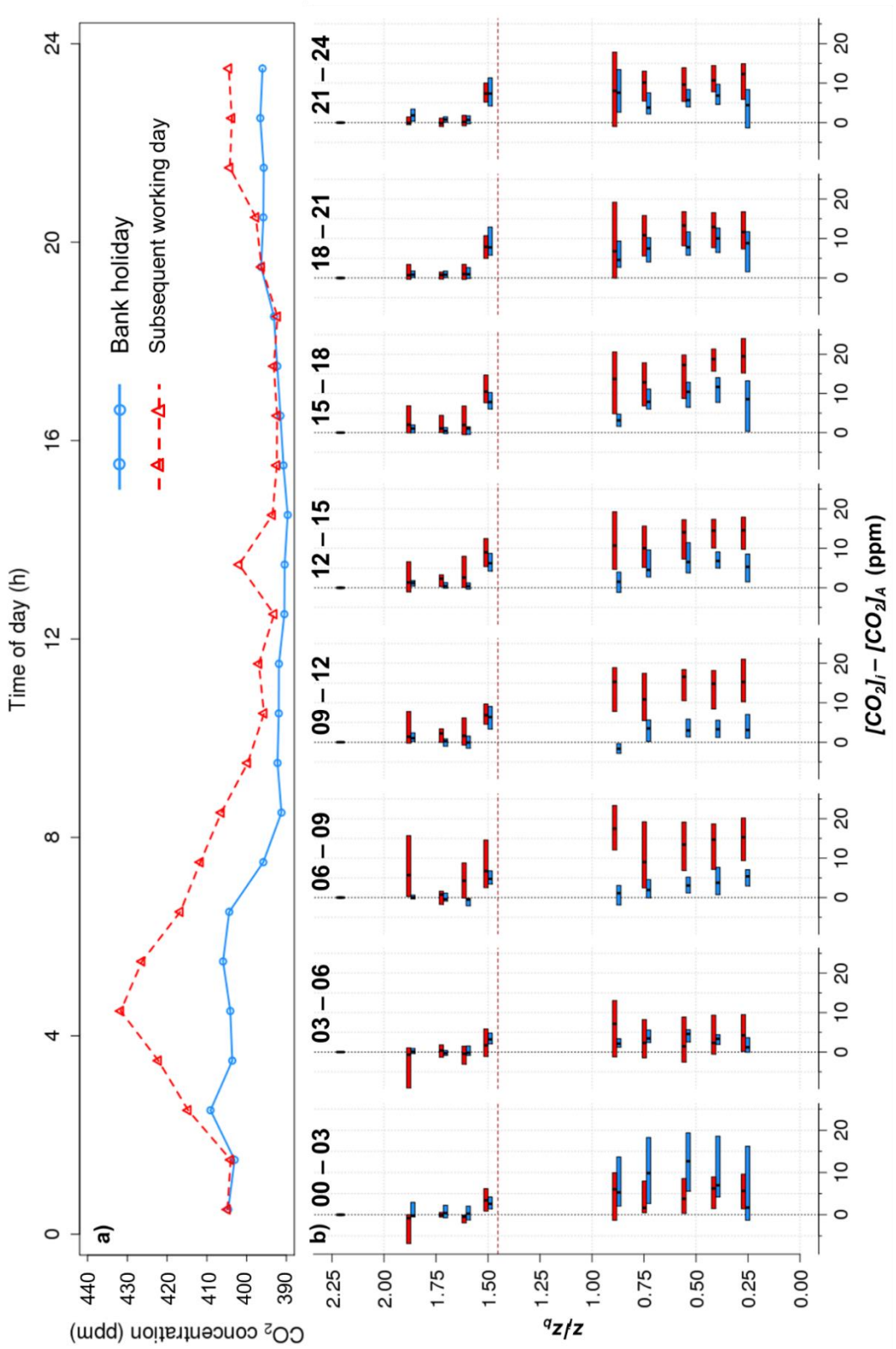

Figure 4.9: (a) Hourly median [CO_2] at z_h for bank holidays (blue, 2012/240, 2013/126, 2013/147) and the following work day (red). (b) Difference from [CO_2] collected at z_h for bank holidays (blue) and the following work day (red) binned into 3 h periods (indicated at the top of the sub-figure). Bars indicate IQR. Heights are given relative to mean building height. Height of the Strand building indicated with horizontal dotted line in (b).

In 2012, Christmas day fell on a Tuesday (day 360). To investigate the changes in human behaviour and subsequent impact on the canyon and above-canyon *[CO_2]*, vertical *[CO_2]* profiles (Figure 4.10) are compared to the following: vertical temperature profiles (Figure 4.10), the vertical temperature gradient (Figure 4.11), automated traffic counts (Figure 4.13), and wind speed and direction (Figure 4.12) for the week beginning on the preceding Saturday (2012/357-363) and the week prior to that (2012/350-356).

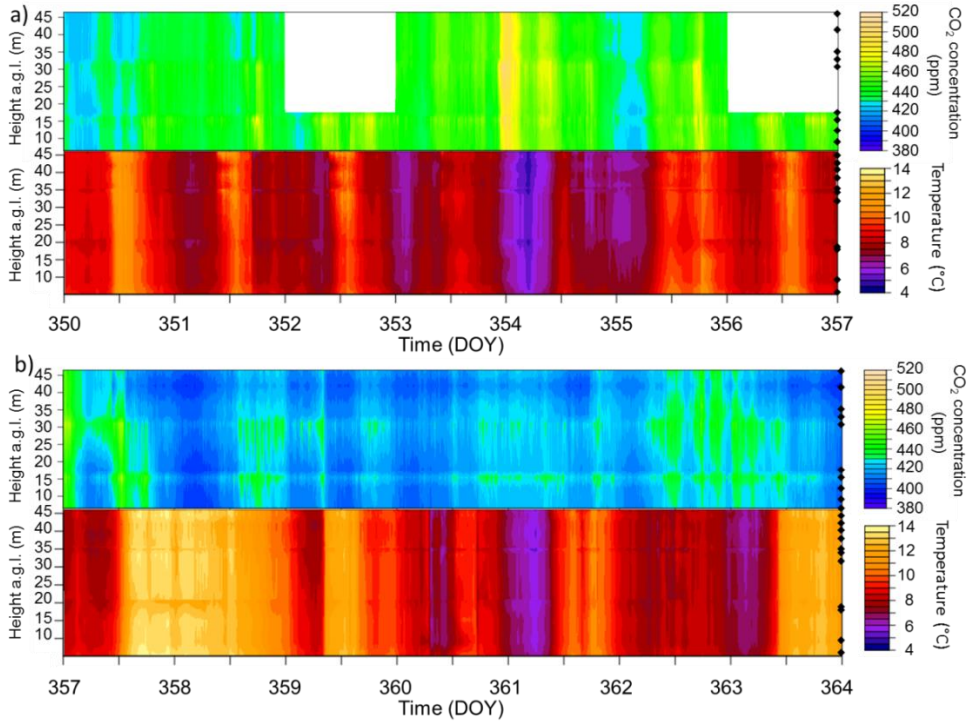

Figure 4.10: CO_2 concentration and temperature profile measured at KS for (a) 2012/350-356 and (b) 2012/357-363. Black diamonds denote measurement locations. White: missing data. Weeks run Saturday to Friday, left to right.

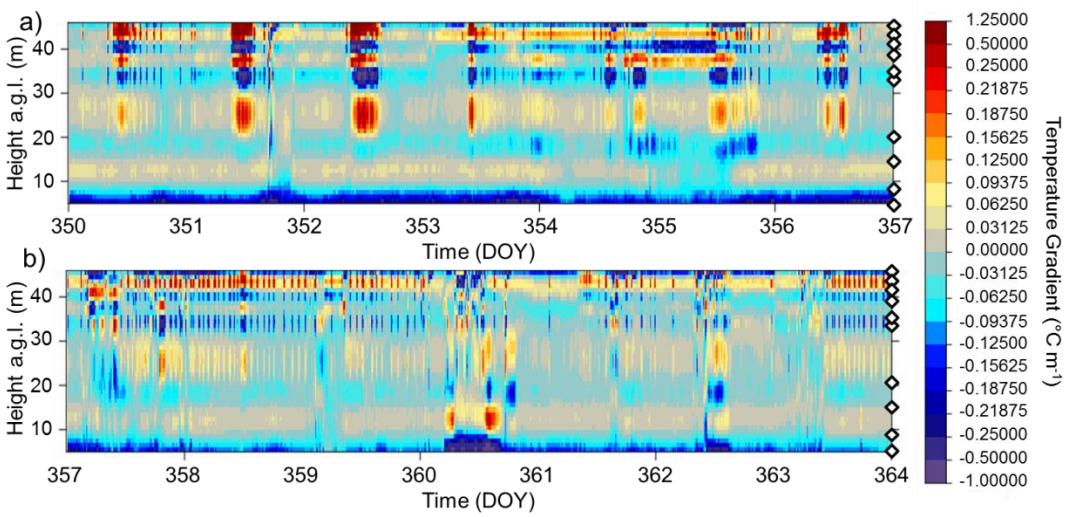

Figure 4.11: 10 minute temperature gradient (°C m^{-1}) vertical profiles at KS for (a) 2012/350-356 and (b) 2012/357-363. Diamonds denote measurement locations used for cubic spline interpolation of temperatures to 1 m spatial resolution.

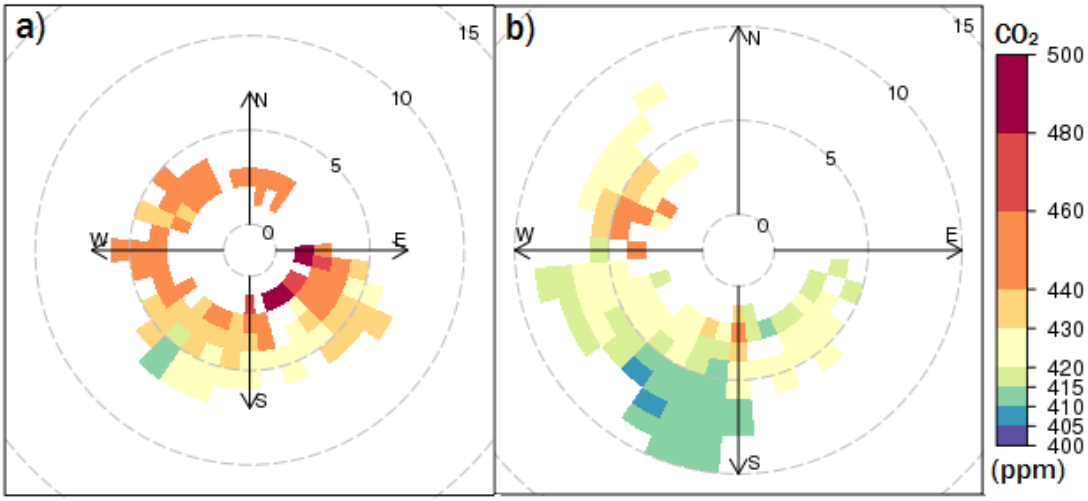

Figure 4.12: CO_2 concentration measured at KSSW z_h plotted by wind speed (m s^{-1}) and direction (KSSW WXT) for (a) 2012/350-356 and (b) 2012/357-363.

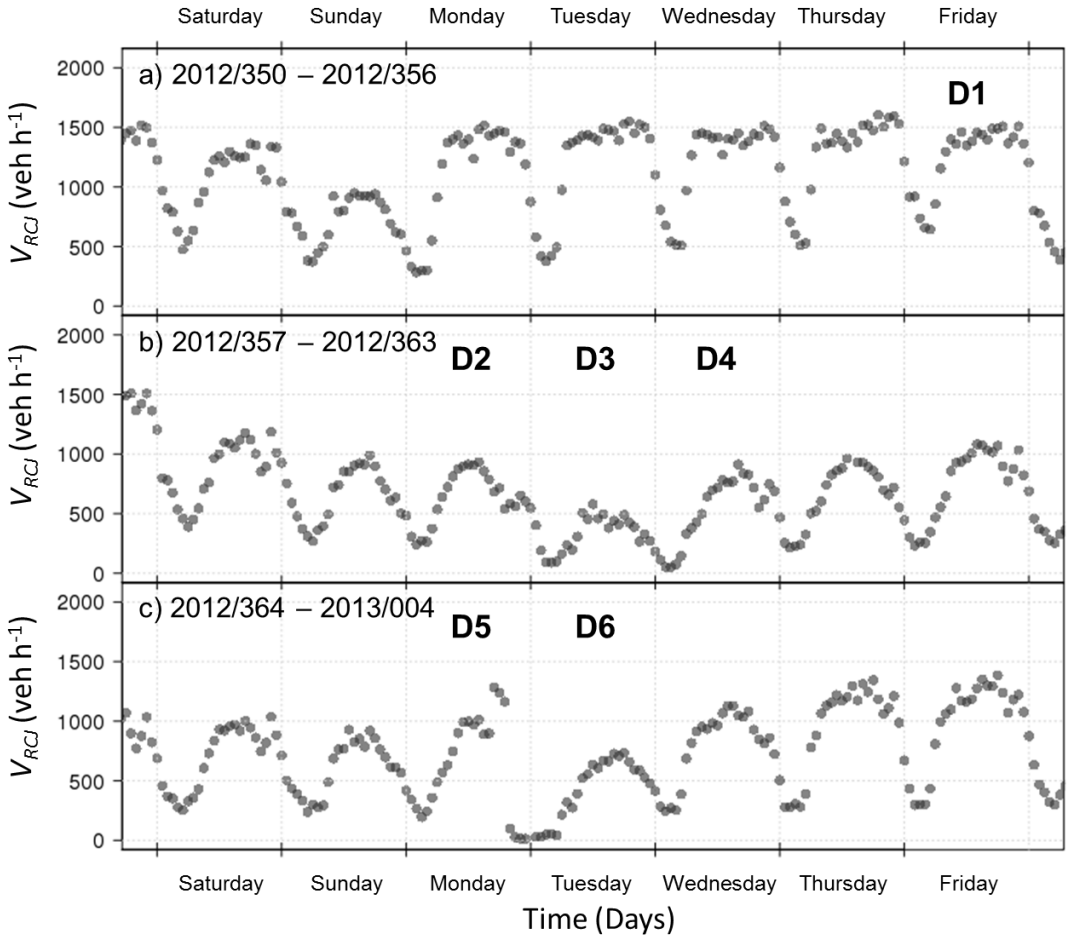

Figure 4.13: Automatic traffic counts at the Royal Courts of Justice (RCJ, Figure 2.1b) for the weeks (a) prior to, (b) during and (c) after Christmas (2013/360), 2012. Weeks run Saturday to Friday left to right. D1: Strand campus closes for the holiday period; D2: Christmas Eve (not a bank holiday); D3 and D4: Christmas and Boxing Day, bank holidays; D5: New Year's Eve (not a bank holiday); D6: New Year's Day, bank holiday.

Both the vertical profile (Figure 4.10) and the wind roses (Figure 4.12) show lower *[CO_2]* during the week surrounding Christmas than the week prior. On average, street level *[CO_2]* was

elevated above local scale measurements by 3.4 ± 7.3 ppm during 2012/350-356. The equivalent figure for 2012/357-363 was -0.9 ± 6.7 ppm, i.e., the gradient for the week prior to Christmas was stronger and had greater concentrations closer to ground level than the week including Christmas. There is little to suggest that the difference was due to anything other than traffic loading (Figure 4.13). Air temperatures were consistent within the canyon, with the greatest change in temperature seen at the very top of the profile (Figure 4.8, Figure 4.11). During 2012/357-363 the temperature gradient generally (with the exception of Christmas day) remained within ± 0.04 °C.m^{-1} of 0 within the canyon - there is no evidence of stable stratification or vigorous, thermally induced turbulence. This is unsurprising as the canyon is essentially north facing and the majority of heat is likely to be generated from anthropogenic sources. The effect of the latter can be seen clearly by comparing Figure 4.11a (term time, air conditioning and boiler turned on) and Figure 4.11b (campus closed, air conditioning and boiler, that is, major sources of CO_2 and warm air, turned off).

Prior to Christmas, high *[CO_2]* values were recorded from all directions, especially during conditions of low wind speeds from the south east which were probably from the vents on the Strand roof (Section 4.3). Whilst there were low student numbers the Strand campus (term ended 2012/249), the campus itself was not closed and other businesses in the vicinity were still operational (as evidenced by the high levels of commuter traffic, Figure 4.13), hence it is likely that emissions due to space heating contributed to the high levels of *[CO_2]* observed. During the following week the Strand campus was entirely closed. There were only 3 working days: Monday, Thursday and Friday, the rest were either weekend or bank holidays. It is likely that the majority of workers in the businesses surrounding the Strand campus took leave, resulting in lower emissions for space heating. *[CO_2]* measured during this week was generally lower than during the previous week, except for when the wind was from the WNW. This wind sector includes Covent Garden, which is a popular market and tends to be especially busy in the run up to Christmas and during the Boxing Day sales. The response to public holidays can be seen to be sector or land use specific: areas with a high percentage of buildings used for retail may have an increase in *[CO_2]*, whereas those used for academic or other public bodies are likely to experience lower concentrations. The topic of *[CO_2]* variation by land use is explored in more depth in chapter 6.

4.5 Vertical variation

4.5.1 Relation to traffic volume

Summer days (configuration C5) are analysed for July 2012 to see the effects of traffic and boundary layer height on the measurements when there is low demand for space heating and therefore few emissions at roof-top level. The diurnal cycle of traffic counts made at RCJ (Section 2.2.8) is somewhat different to those measured at KSNW (Section 2.2.8) (Figure 4.14). Although the RCJ data are not gap filled, and unlike the KSNW data, have no information on vehicle type, they have the advantage of covering a larger timespan and hence were

chosen for the analysis in this chapter. Alternative methods to quantify traffic density, such as linking traffic measurements to those of black carbon within the street canyon, were not successful. The main features of the diurnal cycles of traffic volume in Figure 4.14a are the low overnight (01:00 to 07:00 GMT on weekdays, 02:00 to 09:00 GMT on weekends) and high, sustained daytime (08:00 to 00:00 GMT on weekdays, 10:00 to 01:00 GMT on weekends) traffic volumes with a reasonably rapid transition between the two. 'Peaks' are not observed in the road traffic volume on either side of the normal working day (09:00 to 17:00 GMT/BST); but are very visible in the number of London Underground journeys (e.g., TfL, 2007). This suggests that, despite some similarities, the volume of traffic does not directly relate to the population density and that the results below do not account for the effects of human respiration.

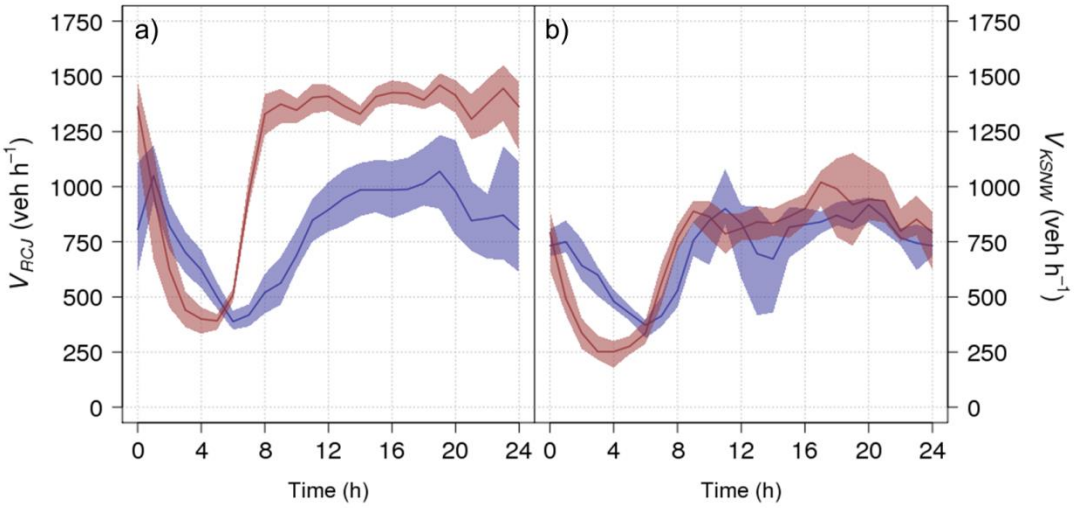

Figure 4.14: Weekday (red) and weekend (blue) hourly traffic, V, at (a) RCJ 2012/001-366, (b) KSNW 2013/189-196. Lines denote median values, shaded areas define interquartile range.

The most distinctive feature of the urban *[CO_2]* diurnal cycle is the week day morning peak, the majority of which occurs before the high traffic volumes shown in Figure 4.14a. To focus on this component of the typical urban diurnal cycle, CO_2 profile data from July 2012, a period with low space heating requirements, low building occupancy and therefore low roof-level emissions, were binned by time of day (1 h bins, Figure 4.15). Peak hourly median weekday and weekend *[CO_2]* at street level were 422 ppm (06:00 - 08:00) and 415 ppm (22:00 – 04:00) (Figure 4.15), giving enhancements of 7.1% and 5.2% above July 2012 GBL respectively. These are much lower than the enhancements reported by Idso *et al.* (2001) (43.3% and 38.3% for weekdays and weekends respectively), but give a higher ratio of average peak weekday enhancement of the air's *[CO_2]* to the average peak weekend enhancement (1.37 vs. 1.13 for this study and Idso *et al.* (2001) respectively).

The diurnal cycle of median hourly *[CO_2]*, measured over the course of one year (2012) shows increases of 15 ppm relative to 1 am (minimum) values within the street canyon (Figure 4.3), which coincide with a doubling of traffic load (Figure 4.14). Perhaps counterintuitively the amplitude of the diurnal cycle of hourly median *[CO_2]* is greater at all heights on the weekend than on weekdays (median amplitude of 18.3 and 15.9 ppm respectively). Weekday *[CO_2]* at all heights and traffic volume at RCJ remain greater than weekend equivalents throughout the

day. Between 00:00 and 04:00 UTC, weekend traffic remains high, whilst weekday traffic drops to a third of the mean value. This is reflected in a weekend *[CO_2]* profile within the street canyon that is 0 – 8 ppm higher than on weekdays. Unlike later in the day, this increase is not transported upwards; weekend *[CO_2]* values are elevated relative to weekday ones only within the canyon. This 'party effect' was also observed by Velasco *et al.* (2009) during the early hours of Saturday and Sunday. As with Vogt *et al.* (2006), *[CO_2]* was observed to decrease with height at all times, with a step change in concentration at the canyon top. As any offset between the two gas analysers is removed using data from an intercomparison point prior to analysis (Section 2.2.1) this step change is not due to a systematic error or difference between the analysers.

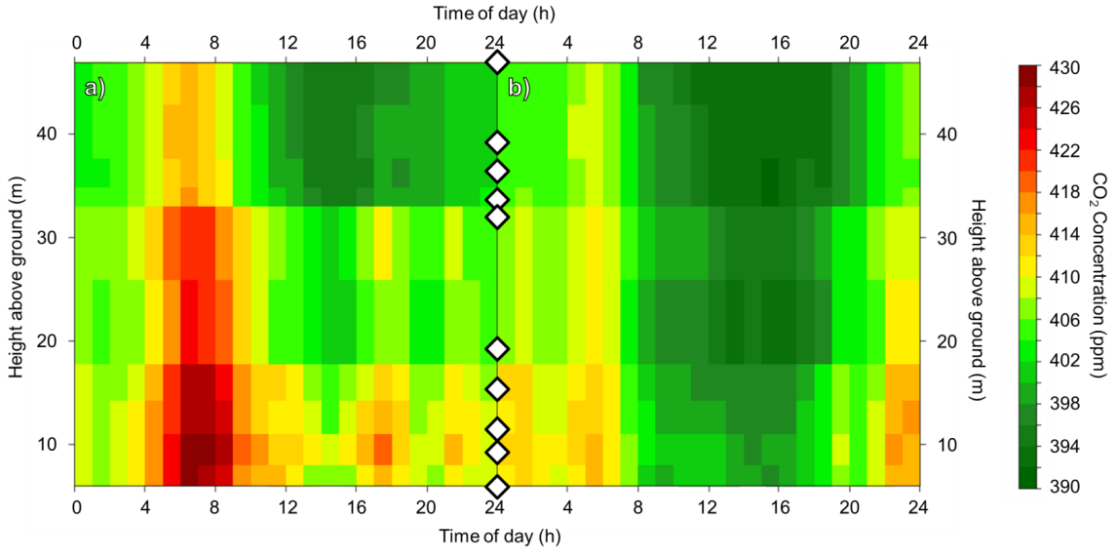

Figure 4.15: Hourly median CO_2 concentration (key: far right) by time of day at 10 heights (white diamonds, Figure 2.1d) at KSSW and KSNW for (a) weekdays and (b) weekends for July 2012 (2012/183-212).

Measured *[CO_2]* correlated reasonably well with traffic load within the canyon and the smallest gradients coincided with the lowest traffic loads. The former contrasts with Vogt *et al.* (2006) who noted no such relation between traffic load and the absolute value of *[CO_2]*, but did see a strong relation between gradient and traffic.

To further investigate the impact of traffic on *[CO_2]* at different heights, the difference between hourly mean weekday and weekend *[CO_2]* at each height (Δ*[CO_2]*) was compared with the difference in hourly weekday vs. weekend traffic flow (ΔV) by fitting a linear model (Figure 4.16). As the data are from the summer time vacation period, it is assumed that heating requirements and hence rooftop CO_2 emissions from space heating are low, hence any difference between the weekday and weekend profiles within the same height is due to traffic. The difference between weekday and weekend *[CO_2]* increased with ΔV (Figure 4.16) until approximately 8 am, after which both decreased, with Δ*[CO2]* becoming negative by 21:00 GMT. The strength of the relation between ΔV and Δ*[CO_2]* varied according to height above street level and time of day. Regression of all hourly Δ*[CO_2]* onto hourly ΔV showed decreasing sensitivity (gradient, Figure 4.17a) and a weaker relation (R^2, Figure 4.17) of Δ*[CO_2]* with ΔV

with increasing height above street level. No such change in the strength of the relation of $\Delta[CO_2]$ to ΔV with height was observed for a regression of values prior to 08:00 GMT, and regression of values after 08:00 GMT showed a stronger relation between $\Delta[CO_2]$ and ΔV with increasing height, though the sign of the slope remained unchanged.

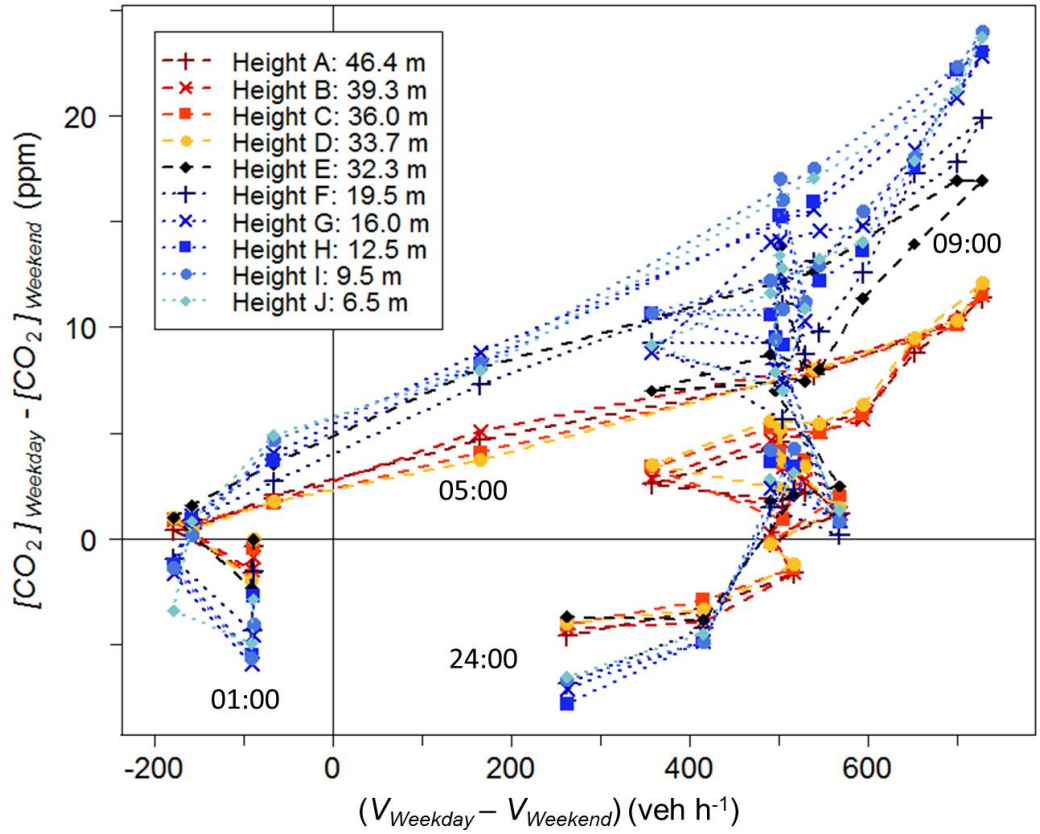

Figure 4.16: Difference between weekday and weekend hourly mean $[CO_2]$ measured at 10 heights above street level plotted with the difference between hourly mean weekday and weekend traffic (V, RCJ). Points are labelled by time period (GMT). Some labels omitted for clarity.

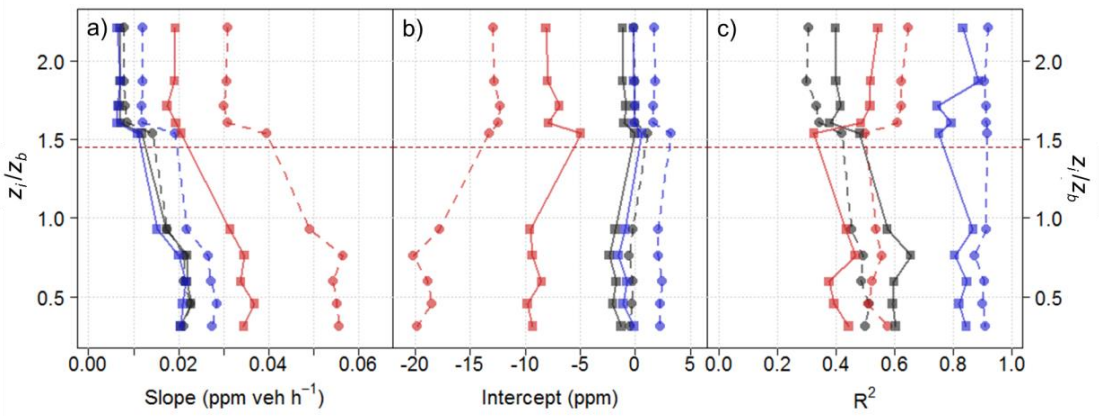

Figure 4.17: (a) Gradient, (b) intercept and (c) R^2 for linear best-fit lines for the difference between hourly mean (circles, dashed lines) and median (squares, solid lines) weekday and weekend $[CO_2]$ for each height plotted against the weekday/weekend difference in hourly mean and median traffic (Figure 4.16). Traffic data derived from 1 hour automated counts, RCJ, 2012. Model fitted to all (black), 'night time' traffic (00:00 – 08:00 GMT, blue) or 'daytime' (08:00 – 24:00 GMT, red) data sets based on form of Figure 4.14.

The relation between ΔV and $\Delta[CO_2]$ can be used to estimate the elevation of $[CO_2]$ due to traffic emissions. A rise in traffic volume of 100 Veh h^{-1} is calculated to increase the CO_2 concentration by 1 – 2 ppm above the Strand roof and 2 – 5 ppm below it. The intercept of Figure 4.17 can be interpreted as the non-traffic elevation of weekday $[CO_2]$ over weekend $[CO_2]$. This is approximately zero and constant with height for regression of all hourly values or values prior to 08:00 GMT, the time of day when the high and sustained 'daytime' weekday traffic volumes begin, suggesting that the difference in traffic volume is the primary cause of observed differences in $[CO_2]$ between weekdays and weekends. However, for the subset of data measured after 08:00 GMT the regression of $\Delta[CO_2]$ onto ΔV suggests that if there were no difference between weekday and weekend traffic then weekend $[CO_2]$ values would be substantially higher. There is a high standard error: at z_i =6.5 m (height J, Figure 2.1d) the intercepts for regressions of mean and median hourly values are -19.8 ± 6.6 ppm and -9.3 ± 5.6 ppm respectively (the intercepts for all other regressions at this height have standard errors of < 2.2 ppm). As these data were measured during a period where space heating requirements are expected to be minimal (Section 4.2), and as plants and soil do not respire differently on weekdays compared to weekends (Ward *et al*., 2015), it is hypothesised that the weekend surplus is due to higher overnight emissions that are stored within the canyon and contribute to higher $[CO_2]$ the following day. The topic of CO_2 storage and traffic volume will be explored further in the following chapter.

4.5.2 Built form and wind direction

The size and orientation of urban roughness elements such as buildings and trees can alter both the speed and direction of airflow. Wind that is close to parallel to a street canyon may be channelled along it, whereas wind perpendicular to a canyon can, depending on the relative height and width of the canyon, result in a number of different flow regimes (Vardoulakis *et al*., 2003).

The Strand canyon is aligned east north east/west south west (Figure 4.18a). The width varies from 20 m at KSB to 54 m a mere 5 m to the east due to the presence of the church in the centre of the road. The height: width ratio accordingly varies from 0.56 (KS to Bush House, Figure 4.18a, c) to 1.21 (KS to the church, Figure 4.18c), and the flow regime can predominantly (for all of the canyon's length except for its widest point) be characterised as skimming flow, with the remainder as wake interference flow (Oke, 1987). The prevailing wind direction is from the southwest (Figure 4.18b), which is approximately 15 degrees off parallel from the street canyon. The exact orientation of the street canyon varies with height and time of year due to the presence of deciduous trees near KSNW (Figure 4.18a). For the purposes of this section, the above-canyon (KSSW, z_h) wind direction has been divided into four sectors, two centred on the 60-240° axis, parallel to the street canyon, and two perpendicular. The sectors parallel to the street are 60° wide and periods with synoptic wind speeds less than 1.5 m s^{-1} were flagged as 'low wind' conditions and removed prior to the analysis in Figure 4.19 (Vardoulakis *et al*., 2003). The wind sectors are colour coded as shown in Figure 4.18a.

The vertical wind components at KSNW (Figure 4.18e) and KSB (Figure 4.18f) show coherent variation in sign and magnitude with local scale wind direction. KSNW has two minima in vertical wind component at around 120° and 300° from north. The vertical wind speed peaks at about 200°, approximately equidistant between the two. As can be seen from Figure 4.18a, 200° is the bearing of the nearest point of the Strand building from the KSNW measurement point. The North Wing roof may therefore be deflecting the wind flow upwards and generating helical motion of air within the canyon.

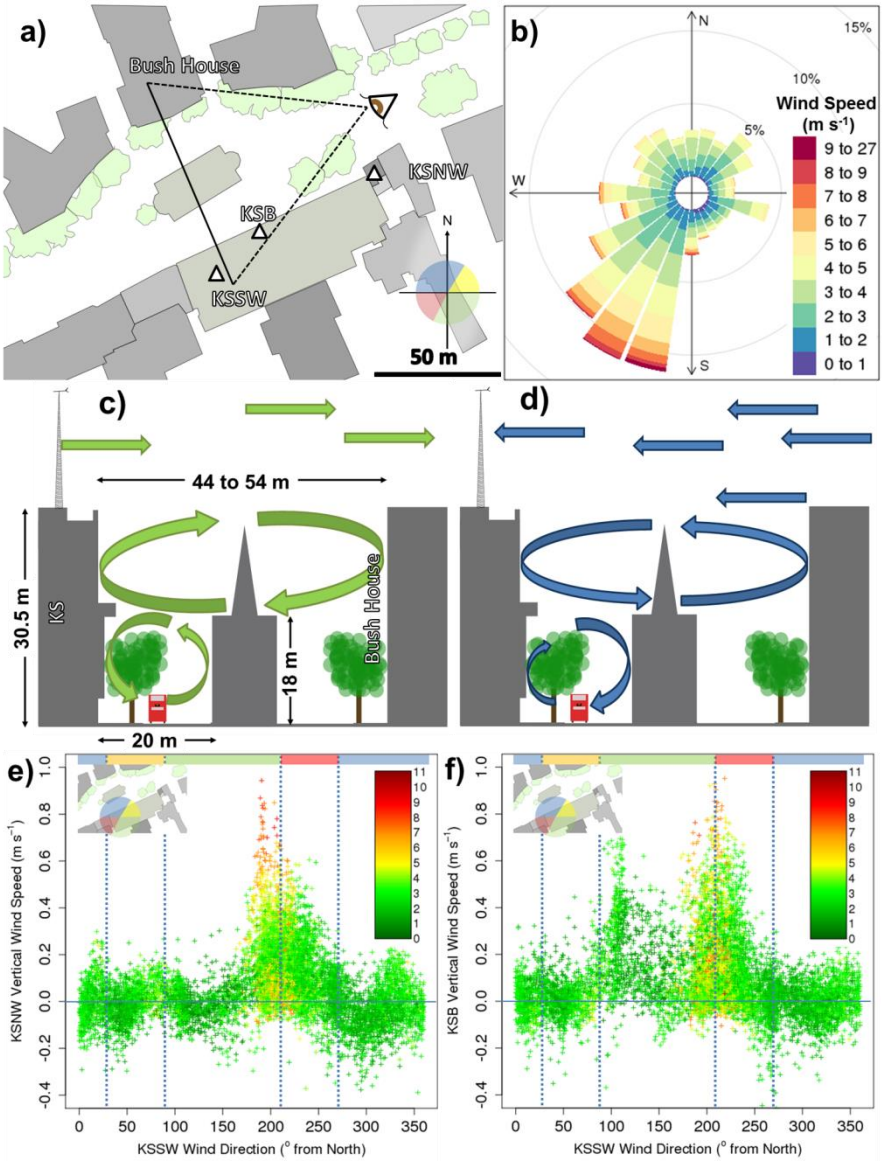

Figure 4.18: (a) Simplified bird's eye view of KCL Strand campus with locations of KSSW, KSB and KSNW marked, inset (lower right) shows scale and four wind sectors: yellow and red: wind along street canyon, blue and green: wind across street canyon. Eye shows point of view depicted in (c) and (d). (b) Wind speed/direction frequency plot for KSSW WXT 2013/100-2014/100. (c) View of Strand street canyon from location and with field of view shown in (a) with building heights and road widths. Above-roof wind direction and suggested street canyon turbulence for wind from green wind sector. (d) As with (c), but with wind from the blue sector. Vertical wind velocity at (e) KSNW (CSAT) and (f) KSB (Gill) plotted with local (KSSW WXT) wind direction, 2013/100-2014/100. Wind speed and direction data in all plots at 30 minute time resolution. Inset colour scale and point colours plots (e and f) is the difference between local (KSSW WXT) and canyon wind speed (m s^{-1}).

The plot of KSB vertical wind speed with local scale wind direction has two peaks in vertical wind component at about 100° and 210°. Wind from both of these directions is effectively perpendicular to the building due to the proximity of the KSB sensor to the Strand building. As the street canyon height: width ratio varies from 0.56 to 1.21, it is possible that the resulting flow regime is closer to wake interference flow, rather than skimming flow (Oke, 1987). Under these conditions the wake created by an upwind building (the Strand building) is disturbed by a downwind building (St Mary le Strand church), creating a downward flow along the side of the building and potentially flushing street level emissions up the side of the Strand building, resulting in the observed positive vertical wind component and the higher than average *[CO_2]* at all canyon heights including roof level for the two sectors (red and green) affected (Figure 4.18e, f; Figure 4.19).

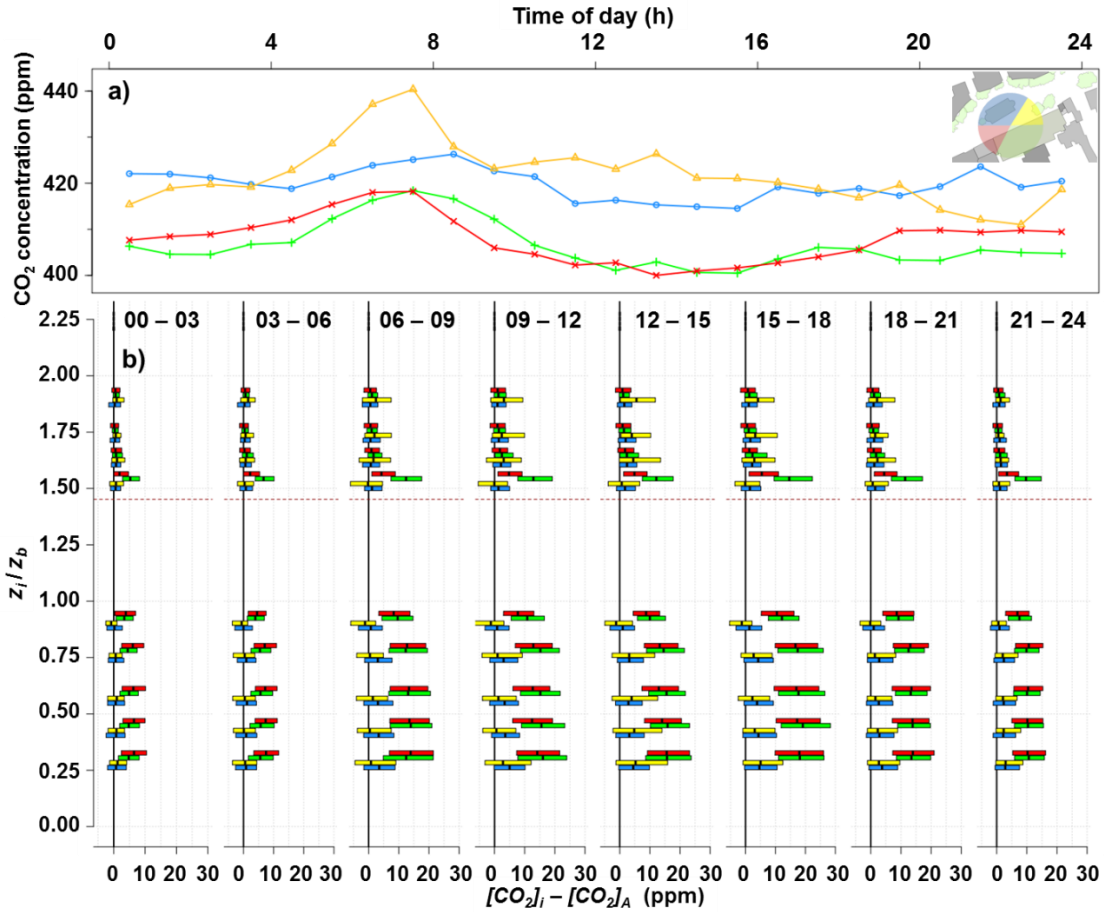

Figure 4.19: (a) Hourly median [CO_2] at KSSW height A (Figure 2.1d) for four wind sectors (Figure 4.18a), 2012/150-2013/150. (b) Difference from [CO_2] collected at KSSW z/z_b=1.52 for four wind sectors (Figure 4.18a) binned into 3 h periods (top of subfigure), 2012/210-2013/210. Bars indicate IQR. Heights are given relative to the mean building height, z_b. Horizontal dashed line indicates Strand building height.

Northerly parallel and perpendicular winds result in the lowest within-canyon *[CO_2]* gradient, but the highest tower-top concentrations, particularly at night. Above-canyon winds from these directions generate the fastest within-canyon airflow, leading to effective shear-based turbulent mixing, and are more likely to have a purely urban fetch compared to the green and red quadrants. Measurements made during conditions with winds from the latter two sectors are likely to have footprints which include the River Thames, and subsequently lower *[CO_2]*. It appears that rather than parallel or perpendicular flow, the Strand canyon experiences a

'northern' condition characterised by efficient vertical mixing and high *[CO_2]* and a 'southern' condition characterised by a more muted diurnal *[CO_2]* cycle and a greater disconnect between above and within canyon air due to shear at the Strand building roof (Caton *et al*., 2003). This is potentially due to the large size of the Strand building relative to the adjacent buildings on the southern side of the street canyon, and the small size of the church to the north, leaving a relatively open structure on both sides with the disruption of air flow caused by the church generating efficient vertical mixing of street level emissions.

4.5.3 Mixing layer depth and atmospheric stability

Measured *[CO_2]* is affected not only by emissions, but also the extent to which these emissions are transported and blended. The atmosphere's tendency to encourage (unstable) or deter (stable) vertical transport of a parcel of air is known as atmospheric stability. Periods of atmospheric instability are associated with mixing and dilution of emissions over a greater vertical extent, in other words, a deeper mixing layer. The two characteristics are therefore linked, but may be calculated from different measurements. In this section the extent to which the emitted CO_2 is blended with local scale concentrations is assessed as the vertical *[CO_2]* gradient and is related to atmospheric stability and mixing layer depth.

The atmospheric stability may be quantified as the ratio of the height of a measurement above ground level less the zero plane displacement height (*z'*), and the Obukhov length (*L*). The ratio *z'/L* was calculated at 30 minute resolution using data from height A, KSSW CSAT3 (Kotthaus and Grimmond, 2014a) for April 2012 to December 2014 (Figure 4.20) and grouped into classes, which were chosen to achieve the following objectives:

1. Reflect atmospheric conditions, that is, not to lump very different conditions within one class.
2. Be sufficiently numerous as to allow detailed examination of the effect of stability on vertical *[CO_2]* gradient.
3. Have a reasonable spread of values across classes.

Conditions were therefore defined as: stable: $0.01 > z'/L$, neutral: $-0.01 < z'/L \leq 0.01$, unstable: $z'/L \leq -0.01$. Due to the large volume of data for $-0.1 < z'/L$ -0.01, neutral conditions were defined more narrowly than in some previous studies (e.g., Kotthaus and Grimmond, 2014b) and the resulting unstable class was further subdivided into four classes at $z'/L = -1$, -0.1 and -0.05. All measurements were made at the local scale using a CSAT3 at KSSW.

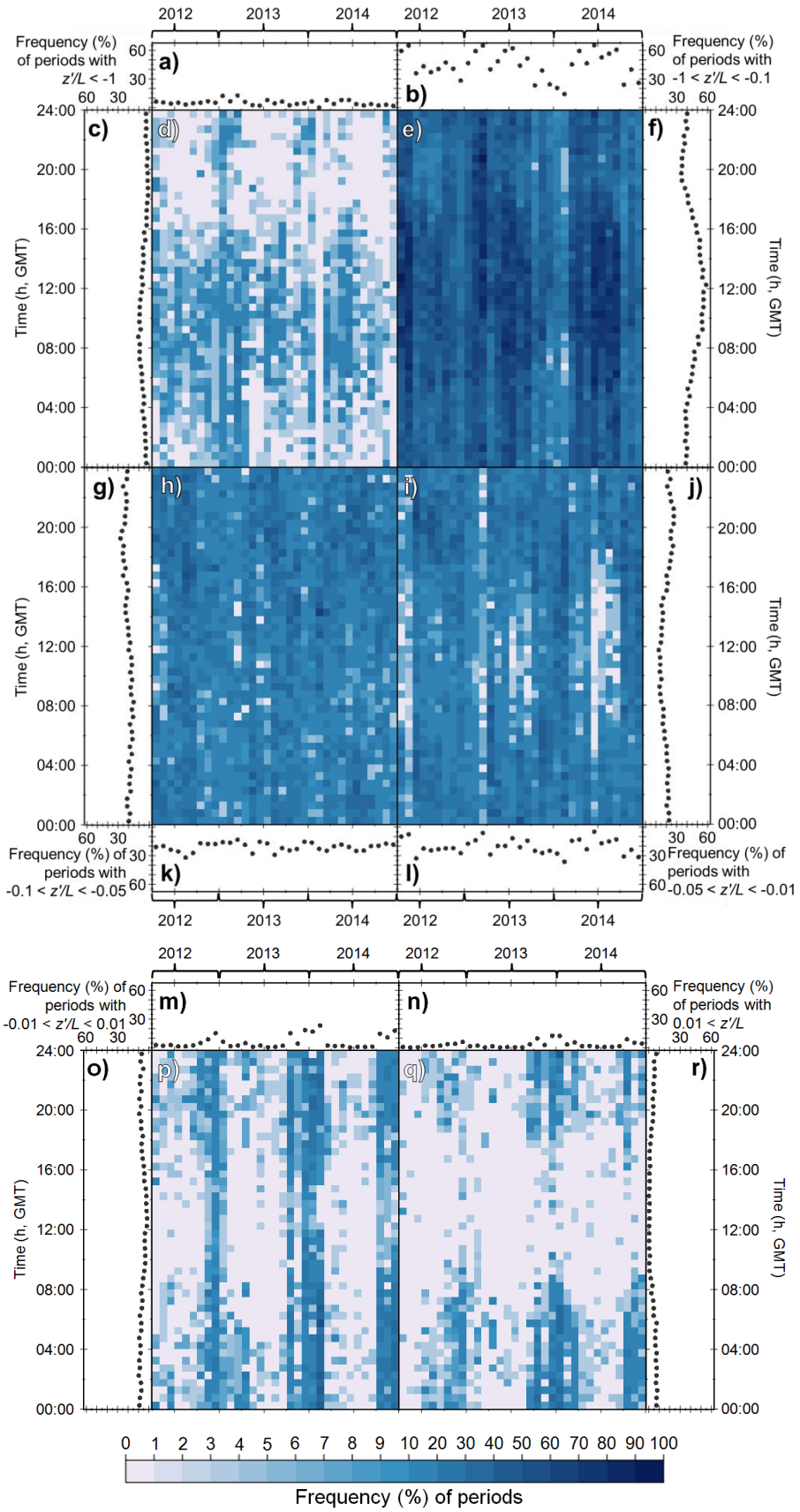

Figure 4.20: Frequency of half hourly periods classified by z′/L measured at height A, KSSW for April 2012 to December 2014, inclusive. Classes are defined as (a, c, d) very unstable (z′/L < -1), (b, e, f) unstable (-1 < z′/L < -0.1), (g, h, k) moderately unstable (-0.1 < z′/L < -0.05), (i, j, l) near neutral (-0.05 < z′/L < -0.01), (m, o, p) neutral (-0.01 < z′/L < 0.01) and (n, q, r) stable (0.01 > z′/L). Frequencies (key: base of graph. Note change in scale) are plotted by time of day (vertical axis) and month of year (horizontal axis).

Overall atmospheric stability was found to be seasonally and diurnally variant. The most unstable conditions ($z'/L < -1$) tended to be observed between 06:00 and 12:00 GMT; however, whilst they were most common January – March 2012, similar frequencies were not observed for January – March 2013 (Figure 4.20a, c, d). Very unstable conditions were distinctly less frequent (5%) than moderately unstable ($-1 < z'/L < -0.1$, 44.9%), unstable ($-0.1 < z'/L < -0.05$, 20.4%) and near-neutral ($-0.05 < z'/L < -0.01$, 19.9%). Moderately unstable conditions were more frequent (approximately 60% of all time periods) between 10:00 and 14:00 (Figure 4.20f) for April to September (Figure 4.20b), i.e., during the periods with greatest direct irradiation. However frequency of moderately unstable periods was observed to have a secondary peak about 00:00, suggesting that nocturnal release of heat from the urban fabric is sufficient to maintain turbulence for > 40% of overnight periods. Periods with ($-0.1 < z'/L < -0.1$ were far more frequent (49.4%) than periods with the narrower definition of neutral ($|z'/L| < 0.01$, 6.3%), with the majority of the difference consisting of the 'unstable' and 'near neutral' periods as defined above.

Less seasonal and diurnal variability was observed for the 'unstable' conditions (Figure 4.20g, h, k), but 'near neutral' conditions (Figure 4.20i, j, l) were observed more frequently 00:00 – 04:00 and 18:00 – 22:00, in essence the inverse of that observed for 'very unstable' conditions. This can also be observed for the 'neutral' (Figure 4.20m, o, p) and 'stable' conditions (Figure 4.20n, q, r). These tend to be most common overnight (20:00 – 04:00) during the colder months (November to February) and are almost entirely absent at other times of day/months of the year.

The variation of the efficacy of vertical mixing of CO_2 with stability was investigated by comparing local scale (height A, KSSW) measurements to $[CO_2]$ from lower elevations for different stability classes (Figure 4.21a). Traffic through the Central London Cordon (Figure 2.1a) is constant throughout the year (TfL, 2012). In other words, there is a seasonally invariant source of CO_2 at ground level, and it is expected that the difference in CO_2 between street level and the top of the canyon would decrease with increasing frequency of unstable periods.

Lowest differences in concentration ($\Delta[CO_2]$) were observed at height B, located closest to height A and within the same vertical 'zone' above the strand roof. Little difference in median $\Delta[CO_2]$ was observed with stability class; however, variation was lowest for the 'unstable' and 'near neutral' classes ($-0.1 < z'/L < -0.01$). The within canyon locations (heights F and J) showed a marked increase in median values for these stability classes, with lower $\Delta[CO_2]$ and higher variability during more stable and more unstable conditions. Height E, at the transition point between the above roof and within canyon zones also showed a sharp increase, but did so for the 'neutral' relative to the 'near neutral' class, suggesting that less intense turbulence is required to reduce the difference in $[CO_2]$ between heights E and A than heights F, J and A, as might be expected due to the smaller distance between height A and height E than height A and heights F and J. Although very unstable conditions were associated with medium to high $\Delta[CO_2]$, this result should not be overstated as they were also associated with maximum variability (and second lowest data availability) in $\Delta[CO_2]$ for all heights.

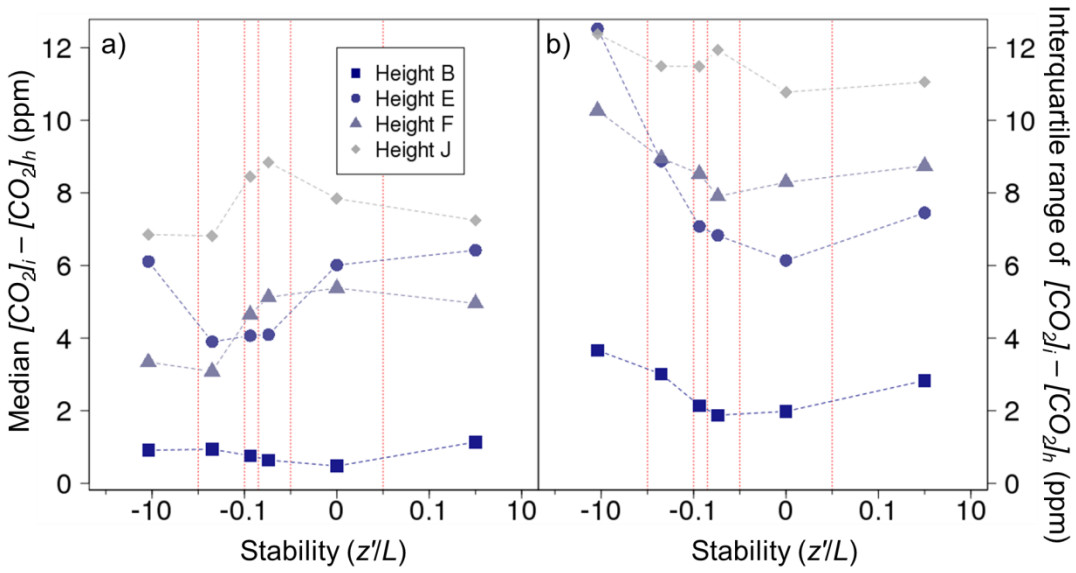

Figure 4.21: (a) Median and (b) interquartile range of differences in mean half hourly CO_2 concentration at four heights (key: inset) z_i ($[CO_2]_i$) to those measured at z_h ($[CO_2]_h$) with atmospheric stability for 2012/150 – 2013/150. Atmospheric stability defined by parameter z'/L, measured at z_h (height A, KSSW). Boundaries of stability classes shown as vertical dotted lines. Points represent value for the entire stability class.

In general, the difference between *$[CO_2]$* at height A, KSSW (Figure 2.1d) and that at heights B, E, F and J increased with distance from height A and more stable atmospheric conditions (Figure 4.21). It should be noted that the variability in the data, as expressed by the interquartile range for each height and stability class (Figure 4.21b), is larger than the median values and also varies with height and atmospheric stability. Variation in *$\Delta[CO_2]$* was lowest during slightly unstable – near neutral conditions. The latter is surprising as the -0.1 < z′/L < -0.01 classes showed the least diurnal and seasonal variation and hence the concurrent *$[CO_2]$* measurements would be affected by the broadest range of meteorological and anthropogenic conditions.

The mixing layer depth (Figure 2.B.5d in Appendix 2.B) was calculated from ceilometer backscatter profiles measured at Marylebone Road using a modified version of Emeis *et al.* (2007)'s gradient method developed by Kotthaus *et al*. (2015). The magnitude and variation of *$[CO_2]$* were found to decrease with increasing boundary height, that is, with increasing mixing up of surface CO_2 emissions and entrainment of low *$[CO_2]$* air from above the nocturnal boundary layer. Linear regression of *$[CO_2]$* at height A on mixing layer depth found poor, negative correlation (slope of -0.014 ppm m^{-1}, R^2 of 0.071), and whilst the slope of the regression was significantly (outside the standard error range) different from 0, the relation between *$[CO_2]$* and mixing layer depth is too weak to be of predictive value in this study.

4.6 Conclusions

The effects of natural and anthropogenic factors on measured CO_2 concentrations ($[CO_2]$) were evaluated using data collected over multiple years in central London. These may be summarised as follows:

- Monthly mean $[CO_2]$ values were almost always greater than Global Background Levels (GBL) as measured at the NOAA monitoring station, often by a considerable margin, and the elevation relative to GBL tended to increase year on year, suggesting that London is net source of carbon dioxide.
- Observed median diurnal cycles are consistent with those observed in other North European cities.
- Space heating requirements varied with both building occupancy and air temperature. Rooftop vents were a source of CO_2 at all times of year, with the greatest emissions observed during high occupancy days in winter.
- Weekends, bank holidays, and the Olympics have reduced $[CO_2]$ compared to the average week day, with the greatest reduction occurring within the street canyon. This is primarily due to a reduction in traffic.
- CO_2 emitted within the canyon was recirculated, and $[CO_2]$ measured at all heights varied more strongly with traffic volume than with boundary layer stability, which in itself was modified by human activity.

Comparison of $[CO_2]$ measured at multiple locations and during different time periods enabled the assignment of changes in CO_2 concentration to anthropogenic and natural factors, the results of which are summarised in Table 4.3. Of the factors examined, CO_2 emissions from vehicles had the largest and clearest impact on both street level and local scale (height A, KSSW, Figure 2.1d) $[CO_2]$. The effect of increasing mixing layer depth was similarly large, but the significance of the relation to $[CO_2]$ was questionable given the low coefficient of determination. Combustion of fuel for building heating was found to affect $[CO_2]$, with the pattern of emissions relative to ambient air temperature varying with building use. The effect of human respiration on $[CO_2]$ was much lower, and that of vegetation and soil was essentially negligible. Some trends in the elevation of $[CO_2]$ at z_i/z_b = 1.87, 1.54, 1.45 and 0.31 (heights B, E, F and J, Figure 2.1d) over those at z_i/z_b = 2.21 ($\Delta[CO_2]$), were observed with atmospheric stability at z_i/z_b = 2.21. However, the difference in $\Delta[CO_2]$ between stability classes was much lower than the variation in $\Delta[CO_2]$ within stability classes and it was not clear that the observed trends were significant. In summary, factors affecting $[CO_2]$ in central London were (in approximate descending order of importance) vehicle emissions, mixing layer depth, combustion for building heating, human respiration, atmospheric stability, and respiration and photosynthesis by vegetation and soil.

Table 4.3: Factors affecting CO_2 concentrations ($[CO_2]$), the methods used to assess their impact on measured $[CO_2]$ and results.

Factor	Method	Impact on measured $[CO_2]$	
Vehicle Emissions	Linear regression of $[CO_2]$ measured at multiple heights on traffic volumes	Above Strand roof: 1 – 2 ppm increase per 100 Veh h^{-1} Below Strand roof: 2 – 5 ppm increase per 100 Veh h^{-1}	
Building Emissions for space heating	Comparison of $[CO_2]$ when building occupied and unoccupied by air temperature.	Absolute $[CO_2]$ decreases with increasing temperature. Demand for space heating changes with temperature and building type but may raise $[CO_2]$ by over 20 ppm.	
Human respiration	Comparison of $[CO_2]$ at heights A and J during a period with no traffic.	$[CO_2]$ at street level increases by 1ppm with an increase in population density of 8196 km^{-2}.	
Mixing layer depth	Linear regression of $[CO_2]$ on mixing layer height.	A growth in mixing layer depth of 100 m is associated with a 1.4 ppm drop in $[CO_2]$ at height A.	
Atmospheric Stability		Comparison of average vertical $[CO_2]$ gradient for different atmospheric stability classes.	Variation of 0.5 – 2 ppm dependent on height above ground.
Vegetation and soil		Regression of $[CO_2]$ at height A with the following variables: 1. Bowen ratio 2. Photosynthetically active radiation (PAR) 3. Time since rainfall	1. Decrease of 1.1 ppm per increase of 10 W m^{-2}/W m^{-2}. 2. Increase in PAR of 100 µmol m^{-2} s^{-1} associated with a decrease of 2.4 ppm; however, the total range of the effect of PAR is virtually identical to that of the mixing layer depth (PAR: -44.4 ppm over 0 – 1880 µmol m^{-2} s^{-1}, mixing layer depth: -41.5 ppm over 180 – 2960 m) and it is likely that the associated change in CO_2 is due to the common driving factor of incoming radiation. 3. Decrease of 0.2 ppm per day of no rainfall.

Appendix 4.A Microscale sources

This section contains a comparison of measurements made above a chiller unit to the south of the KSS tower (Figure 2.1b) to *[CO_2]* measured at the top of the tower for four periods defined in Section 4.3. Results (Figure 4.A.1) are similar to those depicted in Figure 4.4 but the difference between the microscale (chiller) and local scale (tower) *[CO_2]* is smaller.

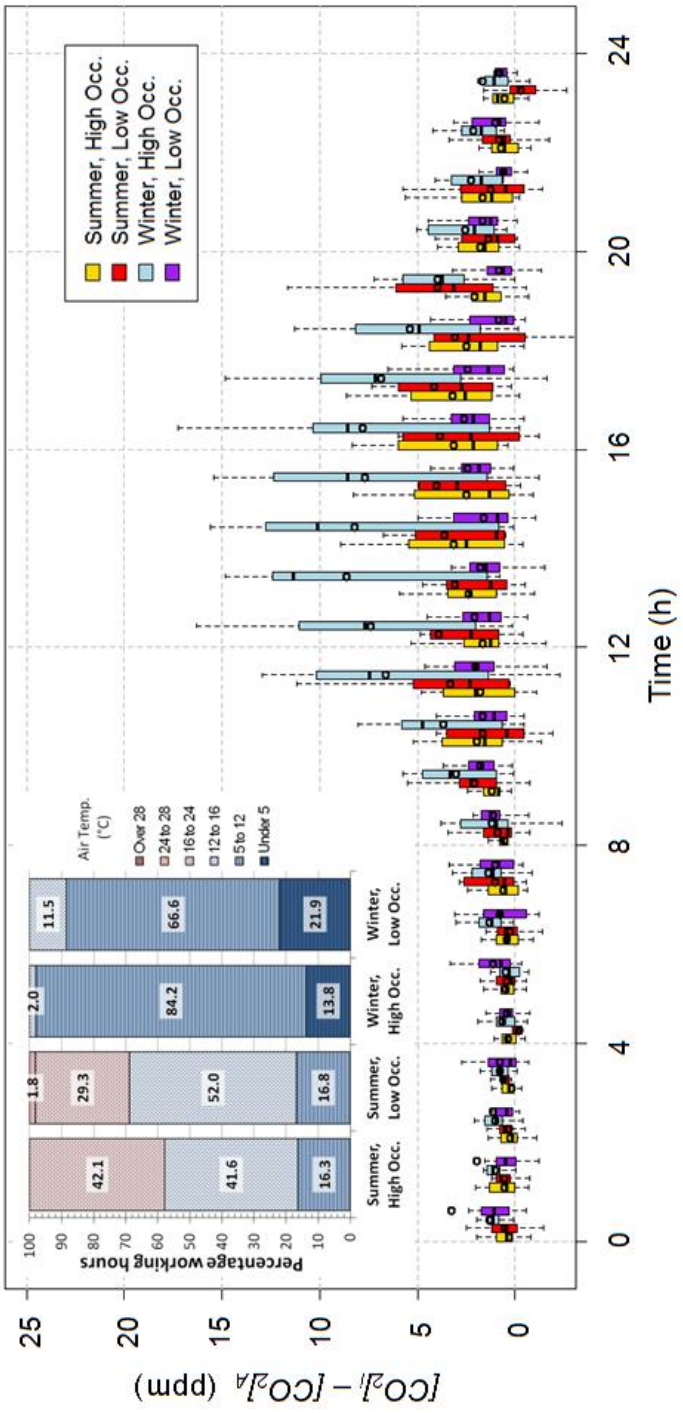

Figure 4.A.1: CO_2 concentration measured over a chiller ($[CO_2]_i$, 4 m to south of KSS) relative to background ($[CO_2]_h$, KSS, z_i=43.18) for two periods of high occupancy (Summer: 2011/141 – 2011/154 & Winter: 2011/336 – 2011/349) and two of low occupancy (Summer: 2011/155 – 2011/168 & Winter: 2011/350 – 2011/363)(key, right inset). Bar: median, circle: mean, box: interquartile range, whiskers: 95% confidence limits. Left inset: Temperature distribution measured at KSK (WXT510) for each period.

Appendix 4.B Hourly mean and median diurnal cycles for various atmospheric variables

This section compares hourly mean and median diurnal cycles in ten variables measured at KSSW and RCJ during June to September, 2012 (Figure 4.B.1). All data were measured on Sundays and have been divided into sets as defined in Section 4.4.2.

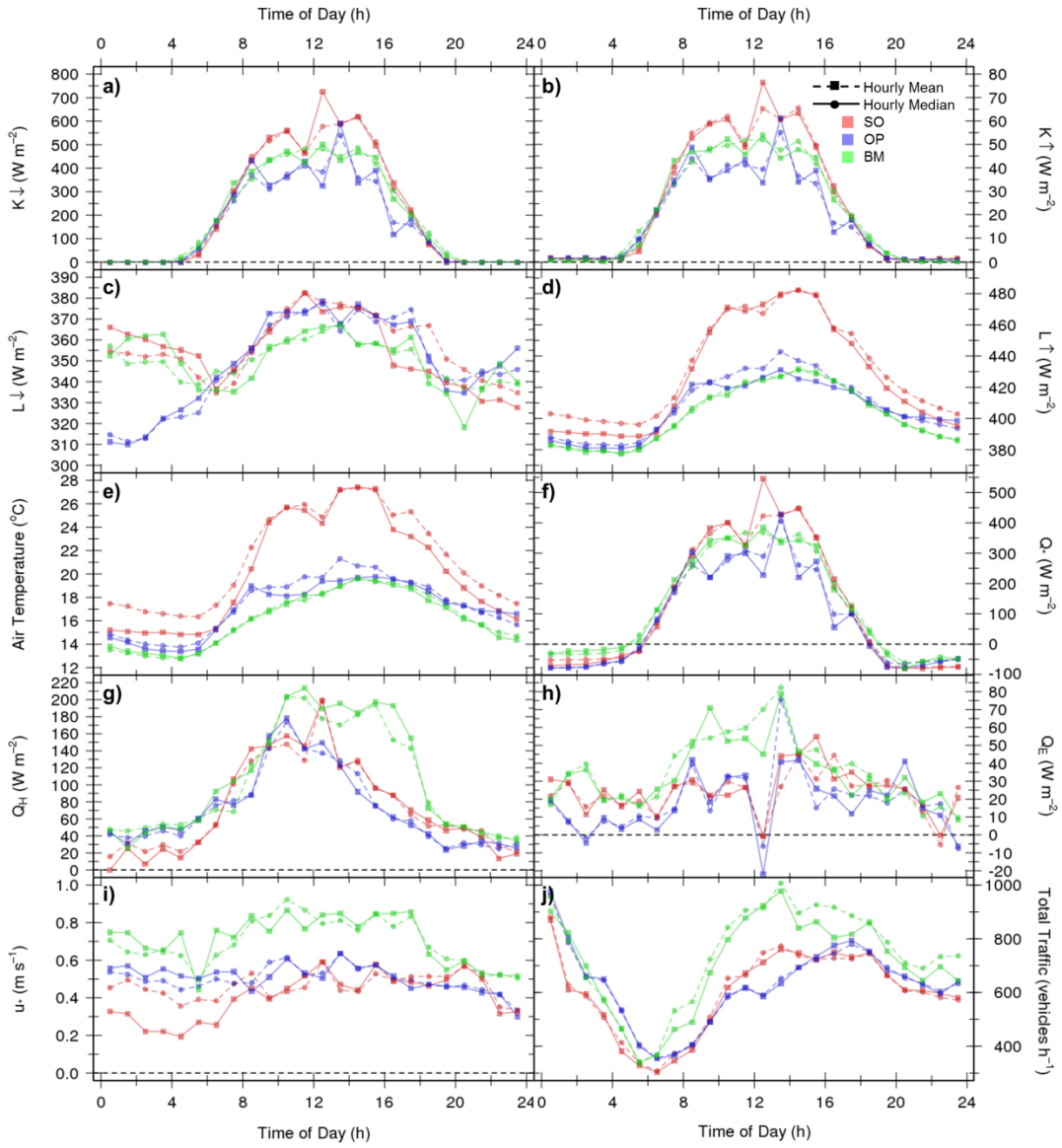

Figure 4.B.1: Hourly mean and median (a) downward shortwave radiation (CNR1, CNR4), (b) upward shortwave radiation (CNR1, CNR4), (c) downward longwave radiation (CNR1, CNR4), (d) upward longwave radiation (CNR1, CNR4), (e) air temperature (CNR1, CNR4), (f) net radiation (CNR1, CNR4), (g) sensible heat flux (CSAT3,), (h) latent heat flux (LI7500), (i) friction velocity (CSAT3), (j) total traffic flow (ATC; RCJ) for three sets of days defined in Section *4.4.2. Measurement site changed from KSS to KSSW, and radiation measurements from CNR1 to CNR4, on 2012/085. See upper right of (b) for key.*

Chapter 5: Storage of carbon dioxide within the urban canyon

The aims of this chapter are to provide a description of CO_2 storage characteristics in an urban environment at timescales ranging from the sub-hourly to the seasonal (Section 5.1) (including loss by venting, Section 5.2), to identify 'best practice' methods of measurement (Section 5.3), and to discuss gap-filling of CO_2 storage data (Section 5.4)[3].

The impact of the spatial (Section 5.3.1), and temporal (Section 5.3.2) density of the CO_2 concentration measurements on calculated CO_2 storage is assessed in Section 5.3. The relation of CO_2 storage to factors such as wind speed, traffic volume and sensible heat flux is investigated in Section 5.4.1. This informs the development of multiple models to gap-fill missing CO_2 storage data (Section 5.4.2). All CO_2 storage data reported were calculated as described in Section 3.1.1 from data collected as described in Section 2.2.

5.1 Temporal variation of CO_2 storage data

The forcings affecting ΔC_{SS} and ΔC_{SP} vary at daily, weekly and seasonal timescales. Analysis of the diurnal and seasonal variation of the CO_2 storage data collected at the Strand campus between 2012/150 and 2013/154 (Configuration C6, Section 2.2), the period for which the profile operated in switching mode, is presented in this section. The general properties of ΔC_{SP} at sub-hourly timescales are illustrated for a typical weekday and rest day, for example, weekend, holiday (Figure 5.1) in June, 2013. These were dry, sunny days, with minimal CO_2 emissions above roof height as there was low building occupancy (summer vacation) and little need for building heating. CO_2 storage data aggregated by hour of day and month of year are presented to illustrate hebdomadal and seasonal variation. The latter are also used to derive qualitative relations between CO_2 storage data and factors such as traffic volume, wind speed and solar irradiation in Section 5.4.1.

5.1.1 Example days

The 10 minute ΔC_{SP} data for 2013/153-154 tended (80% of values) to vary between -0.52 and 0.56 µmol m^{-2} s^{-1} (Figure 5.1a) within an overall range of ±1.5 µmol m^{-2} s^{-1}. Despite the difference in environment, this is comparable to data reported by Iwata *et al.* (2005), who calculated mean daily storage of 0.32 µmol m^{-2} s^{-1}, with skew of -0.32, using a 30 minute profile of 6 heights in the Brazilian rainforest. Larger values (-20 to 5 µmol m^{-2} s^{-1}) were observed by Araujo *et al.* (2010), who made 5 s resolution measurements at 6 heights, cycling through the profile in 15 minutes. They noted a difference in the diurnal cycle of storage depending on whether the profile was situated on a plateau, slope, or valley bottom, with the latter having the most clearly defined cycle of accumulation overnight and dispersal during daylight hours. Similar cycles have been reported from a number of rural sites in Europe (Aubinet *et al.,* 2005), albeit with a smaller range (-5 to 3 µmol m^{-2} s^{-1}). Unlike the aforementioned rural studies, no

[3] Sections 5.1, 5.3 (with the exception of 5.3.2.1 and 5.3.2.4), 5.4.1.1 and 5.4.1.2 have previously been published as part of Bjorkegren *et al.* (2015).

clear diurnal or hebdomadal cycle in the instantaneous ΔC_{SP} values was observed for these particular days (Figure 5.1a) at the Strand. Calculated CO_2 storage values were exceedingly noisy, with increases in ΔC_S tending to be followed by decreases, that is, the time series appears antipersistent; however, autocorrelation values at lag 1 were only -0.03 and -0.25 for Sunday 2013/153 and Monday 2013/154 respectively. There are some small visual and skew differences in the frequency-size distributions (Figure 5.1b) between weekend (dashed blue line) and weekday (solid red line) values (skew of 0.42 and -0.24 for Sunday 2013/153 and Monday 2013/154 respectively).

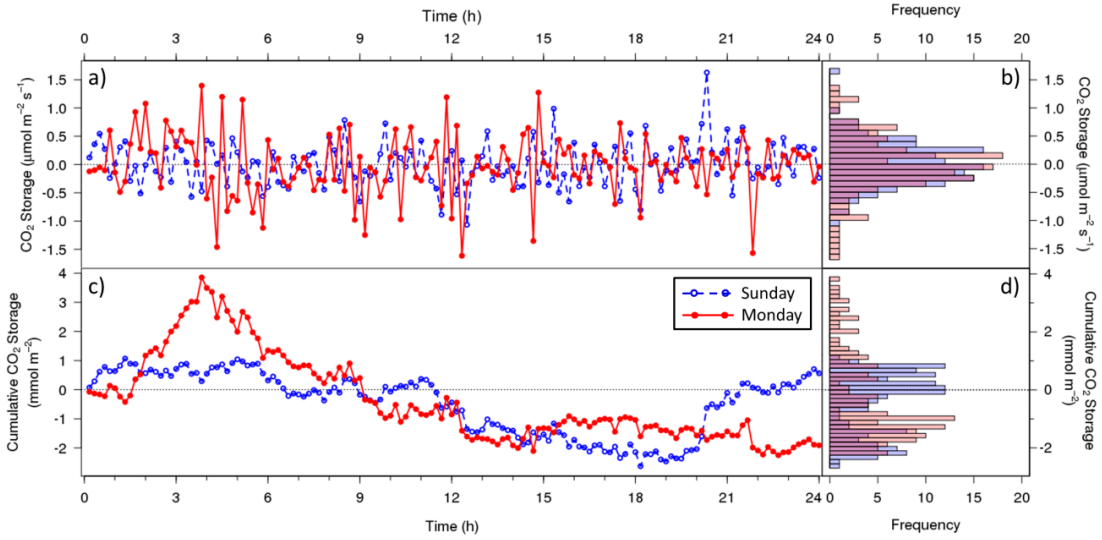

Figure 5.1: Characteristics of weekday and weekend CO_2 storage at KS, London, UK, for two example days in June 2013 (key, upper right (c)). (a) CO_2 storage from 10 minute cycle $[CO_2]$ profile data (all heights, Figure 2.1d) and (c) the running sum for two different days: 2013/153 (dashed blue line, Sunday) and 2013/154 (solid red line, Monday). (b) and (d): histograms of (a) (red, bin width 0.1 µmol m^{-2} s^{-1}) and (c) (blue, bin width = 0.15 mmol m^{-2} s^{-1}).

Changes in the distribution of ΔC_S (Figure 5.1b) impact the cumulative CO_2 storage (Figure 5.1c, d). Weekend ΔC_{SP} accumulated nocturnally is lost during the afternoon. The weekend cycle is more muted than the weekday one. The latter has a larger peak but shorter nocturnal accumulation. From mid-rush "hour" there is loss. The differences between the weekday and weekend ΔC_{SP} may relate to traffic volumes or traffic timing. However, comparison of the change in $[CO_2]$ with time at each profile height, z_i, and traffic volume (Automated traffic count, ATC, 250 m to the north east of KSSW) for 2012/151 – 2013/150 found no relation using a linear model fitted by least-squares between the two at any profile height (R^2<0.01, where R^2 is calculated as the residual sum of squares divided by the total sum of the squares and subtracted from one). The absolute value of the change in $[CO_2]$ with time appeared to increase with increasing traffic volume, with the strongest relation found at the lowest measurement heights. However, no R^2 for a linear regression of the change in $[CO_2]$ with time onto traffic volume exceeded 0.05. The relation of CO_2 storage to traffic and other factors is explored for aggregated data in Section 5.5.1.

5.1.2 Characteristics of the aggregated ΔC_S time series

When describing the characteristics of CO_2 storage on a timescale greater than a day, it is necessary to aggregate or average individual values due to the large number of data points.

This can be achieved by binning the data by e.g., month and/or hour of day and averaging over each bin. The results obtained are very different for the median and the mean of each bin (Figure 5.2).

This section compares ΔC_S calculated via the two approaches described in Section 3.1.1 as they are commonly implemented; in other words, ΔC_{SS} from $[CO_2]$ measurements made by a fast response infra-red gas analyser at several times the height of the local roughness elements (e.g., Nemitz *et al.,* 2002; Crawford and Christen, 2014), and ΔC_{SP} from $[CO_2]$ measurements made by a closed path infra-red gas analyser, with air samples drawn from multiple locations in a vertical profile (e.g., Aubinet *et al.,* 2005). Here aggregated CO_2 storage data calculated from LI840 and from LI7500 measurements are presented for one seasonal cycle (2012/159-2013/154, C6), after which the switched LI840 profile was changed to continuous measurements (C7). Aggregated LI7500 CO_2 storage data for 2012 to 2014 (Appendix 5.A) show little year to year variation.

The diurnal cycle (columns, Figure 5.2) of ΔC_S is not constant throughout the year (rows, Figure 5.2) and varies with measurement method (Figure 5.2a/b vs.c/d). The ΔC_{SP} values calculated from 2 Hz LI840 data averaged to 1 minute values between 2012/160 and 2013/155 were averaged by hour of day and month of year. The majority (80%) of these hourly/monthly medians were within ±0.13 µmol m^{-2} s^{-1} (Figure 5.2); minor in comparison to median turbulent vertical CO_2 flux for the Strand of about 35 µmol m^{-2} s^{-1} (Kotthaus and Grimmond, 2012). For median ΔC_{SS} values calculated in the same fashion from 10 Hz LI7500 data over the same period, 80% of values were within 0.01 to 0.11 mmol m^{-2} s^{-1}, three orders of magnitude larger and significantly less equally distributed about 0. The difference between ΔC_{SP} (LI840) and ΔC_{SS} (LI7500) is also present for the hourly mean values, with 80% of ΔC_{SP} values within ±0.16 µmol m^{-2} s^{-1} when calculated from LI840 data, and between −0.19 and 0.00 mmol m^{-2} s^{-1} for ΔC_{SS} LI7500 data for the same period. Not only does the ΔC_{SS} calculated from the LI7500 data have a greater range of values, it also has a greater (negative) skew than ΔC_{SP} calculated from the LI840 data. The impact of sampling interval and sensor response time are explored further in Section 5.3.

5.1.2.1 LI840 ΔC_{SP}

Both hourly/monthly mean and median ΔC_{SP} calculated from LI840 data show a clear diurnal cycle, the magnitude and timing of which is seasonally variant (Figure 5.2a, b). Peak ΔC_{SP} is observed in the morning, followed by a midday trough and less clearly defined evening peak. Overnight storage values tend to be negative during the colder months (October to April) and weakly positive otherwise (May to September). The timing of the morning peak is closer to midday during January (08:00 GMT) and furthest in June (03:00 GMT), with a steady transition between the two that suggests that the dominant forcing is atmospheric stability and mixing, rather than anthropogenic behaviour (British Summer Time is GMT +1 and is in effect from the last Sunday of March to the first Sunday of October). Comparison of hourly median CO_2 storage for weekdays and weekends for June-August, 2012, found no difference in the timing

of the peak or trough CO_2 storage values despite higher overnight and lower daytime traffic volume on weekends.

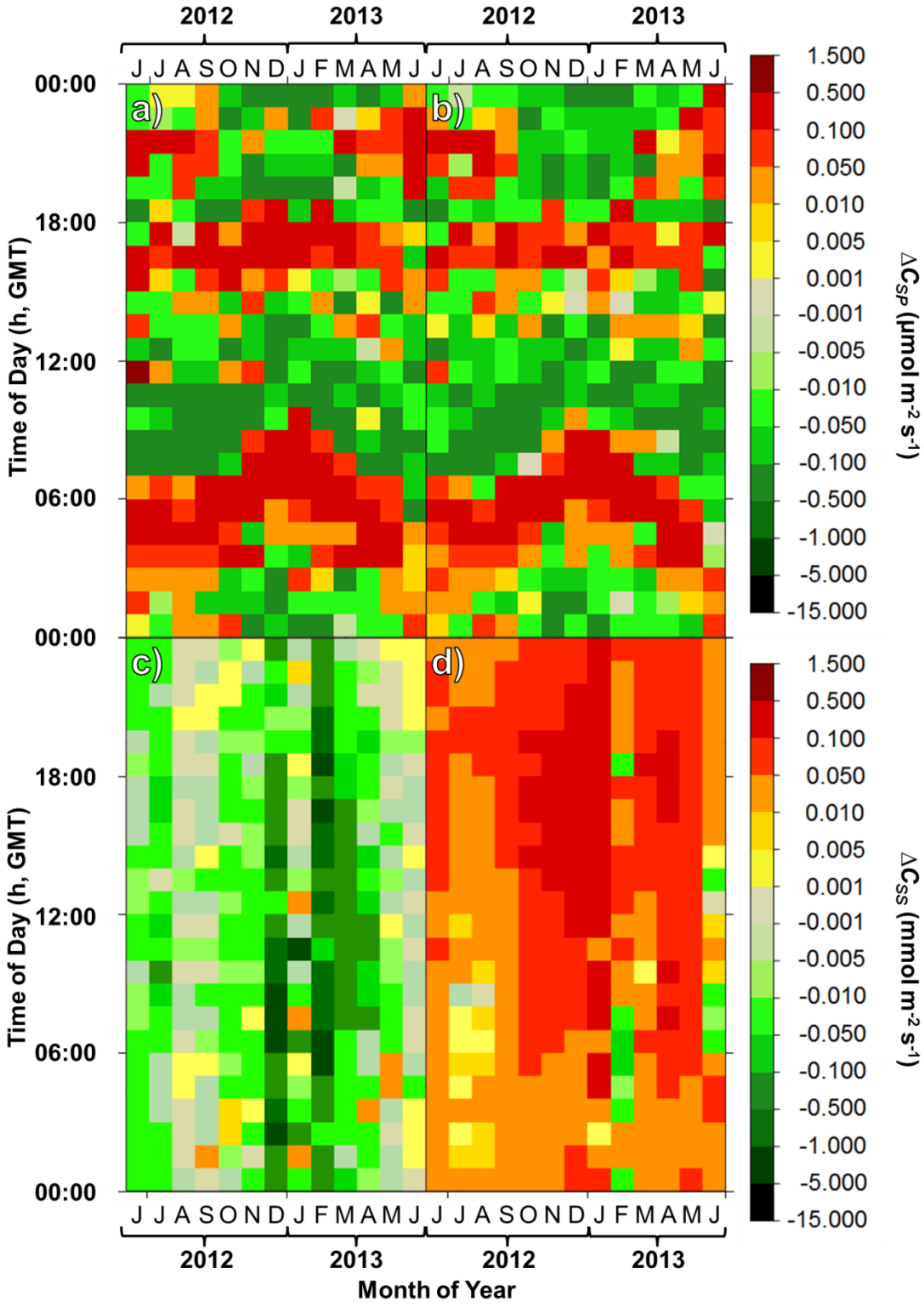

Figure 5.2: Diurnal and seasonal cycle of CO_2 storage (key: far right). Hourly/monthly mean (a, c) and median (b, d) ΔC_{SP} measured at all heights (Figure 2.1d) for 10 minute LI840 (a, b), and ΔC_{SS} measured at Height A (Figure 2.1d) for 10 Hz LI7500 (c, d), 2012/159-2013/154, by month (x-axis) and hour of day (y-axis). LI840 data in units of μmol m^{-2} s^{-1}, LI7500 data in mmol m^{-2} s^{-1}.

Negative overnight values during winter indicate loss of CO_2 from the canyon airspace and coincide with minima in the observed diurnal cycle of vertical CO_2 flux (Kotthaus and

Grimmond, 2012). This is unlikely to be due to photosynthetic uptake. An alternative explanation is drainage flow away from the canyon below z_h, potentially towards the River Thames; however, the EC measurements are predominantly unstable at KSSW even during overnight winter periods (Section 4.5.3). Within canyon temperatures in winter (2012/335-2013/059) exceeded those measured at z_h by approximately 0.8 °C at all times of day on both weekdays and weekends and it is suggested that the losses are either due to sustained thermally induced turbulence as described by Velasco and Roth (2010), or the release of intermittent thermally induced 'bursts' of high CO_2 air from the canyon (Section 5.2) as described by Salmond *et al.* (2005) and Lietzke and Vogt (2013).The temporal resolution of the ΔC_{SP} measurements is not sufficient to distinguish the two and the question is revisited in the following section.

5.1.2.2 LI7500 ΔC_{SS}

ΔC_{SS} calculated from LI7500 data shows a much weaker diurnal cycle relative to seasonality and a much greater difference between mean and median hourly values (Figure 5.2c, d). Hourly means tended to be negative whilst hourly medians tended to be positive, with the difference between the two greatest for November to January, i.e., data during this period had a greater range of values and was more negatively skewed. The larger positive values could be due to greater emissions from space heating, whereas the intermittent but strongly negative values lend credence to the hypothesis of CO_2 venting from the street canyon, which is investigated further in Section 5.2.

5.2 Venting

In this section the processes governing venting from the street canyon are explored at daily to half-hourly timescale using quadrant analysis and lagged cross-correlation of example time series. Scale averaging and a novel spike detection method are then used to identify venting episodes in scalar times series measured at the Strand campus.

Hourly median CO_2 storage values calculated from high (10 Hz) resolution CO_2 concentration data were found to be non-normally distributed (Section 5.1.2) with a negative skew, i.e., numerous small positive values and much fewer, but large in absolute magnitude, negative values. This suggests a slow build-up of CO_2 with intermittent venting and agrees with previous work done by Salmond *et al.* (2005) who used wavelet analysis and manual detection methods to identify venting episodes. It is necessary to distinguish between street canyon venting – the periodic emission of high CO_2 air from the urban canyon, and rooftop venting – the periodic emission of high CO_2 air from air conditioning units or boiler chimneys on the roof. The CO_2 in both cases is likely to have been emitted due to human activity - the events are distinguished by the processes governing their timing and location, which in the latter case are entirely within human control.

Kotthaus and Grimmond (2012) developed a system to automatically identify and remove spikes in CO_2 concentration due to rooftop venting, called IMAS (Identification of Micro-scale

Anthropogenic CO_2, heat and water Sources), at the tower's previous position (KSS). This system continued to be used when the tower was moved to KSSW. On days with high building occupancy and heating demand, the percentage of data points flagged by IMAS can be relatively high, as there are numerous active micro-scale sources of CO_2 from air conditioning units and a natural gas fired boiler (Section 4.3). This section therefore uses data collected between the 20th of December 2013 and the 2nd of January 2014 (2013/354 – 2014/002) when the campus was closed and the building heating was turned off (Olive Byrne, personal communication, 2014) to consider street canyon venting.

5.2.1 Cross Correlation

Day 2013/354 was chosen as a case study day to develop the wavelet analysis method as it was the furthest from major national holidays (Christmas, New Year) and had good data availability (percentage of points flagged by IMAS under 10% for all half hour periods, 6174 points, corresponding to 10.5 minutes removed in total). Conditions were clear and dry throughout daylight hours (8 am to 4 pm GMT), but insolation was low (shortwave radiation peaked at 250 W m^{-2}) and clouds developed after dusk with the collapse of the mixing layer. The air temperature rose from pre-dawn conditions of 5.5 °C to 11 °C at dusk, rising further to 12 °C overnight. The wind speed showed a similar trend, rising from 3.5 m s^{-1} prior to noon, to 8 m s^{-1} by 7 pm and shifting from 240° (approximately parallel to the street canyon) to 205° (aligned with the river to the south west of KCL, Figure 2.1b). Atmospheric stability remained near neutral (z'/L at KSSW of -0.1 to -0.005) throughout the day.

The calculated CO_2 storage shows periodicities at several different temporal scales (Figure 5.3, Figure 5.4). Figure 5.3 shows regular increases in the absolute magnitude of the single height CO_2 storage (ΔC_{SS}) at approximately 30 minute intervals. This pattern is not repeated in the profile values (ΔC_{SP}) on day 354, which vary more gradually over a diurnal cycle (Figure 5.3); however, it is observed for ΔC_{SS} on all days for which there is data during the period 2013/347-2014/002 and for ΔC_{SP} on days 2013/359, 361, 362 and 365 (25th, 27th, 28th, and 31st December respectively) (Appendix 5.E).

At sub-hourly time scales, ramp structures lasting on the order of 60 seconds can be seen in the cumulative ΔC_{SS} ($\Sigma\Delta C_{SS}$) time series (Figure 5.4a). This pattern is not as apparent in the profile data, though some muted structures can be seen between e.g., 3 and 5 minutes in Figure 5.4b. A comparison of time series of the change in $[CO_2]$ with time ($\Delta([CO_2])/\Delta t$, 10 Hz, LI7500, 2013/354) at KSSW and KSNW found maximum cross-correlation with KSNW lagging KSSW by approximately 34 s. However, extension of this analysis to other days between 2013/347 and 2014/002 found no consistent magnitude or direction of the time lag with maximum cross correlation between the KSSW and KSNW $\Delta([CO_2])/\Delta t$. Nor was there any clear difference in lag times for maximum correlation between term (2013/347-2013/353) and vacation (2013/354-2014/002) periods. Rather than showing a smooth trend of increasing correlation in the vicinity of a particular lag, the cross-correlogram for each day was noisy with multiple, very different, lags giving cross-correlations close to the maximum. It is expected that mixing down of low CO_2 concentration air, or 'gusts', would be 'seen' at KSSW first, followed by

KSNW. Conversely, venting or 'bursts' of air with a high CO_2 concentration due to traffic emissions would be measured at KSNW first. Both of these processes can occur at multiple timescales and may not easily be resolved by methods like a cross-correlogram when applied to data for an entire day.

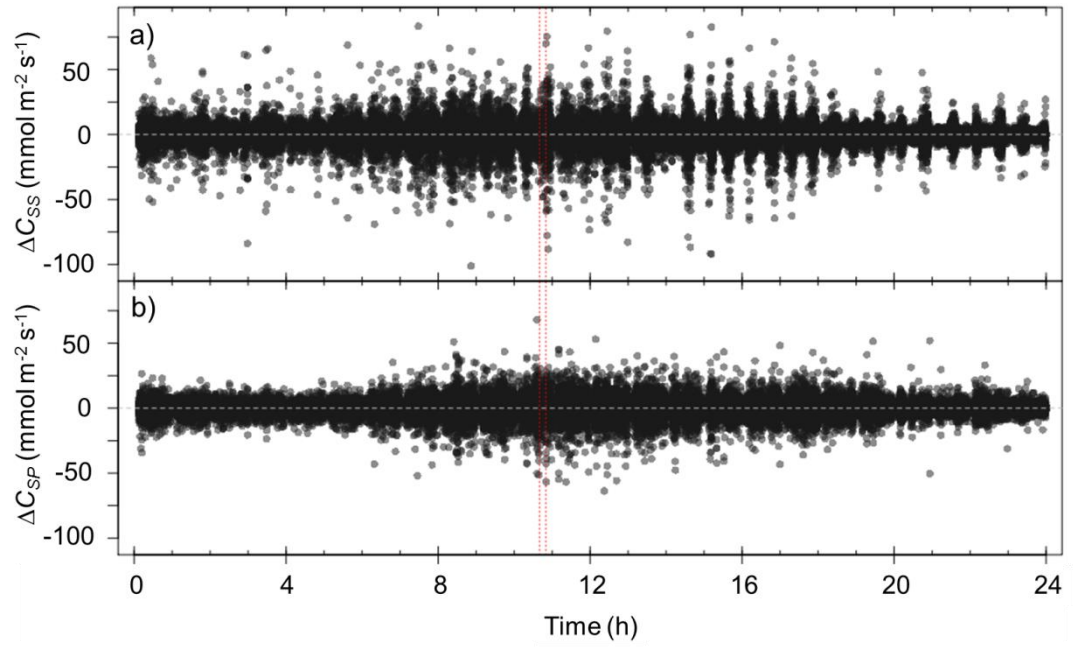

Figure 5.3: (a) ΔC_{SS} (b) ΔC_{SP} calculated from 10 Hz CO_2 concentration data for 2013/354, block averaged to 1 second time resolution. Red lines denote time range in Figure 5.4.

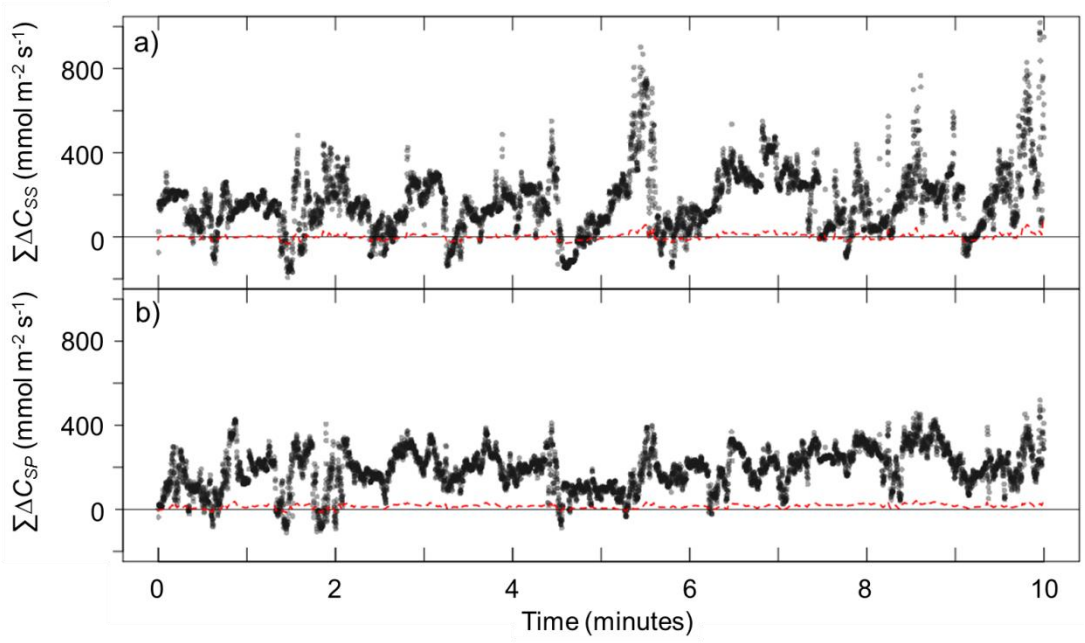

Figure 5.4: (a) Cumulative sum of ΔC_{SS} ($\Sigma\Delta C_{SS}$), (b) cumulative sum of ΔC_{SP} ($\Sigma\ \Delta C_{SP}$) for 2013/354 10:40:00-10:50:00 GMT. Black dots: 10 Hz values; dashed line: one second block average.

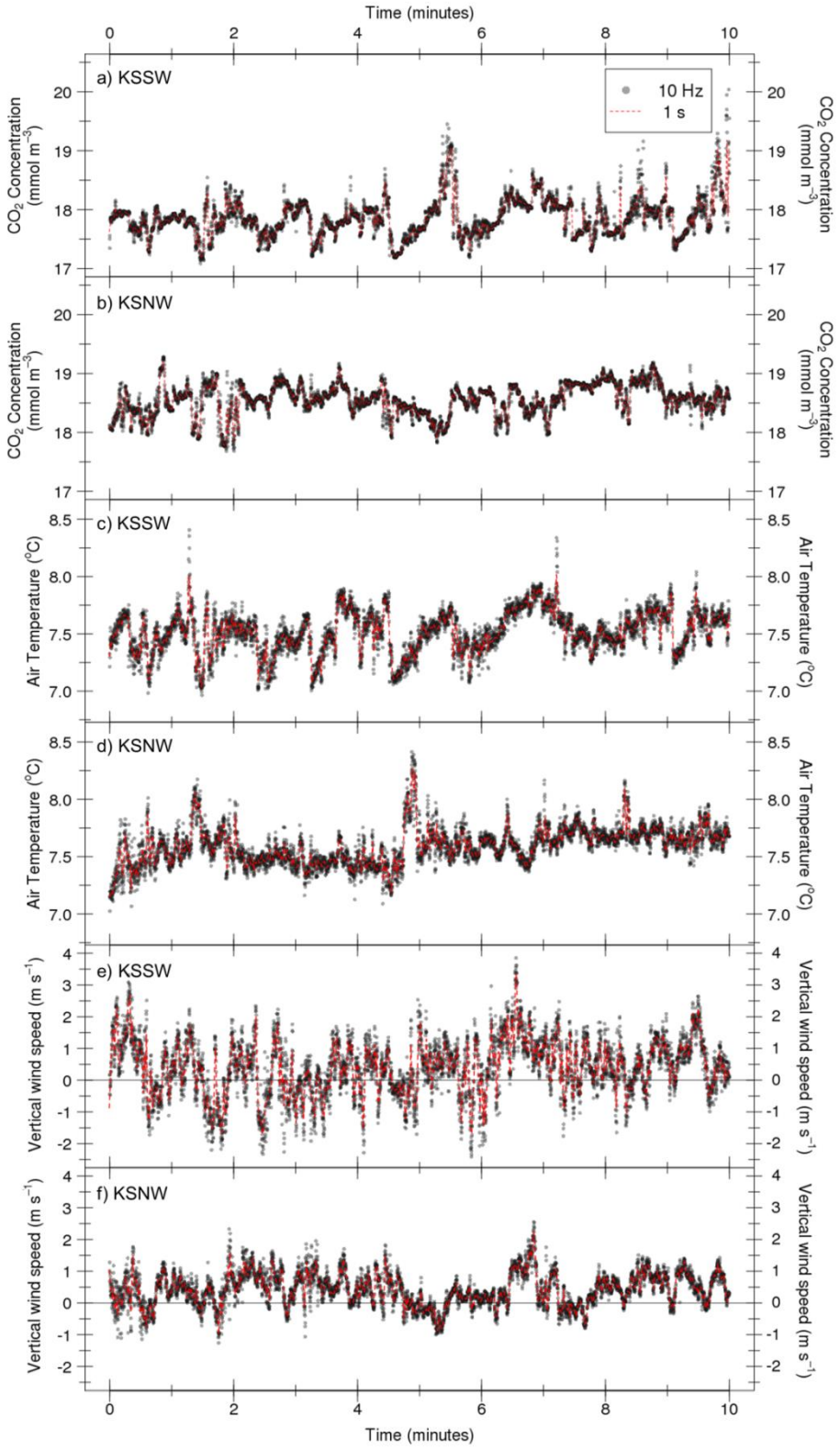

Figure 5.5: (a) and (b): CO_2 concentration measured at 10 Hz by LI7500 at (a) KSSW and (b) KSNW; (c) and (d): Temperature measured at 10 Hz by CSAT3 at (c) KSSW and (d) KSNW ; (e) and (f): Vertical wind speed measured at 10 Hz by CSAT3 at (e) KSSW and (f) KSNW. All plots 2013/354 10:40:00-10:50:00 GMT; Black dots: 10 Hz values; dashed line: one second block average (see key: upper right (a)).

For the period 2013/354 10:40:00-10:50:00 GMT the relation between CO_2 concentration and temperature ($R^2 = 0.52$) is particularly clear for the KSSW data (Figure 5.5). The cross correlation between the KSSW CO_2 concentration and the temperature is 0.72 at zero lag and the highest cross correlation between the KSSW CO_2 concentration and the canyon temperature is 0.22 with a lag of 34 seconds. In contrast, the R^2 for the regression of KSSW CO_2 concentration with vertical wind speed is only 0.08 and it has a cross correlation with CO_2 concentration of 0.28 at a lag of -2 s. The low level of correspondence between vertical wind speed and the CO_2 concentration suggests that the vented parcels of CO_2 are transported horizontally and arise due to shearing across the top of the canyon rather than rising buoyantly. Given the heterogeneity of the CO_2 sources and sinks, particularly in an urban environment, it is unsurprising that a particular turbulent event such as a gust does not always produce the same response in the CO_2 storage time series. This intermittency of response has been noted in other studies (Salmond *et al., 2*005) as an issue when using CO_2 as a tracer in the urban atmosphere. In general, it has been found that the relation between CO_2 concentration and temperature is better than between CO_2 concentration and components of wind speed (Figure 5.5).

The results presented here are relevant to a very specific time period. To extend this analysis, it was first necessary to locate more venting events, particularly those with different wind directions where the shear might be expected to operate differently relative to the canyon. Unfortunately, the superposition of processes on multiple timescales causes the data to be non-stationary. The non-stationarity of the data means a single set threshold is unsuitable to be the sole determinant of which structures are significant, and a sloped threshold fitted to the data might omit a ramp signal. Wavelet analysis was therefore used to decompose signal into time and frequency space as it is robust to intermittent, non-periodic signals. Identification and analysis of venting events using wavelets are therefore the topic of the next section.

5.2.2 Automated venting detection

Wavelet power spectra may be calculated in an analogous way to Fourier power spectra as the sum over all time points of the squared wavelet coefficients, normalised by the scale, the number of data points and the variance of the original times series (Torrence and Compo, 1998) (Section 3.2.3). However, the wavelet coefficients, once squared, may also be averaged over a set range of frequencies or scales and plotted with time to identify events at a particular time and scale. These wavelet time series are the basis for the automated venting (or 'peak') detection described in this section.

Wavelet analysis was conducted after Torrence and Compo (1998) using in-house software, written in R. If a data set of 30 minutes had fewer than 10 minutes of continuous data, the data set was rejected for analysis. Data were normalised by removing the mean and dividing by the standard deviation of the data set prior to processing. The second derivative of a Gaussian, or the Mexican Hat, wavelet was applied at 53 scales ranging from 0.2 s (the highest possible

time resolution given the measurement time resolution of 0.1 s) to 27.3 minutes. The Mexican Hat wavelet was chosen as it has previously been used to successfully identify coherent structures in atmospheric turbulence over an urban area (Feigenwinter and Vogt, 2005), and sudden changes or transitions in a time series may be readily identified in the wavelet coefficients if using the Mexican Hat wavelet as the wavelet coefficients will be 0 at the time and scale at which the event occurred (Salmond *et al., 2*005).

Scale averaged wavelet time series were calculated as the square of the absolute value of the wavelet coefficients, divided by the scale and summed over scales of interest. They were normalised by the reconstruction factor, the sampling time and the scale interval (Equation. 24 in Torrence and Compo, 1998).

5.2.2.1 Peak Detection

Previous studies have tended to assume a chi-square distribution of the wavelet coefficients (due to an assumed normal distribution of the time series data) and calculated the 95% confidence interval accordingly. In this study this test was included for completeness and to allow comparison with previous results. A second test was also developed: the original time series was sampled randomly without replacement to give a series with equivalent statistical properties (mean, variance, etc.) but no coherent structure. This time series was then passed to the same program as the data to be analysed and a 'white noise' spectrum generated. Points in the scale averaged sample spectrum were considered significant and set to 1 if they were greater than 3 standard deviations (Figure 5.6, dashed lines) higher than the mean (Figure 5.6, dash-dot line) of the scale averaged 'white noise' spectrum (Figure 5.6, red points), NA otherwise. The chi-square test has the additional disadvantage of being a very low threshold to clear (Figure 5.6, red dotted line) and in the example case in Figure 5.6, would define the majority of the scale-averaged spectrum as significant.

Both tests have the limitation that they select all data above a certain threshold. However, when identifying spikes or significant events, it is desirable to know the number of times venting has occurred, that is, identify a single point per spike or event, rather than every data point involved. There is the additional problem of defining the extent of a spike – is the signal centred on 5.5 minutes (Figure 5.6) one venting event or several? By choosing the second order derivative of a Gaussian wavelet base, or 'Mexican hat', it is possible to answer this question by identifying the zero-crossing points of the wavelet coefficients. These were identified as the difference in the sign of the wavelet coefficients (Figure 5.7). The zero crossing points were then used to define bin edges and all points flagged as significant within a bin were averaged. The highest value of the scale-averaged spectrum within each bin that had a non-0 mean was defined as the peak or venting event (Figure 5.8).

This method can be fully automated. It is capable of distinguishing between temporally close but structurally unrelated peaks, and multiple peaks for the same event due to noise.

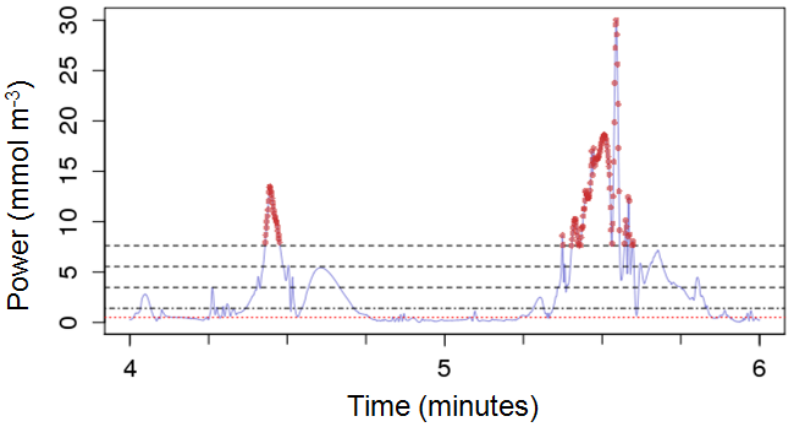

*Figure 5.6: Blue, solid line: 0-8 s scales averaged time series of the wavelet power spectrum for data set 2013/354 10:30:00-11:00:00, focussed on 10:44:00:10:46:00. Red dotted line: Chi-square derived confidence threshold; dash-dot line: mean of the scale averaged 'white noise' wavelet power spectrum; dashed lines: mean of the scale averaged 'white noise' wavelet power spectrum plus 1-3 * the standard deviation of the scale average; red points: 'significant' values.*

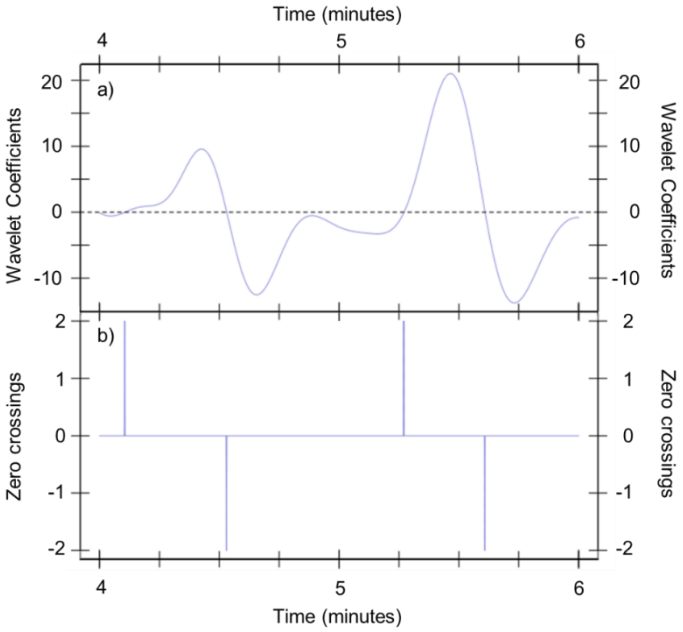

Figure 5.7: (a) Wavelet coefficients for 8 s scale of the wavelet power spectrum for data set 2013/354 10:30:00-11:00:00, focussed on 10:44:00:10:46:00. (b) Zero crossing points.

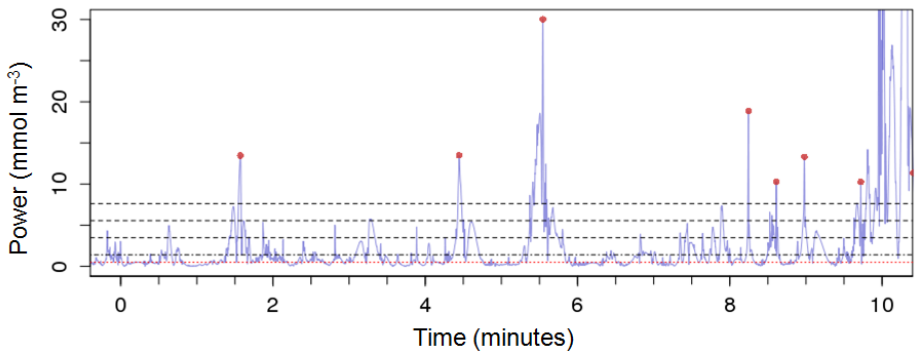

*Figure 5.8: Blue, solid line: 0-8 s scales averaged time series of the wavelet power spectrum for data set 2013/354 10:30:00-11:00:00, focussed on 10:40:00:10:50:00. Red dotted line: Chi-square derived confidence threshold; dash-dot line: mean of the scale averaged 'white noise' wavelet power spectrum; dashed lines: mean of the scale averaged 'white noise' wavelet power spectrum plus 1-3 * the standard deviation of the scale average; red points: venting events.*

5.2.2.2 Results

Automatic peak detection was trialled on 10 Hz data collected on day 2013/354 at KSSW by LI7500 (LICOR, USA) and CSAT3 (Campbell Scientific Ltd, USA) 46.4 m above ground level and 3 s data collected by Picarro (Picarro Inc., USA) 39.3 m above ground level. Peaks in the time series were considered to be co-incident if they were within a certain time span of each other. This time span was set at half the mean time scale of the timescales between 0 and 8 s. The mean timescales were 2.13 s and 6.42 s; peaks were therefore considered co-incident if they were within 10 and 1 adjacent point(s) for the 10 Hz and 3 s data respectively. The daily total peaks and the daily total co-peaks are given in Table 5.1 on the left (daily total: diagonal, light grey; daily total co-peaks: upper right, pink). A measure of the expected co-peaks if there were no underlying physical processes linking the two variables and all co-peaks were merely coincidences is shown in Table 5.1 (lower left, blue). The expected number of co-peaks for two variables, *a* and *b*, is calculated as the fraction of the day classified as 'peak' (number of peaks multiplied by the mean timescale) for variable *a* multiplied by the fraction of the day classified as 'peak' for variable *b*, all multiplied by the length of the day. Variables *a* and *b* can be deemed to co-vary positively if the number of co-peaks is greater than the expected value, and negatively if the number of co-peaks is less than the expected value. The number of observed co-peaks is expressed as a percentage of the number of expected co-peaks on the right hand side of Table 5.1.

Peaks in the *[CO_2]* and *[H_2O]* concentration time series co-occur with peaks in the vertical wind speed with a far greater incidence than would be expected were the two to have no relation (Table 5.1). The highest co-incidence of peaks as a percentage of the expectation value is *[H_2O]* with *[CO_2]*, followed by temperature. The lowest co-incidence is of horizontal wind speed perpendicular to the mean flow (*v*) with *[H_2O]*; however, it is not clear if this low co-incidence (90%) is significant.

Table 5.1: Comparison of the number of co-occurring venting events in two variable time series with the number expected. Left: number of peaks per variable (grey), number of co-peaks (pink) and expected co-peaks if randomly distributed (blue). Right: Number of co-peaks as a percentage of expected co-peaks, colour-coded according to ratio: green: > 110%, grey: 90% – 110%, red: < 90%. Top: 10 Hz data, LI7500 and CSAT 3 46.4 m above ground level. Bottom: 3 s data, Picarro, 39.3 m above ground level.

2013/354	*u*	*v*	*w*	T_A	*[CO_2]*	*[H_2O]*		*u*	*v*	*w*	T_A	*[CO_2]*	*[H_2O]*
u	2619	326	533	240	116	78			153	170	145	105	100
v	213	3092	631	309	133	83				171	158	101	90
w	314	370	4563	460	179	140					160	92	103
T	165	195	287	2396	276	208						271	293
[CO_2]	111	132	194	102	1620	34							753
[H_2O]	78	92	136	71	51	1136							

2013/354	*[CO_2]*	*[CH_4]*	*[H_2O]*		*[CO_2]*	*[CH_4]*	*[H_2O]*
[CO_2]	481	61	57			265	133
[CH_4]	23	480	56				130
[H_2O]	43	43	881				

The analysis was extended to the vacation period and the week prior (2013/347 to 2014/002) (Table 5.2). In general, *[CO_2]* and *[H_2O]* have co-incident peaks in the time series 6 times more

often than would be expected due to chance. This is greater than the co-incidence of any other variables studied. In addition, days with higher percentages of *[CO_2]*-*[H_2O]* co-peaks also tended to have higher *[CO_2]*–temperature and *[H_2O]*-temperature co-peak percentages (R^2 of 0.21 and 0.27 respectively). A paired t-test of the expected and observed co-peaks found the number of copeaks of temperature with *[CO_2]*, temperature with *[H_2O]*, and *[CO_2]* with *[H_2O]* to be significantly different from the expected value (p<0.001). Coupled with the lack of relation between *[CO_2]* peaks and peaks in the wind components (co-peaks of *[CO_2]* and *u*, *v* and *w* have mean ratios of 1.01, 1.02 and 0.99 to expected co-peaks, and a paired t-test gave *p*-values of 0.3, 0.6 and 1.0 to 1 d.p. respectively), this suggests that the venting of *[CO_2]* is primarily due to thermally induced turbulence rather than shear, although it is possible that shear at the Strand building roof height could play a part in preventing the regular emission of high *[CO_2]* warm air by forming a rarely penetrable 'lid' of fast moving air, as suggested by Caton *et al*. (2003). It should be noted that these conclusions are valid only for the measurements at 10 Hz. The results from the Picarro suggest a much weaker *[CO_2]*-*[H_2O]* relation (Table 5.3), with a measured: expected co-peak ratio of 1.15. It is uncertain whether this is due to the difference in time resolution of the measurements or the difference in height above ground level; however, due to the very low *[CO_2]* gradient between the two levels from all wind directions (Section 5.4.1.1), the former seems likely.

Table 5.2: Number of co-incident peaks observed for days 2013/347 to 2014/002 relative to the number expected due to random chance, expressed as a percentage. Data measured at 10 Hz. Number of co-peaks as a percentage of expected co-peaks colour-coded according to ratio: green: > 110%, grey: 90% – 110%, red: < 90%.

DoY	*u* & *v*	*u* & *w*	*u* & T_A	*u* & $[CO_2]$	*u* & $[H_2O]$	*v* & *w*	*v* & T_A	*v* & $[CO_2]$	*v* & $[H_2O]$	*w* & T_A	*w* & $[CO_2]$	*w* & $[H_2O]$	T_A & $[CO_2]$	T_A & $[H_2O]$	$[CO_2]$ & $[H_2O]$
347	166	202	124	107	108	172	145	96	100	139	95	93	204	142	850
348	160	184	141	92	109	174	158	105	105	145	110	124	227	339	759
349	156	187	159	85	82	154	155	90	81	141	85	98	160	139	364
350	178	187	161	108	126	176	187	98	137	162	93	89	176	150	338
351	240	197	167	71	92	196	165	115	82	206	97	114	294	335	711
352	172	171	164	98	93	167	166	114	127	164	121	108	172	119	640
353	169	173	135	108	118	171	153	124	137	168	116	111	329	390	789
354	153	170	145	105	100	171	158	101	90	160	92	103	271	293	753
355	155	174	197	103	108	156	181	79	93	163	94	99	150	79	310
356	153	164	127	118	117	167	145	87	98	140	104	106	351	292	725
357	159	188	190	97	80	161	168	95	84	149	82	98	124	100	381
358	166	187	159	113	107	164	176	110	102	153	107	112	307	223	571
359	208	202	166	103	138	174	169	115	100	163	99	115	319	312	752
360	212	219	154	133	143	215	108	102	93	159	119	109	298	420	1008
361	182	170	184	86	104	155	180	98	97	173	84	92	88	108	576
362	187	169	108	106	96	187	116	87	115	131	117	128	379	315	927
363	167	178	127	101	97	194	126	100	85	144	87	93	276	309	1261
364	168	183	168	88	80	152	164	103	77	148	93	92	176	140	663
365	181	188	159	109	97	163	167	126	106	159	89	109	169	204	728
1	159	187	172			155	154			164					
2	187	188	158			168	140			140					

Table 5.3: Number of co-incident peaks observed for days 2013/347 to 2014/002 relative to the number expected due to random chance, expressed as a percentage. Data measured at 3 s. Number of co-peaks as a percentage of expected co-peaks, colour-coded according to ratio: green: > 110%, grey: 90% – 110%, red: < 90%.

Day of Year	$[CO_2]$ & $[CH_4]$	$[CO_2]$ & $[H_2O]$	$[CH_4]$ & $[H_2O]$
347	129	196	116
348	218	103	167
349	244	109	105
350	317	132	129
351	367	125	245
352	289	114	156
353	260	145	120
354	265	133	130
355	200	65	131
356	195	122	97
357	216	60	141
358	69	105	125
359	413	138	127
360	182	132	126
361	122	109	97
362	443	127	106
363	277	79	86
364	276	104	106
365	378	109	107
1	260	111	151
2	297	106	119

No relation was observed between number of peaks and time of day for any variable, except potentially $[H_2O]$, which had lower median numbers of peaks per half hour between 18:00 and 00:00 (Figure 5.9). However, due to the large scatter this is not conclusive. The number of $[CO_2]$ and $[H_2O]$ peaks increased with wind direction from 180° to 240°, i.e., from approximately perpendicular, to along the Strand street canyon (Figure 5.10). The number of peaks in v decreased across the same range, and u, w and T_A were unaffected. Peaks in scalar concentrations are direction dependent, suggesting that the underlying processes are, at least in part, wind-driven rather than resulting from purely thermally induced turbulence. This conclusion is bolstered by plotting the number of peaks per half hour with stability (Figure 5.11). The wind components, u, v and w, show increases in the number of detected peaks as conditions change from unstable to neutral. Air temperature, $[CO_2]$ and $[H_2O]$ show no trend in number of peaks with stability conditions. The lack of a trend in number of peaks with stability conditions is also observed in the number of co-peaks (Appendix 5.F); however, a maximum is observed for variables co-peaking with $[CO_2]$ at z'/L values of -0.1 to -0.01. This is thought not to simply be due to greater numbers of $[CO_2]$ peaks during these stability conditions, as equivalent numbers of co-peaks were not observed during stable conditions, despite equivalent numbers of $[CO_2]$ peaks being observed for stabilities of $0.001 < z'/L < 0.1$ and $-0.1 < z'/L < -0.001$ for all variables except $[H_2O]$ (Figure 5.F.3, Figure 5.11). It is suggested that both mechanical, direction-dependent, processes and thermal, stability dependent, processes act to remove CO_2 from the street canyon.

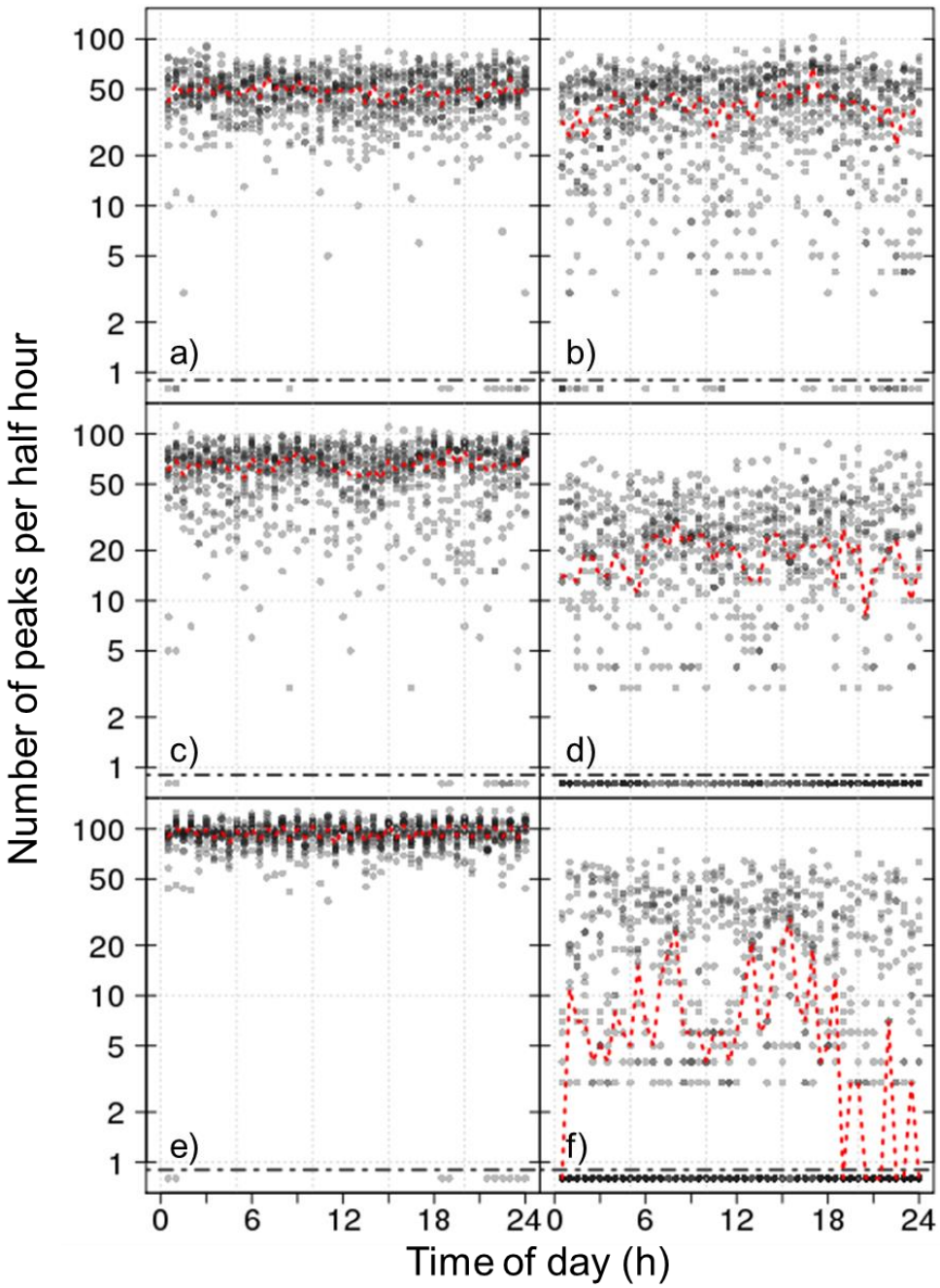

Figure 5.9: Grey points: number of peaks detected per half hour with time of day for (a) u, (b) T_A, (c) v, (d) $[CO_2]$, (e) w and (f) $[H_2O]$. All data collected 2013/354-2014/002, KSSW, by 10 Hz LI7500 and CSAT3. Dotted line: median value for each half hour. Dot-dash line: all values below this line were artificially made greater than zero for ease of plotting on a log scale.

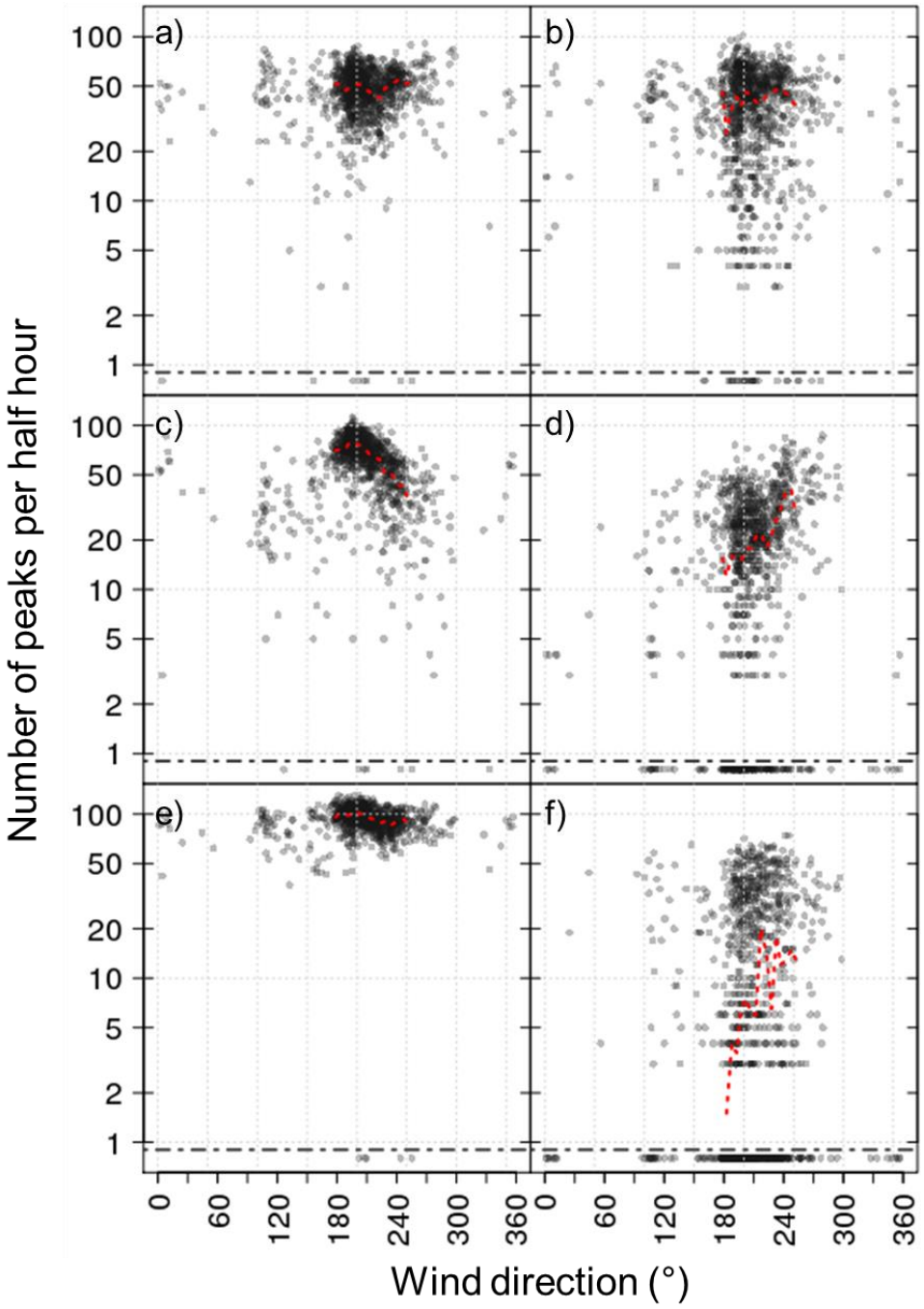

Figure 5.10: Grey points: number of peaks detected per half hour with wind direction at z_h, 2013/354-2014/002, KSSW, 10 Hz LI7500 and CSAT3 for (a) u, (b) T_A, (c) v, (d) $[CO_2]$, (e) w and (f) $[H_2O]$. Dotted line: median value for each 5 degree width bin with greater than 10 values. Dot-dash line: all values below this line were artificially made greater than zero for ease of plotting on a log scale.

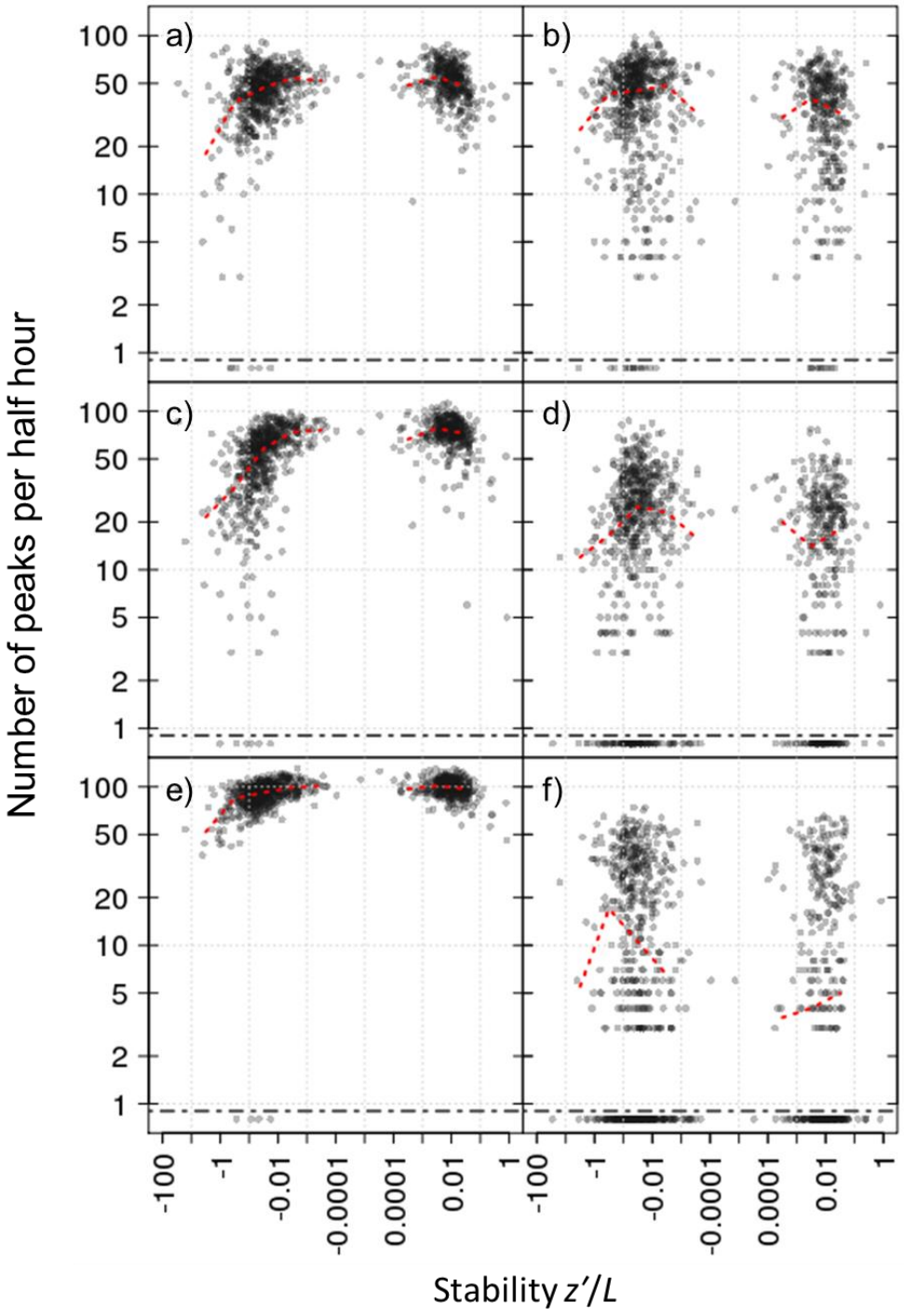

Figure 5.11: Grey points: number of peaks detected per half hour with atmospheric stability at z_h, 2013/354-2014/002, KSSW, 10 Hz LI7500 and CSAT3 for (a) u, (b) T_A, (c) v, (d) $[CO_2]$, (e) w and (f) $[H_2O]$. Dotted line: median value for each bin with greater than 10 values. Bins defined by powers of ten down to ±1E-4, centred on 0. Dot-dash line: all values below this line were artificially made greater than zero for ease of plotting on a log scale.

5.2.2.3 Quadrant analysis

The proportion of a signal which is due to upward 'bursts' rather than downward 'gusts' can be investigated using quadrant analysis. As described in Section 3.2.4, this involves dividing the data into four quadrants depending on the values of the instantaneous deviation from the mean of the zonal and vertical wind speed components (u' and w' respectively). The quadrants are defined: "quadrant 1: $u'>0$, $w'>0$, outward interaction; quadrant 2: $u'<0$, $w'>0$, burst or ejection; quadrant 3: $u'<0$, $w'<0$, inward interaction and quadrant 4: $u'>0$, $w'<0$, sweep or gust" (Shaw *et al.,* 1983) (Q1-Q4, Figure 5.12). To examine extreme events, low wind speeds can be excluded using a 'hole' function. Points are excluded if the absolute value of the product of the u' and w' values for a data point x_t, $|u'w'|_{x_t}$, is less than the absolute value of the mean of the products of u' and w' for the entire time series, $\left|\overline{u'w'}\right|$, multiplied by a constant, H, (Shaw *et al.,* 1983) i.e., a point is included if it satisfies the following:

$$|u'w'|_{x_t} \geq H\left|\overline{u'w'}\right| \tag{5.1}$$

H values of 1, 2 and 3 are plotted in Figure 5.12 for $\left|\overline{u'w'}\right|$ of 0.15 m s^{-1}.

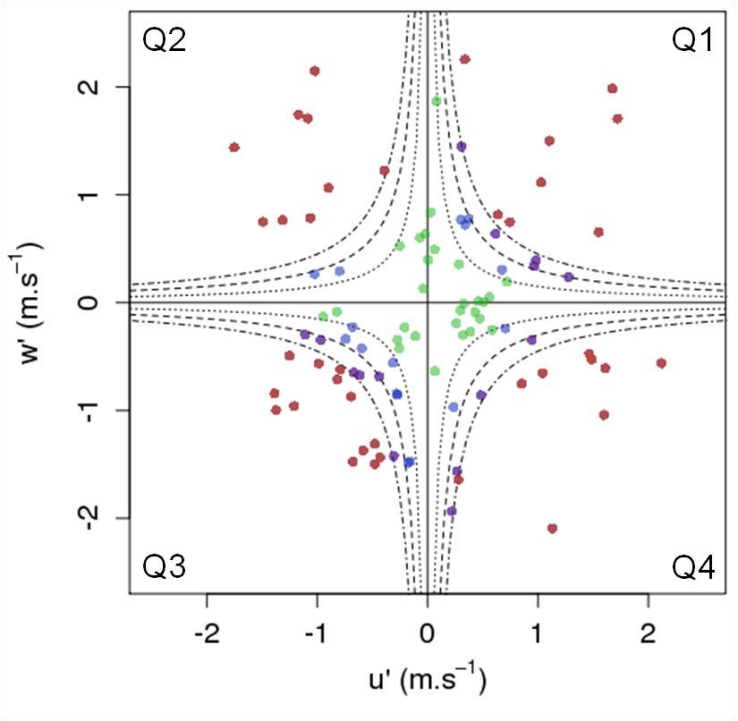

Figure 5.12: Example quadrant plot of u' and w' data synthesised as Gaussian distributed random values. Dotted, dashed and dot-dash lines indicate different 'hole' sizes defined by 7.1 with H equal to 1, 2 and 3 respectively. Green: H<1; blue: 1≤H<2; purple: 2≤H<3; red: 3≤H.

To discover whether extreme events in the CO_2 storage time series were associated with particular turbulence conditions or coherent atmospheric movements, the zonal (u) and vertical (w) components of the 3D wind velocity were binned according to the CO_2 storage value calculated from concurrent CO_2 concentration data. Bins were defined by the number of standard deviations from the daily mean value. Once binned, the wind components were de-trended and averaged over the bins, d, defined by the CO_2 storage ($\langle\overline{u'w'}\rangle_d$) for each half hourly period (T). The bin averages for each time period and ΔC_S bin, d, (Figure 5.B.1 in

Appendix 5.B, $\langle \overline{u'} \rangle_{T,d}, \langle \overline{w'} \rangle_{T,d}$) tend to show a negative relation between *u´*and *w´*with increasing scatter towards the extreme ΔC_S bins. Visual inspection suggests no apparent difference in distribution between the values binned by ΔC_{SS} and those binned by ΔC_{SP}, and the bin averages seem evenly distributed between the burst and sweep quadrants.

The exact contribution of each quadrant can be quantified as the stress fraction, S_q (Shaw *et al.,* 1983):

$$S_q = \langle u'w' \rangle_q / \overline{u'w'} \tag{5.2}$$

S_q can be calculated as the conditional average of the product of the instantaneous deviations from the mean of the longitudinal and vertical wind components within quadrant, *q,* divided by the overall mean of the *u´w´*product. The stress fractions for each quadrant and ΔC_S bin show little systematic variation with the distance of the ΔC_S bin from the mean (Appendix 5.G).

5.3 Measurement density in space and time

5.3.1 Spatial resolution

The focus of this section is the effect the spatial resolution of the *[CO_2]* measurements has on the total calculated CO_2 storage. It will examine which parts of the street canyon contribute most to the overall signal and the effect of multiple vs.single heights on storage data characteristics.

One of the first decisions when preparing to make *[CO_2]* profile measurements is the number and siting of sample locations. The aim, in general, is to accurately characterise the shape of the vertical *[CO_2]* profile with as few sampling points as possible to minimise data loss due to switching, and installation and running costs. Ideally measurements would be more densely spaced where the concentration changes rapidly with height, and sparser where *[CO_2]* is more constant with height. It is commonly accepted that for rural profiles, measurement density should be greater closer to the ground as the major source of CO_2 is sub-surface respiration and the profile changes more quickly at lower elevations (Wofsy *et al.,* 1993; Goulden *et al.,* 1996; Jarvis *et al.,* 1997; Molder *et al., 2*000; Iwata *et al., 2*005; Vogt *et al., 2*006; Araujo *et al., 2*010). Six-hourly median vertical *[CO_2]* profiles measured at the Strand during June and November/December, 2012 suggest this may not be the case for high density urban environments (Figure 5.13a). The median CO_2 concentration with height relative to the mean building height shows weekday concentrations in the canyon relative to those measured at z_i=46.4 m tend to be higher due to the greater volume of traffic.

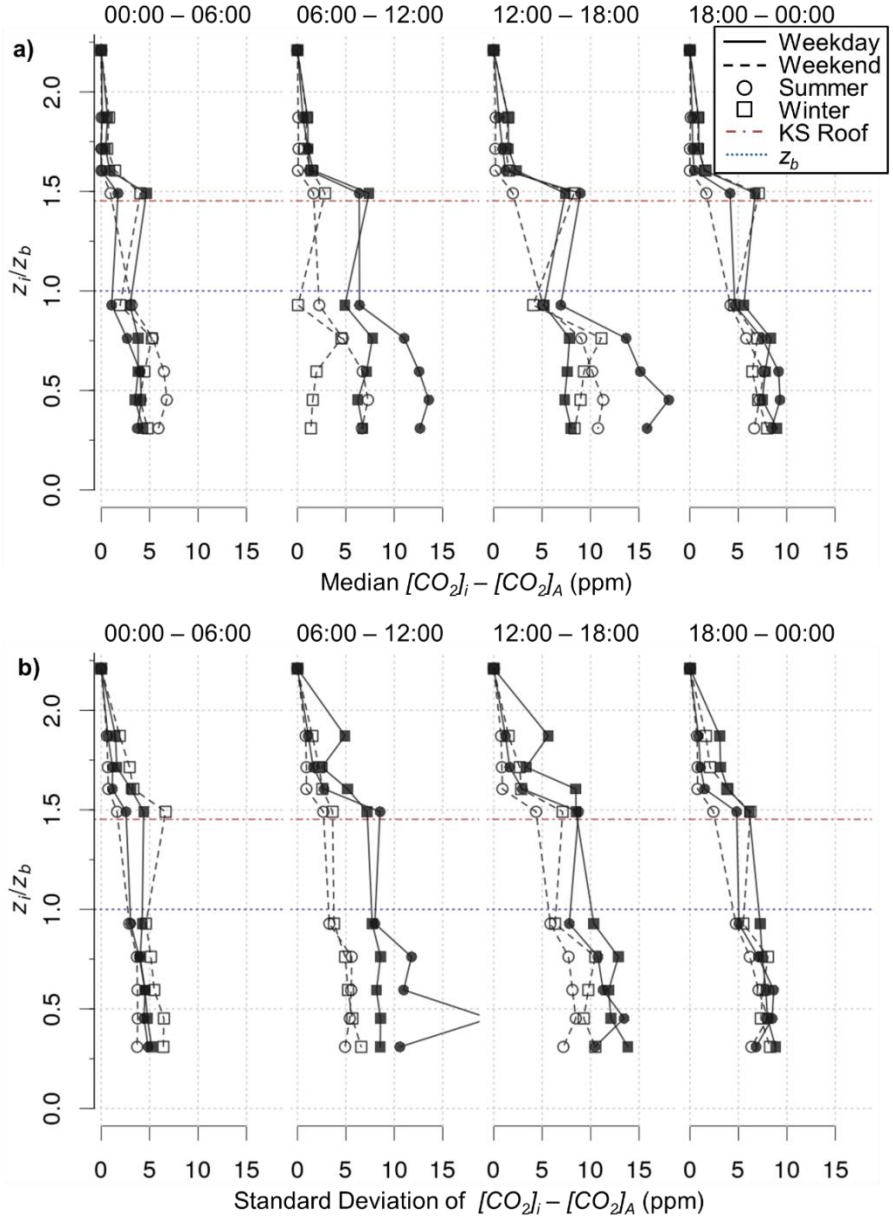

Figure 5.13: a) Strand (London, UK) median enhancement of CO_2 concentrations ($[CO_2]$) in ppm (x-axis) at each height z_i (heights A to J, Figure 2.1d), $[CO_2]_i$, relative to $[CO_2]_h$ measured at z_h,(height A, Figure 2.1d) binned by time of day (left to right: 00:00-06:00, 06:00-12:00, 12:00-18:00, 18:00-00:00) with (y-axis) the height of inlet (z_i) relative to mean building height (z_b, dotted horizontal blue line). Solid points/lines: weekday; hollow points/dashed lines: weekend. Circles: summer (2012/156-183); squares: winter (2012/324-351). Horizontal dot-dash red line: Strand building height. (b) As (a), but standard deviation.

In Figure 5.13a, rather than the smooth, exponentially decreasing concentration curve with height observed in Basel (10 locations spanning 0.17 to 2.3 times the mean building height, z_b, Lietzke and Vogt, 2013), median $[CO_2]$ shows a sharp transition at the Strand building roof level (Figure 5.13, 30.5 m, dot-dash horizontal red line), and potentially another close to the mean building height (Figure 5.13a, 21 m, dotted horizontal blue line) during the day (06:00-18:00 GMT). The difference between observed profiles in Basel and London is likely to be due to the greater street canyon depth at KCL; the height:width ratios for the street canyons in Basel and London are 0.34 – 0.70 and 0.74 – 1.28 respectively. Lietzke and Vogt (2013) characterised the flow regime as 'wake interference' (Oke, 1987), leading to greater mixing out of canyon emissions compared to 'skimming flow' at KCL. The latter would result in a fast moving 'lid' of

air over the roof of the Strand building during the prevailing south-westerly winds and an active vortex within the canyon, leading to two fairly internally homogenous flow regimes, with some exchange at the interface at roof height. This is observed to some extent (Section 5.4.1.1); however, the difference between above and within canyon $[CO_2]$ is more apparent in the standard deviation of the measured $[CO_2]$ for each time period and height (Figure 5.13b). Measurements at or below the Strand building height have consistently higher variance than those above for both summer and winter, weekdays and weekends. This suggests that the CO_2 profile in an urban street canyon with near 1:1 height: width ratio could be adequately measured by two or three points, provided they were placed appropriately.

This hypothesis is tested by extending the analysis of Yang *et al.* (2007) to the urban $[CO_2]$ profile. The method consists of defining a CO_2 storage time series calculated from a particular configuration of sample inlets as 'best practice' (ΔC_{SBP}) and assessing other configurations based on how closely the calculated ΔC_S from each configuration agree with ΔC_{SBP}. In this study, ΔC_{SBP} was defined as the CO_2 storage calculated using data from all ten vertical profile locations. All configurations included z_h, co-located with the eddy covariance system, as this measurement is most likely in other micrometeorological sites. Configurations were grouped by number of sample locations included in the CO_2 storage calculation, for example, all configurations with three sample locations are 'Group 3'. Storage was calculated as the change in $[CO_2]$ weighted by the vertical span for each height and divided by the cycle length. The vertical span (Δz_i) for a sample location z_i was defined as $(z_{i+1} - z_i)/2 + (z_i - z_{i-1})/2$, except for the lowest height, where the span extended to ground level, and the uppermost height, where the span stopped at $z_i = z_h = 46.4$ m.

Cumulative ΔC_S was found to be highly variable with configuration. The ΔC_S time series for each configuration were compared with ΔC_{SBP}. The configurations within each group with the lowest and highest root mean squared error (RMSE) were selected as the 'best' and 'worst' configurations respectively. Configurations with low RMSE tended to maximise Δz_i per sample point and be evenly distributed across the vertical extent of the profile (Figure 5.14a). This is in contrast to previous rural work (e.g., Iwata *et al.,* 2005) which has tended to cluster sample points at the base of the profile. The configurations with the highest RMSE have sample points clustered towards the top of the profile, adding little new information with each new location.

The 'value' of each additional sample point can be assessed by comparing the coefficients of the regression of the ΔC_S calculated from each group's best configuration onto ΔC_{SBP} (Figure 5.15). Increasing the number of sample points from 1 to 2 increases the coefficient of determination (R^2) from 0.15 to 0.80 provided that the second sample point is placed at approximately half the height of the local roughness elements, i.e., $z_i/z_b = 0.5$. This supports the earlier hypothesis for street canyons with height:width ratios of approximately 1:1 that the urban environment can be adequately measured, and perhaps, modelled, as a two-layer system of above and within-canyon air masses with a transition zone at roof level. It is not necessary to monitor the concentration all the way down to street level as the air within the canyon is well mixed and responds quickly to ground-level changes in $[CO_2]$. As expected, air above roof level

is less responsive to street canyon processes and measurements made at 2-3 times mean building height should not be considered directly representative of processes within the street canyon below. The assumption required for the single height calculation of CO_2 storage, also known as the storage flux correction, is not valid – at least one other measurement point is required.

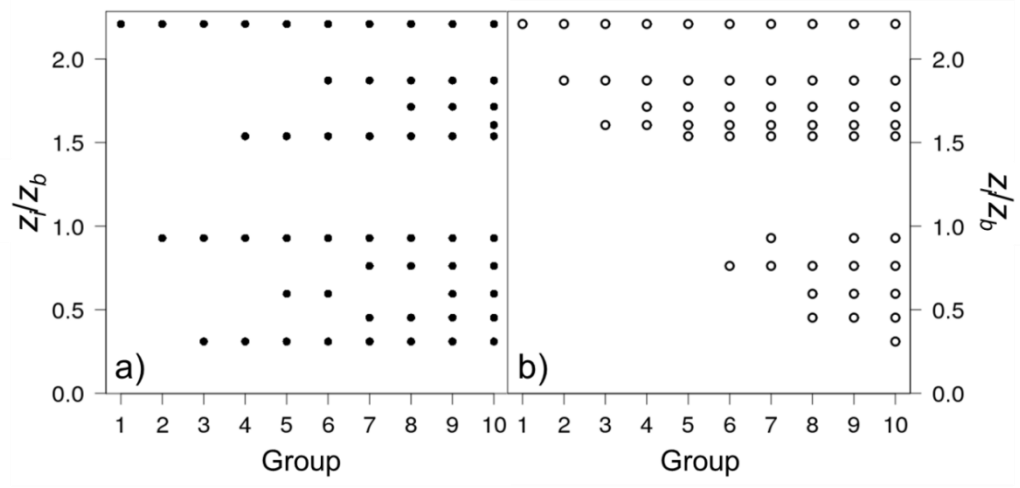

Figure 5.14: The height of inlet (z_i) relative to mean building height (z_b) as a function of configurations for each group with (a) minimum and (b) maximum root mean squared error (RMSE) when the resultant CO_2 storage time series is regressed onto the benchmark CO_2 storage time series (2012/150 – 2013/153, heights A-J, KS, London, UK) calculated from data averaged to 30 minutes. Group number indicates number of inlets for a configuration.

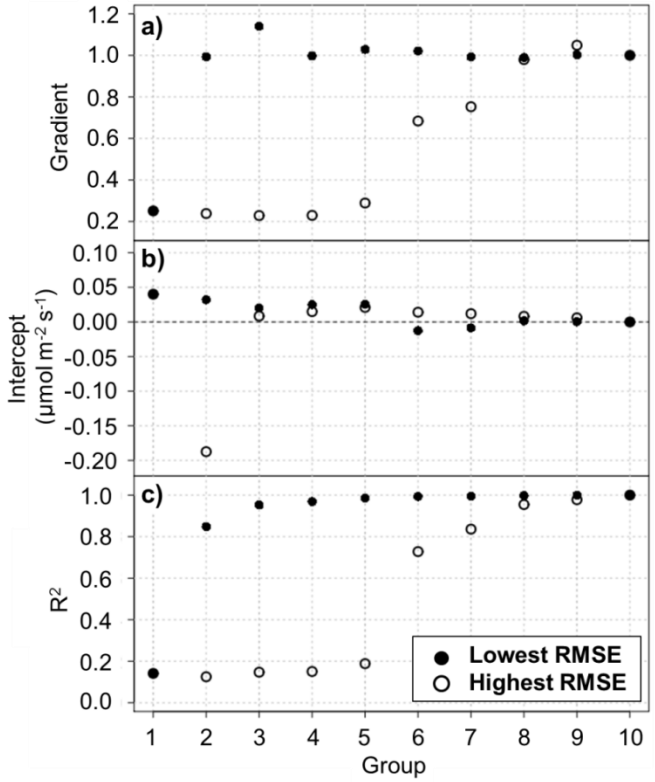

Figure 5.15: The (a) slope, (b) intercept and (c) coefficient of determination for the configurations (Figure 5.14) with highest and lowest root mean squared error (RMSE, see key) when regressed onto the (benchmark) CO_2 storage time series calculated from all ten inlets (see Figure 2.1d) for 2012/150 – 2013/153.

5.3.2 Temporal resolution

5.3.2.1 Introduction

Calculated CO_2 storage values were observed to vary significantly with instrument sensor response time and sampling interval (Section 5.1.2). Peaks and troughs seen in ΔC_{SS} time series measured at different sampling rates occur at approximately the same time (Figure 5.16); however, there are sudden excursions present in higher time resolution series which are not present, or are muted in data measured or averaged to lower temporal resolutions. As noted in Section 5.1.2, Appendix 5.A, and Figure 5.16, CO_2 storage and cumulative CO_2 storage calculated from higher time resolution data also tend to have a larger range of values. In Figure 5.16, the cumulative CO_2 storage peaks at 100, 125 and 200 mmol m^{-2} s^{-1} for 10 minute, 2 Hz and 10 Hz data respectively, suggesting that at lower time resolutions a portion of the signal is lost.

In this section, the measurement time resolution necessary to capture the majority of the CO_2 signal is assessed using the wavelet power spectrum. The effect of under sampling or inadequate sensor response time is simulated by subsampling and progressively smoothing a 20 Hz time series. The loss of measured CO_2 storage with decreasing time resolution is predictable and is shown to be correctable to an extent.

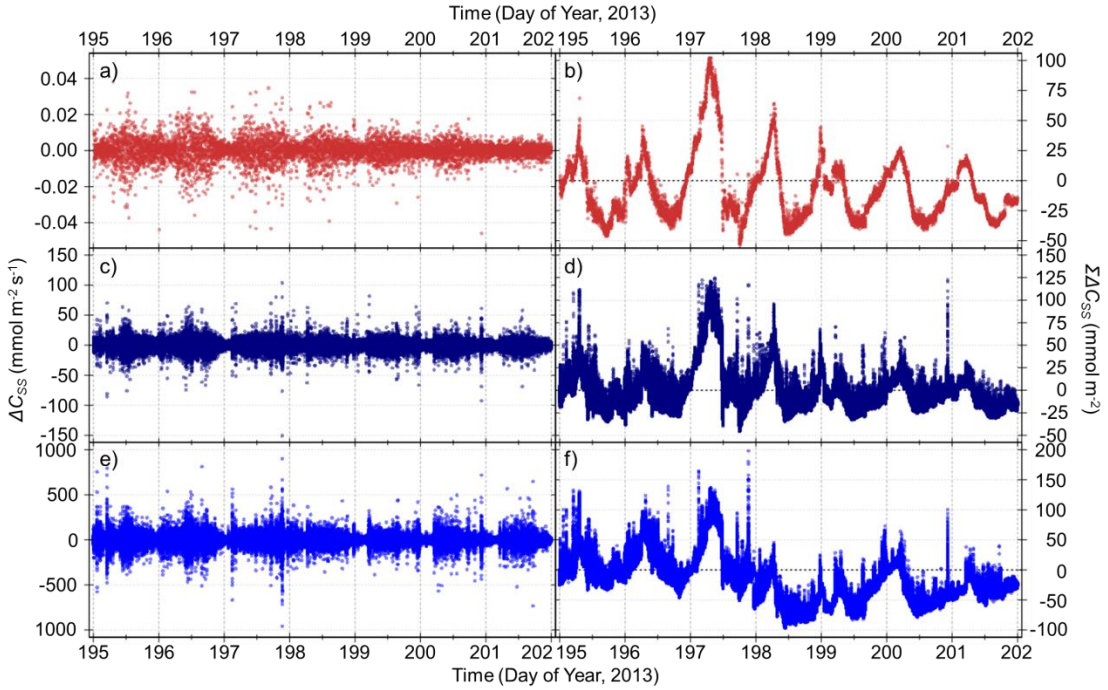

Figure 5.16: Time series plot of (a, c, e) ΔC_{SS} and (b, d, f) $\Sigma\Delta C_{SS}$ calculated from (a, b) 10 minute (LI840, height A, KSSW), (c, d) 2 Hz (LI840, height A, KSSW) and (e, f) 10 Hz (LI7500, height A, KSSW) data for days 2013/195-201. (a, c, e) have units mmol m^{-2} s^{-1}, (b, d, f) have units mmol m^{-2}. Note different scales for each plot.

5.3.2.2 Wavelet analysis

In this section, the measurement time resolution necessary to capture the majority of the CO_2 signal is assessed using the wavelet power spectrum. Wavelet power spectra may be calculated in an analogous way to Fourier power spectra, i.e., as the sum over all time points of the squared wavelet coefficients, normalised by the scale, the number of data points and the variance of the original times series (Torrence and Compo, 1998) (Section 3.2.3). Plotted over a measure of the frequency, they can give an indication of the energy present in processes occurring at each timescale.

Continuous, high frequency (10 Hz) $[CO_2]$ measurements were made by LI7500 at heights A and F (Figure 2.1d) from 2013/073 onwards. Days 2013/347 – 2013/365 were chosen for analysis as the campus was closed and rooftop emissions were likely to be minimal. Winter days were chosen despite the sensitivity of the open path sensor to inclement weather due to the greater probability of stable periods during which CO_2 storage is expected to be significant relative to the vertical flux.

Data were divided into 30 minute periods for wavelet analysis. Wavelet analysis has a number of advantages for atmospheric data relative to traditional Fourier analysis when constructing power spectra. Fourier analysis requires regular, complete data sets as any errors or missing values are delocalised throughout the entire spectrum (Farge, 1992). Fourier analysis also has difficulty resolving sudden transitions or aperiodic signals (Farge, 1992), both of which can occur frequently in an urban CO_2 storage time series due to the prevalence of intermittent, strong CO_2 sources. In contrast, wavelet analysis does not delocalise errors, can resolve sudden step changes or spikes (Salmond *et al.,* 2005), and was found to be considerably quicker to compute than the gap-tolerant (Press and Rybicki, 1988) Lomb-Scargle Periodogram. Wavelet coefficients were calculated as described in Section 3.2.3. Wavelet powers were calculated as the square of the absolute value of the wavelet coefficients, then summed over time and weighted by the original series variance and number of data points to give the global wavelet spectrum. Global wavelet spectra were binned by frequency, and by atmospheric stability for the half hourly period (z'/L, z_i = 46.4 m, KSSW).

The wavelet power spectra for both ΔC_{SP} and ΔC_{SS} were found to increase linearly with frequency on a log-log axis, with approximately a 1:1 relation between 0.005 and 0.1 Hz (200 to 10 s) and approximately 1:2 relation between 0.1 and 0.5 Hz (10 to 2 s) (Figure 5.17a,b). When normalised by the natural frequency the peak spectral energy was found to be between 0.001 and 0.004 Hz (1000 and 500 s or 8 to 16 minutes), although this range has higher frequency during neutral and stable conditions for ΔC_{SP} (Figure 5.17c, d). There was also a secondary peak at approximately 0.1 Hz or 10 s, above which spectral power declines with a slope of approximately −2/3 for all stability classes. It is therefore expected that measurements with a time resolution of better than 1 s should not produce significant improvement in measured CO_2 storage. This is tested in the following section.

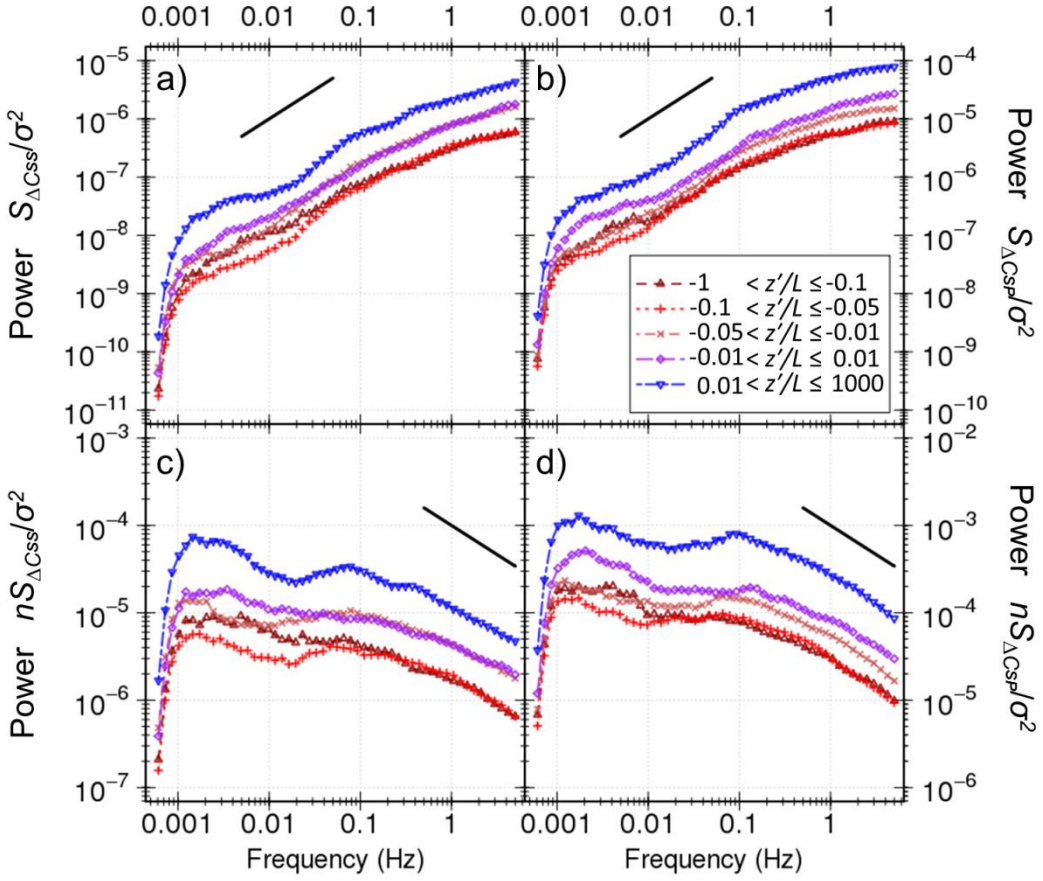

Figure 5.17: Global wavelet power spectra S normalised by the variance σ^2 versus frequency in Hz by stability class (key) for (a) CO_2 storage at a single location, ΔC_{SS}, (b) CO_2 storage from a profile, ΔC_{SP}; (c) and (d) as (a) and (b) but normalised by natural frequency (number of cycles n in 30 minutes). In each subfigure is given a solid black line indicating a power-law exponent: (a and b): 1.00, (c and d): -0.667. Note each y-axis has a different scale. The ΔC_{SS} calculated from 10 Hz LI7500 data at height A (Figure 2.1d), ΔC_{SP} from 10 Hz LI7500 data at heights A and F (Figure 2.1d), 2013/347 – 2013/365. Stability classes correspond to z′/L (effective height z' over the Obukhov length L) ranges as follows: extremely unstable: -1 < z′/L ≤ -0.1, unstable: -0.1 < z′/L ≤ -0.05, unstable/near neutral: -0.05 < z′/L ≤ -0.01, neutral: -0.01 < z′/L ≤ 0.01, stable: 0.01 < z′/L ≤ 1000.

5.3.2.3 Sensor response and sampling rate

Here the effect of altering the two main controls on the temporal resolution of measured *[CO_2]*: the sensor response time and the logging rate, is investigated. A correction factor for cases where the required time resolution could not be attained is proposed.

The basis of both analyses is data from two LI7500 installed at KSSW and KSNW during an intensive observation period between 2014/013 and 2014/043. During this time the sample rate was increased from 10 Hz to 20 Hz to ensure that the normal operating frequency (10 Hz) was resolvable. Different logging rates were simulated by sub-sampling this time series at intervals ranging from 10 Hz to ten minutes. To check that the response was not sensor specific, co-located continuous LI840 data (2 Hz) time series were also subsampled at intervals up to ten minutes. Both LI7500 and LI840 data sets were also used to investigate the effect of sensor response time. This was simulated by smoothing the concentration time series with a modified, single-sided cosine function.

Due to the volume of data it was too computationally expensive to plot the instantaneous values. Instantaneous ΔC_S values at each time resolution were therefore summed over 30 minute periods to give the total storage change within each period. The stability of each 30 minute period was calculated as the effective height (z') over the Obukhov length (L) (Section 2.2) from data measured at KSSW. There was some indication that CO_2 storage values were lowest across all time resolutions for neutral stability but this was not consistent across all time resolutions.

Slowing the sensor response time has the largest impact on calculated ΔC_S between 0.1 and 5 s (Figure 5.18a), corresponding to a resolvable frequency of 5 to 0.1 Hz (as the highest resolvable frequency is half the sample rate). This frequency range corresponds to the aforementioned portion of the natural frequency normalised wavelet power spectrum with a −2/3 power law relation to frequency. Improving the response time beyond 0.1 s does not seem to affect calculated ΔC_S, suggesting that 0.1 s is sufficient. Below 1 s there is little change with increasing smoothing length.

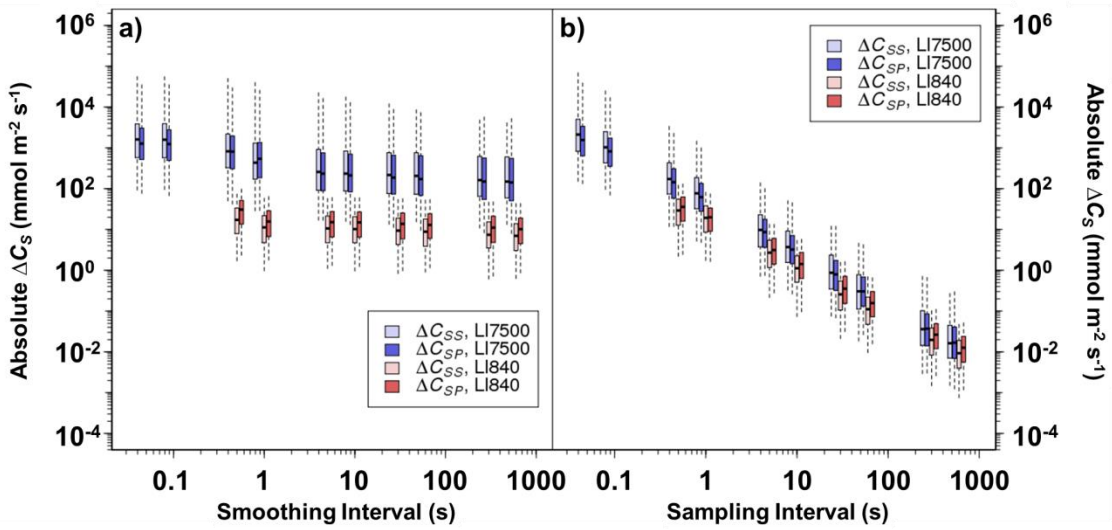

Figure 5.18: Absolute value or modulus of half hourly summed ΔC_S calculated with (a) smoothing and (b) subsampling of the CO_2 concentration ($[CO_2]$) 31 day (2014/013-2014/043) time series collected by LI7500 (20 Hz) and LI840 (2Hz) continuously at KSSW and KSNW (Heights A and F, Figure 2.1d). CO_2 storage at a single location (ΔC_{SS}) calculated from data collected from height A only, CO_2 storage from a profile (ΔC_{SP}) from both heights. Smoothing and subsampling ranges from none to 600 s. Horizontal bar: median; box: interquartile range; whiskers: 5th to 95th percentile.

In contrast, there is a linear decrease in median absolute half-hourly ΔCs with increasing sampling interval length, t_s, (Figure 5.18b) which can be written as:

$$\log_{10}\left(\overline{|\Delta C_S|}\right) = a \log_{10}(t_s) + b \tag{5.3}$$

where a and b are empirically derived constants equal to -1.24 and 1.69 for the LI7500 data, and -1.14 and 1.28 for the LI840 data respectively (all $R^2 > 0.99$). If a time series y_1 has been under-sampled at time interval t_{s1}, a time series y_2 with desired time interval t_{s2}, can be estimated from y_1 using:

$$y_2 = y_1 \frac{10^b t_{s2}^a}{10^b t_{s1}^a} \quad (5.4)$$

If the instrument is the same for both time resolutions, the factor of 10^b may be omitted as the instrument specific constant, *b*, will be the same in both the numerator and denominator of (5.4). However, if converting between instruments then the instrument specific constants for each series must be used. This correction is effective at reducing the under estimation of ΔC_S at a sampling interval of 10 minutes by five orders of magnitude (Figure 5.18b, Figure 5.19). Though simple to apply it is derived from statistical analysis of data only and does not reflect any physical process.

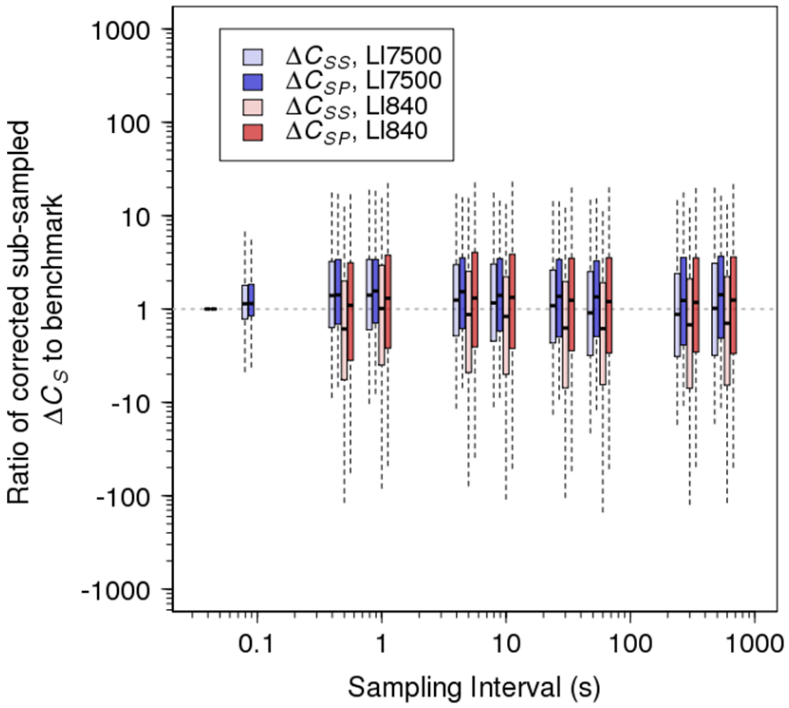

Figure 5.19: Ratio of sampling interval corrected (5.4) absolute 30 minute CO_2 storage values calculated from subsampled [CO_2] time series to CO_2 storage calculated from 20 Hz non-subsampled data, with subsampling time interval. Data were collected and processed as for Figure 5.18 . Bar: median; box: interquartile range; whiskers: 5th to 95th percentile.

5.3.2.4 Relation to the integral timescale of turbulence

Finnigan (2006) hypothesised that the ratio of measured storage to actual storage would depend upon the ratio of the averaging or sample time of the CO_2 profile or point measurements to the ITT. In other words, as the length of the ITT increases towards the length of the averaging interval the measured ΔC_S increases towards the calculated theoretical maximum. Whilst it is not possible to unequivocally calculate the 'true' value of the CO_2 stored within the canyon, if Finnigan is correct then the CO_2 storage should change predictably with the ratio of the time series sample rate to the ITT. In order to test this, it is first necessary to calculate the ITT. For measurements below 100 m, the timescales for vertical and horizontal wind speed fluctuations will differ (Kaimal *et al.,* 1976 via Hanna, 1981), hence in this thesis, the timescales for each wind component are evaluated separately.

The ITT may be calculated as the inverse of the peak natural frequency of the normalised energy spectrum (Hanna, 1981; Oikawa and Meng, 1995). The data were detrended using a fitted linear model, conditioned by applying a bell taper (Stull, 1988) and transferred to the frequency domain using a fast Fourier transform (negligible difference found between fast Fourier transform and discrete Fourier transform, latter calculated as Equation. 3 of Torrence and Compo, 1998). The sums of the squared real and imaginary components above the Nyquist frequency were added to those below (Stull, 1988) and the resultant energy spectrum normalised by the variance and natural frequency (Oikawa and Meng, 1995). Spectra for each stability class were collated and binned into 100 equally spaced non dimensional frequencies (the natural frequency normalised by mean wind speed and displacement height). The peak frequency was derived from the median spectra (Figure 5.20) and corroborated by visual inspection (Hanna, 1981).

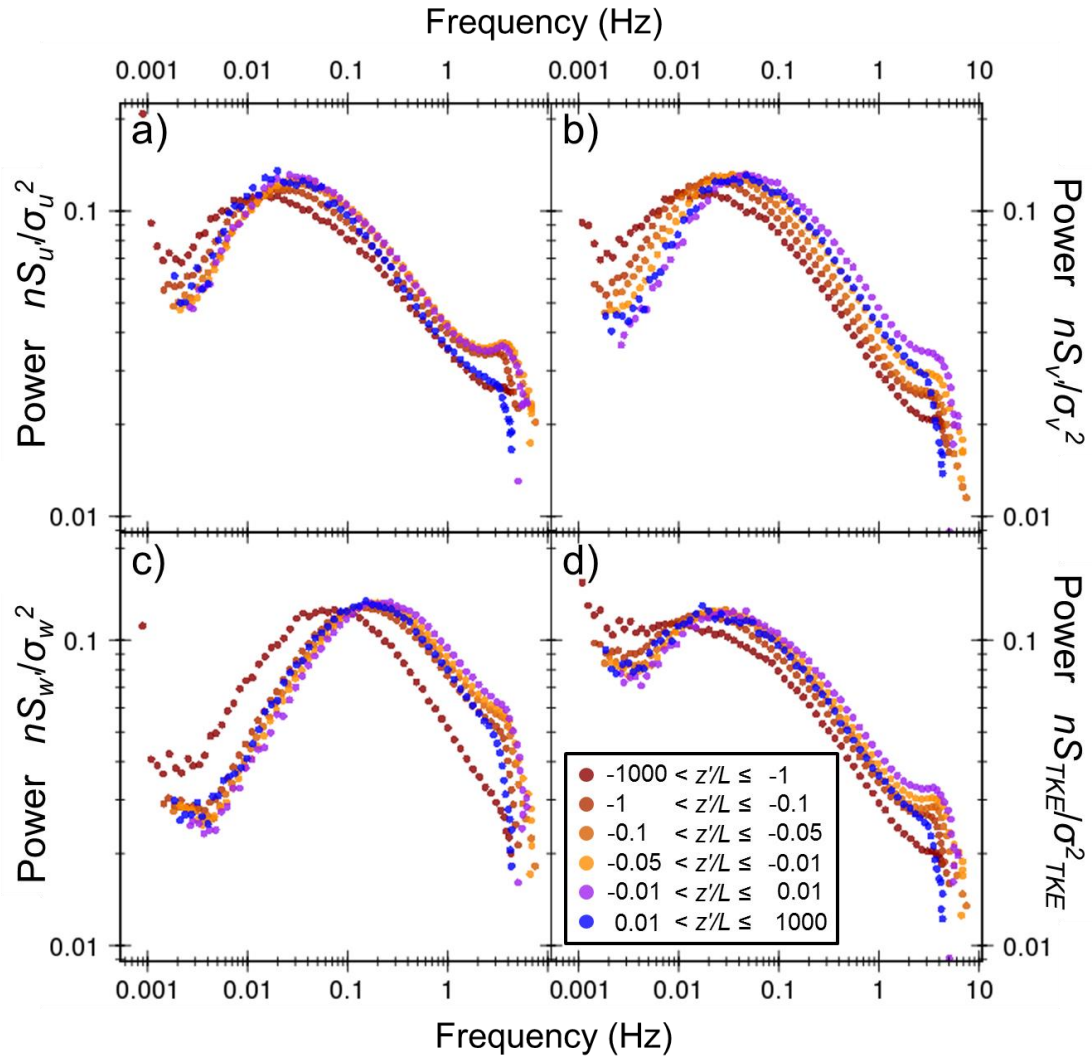

Figure 5.20: Power spectra for wind components (a) u, (b) v, (c) w, and (d) the turbulent kinetic energy divided into six stability classes (inset, d) with natural frequency. Data collected at 10 Hz and 20 Hz (EC5-EC8) at height A, KSSW between 2013/086 and 2014/365.

Data for this analysis were chosen such that each half hourly period had a data availability of at least 90%. This gave a total of 12851 out of 17520 hours between 2013/001and 2014/365 for analysis, which were further subdivided into six stability classes according to z'/L calculated at the top of KSSW tower (see inset, Figure 5.20d). Data availability was good, save for 6 months where the first few minutes of each hourly file were not transferred, leading to the first half of each hour being rejected by the 90% criterion (Figure 5.21).

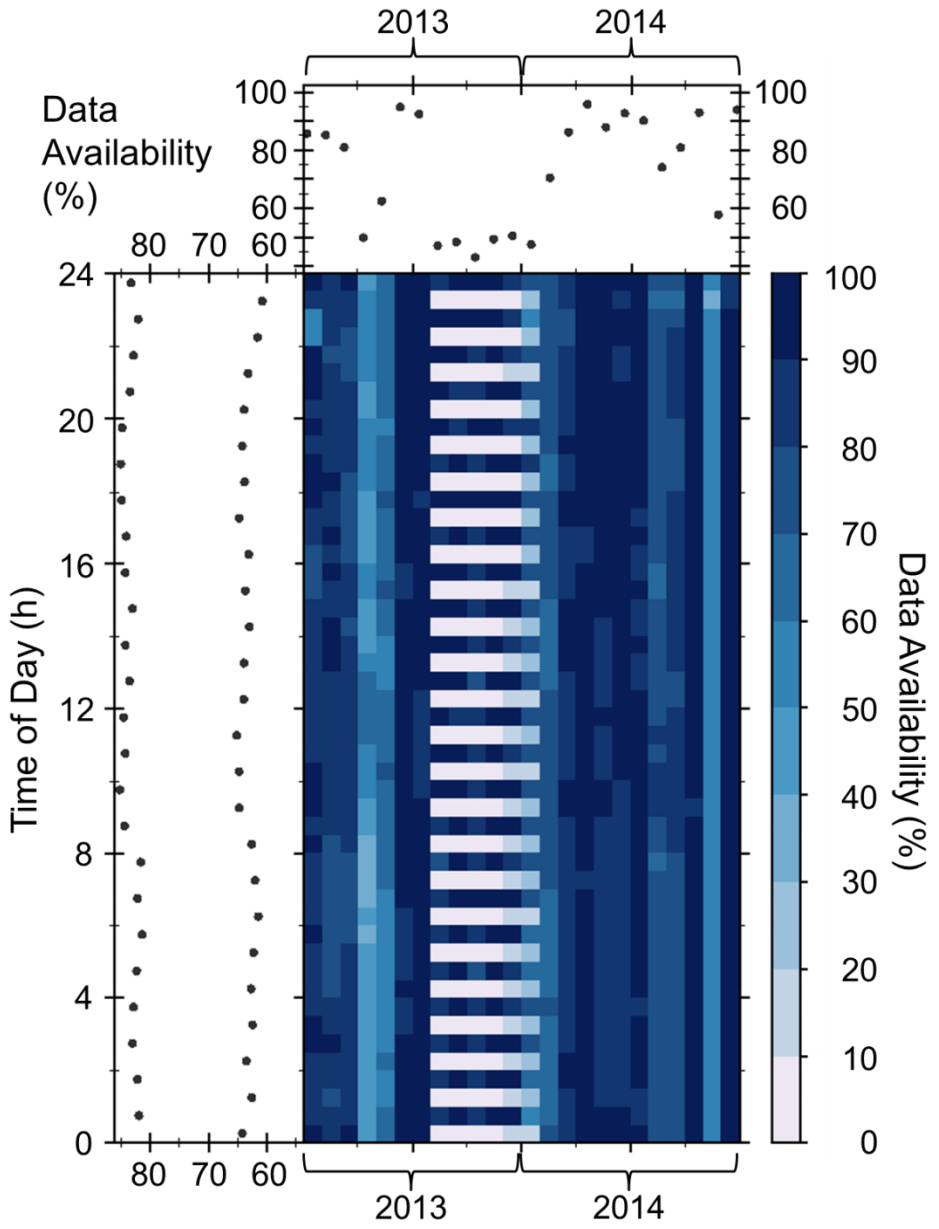

Figure 5.21: Percentage of half hourly periods which were present with sufficient data to be converted to half hourly energy spectra (CSAT3, height A, KSSW) for 2013 and 2014. Horizontal white bars are due to missing data (approximately 3 minutes of each hour were lost due to faulty data processing).

The spectra were normalised by the natural frequency and standard deviation of the quantity transformed (Figure 5.20). The energy spectra peak at slightly higher frequencies than those reported in previous studies (Roth and Oke, 1993, Oikawa and Meng, 1995, Appendix 5.H). The spectra approach the theoretical slope of (-2/3) (Appendix 5.H) when plotted over the non-

dimensional frequency and a slope of -4/9 when plotted over the natural frequency in Hz. The spectral peak shifts to lower frequencies/longer wavelengths with increasing distance from neutrality as expected and the agreement with the theoretical spectrum in the inertial subrange improves with greater instability.

Although the ranges of the estimated integral timescale of turbulence for each of the stability classes tend to overlap, there is a general trend of the timescale, λ, increasing as the atmosphere moves away from neutrality (Figure 5.20, Table 5.4). As mentioned previously, a similar pattern is observed in the variance of the $[CO_2]$ time series, a measure of the magnitude of the CO_2 storage. For a given averaging time of the $[CO_2]$ time series, the neutral stability class has the lowest ITT and the lowest $[CO_2]$ variance, supporting Finnigan's (2006) hypothesis.

Table 5.4: Frequency (f) and time scale (λ) of the peak spectral density for u', v', w' and the turbulent kinetic energy measured at height A by CSAT3, 2013/001-2014/365.

	u'		***v'***		***w'***		**TKE**	
***z'/L* (stability)**	*f* (Hz)	*λ* (s)	*f* (Hz)	*λ* (s)	*f* (Hz)	*λ* (s)	*f* (Hz)	*λ* (s)
-1000 < *z'/L* ≤ -1 (Very unstable)	0.015	66.9	0.010	103.2	0.074	13.6	0.008	119.0
-1 < *z'/L* ≤ -0.1 (Moderately unstable)	0.017	58.7	0.020	50.8	0.150	6.7	0.015	67.9
-0.1 < *z'/L* ≤ -0.05 (Unstable)	0.030	33.9	0.034	29.3	0.168	5.9	0.030	33.9
-0.05 < *z'/L* ≤ -0.01 (Near neutral)	0.026	38.5	0.046	21.6	0.198	5.1	0.026	38.5
-0.01 < *z'/L* ≤ 0.01 (Neutral)	0.026	38.1	0.047	21.3	0.268	3.7	0.047	21.3
0.01 < *z'/L* ≤ 1000 (Stable)	0.020	50.2	0.048	21.0	0.152	6.6	0.017	57.8

5.4 Gap filling

Data availability of CO_2 concentration measurements by the LI840 and the LI7500 for the period 2013 to 2014 were 82% and 71% respectively. Reasons for gaps included instrument failure, power cuts and rain. In order to assess the net ecosystem exchange at a 30 to 60 minute timescale, it is desirable to replace the missing data. In the section the relation of calculated CO_2 storage to various potential predictor variables, such as traffic volume and wind speed, is explored. The relations of such factors to calculated CO_2 storage are then used to model CO_2 concentration.

5.4.1 Relation of CO_2 storage to predictor variables

In this section the relations of calculated CO_2 storage to other measured variables are investigated.

5.4.1.1 Built form and wind direction

CO_2 storage depends not only on emissions but also on the efficacy of transport processes. In this section the effect of above-canyon wind speed and direction on within-canyon CO_2 storage and CO_2 transport is examined.

The asymmetric Strand canyon runs east-northeast to west-southwest (Figure 5.22a), bifurcated opposite the western half of the Strand building by a church (St Mary le Strand).

Airflow through the canyon within 20 m of the ground may, depending on the time of year, be deflected or attenuated by the trees lining the street and, depending on the time of day, be blocked or shifted by the large number of buses on the southern half of the roadway (i.e., the side of the measurements). Both sides of the street vary in height and the canyon is not of uniform width; due to the presence of the church and the curvature of the road it varies from about 15 to 45 m. Comparisons between wind direction and CO_2 storage in this section are therefore limited to this case study and are unlikely to be widely applicable.

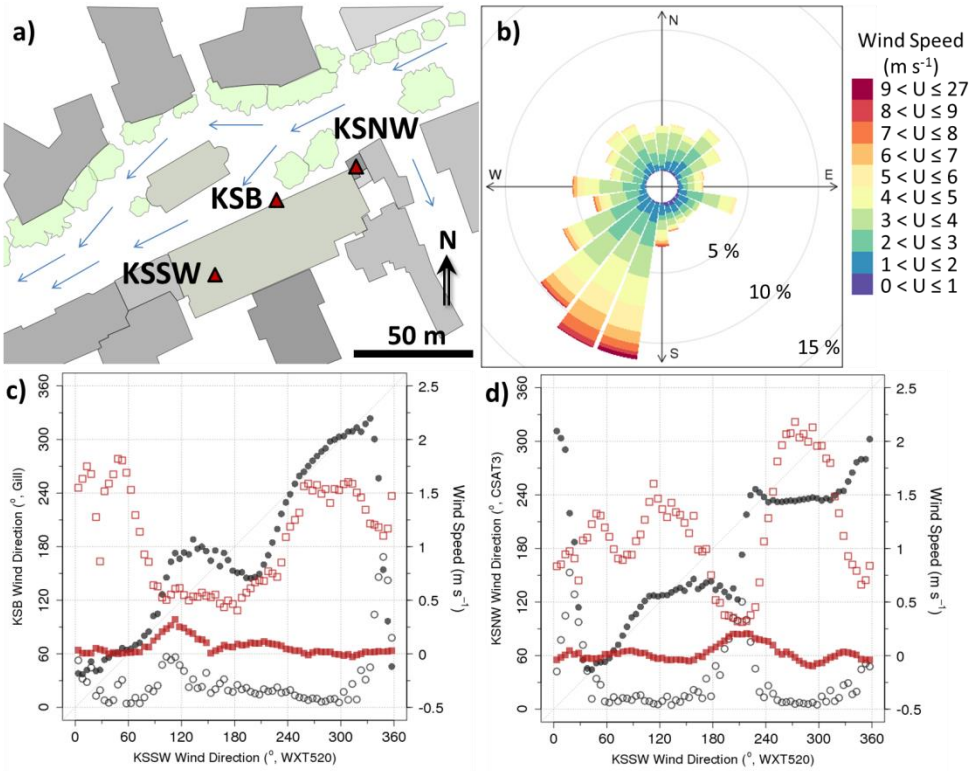

Figure 5.22: Wind speed and direction data relative to the built form of the Strand. (a) Plan view of the Strand canyon buildings (grey), trees (green) and traffic flow (blue arrows) with wind monitoring sites (red triangles); (b) Wind speed (m s^{-1}) and direction measured at KSSW (CSAT, 2013/100-2014/100); 30 minute wind direction (circles, mean: filled; standard deviation: open) and speed (squares, vertical: filled; horizontal: open) binned by wind direction (°, KSSW, WXT, 46.4 m) 2013/100-2014/100, for (c) KSB (Gill, 19.0 m) and (d) KSNW (CSAT, 20.5 m).

As wind speed and direction measurements at KSB (Figure 5.22a) were not available throughout 2012/150 – 2013/154 (the time period for which the CO_2 profile operated in 'switched' rather than 'continuous' mode) a comparison (2013/100 to 2014/100) of data collected by the WXT520s at KSSW and KSNW for both time periods was undertaken. This found that neither the overall wind direction distribution nor the within canyon response differ significantly from year to year.

Wind speed and direction measurements taken at KSSW and KSB are assumed to be representative of the local and canyon air flow respectively, whilst measurements at KSNW represent either the intersection to the east or the canyon to the west. The prevailing wind was from the south-southwest (210°), approximately 30° off parallel to the canyon (245°, Figure 5.22b). Although this direction had the highest mean above canyon wind speed, horizontal wind speeds measured at KSNW were at their lowest due to sheltering by the Strand building

(Figure 5.22d) and were scattered rather than channelled. Horizontal wind speed minima (KSB: 150°, KSNW: 240°) are measured at each site when in the lee of the Strand building and are associated with increasing $[CO_2]$ with time ($\Delta[CO_2]/\Delta t$) for heights G-J (Figure 5.23).

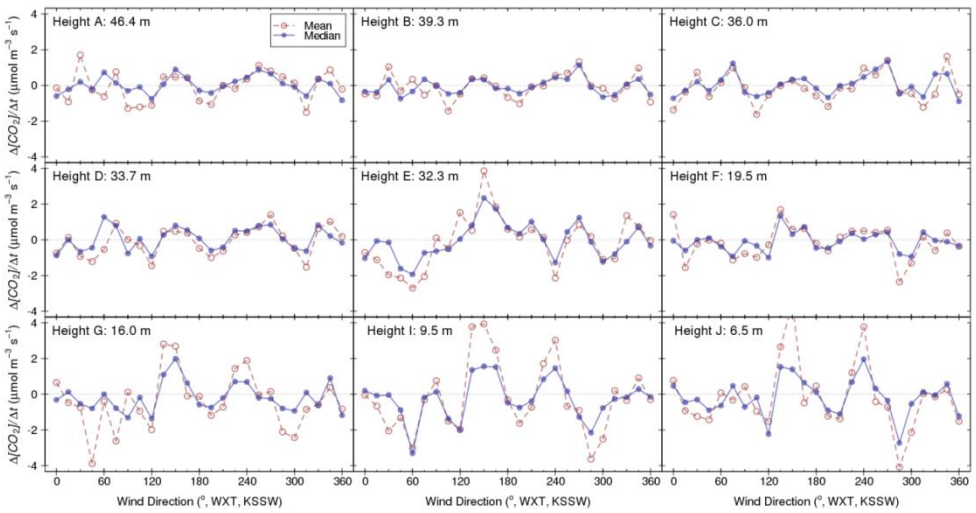

Figure 5.23: Change in $[CO_2]$ with time by above-canyon wind direction for nine different heights (see Figure 2.1d) within and above the Strand canyon (Figure 5.22a) calculated from 10 minute $[CO_2]$ collected 2012/159-2013/150.

Channelling of airflow does not occur for wind from the north east quadrant at either KSB or KSNW, potentially due to the more open canyon structure around the eastern intersection (Figure 5.22a). This sector is associated with a horizontal wind speed minimum and a peak in vertical wind speed. The most negative (downward) vertical wind speeds were measured when above canyon wind at 290° was channelled to 240° (Figure 5.22d), perhaps indicating the presence of a spiral vortex. Both the minimum (290°, KSNW) and the maxima (120°, KSB; 210°, KSNW) in vertical wind speed are associated with a reduction in $\Delta[CO_2]/\Delta t$ at all $z_i \leq 16$ m, suggesting that rather than just recirculating and trapping emissions, vortices act to reduce CO_2 with time at both windward and leeward walls.

5.4.1.2 Shear

Previous work (Lietzke and Vogt, 2013) indicates that even for street canyons with height:width ratios as low as 0.34-0.70, strong wind shear across the top a canyon can act as a 'lid', preventing turbulent mixing out of street level emissions. Intermittent thermally induced turbulent events break through this lid and vent warm, high CO_2 air from the canyon into the airspace above. Periods with high shear (and high friction velocity) might therefore be expected to show negatively skewed CO_2 storage within the canyon relative to periods with lower shear. In this section the lower measurement levels of the vertical $[CO_2]$ profile are shown to be effectively sheltered from shear-based turbulence, even at high above-canyon wind speeds

The friction velocity calculated from data measured at KSSW was used to classify the change in $[CO_2]$ with time at three locations within and above the Strand street canyon (Figure 5.24). The change in CO_2 concentration with time ($\Delta[CO_2]/\Delta t$) was chosen in preference to CO_2 storage as the absolute value of the latter depends upon the vertical separation of the measurement points. Data collected at point J (Figure 2.1d), the lowest measurement location,

showed the least change in either magnitude or variance of $\Delta[CO_2]/\Delta t$ with increasing friction velocity (Figure 5.24, Figure 5.25). $\Delta[CO_2]/\Delta t$ measured above the canyon and at canyon half-height (A and F respectively, Figure 2.1d) decreased from approximately 1.5 to 0 μmol m^{-3} s^{-1} with increased friction velocity (0.1 to 0.5 m s^{-1}); however, there was no consistent shift in skew or sign. Results indicate that increased friction velocity affects the mixing down to about half the canyon height whereas the lowest levels are effectively sheltered.

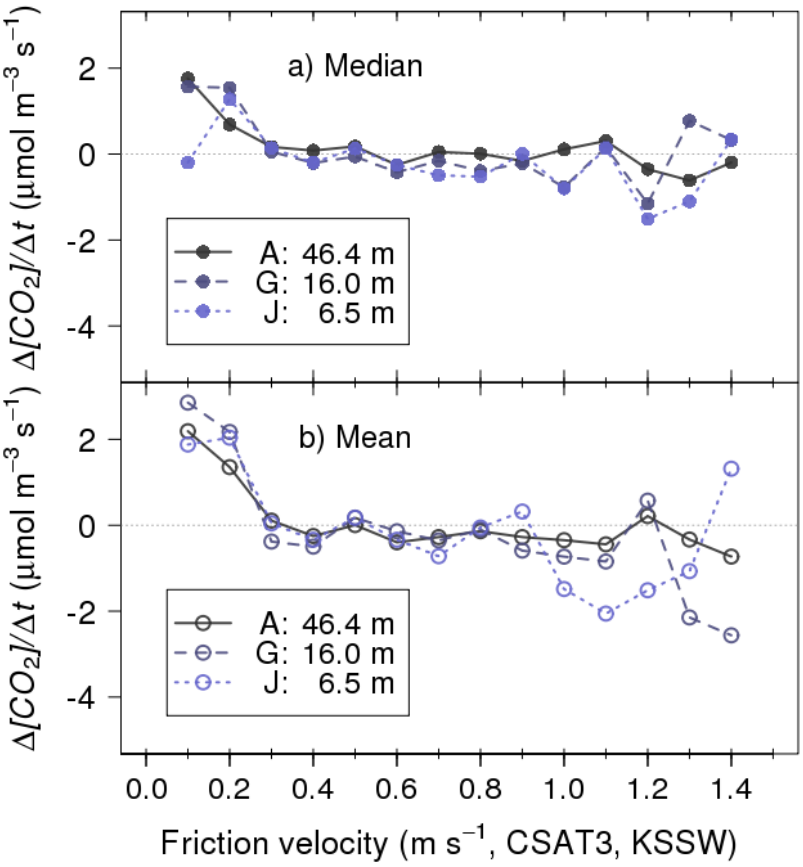

Figure 5.24: a) Median, b) mean change in CO_2 concentration with time ($\Delta[CO_2]/\Delta t$) by above-canyon friction velocity for three different heights (A, G and J, see Figure 2.1d) within the Strand canyon (mean building height within 500 m of KSSW: z_b = 21.7 m) calculated from 10 minute $[CO_2]$ profiles collected 2012/159-2013/154 for all times of day.

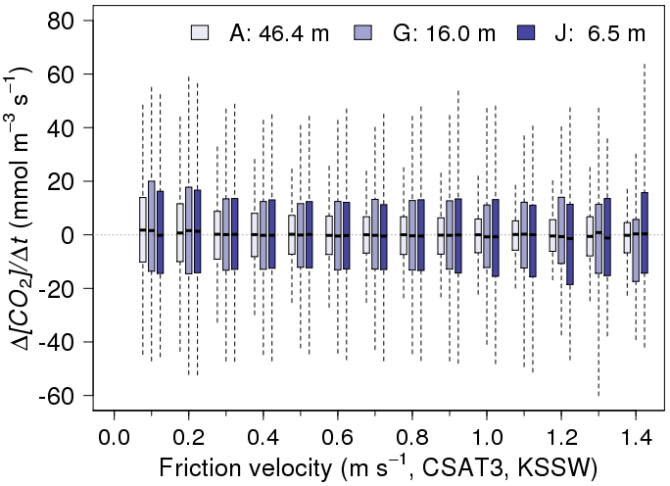

Figure 5.25: Change in $[CO_2]$ with time by above-canyon friction velocity for three different heights (A, G and J, see Figure 2.1d) within the Strand canyon (mean building height, z_b = 21 m) calculated

from 10 minute [CO_2] profiles collected 2012/159-2013/154. Bar: median; box: interquartile range; whiskers: 5th to 95th percentile.

5.4.1.3 Traffic, shortwave radiation and net heat flux

CO_2 storage is affected by both human and meteorological factors. This is illustrated in Figure 5.26 by comparing downward shortwave radiation, sensible heat and total traffic to CO_2 storage by time of day, day of week and season (summer vs. winter). CO_2 storage can be seen to be negative throughout the central portion of the day, with the onset and duration of negative values determined by the incident shortwave radiation (compare Figure 5.26a, e to b, f). Just prior to the central 'trough' in CO_2 storage values is a sharp peak (04:00 Figure 5.26e, 07:00 Figure 5.26f), the height of which varies with day of week (weekday vs. weekend). As meteorological factors tend not to have a hebdomadal cycle, this is likely to be due to anthropogenic factors – namely that traffic, and traffic related emissions, are higher on weekdays than weekends (Figure 5.26g, h). These higher emissions result in higher amounts of CO_2 stored within the canyon airspace as the boundary layer collapses after sunset.

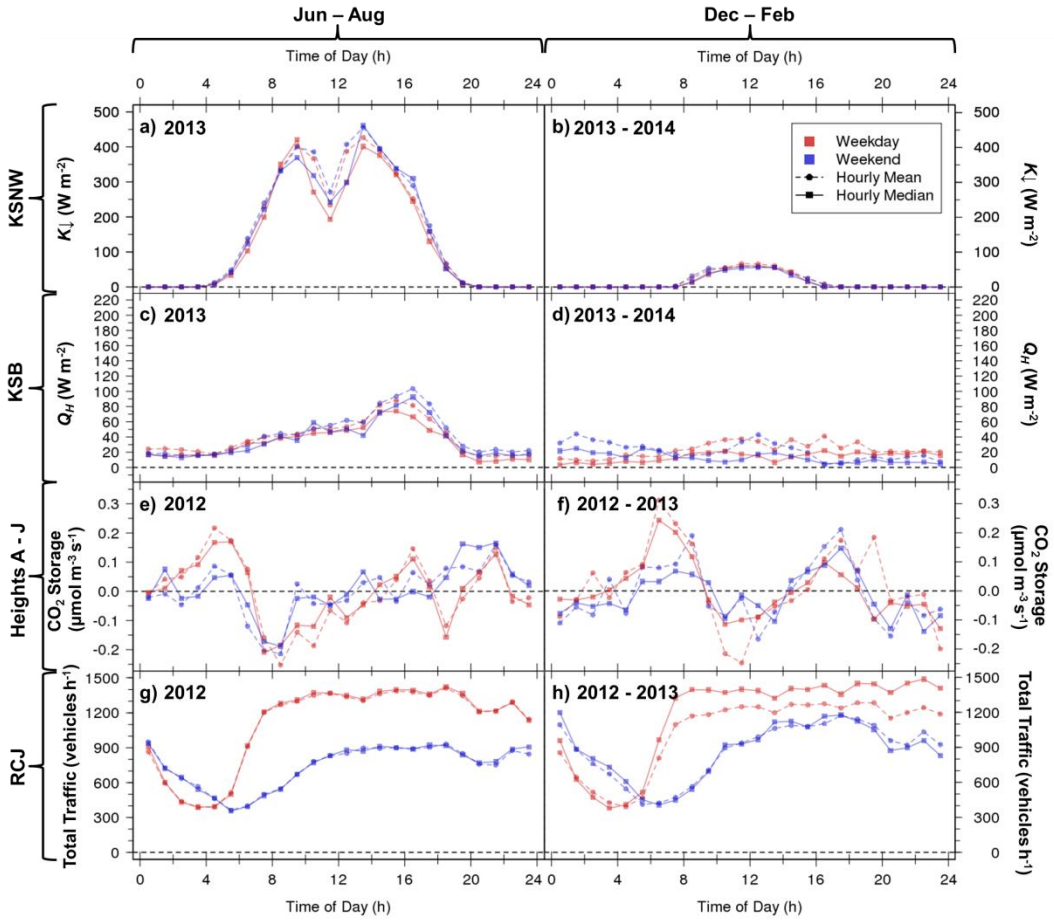

Figure 5.26: Comparison of (a, b) downward shortwave radiation; (c, d) sensible heat flux; (e, f) LI840 $\Delta C_{SP;}$ (g, h) Total traffic flow per hour at RCJ with time of day for summer (a, c, e, g) and winter (b, d, f, h), weekday (red), weekend (blue), mean (dashed line) and median (solid line).

Above the canyon, the sensible heat flux tends to have a symmetrical peak about noon (Appendix 2.B). Within canyon heat fluxes are provided for qualitative comparison (violation of the requirements discussed in section 3.1.2 preclude quantitative comparison). In summer these are highest at 16:00 GMT. In winter within-canyon Q_H are relatively low and constant

throughout the day (Figure 5.26d) compared to those above. This may in part explain the peak in CO_2 storage during the afternoon (17:00, Figure 5.26f). As the above-canyon environment cools, the within-canyon Q_H remains constant and the difference between the two is reduced, allowing thermally driven loss of CO_2 from the canyon (20:00-24:00, Figure 5.26f).

In summary, any statistical model of micro to local scale CO_2 concentrations in an urban environment cannot just consider values of a predictor variable at a point, but also needs to take the vertical change in the variable into consideration and potentially include a lagged response.

5.4.2 Development of a model

Power, sensor, logger, computer and net connection failures can all lead to a loss of data. It is desirable to be able to fill these gaps with a model based on commonly observed variables and to minimise the number required. Previous studies (Iwata *et al., 2*005) have used u^* and time elapsed since dawn to model the behaviour of ΔC_S throughout the day. Purely meteorological variables may be sufficient for an entirely natural ecosystem, however such a model is not suitable for the urban environment which may experience large day-to-day changes in human activity and hence emissions e.g., due to strikes or festivals. As noted earlier in the chapter, whilst the CO_2 storage signal tends to be relatively noisy, the cumulative sum of the CO_2 storage tends to be more predictable. As the cumulative sum of the CO_2 storage is equivalent to CO_2 concentration averaged over the vertical extent of the vertical profile with the mean removed, efforts were focussed on modelling the CO_2 concentration, from which the CO_2 storage term could be derived, rather than the CO_2 storage term itself.

This section discusses the construction and evaluation of CO_2 concentration models. Quantities modelled include the average CO_2 concentration across the vertical extent of the profile, and the CO_2 concentrations at each sample point (heights A – J). All models are empirically derived from observations at the Strand campus during 2012 and 2013 and require 4 to 13 input variables.

The initial sites and variables (except time of day) are presented in Table 5.5. Data were extracted from cleaned, but not gap-filled, annual files. 16 weeks were selected for model development, 4 each from July 2012, October 2012, January 2013 and April 2013; however, one in January had to be discarded due to poor $[CO_2]$ data quality. An estimated power transform to normality was calculated for each variable in each weekly data set (PowerTransform, Fox and Weisburg, 2011). As the transform required data that were strictly positive and performed better when the range was not significantly smaller than the median value, certain variables required the addition (or in the case of pressure, subtraction) of an 'offset' value. Transforms which were consistent (interquartile range of power transform values approximately equal to or less than 1) across all weeks were implemented and others discarded. Principal component analysis on the power transformed data was used to identify major sources of variance and remove duplicate factors. The proportion of the variance explained by each new principal component is presented in Figure 5.27, from which it can be

seen that the first component typically accounts for only a third of the total variance and that subsequent components are of a similar magnitude. The magnitude of the total variance explained by one component does not drop below 10% of that explained by the first component until the 21st principal component, and the total cumulative explained variance does not reach 90% of the total until the 11th principal component. This suggests that it is a very complex data set. A model will require a large number of, potentially interacting, explanatory factors.

Table 5.5: Table of data availability for base data set and weeks chosen to develop [CO_2] model. Weeks are given as year/day of year for the last day in the week. Green indicates data available, red indicates data not available. Grey indicates data from a measurement campaign not concurrent with any selected week, but taken to be representative for any week. Subscripts A-J for [CO_2] indicate [CO_2] time series measured at all heights between heights A and J, whilst subscript z indicates the height weighted average. Subscripts 'East' and 'West' for traffic volumes (V) indicate direction of traffic flow, whilst 'nearside' and 'offside' indicate position of the road lane relative to the kerb (see Figure 2.8).

Site	Instrument	Variables	2012/220	2012/227	2012/234	2012/241	2012/312	2012/319	2012/326	2012/333	2013/017	2013/024	2013/031	2013/097	2013/104	2013/111	2013/118
KSSW	CSAT3	u, v, w, U, wind direction, Q_H, u^*, z'/L															
KSNW	CSAT3	u, v, w, U, wind direction, Q_H, u^*, z'/L															
KSSW	WXT	Wind direction, U, T_A, RH, air pressure															
KSNW	WXT	Wind direction, U, T_A, RH, air pressure															
KSSW	CNR4	$K\downarrow$, $K\uparrow$, $L\downarrow$, $L\uparrow$, Q^*, albedo															
KSNW	CNR1	$K\downarrow$, $K\uparrow$, $L\downarrow$, $L\uparrow$, Q^*, albedo															
RCJ	ATC	$V_{East,\ nearside}$, $V_{East,\ offside}$, $V_{West,\ nearside}$, $V_{West,\ offside}$, V_{East}, V_{West}, V_{Total}															
KSNW	ATC	V_{Total}, V_{Cars}, V_{Buses}, Mean vehicle speed, Street canyon occupancy															
Profile	LI840	$[CO_2]_{A\text{-}J}$, $[CO_2]_z$															

The principal component analysis correctly identified duplicated data series, such as mean wind speed measured by CSAT3 and WXT. It also suggested correlation between sets of data such as shortwave downward radiation and total traffic, both of which tend to rise in the morning and decrease in the evening. This suggests the results from the PCA should be treated with caution as, for example, use of only $K\downarrow$ or total traffic could cause errors on cloudy days. Variables to incorporate into the linear model were chosen based on both the PCA results and the goal of minimising the number of instruments from which data would need to be drawn. This was done over several rounds of model training. In the first round (M_1) the CSAT3 and CNR1 data from KSNW were removed due to low availability and low information contribution given the measurements available at KSSW. This reduced the original set of 51 variables (M_0) to 37. This set was further reduced (M_2) to 32 with the removal of the KSSW WXT data, at which point PCA was re-done. Ten principal components for M_2 were required to cumulatively account for 90% of the total variance, an improvement of one compared to those calculated for M_0; however, at 45% the first principal component accounted for a greater proportion of the overall variance and the magnitude of the total variance explained by one component relative to the first one dropped below 10% after 8 components – a decrease of 13

relative to M_0. This suggests that a considerable degree of redundancy in the dataset has been reduced by the removal of the CSAT and CNR1 data from KSNW, and the WXT data from KSSW.

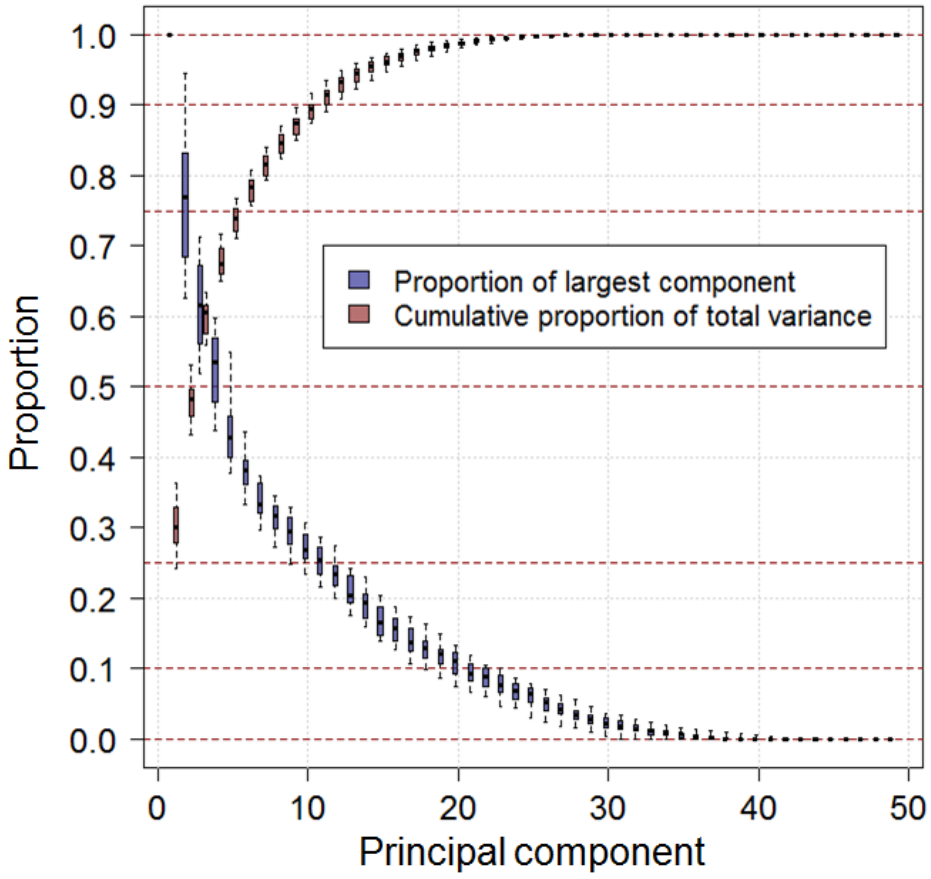

Figure 5.27: Proportion of the total variance explained by each principal component (key: inset) with principal component number for 15 weeks of data (Table 5.5), M_0 (Table 5.6).

Examination of the PCA coefficients found similar structures for each week, for example, moderate coefficients of the same sign for all traffic data from RCJ in the first component, and a very large coefficient for *u* in the last component with the same sign as the traffic data. As the absolute signs of coefficients in PCA are arbitrary (the relation of the sign of one coefficient to another is not), components were multiplied by -1 where necessary to ensure that structures identified as being similar in each week were of the same sign. Coefficients were summed over components for each variable for each week. Median summed coefficients for each variable were compared. Low absolute or relative differences between variable coefficients were interpreted as high similarity between the variables. Likewise, variables with consistently different median coefficients to other variables were considered to contribute unique information to the dataset. Following this analysis $V_{East,\ nearside}$, $V_{East,\ offside}$, $V_{West,\ nearside}$, $V_{West,\ offside}$, V_{Cars} and V_{Buses} (Table 5.5) were removed from the training data set leaving a total of 26 factors (including time of day). Examination of the correlation matrices (*cor,* R Development Core Team, 2013) showed high correlations between $K\downarrow$ and $K\uparrow$, $L\uparrow$, and between V_{Total} (RCJ) and V_{East}, V_{West}. As high correlations were also observed between *u* and *U*, and the factor *v* was not simple to transform for model input, in the next iteration of the model (M_3), $K\uparrow$, $L\uparrow$, $V_{East,}$ V_{West}, *u* and *v* were also removed from the dataset.

Table 5.6: Summary of variables included in each iteration of the model. For list of 'All' variables for each instrument and site, see Table 5.5. All models also included time of day except M_{short}.

Model Iteration	KSSW CSAT3	KSNW CSAT3	KSSW WXT	KSNW WXT	KSSW CNR4	KSNW CNR1	RCJ ATC	KSNW ATC	Total Variables
M_0	All	All	All	All	All	All	All	All	51
M_1	All	None	All	All	All	None	All	All	37
M_2	All	None	None	All	All	None	All	All	32
M_3	w, U, wind direction, Q_H, u^*, z'/L	None	None	All	$K\downarrow$, $L\downarrow$, Q*, albedo	None	V_{Total}	V_{Total}, Mean vehicle speed, Street canyon occupancy	20
M_{short}	U	None	None	T_A, RH	None	None	V_{Total}	None	4
Ml_{ong}	U, wind direction, u^*	None	None	U, T_A, RH, air pressure	$K\downarrow$, $L\downarrow$, Q*	None	V_{Total}	Street canyon occupancy	13

The output of the model included the following for each variable: a coefficient, t statistic (coefficient divided by the standard error of the coefficient) and estimate of the probability that the coefficients could have occurred by random chance (p-value), i.e., if the null hypothesis, that all coefficients are equal to 0, is true. Good agreement was found between the modelled (M_3) and measured $[CO_2]$ for the training weeks (average adjusted R^2 of 0.76); however, the ratios of the standard deviation to the average of the coefficients of the variables for each week of training data ranged from 0.8 (U) to 246.7 (w), with a median ratio of 3.9. This suggests that the values of the model coefficients are highly variable. No seasonality in coefficients was observed for any variable, except Q_H, for which coefficients tended to be negative in summer and positive in winter. The variables were ranked by p-value using a 'score'. Estimates with $0<p<0.001$, $0.001<p<0.01$, $0.01<p<0.05$ and $0.05<p$ were given a score of 3, 2, 1 and 0 respectively. These scores were summed for each variable and divided by the total potential score (the number of training weeks for which data was available multiplied by 3). There was a slight positive (spearman's rank coefficient = 0.22) correlation between the p-value scores and the ratios of the standard deviation of the coefficients to the average. The four variables with the best scores in both categories (both ranks less than or equal to 10) were included as a 'short' model. Nine additional variables (one rank less than or equal to 10) were included in a 'long' model (albedo was not included due to low data availability relative to other variables). The remaining 6 variables (w, Q_H, z'/L, wind direction (KSNW, WXT), V_{Total} (KSNW, ATC) and mean traffic speed) were discarded.

Median R^2 for M_{short} and M_{long} for the training weeks were 0.54 and 0.76 respectively. Results from the test week, 2012/191-197 were less positive. Both models tended to over-estimate the CO_2 concentration and under-respond to diurnal variation (Figure 5.28a). Linear regression of the modelled on the measured vertically averaged CO_2 gave R^2 values of 0.24 and 0.21 for the short and long models respectively. Gap-filling input data did not improve the modelled concentrations.

It was thought that the low agreement could be due to processes at different heights responding to forcings in very different ways. Three new models were therefore constructed to calculate the CO_2 concentration at each height in the vertical profile using the same procedure

as described for M_{Short} and M_{Long}. Agreement between measured and modelled concentrations ranged from R^2 values of 0.02 to 0.42. Linear regression of height averaged CO_2 concentrations calculated from the individually modelled time series at each height in the profile on the measured CO_2 concentrations varied from 0.03 to 0.41. The model with the best fit, M_{Redone}, required only 8 input variables (time since dawn, air temperature difference between KSSW and KSNW, U, T_A, RH, air pressure, $L\uparrow$ and V_{Total}) one of which could be calculated rather than measured. This was clearly an improvement over previous iterations, however comparison of the height averaged $[CO_2]$ (Figure 5.28b) shows that it is still insufficient for gap-filling purposes. It is therefore recommended that data gaps are not filled with the output from a statistical model, but from average values which have been appropriately stratified by e.g., time of day, day of week (Section 3.2.1) as these method does not depend on any variables other than the $[CO_2]$ time series itself.

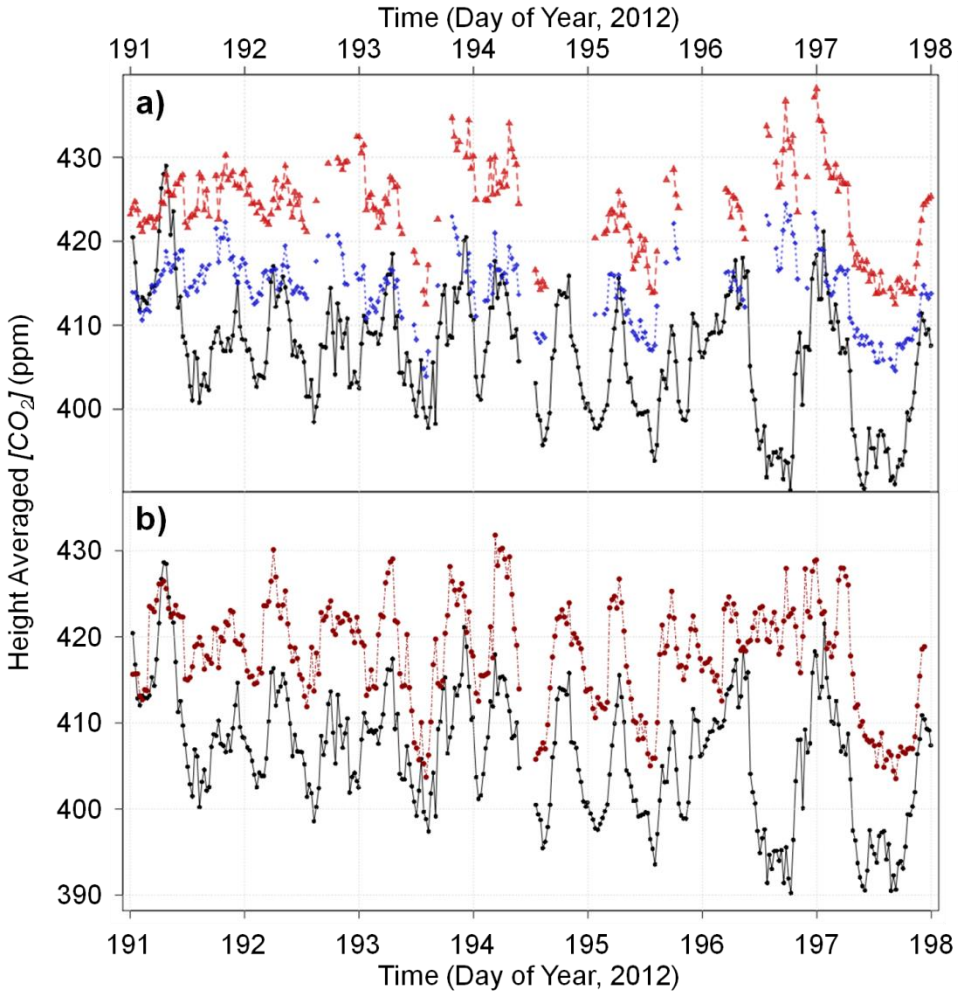

Figure 5.28: Measured (black, solid line) and modelled (a) short model: red, dashed line; long model: blue, dotted line), (b) M_{Redone} CO_2 concentration averaged over the vertical extent (heights A – J) of the CO_2 profile for 2012/191-198 at 30 minute resolution. Missing input data was not gap filled.

5.5 Conclusions

The aim of this chapter was to describe the variation of CO_2 storage in central London at timescales ranging from the sub-hourly to seasonal. Ancillary objectives included identification of venting events, best 'best practice' methods of measurement, and the potential for gap-filling of CO_2 storage time series.

The characteristics of CO_2 storage at all timescales were found to vary with instrument and measurement interval. Values calculated from a switched profile were smaller, and more diurnally and seasonally variant than those calculated from $[CO_2]$ measured by a fast-response open path gas analyser. No seasonal cycle was observed for the latter, but sudden excursions in the time series suggested the possibility of venting of CO_2 from the street canyon.

Regular venting 'events' were observed and a method was developed which could successfully detect these events automatically, greatly increasing the volume of data which could be processed compared to previous manual methods. CO_2 and H_2O venting events were found to co-occur with far greater incidence than would be expected by random chance; however, quadrant analysis did not suggest that this was due to coherent structures.

Two measurement locations were found to be sufficient to characterise CO_2 storage, provided the sampling points were placed appropriately. If possible, sensors should have a response time shorter than 0.1 s. Calculated CO_2 storage has power law relation to sampling frequency and under sampling can be corrected, to an extent.

Comparison of the variation in the $[CO_2]$ time series (a measure of the magnitude of the CO_2 storage) and the integral time scale of turbulence showed both tend to decrease as the atmosphere moves towards neutrality. This supports Finnigan's (2006) hypothesis that the under-estimation of CO_2 storage depends on the ratio of the integral timescale of turbulence to the period over which $[CO_2]$ is averaged in the calculation of CO_2 storage.

Both $[CO_2]$ and CO_2 storage respond to a large number of interacting factors. This complicates prediction as the subsequent uncertainty in the modelled $[CO_2]$ time series is likely to be much greater than the calculated CO_2 storage values.

Appendix 5.A Extended Characteristics of the aggregated ΔC_S time series

When attempting to describe the characteristics of CO_2 storage on a timescale greater than a day, it is necessary to aggregate (e.g., mean, median) individual values due to the large number of data points. This can be achieved by binning the data by e.g., month and/or hour of day and averaging over each bin. The results obtained are very different for the median and the mean of each bin (Figure 5.A.1).

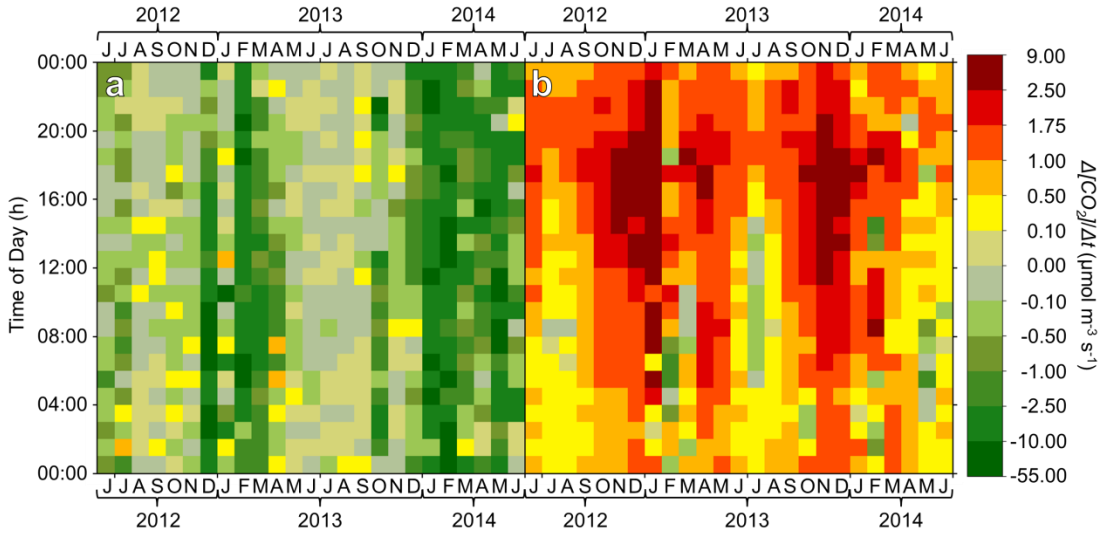

Figure 5.A.1: (a) Mean and (b) median change in CO_2 concentration with time binned by month (x-axis) and hour of day (y-axis) in µmol m^{-3} s^{-1} calculated from 10Hz CO_2 concentration data recorded at a single height (KSSW, LI7500, 2012/160 – 2014/160). Data for January 2013, September 2013 and June 2014 should be treated with caution due to low data availability (<10 h per bin)

The median values (Figure 5.A.1b) show seasonal and diurnal variation, with more positive values peaking between noon and 8 pm between October and January i.e., there is daytime accumulation of CO_2 during the colder months, with lower values occurring at other times. Negative median values are rare. The binned hourly mean values have a much broader range (-51.2 to 0.7 mmol m^{-3} s^{-1}) than the binned hourly medians (-2.3 to 3.7 µmol m^{-3} s^{-1}) for all bins with > 10 h of data, and a more negative skew (-4.70 vs.0.25 for the mean and median values respectively). The mean of the binned $\Delta([CO_2])/\Delta t$ shows less consistent variation than the median with time of day; it is negative for December to March and approximately zero for the rest of the year (Figure 5.A.1). This is the opposite pattern to that observed in the median values plot.

From the hourly mean and median change in $[CO_2]$ with time, it would be expected that the distribution was very asymmetrical about 0. Comparison of the 0.1%, 1%, 10%, 25%, 75%, 90%, 99% and 99.9% quantiles (Figure 5.A.2) shows the hourly/monthly distributions to be almost identical in magnitude, though opposite in sign.

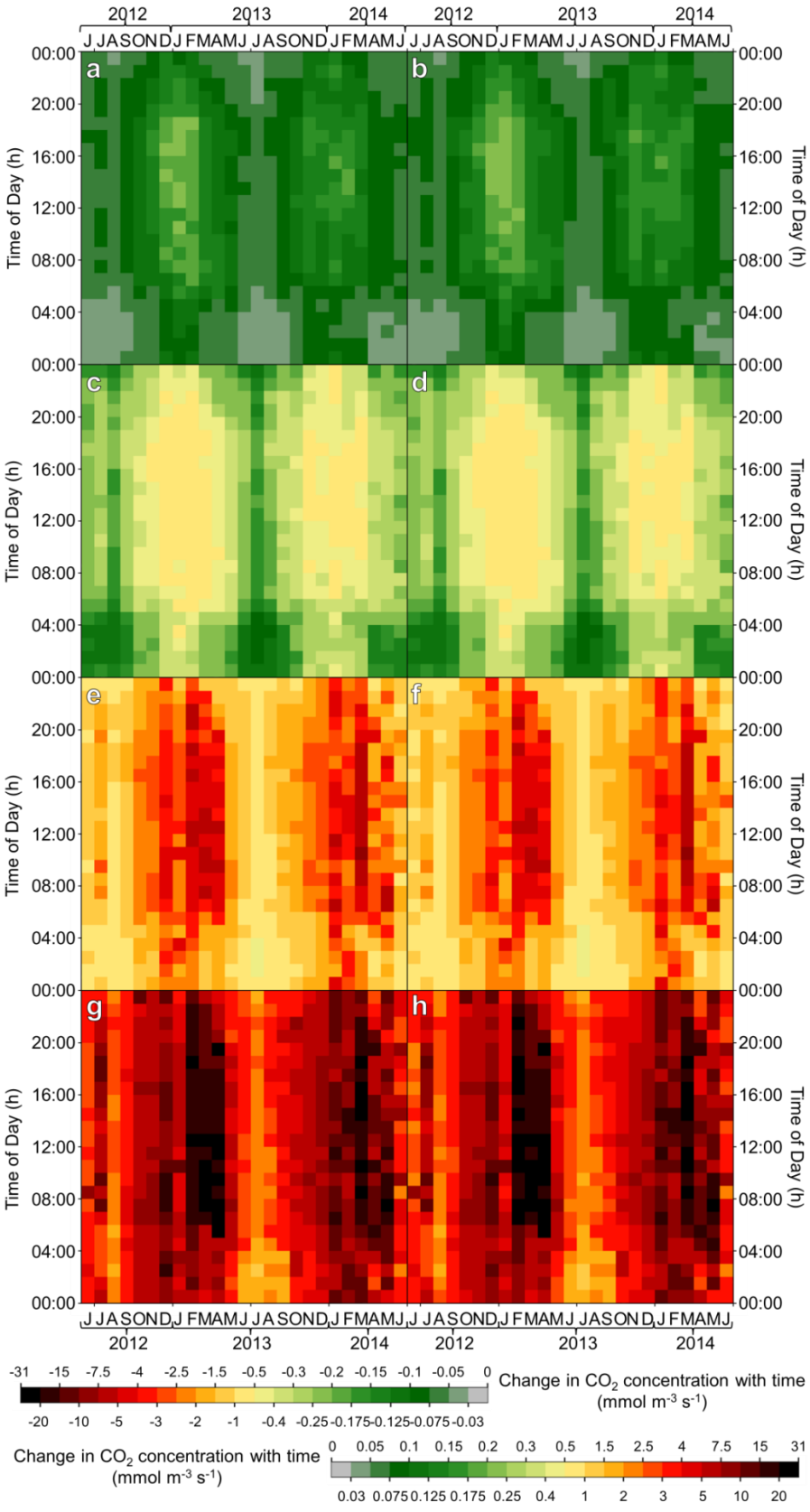

Figure 5.A.2: (a) 25%; (b) 75%; (c) 10%; (d) 90%; (e) 1%; (f) 99%; (g) 0.1%; (h) 99.9% quantiles for the change in CO_2 concentration with time binned by month (x axis) and hour of day (y-axis) in µmol m^{-3} s^{-1} calculated from CO_2 concentration data recorded at a single height: KSSW, LI7500, 2012/160 – 2014/160. Bottom left: scale for a, c, e and g. Bottom right: scale for b, d, f and h. Note change in sign.

Values in Figure 5.A.2 a, c, e and g tend to be slightly more negative than their counterpart is positive, however there is very little difference. The difference between the mean and the median values cannot be accounted for by a comparison of the minimum and maximum values for each bin (Figure 5.A.3) as the absolute magnitude of the maximum values tends to be greater than the absolute magnitude of the minimum values (Table 5.A.1).

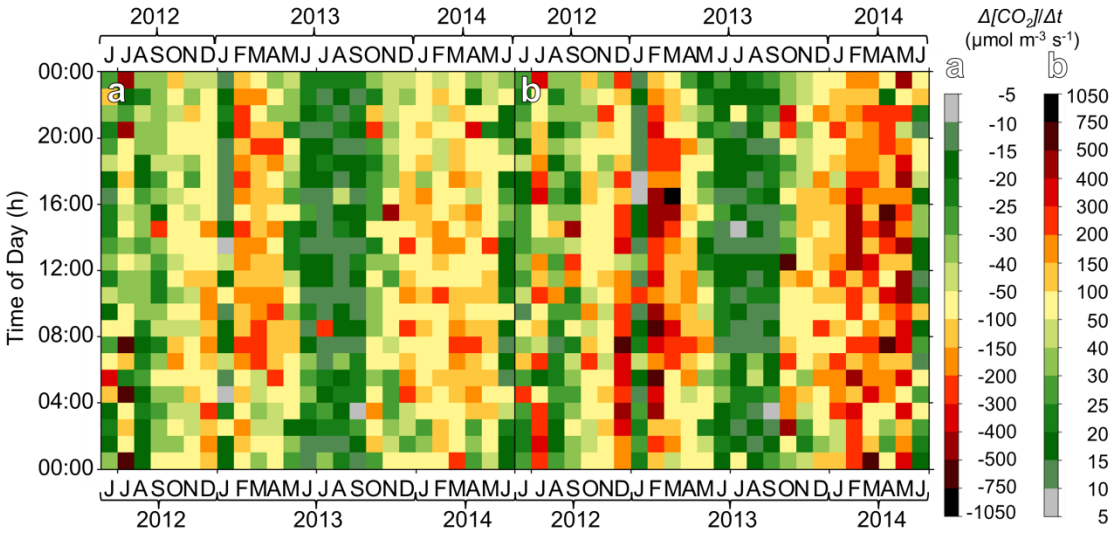

Figure 5.A.3: (a) Minimum; (b) Maximum change in [CO_2] with time binned by month (x axis) and hour of day (y-axis) in μmol m^{-3} s^{-1} calculated from CO_2 concentration data recorded at a single height: KSSW, LI7500, 2012/160 – 2014/160. Left inset: scale for (a); right inset: scale for (b). Note change in sign.

Figure 5.A.1-3 are summarised in Table 5.A.1. The absolute magnitude of the median and the mean of the hourly/monthly 25% (Figure 5.A.2a) values is less than the absolute magnitude of the median and mean of the hourly/monthly 75% (Figure 5.A.2a) values, suggesting that the medial 50% of the data is skewed towards positive $\Delta([CO_2])/\Delta t$. The absolute values of the hourly/monthly 0.1%, 1% and 10% (Figure 5.A.2c, e and g, respectively) are all greater than the absolute values of the hourly/monthly 99.9%, 99% and 90% (Figure 5.A.2h, f and d, respectively), indicating that the majority of the first quartile is more distant from zero than the majority of the fourth quartile, with the difference in absolute values as a percentage of the quantiles being greatest at 10/90%. Overall, the $\Delta([CO_2])/\Delta t$, and by extension, the ΔC_S data has a complex, non-Gaussian distribution. Although half the values lie within a relatively small, positively skewed range (± 100 μmol m^{-3} s^{-1}), a significant portion of the signal is composed of very large excursions from zero with negative excursions tending to be greater in magnitude than positive excursions. For the CO_2 concentration time series, it is expected that this will appear as an asymmetric peak, with concentrations after the event lower than they were prior to the peak, that is, CO_2 will have been 'vented'.

Table 5.A.1: Mean, median, skew and standard deviation of the characteristics of $\Delta([CO_2])/\Delta t$ binned by hour and month plotted in Figure 5.A.1 to Figure 5.A.3. Means, Medians and Standard deviations given in µmol m^{-3} s^{-1}, 3 s.f. Skew to 2 d.p.

Figure	Hourly/Monthly	Mean	Median	Standard Deviation	Skew
Figure 5.A.1	Mean	-2.06	-0.23	4.65	-4.79
	Median	1.20	1.01	1.12	2.23
Figure 5.A.3	Minimum	-72400.00	-49700.00	72200.00	-2.84
Figure 5.A.2	0.1%	-7480.00	-5720.00	5350.00	-1.32
	1%	-2190.00	-1850.00	1310.00	-1.32
	10%	-338.00	-302.00	157.00	-0.67
	25%	-96.2.00	-85.60	40.00	-0.84
	75%	100.00	88.80	42.30	0.84
	90%	337.00	302.00	152.00	0.58
	99%	2060.00	1740.00	1250.00	1.50
	99.9%	7380.00	5520.00	5470.00	1.38
Figure 5.A.3	Maximum	113000.00	60900.00	123000.00	2.02

Appendix 5.B Quadrant plots of day 354, binned by CO_2 storage

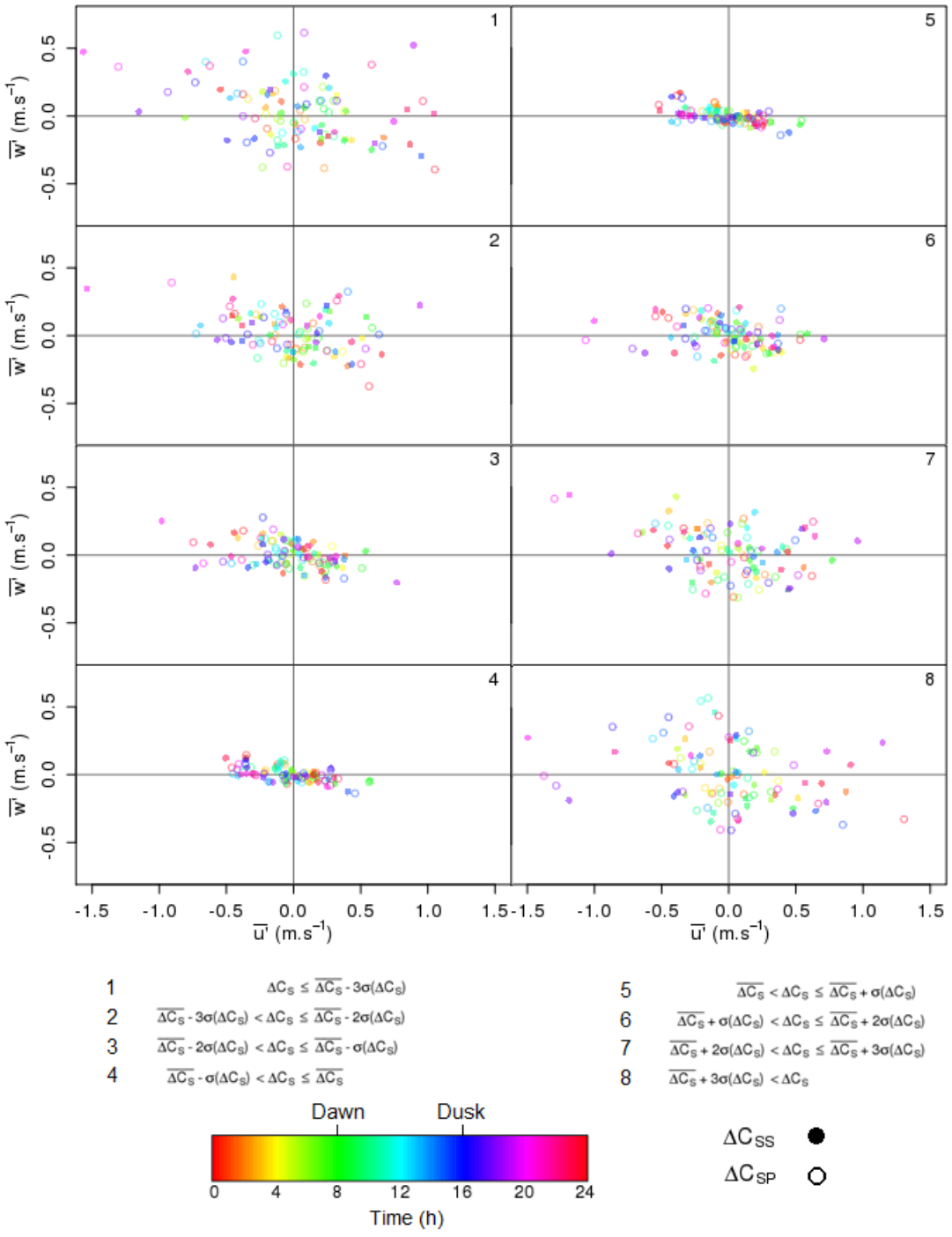

Figure 5.B.1: Mean (30 minute) vertical (w') and horizontal (u') wind characteristics for various classes of ΔC_S for one day (2013/354). Overbar denotes mean and 'σ' standard deviation. 2013/354 coloured according to time of day. Filled circle: ΔC_{SS}, hollow circle ΔC_{SP}. Horizontal and vertical scales are 1:1.

Appendix 5.C Comparison of ΔC_{SS} and ΔC_{SP}

Direct comparison of CO_2 storage calculated from single vs.multiple height data (Figure 5.C.1) indicates that the difference in variance observed between the 10 minute and 10 Hz data in Section 5.3 is not solely an artefact of different time resolutions. The single height method gives greater scatter regardless of base resolution of measurements, albeit to a much lesser extent than decreasing the sampling interval.

All data sets plotted are centred on 0 and appear symmetrical. A diurnal cycle is apparent for all datasets except 10 minute ΔC_{SS} (Figure 5.C.1). Unlike ΔC_{SS} data, the 10 Hz ΔC_{SP} indicates similar variance during the weekend (2013/152-153) as on working days, albeit shifted to later in the day. This supports the importance of measuring within the canyon- it is not sufficient to assume measurements made within the inertial sublayer will accurately reflect conditions within the roughness sublayer at the timescales for which CO_2 storage is relevant.

When ΔC_{SP} is plotted against ΔC_{SS}, conditions with high ΔC_{SP} and low ΔC_{SS} appear as a vertical line centred on the origin (Figure 5.C.2, highlighted). Whilst visually striking, only 1.7% of the 10 Hz 2013/147-153 data is greater than 3 standard deviations (49.7 mmol m^{-2} s^{-1}) away from line of best fit (standard deviation of 18.17 and 16.57 mmol m^{-2} s^{-1} for ΔC_{SS} and ΔC_{SP} respectively). This increases to 1.8% of the data points for 10 Hz 2013/161-267. Removal of this data improves the fit for both weeks (R^2 increases from 0.09 to 0.21 and from 0.04 to 0.09 respectively); however, the gradient is unaffected. Similarly, only 1.1% of the 2 Hz data is outside 3 standard deviations from the line of best fit. Removing this data improves the fit from 0.05 to 0.09 with little alteration to the gradient.

The converse: conditions of very high ΔC_{SS} and low ΔC_{SP}, which would appear as a horizontal line centred on the origin, are not observed. As the excursions only appear in the profile data set, it is possibly a within canyon process missed by the local scale measurement. If so, it is one which occurs throughout the week and at all times of day.

In general, ΔC_{SP} tends to be lower than ΔC_{SS} by a factor of 5 to 10 (Figure 5.C.2, gradient). The strength of the relation between ΔC_{SS} and ΔC_{SP} varies week to week (compare the two 10 Hz plots in Figure 5.C.2), whilst the nature of the relation varies with sampling frequency: the two data sets from week 2013/195-201 (10 Hz and 2 Hz) are much more similar to each other in gradient and coefficient of determination than those from week 2013/149-155 (10 Hz and 10 minutes). The effect of time resolution on calculated ΔC_{SS} and ΔC_{SP} is explored in greater depth in Section 5.3.2.

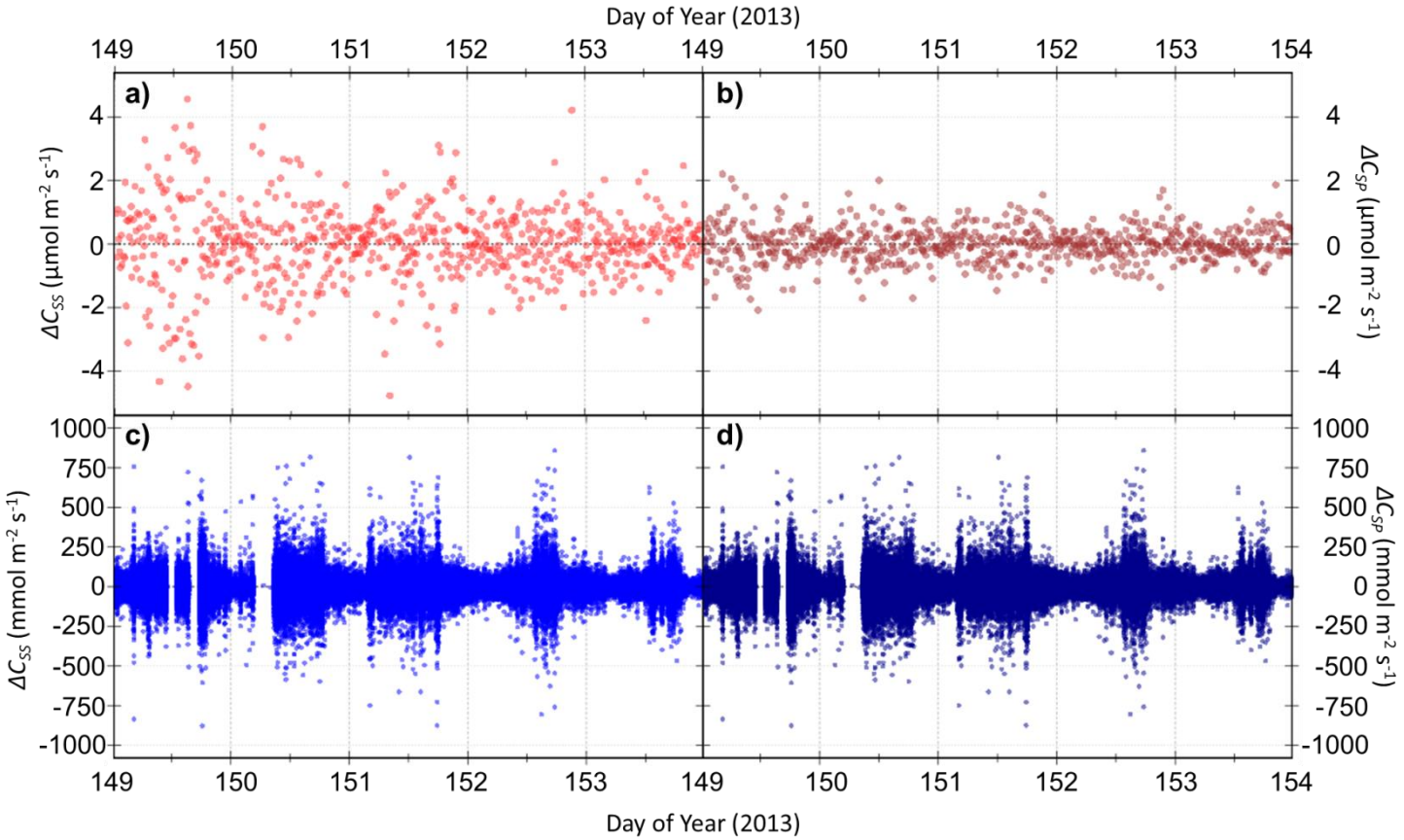

Figure 5.C.1: CO_2 storage time series. (a and c): ΔC_{SS}, (b and d): ΔC_{SP}, (a and b) CO_2 storage data derived from switched profile data (LI840, 2Hz averaged to 1 minute), (c and d) CO_2 storage data derived from continuous measurements at heights A and F (LI7500, 10 Hz). All data collected 2013/149-153, C6, KSSW.

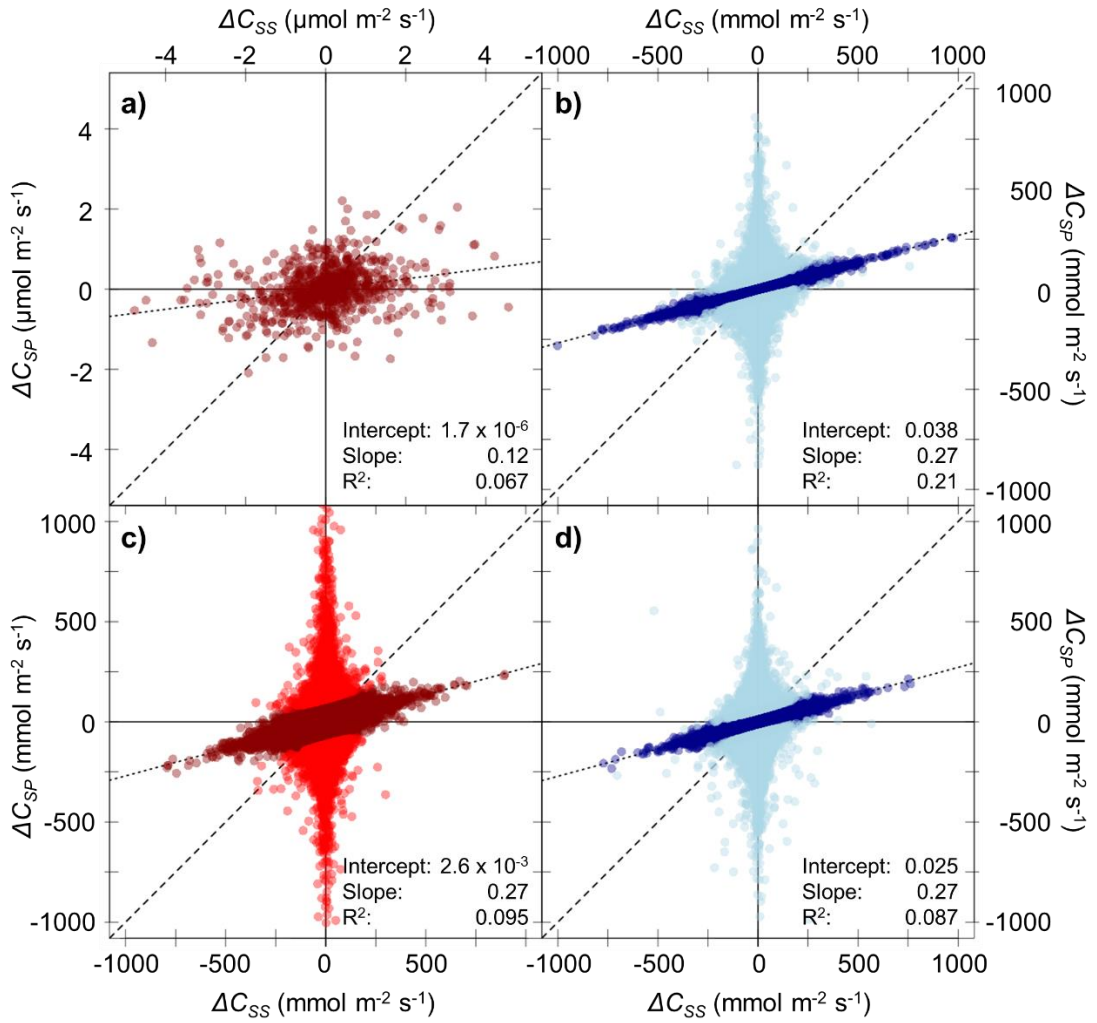

Figure 5.C.2: CO_2 storage calculated from profile measurements (ΔC_{SP}) with concurrent CO_2 storage calculated from measurements at height A only (ΔC_{SS}) for (a and b) 2013/147-153 and (c and d) 2013/161-167. (a) 10 minute switched profile data, LI840, heights A-J, (b and d) 10 Hz continuous measurements, LI7500, heights A and F, (c) 2 Hz continuous measurements, LI840, heights A and F. Solid lines define origin, dashed line: 1:1 slope, dotted line: line of best fit. Points with residual values greater than three times the standard deviation of the ΔC_{SP} data set are plotted in lighter colours in plots (b – d). Intercept, slope and coefficient of determination for the line of best fit with highlighted (lighter) data removed is given in the lower right of each plot.

Appendix 5.D Comparison of power spectra calculated by Fourier and wavelet analysis

This section contains plots comparing power spectra generated by Fourier analysis and by wavelet analysis. This comparison is made for three types of signal: white noise (no change in power with frequency), red noise (decreasing power with increasing frequency) and violet noise (increasing power with increasing frequency) (Figure 5.D.1). The agreement between the two methods is best for white noise. The wavelet global power spectrum under-estimates the power relative to the Fourier power spectrum at the lowest frequencies for all signals, and for the majority of the frequencies analysed for the violet noise spectrum. Despite this, the wavelet method adequately captures the slope of the power with frequency for all signals at frequencies greater than 0.05 rad m^{-1}.

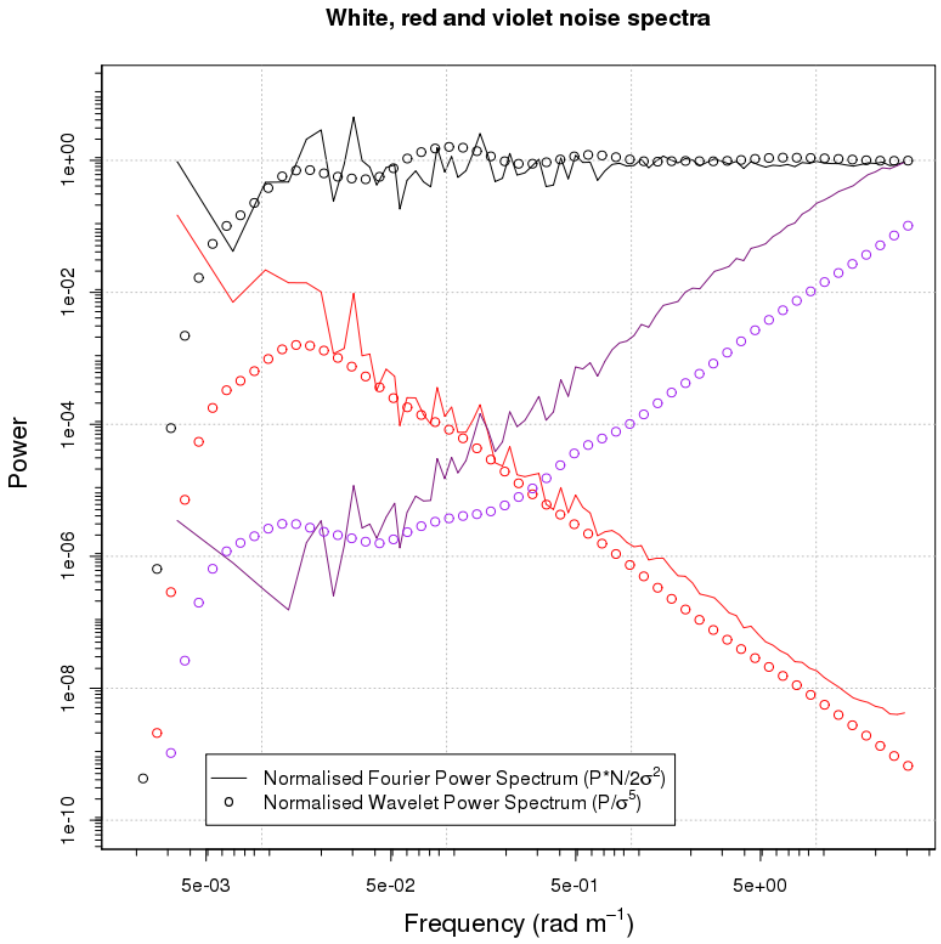

Figure 5.D.1: Comparison of power spectra generated by conventional Fourier transform and by wavelet analysis for synthetic data sets. White noise generated by rnorm (R Development Core Team, 2013), red noise as the integral of the white noise and violet noise as the differential.

The comparison was extended to a subset of real data – the turbulent component of the vertical wind speed measured at KSSW between 00:30 and 01:00 on the 13th January, 2013 (Figure 5.D.2) and the CO_2 storage data between 00:30 and 01:00 on the 25th December, 2013 (Figure 5.D.3). Again, the agreement in slope, if not absolute magnitude, is good.

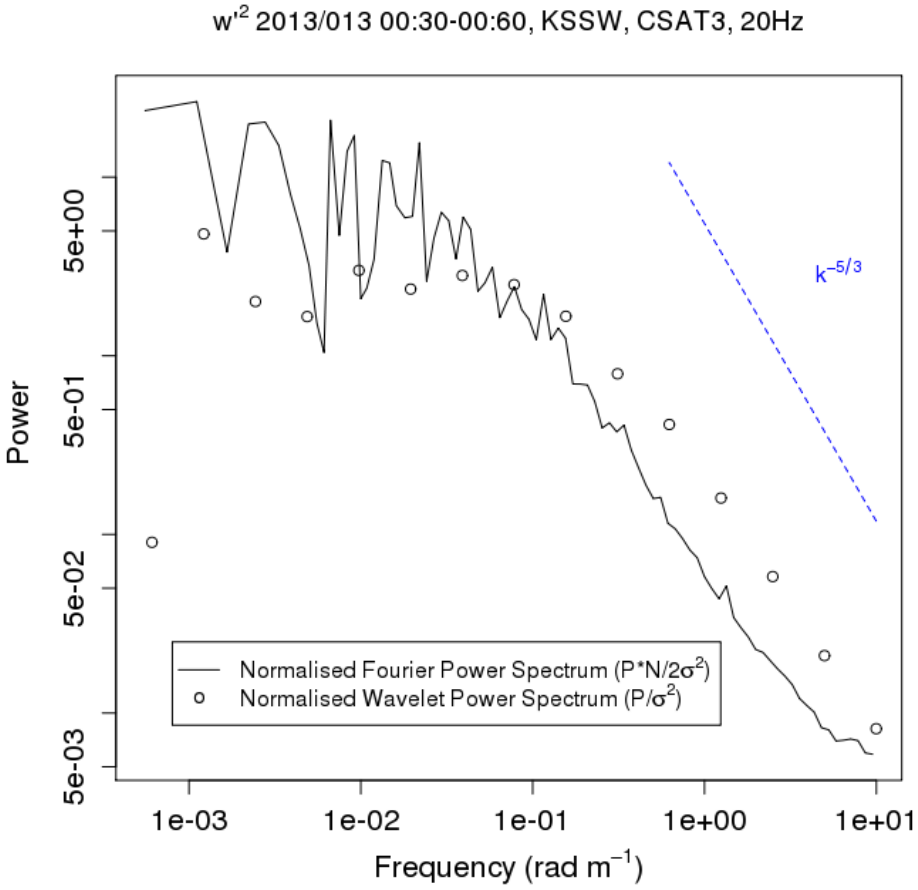

Figure 5.D.2: Comparison of power spectra generated by conventional Fourier transform and by wavelet analysis for a measured data set.

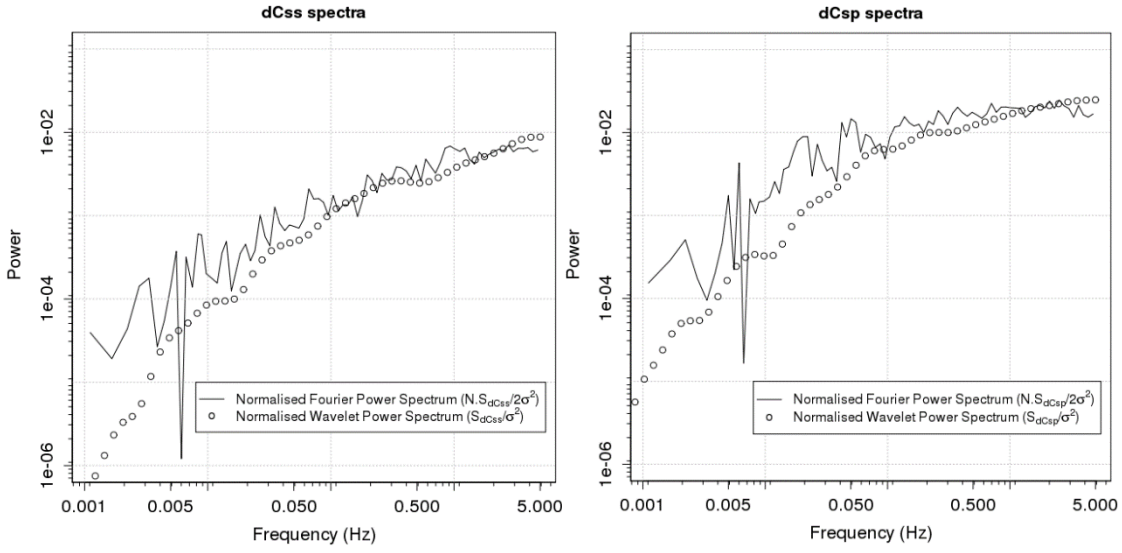

Figure 5.D.3: ΔC_{SS} and ΔC_{SP} spectra for 2013/359 00:30-01:00.

Appendix 5.E ΔC_{SS} and ΔC_{SP} for 2013/347 to 2014/002.

This section contains one second average time series plots of ΔC_{SS} and ΔC_{SP} for 2013/347 to 2014/002. The majority of ΔC_{SS} time series show regular spikes at approximately 40 minute intervals. Due to the similarity of the plots, individual captions are not given. Each plot presents data for one day, which is given in the plot title.

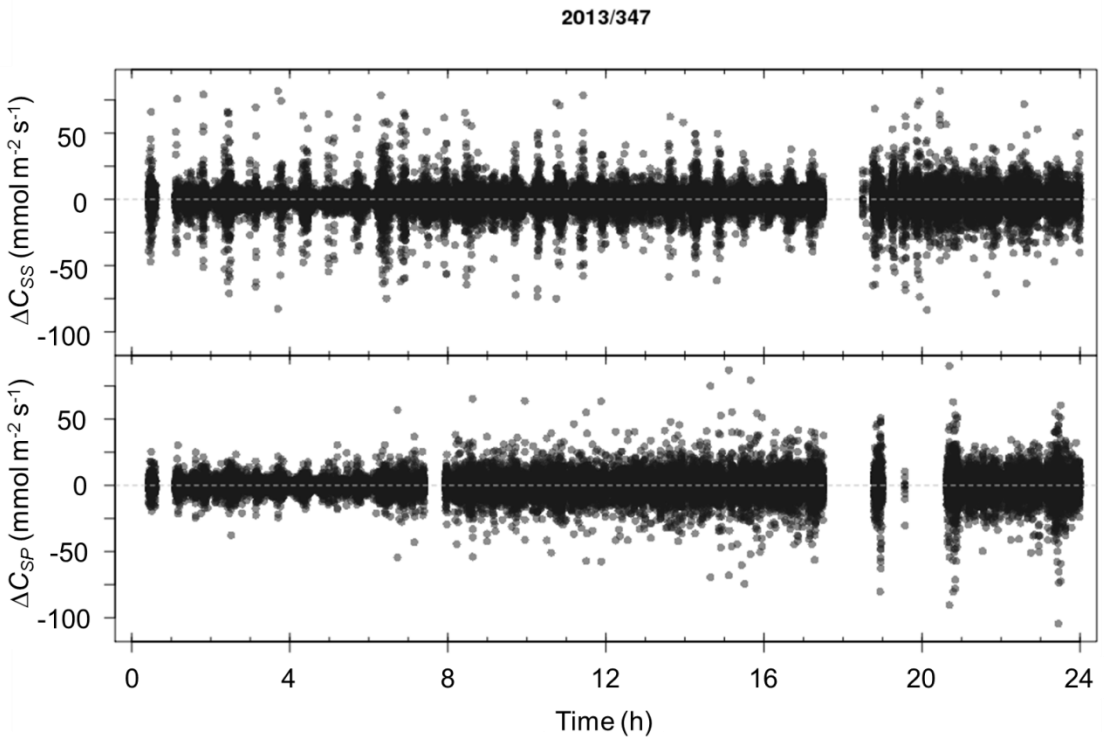

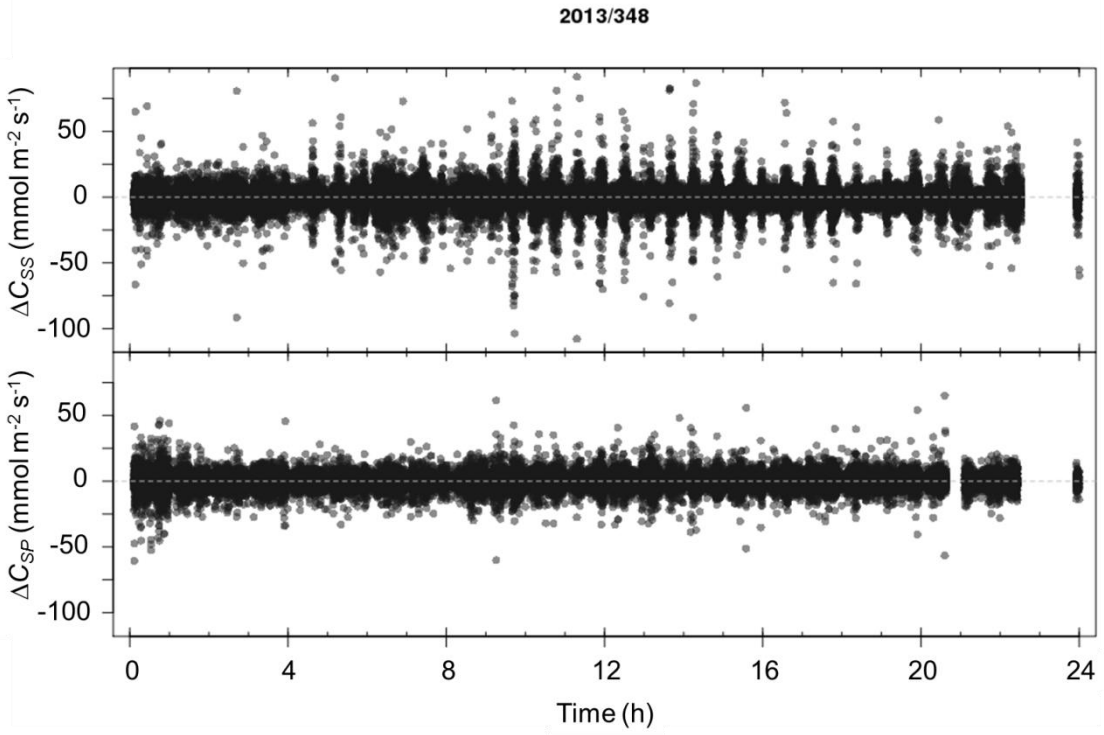

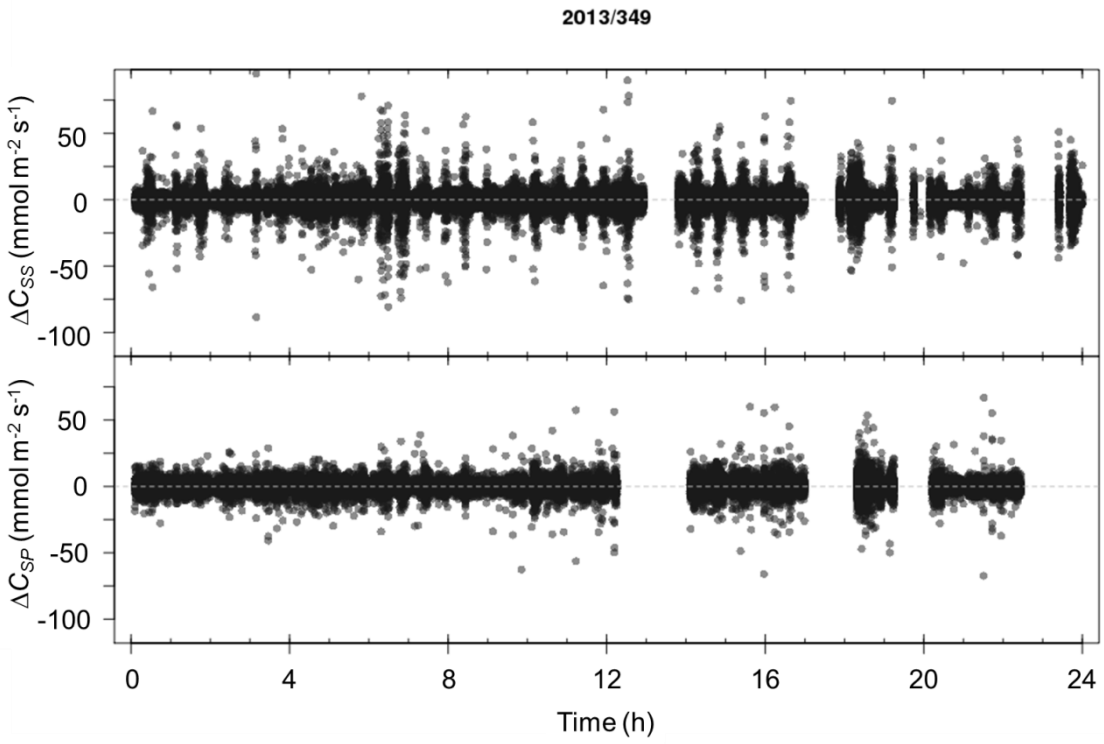
2013/349
ΔCSS (mmol m-2 s-1)
ΔCSP (mmol m-2 s-1)
50
0
-50
-100
0
4
8
12
16
20
24
Time (h)

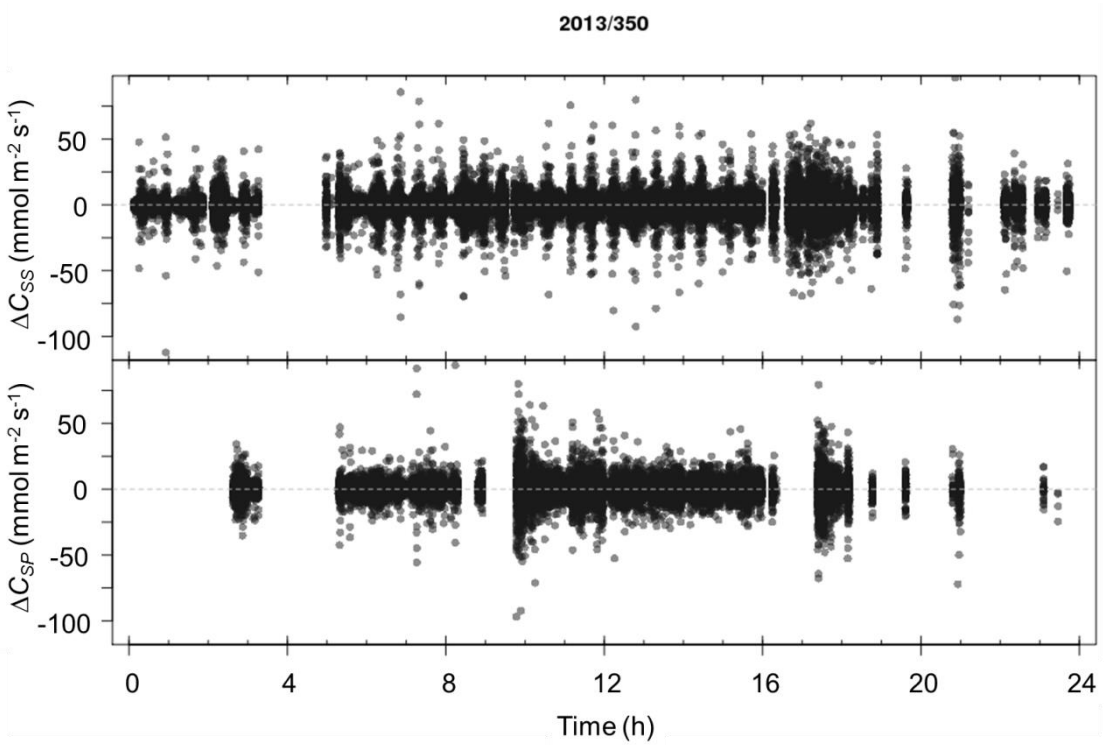
2013/350
ΔCSS (mmol m-2 s-1)
ΔCSP (mmol m-2 s-1)
50
0
-50
-100
0
4
8
12
16
20
24
Time (h)

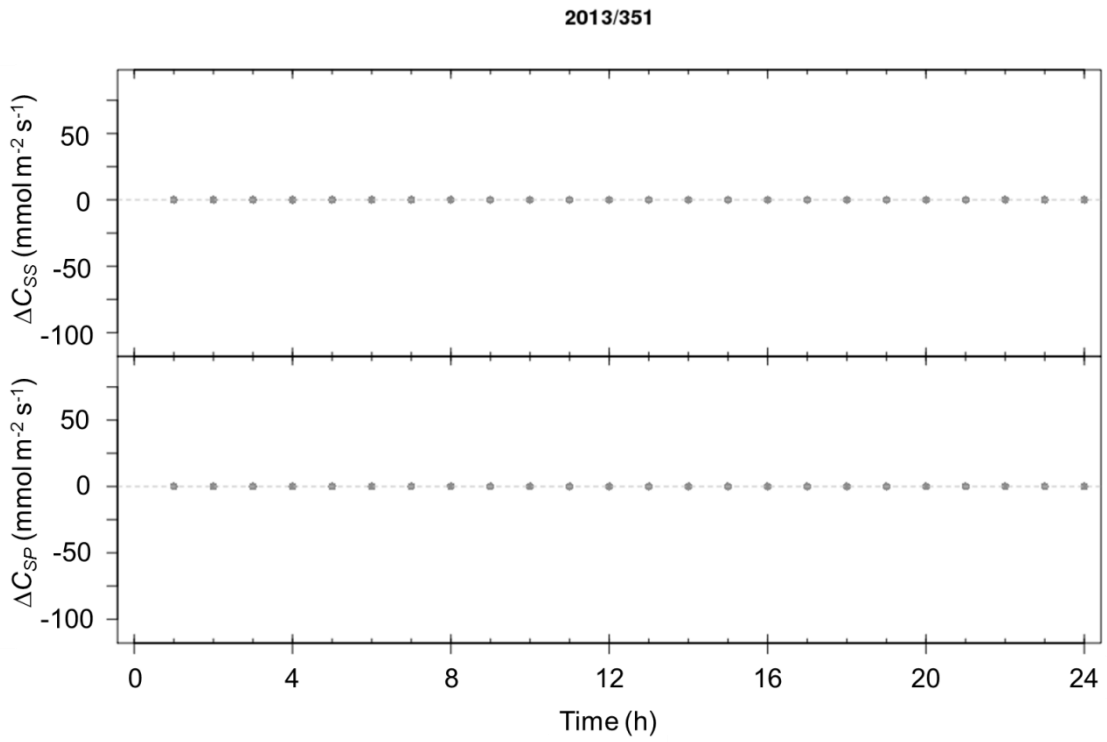
2013/351
ΔCSS (mmol m-2 s-1)
ΔCSP (mmol m-2 s-1)
50
0
-50
-100
0
4
8
12
16
20
24
Time (h)

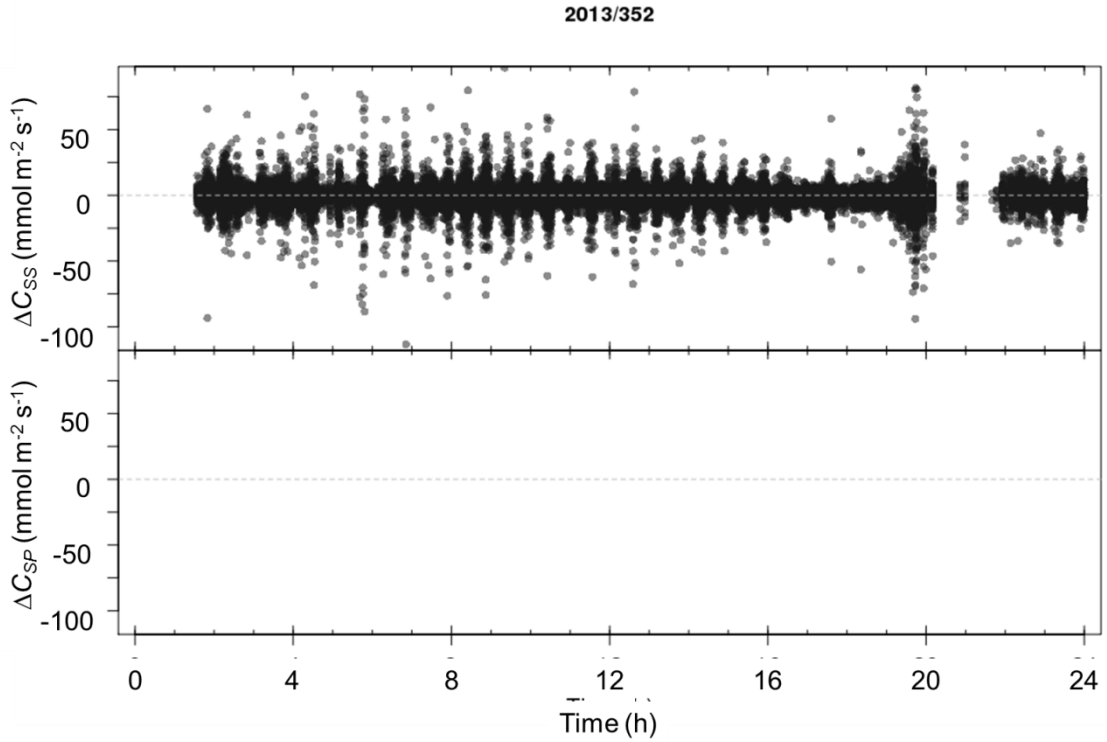
2013/352
ΔCSS (mmol m-2 s-1)
ΔCSP (mmol m-2 s-1)
50
0
-50
-100
0
4
8
12
16
20
24
Time (h)

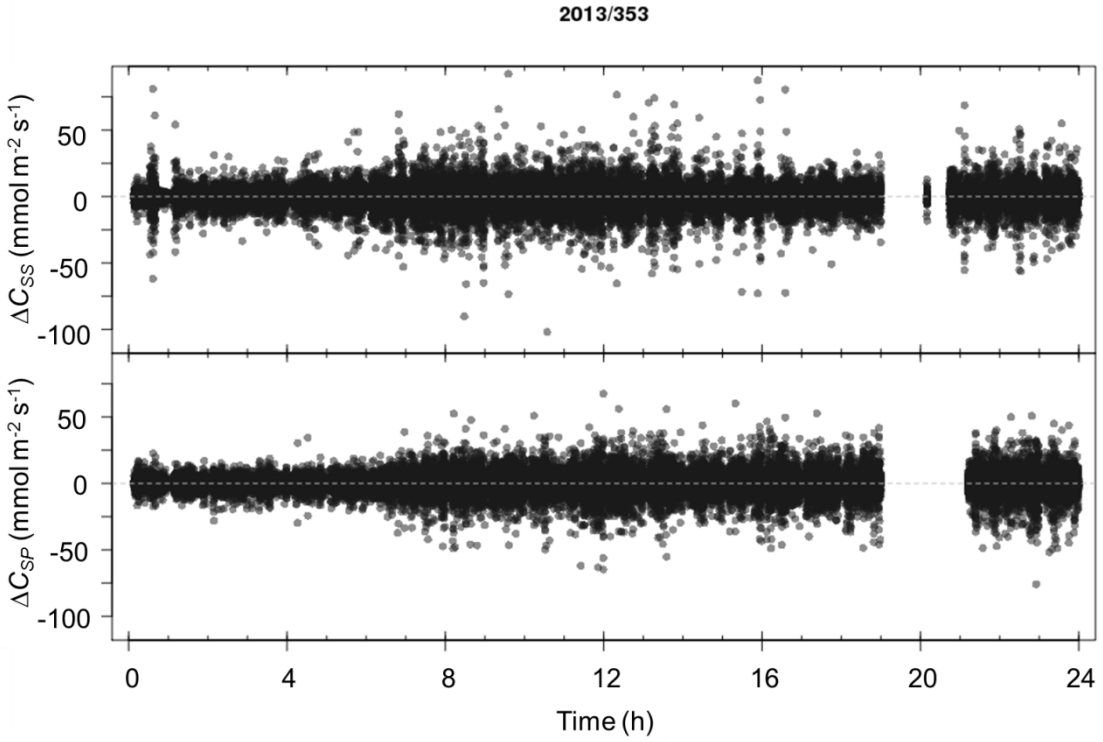
2013/353
ΔCSS (mmol m-2 s-1)
ΔCSP (mmol m-2 s-1)
50
0
-50
-100
0
4
8
12
16
20
24
Time (h)

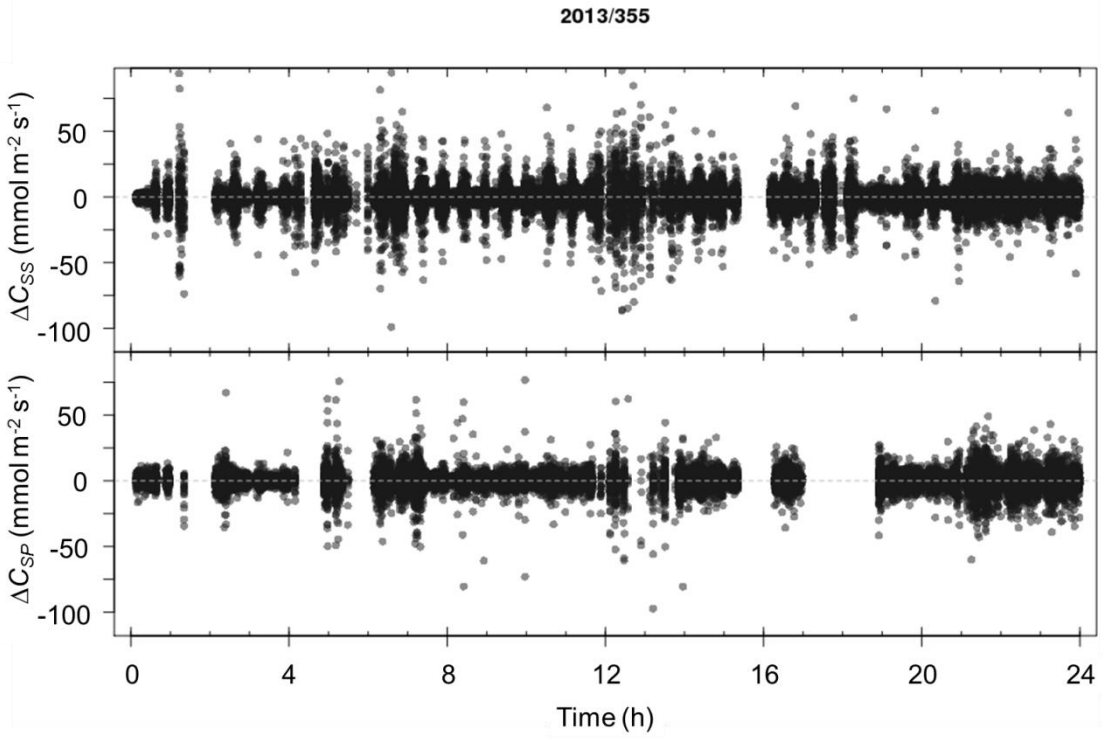
2013/355
ΔCSS (mmol m-2 s-1)
ΔCSP (mmol m-2 s-1)
50
0
-50
-100
0
4
8
12
16
20
24
Time (h)

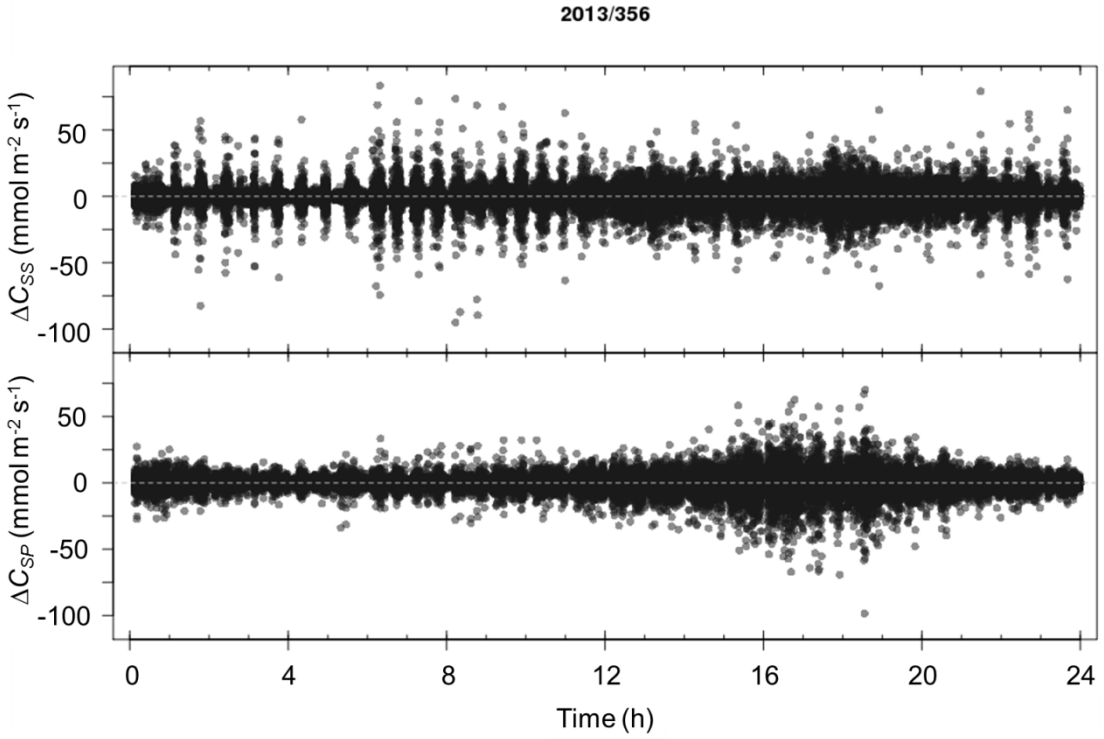
2013/356
ΔCSS (mmol m-2 s-1)
ΔCSP (mmol m-2 s-1)
50
0
-50
-100
0
4
8
12
16
20
24
Time (h)

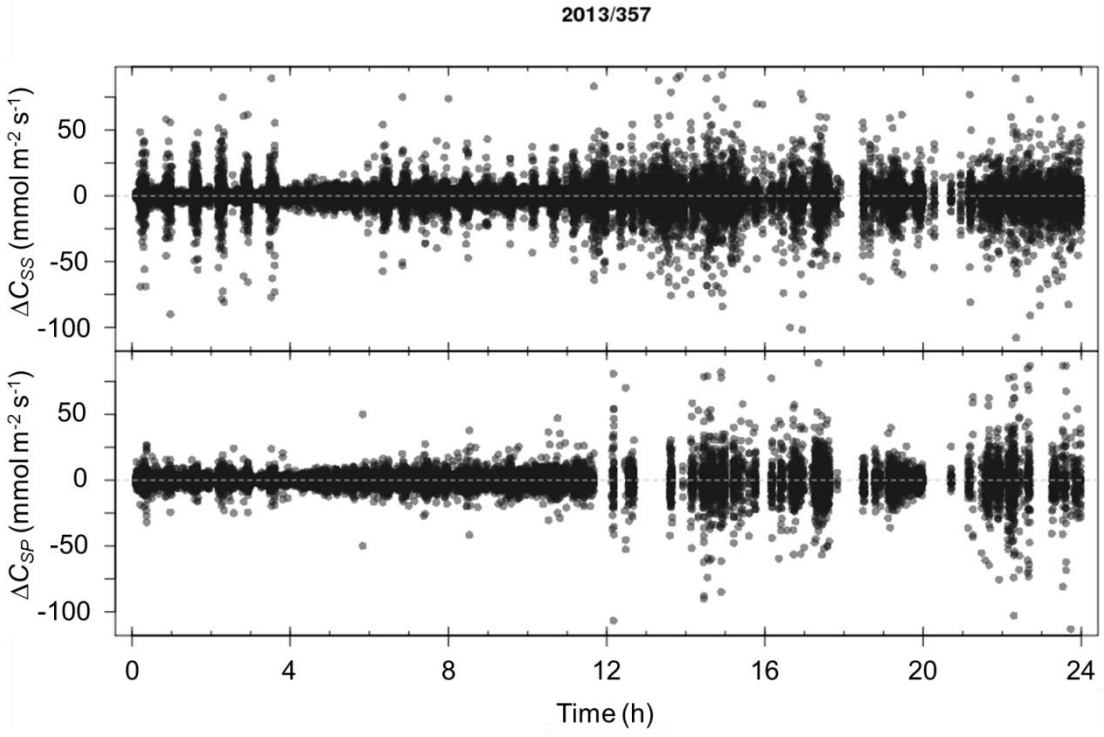
2013/357
ΔCSS (mmol m-2 s-1)
ΔCSP (mmol m-2 s-1)
50
0
-50
-100
0
4
8
12
16
20
24
Time (h)

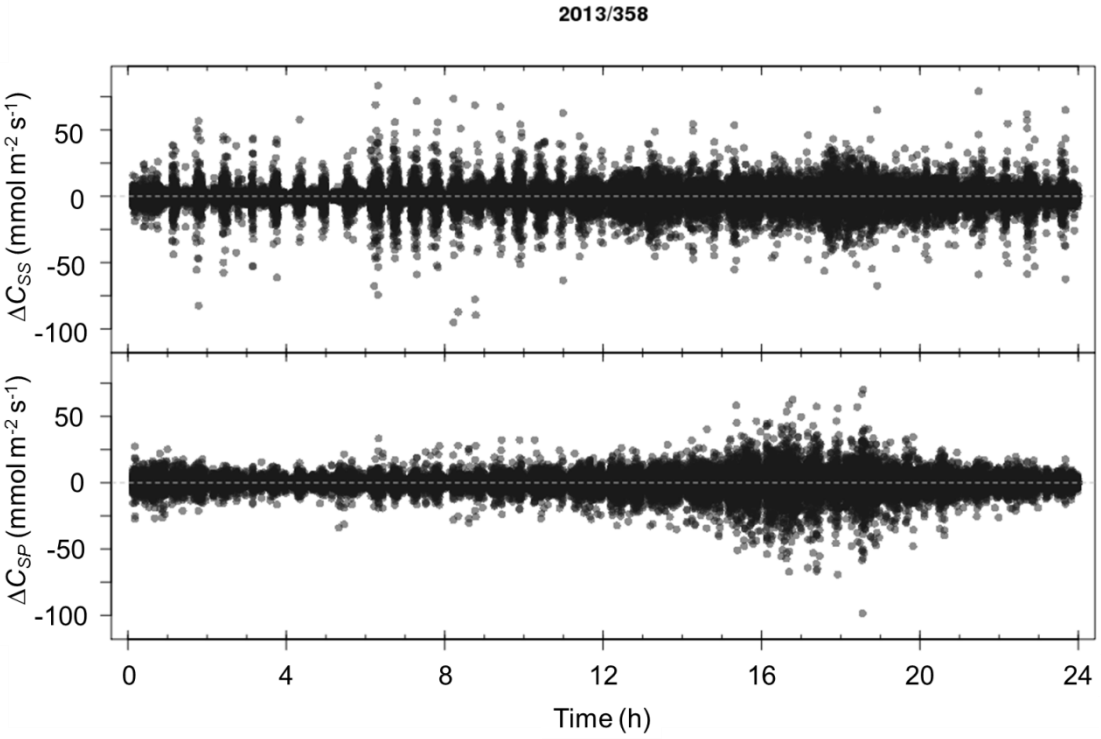
2013/358
ΔCSS (mmol m-2 s-1)
ΔCSP (mmol m-2 s-1)
50
0
-50
-100
0
4
8
12
16
20
24
Time (h)

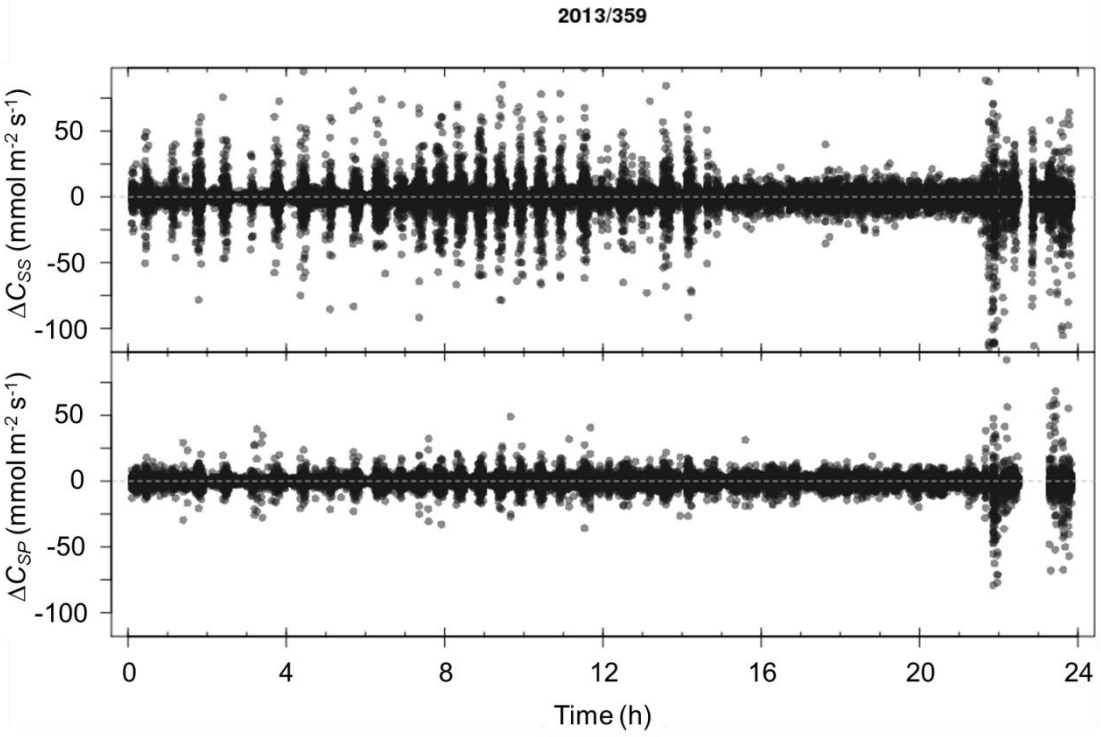
2013/359
ΔCSS (mmol m-2 s-1)
ΔCSP (mmol m-2 s-1)
50
0
-50
-100
0
4
8
12
16
20
24
Time (h)

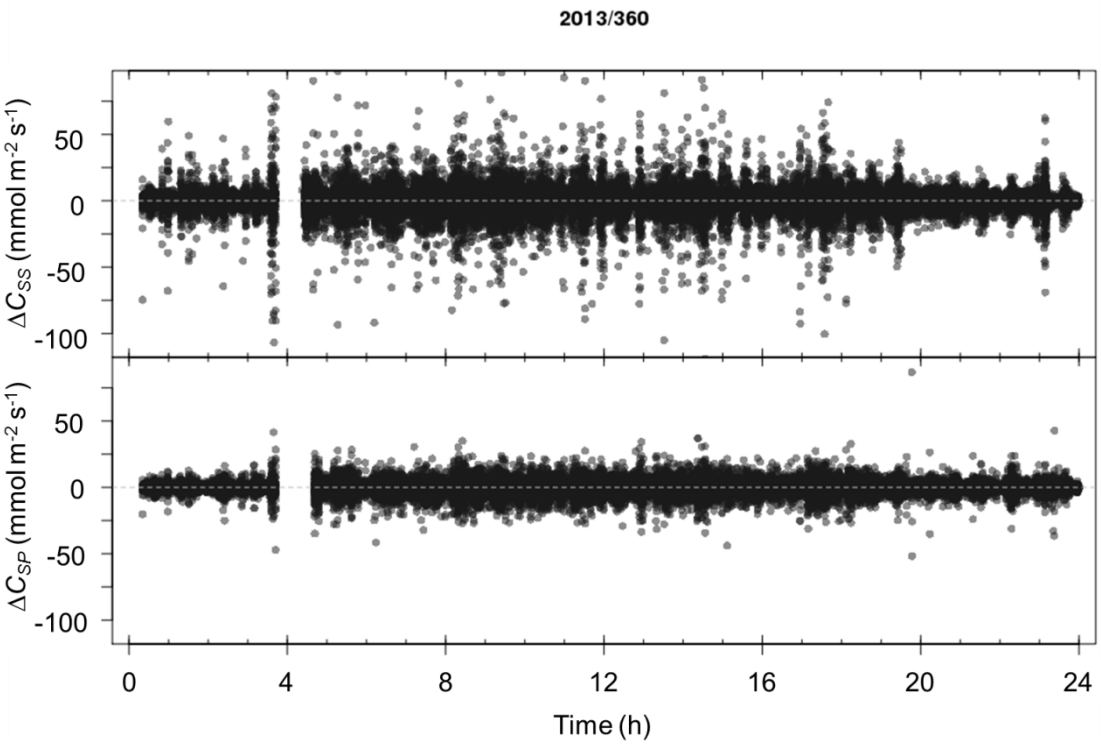
2013/360
ΔCSS (mmol m-2 s-1)
ΔCSP (mmol m-2 s-1)
50
0
-50
-100
0
4
8
12
16
20
24
Time (h)

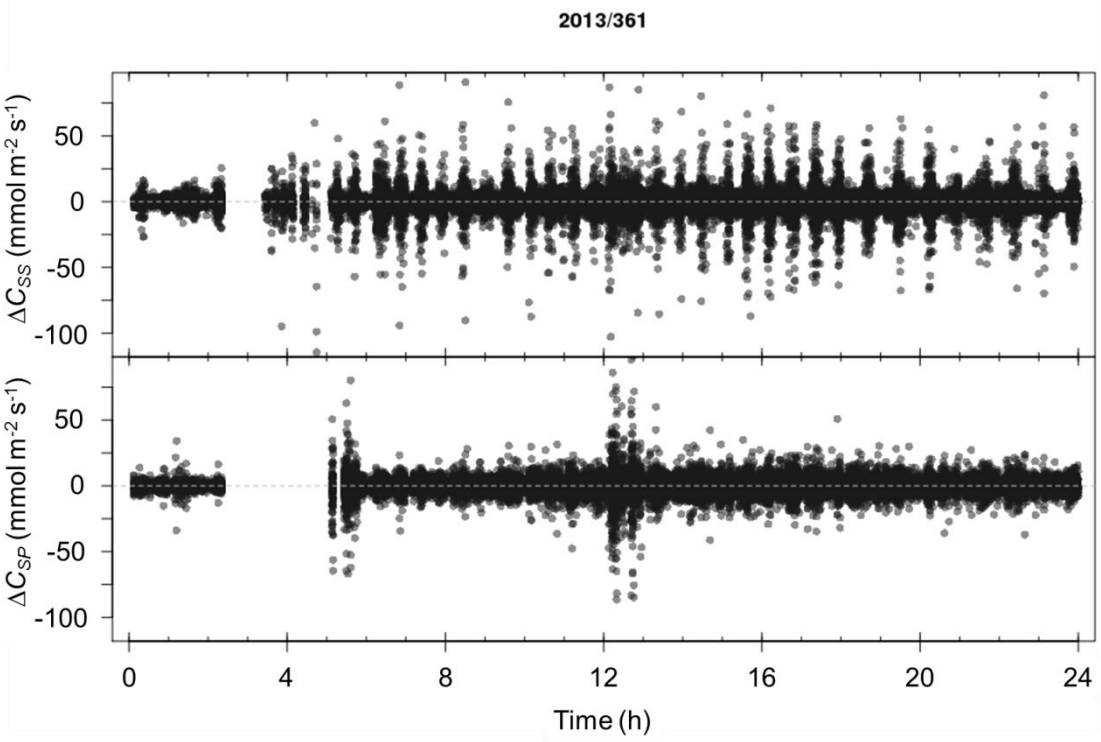
2013/361
ΔCSS (mmol m-2 s-1)
ΔCSP (mmol m-2 s-1)
50
0
-50
-100
0
4
8
12
16
20
24
Time (h)

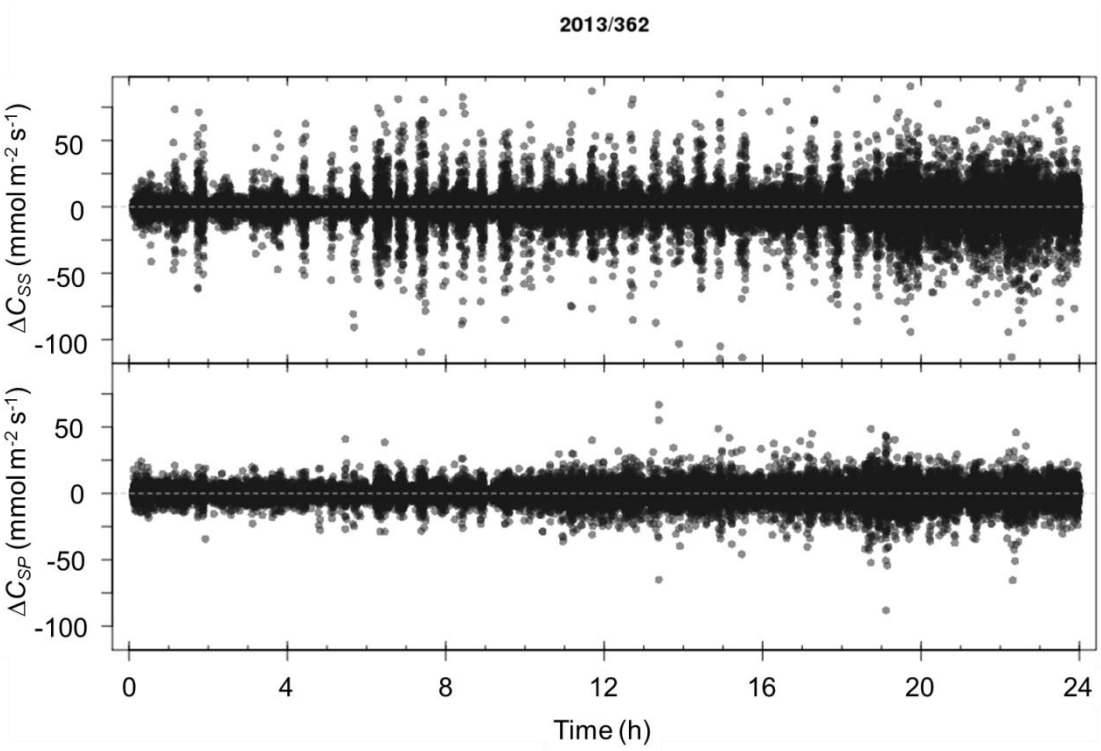
2013/362
ΔCSS (mmol m-2 s-1)
ΔCSP (mmol m-2 s-1)
50
0
-50
-100
0
4
8
12
16
20
24
Time (h)

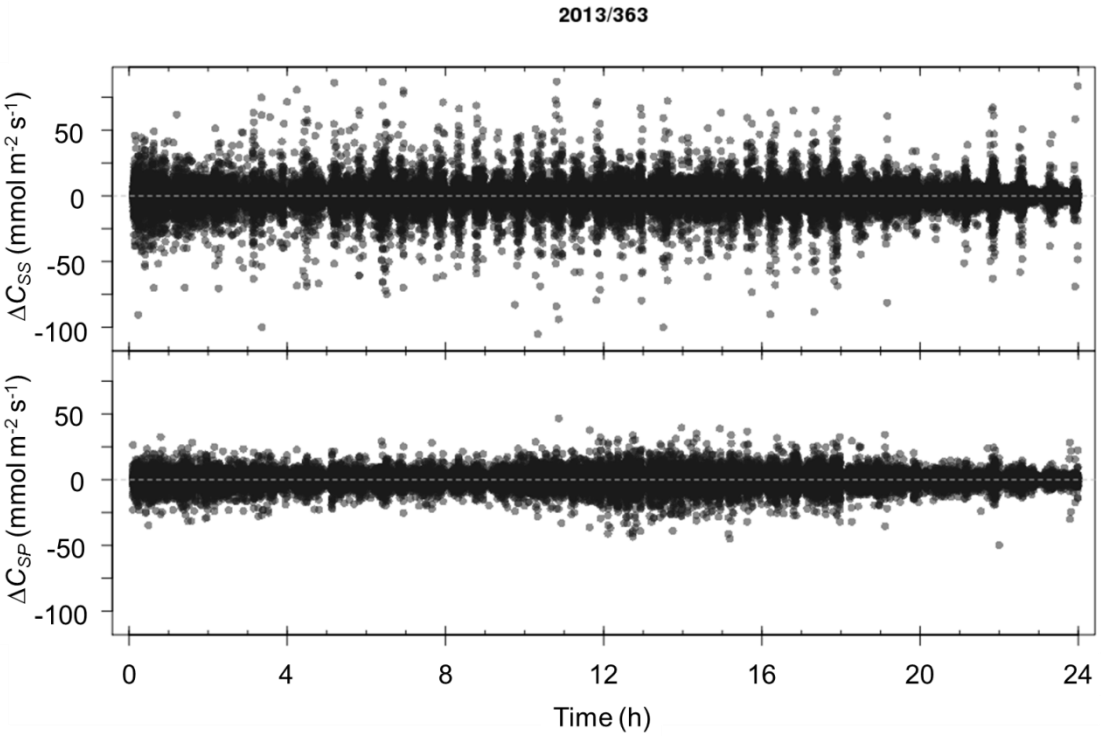
2013/363
ΔCSS (mmol m-2 s-1)
ΔCSP (mmol m-2 s-1)
50
0
-50
-100
0
4
8
12
16
20
24
Time (h)

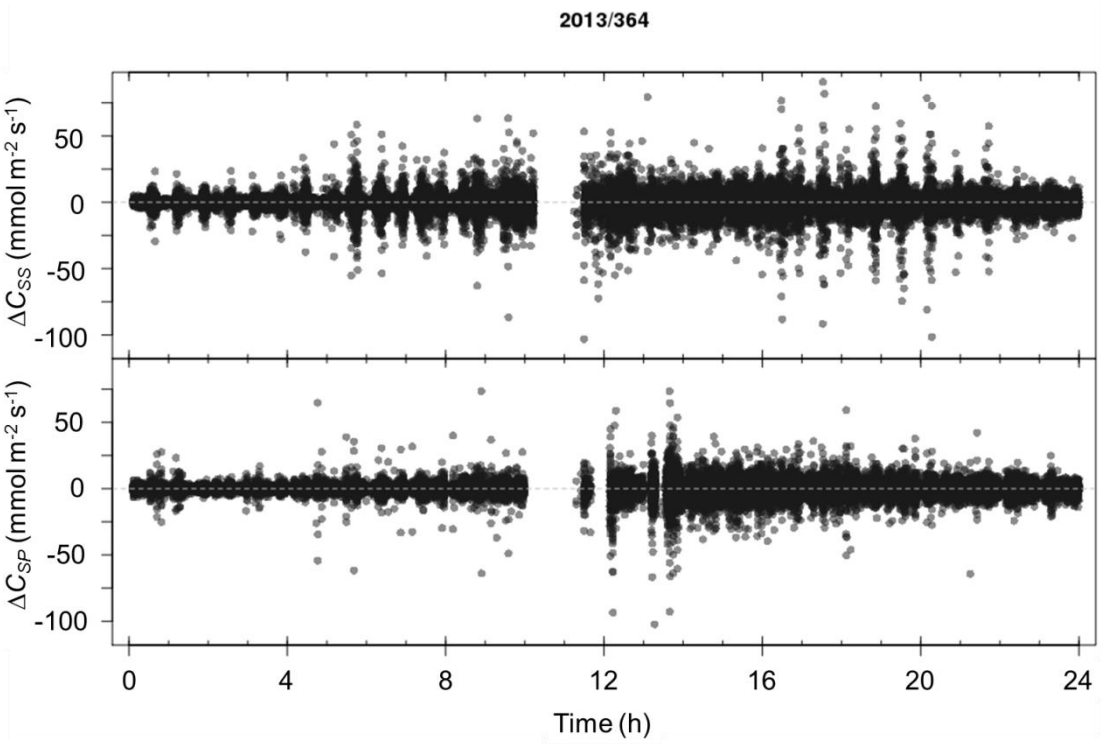
2013/364
ΔCSS (mmol m-2 s-1)
ΔCSP (mmol m-2 s-1)
50
0
-50
-100
0
4
8
12
16
20
24
Time (h)

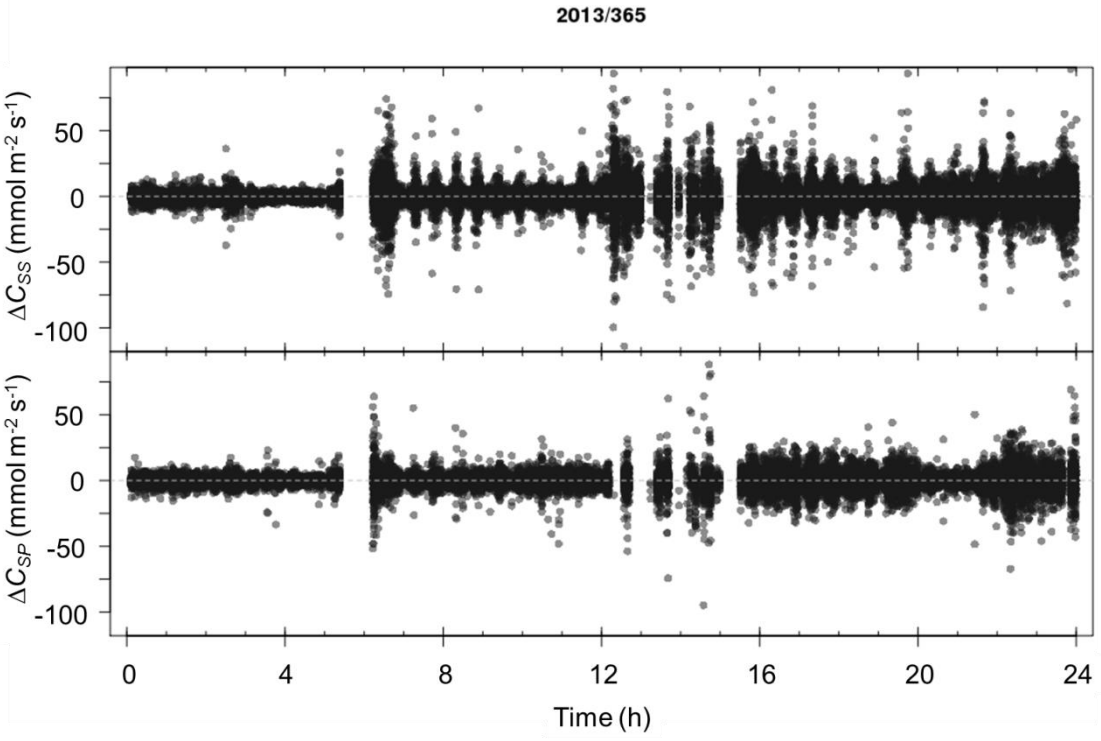
2013/365
ΔCSS (mmol m-2 s-1)
ΔCSP (mmol m-2 s-1)
50
0
-50
-100
0
4
8
12
16
20
24
Time (h)

Appendix 5.F Copeaks

This appendix contains plots of the number of co-peaks per half hour for the following variables: *u* (zonal wind component, m s^{-1}), *v* (meridional wind component, m s^{-1}), *w* (vertical wind component, m s^{-1}), T_A (air temperature in degrees Centigrade), $[CO_2]$ (CO_2 concentration, mmol m^{-3}), and $[H_2O]$ (H_2O concentration, mmol m^{-3}). They are plotted with time of day (h), wind direction (degrees from true north) and stability (z'/L, calculated from data at KSSW).

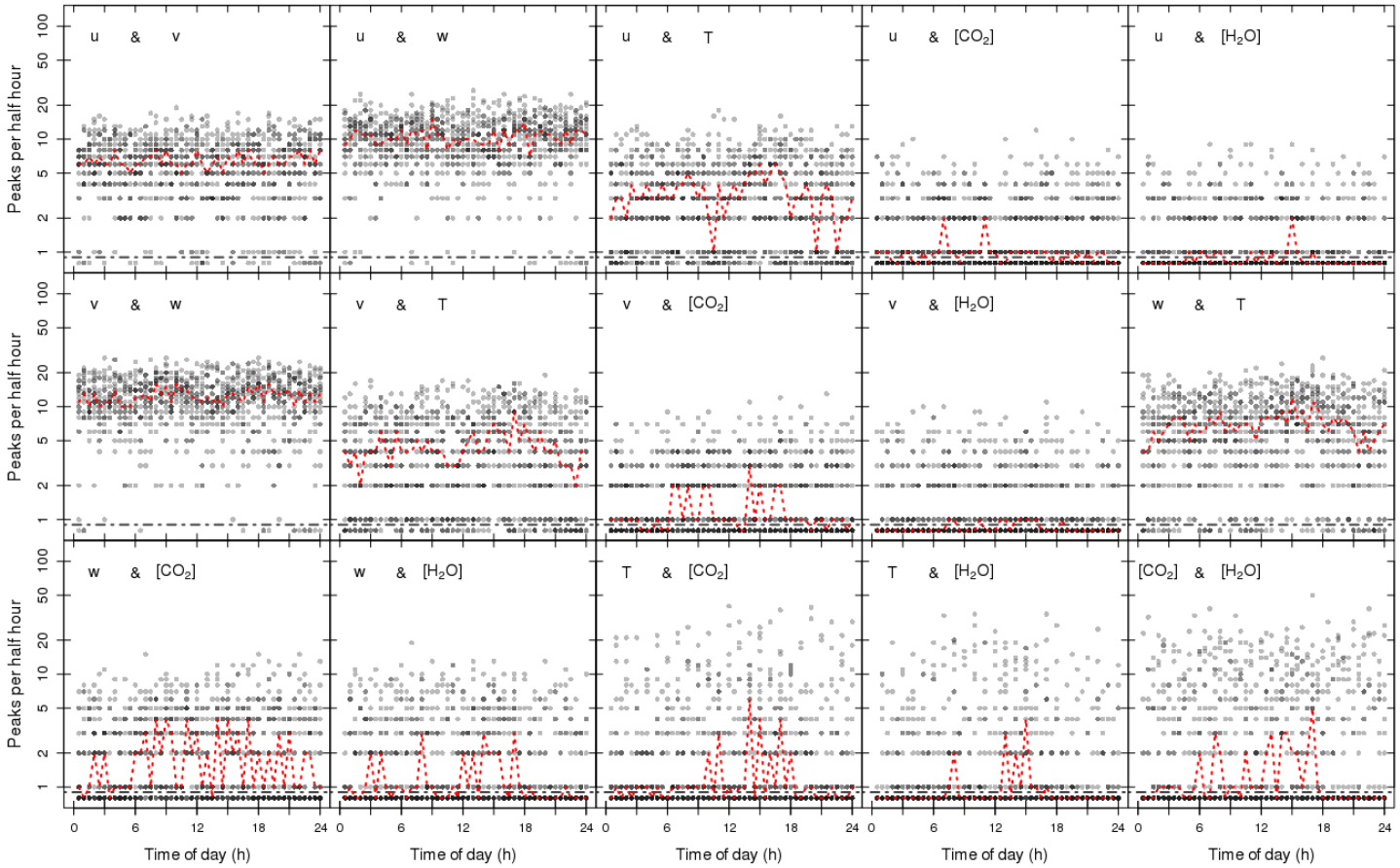

Figure 5.F.1: Grey points: number of peaks detected per half hour with time of day, 2013/354-2014/002, KSSW, 10 Hz LI7500 and CSAT3. Dotted line: median value for each half hour. Dot-dash line: all values below this line were artificially made greater than zero for ease of plotting on a log scale.

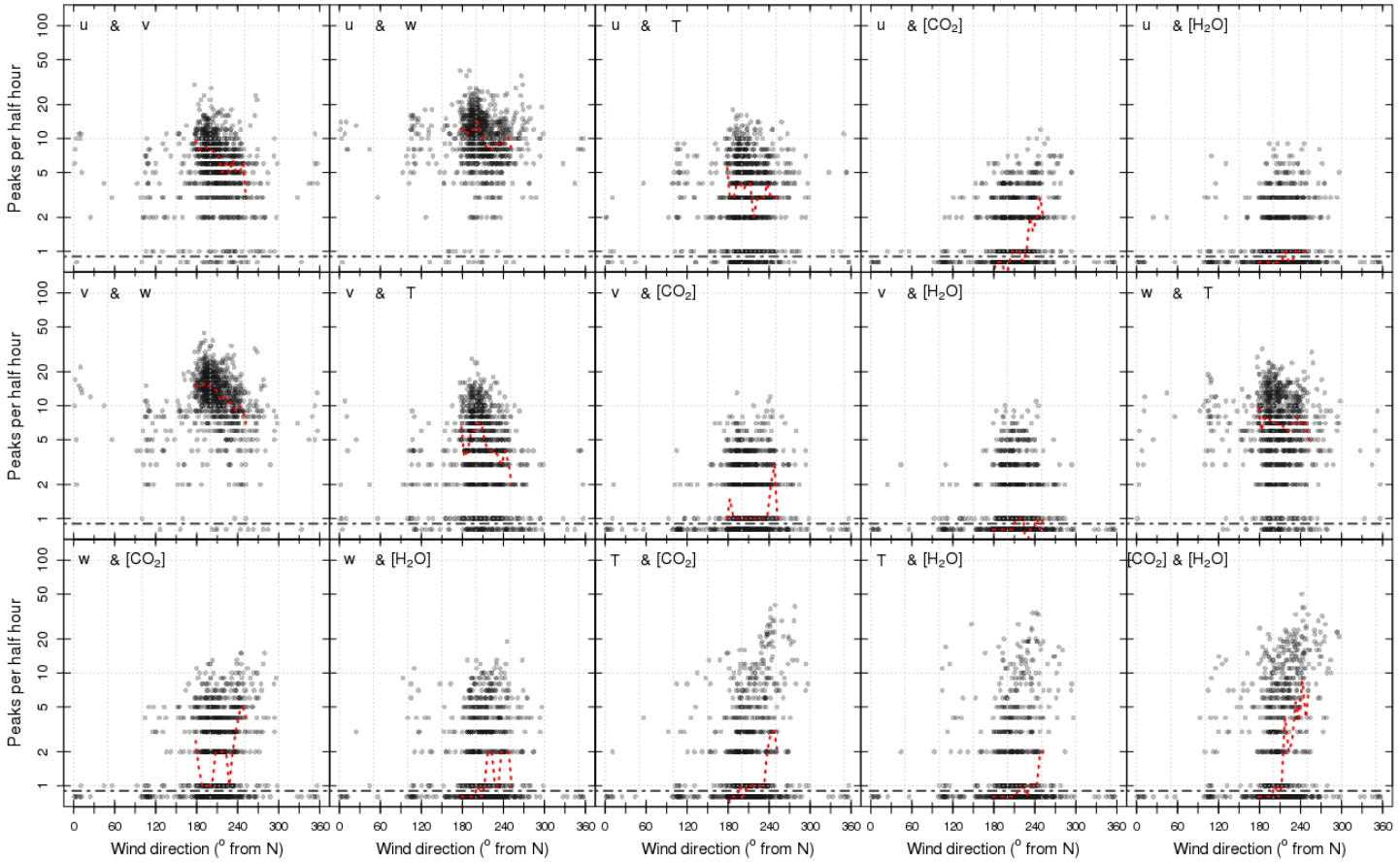

Figure 5.F.2: Grey points: number of peaks detected per half hour with wind direction, 2013/354-2014/002, KSSW, 10 Hz LI7500 and CSAT3. Dotted line: median value for each 5 degree width bin with greater than 10 values. Dot-dash line: all values below this line were artificially made greater than zero for ease of plotting on a log scale.

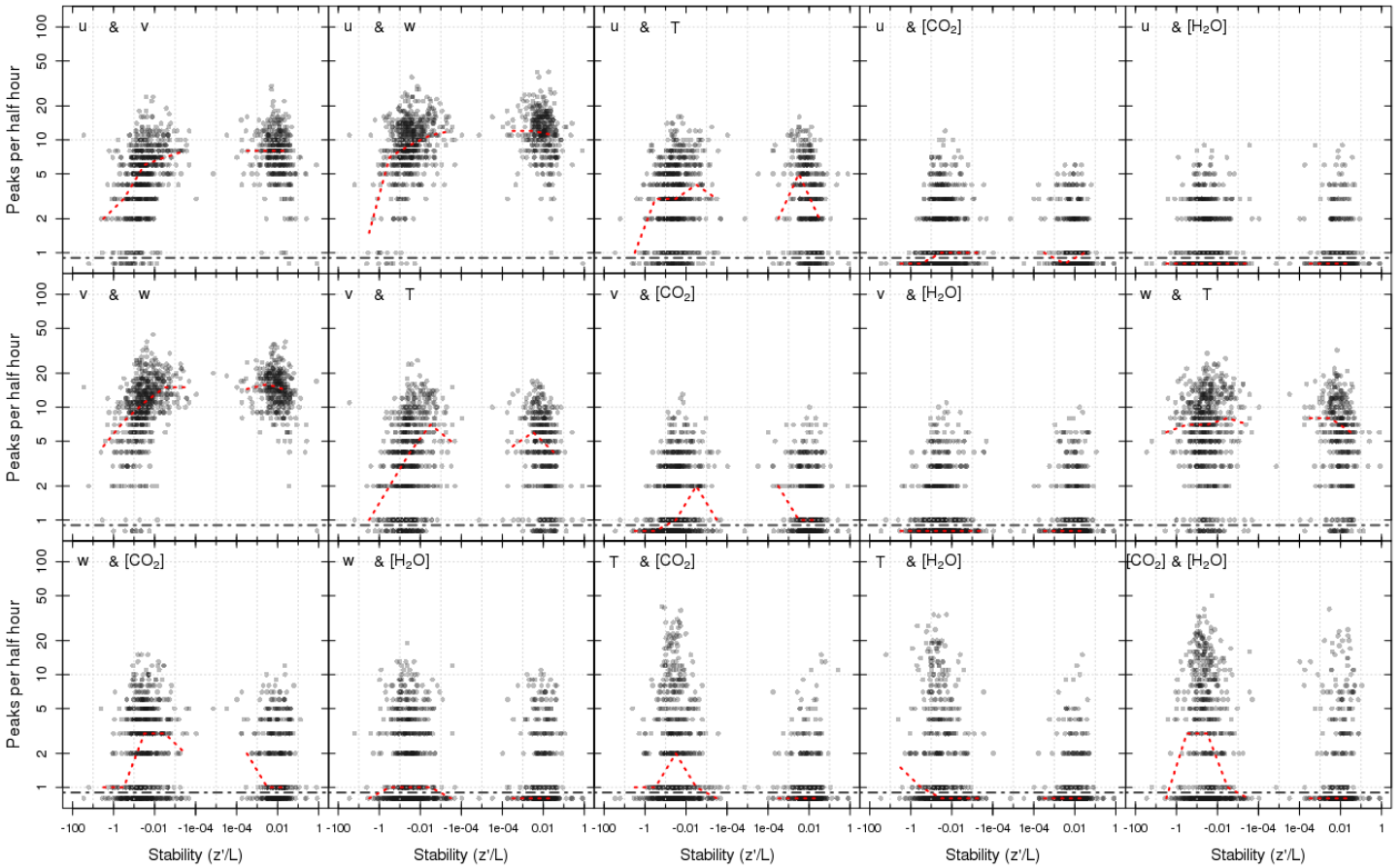

Figure 5.F.3: Grey points: number of peaks detected per half hour with atmospheric stability, 2013/354-2014/002, KSSW, 10 Hz LI7500 and CSAT3. Dotted line: median value for each bin with greater than 10 values. Bins defined by powers of ten down to ±1E-4. Dot-dash line: all values below this line were artificially made greater than zero for ease of plotting on a log scale.

Appendix 5.G Stress fractions

Stress fraction for each quadrant and half hourly period 2013/347-2014/002, as described in Section 5.2.4.3, binned by stability and ΔC_S value for ΔC_{SS} (Figure 5.F.2) and ΔC_{SP} (Figure 5.F.3). Data for stable conditions excluded due to low quantity compared to other stability classes. Stability and ΔC_S classes defined in Figure 5.F.1.

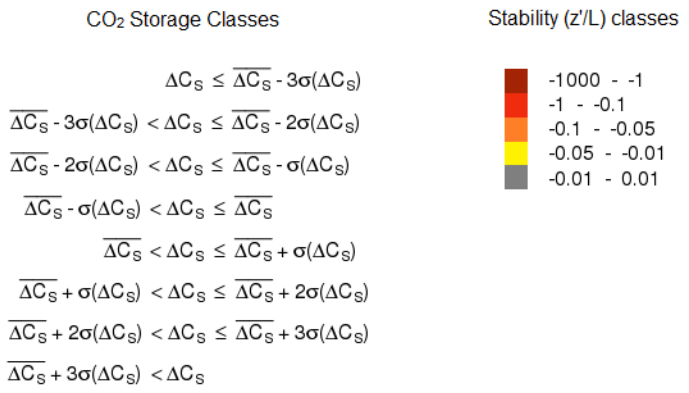

Figure 5.G.1: ΔC_S and stability classes used in Figure 5.G.2-Figure 5.G.3.

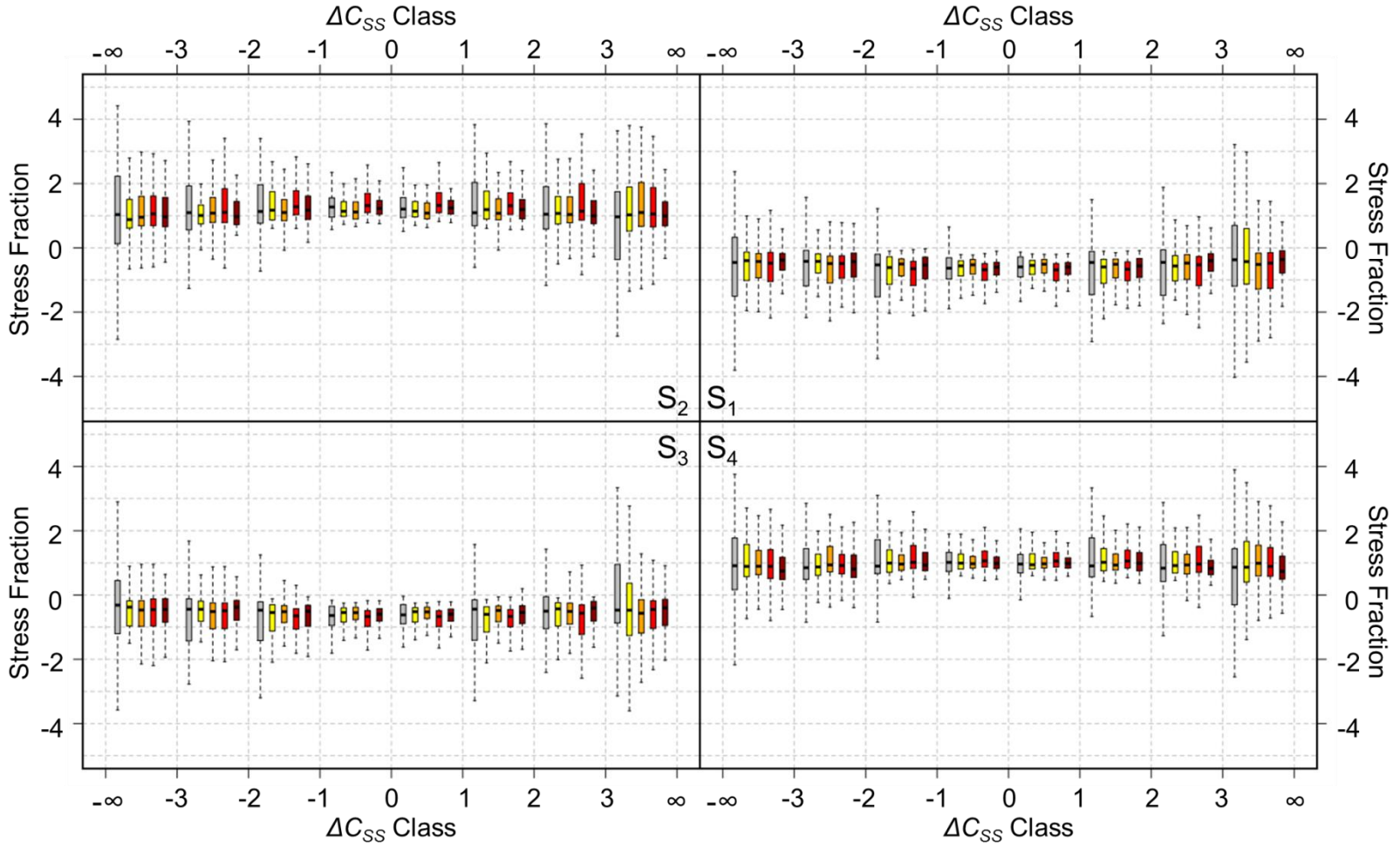

Figure 5.G.2: Anti-clockwise from top right: Half hourly stress fractions for quadrants 1, 2, 3 and 4, 2013/347-2014/002, binned by stability and ΔC_{SS}. Key: Figure 5.G.1.

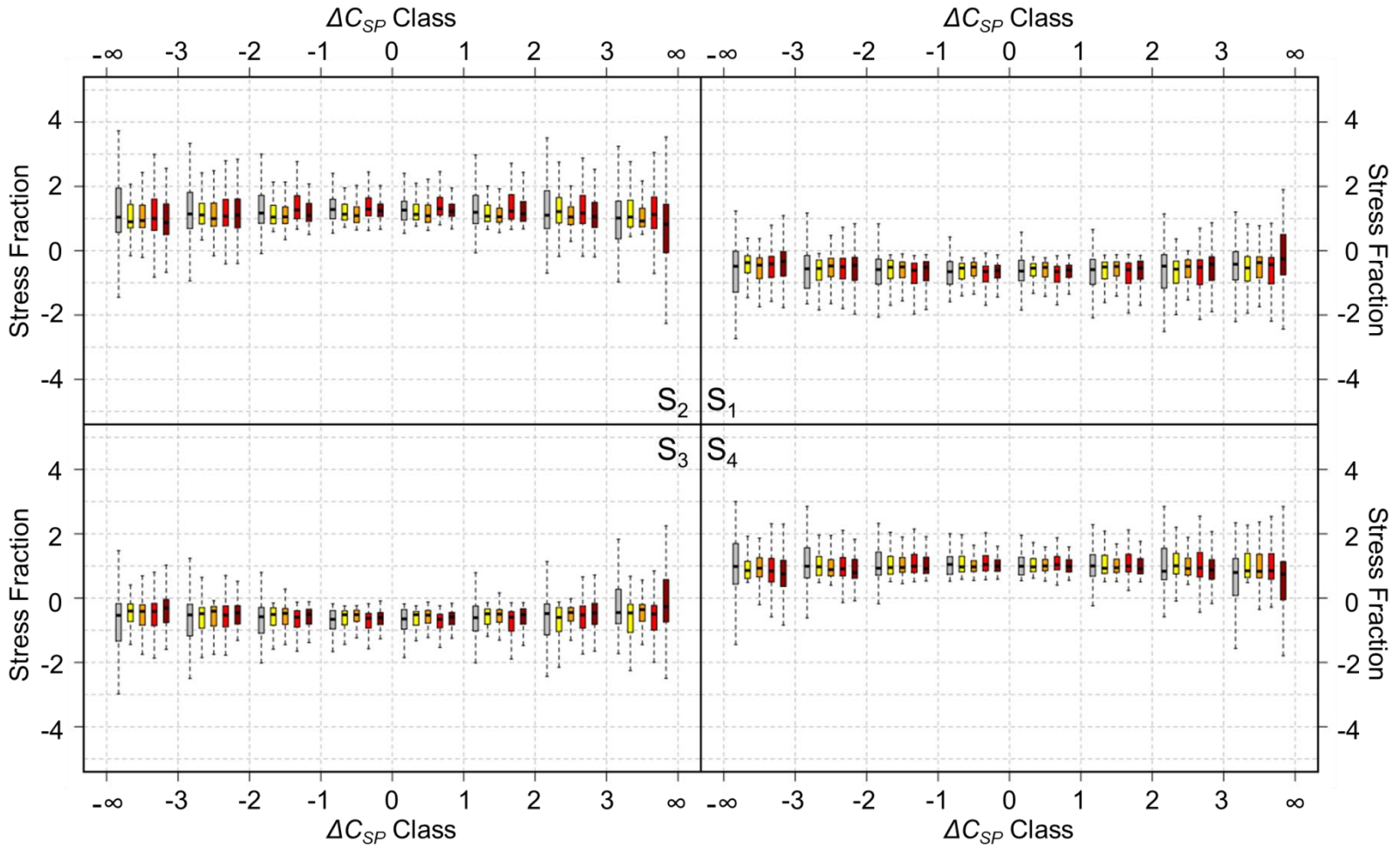

Figure 5.G.3: Anti-clockwise from top right: Half hourly stress fractions for quadrants 1, 2, 3 and 4, 2013/347-2014/002, binned by stability and ΔC_{SP}. Key: Figure 5.G.1.

Appendix 5.H Energy spectra and data availability

In this section energy spectra with natural and with non-dimensional frequency are presented for sites KSSW, KSNW and KSB. The data availability for the CSAT3 at site KSNW and the Gill anemometer at KSB are also reported.

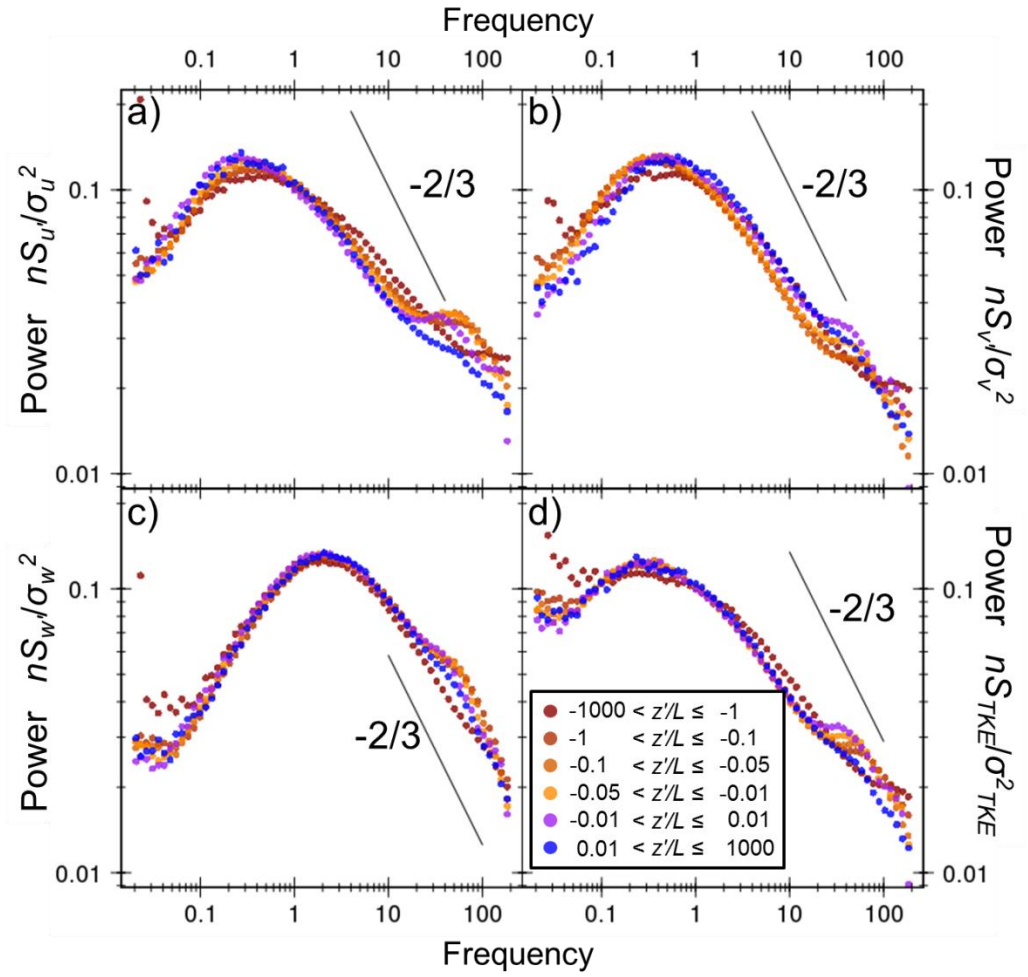

Figure 5.H.1: Power spectra for wind components (a) u, (b) v, (c) w , and (d) the turbulent kinetic energy divided into six stability classes (inset, d) with nondimensional frequency (f=nz'/U). Data collected at 10 Hz and 20 Hz (EC5-EC8) at height A, KSSW between 2013/086 and 2014/365.

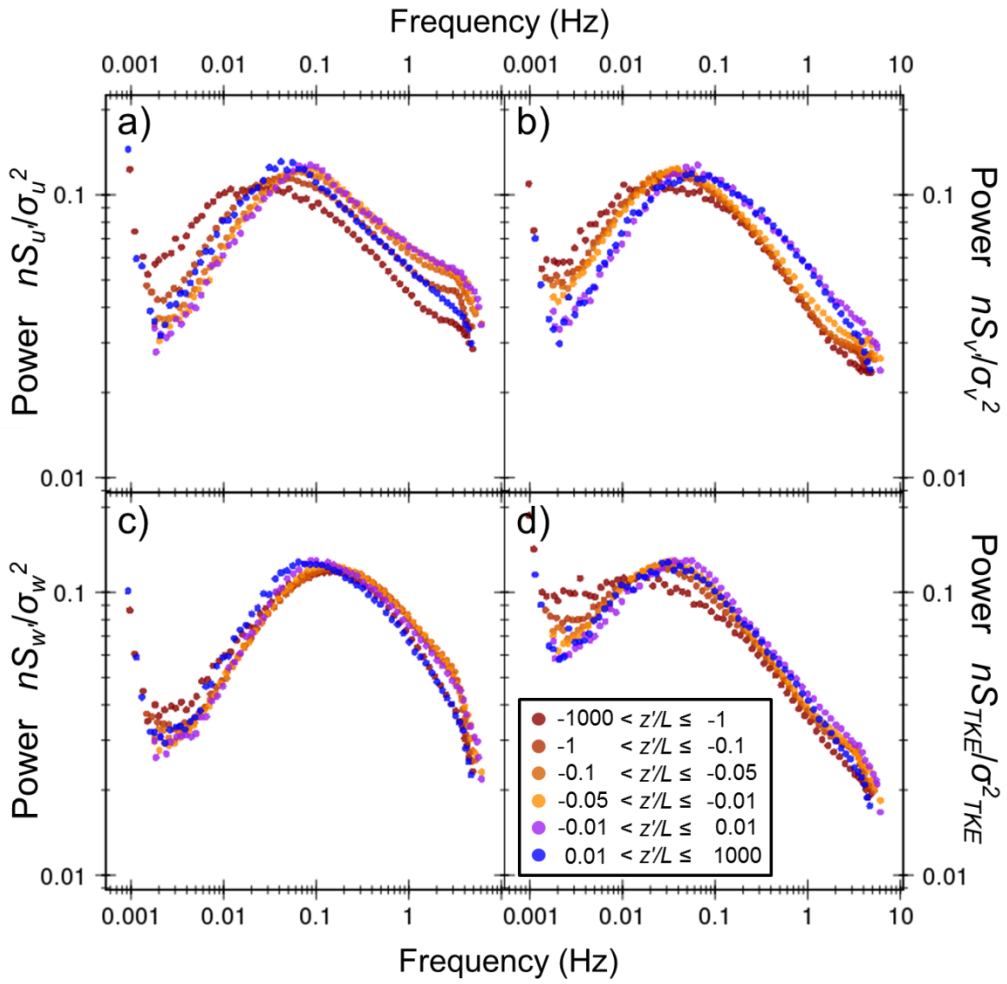

Figure 5.H.2: Power spectra for wind components (a) u, (b) v, (c) w , and (d) the turbulent kinetic energy divided into six stability classes (inset, d) with natural frequency. Data collected at 10 Hz and 20 Hz (EC5-EC8) at height F, KSNW between 2013/086 and 2014/365.

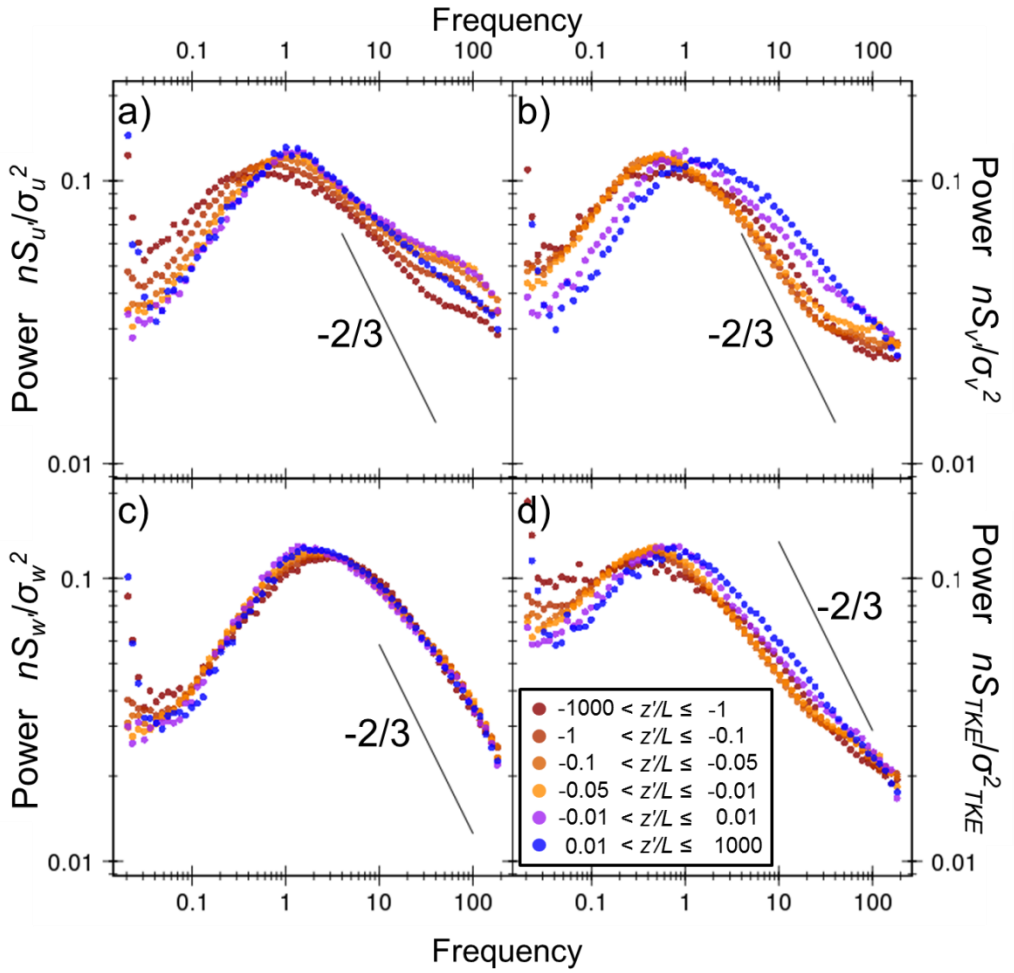

Figure 5.H.3: Power spectra for wind components (a) u, (b) v, (c) w , and (d) the turbulent kinetic energy divided into six stability classes (inset, d) with nondimensional frequency (f=nz'/U). Data collected at 10 Hz and 20 Hz (EC5-EC8) at height F, KSNW between 2013/086 and 2014/365.

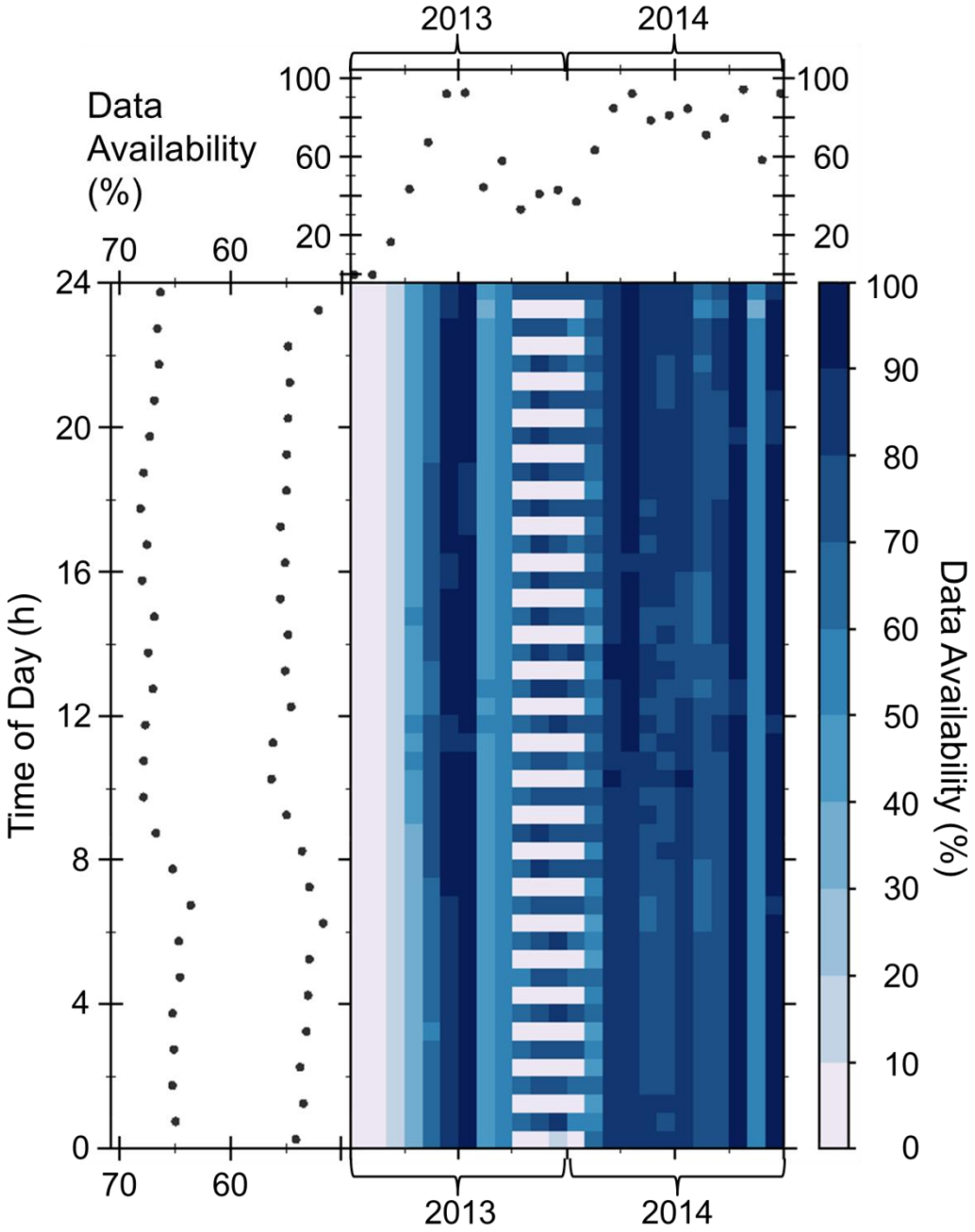

Figure 5.H.4: Percentage of half hourly periods which were present with sufficient data to be converted to half hourly energy spectra (CSAT3, height F, KSNW) for 2013 and 2014.

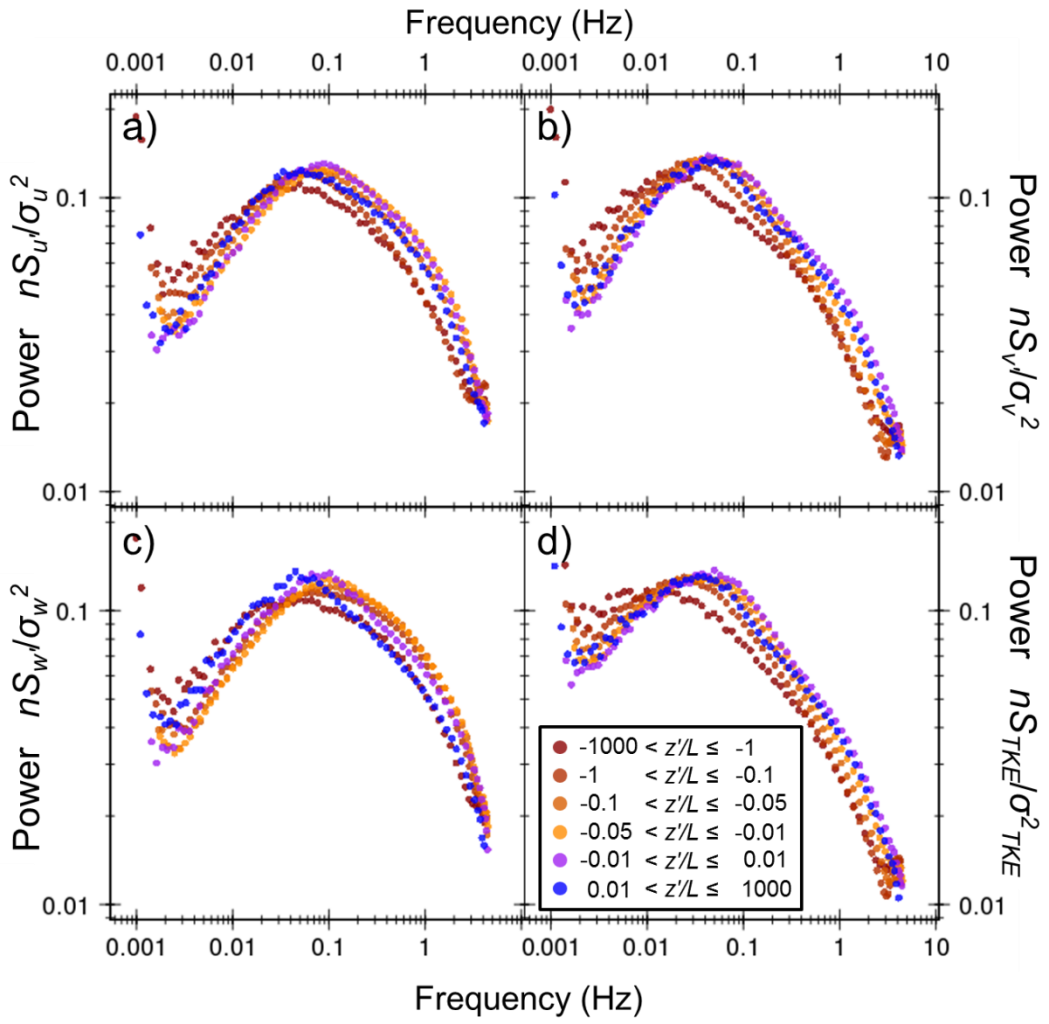

Figure 5.H.5: Power spectra for wind components (a) u, (b) v, (c) w, and (d) the turbulent kinetic energy divided into six stability classes (inset, d) with natural frequency. Data collected at 10 Hz and 20 Hz (EC5-EC8) at height F, KSB between 2013/086 and 2014/365.

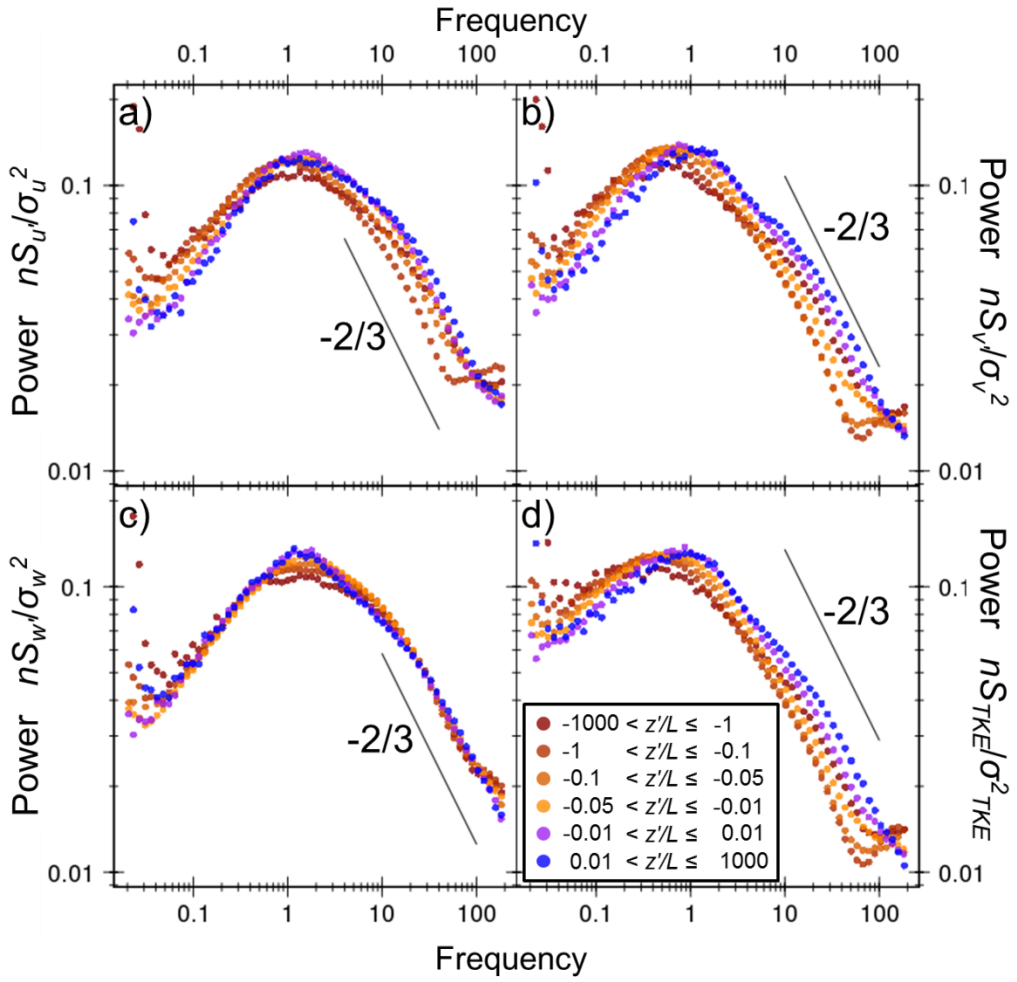

Figure 5.H.6: Power spectra for wind components (a) u, (b) v, (c) w , and (d) the turbulent kinetic energy divided into six stability classes (inset, d) with nondimensional frequency (f=nz'/U). Data collected at 10 Hz and 20 Hz (EC5-EC8) at height F, KSB between 2013/086 and 2014/365.

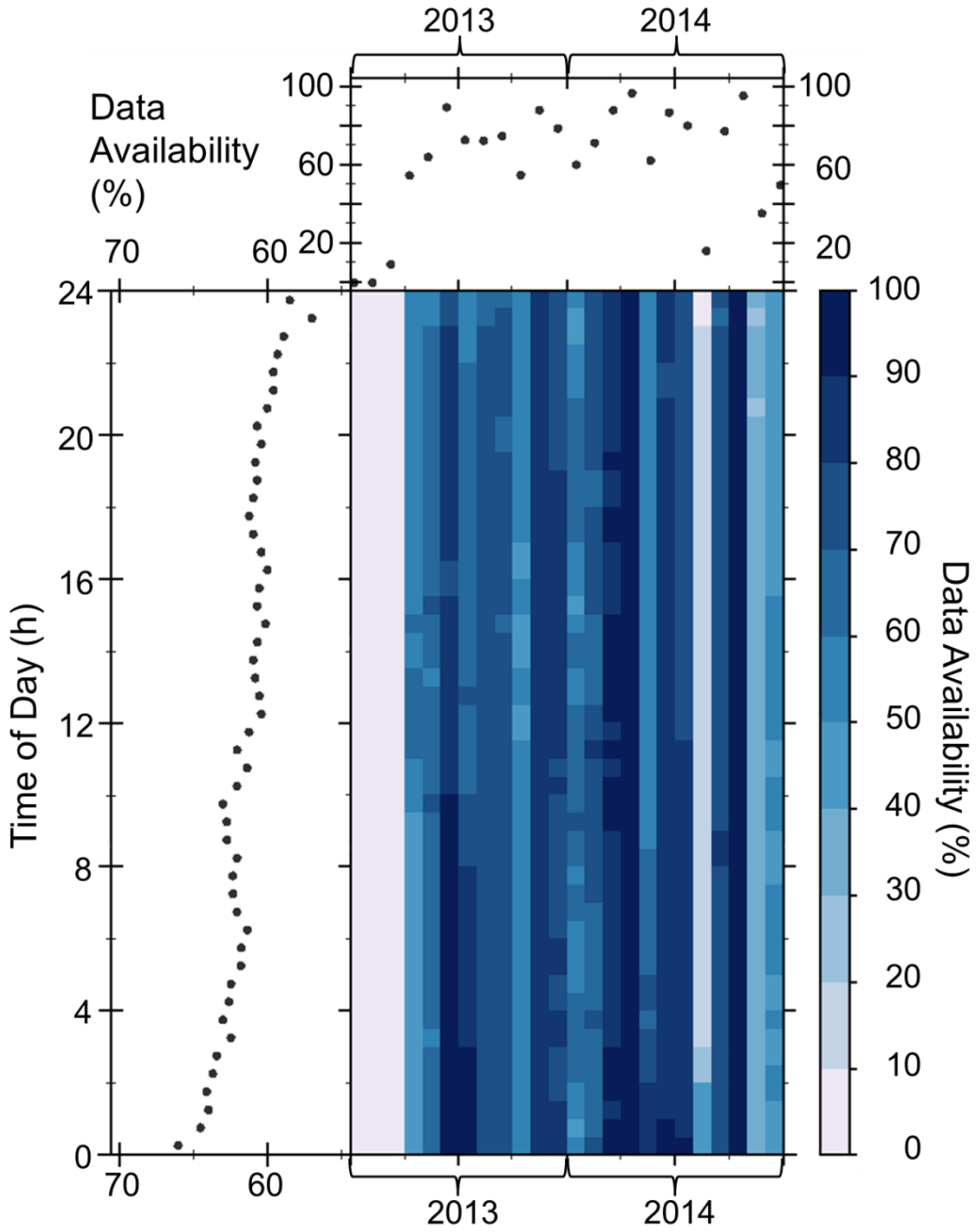

Figure 5.H.7: Percentage of half hourly periods which were present with sufficient data to be converted to half hourly energy spectra (Gill, height F, KSB) for 2013 and 2014.

Chapter 6 Land cover and carbon dioxide in central London

This chapter reports atmospheric carbon dioxide (CO_2) concentrations measured by a horizontal profile and mobile transects between 2012 and 2015. The variation of CO_2 mixing ratios and horizontal gradients with different urban land use and forms is investigated for three different land use schemes. The horizontal profile and walking transect measurements were measured in Central London, whilst bicycle and car mounted sensors provided measurements from the inner and outer zones as well.

6.1 Introduction

Partitioning of local scale CO_2 concentrations or vertical fluxes by e.g., source area may allow some inferences to be drawn regarding relative source and sink strength of different land use classes; however, ultimately measurements made within each land use class at a sufficient distance from the boundary for the signal to reflect only the land use class are necessary to quantify the effect of land use and land cover on urban CO_2 concentrations. The objective of this chapter is to investigate the horizontal variation of CO_2 concentrations and gradients and determine whether these are consistent with any land use or cover classification using a combination of mobile CO_2 sensors and a switched CO_2 profile.

Mobile CO_2 measurements along rural-urban transects have been made in Nottingham, UK (Berry and Colls, 1990), Phoenix, USA (Idso *et al.*, 2001) and Essen, Germany (Henninger and Kuttler, 2010). Measured daytime concentrations were typically found to be lower in areas with higher vegetation fraction such as the rural ends of the transect (Henninger and Kuttler, 2007). Urban enhancement of background rural CO_2 concentrations varied from 1.2% (Berry and Colls, 1990) to 41.9% for the inner city (Idso *et al.*, 2001). Within urban areas, both Henninger and Kuttler (2010) and Crawford and Christen (2014) measured lower daytime CO_2 concentrations over parkland than in residential areas (difference of 7 and 10.2 ppm respectively). Mobile CO_2 flux measurements made by Soegaard and Møller-Jensen (2003) 10 m above the ground in Copenhagen also found large differences between land use classes (22.3 and 38.4 g CO_2 m^{-2} day^{-1} for outer and inner residential areas compared to 14.4 and 302.6 g CO_2 m^{-2} day^{-1} for mixed green areas and roads respectively). It is clear that the surface characteristics can strongly affect CO_2 measured at the micro scale.

The objective of this chapter is to investigate the effect of different land cover, land use and neighbourhood factors on CO_2 concentration. In this chapter ‘land cover’ refers to the surface type, e.g., road, vegetation, river water, directly beneath the point at which a measurement was made, whilst ‘land use’ refers to the purpose of the immediate surroundings normal to the direction of travel, e.g., residential, retail, office. Neighbourhood factors include larger structures that might be expected to influence measurements from a distance, such as sewage works, motorways and the River Thames. In this chapter land cover, land use and neighbourhood factors are collectively referred to as ‘land categories’. Further aims include characterising the spatial scale of CO_2 variation in urban areas and the impact of street height to width ratio on CO_2 mixing ratios.

6.2 Site

All measurements reported in this chapter were made within the bounds of Greater London, a 1,570 km^2 (Nomis, 2011) metropolitan region in the United Kingdom that includes London, the capital city, and has a population estimated as 8.4 million in 2013 (ONS, 2014). Greater London has a relatively high vegetation fraction (47%, GiGL, 2015). Like many European cities, London has a densely urbanised historic core surrounded by more recent (mid-20^{th} century) residential developments. Due to 'protected view' legislation there are restrictions on the location of high rise buildings (GLA, 2012); as such the majority of office developments within the Central Activity Zone (CAZ) are concentrated in the vicinity of London Bridge. For further site details see Section 2.1.1.

6.3 Data

The data reported in this chapter were collected by a switched profile (Section 6.3.1) at the Strand campus of King's College London (KS) and three sets of transects (Section 6.3.2). The majority of the transect routes centre on KS, and CO_2 concentration (hereafter denoted as $[CO_2]$) data collected at KS at 2.21 times the mean building height is taken as a measure of local-scale CO_2 concentration, with the difference between local-scale and transect measurements denoted by $\Delta[CO_2]$.

6.3.1 Profile data

The profile measurements reported were measured along the front of the Strand building (Figure 2.1) by two LI840 gas analysers (LICOR, USA). Sample points were selected sequentially for 75 s using a valve array with a total cycle time of 10 minutes and concentrations were recorded at 2 Hz. See Section 2.2.1 for a description of the switched profile equipment and data processing.

6.3.2 Transect data

The $[CO_2]$ data was recorded by mobile CO_2 sensors along three sets of transects, TK, JD and GZ (Table 6.1) between 2012 and 2015. Transects TK1 – TK10 were located in the city centre and sampled only high density commercial urban environments (Figure 6.1c). JD1 – JD4 included the city centre but also sampled lower density terraced housing to the east and west of the CAZ (Figure 6.1b). GZ1 covered the widest range of land use categories, including open parkland, light industrial and low density detached housing (Figure 6.1a).

6.3.2.1 JD1 – JD4

Position data were recorded for the first four transects (JD1 – JD4) by Trackstick Mini GPS tracker at 4 to 10 s intervals. Latitude and longitude values were given to 5 and 6 decimal places respectively. The $[CO_2]$ data were collected using a mobile CO_2 sensor (Extech CO210 CO_2 analyser with built in data-logger, here referred to as the 'Extech') mounted at 1.2 m above ground level on the front of a bicycle. The Extech is a non-dispersive infrared gas analyser with 1 ppm resolution and an accuracy of ± 5% of reading + 50 ppm (FLIR Systems, 2014). The response time was found to be 23 seconds (Durrans, 2012).

Table 6.1: Transects reported in this chapter in sets of increasing number of London Zones sampled. All transects sampled air at 1 m a.g.l., apart from GZ1 which sampled air at 1.5 m a.g.l.

Transect	Mode of transport	Instrument	Date	Time (GMT)	London zones sampled
TK1	Walking	Greeneye/Extech	15/05/2013	15:08 – 16:39	CAZ
TK2	Walking	Greeneye/Extech	21/05/2013	12:10 – 14:26	CAZ
TK3	Walking	Greeneye/Extech	23/05/2013	11:18 – 11:54	CAZ
TK4	Walking	Greeneye/Extech	03/06/2013	12:28 – 14:41	CAZ
TK5	Walking	Greeneye/Extech	05/06/2013	13:34 – 16:29	CAZ
TK6	Walking	Greeneye/Extech	15/06/2013	12:08 – 14:18	CAZ
TK7	Walking	Greeneye/Extech	27/06/2013	09:42 – 11:42	CAZ
TK8	Walking	Greeneye/Extech	29/06/2013	13:33 – 15:39	CAZ
TK9	Walking	Greeneye/Extech	04/07/2013	06:55 – 09:06	CAZ
TK10	Walking	Greeneye/Extech	08/07/2013	07:55 – 10:08	CAZ
JD1	Cycling	Extech	10/07/2012	13:58 – 14:42	Inner, CAZ
JD2	Cycling	Extech	11/07/2012	10:15 – 11:44	Inner, CAZ
JD3	Cycling	Extech	12/07/2012	05:16 – 06:10	Inner, CAZ
JD4	Cycling	Extech	12/07/2012	12:55 – 13:55	Inner, CAZ
GZ1	Driving (car)	Picarro	20/03/2015	05:21 – 11:16	Outer, Inner, CAZ

CAZ: Central Activity Zone; Inner: boroughs defined as 'Inner London' by the Office of National Statistics (ONS, 2015b); Outer: boroughs defined as 'Outer London' by ONS (2015b).

Note: All transects except GZ1 were measured during 'British Summer Time', when the time zone is GMT+1.

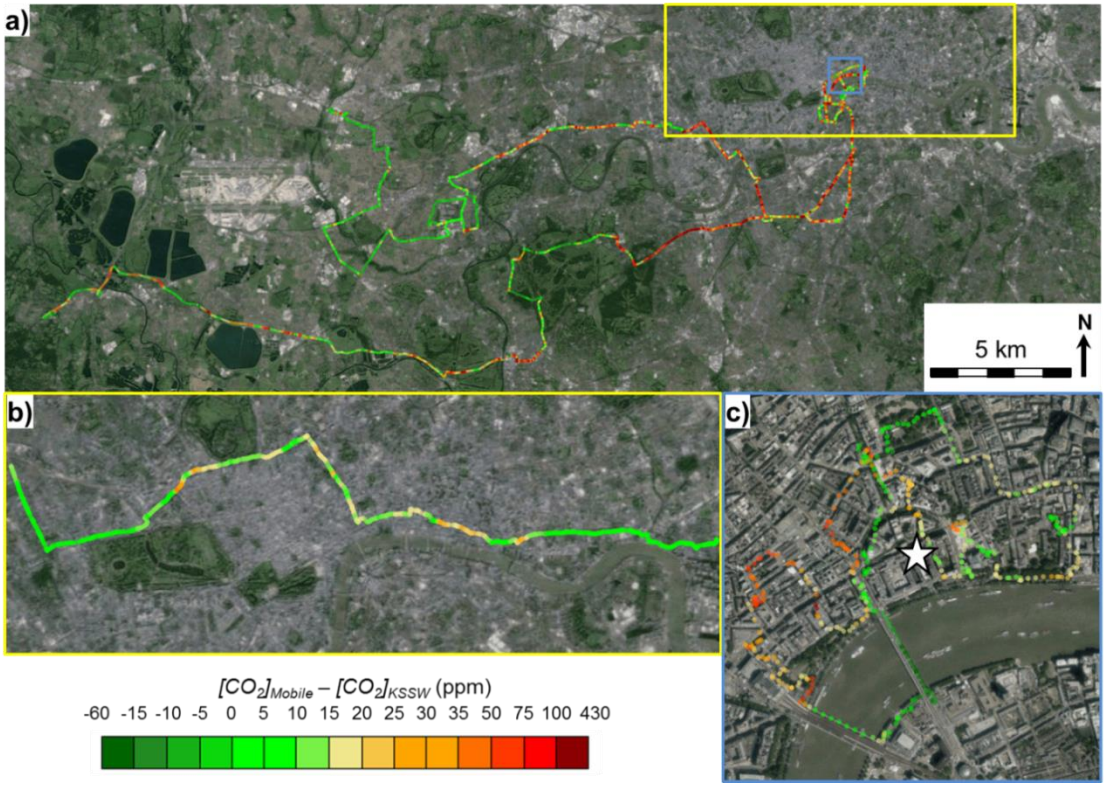

Figure 6.1: Three example transect routes and CO_2 concentrations (key: lower right) measured relative to those at KSSW height A (Figure 2.1d). (a) GZ1, (b) JD4, (c) TK6 (Table 6.1). Coloured rectangles (upper right, a) show location of b (yellow) and c (blue) relative to a. Position of KSSW shown as a white star, approximate centre of (c).

To protect the Extech from rain it was contained within a plastic box. Holes of 1 cm diameter were drilled in every side other than the lid to enable airflow to the sensor, which was cushioned with polyethylene foam. The Extech is capable of recording up to 5333 CO_2 values (FLIR Systems, 2014). The logging interval was set to 1 s, giving a total potential transect time of 88.9 minutes.

Both the Trackstick and the Extech were set to GMT (UTC+0) and the data were merged in R. Only *[CO_2]* data for which there was a concurrent location measurement were included for analysis – the position data were not interpolated. Prior to the transect measurements the Extech was co-located with a sample point of the vertical *[CO_2]* profiling system.

To ensure a smoothly varying local-scale signal and to interpolate the switched profile data, a loess curve with span 0.2 (4.8 h) was applied to the *[CO_2]* measurements at height A, KSSW (Figure 2.1d). The span was chosen after visual inspection showed it to capture the main features of the daily cycle, but not smaller scale variation less than 30 minutes in duration. This background signal was subtracted from the transect data.

6.3.2.2 TK1 – TK10

Position data for the 2013 transects (TK1 – TK10) were recorded by Garmin Foretrex 301 (Garmin, UK) to a precision of 5 and 6 decimal places for latitude and longitude respectively at irregular intervals ranging from 1 to 74 s with a mean of 13.3 s. Two model 7798 (AZ Instruments, Taiwan) CO_2 sensors, under the brand names Extech CO210 and Green Eye (Global Sensors, Belmont, USA) were used to record the CO_2 concentrations at regular 10 s intervals. Analysis reported in Appendix 3.A supports the use of linear interpolation of *[CO_2]* time series where the time series is not measured at the desired time points, and hence the CO_2 concentration data were interpolated to the position data. The Green Eye/Extech sensors assume atmospheric pressure of 1013 hPa. Measured *[CO_2]* data were therefore converted to mmol mol^{-1} using the assumed pressure, then converted to ppm using the measured pressure (WXT520, KSSW). The local-scale *[CO_2]* signal was subtracted from the street level CO_2 concentration measurements as with the JD1 – JD4 transects. As KSSW data were not available for TK1 the values from this transect are not included in the analysis.

6.3.2.3 GZ1

As position and *[CO_2]* data were measured by a Picarro (G2301, Picarro Inc., USA), no interpolation or matching was necessary. As with the other transects, ground level *[CO_2]* measurements were related to local scale measurements at KSSW.

6.3.3 Land use and land cover assignment

The three land cover schemes used in this chapter are as follows:

1) Land cover classification developed by Lindberg and Grimmond (2011) based on LiDAR data, referred to here as MM7C.

2) Land use and cover classification developed by Urban Atlas (European Union, 2011a) based on earth observation and “common off the shelf” navigation data, referred to here as UA.
3) Author defined scheme which includes land cover, land use, and neighbourhood factors such as sewerage works, referred to here as LCUN.

The first scheme has a horizontal resolution of 4 m x 4 m and covers 4000 m by 4000 m, approximately centred on KS (Figure 6.2a). The categories are building, road, open water, grass, shrub, deciduous trees and coniferous trees. No information about land use, such as retail vs. residential buildings, is provided. The second scheme is more detailed with 20 categories based on building density and land use (Figure 6.2b), and has been applied to cities in several European cities besides London. These categories were assigned with an overall accuracy of 86.8% (92.9% rural, 87.5% urban, European Union 2011b).

The third scheme was developed by visual inspection of transect routes either in person or via google maps. Although the position of each point on the transects relative to those before and after it was found to be reasonable, and the overall reported route agreed well with London’s unique street pattern, in areas of London with particularly deep street canyons the absolute position given by the Trackstick was sufficiently far from the road that automatic assignment of land use and cover was difficult and a combination of manual correction and 20 m ‘buffer zones’ around each point were used to determine the relevant land categories for the MM7C and UA LCSs. Manual assignment (LCUN) of land categories proceeded as follows: land cover was assigned as the surface over which the measurement was recorded and land use was assigned according to the buildings or lack thereof on either side of the point at which the measurement was recorded, and normal to the transect route. All cases where the land cover on either side of the transect was primarily vegetation were defined as ‘park’. Land cover classes were: A road, B road, cycle path, footpath and carpark. A roads and B roads are road classes for non-motorway roads in the UK, with A roads typically being larger and more traversed than B roads. Land use classes were: academic, bridge, carpark, hotel, light industrial, motorway, office, park (any predominantly vegetated space), residential, retail, stadium and tunnel. Whilst land cover classes are mutually exclusive (the measurement vehicle cannot be both on an A road and a footpath), the land use classes are not. In particular, the residential and retail classes were found to have significant overlap along main roads; the lower storey of buildings is used for retail and the upper for housing. ‘Neighbourhood’ factors were: London Underground stations, London Overground or National Rail stations, motorway, railway, reservoir or dock, the River Thames, sewage works and Thames Water Utilities Ltd. plant.

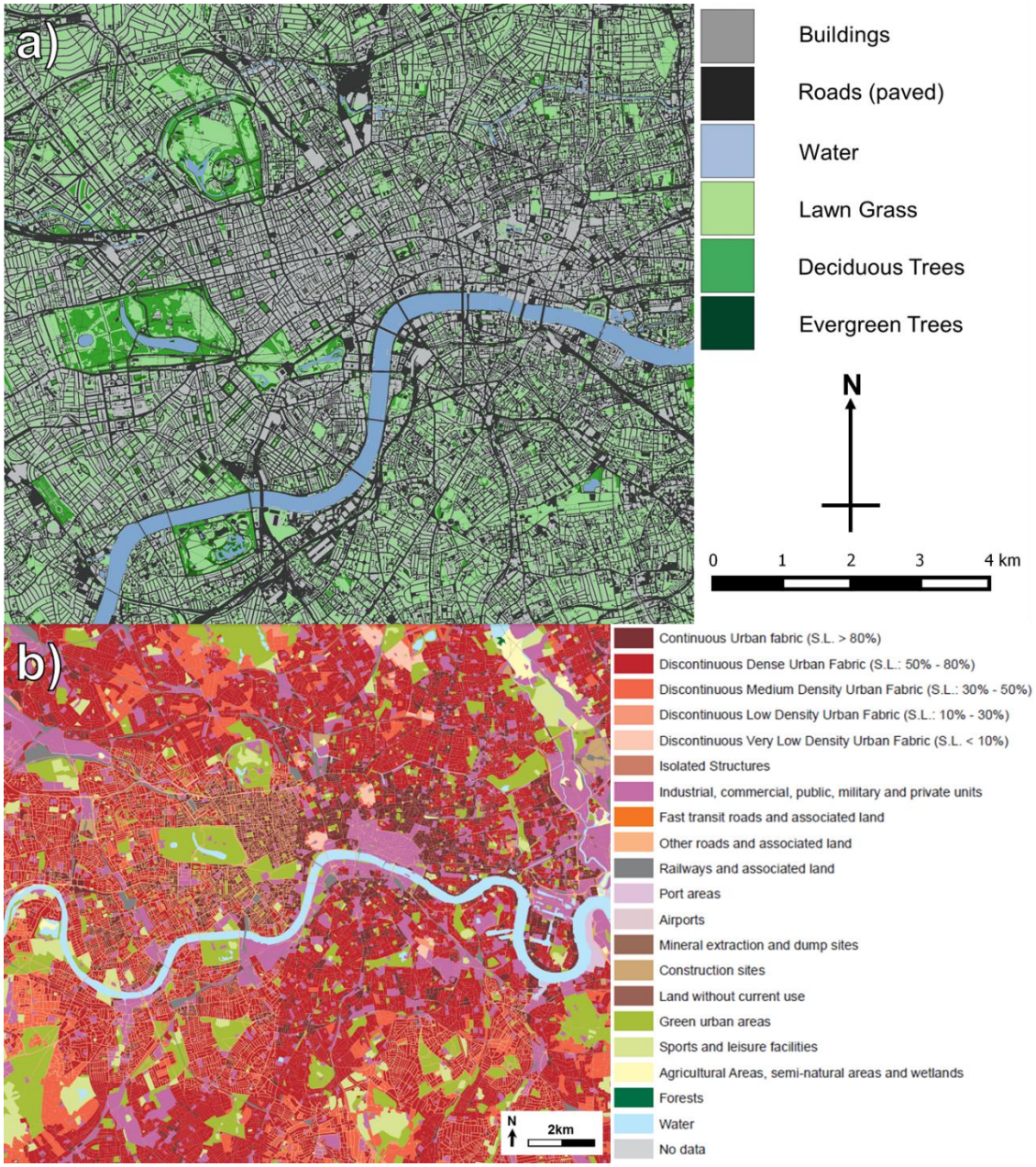

Figure 6.2: Two land classification schemes used in this study; (a) MM7C, plotted using British National Grid coordinate reference system, (b) UA, plotted using ETRS-LAEA coordinate reference system. "S.L. refers to 'sealed layer', see European Union (2011a). Land cover classes are given in the key on the right hand side of both maps.

6.3.4 Distance travelled

Position data for the mobile measurements were recorded as digital latitude and longitude. To calculate the horizontal *[CO_2]* gradient it was necessary to convert these to Cartesian grid co-ordinates. A set of *x*-*y* coordinates is part of the output of the PlotOnStaticMap (RgoogleMaps library, R) function (subfunctions: LatLong2XY.centred, LatLon2XY). The relevant parts of the subfunctions were extracted. Fourteen pairs of coordinates (Table 6.2) were located from google maps. They were chosen to span a range of distances from the tens of m (length of the KS building) to over a km (site ref. 11, Table 6.2), and to have a roughly equal number of north-south and east-west bearings. The distance between each pair of coordinates was calculated

from manual measurement of google maps and from an online geodesic calculator (GeodSolve, 2015; Karney, 2013) as a secondary check against measurement errors.

A linear regression of the manually measured distances with the plotting output of the modified LatLong2XY function (LatLong2XY_M) showed good agreement (R^2>0.999). The coefficients of the line of best fit (forced through the origin) were used to convert the LatLong2XY_M output to Cartesian coordinates. This function and conversion factor was applied to the transect position data and the distance between consecutive position measurements calculated as the hypotenuse of a triangle constructed of the change in x and y co-ordinates. Measurements closer than 5 m or greater than 50 m apart on the transect were removed prior to calculation of the horizontal $[CO_2]$ gradient, which was only calculated along the direction of the transect. Measurements made in e.g., parallel streets were not considered for comparison as transfer of CO_2 at 1.2 m above street level is more likely along streets than through buildings.

6.3.5 Identification and removal of 'edge effects' between land use and cover categories

One of the objectives of this chapter is to investigate the effect of different land cover, land use and neighbourhood factors on $[CO_2]$. It is therefore not ideal if measurements listed as one land use or cover type are influenced by a neighbouring one, i.e., if the surface layer has not fully adjusted to the surface type. To try and define a 'buffer' distance beyond which measurements could reasonably be considered to be representative of the assigned land cover, the distance from the closest 'border' for each land cover/use class was calculated for each transect measurement. This was done as follows: the distance of each measurement from the previous measurement point was calculated in metres using the method described in Section 6.3.4. A land use/cover type was selected, and all distances for points not of that category were set to NA. This allowed the vector of distances to be divided into factors for each contiguous set of measurements within a land use/cover category. The distance was cumulatively summed for each factor to give the distance from the entry point of the land use/cover type. The factorised vector of distances was then reversed and the cumulative sum taken again to get the distance of each measurement from the exit point of the land use/cover type. The distance from the boundary for each measurement location was then defined as the minimum of these two values. It should be noted that this method only considers the distance long the transect from the land use/cover border. It does not consider the distance perpendicular to the direction of travel, that is, it assumes the primary horizontal movement of CO_2 is parallel to the transect. Within street canyons this assumption is probably reasonable; it is less likely to hold in more open spaces, such as parks, bridges and lower density residential areas. It also does not account for mixed land use, for example spaces that are purely residential vs. residential and retail.

Mean $\Delta[CO_2]$ was calculated for data subset by distance from the boundary at 10 m intervals i.e., all data > 0 m, all data > 10 m, etc. No coherent or consistent trend for the majority of land use/cover types was found for any of the sets of transect data, and therefore in this chapter all measurements have been used.

Table 6.2: Table of distances in metres between selected sites as calculated from a map, online arc-length calculator GeodSolve (Geod), and in-house function LatLong2XY_M (LL2XY_M). Calculated Root Mean Squared Error (RMSE) given for comparison of calculated distances. All values given to three decimal places. Where stations are named sites, the London Underground station was used. Latitude and Longitude values used to calculate distances were recorded to 5 d.p. and have been truncated for presentation.

Sites			From		To		Distance (m)			RMSE (m)		
Ref	From	To	Lat	Lon	Lat	Lon	Map	Geod	LL2XY_M	Map to Geod	Map to LL2XY_M	Geod to LL2XY_M
1	Charing Cross	BFI Imax	51.507	-0.127	51.505	-0.114	1053.125	984.243	990.394	6.382	0.231	6.151
2	Blackfriars Bridge, south west	Blackfriars Bridge, north west	51.509	-0.105	51.511	-0.105	250.000	247.345	249.505	2.655	0.495	2.160
3	HMS President, west	HMS President, east	51.511	-0.109	51.511	-0.108	84.706	83.834	84.348	0.872	0.358	0.514
4	King's Strand, north east	King's Strand, north west	51.512	-0.116	51.512	-0.117	71.346	68.120	68.570	3.226	2.776	0.450
5	St Clement Danes (spire)	St Mary-le-Strand (spire)	51.513	-0.114	51.512	-0.117	227.451	230.840	232.402	3.389	4.951	1.562
6	Lincoln's Inn Fields, south west	Lincoln's Inn Fields, north east	51.515	-0.118	51.518	-0.115	353.125	348.815	351.582	4.310	1.543	2.767
7	Tottenham Court Road	Holborn	51.516	-0.130	51.518	-0.120	732.813	698.848	703.291	33.965	29.521	4.443
8	Tottenham Court Road	Leicester Square	51.516	-0.130	51.511	-0.128	581.250	574.827	579.817	6.423	1.433	4.990
9	St Stephen's Tower	The Old Vic	51.501	-0.125	51.502	-0.109	1075.000	1077.354	1083.791	2.354	8.791	6.437
10	Smithfield Market, north west (spire)	Smithfield Market, north east (spire)	51.519	-0.103	51.520	-0.100	185.098	184.349	185.615	0.749	0.517	1.266
11	Warren Street	King's Cross	51.525	-0.138	51.531	-0.123	1231.250	1226.602	1235.452	4.648	4.202	8.850
12	Leicester Square	Charing Cross	51.511	-0.128	51.507	-0.127	450.000	449.389	453.275	0.611	3.275	3.886
13	Aldwych junction	BFI Imax	51.511	-0.119	51.505	-0.114	818.750	818.268	824.895	0.482	6.145	6.627
14	London Eye Pier, north	London Eye Pier, south	51.504	-0.120	51.503	-0.121	94.118	94.115	94.920	0.003	0.802	0.805
									Total	70.068	65.043	50.910

6.3.6 Derivation of street height: width ratios from a London Digital Elevation Model (DEM)

A 4 m resolution DEM of the Greater London region in '.asc' format was divided into 1 x 1 km regions or 'tiles' for processing in Matlab (see Lindberg *et al., 2*015 for details). It was necessary to divide the data as processing time increased with the square of the grid size. The output files consisted of matrices with location defined by row and column position. All entries were set to NA except for those in the centre of a street, which gave the associated height: width ratio (Figure 6.3). The relevant output tiles for each transect were collated in R and each non-NA entry assigned a position relative to fixed reference point, which was chosen to be the Queen Eleanor Memorial Cross (QEMX) as this was a clearly defined single point in the output and was close to a portion of all transect routes. The program described in Section 6.3.4 was used to convert all transect data to x and y co-ordinates in m relative to QEMX. Transect points were matched to the closest height:width ratio value, with values excluded from analysis if the distance was greater than 2 grid points in the x and/or y direction (as the grid was 4 m resolution this distance was 11.3 m).

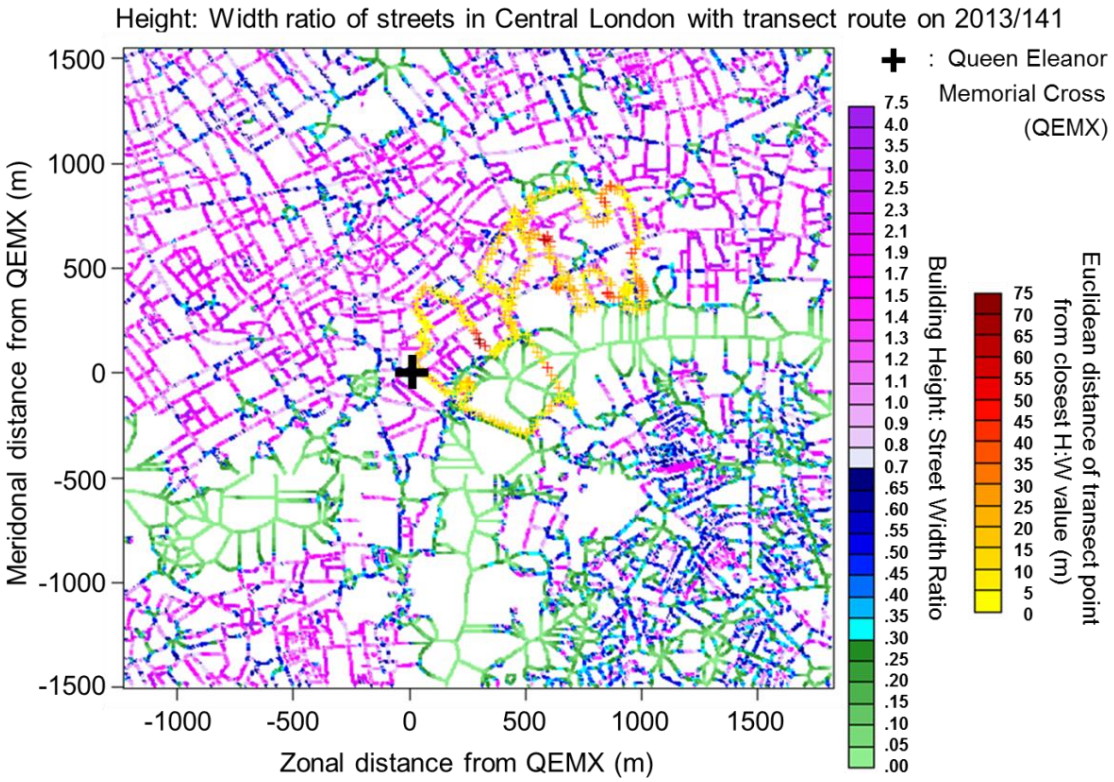

Figure 6.3: Height: Width ratio of streets in Central London with transect route TK2 (Table 6.1). Figure shows approximately the same area as Figure 6.1c. Position of QEMX indicated with a black cross.

6.4. CO_2 Concentration by land use and land classification scheme

In this section measured CO_2 concentrations over different land use and cover types are compared and the statistical significance of any difference found is evaluated.

Visual inspection of transect measurements (Figure 6.4a) shows distinct spatial patterns with e.g., measurements made on bridges or along the southern river bank are substantially (up to 40 ppm) lower than those made further inland. Green spaces can have lower concentrations (e.g., Lincoln's Inn fields), but this is not observed for those adjacent to major roads (e.g., Embankment gardens) (Figure 6.4a). There does not appear to be a discernible difference in $\Delta[CO_2]$ measured on A roads and B roads (Figure 6.4b), both tending to be higher than footpaths. Despite the ability of traffic along major roads to elevate $[CO_2]$ in urban greenspace, the low and negative $\Delta[CO_2]$ along bridges and riverside footpaths (Figure 6.4b, 1 – 2 km) suggest ventilation is key to reducing pollutant concentrations in highly urbanised environments. These hypotheses are investigated further in the following sections.

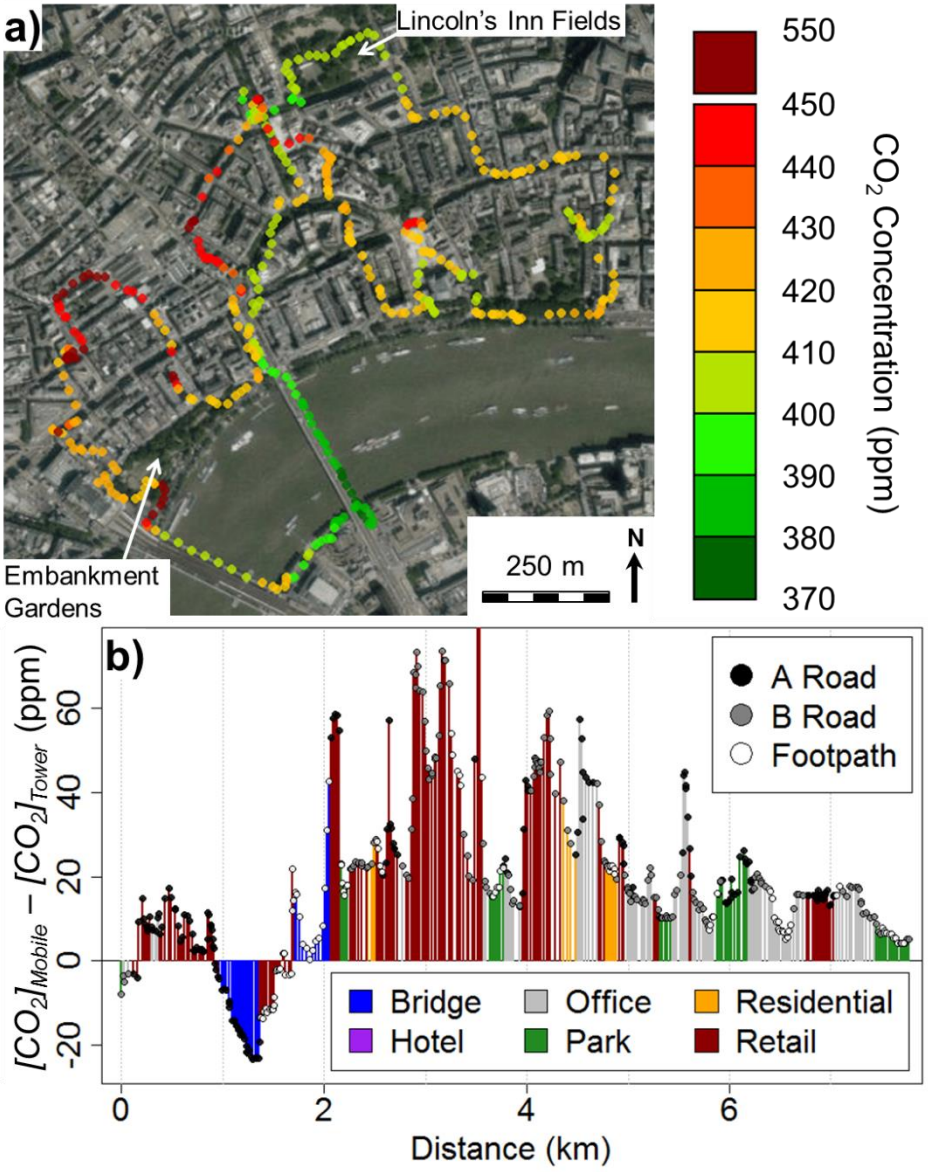

Figure 6.4: CO_2 concentrations measured on transect TK6 (Table 6.1) (a) as absolute values plotted over their mapped position (key: upper right); (b) as differences from KSSW coloured by (points, key: upper right) land cover and (lines, key: lower right) surrounding land use derived from land cover scheme LCUN.

6.4.1 Central London: TK2 – TK10

CO_2 concentration measurements from transects TK2 – TK10 (1 m a.g.l., Section 6.3.2.2) range from 23 ppm below to 143 ppm above measurements at height A, KSSW (46.4 m, a.g.l., Figure 2.1d), with the majority (80%) of $\Delta[CO_2]$ values 3 – 49 ppm greater than the background. Although some land use/cover classes tended to have higher median values than others (e.g., A roads vs. B roads, Figure 6.5; roads vs. water, Figure 6.6a, b), negative $\Delta[CO_2]$, where observed, tends to occur in the majority of classes for a particular transect, rather than a particular class for the majority of transects. Negative $\Delta[CO_2]$ values were not associated with any particular stability class or wind direction and although they were observed on both Saturday transects (TK6 and TK8), the results from TK5 (Wednesday the 5th June) suggest that negative relative concentrations are not associated with any particular day of week.

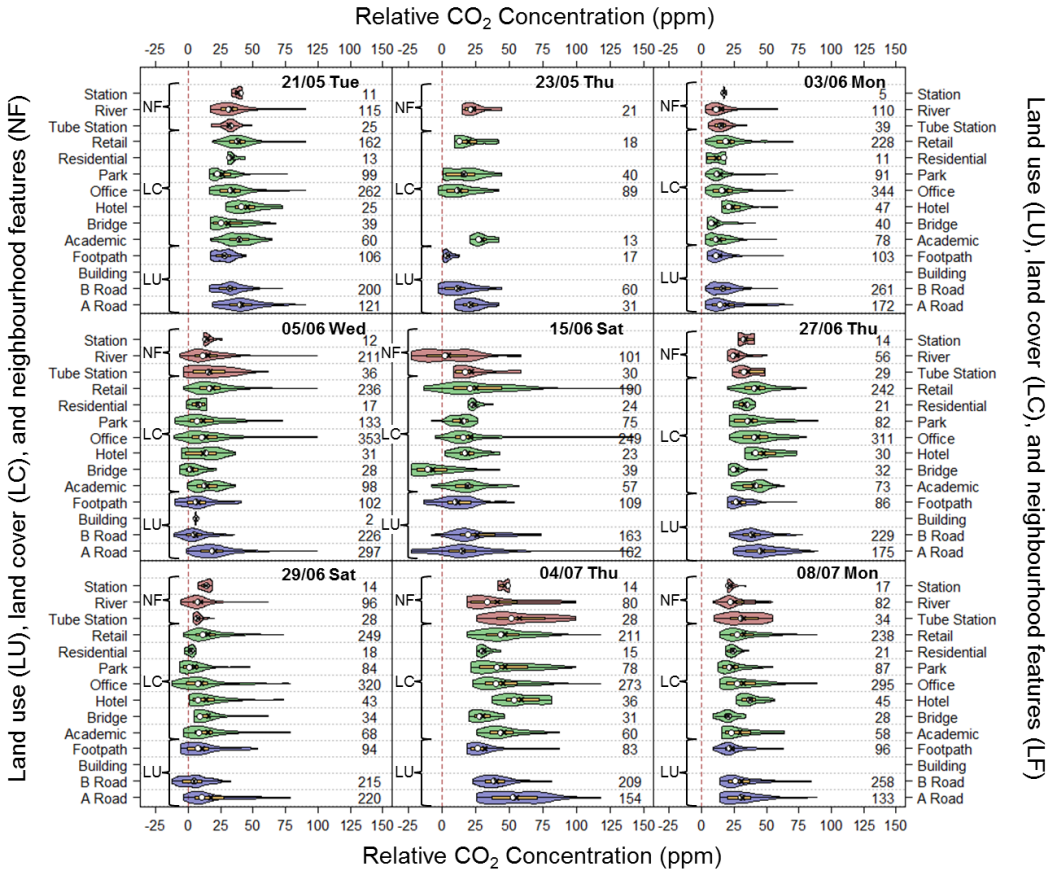

Figure 6.5: Violin plot of CO_2 concentration measured by Greeneye/Extech relative to CO_2 measured at height A, KSSW (Figure 2.1d) in ppm binned by the land use (LU), land cover (LC) and neighbourhood features (NF) (y-axis) (LCUN). Number of measurements within each class listed at 150 ppm. Median: white circle, mean: black cross, interquartile range: pale bar, data distribution: coloured envelope. Date and day of week of transect upper right of each plot. Code modified from vioplot (Adler, 2005).

There was no significant difference in mean half hourly wind speeds (Welch two sample t-test, *t.test* function, R Development Core team, 2013) for transects with negative $\Delta[CO_2]$ compared to those without. The mean above-canyon $[CO_2]$ is 5 ppm lower on transects with negative $\Delta[CO_2]$ than on the others (396 and 401 ppm respectively) and this difference is significant (p = 0.002). This suggests that the phenomena are not due to higher than average roof top CO_2 emissions from building vents, boilers, etc. Comparison of the mean time since dawn for TK5,

TK6 and TK8 to the mean time since dawn for the other transects with a Welch two sample t-test suggested the difference in mean time (10 h, 32 minute and 7 h, 10 minute respectively) was significant at the 5%, but not the 1% level (p=0.015). The indicated hypothesis, that ground level concentrations are likely to be lower than those measured at height A, KSSW (Figure 2.1d) layer with increasing time since dawn, is revisited in the following section.

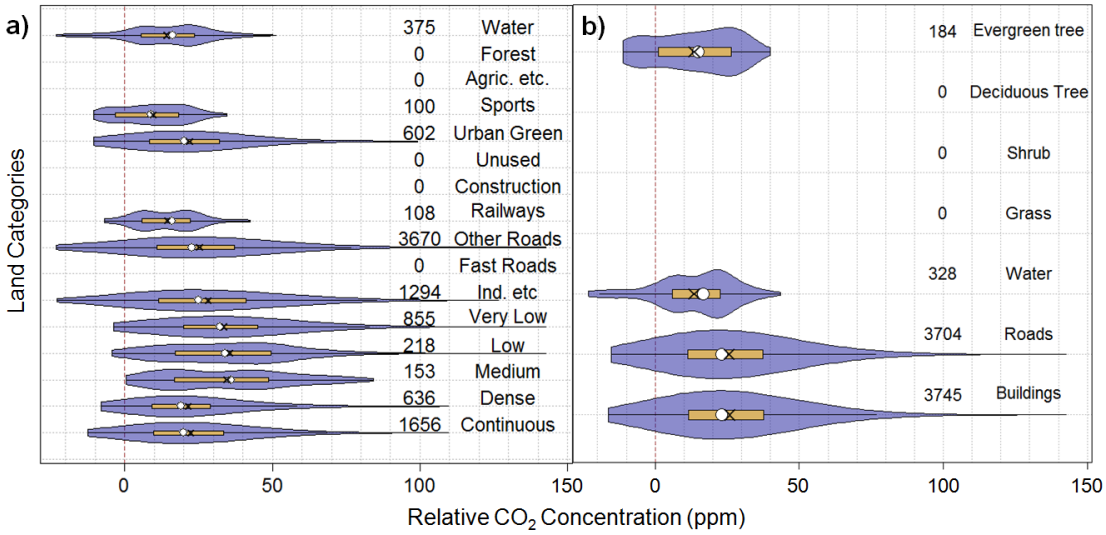

Figure 6.6: Violin plot of CO_2 concentration measured by Greeneye/Extech during TK2 – TK10 relative to CO_2 measured at height A, KSSW (Figure 2.1d) in ppm binned (a) UA and (b) MM7C land categories. Number of measurements within each class listed at 125 ppm. Median: white circle, mean: black cross, interquartile range: pale bar, data distribution: coloured envelope. Code modified from vioplot (Adler, 2005).

CO_2 concentrations relative to those at height A tended to be positively skewed across all land categories and land classification schemes (Figure 6.5, Figure 6.6). In other words, extremely high $\Delta[CO_2]$ occurred more frequently than extremely low $\Delta[CO_2]$. Higher $\Delta[CO_2]$ was observed across all land categorisation schemes (LCSs) for classes which contained buildings or roads compared to those with predominantly unsealed surfaces such as water (or river) and greenspace (park or trees); however, $\Delta[CO_2]$ was not found to increase with building density (Figure 6.6a). Instead, $\Delta[CO_2]$ was highest for medium to low density areas (UA, 10% - 50% of the surface covered by buildings) with $\Delta[CO_2]$ in areas categorised as having dense to continuous urban fabric (UA, >50% of the surface covered by buildings, Figure 6.2b) equal or lower, on average, to that observed in urban green spaces. Inspection of the transect route suggests that this may be due to characteristics unique to central London, rather than those inherent in the land classification. These consist of high traffic emissions adjacent to the sampled urban greenspace (the Victoria Embankment A road) and low traffic emissions due to pedestrianisation of the high density to continuous urban fabric areas (Covent Garden market). This hypothesis is examined in Section 6.4.3.

6.4.2 Central and inner London: JD1 – JD4

Despite the greater spatial scale, the range of $\Delta[CO_2]$ observed during transects JD1-4 (-10.6 to 63.4 ppm) was smaller than for TK2-10. Again, slightly more than 80% of the data were greater than 0, with a median elevation of 6.8 ppm (8.8 ppm if JD3, a transect with negative $\Delta[CO_2]$ in all categories, was excluded). All LCUK land categories except cycle path had

positive median $\Delta[CO_2]$; however, half of the cycle path values were measured during JD3 and if data from this transect is excluded, median $\Delta[CO_2]$ measured over cycle paths was 5.6 ppm. In other words, all land categories show raised CO_2 relative to background levels.

LCUK land categories whose median $\Delta[CO_2]$ was greater than 1 ppm above the overall median $\Delta[CO_2]$, both when JD3 was included and when it was not, are the A road, academic, office, retail, London Underground station and Overground/railway station categories (1.7, 3.7, 3.1, 1.6, 1.4, 2.3 ppm above the overall median respectively when JD3 is included). Lowest $\Delta[CO_2]$ values were observed for the following land categories: cycle path, bridge, tunnel, motorway and reservoir but all of these bar the cycle path and motorway category had fewer than 20 data points. Concentrations measured within or adjacent to parks were approximately equal to the overall median. This may be because transects JD1-4 were measured on roads adjacent to parks, rather than through them, as with TK2-10 and GZ1.

Median $\Delta[CO_2]$ was positive for all UA land categories with the exception of water (Figure 6.8b). Lower $\Delta[CO_2]$ values were measured in areas categorised as having higher building density (medium, dense and continuous urban fabric) compared to areas categorised as very low to low building density; however, the low number of $\Delta[CO_2]$ values in the very low (52) and low (46) building density classes limits confidence in this observation. Median $\Delta[CO_2]$ in the medium to high building density areas were approximately equal to that observed on roads adjacent to urban greenspace (no transects were made off road through parkland) and to that observed for the 'other roads' class. This suggests that the primary source of CO_2 in the medium to high building density areas, and adjacent to the urban greenspace, is vehicle emissions. Traffic is also likely to be the cause of the elevated $\Delta[CO_2]$ recorded in the very low to low building density classes – all values in these classes were recorded close to traffic lights on major thoroughfares.

As with the results from TK2 – TK10, the $\Delta[CO_2]$ distributions in the road and building MM7C land categories are very similar. The median values for 'evergreen trees' are slightly higher, potentially due to the presence of a main road adjacent to the parks sampled in these transects.

Like the TK transects, a JD transect was measured with predominantly negative $\Delta[CO_2]$. Unlike TK 5, 6 and 8, this transect (JD3, Figure 6.7c) was performed only one hour, 45 minutes after dawn, between 06:16 and 07:10 BST (GMT +1). During this time period the traffic intensity rises from the nocturnal trough to 2/3 of the day-time maximum (Section 4.5.1). Incoming shortwave radiation also increases rapidly and net radiation changes from negative to positive (Appendix 2.B). Overall, lower CO_2 concentrations at ground level compared to those aloft seem to be associated with transitional periods as the land surface begins to heat or cool, and residential, rather than commercial (office, retail, hotel) or institutional (academic) building use (Figure 6.7).

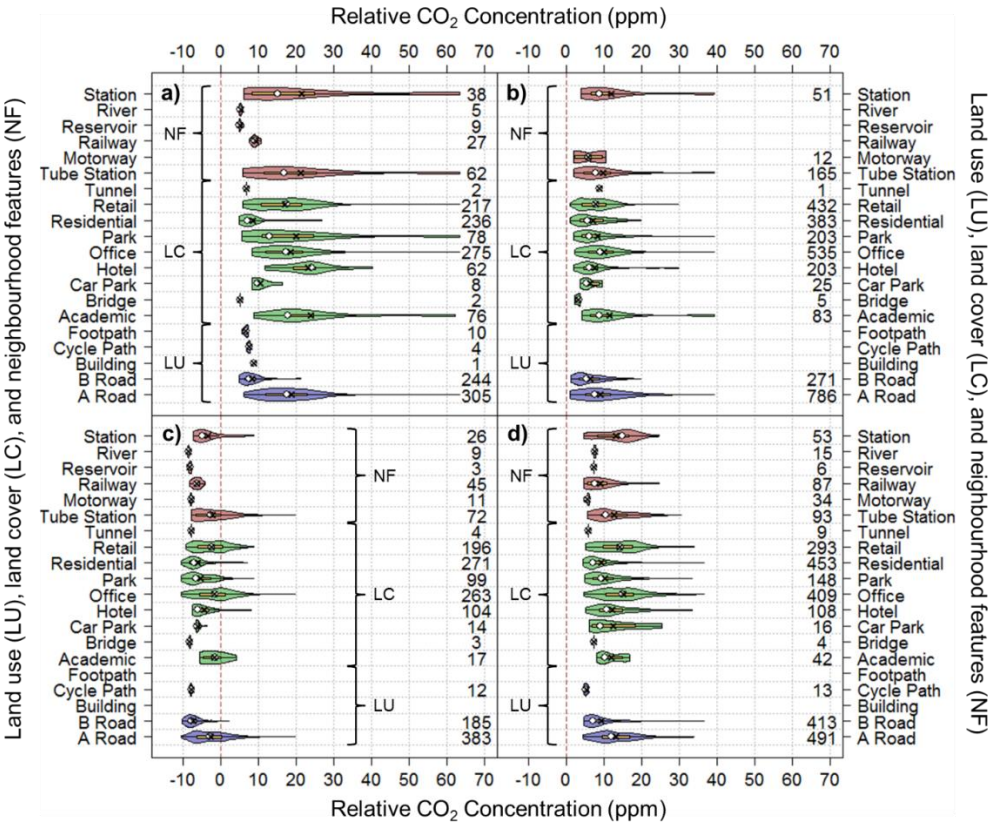

Figure 6.7: Violin plot of CO_2 concentration measured by Extech relative to CO_2 concentration measured at height A, KSSW (Figure 2.1d) in ppm for (a) Tuesday 10/07/2012, 13:58 – 14:42; (b) Wednesday 11/07/2012, 10:15 – 11:44; (c) Thursday 12/07/2012, 05:16 – 06:10; (d) Thursday 12/07/2012, 12:55 – 13:55. Data are binned by the land use (LU), land cover (LC) and neighbourhood features (NF) (y-axis) (LCUN). Number of measurements within each class listed at 65 ppm. Median: white circle, mean: black cross, interquartile range: pale bar, data distribution: coloured envelope. Code modified from vioplot (Adler, 2005).

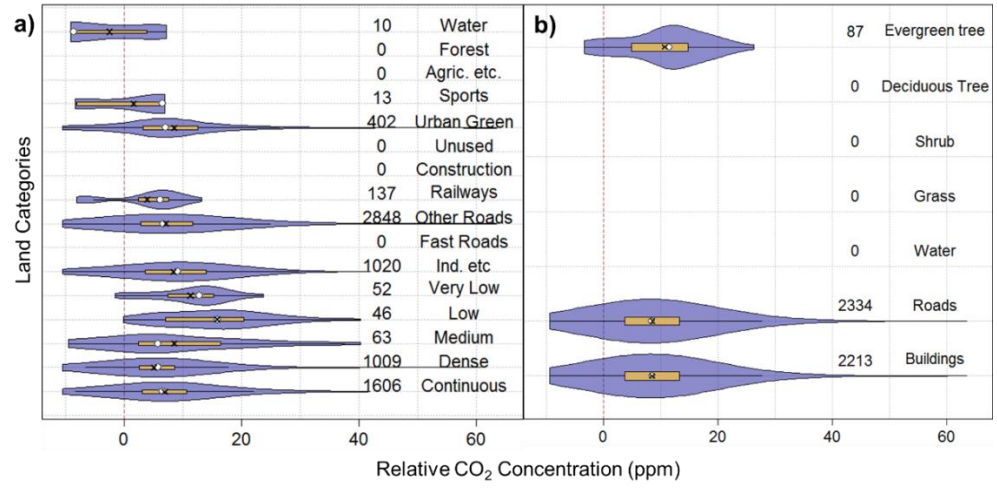

Figure 6.8: Violin plot of CO_2 concentration measured by Greeneye/Extech relative to CO_2 measured at height A, KSSW (Figure 2.1d) in ppm binned (a) UA and (b) MM7C land categories. Number of measurements within each class listed at 50 ppm. Median: white circle, mean: black cross, interquartile range: pale bar, data distribution: coloured envelope. Code modified from vioplot (Adler, 2005).

6.4.3 Greater London: GZ1

Transect GZ1 covers the greatest horizontal distance and number of land categories. It is the only transect to include the semi-rural (Egham, UK), and low-density industrial (Hounslow, UK)

fringe of the Greater London region. It is therefore not unexpected that the GZ1 transect records the greatest range in $\Delta[CO_2]$ (-51.3 to 429.2 ppm) of all the transects. The variability within each land category is greater than between land categories (Figure 6.9, Figure 6.10). Despite this some general trends can be discerned.

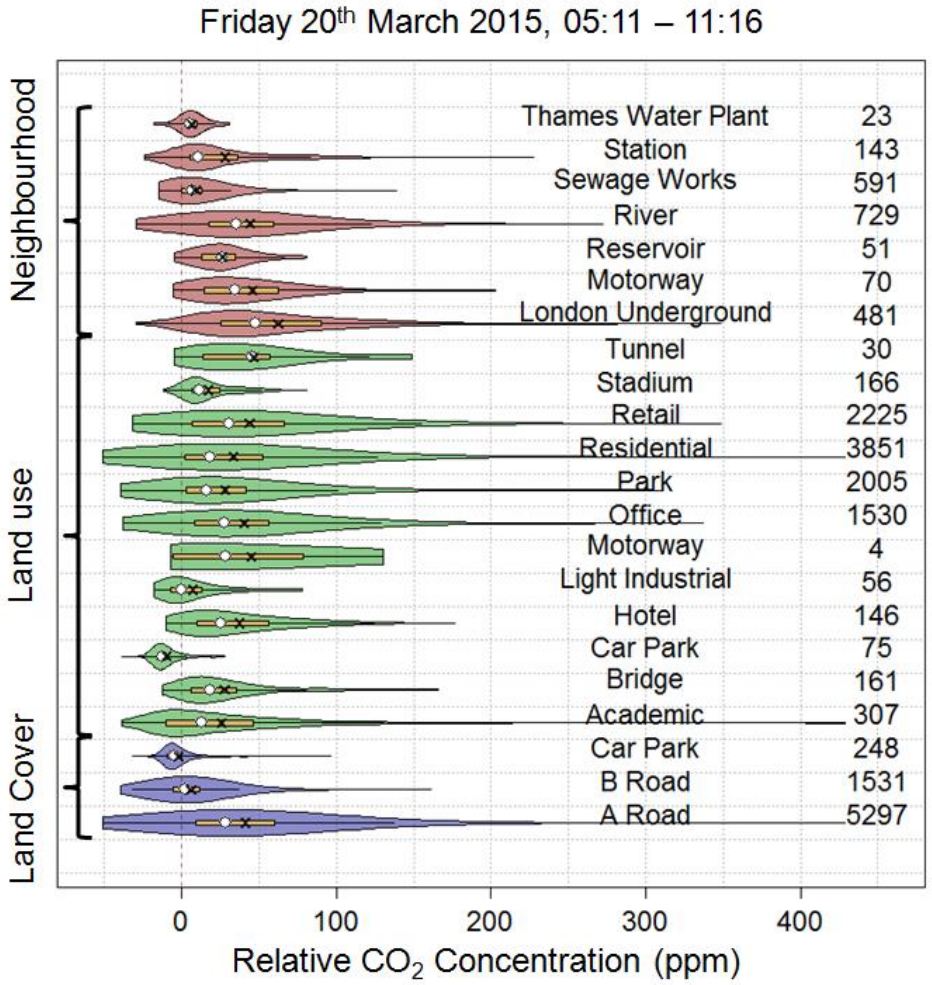

Figure 6.9: Violin plot of CO_2 concentration measured by Picarro relative to CO_2 concentrations measured at height A KSSW (Figure 2.1d) in ppm binned by the land use, land cover and neighbourhood features (LCUN) listed at 300 ppm. Number of measurements within each class listed at 450 ppm. Median: white circle, mean: black cross, interquartile range: pale bar, data distribution: coloured envelope. Code modified from vioplot (Adler, 2005).

High traffic (LCUN: Motorway, A road) land categories generally have higher $\Delta[CO_2]$ than lower traffic (LCUN: B road) categories, and land categories associated with the city centre (LCUN: London Underground stations, retail, office and hotel) tend to have higher $\Delta[CO_2]$ than those associated with the suburbs (LCUN: Thames Water plant, sewage works, reservoir, residential and park). Park in this transect was primarily Richmond park, a 995 hectare (HC Deb (2001-02) 379 col. *1113W*) nature reserve approximately 8 km to the south west of KS. In this transect $\Delta[CO_2]$ measured within very low and low building density areas (UA) were again higher than those measured in medium and high building density areas; however, 'continuous urban fabric', the land category with the highest building density, also has the highest median $\Delta[CO_2]$ of all land categories with greater than 20 values (Figure 6.10a). This may be due to the spatial distribution of the categories within the city. Medium and dense building densities are found

primarily outside the central activity zone (CAZ, Section 2.1) of London (only 0.9% and 4.3% of $\Delta[CO_2]$ measurements for those land classes respectively were within the CAZ), whilst continuous urban fabric (44.1%), low (86.1%) and very low (100%) all had much higher percentages of $\Delta[CO_2]$ measurements within that land category made within the CAZ. A linear regression of the median $\Delta[CO_2]$ for the UA land categories on the percentage of the $\Delta[CO_2]$ values for each land category that were measured within the CAZ had a non-adjusted R^2 value of 0.27, suggesting there may be some effect but that other factors also play a role.

This analysis can be extended by examining periods with negative $\Delta[CO_2]$ before, during, and after the measurement vehicle drove through the central activity zone (CAZ) of London. Of all measurements with negative $\Delta[CO_2]$ and a horizontal separation from the adjacent measurement of greater than 5 m (i.e., vehicle speed of greater than 1.67 m s^{-1}), 62.5% were made prior to the CAZ, 10.2% within the CAZ, and 27.3% after the CAZ. Conversely, 36%, 36% and 28% of all $\Delta[CO_2]$ measurements greater than 200 ppm were made prior, during and after the CAZ respectively, compared to a horizontal distance travelled of 42.2%, 18.8% and 39.0%. Overall it can be seen that low (negative $\Delta[CO_2]$) is greater in the morning and outside the city centre, whereas high ($\Delta[CO_2]$ > 200ppm) is elevated relative to distance travelled within the high density, high traffic city centre.

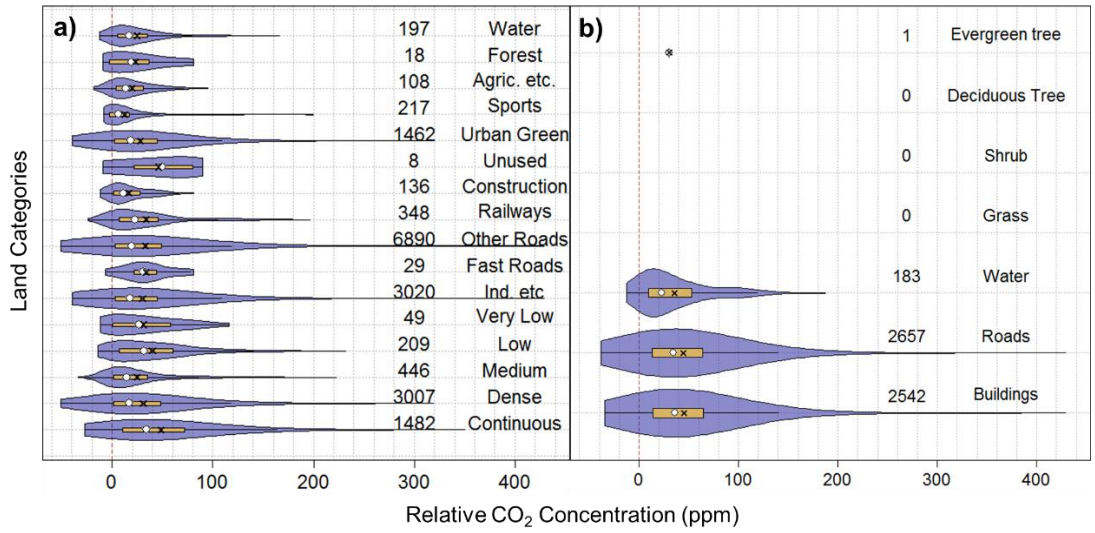

Figure 6.10: Violin plot of CO_2 concentration measured by Picarro relative to CO_2 measured at height A, KSSW (Figure 2.1d) in ppm binned (a) UA and (b) MM7C land categories. Number of measurements within each class listed at 300 ppm. Median: white circle, mean: black cross, interquartile range: pale bar, data distribution: coloured envelope. Code modified from vioplot (Adler, 2005).

6.4.4 Discussion

This section focuses on whether differences between aggregated $\Delta[CO_2]$ for each land category within an LCS are significant, and which LCS has the lowest intra: inter-category variation of $\Delta[CO_2]$, or in other words, which LCS generates subsets of $\Delta[CO_2]$ which are most distinct from each other and therefore have the greatest value if attempting to predict $\Delta[CO_2]$ from a land cover map.

By aggregating data from multiple transects (Figure 6.5 to Figure 6.10; Table 6.A.1 to Table 6.A.3 in Appendix 6.A) it can be seen that categories associated with human activity, such as buildings and roads tended to have higher $\Delta[CO_2]$ compared to more 'natural' classes such as water or river. The exceptions are railways (London lines are electrified, rather than burning diesel or other fuel), which tend to have very low $\Delta[CO_2]$, and parks, which tended to have concentrations similar to those measured on roads. This suggests that the primary means of removal of CO_2, or of generating low CO_2 air in central London is ventilation along land categories with low roughness length, rather than absorption by vegetation during photosynthesis

Multiple t-tests were applied to the relative concentration data to test if data from different land use categories had significantly different CO_2 concentrations (Table 6.3), and the percentage of comparisons with significantly different $\Delta[CO_2]$ for the land categories compared was calculated. The significance level was chosen as p=0.001 to minimise the likelihood of type 1 errors. The likelihood of at least one type 1 error occurring is reported in Table 6.3 and scales with the number of unique comparisons between $\Delta[CO_2]$ binned by land category from 0.003 (JD1 – JD4, MM7C) to 0.206 (GZ1, all data, LCUN), so the reported percentage of comparisons which are significantly different for the former has less uncertainty associated with it than the latter. This analysis was applied to all the data for each set of transects (TK, JD, GZ) without categorisation by transect, and to the data for each individual transect. The median of the percentages of comparisons which were significant are reported for the latter in Table 6.3.

Table 6.3: Summary of t-test results comparing $\Delta[CO_2]$ within each land category and LCS. T-tests results are reported for the entire data set (% p<0.001, all data) and for the median percentage of comparisons with p<0.001 for each individual transect (Median % p<0.001). Also reported are the number of unique comparisons between land categories and the probability of getting at least one false positive (P(FP>1)). Results for transect GZ1 are reported using all data, and using date only from land categories with greater than 100 points (n > 100).

Transect data	LCS	Unique LC comparisons	*P*(FP>1)	% *p*<0.001, all data	Median % *p*<0.001
TK2 – TK10	LCUN	78	0.0750	68%	49%
	UA	55	0.0535	78%	53%
	MM7C	6	0.0060	67%	67%
JD1 – JD4	LCUN	153	0.1419	51%	66%
	UA	55	0.0535	44%	54%
	MM7C	3	0.0030	0%	33%
GZ1, all LC comparisons	LCUN	231	0.2064	63%	-
	UA	120	0.1131	35%	-
	MM7C	3	0.0030	0%	-
GZ1, all n > 100	LCUN	105	0.0997	75%	-
	UA	66	0.0639	73%	-
	MM7C	3	0.0030	0%	-

Approximately half of the land category comparisons show a significant (p<0.001) difference in $\Delta[CO_2]$ (Table 6.3). This proportion is generally larger for the more detailed land classification schemes (UA and LCUN) compared to MM7C, although the reverse is true for the median percentage of the within-transect comparisons for the TK transects. Removing classes with

fewer than 100 data points (GZ1, all n > 100, Table 6.3) increases the percentage of comparisons which were classified as significant, but also reduces the difference between the UA and LUCN results, with the greatest improvement seen for the UA LCS. Examination of the number, rather than the proportion, of interactions which were significant shows that the removal of categories with fewer than 100 data points removed only 3 significant comparisons for the UA LCS, but removed 67, almost half, of the significant comparisons for the LUCN LCS. This suggests that the LUCN LCS is more appropriate for resolving differences between less common land categories than the UA LCS; however, to put these results in context the same analysis was applied to the transects themselves. In other words, to see if $\Delta[CO_2]$ measured on each transect was significantly different from the $\Delta[CO_2]$ measured on other transects within the same set. For, GZ1, the data were split depending on whether they were recorded before, during, or after measurements within the CAZ. The results are summarised in Table 6.4 and show that the differences between $\Delta[CO_2]$ values measured on different transects within the same set are far greater than the differences between $\Delta[CO_2]$ measured in different land categories. Whilst the land category has some impact on measured $\Delta[CO_2]$, it seems that at this site other factors on much larger spatial (within or outside the CAZ) and temporal (time of day, time of year) scales are more important in determining the difference in $[CO_2]$ above a particular surface relative to that measured above the blending height. It also suggests that the characteristic spatial scale of variation of horizontal $[CO_2]$ distribution in London is much larger than 10 m – 1 km (micro) scale of the land category variation sampled by transects TK2 – TK10 and JD1 – JD4, i.e., ground level $[CO_2]$ can be considered distinct from each other at the local scale (0.1 – 80 km, Oke, 1987).

Table 6.4: Summary of t-test results comparing $\Delta[CO_2]$ within each transect or sub-transect category (GZ1). Nomenclature is as Table 6.3.

Transect data	Unique Transect Comparisons	*P*(FP>1)	% comparisons $p<0.001$
TK2 – TK10	36	0.0354	83%
JD1 – JD4	6	0.0060	100%
GZ1: pre, during, and post CAZ	3	0.0030	100%

The ability of each LCS to divide the $\Delta[CO_2]$ data into distinct groups was assessed by comparing the standard deviation of the $\Delta[CO_2]$ in each group to the mean value for each land category (for these values, see Table 6.A.1 to Table 6.A.3 in Appendix 6.A). The average ratio of the standard deviation to the mean is reported for each set of transects and LCS in Table 6.5, with higher values indicating greater variation in $\Delta[CO_2]$ and lower values less variation. LCUN has the lowest average ratio for transects TK2 – TK10, i.e., those closest to KS, which suggests that for analysis within approximately 1km of KS it may be the most appropriate land classification scheme. However, it also has the highest average ratio for transects JD1 – JD4, which indicates that it is not appropriate for analysis which may include areas even slightly further afield. The UA scheme has a much smaller range of average ratios, but it is the MM7C LCS which has an average standard deviation to mean $\Delta[CO_2]$ ratio of less than or equal to 1 for all sets of transects. Given this consistent, relatively low ratio and the greater ease of application (it does not require manual assignment of building use), the MM7C LCS seems the

most appropriate LCS for prediction of $\Delta[CO_2]$, and hence, land category specific CO_2 emissions. This topic is revisited in Chapter 7.

Table 6.5: Average ratio of the standard deviation to the mean of the $\Delta[CO_2]$ for each land category (Table 6.A.1 to Table 6.A.3 in Appendix 6.A) by land category scheme. Values are colour coded low to high (green to red)

LCS	TK2-TK10	JD1-JD4	GZ1
LCUN	0.69	2.27	0.88
UA	0.79	1.17	1.24
MM7C	0.89	0.95	1.00

6.5 CO_2 concentration and street height: width ratio

Tall, narrow street canyons are known to trap and recirculate pollutants, whereas broader streets are associated with periodic flushing of street level emissions (Vardoulakis *et al., 2*003). It is therefore expected that higher height:width ratios (H/W) will be associated with higher CO_2 concentrations. In this section $\Delta[CO_2]$ from all three sets of transect measurements is compared to street height:width ratio, the latter calculated as described in Section 6.3.6.

When measured transect concentration relative to KSSW is plotted with the closest H/W ratio (Figure 6.11), there is a slight increase but the concentrations are scattered. Comparison of relative concentrations binned by H/W class (Isolated roughness flow: H/W<0.3, Wake interference flow: 0.3<H/W<0.7; skimming flow: 0.7<H/W, Oke, 1987) showed significant differences between all classes for all three sets of transects at the 5% level for all except wake interference flow and skimming flow for TK2 – TK10; however, linear regression of the relative concentration onto the H/W ratio had very low coefficients of determination (<0.1 in all cases). Whilst building height compared to street width has an impact on CO_2 concentrations, the intra-class variation is much greater than the inter-class variation.

6.6 CO_2 concentration gradient between land use categories

In this section the intra land category gradient for the street canyons in the vicinity of the Strand campus is compared to the inter land category gradient for all transects.

Transect data for the Strand (road adjacent to KSSW), Aldwych (road to the north of the campus with very similar traffic patterns and morphometric characteristics), and Surrey Street (one-way street along the eastern side of the Strand campus) were extracted and the average gradient calculated. Of these only one (TK2-10, Aldwych) was found to be significantly different from 0 at the 5% level (p = 0.011) and another at the 10% level (TK2-10, Strand, p = 0.094). These values were 56.76 and 54.20 ppb m^{-1} respectively, which are of similar magnitude to the gradients observed between categories (Table 6.6, Table 6.7).

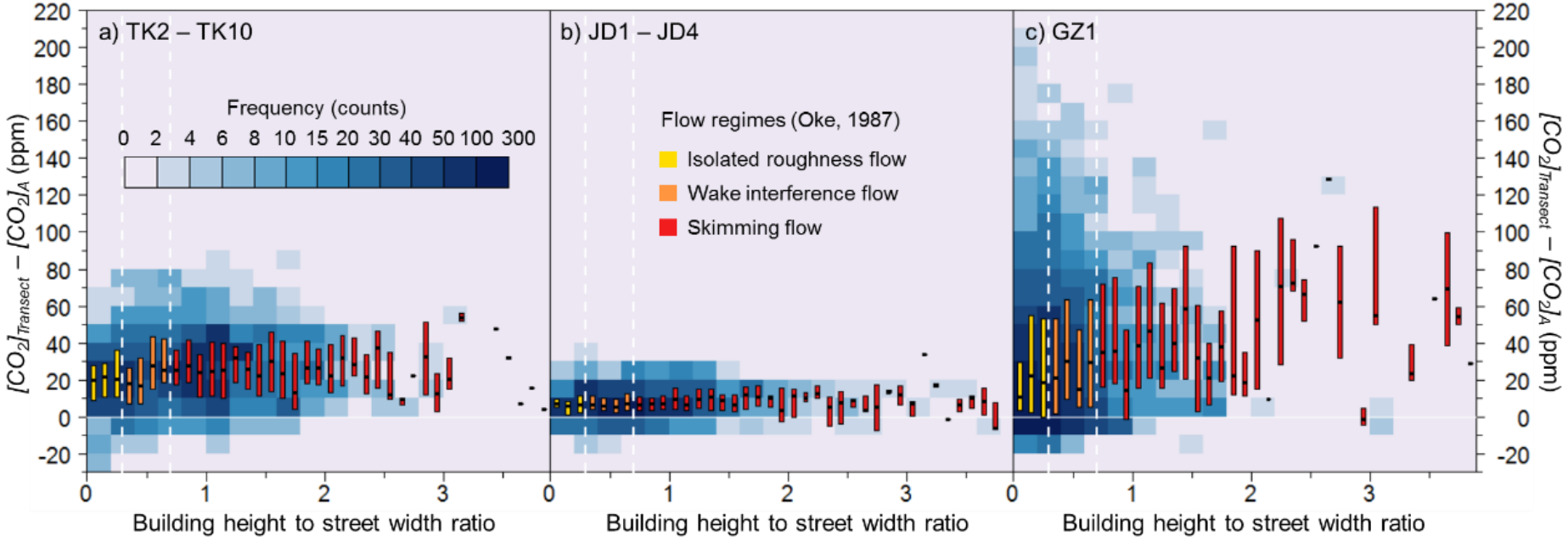

Figure 6.11: Frequency (see key in (a)) of CO_2 concentrations relative to local scale values ($[CO_2]_A$) in ppm plotted over building height: street width ratio for all three sets of transect measurements. Vertical dashed lines: street canyon height/width values of 0.3 and 0.7, solid horizontal line: origin. Coloured bar: interquartile range, black tick: median. Colours of bars denote flow regime (Oke, 1987): see key in (b).

Mean gradients between LCUN land categories tended to be larger, and in some cases were the opposite sign, to the median value (Table 6.6, Table 6.7). All mean inter-land category gradients (LCUN, UA) for JD1-4 were lower than that observed during TK1-10 in the Strand and Aldwych street canyons. Half (16/30) and a third (7/22) of TK2-10 and GZ1 mean inter land category gradients for the LCUN LCS were also smaller in magnitude (UA: TK 6/14, GZ: 0/2; MM7C: TK 5/5, GZ 0/1). The horizontal *[CO_2]* gradient observed in the Strand and Aldwych street canyons was approximately a fifth of typical vertical CO_2 gradients (ca. 250 ppb m^{-1}, Figure 5.13, Section 5.3.1). The only horizontal gradients of similar magnitude between land categories were both observed during the GZ1 transect between the office and retail land categories (LCUN), and the water and roads categories (MM7C). This suggests that intra-land category horizontal transport of CO_2 is likely to be as important as inter-land category transport, and that both will be much less important to the overall CO_2 concentration in any particular area than vertical CO_2 transport.

6.7 Horizontal CO_2 concentration gradient with height

In this section the differences in horizontal gradients of CO_2 concentration at two different heights are explored.

CO_2 concentration measurements were made along the northern edge of the Strand roof (KSUH, Figure 2.1c) and the Strand building balcony (KSLH, Figure 2.1c) using switched profiles as described in Section 2.2.1. between 2012/153 and 2013/151 (C6, Table 2.2). When averaged over time of day and month of year (Figure 6.12), a seasonal cycle is apparent in the data measured at KSLH (Figure 6.12a, 19.5 m a.g.l.), but not that at KSUH (Figure 6.12b, 30.5 m a.g.l.). The range of values for both KSLH and KSUH were largely the same, approximately -50 to 60 µmol m^{-1}, with over 90% of the data from both levels within ± 10 µmol m^{-1}. Gradients were calculated parallel to the Strand street canyon such that higher concentrations of CO_2 in the west compared to the east resulted in a positive gradient, and higher concentrations in the east than the west gave a negative gradient. Hence Figure 6.12 shows that at a smaller height above ground level, there tend to be higher CO_2 concentrations at the western end of the profile in summer (June to August), and higher concentrations to the east of the profile in winter (December to February).

Table 6.6: Median and mean horizontal CO_2 gradient (ppb m^{-1}) between land categories (LCUN), colour coded from green (negative) to red (positive). Associated p values are for a t-test with the null hypothesis that the mean of the horizontal CO_2 concentration gradient for a combination of land categories is equal to 0. Tables left to right are for data derived from transects TK2-10, JD1-4 and GZ1 respectively. Only results with p values < 0.01 (shaded green, right hand column) and 0.01 < p < 0.05 (shaded yellow, right hand column) are included.

From	To	Median	Mean	*p* value
A Road	A Road	-1.02	46.32	0.002
	Bridge	-46.99	-67.38	0.000
	Retail	5.13	53.78	0.003
B Road	A Road	24.81	105.69	0.007
	B Road	-13.55	-26.17	0.000
	Park	-6.02	-32.07	0.006
	Residential	-32.27	-89.49	0.001
Academic	B Road	-13.06	-57.47	0.004
	Residential	-37.02	-77.15	0.005
Hotel	B Road	-35.92	-58.01	0.009
	Park	-87.03	-141.38	0.003
Office	A Road	4.41	55.88	0.003
	B Road	-13.33	-27.96	0.000
	Park	-87.03	-42.48	0.001
Park	Office	-5.74	-38.19	0.004
Retail	A Road	8.49	62.85	0.000
B Road	Footpath	-11.67	-53.14	0.038
	Academic	-13.06	-45.11	0.024
	Office	-8.69	-15.57	0.036
Bridge	A Road	-42.94	-42.91	0.036
	Footpath	2.58	54.46	0.027
Hotel	Office	-58.33	-63.94	0.011
Office	Footpath	-11.49	-67.74	0.043
	Hotel	-42.05	-63.05	0.036
	Retail	-0.90	35.14	0.018
Park	A Road	0.06	97.63	0.043
Residential	Academic	-29.77	-56.70	0.039
	Residential	-12.43	-38.38	0.042
Retail	Office	-1.32	30.39	0.044
	Retail	-1.46	26.05	0.014

From	To	Median	Mean	*p* value
B Road	B Road	0.00	-3.61	0.001
	Residential	0.00	-3.61	0.003
Office	B Road	-7.75	-12.49	0.010
B Road	Office	-5.67	-11.44	0.013
Park	B Road	0.00	-7.42	0.048
Residential	A Road	0.00	7.29	0.011
	B Road	0.00	-2.67	0.010
Retail	Academic	-15.39	-19.27	0.014

From	To	Median	Mean	*p* value
A Road	A Road	-25.96	43.10	0.002
	Hotel	-9.09	74.08	0.000
	Retail	-51.81	91.85	0.003
B Road	B Road	-6.12	-18.03	0.000
	Park	-5.72	-4.63	0.006
	Residential	-6.63	-12.24	0.001
Office	A Road	-37.66	143.91	0.003
	B Road	8.63	-96.57	0.000
	Park	18.68	121.32	0.001
Park	Office	23.36	106.47	0.004
Retail	A Road	-51.81	92.53	0.000
B Road	Office	7.05	-49.31	0.036
Hotel	A Road	-117.63	-120.33	0.036
Office	Retail	-31.87	225.80	0.018
Park	A Road	-28.73	10.50	0.043
	Sewage Works	-2.25	-65.55	0.040
Residential	Residential	-17.84	22.30	0.042
Retail	Office	-31.87	222.72	0.044
	Retail	-50.71	110.12	0.014
Stadium	Sewage Works	4.33	-150.53	0.037
Sewage Works	Park	-7.32	-62.46	0.043
	Stadium	3.69	-188.94	0.018

Table 6.7: Median and mean horizontal CO_2 gradient (ppb m^{-1}) between land categories, colour coded from green (negative) to red (positive). Associated p values are for a t-test with the null hypothesis that the mean of the horizontal CO_2 concentration gradient for a combination of land categories is equal to 0. Upper table for data classified by UA, lower by MM7C. Only results with p values < 0.01 (shaded green, right hand column) and 0.01 < p < 0.05 (shaded yellow, right hand column) are included.

From	To	Median	Mean	*p* value
TK2 - TK10				
Other roads and associated land	Green urban areas	2.14	72.86	0.000
Railways and associated land	Other roads and associated land	48.98	157.10	0.007
Green urban areas	Other roads and associated land	4.03	70.66	0.000
Water	Water	-15.15	-35.33	0.008
Discontinuous Dense Urban Fabric (S.L.: 50% - 80%)	Green urban areas	2.12	90.27	0.039
	Sports and leisure facilities	21.88	43.61	0.030
Discontinuous Low Density Urban Fabric (S.L.: 10% - 30%)	Discontinuous Medium Density Urban Fabric (S.L.: 30% - 50%)	-99.33	-101.16	0.025
	Discontinuous Low Density Urban Fabric (S.L.: 10% - 30%)	-61.17	-96.44	0.022
Other roads and associated land	Railways and associated land	37.98	129.42	0.025
	Sports and leisure facilities	9.02	39.94	0.035
	Water	-17.85	-42.90	0.012
Green urban areas	Discontinuous Medium Density Urban Fabric (S.L.: 30% - 50%)	77.20	135.23	0.014
Sports and leisure facilities	Discontinuous Dense Urban Fabric (S.L.: 50% - 80%)	2.73	32.22	0.035
Water	Other roads and associated land	-10.88	-29.68	0.049
JD1 - JD4				
Continuous Urban Fabric (S.L. > 80%)	Railways and associated land	0.00	-3.98	0.022
GZ1				
Industrial, commercial, public, military and private units	Construction sites	-56.54	-185.11	0.011
Construction sites	Industrial, commercial, public, military and private units	4.33	-116.51	0.042

From	To	Median	Mean	*p* value
TK2 - TK10				
Building	Evergreen tree	-33.02	-45.01	0.000
Road	Evergreen tree	-22.93	-31.18	0.000
Evergreen Tree	Building	-20.90	-27.45	0.001
	Road	-14.03	-22.67	0.001
	Evergreen tree	-19.05	-27.04	0.000
GZ1				
Water	Road	-155.87	-295.11	0.045

If this effect were observed at KSUH it might be thought that this was due to roof-top emissions entrained into the canyon, as the boiler chimneys, air vents, etc. are all located at the eastern end of the Strand building roof. Further, unlike the vertical CO_2 gradient (Section 4.3), there does not seem to be any significant relation between the horizontal CO_2 gradient and air temperature (Figure 6.13) as the interquartile ranges of all horizontal CO_2 gradients aggregated by air temperature (bin width 1ºC) overlap with 0, i.e., none can be said to be significantly different from 0. The effect is unlikely to be due to traffic intensity, as this is reasonably constant all year round (Figure 2.B.9 in Appendix 2.B). There are two mature London Plane trees at the eastern end of the profile which would act to reduce the CO_2 concentrations (and make the CO_2 gradient more positive) during the daylight hours between April and November; however, weakly positive gradients were observed overnight (Figure 6.12a) when the trees would be a source, rather than a sink of CO_2. The effect of street trees on *[CO_2]* measured at KS is explored more thoroughly in the following chapter. What is clear is that the effect is not observed at KSUH. This could suggest that the air is sufficiently mixed as to remove coherent (rather than random) horizontal concentration differences at the scale of 10 – 100 m by the time it reaches 30 m a.g.l. or approximately two thirds of the height of the eddy covariance equipment at KSSW.

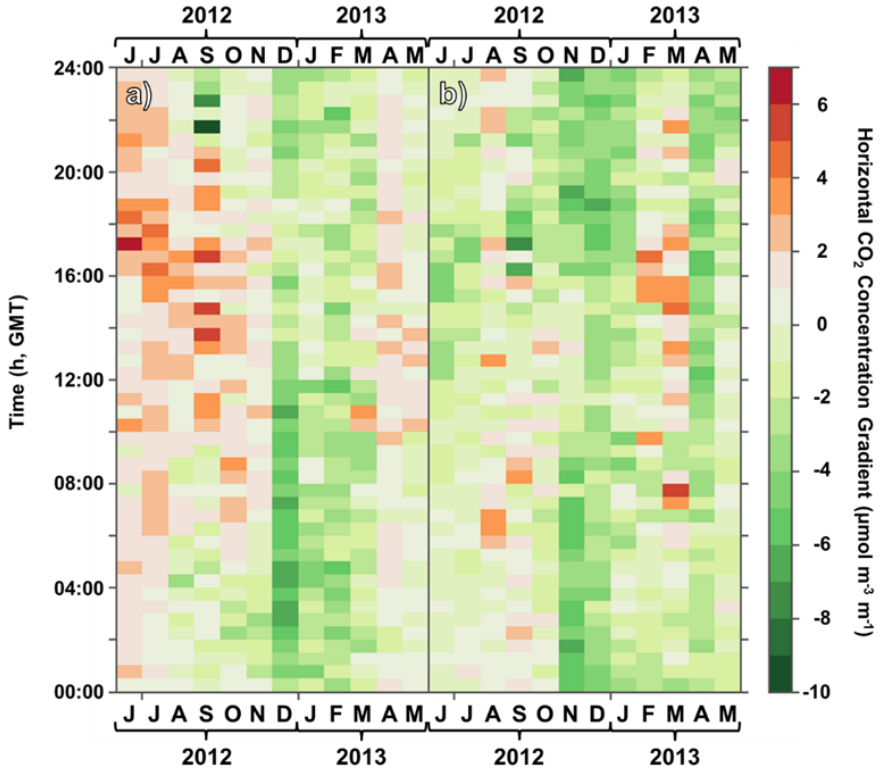

Figure 6.12: Half hourly/monthly mean horizontal CO_2 concentration gradients measured at (a) KSLH and (b) KSUH (Figure 2.1c) for 2012/153 to 2013/151.

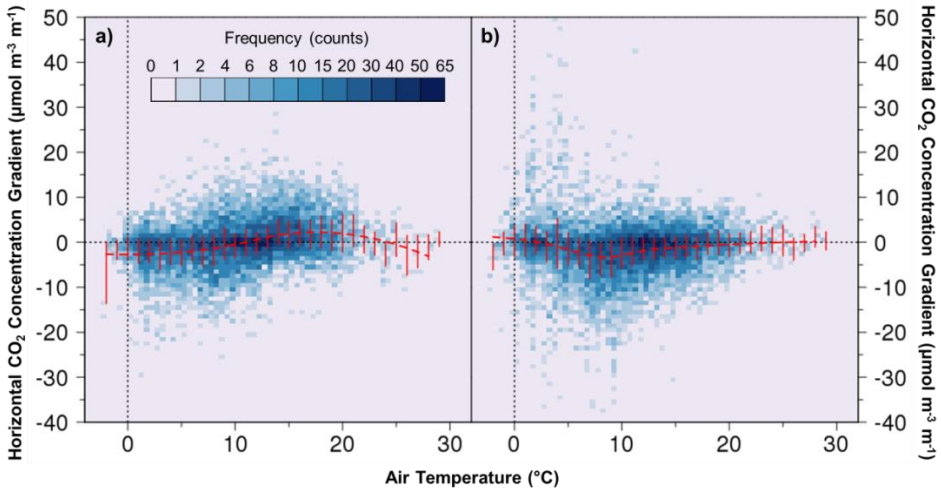

Figure 6.13: Frequency (see key, (a)) of half hourly horizontal CO_2 concentration gradients measured at (a) KSLH and (b) KSUH (Figure 2.1c) for 2012/153 to 2013/151 with air temperature measured at height A by WXT520. Curved dashed line: loess curve; vertical solid lines: central 50% (interquartile range) of data at 1 °C intervals; dotted lines: origin.

6.8 Horizontal advection

The horizontal advection was calculated following Section 3.1.3 using the horizontal gradients reported in Section 6.7 and the wind speed and direction data collected at KSNW (Table 2.A.1 in Appendix 2.A). The wind data were used to calculate the component of the wind vector parallel to the street canyon, called the 'along road wind component' (Figure 6.14a). This was positive with easterly (east to west) winds, and negative with westerly winds. When combined with a positive (*$[CO_2]$* higher in the west) horizontal *$[CO_2]$* gradient, a positive wind can be interpreted as the air becoming enriched in CO_2 as it passes along the span of the horizontal profile, i.e., the horizontal advection is positive. Conversely, when the gradient is positive, but the wind blows from the higher *$[CO_2]$* in the west to the lower *$[CO_2]$* in the east, this can be interpreted as a loss of CO_2, i.e., negative advection.

From Figure 6.14b it can be seen that advection tends to be strongly positive when the street canyon is in the lee of the Strand building (KS, blue box), and when the wind comes from the north west quadrant, when part of the horizontal profile is downwind of the Mary-le-Strand church. Both wind directions are associated with negative mean vertical wind speeds but no decrease in within-canyon horizontal wind speed (Figure 5.22d). It therefore seems unlikely that the majority of the high, positive advection values are due to CO_2 accumulated within the airspace due to lack of ventilation, particularly as the positive horizontal advection values are an order of magnitude larger than the CO_2 storage values calculated at the same time resolution and from the same instruments.

Horizontal advection data aggregated by time of day, month of year and weekday/weekend (Figure 6.15) show both seasonal (compare December to January with June to August, Figure 6.15b) and hebdomadal variation. Wind speed and direction are not seasonally variant (Figure 2.B.6 in Appendix 2.B), hence the differences observed must be due to changes in horizontal

gradient (Figure 6.14). The high positive advection in Figure 6.14b is associated with negative along road wind components (west to east), and therefore negative horizontal *[CO_2]* gradients (higher *[CO_2]* in the east). Given the negative (i.e., downward moving) vertical wind speed also associated with the positive advection, it may be necessary to re-consider the possibility that these negative horizontal *[CO_2]* gradients are due to roof level emissions from the boiler chimneys and air conditioning vents on the eastern end of the Strand building. Downward transport of air with high CO_2 concentrations was observed in a residential neighbourhood of Tokyo by Moriwaki *et al*. (2006) under similarly cold conditions, albeit with a much lower mean building height. As the KSUH horizontal profile does not extend along the full length of the Strand roof, it is possible that movement of CO_2 from vents and chimneys on the Strand roof was transported into the street canyon beyond the eastern extent of KSUH. As it moved downward it dispersed horizontally until it was registered at KSLH. This hypothesis would explain the positive advection values with above-canyon wind from 120 -180º, but does not explain the positive advection values when the wind is from the north west quadrant. Further, elevated *[CO_2]* relative to that at height A is not observed at the eastern end of the profile during north-west wind conditions (Figure 4.19).

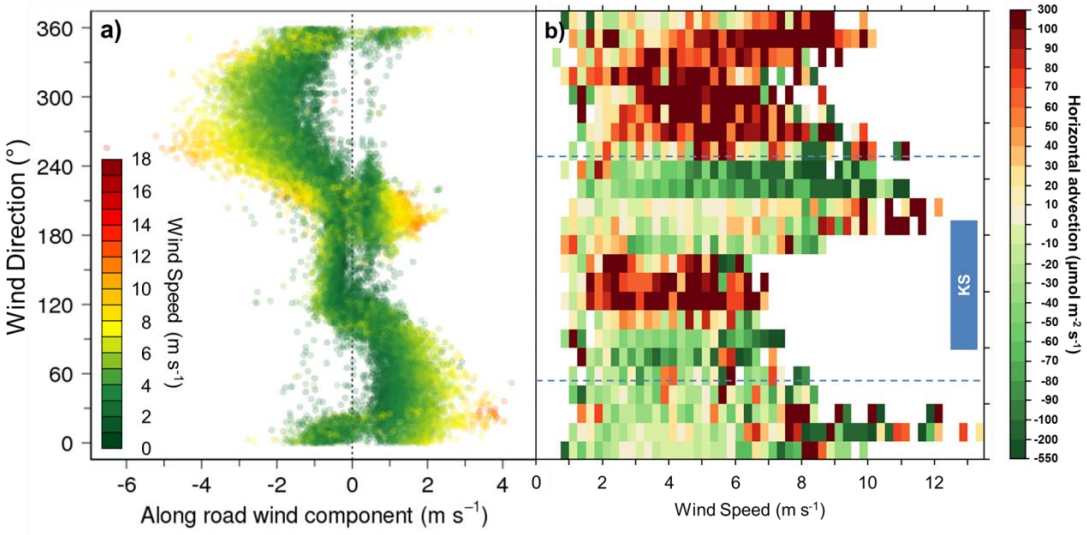

*Figure 6.14: (a) Along road wind component with wind direction, colour coded by wind speed, (b) mean horizontal advection (2012/153 – 2013/151) by wind speed (x-axis) and direction (y-axis). Advection data calculated from KSLH and KSUH (Figure 2.1c) LI840 data (*Section *2.2.1). Blue dotted lines denote approximate angle of the Strand, blue box denotes approximate angles over which the Strand street canyon is shadowed by the KCL Strand building (KS). All wind speed and direction data collected at height A, KSSW. Along road wind component calculated from data collected at height F, KSNW.*

Despite a visible difference in seasonality between weekday and weekend horizontal advection, no relation was found between either the value or the magnitude of the horizontal advection and traffic volume. It is suggested that the negative gradient during conditions with winds from the northwest is therefore either due to emissions from combustion of fuel for space heating which have been preferentially transported to one end of the street canyon, which seems unlikely, or due to preferential venting of traffic emissions at the western end of the street canyon, resulting in lower concentrations. Ultimately, the complex nature of the street

canyon geometry may result in multiple interactive processes which together affect the horizontal advection parallel to the street canyon.

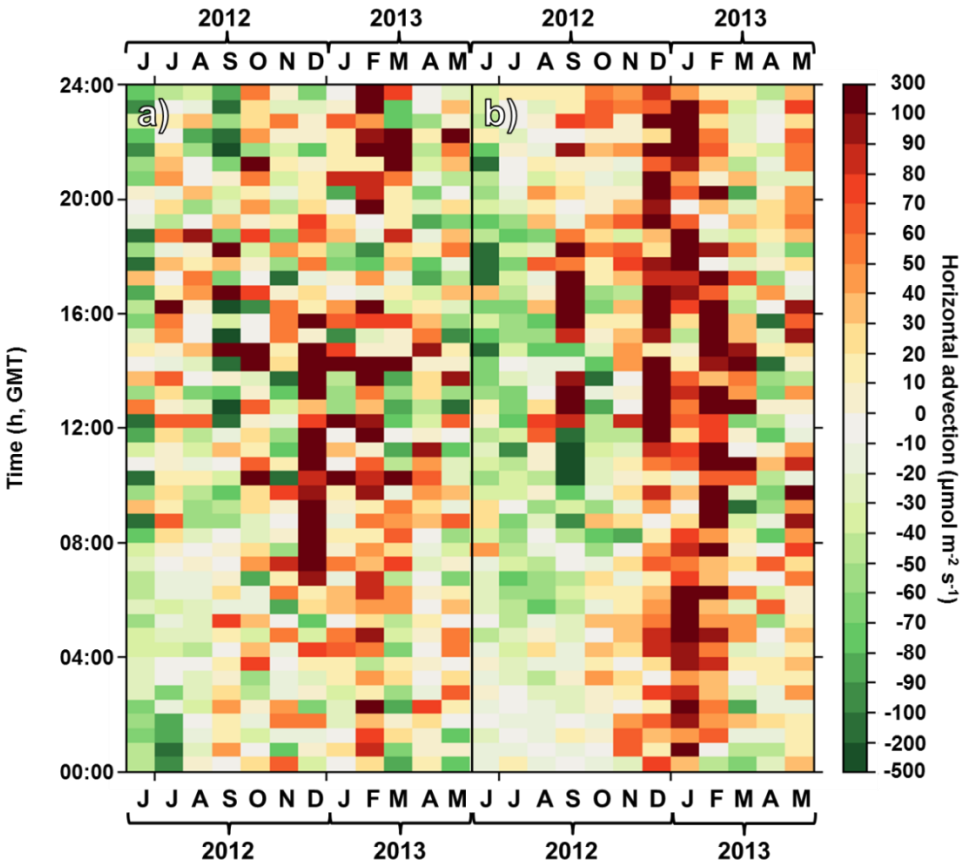

Figure 6.15: Mean horizontal advection at KS for 2012/153 – 2013/151 averaged over time of day (30 minute periods), month of year and (a) weekends (Saturday and Sunday) and (b) weekdays (Monday to Friday).

6.9 Contributions

The primary aim of this chapter was to investigate the effect of different land cover, land use and neighbourhood factors on CO_2 concentration ($[CO_2]$) and to determine whether any particular land cover scheme was able to partition measured street level $[CO_2]$ relative to local scale values into subsets that were internally homogenous and significantly different from other subsets. Further aims included characterising the spatial scale of CO_2 variation in urban areas, quantifying the impact of street height to width ratio on CO_2 mixing ratios, determining the variation of horizontal $[CO_2]$ gradients with factors such as land cover and height above ground, and assessing the size and variability of horizontal advection.

CO_2 concentration was found to increase with proximity to the city centre, greater building density, i.e., decreasing access to ventilation, and higher traffic load. Urban green space was not sufficient to decrease CO_2 concentrations below background levels. A land categorisation scheme derived from LiDAR data was found to be the most effective and efficient means of associating $\Delta[CO_2]$ with a land category. Land use and cover, as well as street height: width ratio, have a distinct impact on measured CO_2 concentrations and horizontal gradients. This impact is heavily modified by factors such as wind direction and time of day. Within land category CO_2 gradients are comparable in size to between category gradients and both are small compared to observed vertical gradients. Given the relatively small horizontal gradients, the horizontal advection term is surprisingly large compared to the CO_2 storage term; however, it should be noted that only the component of the horizontal advection parallel and not perpendicular to the street was calculated.

.

Appendix 6.A Elevation of transect CO_2 concentration measurements above local scale concentrations by land category and land categorisation scheme

Table 6.A.1: CO_2 concentrations (ppm) relative to KSSW from each set of transects aggregated by land category (LCUN). Means are shaded green to red low to high, standard deviations (σ) grey to red, and number of values (n_v) white to green. Means and standard deviations given in ppm.

Land Categories		TK2-TK10			JD1-JD4			GZ1		
		Mean	σ	n_v	Mean	σ	n_v	Mean	σ	n_v
Land Cover	A Road	29.06	22.03	1463	8.69	9.35	1660	40.89	45.20	5297
	B Road	23.89	17.75	1812	4.63	7.55	856	6.07	19.67	1531
	Building	5.85	0.59	2	-	-	0	-	-	0
	Car park	-	-	0	-	-	0	-2.33	11.90	248
	Cycle Path	-	-	0	-1.24	7.12	23	-	-	0
	Footpath	18.91	14.81	787	6.66	0.54	10	-	-	0
Land Use	Academic	26.12	17.62	564	13.02	11.31	156	25.80	48.16	307
	Bridge	16.14	17.16	271	1.24	5.99	12	27.68	32.66	161
	Car park	-	-	0	4.78	8.00	53	-9.83	10.35	75
	Hotel	31.77	20.09	280	7.06	9.16	451	37.02	37.29	146
	Light Industrial	-	-	0	-	-	0	-	-	0
	Motorway	-	-	0	-	-	0	44.85	65.02	4
	Office	26.25	20.17	2488	9.96	9.59	1150	40.08	43.40	1530
	Park	21.43	18.18	759	7.22	10.65	451	27.91	38.68	2005
	Residential	21.11	12.25	139	4.70	7.52	1144	33.53	44.90	3851
	Retail	29.73	19.49	1772	8.53	8.66	902	43.89	49.27	2225
	Stadium	-	-	0	-	-	0	17.21	16.86	166
	Tunnel	-	-	0	1.92	6.86	13	46.43	40.33	30
Neighbourhood	London Underground	26.42	19.02	248	9.61	11.14	348	62.33	54.20	481
	Motorway	-	-	0	1.69	6.57	38	45.65	43.09	70
	Railway	-	-	0	2.82	8.12	112	-	-	0
	Reservoir	-	-	0	2.91	5.82	15	26.56	18.99	51
	River	20.16	18.69	863	0.43	7.67	22	43.97	38.44	729
	Sewage Works	-	-	0	-	-	0	9.02	15.96	591
	Station	27.23	12.66	87	11.86	13.84	140	27.73	37.80	143
	Thames Water Plant	-	-	0	-	-	0	6.70	9.46	23

Table 6.A.2: CO_2 concentrations (ppm) relative to KSSW from each set of transects aggregated by land category (UA). Means are shaded green to red low to high, standard deviations (σ) grey to red, and number of values (n_v) white to green. Means and standard deviations given in ppm. Categories are sub-divided according to land cover type (buildings, transit, construction/disused, vegetated, water).

Land Categories	TK2 - TK10			JD1 - JD4			GZ1		
	Mean	σ	n_v	Mean	σ	n_v	Mean	σ	n_v
Continuous Urban Fabric (S.L. > 80%)	22.26	17.62	1648	6.93	9.00	1334	48.77	52.76	1482
Discontinuous Dense Urban Fabric (S.L.: 50% - 80%)	21.59	17.15	626	5.07	7.40	900	30.93	41.29	3007
Discontinuous Medium Density Urban Fabric (S.L.: 30% - 50%)	34.59	21.25	153	8.49	12.15	60	24.66	35.01	446
Discontinuous Low Density Urban Fabric (S.L.: 10% - 30%)	35.69	23.15	218	15.80	9.08	45	39.84	42.43	209
Discontinuous Very Low Density Urban Fabric (S.L.: < 10%)	33.62	19.75	854	11.31	6.37	46	31.42	34.66	49
Industrial, commercial, public, military and private units	28.16	20.99	1294	8.36	8.86	726	30.12	40.50	3020
Fast transit roads and associated land	-	-	0	-	-	0	33.66	23.12	29
Other roads and associated land	25.28	19.53	3660	7.09	9.15	2323	32.75	43.28	6890
Railways and associated land	14.47	10.64	108	3.91	5.98	103	33.51	38.52	348
Construction sites	-	-	0	-	-	0	16.56	19.70	136
Land without current use	-	-	0	-	-	0	-	-	8
Green urban areas	21.90	18.61	601	8.52	11.48	341	28.17	37.70	1462
Sports and leisure facilities	9.61	11.23	100	-	-	13	12.20	24.36	217
Agricultural areas, semi-natural areas and wetlands	-	-	0	-	-	0	19.69	21.68	108
Forests	-	-	0	-	-	0	-	-	18
Water	14.24	14.18	375	-	-	10	25.03	29.63	197

Table 6.A.3: CO_2 concentrations (ppm) relative to KSSW from each set of transects aggregated by land category (MM7C). Means are shaded green to red low to high, standard deviations (σ) grey to red, and number of values (n_v) white to green. Means and standard deviations given in ppm.

	TK2 - TK10			JD1 - JD4			GZ1		
	Mean	σ	n_v	Mean	σ	n_v	Mean	σ	n_v
Buildings	25.88	19.36	3732	8.46	9.22	1776	45.22	43.76	2542
Roads	25.61	19.42	3691	8.52	9.27	1871	44.41	43.47	2657
Water	13.50	13.88	328	-	-	0	35.95	37.89	183
Grass	-	-	0	-	-	0	-	-	0
Shrub	-	-	0	-	-	0	-	-	0
Deciduous Tree	-	-	0	-	-	0	-	-	0
Evergreen Tree	13.46	14.03	184	10.67	7.25	76	-	-	1

Chapter 7: Net exchange of CO_2 from an urban environment as calculated by inventory and micrometeorological methods.

7.1 Introduction

In this chapter the net CO_2 emissions calculated by two methods (micrometeorological and inventory) are evaluated and compared. The micrometeorological method is described in Section 3.1. The inventory method involves identifying all sources and sinks of CO_2 within a defined area. The rate of CO_2 emission for each is then measured or calculated from inventory data, such as the National Atmospheric Emissions Inventory (NAEI), and summed to give the net emissions for that area. Common components in urban systems (e.g., Velasco *et al.*, 2014) are vehicle emissions, human respiration, etc. Previous studies in central London have found a wide range of net emissions, for example, Sparks and Toumi (2010) calculated a mean CO_2 flux that would result in emissions of 27.35 kg CO_2 m^{-2} yr^{-1} from eddy covariance measurements 50 m above ground level, and estimated emissions to be 43.89 and 31.39 kg CO_2 m^{-2} yr^{-1} using the NAEI and London Atmospheric Emissions Inventories (LAEI) respectively (with point sources excluded). Net CO_2 emissions of similar magnitude (35.5 kg CO_2 m^{-2} yr^{-1}) were calculated by Helfter *et al.* (2011) from EC measurements 190 m above street level, and Ward *et al*. (2015, 46.6 kg CO_2 m^{-2} yr^{-1}) from measurements made 45.1 and 46.4 m above ground level (configurations E3-E5, Section 2.2.2). Emissions from building heating have generally been found to contribute the most to net emissions, followed by traffic and human respiration. Reduction of CO_2 emissions due to sequestration by vegetation was calculated as 0.4% of total emissions (Helfter *et al.*, 2011).

In this chapter the emissions from space heating (E_B), freshwater (E_W), human respiration (E_R), animal respiration/decomposition (E_A), traffic (E_V), and respiration of organisms in bare soil (E_S) are estimated separately. For the majority of the inventory components these emissions are calculated as a land-category specific (e.g., building) flux and multiplied by the land area over which that flux is likely to apply in order to calculate the total emissions for, e.g., combustion for building heating. The rate of exchange of CO_2 between the atmosphere and vegetation (F_P) can be evaluated as several components: photosynthetic uptake of CO_2 by leaves ($F_{P,\,leaf}$), emission of CO_2 by leaf respiration, emission of CO_2 by stem and branch respiration (by woody vegetation, i.e., trees, large shrubs), and emission of CO_2 by root respiration. The net exchange of CO_2 by leaves (i.e., the sum of the leaf respiration and photosynthesis) is evaluated for grass as one component from leaf chamber measurements, whilst the exchange due to root respiration is evaluated using soil chamber measurements. For woody vegetation, the sum of all four components is evaluated using survey measurements. The sum of the total emissions for both woody vegetation and grass (E_P), as well as the aforementioned space heating, freshwater, human, animal, traffic and soil emissions is taken to be the Net Ecosystem Exchange (NEE) of the central London environment, and should be equal to the sum of the micrometeorological components of the NEE, namely vertical flux (F_{CO2}), change in CO_2 stored within the airspace below the EC sensor (ΔC_S) and advection (A_{xy}, A_z).

$$NEE = E_B + E_R + E_A + E_W + E_V + E_S + E_P = \Delta C_S + F_{CO_2} + A_z + A_{xy} \qquad (7.1)$$

The NEE was calculated via both methods for the period 2012/153 to 2013/151 (June 2012 to May 2013). There were two periods (2012/152 – 2013/151, C6 – C7; 2014/160 -2015/124, C10) during which the switched profile was in operation both above and within the canyon. Data from an automated traffic count at the Royal Courts of Justice (Section 2.2.8), which were used in the calculation of E_V, were available for 2010/336 to 2013/137. The period 2012/152 – 2013/151 was therefore chosen as it had the best data availability for both the micrometeorological and the inventory methods of calculating NEE.

The components for the inventory method, the means of calculating each and the assumptions made in doing so are listed briefly in Table 7.1 and discussed in Section 7.3 (the assumptions and methods used in the calculation of the micrometeorological components of NEE are discussed in Section 3.1 with filling of gaps in the data discussed in Section 3.2). The remainder of this chapter includes methods and results of flux footprint calculation (7.2), results from the inventory and micrometeorological methods (7.3 and 7.4) and comparison of the two (7.5).

Table 7.1: Components of total CO_2 emissions in central London, methods to measure the associated processes and assumptions made.

Components	Influenced by	Measurement/Data	Method/Assumptions
Traffic (F_V)	Volume Vehicle type Vehicle speed	Vehicle emission factors Traffic counts: 1. Annual average daily flows (include vehicle type) 2. Hourly total vehicles	Section 7.3.4, assumptions summarised in Table 7.8
Net Vegetation Photosynthesis in Leaves ($F_{P, leaf}$)	Leaf on/off time Species Leaf area index % land cover Position relative to measurements Water availability Light availability Disease/insect damage Soil quality Humidity Temperature	PAR at height A (KSS/W) Phenology- half hourly webcam images of street trees Light response curves (lawn grass, London Plane) Tree survey (diameter at breast height)	Section 7.3.1 Assumptions: all lawn grass is the same species and experiences the same conditions as that measured in Embankment gardens. Leaf area index of grass is one. The grass receives all the PAR measured at height A. Water availability and temperature do not limit photosynthesis The chosen allometric equations are appropriate Disease/insect damage is negligible
Vegetation Respiration (F_{PR})	Species % land cover Position relative to measurements Disposal of leaf litter & associated CO_2 release. Humidity Temperature	Light response curves (lawn grass, London Plane) at 0 PAR Tree survey (diameter at breast height) RH and air temperature measurements at Height A (KSS/W). Soil chamber measurements.	Section 7.3.1 See prev. All grass clippings and litterfall are disposed of outside the footprint and do not contribute to local CO_2 emissions
Soil Respiration (F_{Soil})	Temperature Moisture Carbon/organic content (sand will not respire, loam will)	Soil temperature and moisture probes in Embankment and Middle Temple gardens	Section 7.3.2 Soil moisture is not a limiting factor
Buildings (F_B)	Building occupancy Energy source Air temperature Building heat transfer resistance (insulation) Building function	Direct measurements of vents and boiler emissions for short periods Monthly gas consumption (Strand building) Census population data	Section 7.3.5, Iamarino *et al.* (2012) and Ward *et al.* (2015)
River (F_W)	Temperature Water carbon content Atmospheric CO_2 concentration	CO_2 concentration of air passed over river water samples relative to that passed over an inert surface.	Section 7.3.3
Human respiration (F_R)	Population Activity Age Weight	Average respiration rate per person (Koerner and Klopatek, 2002)	Section 7.3.5, Iamarino *et al.* (2012)
Animal respiration and decomposition (F_A)	Species Population Activity	No population data.	Assume negligible.

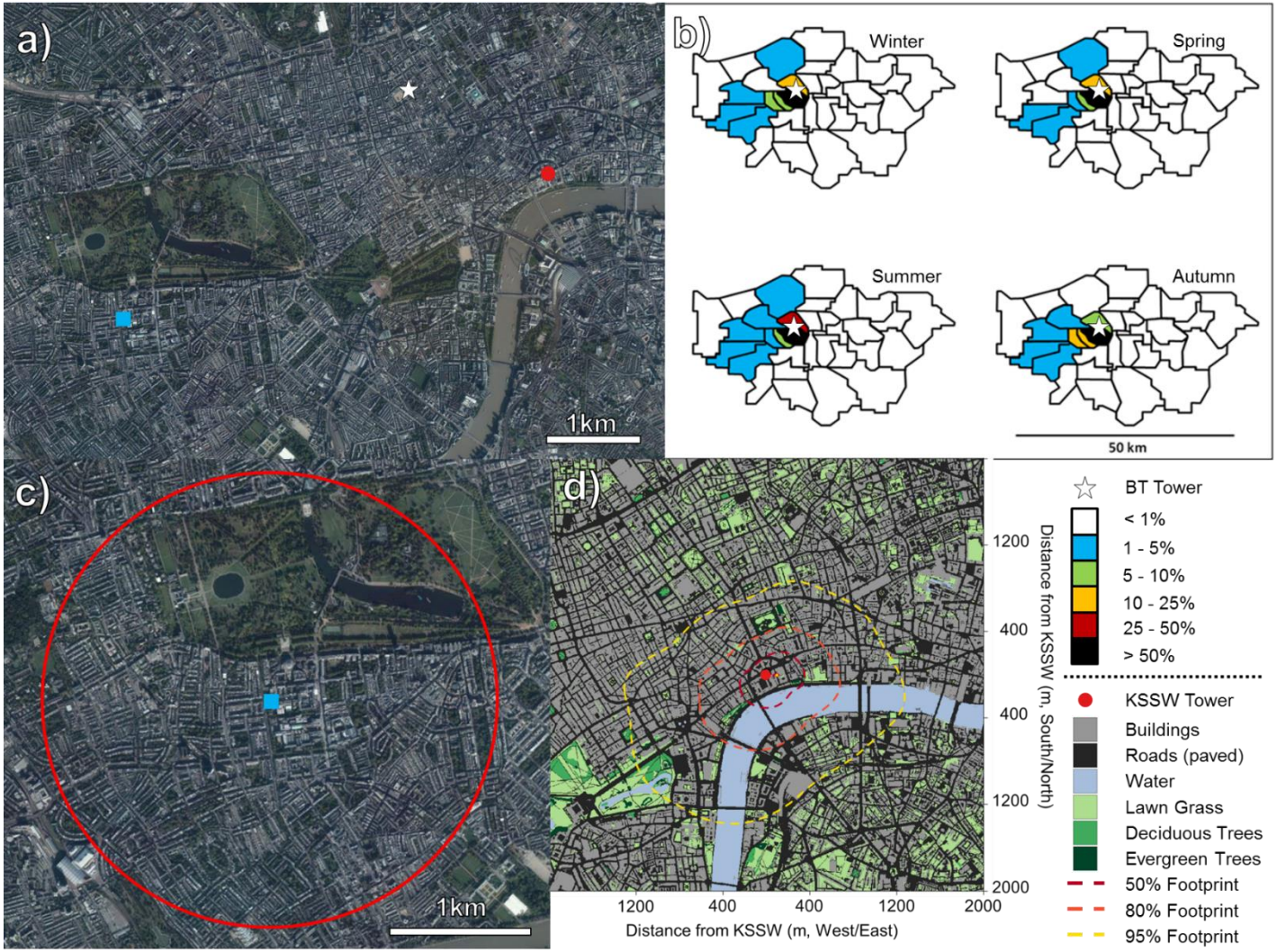

*Figure 7.1: Locations (a) and (b-d) source areas of studies which have calculated net CO_2 emissions in London. Studies are (b) Helfter et al. (2011) (a: white star), (c) Sparks and Toumi (2011) (a: blue square) and (d) Ward et al. (2015) and this study (a: red dot). (b) Indicates the percentage of the flux footprint of the BT tower (see key to the upper right of (d)) over Greater London for each season and was reproduced with permission from Fig 3a in Helfter et al. (2011). (c) Shows the sampling location and the land within 1.6 km, the distance containing 90% of the upwind flux, for Sparks and Toumi (2011). (d) Land cover around the KSSW tower (red dot, key: lower far right) overlain with the 2012-2014 CO_2 flux source areas: 50% (dark red), 80% (orange) and 95% (yellow) of the average non-gap filled footprint (*Section *7.2). X and y axes are British national grid east/west and north/south respectively*

7.2 Land use partitioning/footprint method

7.2.1 Introduction

In order to link the measured CO_2 flux to processes, and develop a greater understanding of the factors affecting vertical CO_2 fluxes and by inference, net CO_2 emissions, it is necessary to know which sources or sinks are in the field of view for the equipment used for each measurement (Schmid, 2002; Vesala *et al.*, 2007). This information is also important to determine whether the flux measurements are representative of the land cover/use of interest and whether the inventory measurements used for comparison with the micrometeorological measurements are appropriate (Schmid, 2002). Because the urban surface is heterogeneous with unevenly distributed sources and sinks that vary in position and magnitude at multiple temporal scales (Grimmond *et al.*, 2002) the characteristics of the source area (the fraction of the earth's surface containing the sources and sinks which contribute to the measured signal) will vary with wind direction, wind speed, atmospheric stability and surface roughness (Rannik *et al.*, 2012). As the source area technically includes the entirety of the earth's surface (as, in theory, sources and sinks on any one part of the globe may contribute to the signal in any other part), it is typically given as the area of land containing processes which contribute a set proportion of the flux measurement within a given time period, e.g., 80% of the flux for one 30 minute period (Schmid, 1994). The emissions or sinks within a source area are linked to the flux measurements by a spatial weighting known as a flux footprint, which can be defined as the relative contribution of each element of the source area to the measured signal (Schuepp *et al.*, 1990). The peak of this footprint tends to be closer to the flux measurement point under unstable atmospheric conditions, lower wind speeds and lower measurement heights above ground level. These effects are illustrated and discussed in more detail in Section 7.2.3.

There are four basic approaches (and numerous parameterisations) to estimate the flux footprint, typically termed 'flux footprint models', namely (Vesala *et al.*, 2007): analytical, Lagrangian stochastic particle dispersion (LSPD), large eddy simulations (LES) and ensemble averaged closure models. The characteristics of each, discussed in detail by Rannik *et al.* (2012), are summarised in Table 7.2.

Table 7.2: Summary of footprint model characteristics based on a review by Vesala et al. (2008).

	Computing Time	Atmospheric Stability	Accuracy	Number of Inputs	Examples
Analytical	Low	All	Low	Low	Kormann and Meixner (2001)
LSPD: Forward Backward	Medium Medium	Dependent upon imposed turbulence statistics	- -	Turbulence statistics	Rannik *et al.* (2000) Kljun *et al.* (2002)
LES	Very High	Best under convective conditions	High	Very high	Cai *et al.* (2010)
Ensemble	Increases with order of model	Neutral only	Increases with order of model	Increases with order of model	Sogachev and Panferov (2006)

The criteria for choosing a flux footprint model depend upon whether the model is intended for general use or for analysis of case studies. The main requirement for the former is that it

should be ‘computationally cheap’, i.e., it should be efficient and time short, so that the ‘computer time’ is much less than real time. This constraint is removed for analysis of single days of interest and the accuracy of the result is of much greater importance. In both cases the model should be applicable over the range of atmospheric stabilities observed in London (Section 4.5.3). All other factors being equal, a model requiring fewer or more commonly measured variables as input is preferable.

As the range of stabilities observed in central London is quite large and it is desirable to have half hourly source area estimations for multiple years’ of data, computing time and the ability to model source areas over a wide range of atmospheric stabilities were the key criteria for model selection. The analytical model proposed by Kormann and Meixner (2001) fulfils these criteria and has previously been used successfully to estimate CO_2 flux footprints over urban landscapes (Christen *et al.,* 2011; Crawford *et al.,* 2011; Liu *et al.,* 2012).

7.2.2 Method

The flux footprint was evaluated following Kormann and Meixner (2001) with roughness length calculated according to Macdonald *et al.* (1998). The software was originally provided in IDL by Andreas Christen and adapted for use at KS by Simone Kotthaus. The adaptations consist of a dynamic calculation of the morphometric parameters and roughness length (achieved by iteratively calculating the footprint) using Macdonald *et al*. (1998) and using measured values of the friction velocity rather than calculating it from roughness/stability parameters and mean wind speed. The software was translated into R by the author, copies are provided in Appendix 7.A and a comparison of the program output by the Kotthaus IDL version and the author’s R version is provided in Appendix 7.B.

The footprint calculation follows Kotthaus and Grimmond (2012, 2014a) (Figure 7.2). This method uses morphometric parameters (plan area index, frontal area index, height of buildings above ground level, height of ground above sea level) that are calculated for individual 1° directions from a digital elevation model (DEM) for a 500 m radius (a first order approximation of the source area, Kotthaus and Grimmond, 2014b, contains 70.2% of the final footprint for 2012-2014) around KSSW. The parameters for the mean wind direction are used with EC meteorological data for each 30 m period to generate the first footprint estimates. These estimates are used in the next iteration to sample the DEM to obtain a final footprint after three iterations. This was done for 2012 to 2014. Missing EC data periods were filled with footprints from periods with the same wind speed and direction data (WXT, KSSW, height A). Initial data availabilities for 2012 to 2014 (excluding 2012/001 – 2012/084 when the tower was at KSS) were 78.5%, 77.4% and 83.2% respectively. Data availability of the gap filled flux footprint files was 96.8%, 96.4% and 99.5% in 2012, 2013 and 2014 respectively.

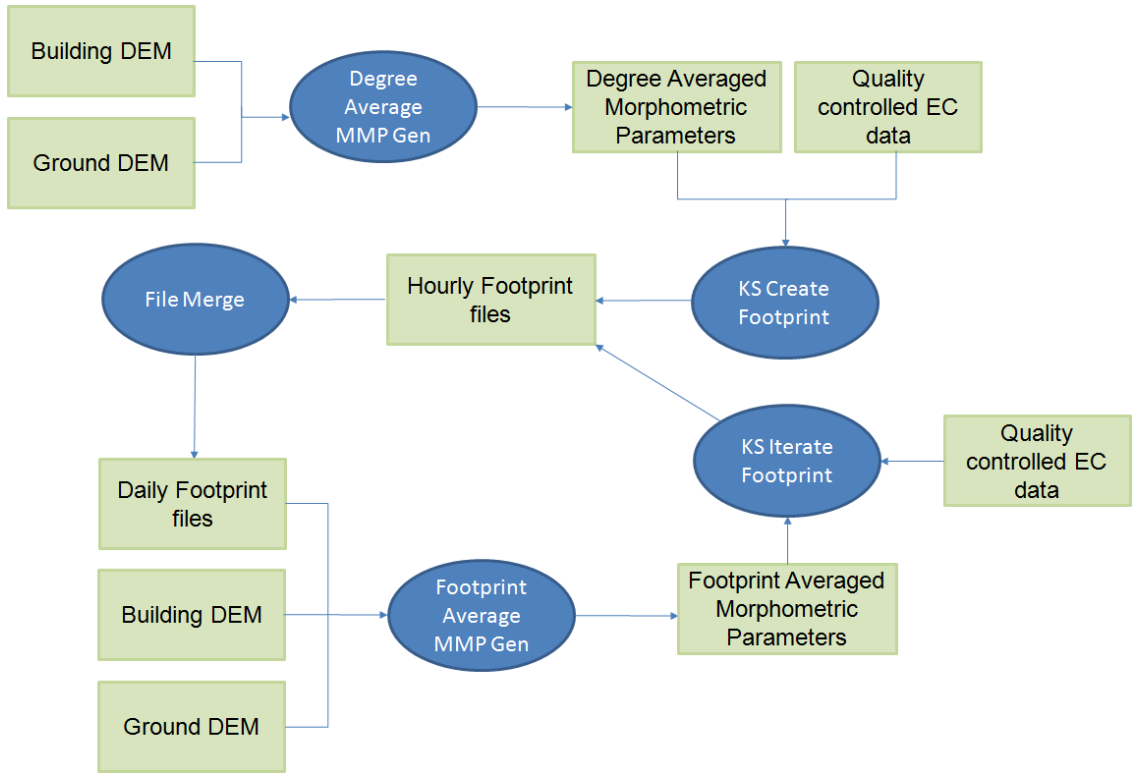

Figure 7.2: Flow diagram of flux footprint processing. Pale green boxes: inputs/data, dark blue ovals: programs (Appendix 7.A). The final files contain the parameters listed in Table 7.B.1 in Appendix 7.B.

The footprint weighted source areas (e.g., Figure 7.B.1, Appendix 7.C) were used to calculate the land cover fractions for each 30 minute period from land cover data (Figure 7.1d, Lindberg and Grimmond, 2011). Seven land cover classes (building, road, water, grass, shrub (no instances in the area mapped), coniferous and deciduous tree) at 4 m horizontal resolution are used (Table 7.3).

The land cover fractions were multiplied by emission/sink strengths for the following classes: buildings (space heating), roads (vehicle emissions), river (efflux), bare soil in parks or on private land (respiration) (the position of street trees and the bare soil around their roots was not recorded in the land cover data), lawn grass (sequestration by photosynthesis and release by plant and soil respiration). Human respiration was assumed to be delocalised over all non-open water land classes. Sequestration of CO_2 by trees was estimated only at the annual scale rather than 30 minute intervals.

7.2.3 Results

The multiple year aggregated flux source area has a generally SW-NE axis (Figure 7.1d, Figure 7.3) which is elongated towards the prevailing wind direction (south west) and contracted to the north west of KS. The overall shape of the source area is possibly more circular than might be expected from the distribution of wind directions recorded at the site (e.g., Figure 2.B.6 in Appendix 2.B, Figure 5.22b, Figure S.5 in the supplementary material of Björkegren *et al.*, 2015) which were heavily skewed (>50% of all half hourly periods) to the south to southwest octant. Examination of the typical shape of the half hourly flux source areas (e.g., Figure 7.C.1 and Figure 7.C.2 in Appendix 7.C) shows that even under conditions of high wind speeds,

where the effect of the crosswind variation might be expected to be relatively low, the source area is wide and the flux will be affected by sources or sinks that are on a bearing quite different from the mean wind direction. A source area 'hole', or area which contributes less to the flux than its surroundings is visible about 50 m to the east of the tower (Figure 7.1d). This was observed in all annual aggregations of the flux footprint (Figure 7.3), and the shape of the cumulative annual source area varies very little by year (Figure 7.3) for three weights considered (50%, 80% and 95%).

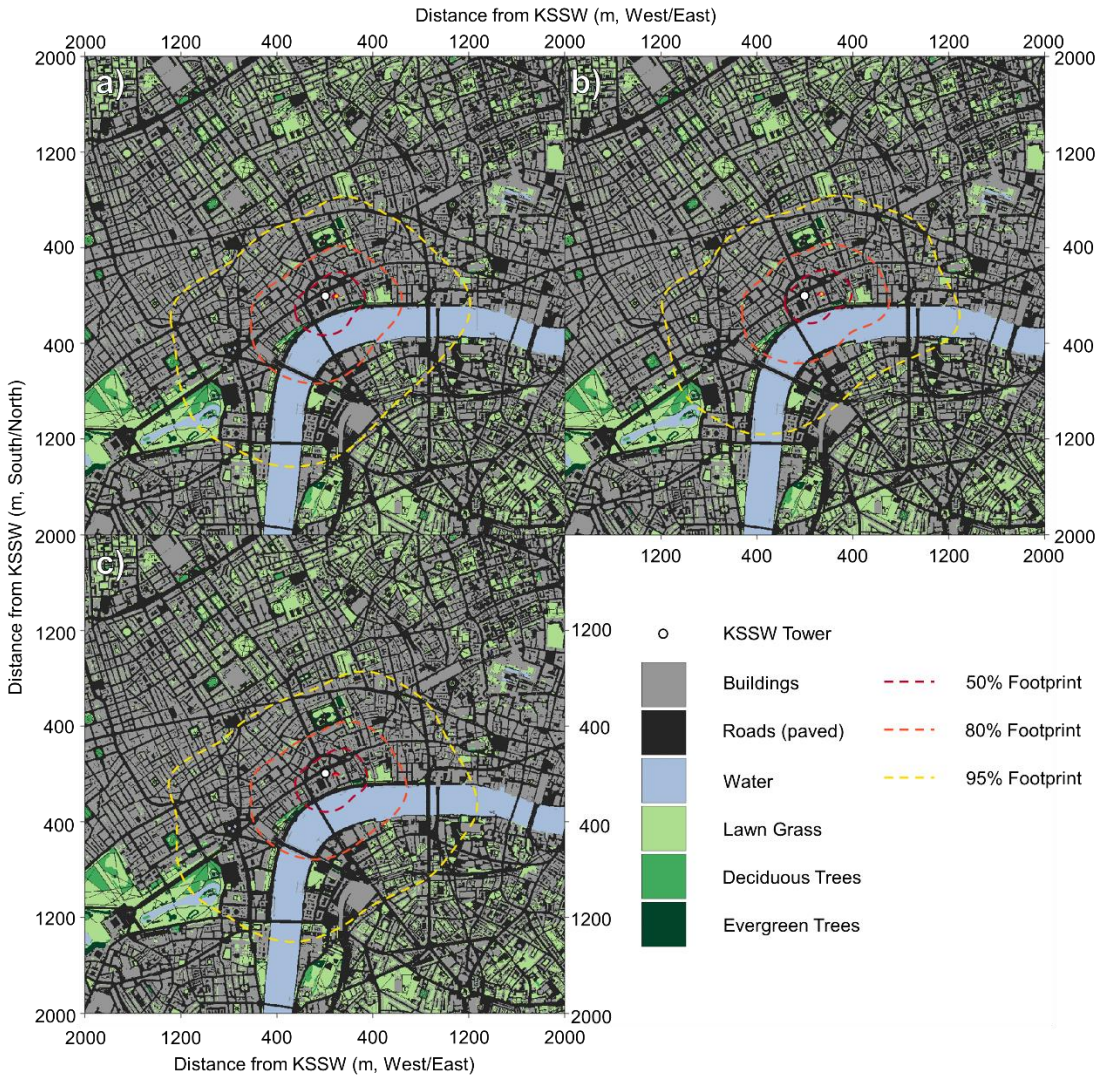

Figure 7.3: Annual average footprint for the KSSW tower in (a) 2012, (b) 2013, (c) 2014. Data not gap filled.

Variation in the land surface characteristics of the flux footprint were observed between different years (Table 7.3) however the differences were small. In all years 'road' was the most common land use class, closely followed by 'building', then 'water', 'lawn grass' and the two tree classes. It should be noted that the tree classes are only defined for areas where trees are the primary land cover class and do not include street trees; however, as emissions/uptake for trees are calculated on an annual basis from survey measurements (Section 7.3.1.1) this will not lead to an underestimation of the contribution of trees to the annual CO_2 emissions.

Table 7.3: Land cover (%) for (weighted by) the KSSW flux footprint by year (2012-2014) assuming the 4000 m x 4000 m area (Figure 7.1d) contains 100% of the total footprint (actual value ca. 90%). Percentages are given to one decimal place.

Primary Land cover	*2012*	*2013*	*2014*	*All years*
Buildings	38.3	41.0	38.8	39.4
Roads	41.7	42.6	41.6	42.0
Water	15.4	11.8	15.0	14.0
Lawn Grass	3.5	3.6	3.6	3.6
Deciduous Trees	0.7	0.6	0.6	0.6
Evergreen Trees	0.4	0.4	0.4	0.4

7.3 Inventory results and estimation of errors

Each sub-section contains the method used to generate an emission factor per m^2 of vegetation, bare soil, river water, road and building.

7.3.1 Vegetation

This section covers uptake and emission of CO_2 by trees and grass, which composed 3.9% and 1.4% of the land cover within 500 m of KS respectively. Loss of vegetation to animals, and subsequent release of CO_2 to the atmosphere by animal respiration and decomposition, is not considered due to the difficulty of estimating populations with any certainty. Decomposition of leaf litter and lawn clippings are also not considered as both are removed regularly and are not composted or burnt on site. The sequestration of CO_2 each year is therefore calculated as the difference between the uptake of CO_2 by photosynthesis and the CO_2 released to the atmosphere by respiration above (leaves) and below (roots) ground. The sequestration of CO_2 was calculated separately for woody (trees, shrubs > 2 m tall) and ground (lawns, shrubs < 2 m tall) vegetation. The two methods and their results are described in Sections 7.3.1.1 and 7.3.1.2 respectively.

7.3.1.1 Woody vegetation

Flux footprint calculations (Section 7.2) suggested that vegetation within 500 m of KS in the prevailing wind direction (south to west quadrant) and 250 m for the other three quadrants had the greatest influence on the measured CO_2 fluxes. The woody vegetation within this area was predominantly (51.3% stems or tree trunks, 67.8% basal area) street trees, of which 95.9% stems and 99.6% of the basal area were London Plane with all the remainder Oak (*Quercus Cerris*). Approximately a third (37.8% stems, 23.8% basal area) of trees surveyed were in public parks, with the remainder (10.9% stems, 5.9% basal area) on privately owned land. The majority of trees, particularly those with a large basal area and hence biomass were therefore accessible for ground based measurements or surveys. Remote sensing or satellite measurements (e.g., Potter *et al.*, 2007) were considered; however, there were concerns that the presence of multiple canopy layers in the public park could result in under counting of vegetation and photosynthetic uptake.

Leaf chamber measurements of London Plane trees near Embankment gardens were made during the summer of 2014 from which light response curves could be constructed. This

approach was abandoned for calculation of sequestration of CO_2 by woody vegetation for the reasons discussed in the following paragraph.

Visual inspection of leaves sampled found a build-up of dust and other deposits on the leaf surface. This is likely to affect leaves closest to the ground (all leaves sampled were by necessity < 2 m above ground level) due to the proximity of the road and the sheltering from rain by the rest of the canopy. The response to PAR of these sampled leaves may therefore not adequately reflect the response of the leaves in the rest of the canopy. Other considerations include potential inaccuracies in scaling up from sampled leaves to an entire canopy, and the difficulty of measuring the release of CO_2 by respiration of non-leaf tissue. The latter was particularly important as the majority of the trees within the area of interest are deciduous and will release, but not store, CO_2 to the atmosphere during the leaf-off period (approximately late October to March). Making direct measurements of the rate of CO_2 exchange for a statistically valid sample of the trees within the KSSW tower flux footprint for a long enough period to characterise the range of atmospheric and seasonal conditions within central London would require resources beyond the scope of the project.

A third approach is to relate a surveyed tree characteristic to tree volume or dry weight and calculate the difference over the time period of interest. Typical characteristics are tree height or diameter and these are converted to the quantity of interest (above ground biomass, total biomass, leaf biomass, etc.) using allometric equations. As the form of a tree varies with site conditions and climate, e.g., windswept coastline vs. more sheltered inland forest or hedgerow, allometric equations developed in one location may not be accurate in another (Clark *et al.*, 2001). A further problem is that whilst most allometric equations in the literature use measurement of tree diameter at breast height (DBH), this is not useful for monocots such as bamboo or palm trees (present in Embankment gardens) which do not have continued outward growth. Additionally, there are region-specific differences in the height above ground at which DBH measurements are made. This suggests that whilst tree surveys can be a relatively low-cost and simple means of gathering the data required to calculate CO_2 sequestration, care must be taken to ensure that the allometric equations used are appropriate for the site studied. The alternative, developing site specific equations by destructive sampling of surveyed trees, was not practical given that all trees within the footprint were publicly or privately owned and the limited facilities available. Calculation of the change in above ground biomass in this manner accounts for carbon fixed as part of the trunk and woody canopy matter (and, depending on the allometric equation or conversion used, the root matter). It does not account for fine litter fall such as small twigs and leaves. It is recommended that the latter be estimated using litter traps (Clark *et al.*, 2001); however, this was not practical in central London as it would obstruct pedestrian walkways and potentially be a target of theft or vandalism. The percentage of carbon fixed in leaf matter decreases rapidly with increasing tree size (approximately 22% for beech trees < 5 cm in diameter to about 2% for beech trees > 20 cm in diameter, Bartelink, 1997). Given the median diameter of the surveyed trees was 38 cm the error introduced by not measuring the carbon fixed as leaves was deemed negligible relative to

the uncertainties associated with using non-site specific allometric equations (-24 to +93%, Grier *et al.*, 1984).

All woody vegetation within 250 m of KSSW, and all woody vegetation within 500 m to the south west of KSSW (Figure 7.4) were surveyed (3-4 October 2015). Observations included species type (if unidentifiable, the entry was noted as deciduous or evergreen), position (drawn on a map and Latitude and Longitude provided by '*My GPS Coordinates*' Android app), tree vitality, and diameter at breast height (DBH). Although possible to use this information within various models (e.g., CUFR Tree Carbon Calculator, 2008) to obtain estimates of CO_2 sequestered each year, these are predominantly non-UK so the meteorological conditions are likely inappropriate.

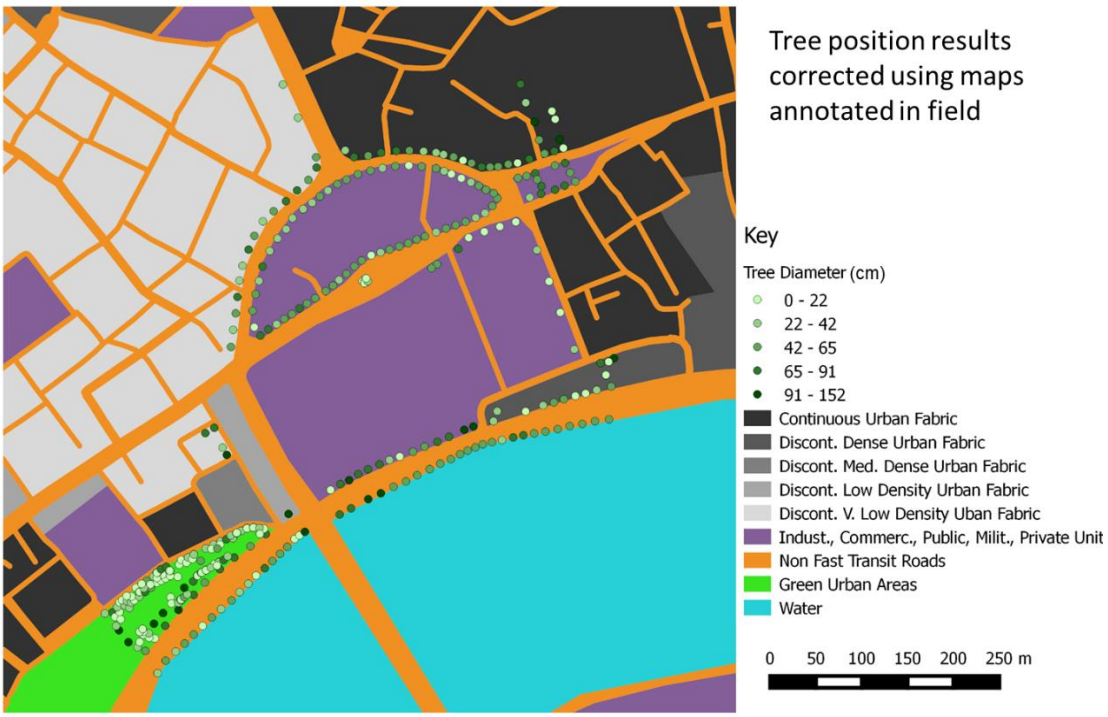

Figure 7.4: Vegetation (points) stem diameter by land class (see key: right) as surveyed 3rd – 4th October, 2015.

The age of each tree was calculated following Forestry Commission guidelines (White, 1998) as information regarding planting dates and tree ages were not held by the local council. Where age/ring width data were not available, data for the closest species were substituted. Following the method of Velasco *et al.* (2014), the tree ages were used to estimate the trees' radii for the preceding five years for both average and good conditions, and all trees less than one year old (replacement street trees) were excluded from further calculations. The above ground dry weight biomass for each tree for each year was calculated from the radii using allometric equations (Bunce, 1968; Brandini and Tabacchi, 1996; Jenkins *et al.*, 2003; Table 7.4). To minimise errors due to climate differences, allometric equations for each species (where available) were chosen based on the proximity of the study site to KS (UK equations were preferred, followed by European and other temperate regions). Where no allometric equations

for a species were available, equations for a species with similar growth characteristics were used.

Table 7.4: Allometric equations for above ground biomass (kg) with their source used. Equation Type [1]: exp(a+b.ln(DBH)); [2] a+b.DBH^2; [3] $10^{-3}.10^{(a+b.log(\pi.DBH))}$ where DBH is tree diameter (cm), ln denotes log_e and log denotes log_{10}. a and b are constants used (some are the averages). Species surveyed are given using their common names, species of the allometric equation used are given as listed in the study referenced.

Species Surveyed	Allometric Eq. Species	Eq.	Study site	a	b	Reference
London Plane	*Acer Pseudoplatanus*	1	UK	-2.7312	2.547	Bunce, 1968
Oak	*Quercus*	1	UK	-2.7467	2.5955	Bunce, 1968
Holly	*Arbutus Unedo*	2	Italy	-2.7563	0.3045	Brandini and Tabacchi, 1996
Sequoia	*Softwood (Cedar/Larch)*	1	USA	-2.0336	2.2592	Jenkins *et al.*, 2003
Sycamore	*Acer Pseudoplatanus*	1	UK	-2.7312	2.547	Bunce, 1968
Chestnut	*Hardwood (Maple/ Hickory/ Beech)*	1	USA	-2.0127	2.4342	Jenkins *et al.*, 2003
Lime	*Tilia Cordata*	1	UK	-2.6788	2.4542	Bunce, 1968
Ash	*Fraxinus Excelsior*	1	UK	-2.4658	2.5174	Bunce, 1968
Conifer	*Pinus Sylvestris*	3	UK	0.981	2.289	Lim and Cousens, 1986
Magnolia	*Arbutus Unedo*	2	Italy	-2.7563	0.3045	Brandini and Tabacchi, 1996
Deciduous	*Quercus*	1	UK	-2.7467	2.5955	Bunce, 1968
Evergreen	*Arbutus Unedo*	2	Italy	-2.7563	0.3045	Brandini and Tabacchi, 1996
Apple	*Hardwood (Mixed)*	1	USA	-2.48	2.4835	Jenkins *et al.*, 2003
Cherry	*Hardwood (Mixed)*	1	USA	-2.48	2.4835	Jenkins *et al.*, 2003
Fig	*Hardwood (Mixed)*	1	USA	-2.48	2.4835	Jenkins *et al.*, 2003
Laurel	*Arbutus Unedo*	2	Italy	-2.7563	0.3045	Brandini and Tabacchi, 1996
Maple	*Acer Pseudoplatanus*	1	UK	-2.7312	2.547	Bunce, 1968

The below ground biomass was assumed to be 1.28 the above ground biomass (Cairns *et al.*, 1997; Husch *et al.*, 1982; Wenger, 1984 all cited by McPherson *et al.*, 2013). The carbon mass was assumed to be 0.5 of the biomass (Lieth *et al.*, 1975 cited by McPherson *et al.*, 2013; Agueron and McPherson, 2011, Thomas and Martin, 2012). The mass of CO_2 is 3.67 times the carbon mass.

Annual totals for the area surveyed (0.34 km^2) give a per km estimate of CO_2 sequestration by woody vegetation (Figure 7.5). This estimate is biased by the lack of prior survey measurements. Of 384 stems surveyed, 60 were smaller than 10 cm diameter, of which 10 were London Plane and likely to be replacements for older, larger trees capable of sequestering more CO_2 (Stephenson *et al.*, 2014). The values in Figure 7.5 prior to 2014 should therefore be considered as lower bounds estimates. Estimates of CO_2 emissions for central London vary from 35,500 t CO_2 yr^{-1} (Helfter *et al.*, 2011) to 46,600 t CO_2 yr^{-1} (Ward *et al.*, 2015). The maximum impact of the sampled trees on London CO_2 emissions, i.e., using the lower Helfter *et al.* (2011) estimate of emissions and the very uppermost estimate of CO_2 sequestration of 154.93 t km^{-2} yr^{-1} (2014-2015, 'Good' conditions) is -0.32%. The trees in central London may therefore be considered to have a negligible impact on total CO_2 emissions.

The stem density (1120 trees km^{-2}) and plan area fraction covered by trees (2%) at KS is much lower than those reported by similar studies in Sacramento (1480-6880, 8%-28.1%, McPherson *et al.*, 2013), Los Angeles (2280-7080, 3.5%-21.9%, McPherson *et al.*, 2013), Singapore (5545

km^{-2}, 11%, Velasco *et al.*, 2013) and Mexico City (5276 km^{-2}, 6%, Velasco *et al.*, 2014). As expected, the amount sequestered, (155 tCO_2 km^{-2} yr^{-1}) is also much lower (Table 3 in McPherson *et al.*, 2013; Velasco *et al.*, 2013; Velasco *et al.*, 2014).

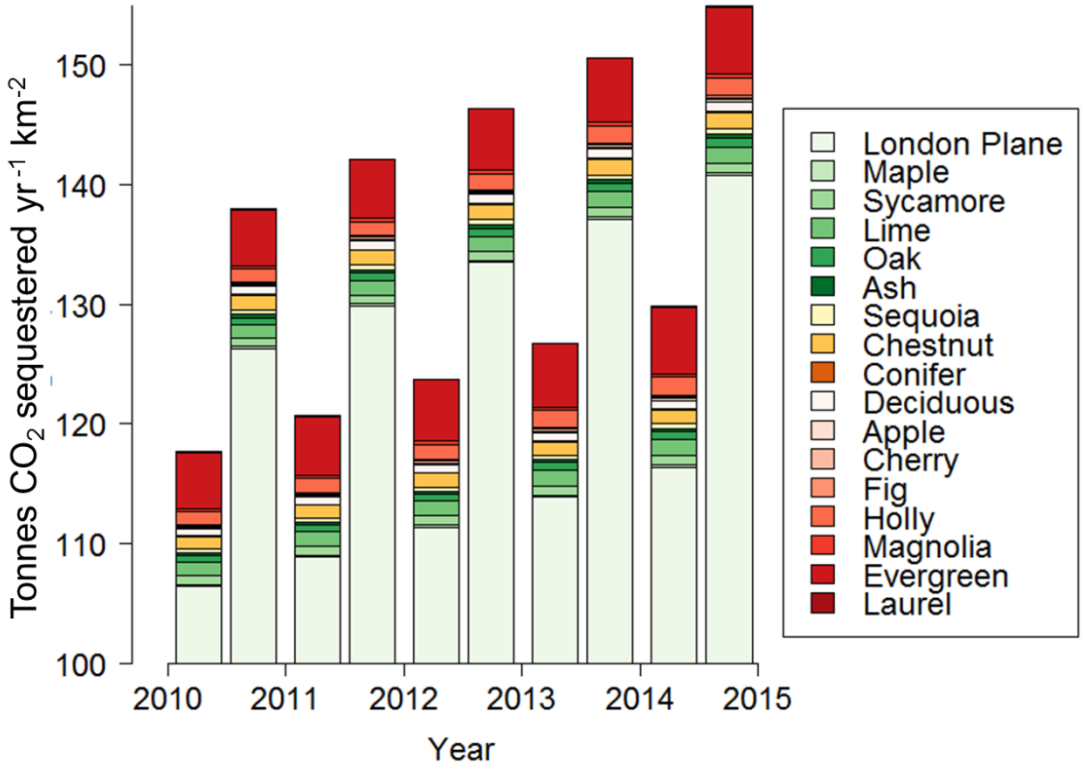

Figure 7.5: Carbon dioxide sequestered by sampled trees (see key for species) per year per km^2 (September 2010 to September 2015) for (left) average and (right) good growing conditions for each year.

7.3.1.2 Lawn Grass

As described in Section 2.2.7, photosynthetic light response curves for lawn grass and London Plane trees were measured during the summer of 2014 using an LI6400. Due to the great variety of non-lawn low vegetation (e.g., flowering plants), the small land cover fraction, and their impermanence (once the plants have ceased to flower, they are often dug up and replaced with different varieties), only photosynthetic uptake from lawn grass was calculated.

Net photosynthetic uptake ($F_{P,\,leaf}$) was found to vary consistently with photosynthetically active radiation (PAR), but not air temperature, leaf temperature or carbon dioxide concentration (Section 2.2.7), hence the uptake of CO_2 was fitted only to PAR. A linear model was fitted for PAR values less than 200 µmol m^{-2} s^{-1} (7.2), and $F_{P,\,leaf}$ values were fitted to the natural log of the PAR values for PAR greater than 200 µmol m^{-2} s^{-1} (7.3) (all constants given to 3 d.p.). In both cases the negative of $F_{P,\,leaf}$ was used for ease of calculation.

$$-F_{P,leaf} = 0.044 \times \mathrm{PAR} - 2.215 \qquad \mathrm{PAR} < 200\ \mu mol\ m^{-2}s^{-1} \tag{7.2}$$

$$-F_{P,leaf} = 4.201 \log_e \mathrm{PAR} - 15.881 \qquad \mathrm{PAR} \geq 200\ \mu mol\ m^{-2}s^{-1} \tag{7.3}$$

Agreement between measured and modelled $F_{P, leaf}$ was reasonable (R^2 of 0.63 and 0.39 for (7.2) and (7.3) respectively) given the large scatter in the light response curve data. The light compensation point (point at which the CO_2 absorbed by photosynthesis is equal to that emitted by plant respiration) and the dark respiration rate were calculated as 50 µmol m^{-2} s^{-1} and +2.5 µmol m^{-2} s^{-1} respectively. $F_{P, leaf}$ for 2012 to 2014 was calculated from PAR measured at KSS, KSSW and KSS45W at 15 minute intervals (Figure 7.6). This calculation assumed a leaf area index of 1, that all grass always received the maximum PAR available, and that all areas designated as 'grass' are always in full leaf with no bare patches. The leaf area index at Embankment was not measured due to safety concerns (discarded needles had been found in the lawn). Measurements made at a similar site in Norfolk (UK) found a leaf area index of 1.62, which is much closer to that used in other studies (e.g., Grimmond and Oke, 1991) but due to site separation this value was not used and the effect of this assumption is to reduce the magnitude of the calculated $F_{P, leaf}$ relative to the 'real' value. Conversely, the grass is likely to be shaded during the day, either by tree canopies or by the city workers and tourists who picnic on the grass. Human trampling has been observed to reduce the grass cover, with large semi-bare patches found near walkways. The second and third assumptions are therefore likely to increase the calculated $F_{P, leaf}$ relative to the 'real' value.

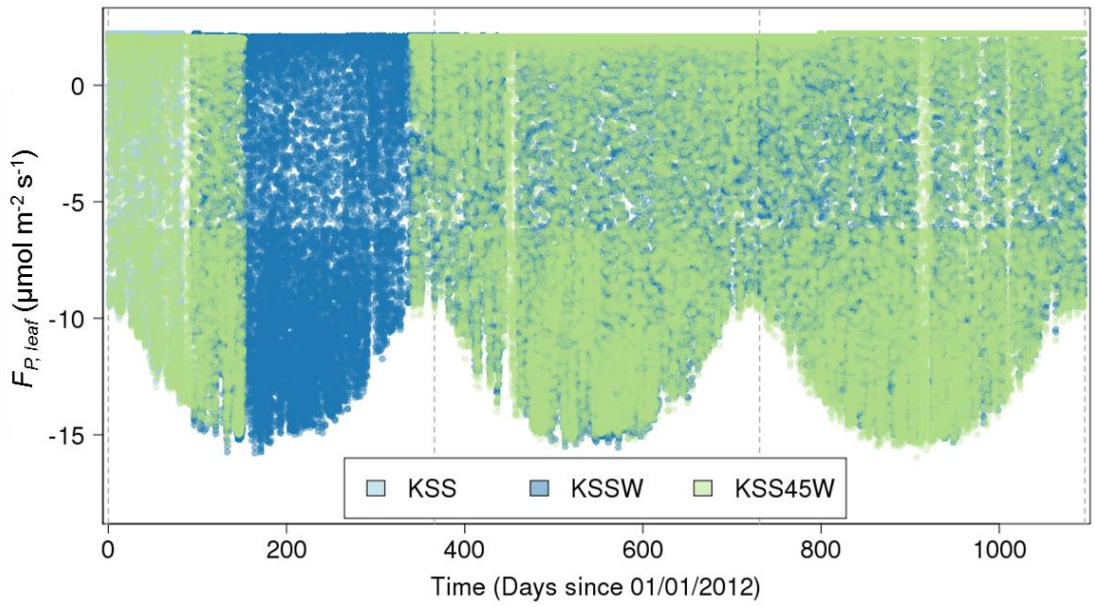

Figure 7.6: Modelled vertical CO_2 flux over lawn grass in central London using PAR data collected at three sites (see key). Negative fluxes denote net uptake of CO_2 by the grass, whilst positive fluxes denote net source of CO_2 to the atmosphere.

For 2014 the total modelled CO_2 uptake by lawn grass per km^2 for an urban environment with the land cover characteristics of the KSSW tower flux footprint was 107 tCO_2 km^{-2} yr^{-1}, of the same order of magnitude as the contribution calculated by Velasco *et al*. (2013) of 128.8 tCO_2 km^{-2} yr^{-1} for turf grass with a plan area fraction of 4%, which suggests that even with the assumed leaf area index of 1 the London figure is an over-estimate (the annual uptake due to lawn grass assuming a LAI of 1.62, and no change to the other assumptions increases to 173 tCO_2 km^{-2} yr^{-1}). Even so, the calculated uptake of CO_2 by lawn grass is equivalent to 0.29% of

the yearly emissions calculated by Helfter *et al.* (2011). As with the trees, this suggests that photosynthetic uptake of CO_2 has a negligible impact on net emissions in central London.

7.3.2 Soil respiration

As measurement of soil CO_2 emissions is labour intensive (Section 2.2.6) and the percentage of unsealed land cover is very low, continuous soil fluxes were calculated from the van't Hoff equation following Velasco *et al.* (2014), rather than measured throughout the year. The van't Hoff equation relates the soil CO_2 flux (F_{soil}) to the soil temperature (T_{Soil}), soil CO_2 flux at 10 °C ($F_{soil,\ 10}$) and the increase in respiration rate per 10 °C (Q_{10}):

$$F_{soil} = F_{soil,10} Q_{10}^{((T_{soil}-10)/10)} \quad (7.4)$$

This equation does not take soil moisture into account; however, as the unsealed surfaces are primarily in irrigated public parks and private (commercial) gardens, soil moisture is not expected to be a limiting factor. The constants $F_{soil,\ 10}$ and Q_{10} are site specific. As soil flux measurements were made towards the end of summer, soil temperatures were too high to measure $F_{soil,\ 10}$. Instead, the $\log_{10}$ of (7.4) can be rearranged to give a linear equation:

$$\log_{10}(F_{soil}) = \frac{T_{Soil}-10}{10} \log_{10}(Q_{10}) + \log_{10}(F_{soil,10}) \quad (7.5)$$

from which $F_{soil,\ 10}$ and Q_{10} may be calculated. The results from the soil flux measurement campaign showed land-cover specific differences, but suggested $F_{soil,\ 10}$ and Q_{10} values at odds with the literature (Figure 7.7, Table 7.5). Instead, values for $F_{soil,\ 10}$ and Q_{10} were taken from measurements made at Alice Holt, UK (Bond-Lamberty and Thomson, 2010). The soil temperature data (T_{Soil}, Figure 7.8) were gap-filled by air temperature (T_A) measurements at KSSW (height A, Figure 2.1d) with a lag of about 2 hours using the following conversion:

$$T_{Soil,t} = aT_{A,t-2} + b \quad (7.6)$$

where *a* and *b* are empirically derived constants of 0.76 and 2.75 ºC respectively (2 d.p.), and *t*-2 denotes the time two hours prior to time, *t*. The gap filled data were used with (7.4) to calculate soil CO_2 fluxes for 2012-2014. Using the two Q_{10} values (3.2, Alice Holt UK (Bond-Lamberty and Thomson, 2010); 1.4 'global' (Velasco *et al.,* 2014)) (Figure 7.9) the overall range of F_{soil} was much larger with the Alice Holt Q_{10} value than when the smaller value was used.

The median F_{soil} values for 2012 – 2014 were similar at 2.02 and 1.76 µmol m^{-2} s^{-1}, respectively. After visual inspection, the ground below trees in parks and adjacent to the tree trunks on streets in central London is assumed to be bare soil. For trees in parks, the areal extent of the bare soil is assumed equal to the extent of the canopy (derived from LiDAR data). For street trees it is either 1 m^2 (if the tree trunk diameter was less than 1 m) or, due to the square paving stones used on the surveyed streets, the square of the trunk diameter (if > 1 m). The plan area of bare soil in the vicinity of KS was 5.4%. The F_{soil} values calculated previously

therefore give upper and lower estimates of the contribution of soil respiration to the measured NEE at KSSW height A of 150.3 and 128.0 gCO_2 km^{-2} yr^{-1}, i.e., the contribution of soil respiration to net emissions is approximately equal in magnitude and opposite in sign to the amount sequestered by woody vegetation and can be considered negligible.

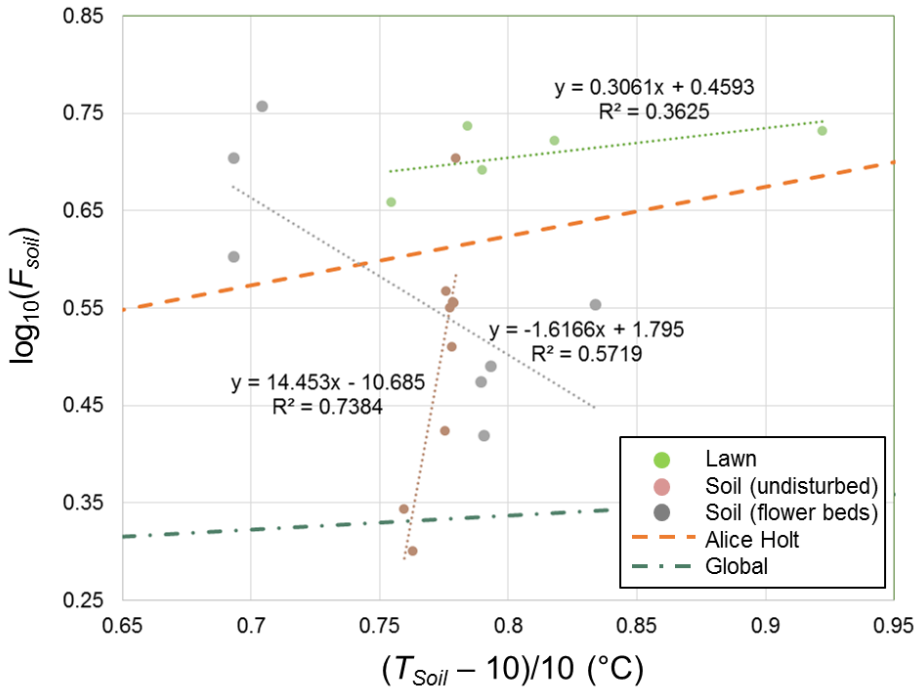

Figure 7.7: Relation of the soil flux (F_{Soil}) to soil temperature (T_{Soil}) measured at Embankment gardens (Figure 2.1b), 2nd September 2014 for three land cover types. Equations for lines of best fit and R^2 values determined by linear regression of $log_{10}(F_{Soil})$ on $(T_{Soil}-10)/10$ are shown. Two lawn measurements were omitted due to poor data quality. Also plotted are the relations calculated using Alice Holt, UK (orange dashed line, Bond-Lamberty and Thomson, 2010) and 'global' (dot-dash teal line, Velasco et al., 2014) results (Table 7.5).

Table 7.5: Values for Q_{10} and $F_{soil,\ 10}$ derived from the lines of best fit (Figure 7.7) for soil flux measurements conducted in Embankment gardens (02/09/2014, Section *2.2.6) over three unsealed surface types: lawn grass, undisturbed bare soil, and disturbed (fertilised and forked over) soil, as well as those derived from measurements at Alice Holt (Bond-Lamberty and Thomson, 2010) and around the globe (Velasco et al., 2014). All values given to 2 d.p.*

	$log_{10}\ Q_{10}$	Q_{10}	$log_{10}\ F_{soil,\ 10}$	$F_{soil,\ 10}$ (µmol m^{-2} s^{-1})
Lawn	0.31	2.02	0.46	2.88
Soil (undisturbed)	14.45	$2.84x10^{14}$	-10.69	$2.07x10^{-11}$
Soil (disturbed)	-1.62	0.02	1.80	62.37
Alice Holt	0.51	3.20	0.22	1.66
Global	0.15	1.40	0.22	1.66

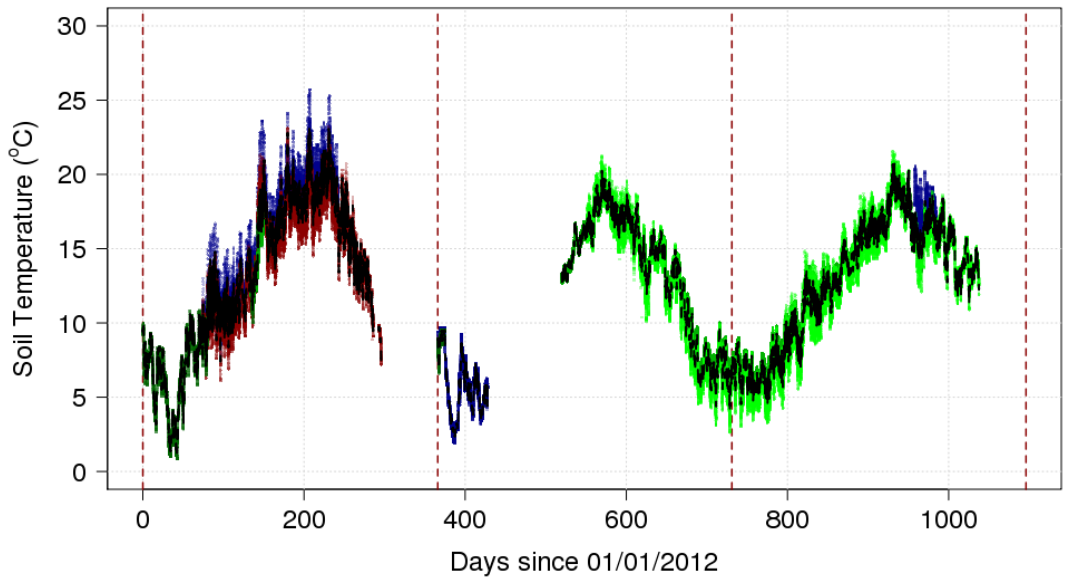

Figure 7.8: Mean (black) 30 minute soil temperature (°C) measured with SM300 (various sensors) at Embankment gardens (blue), Hanover Square (red), and Middle Temple gardens (green) (see Figure 2.1b for locations) with time. Vertical red dashed lines denote start of year.

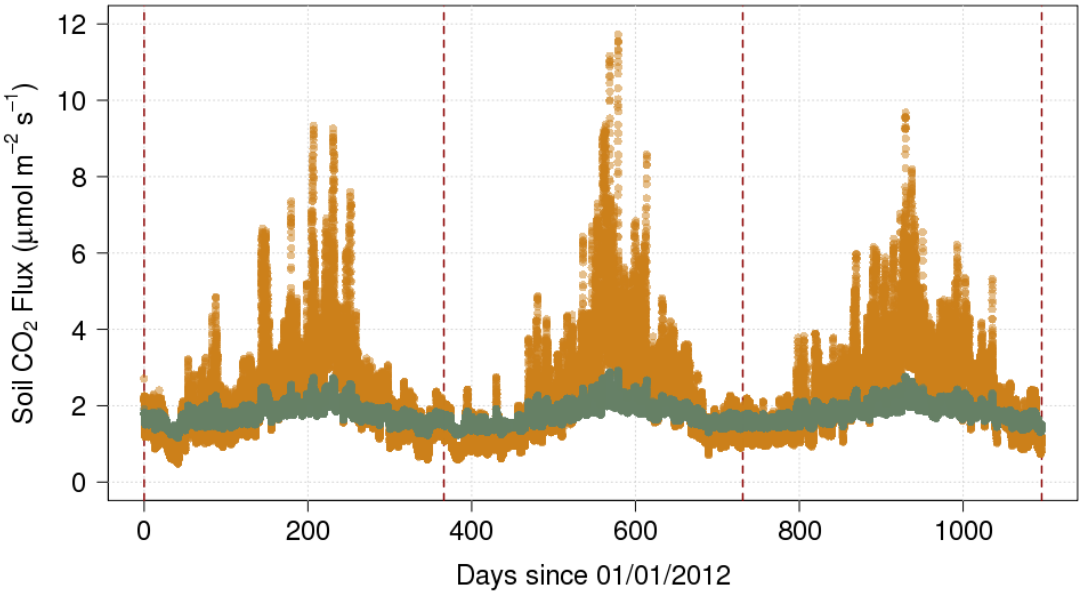

Figure 7.9: Calculated 30 minute soil CO_2 flux for central London using the van't Hoff equation with different Q_{10} values: (orange) 3.2 observed at Alice Holt (Bond-Lamberty and Thomson, 2010), (grey) 1.4 'global' value of Velasco et al. (2014).

7.3.3 River water CO_2 flux

Examination of the measurements described in Section 2.2.4 (Appendix 7.D) suggested that they were unsuitable for calculating the flux of CO_2 from the surface of the Thames and it was necessary to use values from the literature instead.

Studies of CO_2 fluxes from inland waters have tended to focus on rural, rather than urban environments. It is possible that the results in Table 7.6 underestimate CO_2 fluxes due to lower

water temperatures in rural compared to urban areas. Alternatively, the CO_2 fluxes from boreal lakes may be higher than those from the River Thames due to the higher carbon content. The studies summarised below were chosen as they were performed in approximately the same climatic zone to provide an order of magnitude estimate of the CO_2 flux that might be expected from the River Thames.

The highest calculated flux reported in the literature surveyed was derived from measurements made in a highly productive pond in the Lake District, UK (Casper *et al.*, 2000). It is two to eight times larger than the other values in Table 7.6 and is equivalent to 900 $tCO_2\ yr^{-1}$ for 1 km^2 of land with the same land cover characteristics as the KSS tower footprint (14% water, Ward *et al.*, 2015). Although this is much larger than the carbon sequestered by the vegetation as calculated in Section 7.3.1, it is still only 2.5% of the lowest estimate of yearly emissions (35,500 $tCO_2\ km^{-2}\ yr^{-1}$, Helfter *et al.*, 2011) and less than one ninth of the size of the difference between the traffic emissions calculated using the original and edited software (Section 7.3.4). Hence assuming the river to be a non-absorbing or emitting surface for the purpose of calculating CO_2 fluxes is likely to have a lower impact on the total calculated emissions than the uncertainty in the traffic emission calculation.

Table 7.6: Calculated CO_2 fluxes ($gCO_2\ m^{-2}\ yr^{-1}$) from inland waters in the temperate and boreal climate zones. All values are given to the nearest integer. Values in brackets denote the range. In some cases different values are given for different years.

Reference	Location	Description	CO_2 emissions ($gCO_2\ m^{-2}\ yr^{-1}$)
Sellers *et al.* (1995)	Western Ontario, Canada	Experimental wetland pond	291
Casper *et al.* (2000)	Lake District, UK	Hypertrophic lake (0.01 km^2)	643
Rantakari and Kortelainen (2005)	Finland	37 natural lakes, each with an area >100 km^2	1996: 78 1997: 66 1998: 101 1999: 85 2000: 92 2001: 96
Buffam *et al*. (2011)	Wisconsin and Michigan, USA	Northern Highlands Lake District	Lakes: 117 (92 – 143) Rivers: 172 (37 – 308)
Huotari *et al.* (2011)	South Finland	Natural lake (0.041 km^2)	2003: 355 2004: 271 2005: 271 2006: 271 2007: 249
Algestan *et al.* (2004) *via.* Koehler *et al*. (2014)	Sweden	Boreal inland freshwater	121

7.3.4 Traffic emissions

The road system surrounding the Strand campus consists of three major roads (The Strand/Aldwych, Kingsway, and Embankment) and numerous minor roads, alleyways and cul-de-sacs, some of which are partially or wholly pedestrianised (Figure 7.10). Waterloo bridge and Kingsway are connected above ground by Aldwych and belowground by the Strand underpass (northbound only except during the London Olympics during which it was southbound only). The major roads are all 4-lane single carriageways approximately 16 m in

width with traffic flow in both directions, except for the Strand located ca. 100 m to the east and west of KS, which divides into Aldwych to the north (traffic flow west to east) and the Strand to the south (traffic flow east to west). The southern half is further divided by a church (St Mary-le-Strand) with buses and southbound (Waterloo bridge) vehicles tending to travel to the south of the church and all other traffic to the north. The complex road network and potential for delayed release of traffic emissions (from the Strand underpass) represent a significant challenge to modelling of CO_2 emissions from vehicles at KS.

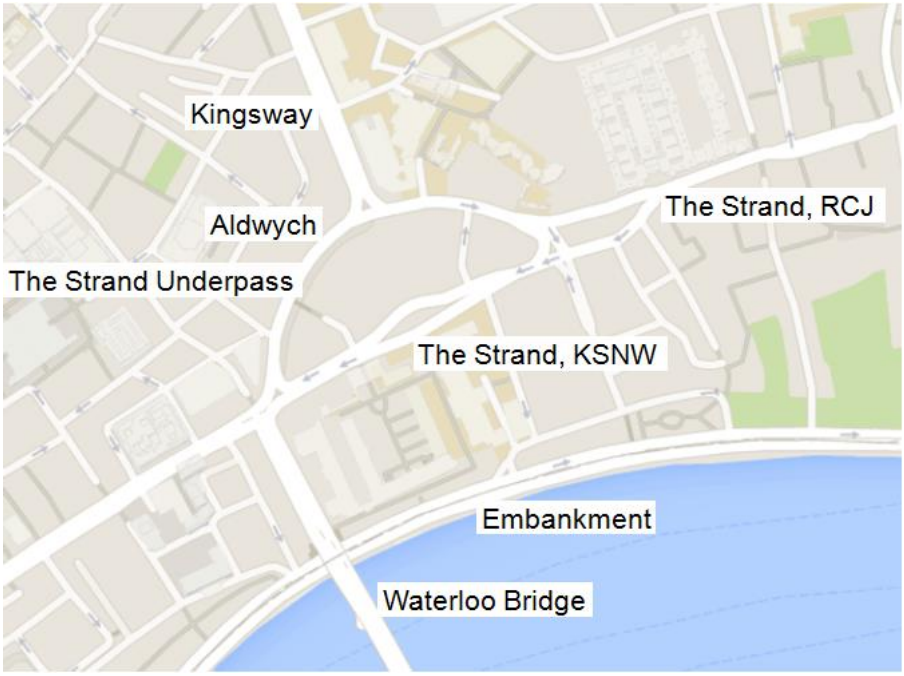

Figure 7.10: Major (thicker) and minor (thinner) roads around the Strand campus of King's College London. One way-traffic is indicated by small blue arrows. Google (2016)

Annual Average Daily Flows (AADFs) were available for 2000-2014 for all major road connections (junction to junction) in the vicinity of KS (Figure 7.11, Figure 7.12, Department for Transport, 2014). Also available were hourly total vehicle counts for 2010-2013 on the Strand outside the Royal Courts of Justice (RCJ) and one week of traffic count data at KSNW (Section 2.2.8).

A report of average daily traffic flows at 35 sites in Westminster derived from a seven day automated traffic count (Buchanan, 2011) showed peak flows varying from about 100 vehicles per hour to over 1500 vehicles per hour. Flows were not easily separable by road class, with some apparently minor roads having peak flows of approximately 1000 vehicles per hour. In general flows on minor (B) roads are lower than the AADFs recorded by TfL (Transport for London), but not low enough to be negligible.

Comparison of AADFs provided by TfL and an AADF generated from the 7 day KSNW ATC by vehicle type (Table 7.7) showed good agreement between most traffic count points within 250 m of KS, with the exception of the Strand underpass, which has a signposted height restriction of 3.6 m and a much lower proportion of vehicles larger than a car. This suggests that despite differences in total traffic volume, fleet characteristics are similar across the roads surrounding

the Strand campus and that it is reasonable to apply a fleet profile, generated from the 7 day KSNW ATC to the surrounding area.

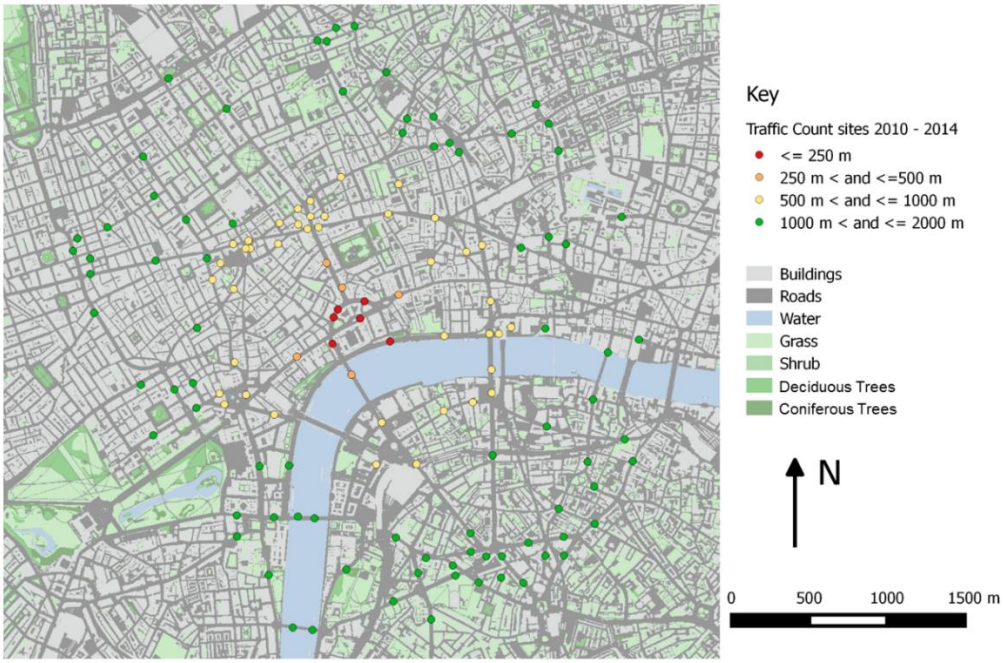

Figure 7.11: Location of traffic counts and AADF data for 2010 to 2014 coloured by distance from KSSW (see key: right).

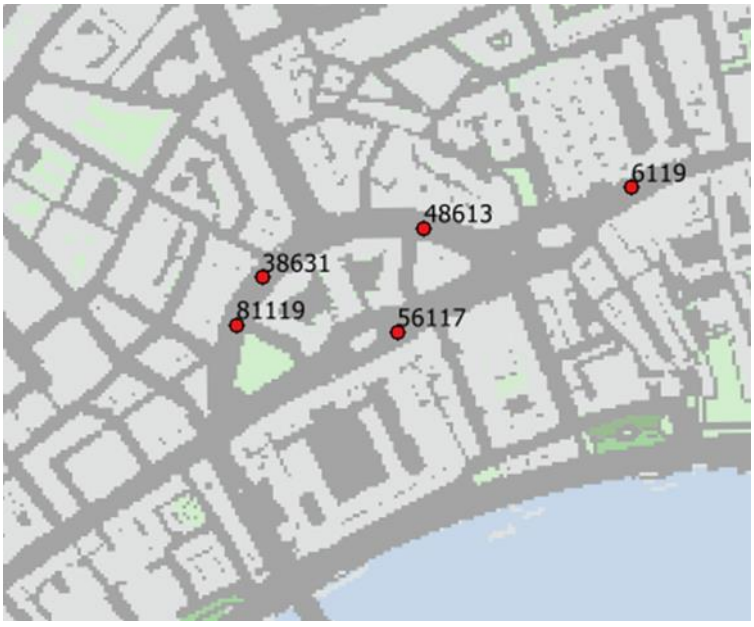

Figure 7.12: Location of AADF traffic count points compared with the 7-day KSNW count (close to 56117) in Table 7.7.

Ward *et al.* (2015) initially estimated the contribution of traffic to the overall flux by generating traffic profiles (hourly percentages of total traffic flow for each vehicle class, for weekdays, Saturdays and Sundays from the KSNW data. The hourly total traffic flow data for 2010-2013 measured at RCJ were averaged over the two east-bound lanes, then aggregated by hour of day, day of week (weekday, Saturday, Sunday) and month of year, and the median value taken from each subset. These median total flows were used to scale the vehicle class profiles derived from the KSNW data. Major roads were assumed to have the same traffic volume and

vehicle profile as the Strand, whilst minor roads were assumed to have no vehicles larger than a car (buses, heavy goods vehicles) and to have 25% of the traffic volume of the major roads. Emission factors for the vehicle classes were provided by the National Atmospheric Emissions Inventory for the 2010 vehicle fleet as gCO_2 per km of road driven. As yet, the emission factors for the 2013 vehicle fleet are still under revision.

Table 7.7: Percentage of total flow for each vehicle class for AADFs measured at the sites shown in Figure 7.12 and KSNW (ATC, Figure 2.1c). Values are colour coded blue (low) to red (high). Site 81119 is the Strand underpass

Site ID	Location	Two wheeled	Car/Taxi/LGV	Bus/Coach/2 axle rigid	3 - 5 axles	Axles ≥ 6
6119	The Strand/RCJ	16.14	73.88	9.77	0.20	0.00
56117	The Strand/KSNW	14.58	73.57	11.37	0.48	0.00
48613	Aldwych East	12.81	74.29	12.43	0.47	0.01
38631	Aldwych Mid	22.62	57.75	19.07	0.55	0.01
81119	The Strand Underpass	11.51	83.96	4.52	0.02	0.00
KSNW	The Strand/KSNW	10.49	71.99	12.62	4.42	0.48

To convert from emissions per km of road length to per m^2 road area, the emissions were divided by the road area per km^2. In the Ward *et al*. (2015) calculation, the road area per km^2 was calculated using an assumed lane width (assumption 7, Table 7.8). The overall traffic emissions per m^2 were calculated as the average of the emissions for the major and minor roads, weighted by the relative road areas (47% and 53% of the total road area for major and minor roads respectively, derived from a 4 m LiDAR data set (Lindberg and Grimmond, 2011)).

Some of the assumptions made in the calculation of emissions from traffic are listed in Table 7.8. The validity of these assumptions is explored in this section and it is shown that they significantly impact the calculated vehicle emissions per year (Figure 7.13). The first assumption listed in Table 7.8 has already been discussed; the data reported in Table 7.7 shows that it is reasonable to assume that the fleet characteristics, i.e., proportion of vehicles in each traffic class, is similar to that measured at KSNW for the majority of the roads surrounding KS.

The second assumption, that traffic counts at RCJ accurately represent local (to KS) traffic volumes, was investigated by comparing average total daily flows measured at the AADF points with the ATC measurements at RCJ and KSNW. Average total daily flow for all four lanes at RCJ in 2012 was 25,000 vehicles. This is slightly less per lane than the average daily flow measured by the 7 day count at KSNW over two lanes of 17,000 vehicles. The KSNW AADF (site 56117) was the highest of those in Figure 7.11 at 35,000 vehicles per day (it is likely that this measurement was taken up-stream of the split about St Mary-le-Strand church and hence is over 4 lanes), followed by Aldwych East (site 48613, 30,000, 3 lanes), RCJ (site 6119, 28,000, 4 lanes), Aldwych Mid (site 38631, 13,000, 3 lanes) and the Strand underpass (site 81119, 6,500, 2 lanes) (all figures given to 2 s.f.). Given that the per lane counts at RCJ were lower than most of the AADFs closer to KS, it is likely that using the RCJ hourly total flows will result in under, rather than over-estimations of the contribution of vehicle emissions to the

total flux. Although comparison of automated traffic counts with manual traffic counts (Buchanan, 2011) found that automated traffic counts under-estimated total traffic flow by approximately 20% relative to the manual counts, the proportions of vehicles counted were approximately the same (Buchanan, 2011).

Table 7.8: Assumptions made in the calculation of CO_2 emissions by vehicles at KS, their outcome in the original calculation and in the processing reported here.

No.	Assumption/choice	Original Value	Discussion	Final Value
1	Fleet characteristics measured at KSNW accurately represent the surrounding area	Yes	Comparison with AADFs in the surrounding area (Figure 7.12, Table 7.7) support this.	Yes
2	Traffic volume measured at RCJ accurately reflect local traffic volumes.	Yes, with caveats (see row 5).	Comparison with AADFs in surrounding area (Figure 7.12, Table 7.7) support this.	Yes
3	NAEI emissions factors: are accurate and average vehicle class values reflect those found at KS.	Yes	Comparison with values provided DEFRA found significant differences in estimated fluxes. NAEI chosen due to more detail (rural vs. urban).	Yes
4	Traffic count and emissions factor vehicle classes can be matched.	Motorbike: Tc1, Car: Tc2, Bus: Tc4, Truck: Tc3, Tc6-10	As Tc3 is listed as a 'short-towing' vehicle in the Automated Traffic Counts Classification Scheme, the class was changed to 'car'. HGVs (previously trucks) were divided to allow more detailed calculation.	Motorbike: Tc1, Car: Tc2 and Tc3, Bus: Tc4, Rigid HGVs: Tc5 and Tc6, Articulated HGVs: Tc7-10
5	Diurnal cycles of each traffic class vary by day of week.	Hourly traffic profiles constructed for an average weekday and average weekend.	Construction of profiles for each weekday is possible but due to lack of repetition is not statistically robust.	Hourly traffic profiles constructed for an average weekday and average weekend.
6	Lanes 1 and 2 (eastbound) accurately reflect total traffic flow.	Lanes 3 and 4 removed from lane average calculation due to very low flows observed in lane 4.	At the RCJ ATC site lane 4 was downstream of the lane used for turning right at a set of traffic lights, whereas lane 3 was downstream of the 'straight on' lane.	Emissions from traffic in all lanes would have contributed to the CO_2 flux. Average total flow derived from measurements from all four lanes.
7	Total road length is the road area (known) divided by an estimated road width.	Estimated road width: 3 m.	Main roads consist of 2 lanes, one of which tends to be a bus lane, per direction of traffic flow and a pedestrian walkway.	1. Average lane width of 4.4 m derived from Newcastle City Council (2011) guidance on road planning. 2. Average road width of 6.6 m derived from DEM, assumed to be two lanes.
8	Volume of traffic on minor roads is 25% of that on major roads and contains no vehicles larger than a car.	Yes	The 4:1 ratio is derived from visual inspection of graphs provided within Buchanan (2011). Values were not available at the time of writing.	Yes.

The effects of assumptions 3 and 4 (Table 7.8) were investigated by first varying the assignment of KSNW traffic counts to different emission factor classes (NAEI emission factors, Figure 7.13), then using the amended assignment with DEFRA conversion factors (DEFRA, 2013; Figure 7.13). The change in class assignment (ARX class 3 from truck to car, classes 5 to 10 split into two heavy goods vehicle classes) had limited (+5.9%) impact on calculated total yearly emissions, whereas the change with emissions factor provider was greater (-12.0%). As urban emission factors tend to be greater than rural emission factors due to lower vehicle speeds (NAEI, 2010) and as the DEFRA factors were fleet averaged over both urban and rural areas, it is thought that the DEFRA values are an under-estimate and hence were not used in the final calculation.

The effect of the assumption that the variability of traffic flow can be adequately represented by a weekday and weekend traffic profile was tested by constructing profiles for each day of the week. This increased estimated emissions by 7.2%. As only one day of data was available for constructing each daily traffic profile this approach was no used in the calculation of the reported values due to the high risk of bias.

Assumption 6 (that the traffic flow in the two eastbound lanes at RCJ accurately reflect overall traffic flow) has to some extent already been discussed above. The difference between the flow in each lane is presented in Appendix 2.B. Emissions calculated using an average flow over all four lanes are slightly (-3.4%) lower than unedited estimates.

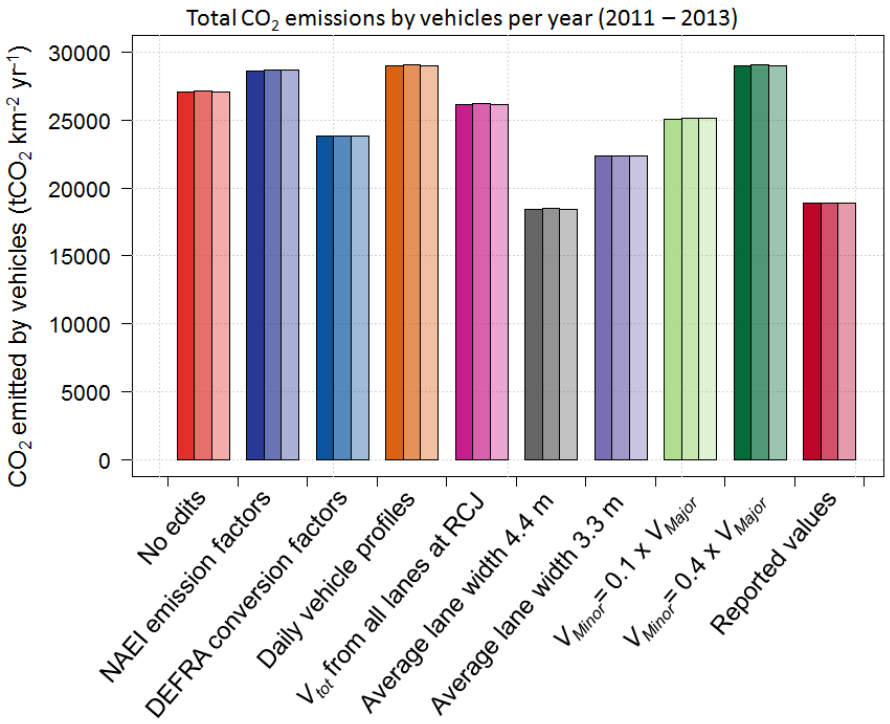

Figure 7.13: Total annual CO_2 emitted by vehicles per km^2 for land with the land cover fractions in the vicinity of KS for (left to right, dark to light shading) 2011 to 2013 calculated with different assumptions and methods (Table 7.8).

The assumed average lane width of 3 m (assumption 7, Table 7.8) is correct if bus lanes, cycle lanes and pavements are not considered; however, the file from which the measurements of

road area are derived does not distinguish between footpath, bus lane and car lane. Visual inspection of the major roads in the vicinity of KS found that each side of the road tended to have one car lane, one bus lane and one pavement. From Newcastle City Council guidance (2011) this gives an overall road width of approximately 8.8 m per direction of travel, or 4.4 m per lane. Conversely, calculation of the total road length (*r.thin*, GRASS) and road area (*GroupStats*, QGIS) gave an average road width of 6.6 m, assumed to be two lanes of 3.3 m each. It should be stressed that due to the eccentricities in the development of London's road network, that this is an exceedingly broad estimate and that many roads, such as Aldwych, do not have defined lanes at all. There were further issues with the calculation of an average road width from the MM7C data set, such as the difficulty of separating non-road structures such as carparks and footpaths in parks from the road dataset. For this reason, the 4.4 m estimate of lane width was chosen rather than the 3.3 m estimate from the land cover map (Figure 7.13), a choice which had the largest impact on estimated traffic emissions (-31.8%) of those examined in this section.

The final assumption, that the traffic flow on minor roads was 25% of that on major roads with no heavy vehicles, was assessed by varying the proportion of traffic on minor roads from 10% to 40% of that on major roads. The impact of excluding heavy goods vehicles from minor roads was not assessed as in many cases on street parking makes these roads too narrow for such vehicles and visual inspection of a photographic survey of roads in Westminster suggested that the number of vehicles larger than a car or van on such roads was very limited. Variation of the flow on minor roads by ±15% of the flow on major roads resulted in a change of ±7.2% in total yearly emissions (Figure 7.13) and the original ratio of 1:4 was retained for the final calculation.

The final emission estimates were calculated using amended vehicle classifications with the NAEI emissions factors, total traffic estimates derived from all four lanes at RCJ and an estimated lane width of 4.4 m, giving an overall estimate 30.5% lower than those reported using the method of Ward *et al.* (2015). The emissions per km^2 were 18,850, 18,910, and 18,880 $tCO_2\ km^{-2}\ yr^{-1}$ for 2011 to 2013 respectively, or approximately 53% of the total emissions per km^2 of 35,500 $tCO_2\ km^{-2}\ yr^{-1}$ calculated by Helfter *et al.* (2011). If the automated traffic counts are, as suggested by Buchanan (2011), an under estimate of 20%, then the emissions from traffic rise to 22,680 $tCO_2\ km^{-2}\ yr^{-1}$ or 64% of the overall exchange of CO_2, a substantial difference. As expected, both figures are much larger than those reported for a residential suburb of Vancouver (10,740 $tCO_2\ km^{-2}\ yr^{-1}$, Christen *et al.*, 2011) and approximately equivalent in magnitude (but not percentage contribution to total emissions) to those reported for a compact midrise, densely populated neighbourhood of Mexico City (19,490 $tCO_2\ km^{-2}\ yr^{-1}$, Velasco *et al.*, 2014). These results suggest it is important but difficult to accurately assess the contribution of vehicle exhaust to total CO_2 emissions.

7.3.5 Building heating and human respiration

Estimates of the heat flux from human metabolism and space heating of buildings were calculated at 200 m x 200 m (30 minute) resolution for EC flux source areas using the GreaterQf model (Iamarino *et al.*, 2012) using the modifications described in Ward *et al.* (2015). The output for the relevant 200 m x 200 m grid squares were combined with the output from the flux footprint model to generate footprint average values for the heat flux from human respiration ($Q_{F,R}$) and space heating of buildings ($Q_{F,B}$). The heat fluxes were converted to CO_2 emissions as described below.

Both heat and CO_2 fluxes due to human respiration depend, upon other things, on the size, age and activity level of the population; these factors are accounted for in the GreaterQF model. The calculated heat flux due to respiration can be divided by the heat flux per person to give a population density of 'average' people. The average person in the UK consumes 3,450 kcal day^{-1}. If it is assumed that all energy consumed is eventually released as heat (i.e., not stored as extra tissue due to growing or fat deposition), this is equivalent to about 167 J $person^{-1}$ s^{-1} or 167 W $person^{-1}$. It is important to note that during the night time, when metabolic rates are expected to be lower than average due to low activity levels, this 'average' density is likely to be lower than the real values, and vice versa during the day. As the 'average' rather than activity specific respiration rate of 365 µmol CO_2 $person^{-1}$ s^{-1} (Koerner and Klopatek, 2002) is multiplied by the calculated population density to give the rate of CO_2 emitted by respiration per m^2, these effects should cancel out. The calculation also assumes that the people within the flux footprint reflect the population average, that the rate of heat emission is directly proportional to the rate of CO_2 emission and that all respiration is aerobic.

Calculated CO_2 fluxes from respiration range from 0.071 to 24.495 µmol m^{-2} s^{-1} ($3.11x10^{-06}$ to $1.08x10^{-03}$ gCO_2 m^{-2} s^{-1}), with mean annual total emissions for 2009 to 2014 of 9.056 kg CO_2 m^{-2} yr^{-1}. The slightly larger mean (but not median, not shown) summer weekday values than winter weekday values are not due to the Olympic Games and are observed for every year from 2009 to 2014. Emissions are highest during the working day and lowest overnight, with minimal seasonal variation (Figure 7.14). This is due to the predominantly commercial/office/institutional use of the buildings surrounding the flux tower and low overnight/weekend population recorded in the census data, which is the basis for the GreaterQF calculation. In reality, the overnight and daytime weekend respiration is likely to be higher than shown in Figure 7.14 due to patrons of the nearby tourist attractions (Aldwych theatre, Somerset House), numerous restaurants, and public houses, which are not recorded in the census. In other words, the annual totals are likely to under-estimate the actual contribution of respiration to the net annual emissions. The mean values for 2011-2012 (9.021 kg CO_2 m^{-2} yr^{-1}) comprise 19.3% of the mean annual total emissions reported by Ward *et al.* (2015) or 25.4% of the annual total emissions reported by Helfter *et al.* (2011), indicating that emissions of CO_2 by human respiration are a significant source of CO_2 in central London.

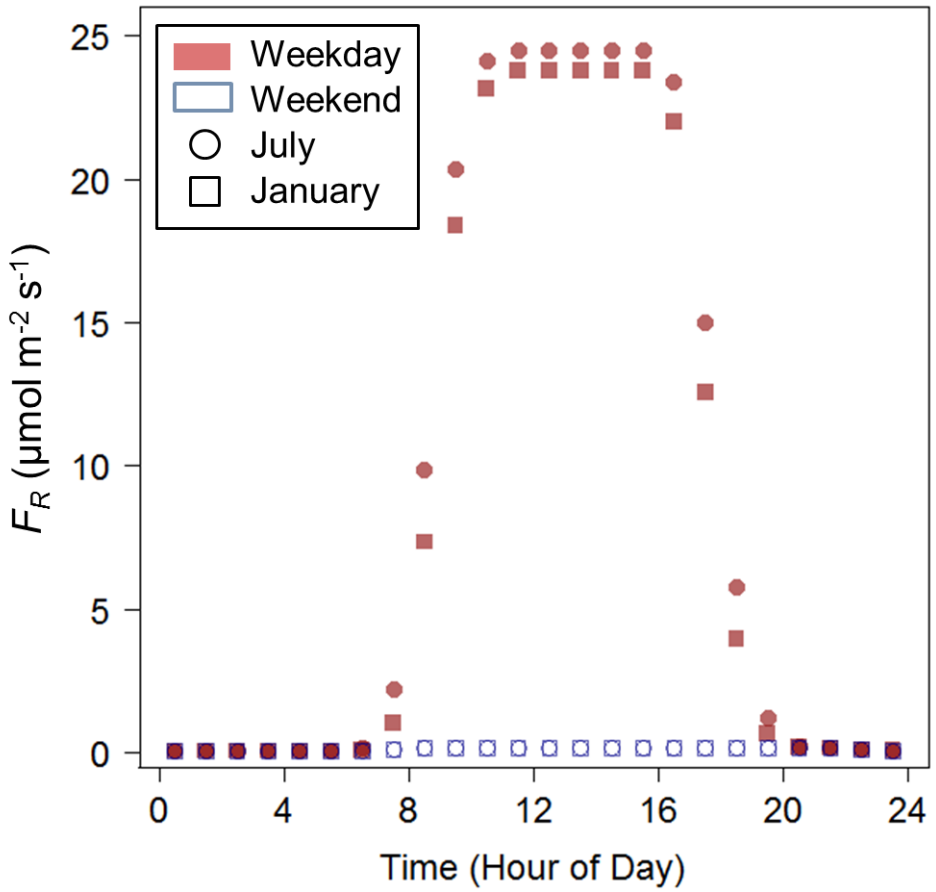

Figure 7.14: Hourly mean CO_2 fluxes due to human respiration (F_R) in the flux footprint of the KS tower for 2008 to 2015. Values averaged over month of year (squares: January, circles: July) and day of week (red filled: working day, blue hollow: weekend).

Building emissions, calculated with GreaterQf, had mean and median values for 2008 – 2015 heat fluxes from space heating and lighting of 83 and 66 W m^{-2} respectively when adjusted for reduced fuel demand (DECC, 2011). The energy sources were 59.1% from electricity, which was assumed to not generate any CO_2 emissions within the tower flux footprint, 40.2% natural gas and 0.7% other fuels. The heat generated by each fuel type was multiplied by total heat to CO_2 conversion factors (Ward *et al.*, personal communication, 2015). These conversion factors were based on those provided for CO_2 and sensible heat by the Natural and bio Gas Vehicle Association of Europe (NGVA Europe, 2015) but modified to account for latent heat. The mean annual emissions from building heating for 2011 and 2012 were calculated as 52.5 and 52.6 kg CO_2 m^{-2} yr^{-1} respectively, making emissions from space heating the largest contributor to total emissions.

This is larger than the estimation of total emissions reported in Ward *et al.* (2015) and Helfter *et al.* (2011), suggesting either that the model grossly over-estimates CO_2 emissions or that a large portion of the net emissions are not measured by the flux tower. Work by Ward *et al.* (personal communication, 2015) found that this was due to large, highly localised, non-domestic gas emissions and instead recommended estimating emissions due to building space heating from the spatially averaged modelled building heat flux for the borough of Westminster, which contains the majority of the flux footprint. The calculated Westminster borough CO_2 emissions from building heating have a higher baseline but smaller range of values than those

calculated for the flux footprint on a 200x200 m grid. Calculated CO_2 emissions ranged from 22.84 to 28.91 kg CO_2 m^{-2} yr^{-1} from 2011 to 2014. When adjusted for land cover fraction this is approximately 10.35 kg CO_2 m^{-2} yr^{-1}, equivalent to 29.2% and 22.2% of the total emissions estimated by Helfter *et al.* (2011) and Ward *et al.* (2015) respectively. Emissions are highest on weekdays (Figure 7.15) December to February, 10:00 to 14:00, GMT and lowest overnight in summer, i.e., they are higher during periods of higher building occupancy and lower temperatures as described in Section 4.3. A second peak in summer due to emissions from building cooling is not observed as air conditioning is typically powered by mains electricity and this study focuses on emissions within the flux footprint (the flux footprint does not contain any power stations), hence increased energy use by air conditioning would not be observed as a peak in CO_2 emissions. Indeed, comparison of term time and holiday *[CO_2]* at height A, KSSW (Section 4.3) found term time *[CO_2]* to be below holiday *[CO_2]* for air temperatures greater than 20ºC, albeit with low certainty due to the low number of data points.

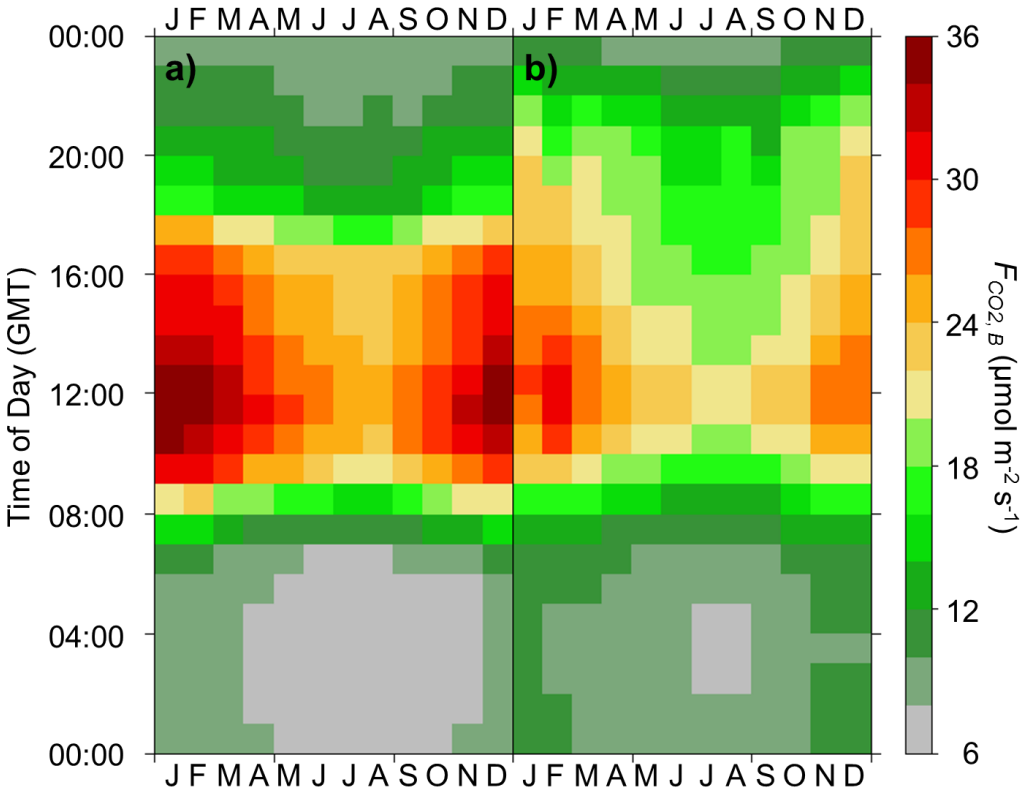

Figure 7.15: Hourly mean CO_2 emissions (µmol m^{-2} s^{-1}, key: far right) due to space heating of buildings aggregated over month of year (x axis), hour of day (y-axis) and (a)weekdays or (b) weekends, calculated from output of the GreaterQf model for the borough of Westminster, 2008/275 – 2014/365.

The assumptions required for this calculation include that the natural gas burnt for heating is entirely composed of methane (natural gas is typically 95% methane, Union Gas, 2015) and that the fuel is completely combusted, that is, all hydrocarbons are completely converted to carbon dioxide. As longer chain hydrocarbons release less heat when burnt per kg fuel and are less likely to be fully converted to CO_2, the aforementioned assumptions are likely to result in under and over estimates of the total CO_2 emitted due to building heating respectively.

7.4 Micrometeorological results

Calculation of the four components of the net ecosystem exchange as measured by the micrometeorological method is described in Section 3.1. Gap filling of the half-hourly values is described in Section 3.2.

Hourly/monthly mean values of the vertical flux were always positive (6.8 to 97.4 μmol m^{-2} s^{-1}), highest during the afternoon (12:00 to 17:00 GMT) in winter (December to February) and in the early morning hours (01:00 to 05:00 GMT) in summer (June to August) (Figure 7.16a). CO_2 storage has both positive and negative values with equal proportions of both and a much smaller range of hourly/monthly mean values (-0.4 to 1.1 μmol m^{-2} s^{-1}) that are positive for the four hours prior to sunrise, for the two to three hours just after the daily peak in incident shortwave radiation, and negative otherwise (Figure 7.16b). The range of values for the vertical advection was an order of magnitude larger (-11.5 to 10.1 μmol m^{-2} s^{-1}), tended more towards negative values (55.6% of gap filled data) and have no obvious diurnal or seasonal cycle (Figure 7.16d). This is very different to the calculated horizontal advection, which not only seems to tend towards positive values in winter (Figure 7.16c), but also has a much large range of hourly/monthly mean values (-102.0 to 165.9 μmol m^{-2} s^{-1}).

Observations regarding the characteristics of the calculated horizontal advection should be considered with caution. The horizontal profile measurements available can only be considered representative of CO_2 concentration distributions up to the Strand building roof level as significant differences were found between the above and below roof portions of the vertical CO_2 profile (Section 5.3.1). As there is only one set of tower data and horizontal advection requires at least two horizontal concentration measurements along the wind direction (or three with triangulation for any wind direction), it is not possible to calculate horizontal advection above Strand roof level. Horizontal advection values were therefore calculated by integration only up to Strand roof height, with advection between the roof level and the top of the tower not calculated. A further drawback is the lack of horizontal CO_2 profile measurements normal to the Strand, i.e., across the street. This inhibits the calculation of horizontal advection in this direction. The values presented in Figure 7.16c therefore represent only the horizontal advection parallel to the Strand street canyon below the Strand building roof level. They suggest that the magnitude of horizontal advection in urban street canyons may be large, but they do not provide a measure of the total horizontal advection term. To distinguish between the two, the total horizontal advection is referred to here as A_{xy}, and the calculated horizontal advection term as $A_{x,\,zs}$.

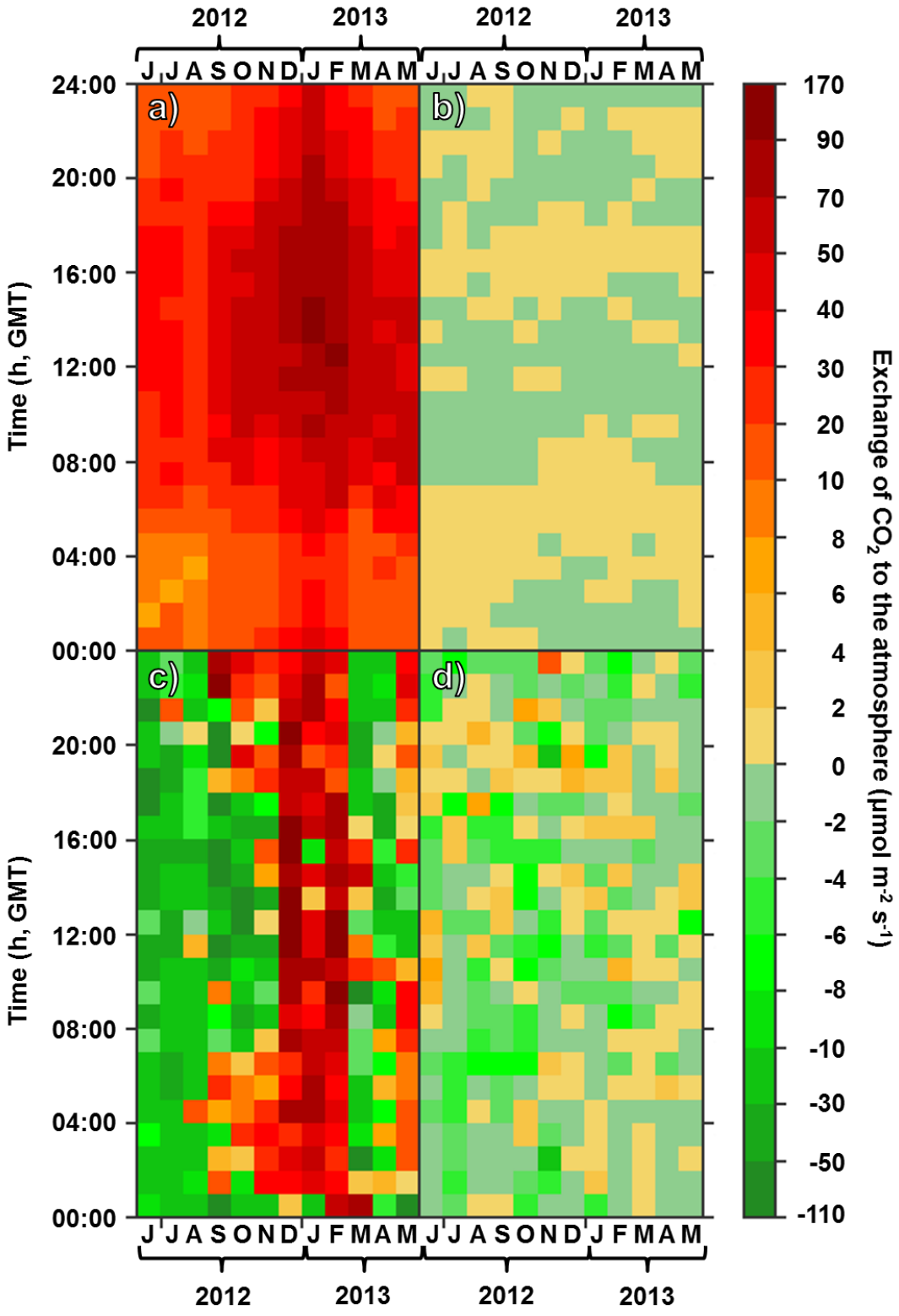

Figure 7.16: Mean values for each hour of day (y-axis) and month of year (x-axis) for 2012/153 – 2013/151. (a) Vertical CO_2 flux (Height A, KSSW), (b) ΔC_{SP} (LI840, C6), (c) calculated horizontal advection, (d) vertical advection. All values given in µmol m^{-2} s^{-1}. Note the non-linear scale (far right).

Inclusion of $A_{x,\,Zs}$ increases the range of half hourly net emissions from -270.8 to 466.7 µmol m^{-2} s^{-1}, to -1229.8 to 1839.0 µmol m^{-2} s^{-1} and suggests that during June, 2012, that central London was, on average, a net sink of CO_2 (Figure 7.17a). Whilst peak traffic loads (the largest source of CO_2) were slightly reduced by the London Olympic games travel restrictions, the

difference was minor and overnight traffic loads increased (Section 4.4.1). It is therefore suggested that the calculated $A_{x,\,zs}$ are unrealistic and suffer from not capturing the movement of CO_2 above the Strand building roof level and across, as well as along, the Strand. As the above roof and across street components are not calculable from the available data the horizontal advection is omitted from the annual emissions reported in the following sections (i.e., horizontal homogeneity is assumed). This reduces the estimates of annual emissions by 8.2 kg CO_2 m^{-2} yr^{-1} (16.0% of the 3-component annual net emissions).

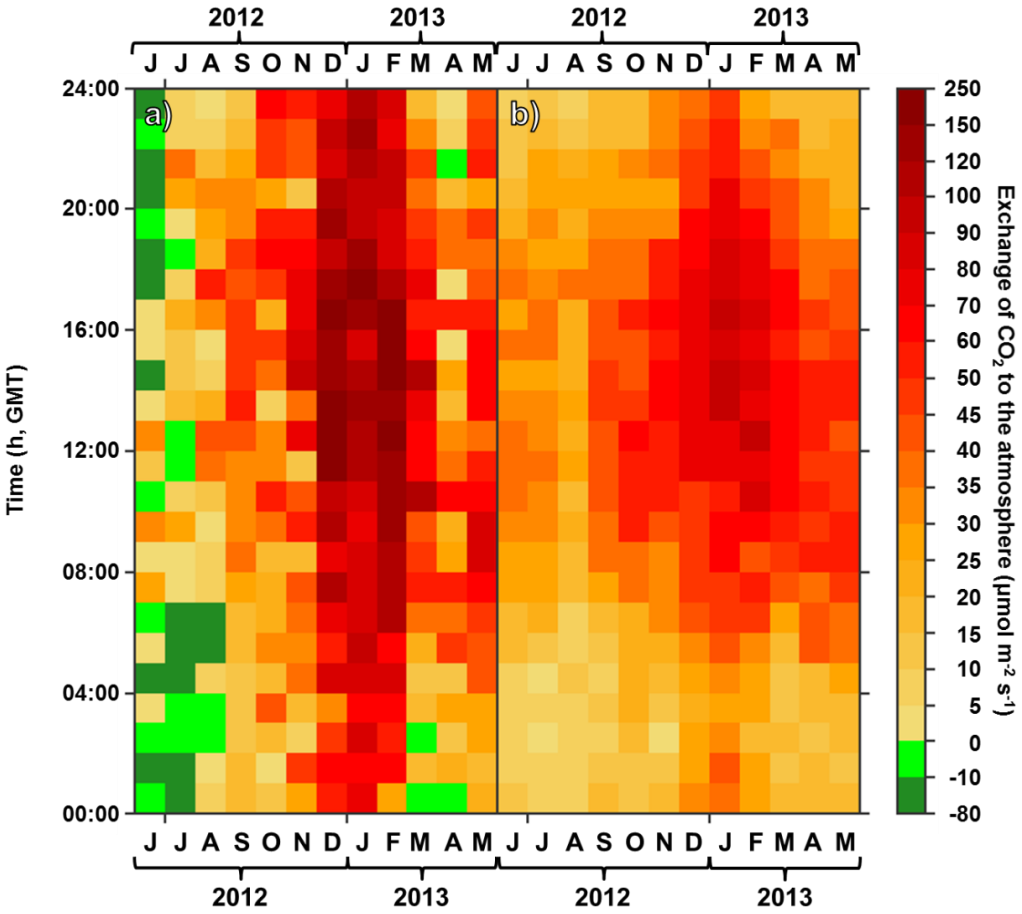

Figure 7.17: Mean total emissions (key: far right) by hour of day (y-axis) and month of year (x-axis) for June 2012 to May 2013 calculated from (a) all components of the net ecosystem exchange (Figure 7.16) and (b) all components of the net ecosystem exchange except the calculated horizontal advection (Figure 7.16c).

7.5 Comparison and conclusions

The annual net emission of CO_2 per km^2 for central London has been estimated using the inventory and the micrometeorological approaches. If horizontal homogeneity is assumed (horizontal advection is neglected), then the results from the two approaches differ by only 3.2% (Table 7.9). If all terms other than vertical flux were neglected the two estimates would still be within 6% of each other and could be achieved with considerably less equipment and measurements at far fewer sites. Overall, this study verifies the use of vertical fluxes calculated from eddy covariance measurements to estimate total emissions from high density urban environments. This result may not be applicable to lower density urban environments, such as residential suburbs, where stable atmospheric conditions are more common (Feigenwinter *et*

al., 2012) and CO_2 emitted at ground level may be lost via drainage flow without reaching the eddy covariance measurement height. It should also be noted that the calculation of horizontal advection and emissions from river water and the animal population in this study are incomplete and that this may affect both the overall annual emissions and the significance of each component in the inventory and micrometeorological calculations of net emissions.

Table 7.9: Total CO_2 emissions ($gCO_2\ m^{-2}\ yr^{-1}$) for central London 2012/153-2013/151 as estimated by inventory and micrometeorological methods. All values are given to the nearest 10 grams.

Inventory		Micrometeorological	
Component	Annual Contribution ($g\ CO_2\ m^{-2}\ yr^{-1}$) (%)	Component	Annual Contribution ($g\ CO_2\ m^{-2}\ yr^{-1}$) (%)
Total	49,837 (100%)	Total	51,430 (100%)
Vehicles	33,992 (68.2%)	Vertical Flux	52,790 (102.6%)
Building heating	8,566 (17.2%)	Vertical advection	-1,365 (-2.7%)
Human respiration	7,390 (14.8%)	CO_2 storage	6 (0.0%)
Soil	130 (0.3%)	Horizontal Advection	Calculated as 8,243 (16.0%), set to 0 (0.0%) due to not being able to measure A_x above Strand roof level and A_y (advection across the street).
Vegetation	-86 (Grass), -155 (uppermost estimate, woody vegetation) (-0.2%, -0.3%)		
River efflux	Assumed 0 (0.0%)		
Animal respiration	Assumed 0 (0.0%)		

Emissions from traffic were much higher than expected; Helfter *et al.* (2011) and Ward *et al.* (2015) both calculated the contribution of traffic to total emissions as ca. 35%, with that of combustion for building heating much higher at ca. 60%. It should be noted that Helfter *et al.* (2011) calculated the contribution by vehicle emissions as the difference between NAEI estimates of emissions from building heating and observed fluxes, rather than from traffic counts. As Ward *et al.*, (2015) report that the total estimated emissions from traffic and building heating was greater than the observed fluxes, the NAEI may over-estimate emissions, resulting an under-estimate of CO_2 released by vehicles. Ward *et al.* (2015) also noted that their method of calculating traffic emissions (GreaterQF model, Iamarino *et al*., 2012) was likely to under-estimate traffic emissions. Nevertheless, there is a significant difference in the estimated contribution of emissions from building heating and vehicles to the total.

The reported contribution of human respiration to total emissions in previous studies varies from 5% (Vancouver, Crawford and Christen, 2015; London, Helfter *et al*., 2011) to 38% (Tokyo, Moriwaki and Kanda, 2004). In this study the percentage of total emissions due to human respiration is 14.8%, but ranges between 0.2% and 24.7%, with the highest values observed during the working day (09:00 to 05:00 GMT) and the lowest overnight (Figure 7.18e), as expected given the large difference between the daytime and night time population (2.1 million and 0.4 million respectively, GLA Opinion Research and Statistics, 2013).

Respiration from soil and net photosynthetic uptake by lawn grass (Figure 7.18d, c) contribute much less to the total emissions (soil: 0.1 to 1.3%, grass: -1.6 to 0.7%). Soil respiration contributes more as a percentage of the total overnight, though this is due to lower overall emissions, whilst net photosynthetic uptake is more important between 06:00 and 10:00 in summer, when photosynthesis is greatest and emissions from combustion for space heating are low. Emissions from space heating range from 9.7 to 33.9% of the total emissions and are highest as a percentage of the total in December and January. The emissions from buildings heating have less of a seasonal cycle than might be expected and this may explain the relatively low seasonal variation in total emissions calculated from inventory measurements (Figure 7.18f) compared to those calculated from micrometeorological measurements (Figure 7.17). The range of hourly/monthly mean total emissions for 11:00 to 12:00 GMT for the inventory method was 51.1 to 71.5 μmol m^{-2} s^{-1}, a difference of approximately 20 μmol m^{-2} s^{-1}. The equivalent range for the micrometeorological results was 29.1 to 79.1 μmol m^{-2} s^{-1}, 50 μmol m^{-2} s^{-1}. As might be expected from the low spatial and temporal resolution at which inventory data tends to be reported, the inventory method fails to capture the variability of emissions with time. Comparison of the annual total emissions (Table 7.9) show this resolution to be sufficient for calculation of net emissions over long timescales, but Figure 7.18 demonstrates that this method is unsuitable for evaluating emissions at hourly to monthly timescales.

Evaluation of net emissions from central London by two different methods found annual totals which were in good agreement with prior literature. A combination of survey, census and inventory data was used to calculate emission factors for the following land cover components: buildings, roads, river water, lawn grass, soil and woody vegetation. These were multiplied by land cover fractions derived by combining half hourly flux footprint data with a 4 m x 4 m land cover map of central London to generate half hourly estimates of total emissions in the footprint of the KSSW flux tower. The half hourly estimates were compared to estimates of total emissions derived from measurements made with standard eddy-covariance equipment and a vertical $[CO_2]$ profile. The difference between the annual totals derived via the two methods was ca. 3%; however, comparison of emissions estimates at higher time resolutions found greater disparities between the two. It is suggested that this is due to the coarser time resolution of some of the inventory data available.

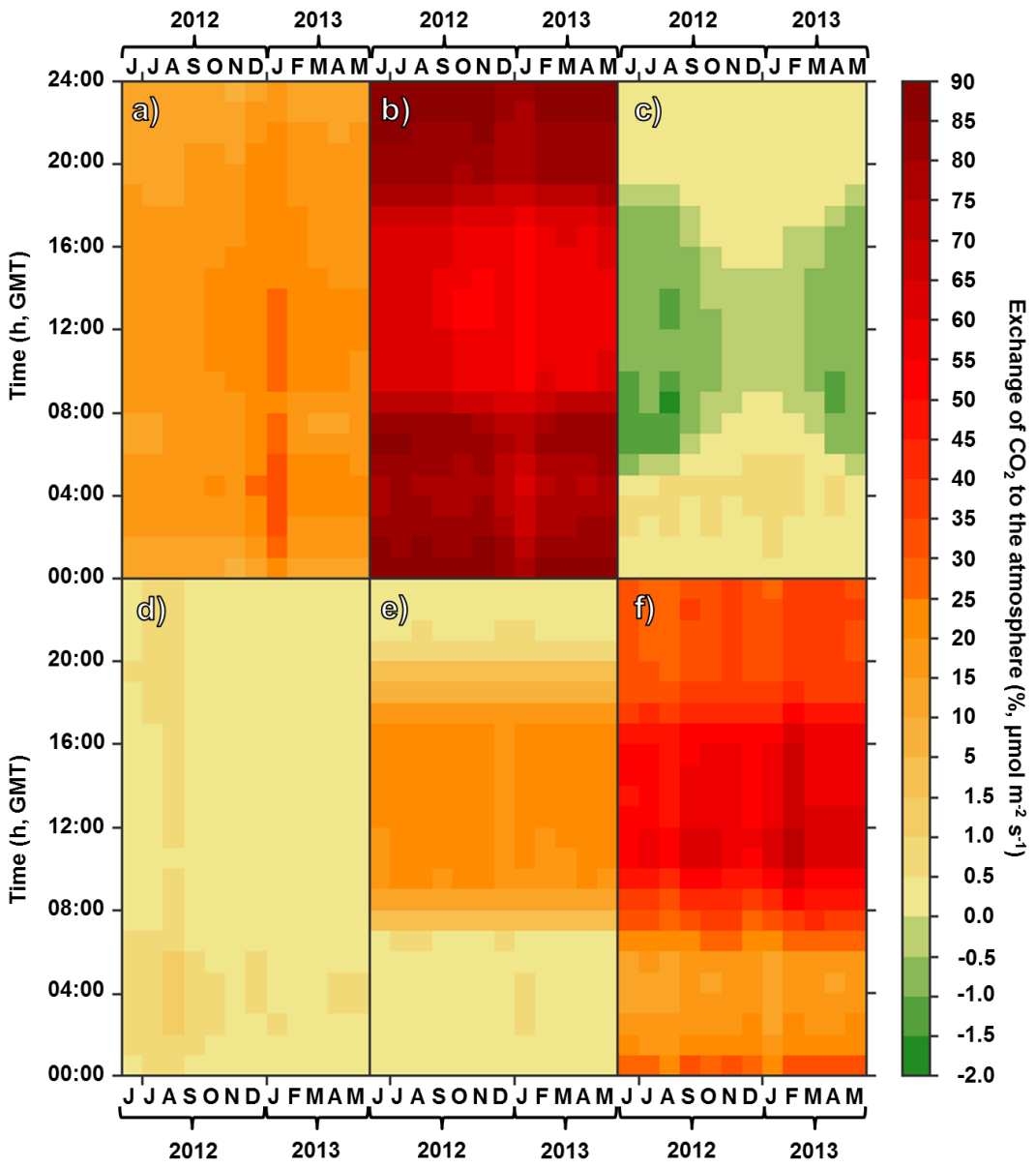

Figure 7.18: The percentage contributions of each component of the inventory estimate to the total CO_2 emissions in central London by hour of day and month of year for June 2012 to May 2013 (C6 and C7, Table 2.2). Components are from: (a) building heating, (b) vehicles, (c) lawn grass, (d) soil respiration, (e) human respiration. These are summed to give the total emissions (f) in µmol m^{-2} s^{-1}. All components (a to e) are given as percentages of this total.

Appendix 7.A: Software used in the flux footprint calculation

The footprint contains all software listed in Figure 7.2 as well as subsidiary files containing flux-footprint specific functions. The first program is 'kcl_create_footprint', which creates the first estimate of the footprint function. The second is 'kcl_iterate_footprint' which calculates the second to fourth iterations of the footprint. The third is a collection of functions called by the previous two programs. The fourth and fifth programs are those used to calculate the morphometric parameters (Table 7.B.1) used as input for the 'create' and 'iterate' footprint programs respectively. The final program is that used to merge the individual half hourly footprint files to daily files.

```
###kcl_create_footprint
##
## function to generate input for footprint calculations based on epicc_create_footprint.pro from
## Andreas Christen, UBC 2009. Adapted to use at KCL by Simone Kotthaus, Jan 2011
## Translated from IDL to R by Alex Björkegren, Sep 2015

rm(list=ls())
## basic settings
TIMEZONE<-"UTC"
SITE    <-"KSS"
DATA_DIR<-"/data/its-tier2/micromet/data/"
WORK_DIR<-"/net/glusterfs/micromet/users/micromet/works/"
FUNC_DIR<-"/home/micromet/Roofprograms/Alex_Analysis/"
source(paste(FUNC_DIR,"Footprint_functions.R", sep=""))
library(ncdf); library(imager)

##time settings
YEAR<-2012; off_set<-32  ##off_set controls which days of year to process

##constants
g<-c(9.81) ##acceleration due to gravity
karman<-0.40 ##von Karman constant

##model settings
SPV     <- c(-999)
D_INPUT <- c(4.0)  ##model resolution
DOMAIN_X<- c(2000.0)  ##modelled area in longitudinal direction
DOMAIN_Y<- c(500.0)   ##modelled area in lateral direction
DOMAIN_OUTPUT<-c(4000.0)  ##area ouput into file after rotation (the area in m east x m
north)

###Read in micromet data
 FILE<-paste(DATA_DIR,YEAR,"/London/L2/",SITE,"/ANNUAL/CSAT3_ECpack_",SITE
                ,"_",YEAR,"_30min.nc",sep="")

 if(file.exists(FILE))
 {ncID<-open.ncdf(FILE)
  TIME<-ncID$dim$time$vals
  TUNITS<-att.get.ncdf(ncID,"time","units")
  S_DATE<-strsplit(TUNITS[[2]]," ")[[1]][3]
  S_TIME<-strsplit(TUNITS[[2]]," ")[[1]][4]
  T_DIFF<-difftime((paste(S_DATE,S_TIME))  ##put relative to start of year
              ,paste(YEAR,"-01-01 00:00:00",sep=""), units="mins")
  TIME<-TIME+as.numeric(T_DIFF); rm(TUNITS,T_DIFF,S_DATE,S_TIME)
  HEIGHT<-ncID$dim$height$vals
  DIR   <-get.var.ncdf(ncID,"dir") #wind direction -magnetic north
  WS    <-get.var.ncdf(ncID,"WS")  #horizontal wind speed
  USTAR <-get.var.ncdf(ncID,"ustar")  #friction velocity
```

```
SD_V  <-get.var.ncdf(ncID,"sd_v")   #crosswind variation
OBKHV <-get.var.ncdf(ncID,"L")      #obukhov length
close.ncdf(ncID); rm(ncID)

DIR[which(  DIR==SPV)]<-NA   ##if data is equal to a value
WS[which(   WS==SPV)]<-NA   ##mean to represent NA, but which
USTAR[which(USTAR==SPV)]<-NA   ##is not NA, set all instances of
SD_V[which( SD_V==SPV)]<-NA   ##this data to NA
OBKHV[which(OBKHV==SPV)]<-NA

pcs<-which(is.finite(DIR)) ##indices to process for footprint
SEL<-round(DIR[pcs])
num<-length(pcs)
WID<-ceiling(SD_V[pcs]/0.46)

###morphometric calculations
M_FILE<-paste(DATA_DIR,YEAR,"/London/L1/",SITE,"/META/L1_"
                    ,SITE,"_MORPH_1d500.txt",sep="")
DATA<-read.table(M_FILE, header=T)

for(id in 1:num)
{ k<-pcs[id]
  DOY<-formatC(1 + floor(TIME[k]/1440), width=3, flag="0")
  TDIM<-TIME[k]-1440*floor(TIME[k]/1440)
  if(TDIM==0){TDIM<-1440; DOY<-formatC(floor(TIME[k]/1440), width=3, flag="0")}
  if(as.numeric(DOY)<off_set)  ###controls which days to process
  { if(is.finite(OBKHV[k]) & is.finite(SD_V[k]) & is.finite(WS[k]) & is.finite(DIR[k]) )
    { Tinfo<-ff_Tinfo(as.Date(paste(YEAR,DOY,sep=""),"%Y%j"))  ###get time information
      TUNIT<-paste("minutes since ",Tinfo["tD","YEAR"],"-",Tinfo["tD","MONTH"],"-"
                        ,Tinfo["tD","DAY"]," 00:00:00",sep="")
      OT_DIR <-paste(WORK_DIR,Tinfo["tD","YEAR"],"/London/Level_1/FPR/",DOY,"/",sep="")
      if(!file.exists(OT_DIR)){dir.create(OT_DIR)}
     OT_FILE<-paste(OT_DIR,"FPR_AB_",SITE,"_",Tinfo["tD","YEAR"],Tinfo["tD","DOY"],"_"
                  ,formatC(TDIM%/%60,width=2,flag="0"),formatC(TDIM%%60,width=2,flag="0")
                  ,".nc",sep="")
     print(paste(Tinfo["tD","YEAR"],"/",Tinfo["tD","DOY"],", "
          ,formatC(TDIM%/%60,width=2,flag="0")
          ,formatC(TDIM%%60,width=2,flag="0"),sep=""))
     ###select roughness parameters and average over a sector proportional to sd_v's size
     SECTOR<-c(360+SEL[id]-WID[id],360+SEL[id]+WID[id])%%360
     if(SECTOR[1]<=SECTOR[2])
     {Z_G<-mean(DATA[SECTOR[1]:SECTOR[2],2])
      Z_H<-mean(DATA[SECTOR[1]:SECTOR[2],3])
      PAI<-mean(DATA[SECTOR[1]:SECTOR[2],5])
      FAI<-mean(DATA[SECTOR[1]:SECTOR[2],6])
     }else{
      Z_G<-mean(DATA[c(1:SECTOR[2],SECTOR[1]:360),2])
      Z_H<-mean(DATA[c(1:SECTOR[2],SECTOR[1]:360),3])
      PAI<-mean(DATA[c(1:SECTOR[2],SECTOR[1]:360),5])
      FAI<-mean(DATA[c(1:SECTOR[2],SECTOR[1]:360),6])
     }

     ###roughness calculation, Macdonald et al 1998
     Z_D<-Z_H*(1+(PAI-1)*4.43^(-PAI))
     Z_0<-Z_H*((1-Z_D/Z_H)*exp(-(0.5*1*1.2*0.4^(-2)*(1-Z_D/Z_H)*FAI)^(-0.5)))
     Z_M<-(HEIGHT-Z_G)-Z_D

     ###Restrict to unstable conditions of <= -1
     L<-OBKHV[k]
     if(L<0 & abs(L)<(2*Z_0)){L<-c(-2*Z_0)}

     ###call kcl_fpr_write_ncdf function
```

```
      ##create directory if not already created
      METAFILE<-paste(DATA_DIR,YEAR,"/London/L1/",SITE,"/META/L1_",SITE
                              ,"_FPR_30min.csv",sep="")

      try(kcl_fpr_write_ncdf(OT_FILE, "L1", Z_0, Z_M
                          ,WS[k], DIR[k], SD_V[k], L, USTAR[k]
                          ,DOMAIN_X, DOMAIN_Y, DOMAIN_OUTPUT, D_INPUT
                          ,TDIM, TUNIT, SITE, TIMEZONE, METAFILE)
          , silent=TRUE)
      rm(L,Z_D,Z_0,Z_M,Z_G,Z_H,PAI,FAI,SECTOR,TDIM)
    } ###finite data
   } ##day if year in correct range
  } ##half hourly loop
 }else{
 TIME<-NA; height<-NA; DIR<-NA; WS<-NA; USTAR<-NA; SD_V<-NA; L<-NA
 print(paste(FILE,"does not exist"))
 } ##FILE exists
```

```
###kcl_iterate_footprint
##
## function to generate input for footprint calculations based on epicc_create_footprint.pro
## from Andreas Christen, UBC 2009. Adapted to use at KCL by Simone Kotthaus, Jan 2011
## Translated from IDL to R by Alex Bjorkegren, Sep 2015

rm(list=ls())
## basic settings
TIMEZONE<-"UTC"
SITE    <-"KSS"
DATA_DIR<-"/data/its-tier2/micromet/data/"
WORK_DIR<-"/net/glusterfs/micromet/users/micromet/works/"
FUNC_DIR<-"/home/micromet/Roofprograms/Alex_Analysis/"
source(paste(FUNC_DIR,"Footprint_functions.R", sep=""))
library(ncdf); library(imager)

##time settings
#DSTART<-c("12001"); DSTOP<-("12366")
#DATE_STR<-as.Date(DSTART,"%y%j") ; DATE_STP<-as.Date(DSTOP, "%y%j")
#DATE_LIST<- c(seq(DATE_STR,DATE_STP,1))
YEAR<-2012
ITER<-2
OFF_ST<-0  ###control which days to process
OFF_ED<-32

##constants
g<-c(9.81) ##acceleration due to gravity
karman<-0.40 ##von Karman constant

##model settings
SPV     <- c(-999)
D_INPUT <- c(4.0)  ##model resolution
DOMAIN_X<- c(2000.0)  ##modelled area in longitudinal direction
DOMAIN_Y<- c(500.0)   ##modelled area in lateral direction
DOMAIN_OUTPUT<-c(4000.0)  ##area ouput into file after rotation (the area in m east x m
north)

###Read in micromet data
 FILE<-paste(DATA_DIR,YEAR,"/London/L2/",SITE,"/ANNUAL/CSAT3_ECpack_",SITE
                ,"_",YEAR,"_30min.nc",sep="")

 if(file.exists(FILE))
 {ncID<-open.ncdf(FILE)
  TIME<-ncID$dim$time$vals
  TUNITS<-att.get.ncdf(ncID,"time","units")
  S_DATE<-strsplit(TUNITS[[2]]," ")[[1]][3]
  S_TIME<-strsplit(TUNITS[[2]]," ")[[1]][4]
  T_DIFF<-difftime((paste(S_DATE,S_TIME))  ##put relative to start of year
               ,paste(YEAR,"-01-01 00:00:00",sep=""), units="mins")
  TIME<-TIME+as.numeric(T_DIFF); rm(TUNITS,T_DIFF,S_DATE,S_TIME)
  HEIGHT<-ncID$dim$height$vals
  DIR   <-get.var.ncdf(ncID,"dir") #wind direction -magnetic north
  WS    <-get.var.ncdf(ncID,"WS")  #horizontal wind speed
  USTAR <-get.var.ncdf(ncID,"ustar")  #friction velocity
  SD_V  <-get.var.ncdf(ncID,"sd_v")   #crosswind variation
  OBKHV <-get.var.ncdf(ncID,"L")      #obukhov length
  close.ncdf(ncID); rm(ncID)

    DIR[which(  DIR==SPV)]<-NA   ##if data is equal to a value
     WS[which(   WS==SPV)]<-NA   ##mean to represent NA, but which
  USTAR[which(USTAR==SPV)]<-NA   ##is not NA, set all instances of
   SD_V[which( SD_V==SPV)]<-NA   ##this data to NA
```

```
 OBKHV[which(OBKHV==SPV)]<-NA

 pcs<-which(is.finite(DIR)) ##indices to process for footprint
 SEL<-round(DIR[pcs])
 num<-length(pcs)
 WID<-ceiling(SD_V[pcs]/0.46)

 for(id in 1:num)
 { k<-pcs[id]
   DOY<-formatC(1 + floor(TIME[k]/1440), width=3, flag="0")
   TDIM<-TIME[k]-1440*floor(TIME[k]/1440)
   if(TDIM==0){TDIM<-1440; DOY<-formatC(floor(TIME[k]/1440), width=3, flag="0")}
  if(as.numeric(DOY)>OFF_ST & as.numeric(DOY)<OFF_ED)
  {if(is.finite(OBKHV[k]) & is.finite(SD_V[k]) & is.finite(WS[k]) & is.finite(DIR[k]) )
   {Tinfo<-ff_Tinfo(as.Date(paste(YEAR,DOY,sep=""),"%Y%j")) ###get time information
   TUNIT<-paste("minutes since ",Tinfo["tD","YEAR"],"-",Tinfo["tD","MONTH"],"-"
         ,Tinfo["tD","DAY"]," 00:00:00",sep="")

   ###morphometric calculations
   M_FILE<-paste(DATA_DIR,YEAR,"/London/L",ITER,"/",SITE,"/DAY/",DOY,"/MORPH_AB_"
            ,SITE,"_",YEAR,DOY,".txt",sep="")
   DATA<-read.table(M_FILE, header=T)

   OT_DIR <-paste(WORK_DIR,Tinfo["tD","YEAR"],"/London/Level_",ITER
                  ,"/FPR/",DOY,"/",sep="")
   if(!file.exists(OT_DIR)){dir.create(OT_DIR)}
   OT_FILE<-paste(OT_DIR,"FPR_AB_",SITE,"_",Tinfo["tD","YEAR"],Tinfo["tD","DOY"],"_"
             ,formatC(TDIM%/%60,width=2,flag="0"),formatC(TDIM%%60,width=2,flag="0")
             ,".nc",sep="")
    print(paste(Tinfo["tD","YEAR"],"/",Tinfo["tD","DOY"],", "
             ,formatC(TDIM%/%60,width=2,flag="0")
            ,formatC(TDIM%%60,width=2,flag="0"),sep=""))

    ###select roughness parameters and average over a sector proportional to sd_v's size

    Z_G<-(DATA[TDIM%/%30,3])
    Z_H<-(DATA[TDIM%/%30,4])
    PAI<-(DATA[TDIM%/%30,5])
    FAI<-(DATA[TDIM%/%30,6])

    ###roughness calculation, Macdonald et al 1998
    Z_D<-Z_H*(1+(PAI-1)*4.43^(-PAI))
    Z_0<-Z_H*((1-Z_D/Z_H)*exp(-(0.5*1*1.2*0.4^(-2)*(1-Z_D/Z_H)*FAI)^(-0.5)))
    Z_M<-(HEIGHT-Z_G)-Z_D

    ###Restrict to unstable conditions of <= -1
    #L<-OBKHV[k]       ###not included in iterate
    #if(L<0 & abs(L)<(2*Z_0)){L<-c(-2*Z_0)}

    ###call kcl_fpr_write_ncdf function
    METAFILE<-paste(DATA_DIR,YEAR,"/London/L",ITER,"/",SITE,"/META/L",ITER,"_"
                    ,SITE,"_FPR_30min.csv",sep="")
    try(kcl_fpr_write_ncdf(OT_FILE, paste("L",ITER,sep=""), Z_0, Z_M
                    ,WS[k], DIR[k], SD_V[k], OBKHV[k], USTAR[k]
                    ,DOMAIN_X, DOMAIN_Y, DOMAIN_OUTPUT, D_INPUT
                    ,TDIM, TUNIT, SITE, TIMEZONE, METAFILE))

    rm(L,Z_D,Z_0,Z_M,Z_G,Z_H,PAI,FAI,SECTOR,TDIM)
    } ###finite data
   } ###day of year in correct range
  } ##half hourly loop
 }else{
```

```
TIME<-NA; height<-NA; DIR<-NA; WS<-NA; USTAR<-NA; SD_V<-NA; L<-NA
print(paste(FILE,"does not exist"))
} ##FILE exists
```

```
## Footprint_Functions
##
## Functions used in calculating the flux footprint
##
## Tinfo
## kcl_write_ncdf
## kcl_fpr_kormann_and_meixner
## psi_m
## phi_c
## I_1
## I_2
## I_3
## j_1
## j_2
## f_psi_m
## f_z_phi_c
## fequ_m
## fequ_n
## linspace
########


ff_Tinfo <- function(Date){
      # generate time information for daily processing
      # specify yesterday, today and tomorrow
      Tinfo <-
matrix(NA,3,6,dimnames=list(c("yD","tD","tM"),c("YEAR","YY","MONTH","DAY","DOY","YD")))
      for(d in seq(1,3)){
        Tinfo[d,"YEAR"]  <- format(Date-2+d,"%Y")
        Tinfo[d,"YY"]    <- format(Date-2+d,"%y")
        Tinfo[d,"MONTH"] <- format(Date-2+d,"%m")
        Tinfo[d,"DAY"]   <- format(Date-2+d,"%d")
        Tinfo[d,"DOY"]   <- format(Date-2+d,"%j")
        Tinfo[d,"YD"]    <- paste(Tinfo[d,"YEAR"],Tinfo[d,"DOY"],sep="")
      }
      return(Tinfo)
}


ff_getMETA<- function(FILE){
  # function to extract list of global and variable attribute from META-data file in csv format
  # variable attributes: name, units, longndame, linked_variables, precision
  INFO<-read.csv(FILE,head=FALSE,sep=',')
  Vstart=which(INFO[,1]=="###")+1                    # '###' indicates start of information on
variables
  gAtt<-as.matrix(INFO[1:(Vstart-2),1:2])            # extract global attribute names and values
  vAtt<-as.matrix(INFO[Vstart:dim(INFO)[1],])        # extract information on vaiables
  return(list(gAtt,vAtt))
}



kcl_fpr_write_ncdf<-function(FILE_NAME, LEVEL, Z_0_INPUT, Z_M_INPUT
                  ,U_INPUT, WD_INPUT, SIGV_INPUT, L_INPUT, USTAR_INPUT
                  ,DOMAIN_X, DOMAIN_Y, DOMAIN_OUTPUT, D_INPUT
                  ,TDIM, TUNIT, SITE, TIMEZONE, METAFILE){
 ##calculates the fluxsource area based on the Kormann and Meixner 2001
 ##footpint model, rotates output into mean wind and writes a geographically
 ##referenced raster to a ncdf file
 ##run model
 FOOTPRINT<-kcl_fpr_kormann_and_meixner(Z_0_INPUT, Z_M_INPUT ,U_INPUT
                              ,SIGV_INPUT, L_INPUT, USTAR_INPUT
```

```
                                ,DOMAIN_X, DOMAIN_Y, D_INPUT)
 ##variables are (1:10): PHI, F_VAL, D_Y, X_ARR, M, N, U_VAL, KAPPA, USTAR, XSI
 ##extract max distance footprint
 IXS<-which(FOOTPRINT[[2]]==max(FOOTPRINT[[2]],na.rm=T))
 if(length(IXS)>0){
  X_DISTANCE<-FOOTPRINT[[4]][,,1]
  X_MAX<-X_DISTANCE[IXS[1]]
 }
 ##pad and rotate footprint
 FX<-DOMAIN_OUTPUT*2/D_INPUT; FY<-FX
 FULL<-array(0,c(FX,FY,1,1))
 X_LIM<-c((1+(FX)/2):((FX)/2+(DOMAIN_X/D_INPUT)))
 Y_LIM<-c(((1+(FY/2))-DOMAIN_Y/D_INPUT):(((FY/2))+DOMAIN_Y/D_INPUT))
 FULL[X_LIM,Y_LIM,1,1]<-FOOTPRINT[[1]]
 UNDEF<-which(!is.finite(FULL))
 if(length(UNDEF)>0){FULL[UNDEF]<-0}
 ROTANG<-WD_INPUT-90          ##will need to make into a 4D array then transform back
 ROTATED<-rotate_xy(FULL,-ROTANG,cx=((FX-1)/2), cy=((FY-1)/2))  ##rotate_xy  goes anti-
clockwise
 ROTATED<-as.matrix(ROTATED[,,1,1])
 ###define the cut bounds for ROTATED array - split this up to make it easier to understand
  LOWER_X<-((FX)/2)-DOMAIN_OUTPUT/(2*D_INPUT)
  UPPER_X<-((FX)/2)+DOMAIN_OUTPUT/(2*D_INPUT)
  LOWER_Y<-((FY)/2)-DOMAIN_OUTPUT/(2*D_INPUT)
  UPPER_Y<-((FY)/2)+DOMAIN_OUTPUT/(2*D_INPUT)
 ROTATED<-ROTATED[LOWER_X:UPPER_X,LOWER_Y:UPPER_Y]
  rm(LOWER_X,UPPER_X,LOWER_Y,UPPER_Y)
 COORDINATES<-c(0:(2*DOMAIN_X/D_INPUT))*D_INPUT-DOMAIN_X
 NX<-length(ROTATED[,1])
 NY<-length(ROTATED[1,])

  ##write to ncdf file
    ###define dimensions   #name ##units  #values  #unlim?  #create as a dim/coord var
  dim_x<-dim.def.ncdf("easting", "m", COORDINATES, create_dimvar=TRUE)
  dim_y<-dim.def.ncdf("northing", "m", COORDINATES, create_dimvar=TRUE)
  dim_t<-dim.def.ncdf("time",TUNIT,TDIM,unlim=TRUE, create_dimvar=TRUE)
  dim_i<-dim.def.ncdf("MODEL_INPUT","",1, create_dimvar=TRUE)
  dim_p<-dim.def.ncdf("MODEL_PARAMETER","",1, create_dimvar=TRUE)

  ###define global attributes
  INFO  <-ff_getMETA(METAFILE)
  gAtt  <-INFO[[1]]

  ###define variables
  vAtt  <-list(INFO[[2]][,1],INFO[[2]][,2],INFO[[2]][,3],INFO[[2]][,4],INFO[[2]][,5],INFO[[2]][,6])
  ncVar<-vector("list",15)
  ##define variable -phi
  ncVar[[1]]<-var.def.ncdf(as.character(vAtt[[1]][1]),as.character(vAtt[[2]][1])
                           ,list(dim_x,dim_y,dim_t)
                           ,as.numeric(gAtt[which(gAtt[,1]=='missing_value'),2])
                                   ,prec=as.character(vAtt[[5]][1])
                           ,longname=as.character(vAtt[[3]][1]))

  for (n in 2:8){    ###define variables - inputs
      ncVar[[n]] <- var.def.ncdf(as.character(vAtt[[1]][n]),as.character(vAtt[[2]][n])
                           ,list(dim_i,dim_t)
                           ,as.numeric(gAtt[which(gAtt[,1]=='missing_value'),2])
                                   ,prec=as.character(vAtt[[5]][n])
                           ,longname=as.character(vAtt[[3]][n]))}

  for (n in 9:15){    ###define variables - model parameters
      ncVar[[n]] <- var.def.ncdf(as.character(vAtt[[1]][n]),as.character(vAtt[[2]][n])
```

```
                        ,list(dim_p,dim_t)
                        ,as.numeric(gAtt[which(gAtt[,1]=='missing_value'),2])
                                ,prec=as.character(vAtt[[5]][n])
                        ,longname=as.character(vAtt[[3]][n]))}

 # create netCDF file
 ncID <- create.ncdf(FILE_NAME,ncVar)
 # write data  - inputs
 put.var.ncdf(ncID,ncVar[[1]],ROTATED) #phi
 put.var.ncdf(ncID,ncVar[[2]],D_INPUT) #resolution
 put.var.ncdf(ncID,ncVar[[3]],Z_0_INPUT) #roughness length
 put.var.ncdf(ncID,ncVar[[4]],Z_M_INPUT) #effective height
 put.var.ncdf(ncID,ncVar[[5]],L_INPUT) #obukhov length
 put.var.ncdf(ncID,ncVar[[6]],SIGV_INPUT) #std dev v
 put.var.ncdf(ncID,ncVar[[7]],U_INPUT) #horizontal wind speed
 put.var.ncdf(ncID,ncVar[[8]],WD_INPUT) #hoz wind direction
 # write data - outputs
 put.var.ncdf(ncID,ncVar[[9]],FOOTPRINT[[5]]) # parameter m
 put.var.ncdf(ncID,ncVar[[10]],FOOTPRINT[[6]]) #parameter n
 put.var.ncdf(ncID,ncVar[[11]],FOOTPRINT[[7]]) #u val
 put.var.ncdf(ncID,ncVar[[12]],FOOTPRINT[[9]]) #ustar
 put.var.ncdf(ncID,ncVar[[13]],FOOTPRINT[[8]]) #kappa
 put.var.ncdf(ncID,ncVar[[14]],FOOTPRINT[[10]]) #xsi
 put.var.ncdf(ncID,ncVar[[15]],X_MAX) # position max footprint
 close.ncdf(ncID)
}  ##close function kcl_write_ncdf


kcl_fpr_kormann_and_meixner<-function(Z_0_INPUT, Z_M_INPUT ,U_INPUT
                                ,SIGV_INPUT, L_INPUT, USTAR_INPUT
                                ,X_MAX, Y_MAX, D_INPUT)
{V_K<-0.4 #von_karmann constant

 ##bounds for integration
 Z_1<-3*Z_0_INPUT
 Z_2<-(1+V_K)*Z_M_INPUT

 ##roof finding for equations 39 and 40
 M<-uniroot(f=fequ_m
        ,Z_0_INPUT,Z_M_INPUT,L_INPUT,Z_1,Z_2  #inputs
        ,interval=c(0.6,0.1),maxiter=1000); M<-Re(M$root)
 N<-uniroot(f=fequ_n
        ,Z_0_INPUT,Z_M_INPUT,L_INPUT,Z_1,Z_2  #inputs
        ,interval=c(0,1.5),maxiter=1000)  ; N<-Re(N$root)

 #Eq 41
 NOM<-(I_2(M,Z_0/Z_M,Z_1,Z_2,Z_M) + j_1(M,Z_1,Z_2,Z_M,L_INPUT,f_psi_m))
 DENOM<-(I_1(2*M,Z_1,Z_2,Z_M)*Z_M^M)
 U_VAL<-(USTAR_INPUT/V_K)*(NOM/DENOM) ; rm(NOM,DENOM)
 U_VAL<-as.numeric(U_VAL)

 #Eq 41
 NOM<-j_1(N,Z_1,Z_2,Z_M,L_INPUT,f_z_phi_c)
 DENOM<-(I_1(2*N,Z_1,Z_2,Z_M)*Z_M^(N-1))
 KAPPA<-(V_K*USTAR_INPUT)*(NOM/DENOM);  rm(NOM,DENOM)
 KAPPA<-as.numeric(KAPPA)

 ###define grid over which footprint phi is to be calculated
 X_SERIES<-seq(1,X_MAX,D_INPUT)
 Y_SERIES<-seq(-Y_MAX,(Y_MAX-1),D_INPUT)
 X_ARR<-array(0,dim=c(length(X_SERIES),length(Y_SERIES),2))
 for(j in 1:length(Y_SERIES)){X_ARR[,j,1]<-X_SERIES}
```

```
 for(j in 1:length(X_SERIES)){X_ARR[j,,2]<-Y_SERIES}

 ##Crosswind integrated footprint
 R_VAL <- 2 + M - N    # Top of p 213
 MU_VAL<-(1 + M)/R_VAL  ## defined after Eq 18

 XSI<-(U_VAL*(Z_M^R_VAL))/(KAPPA*(R_VAL^2)) ##Eq 19

 if(length(XSI)>1){print("XSI more than one value")
 }else{XSI<-as.numeric(XSI)}
 ##Exclude values on edge of matrix leading to floating underflow error
 ##following Simone Kotthaus in IDL version 28/02/2011
 EXC<-(-XSI)/X_ARR[,,1]
 IDX<-which(EXC<(-87))
 if(length(IDX)>0){EXC[IDX]<-NA}  ; rm(IDX)

 F_VAL<-(1/(gamma(MU_VAL)))*((XSI^MU_VAL)/(X_ARR[,,1]^(1+MU_VAL)))*exp(EXC) #Eq
21

 ##Crosswind diffusion: Eq 18
 U_BAR<-
(gamma(MU_VAL)/gamma(1/R_VAL))*U_VAL*(((KAPPA*R_VAL^2)/U_VAL)^(M/R_VAL))*(X_
ARR[,,1]^(M/R_VAL))
 SIG<-SIGV_INPUT*X_ARR[,,1]/U_BAR  ##Definition after Equation 9

 ##Exclude values on edge of matrix leading to floating underflow error
 ##following Simone Kotthaus in IDL version 28/02/2011
 INM<-(-X_ARR[,,2]^2)/(2*SIG^2)
 IND<-which(INM < (-87))
 if(length(IND)>0){INM[IND]<-NA} ; rm(IND)
 ##Equation 9
 D_Y<-(1/(SIG*sqrt(2*pi)))*exp(INM)
 IND<-which(D_Y<(1E-38))
 if(length(IND)>0){D_Y[IND]<-NA} ; rm(IND)

 PHI<-D_Y*F_VAL  ##Eq 8
 PHI<-matrix(PHI*D_INPUT^2, length(X_SERIES), length(Y_SERIES))
 D_Y<-matrix(D_Y*D_INPUT, length(X_SERIES), length(Y_SERIES))
 F_VAL<-matrix(F_VAL*D_INPUT, length(X_SERIES), length(Y_SERIES))

 MODEL<-list(PHI, F_VAL, D_Y, X_ARR, M, N, U_VAL, KAPPA, USTAR_INPUT, XSI)
 return(MODEL)
} ##end function kcl_fpr_kormann_and_meixner


psi_m<-function(Z,L_INPUT)
{##calculate phi m Equation 35
 if(L_INPUT>0)
 {PHI_M<-5*Z/L_INPUT
 }else{
  ZETA<-(1-16*Z/L_INPUT)^0.25
  PHI_M<-(-2)*log((1+ZETA)/2)-log((1+ZETA^2)/2)+2*atan(ZETA)-pi/2
 }
 return(PHI_M)
} #end of function psi_m

phi_c<-function(Z,L_INPUT)
{##calculate phi C Equation 34
 if(L_INPUT>0)
 {PHI_C<-1+5*Z/L_INPUT
 }else{
  PHI_C<-(1-(16*Z/L_INPUT))^(-0.5)
```

```
 }
 return(PHI_C)
}

I_1<-function(P,Z_1,Z_2,Z_M_INPUT)
{##Eq 42
 Z<-linspace(Z_1/Z_M_INPUT,Z_2/Z_M_INPUT,1000)
 DZ<-diff(Z)
 Z<-Z[1:(length(Z)-1)]+DZ/2
 D1<-sum((Z^P)*DZ)
 return(D1)
}

I_2<-function(P,Z_0_INPUT,Z_1,Z_2,Z_M_INPUT)
{##Eq 43
 Z<-linspace(Z_1/Z_M_INPUT,Z_2/Z_M_INPUT,1000)
 DZ<-diff(Z)
 Z<-Z[1:(length(Z)-1)]+DZ/2
 D1<-sum((Z^P)*(log(Z/Z_0_INPUT))*DZ)
 return(D1)
}

I_3<-function(P,Z_0_INPUT,Z_1,Z_2,Z_M_INPUT)
{##Eq 44
 Z<-linspace(Z_1/Z_M_INPUT,Z_2/Z_M_INPUT,1000)
 DZ<-diff(Z)
 Z<-Z[1:(length(Z)-1)]+DZ/2
 D1<-sum((Z^P)*log(Z)*(log(Z/Z_0_INPUT))*DZ)
 return(D1)
}

j_1<-function(P,Z_1,Z_2,Z_M_INPUT,L_INPUT,called_func)
{##Eq 45
 Z<-linspace(Z_1/Z_M_INPUT,Z_2/Z_M_INPUT,1000)
 DZ<-diff(Z)
 Z<-Z[1:(length(Z)-1)]+DZ/2
 D1<-sum((Z^P)*DZ*called_func(Z*Z_M_INPUT,Z_M_INPUT,L_INPUT))
 return(D1)
}

j_2<-function(P,Z_1,Z_2,Z_M_INPUT,L_INPUT,called_func)
{##Eq 46
 Z<-linspace(Z_1/Z_M_INPUT,Z_2/Z_M_INPUT,1000)
 DZ<-diff(Z)
 Z<-Z[1:(length(Z)-1)]+DZ/2
 D1<-sum((Z^P)*DZ*log(Z)*called_func(Z*Z_M_INPUT,Z_M_INPUT,L_INPUT))
 return(D1)
}

f_psi_m<-function(Z,Z_M_INPUT,L_INPUT)
{D1<-psi_m(Z,L_INPUT)
 return(D1)
}

f_z_phi_c<-function(Z,Z_M_INPUT,L_INPUT)
{D1<-Z/(Z_M_INPUT*phi_c(Z,L_INPUT))
 return(D1)
}

fequ_m<-function(M,Z_0_INPUT,Z_M_INPUT,L_INPUT,Z_1,Z_2)
{##Equation 39
 ALL_D<-rep(0,length(M))
```

```
 for(j in 1:length(M))
 {A<-
l_1(2*M[j],Z_1,Z_2,Z_M_INPUT)*(l_3(M[j],Z_0_INPUT/Z_M_INPUT,Z_1,Z_2,Z_M_INPUT)+j_2(
M[j],Z_1,Z_2,Z_M_INPUT,L_INPUT,f_psi_m))
  B<-
l_2(2*M[j],1,Z_1,Z_2,Z_M_INPUT)*(l_2(M[j],Z_0_INPUT/Z_M_INPUT,Z_1,Z_2,Z_M_INPUT)+j_
1(M[j],Z_1,Z_2,Z_M_INPUT,L_INPUT,f_psi_m))
  ALL_D[j]<-B-A
 }
 return(ALL_D)
}

fequ_n<-function(N,Z_0_INPUT,Z_M_INPUT,L_INPUT,Z_1,Z_2)
{ ##Equation 40
 ALL_D<-rep(0,length(N))
 for(j in 1:length(N))
 {A<-l_1(2*N[j],Z_1,Z_2,Z_M_INPUT)*j_2(N[j],Z_1,Z_2,Z_M_INPUT,L_INPUT,f_z_phi_c)
  B<-l_2(2*N[j],1,Z_1,Z_2,Z_M_INPUT)*j_1(N[j],Z_1,Z_2,Z_M_INPUT,L_INPUT,f_z_phi_c)
  ALL_D[j]<-B-A }
 return(ALL_D) }

linspace<-function(X1,X2,N=100,PERI=F,GHOST=c(0),UNIQUE=TRUE)
{ ###returns a real vector of length N, containing equidistant values between
  ##x1 and x2 exclusively. If N is omitted, 100 is used.
 if(length(GHOST)==1){NGHOST<-rep(GHOST,2)
 }else if(length(GHOST)>2 ){
  NGHOST<-c(min(abs(GHOST),na.rm=T),max(abs(GHOST),na.rm=T))
 }else{ NGHOST<-GHOST}
 if(PERI==TRUE){NGHOST<-c(0,-1)}

 if(length(X1)>=2)
 {XX1<-X1[1]; XX2<-X1[2]
  if(length(X2)!=0){NN<-X2}
 }else{ XX1<-X1;  XX2<-X2
  if(length(N)!=0){NN<-N}
 }
 if(length(N)==0){UNIQUE<-TRUE}

 N_REAL<-NN-NGHOST[1]-NGHOST[2]
 OUT<-XX1+(seq(0,NN-1)-NGHOST[1])*(XX2-XX1)/(N_REAL-1)
 if(UNIQUE==TRUE){OUT<-unique(OUT)}
 return(OUT)
}
```

```
%ImageMorphometricParms.m
%calculates morphometric parameters for an image based on prevailing wind
%direction. Specify a dem on a square grid to load and averaging dimension
%(ny)
%
%Date: 26 February 2004
%Author:
%   Offerle, B.
%   Geovetarcentrum
%   Goteborg University, Sweden
%   Modifyed by Fredrik Lindberg 2010-01-09, fredrik.lindberg@kcl.ac.uk
%   Modified by Simone Kotthaus 2011-02-09, KCL
%    V2 include KSSW and move to UR, SK 2013/11/22
%-------------------------------------------------------------------------

clear

maps='/data/its-tier2/micromet/data/MAPS/Footprint/DEM/';
% plot settings
screensize=get(0,'ScreenSize');
screenwidth=screensize(3);
screenheight=screensize(4);

% radius for 1deg calculations
R = 500;
% which site to run for
site='KSSW';

nx=0;
pcrop=0;%percent of pixels to crop from left, should be a factor of y, so no zero pixesl are used
canyondir=0.0;

% read builing DEM from LiDAR, ground DEM from LiDAR
[s,scale,header,headernum,headername,sizey,sizex]=Solweig_10_loaddem([maps
'lidar_builddem_4m.asc']);
g=Solweig_10_loaddem([maps 'lidar_grounddem_4m.asc']);

% specify subset and center of rotation
dtheta=1;
nsub=R*scale;

if strcmp(site,'KSS') ;      yc=1454; xc=1021;
elseif strcmp(site,'KSK') ;  yc=1457; xc=1036;
elseif strcmp(site,'KSSW') ; yc=1446; xc=1026;
elseif strcmp(site,'Wood') ; yc=1480; xc=1100;
else
  error('site not found!')
end

if xc<nsub||xc+nsub>length(s)||yc<nsub||yc+nsub>length(s)
   error('Image too small for specified center and subset')
end
a=s(xc-nsub:xc+nsub,yc-nsub:yc+nsub); %subset and center
g=g(xc-nsub:xc+nsub,yc-nsub:yc+nsub); %subset and center
clear s

a(a==-9999)=0;% ground and building dem
p=a-g;        % buildingheight above ground
f=p;
f(f>0)=1;
f(f<0)=0;
f=f.*a;       % building height above zeroplane
```

```
n=length(a);
%this is for the averaging function
imid=floor(n/2);
dY=(pcrop/100*imid+1):imid;
dX=imid-nx:imid+nx;
lx=length(dX);
ly=length(dY);

% plot settings
figure('Position',[100 100 screenwidth*0.8 screenheight*0.8],'Numbertitle','off');
set(clf,'color',[1 1 1])
subplot(2,2,1)
image(a)
pbaspect([1 1 1])

% textfile generation
% Specify location of output textfile
fn=fopen(['L1_MORPH_',site,'_1d',num2str(R),'.txt'],'w');
fprintf(fn,'%9s','DIR','zG', 'zHground','zHsea', 'PAI', 'FAI');
fprintf(fn,'\r\n');
j=1;
for angle=(canyondir:dtheta:360-dtheta+canyondir);
   c=zeros(n,n);
   ground=imrotate(g,angle,'nearest','crop');
   buildandground=imrotate(a,angle,'nearest','crop');
   buildfromground=imrotate(p,angle,'nearest','crop');
   buildfromsea=imrotate(f,angle,'nearest','crop');

   bld=buildfromground(dY,dX); %building array

   subplot(2,2,2)
   image(buildandground)
   pbaspect([1 1 1])
   % base=mean(mean(b)); %this is to account for ground height.
   % convolve leading edge filter with domain
   c(2:n,:)=buildandground(2:n,:)-buildandground(1:(n-1),:);
   subplot(2,2,3)

   imagesc(c)
   pbaspect([1 1 1])
   wall=c(dY,dX);                %wall array
    % select "walls" of any height on building pixels or
    % extreme ground height changes of more than 2m
   wall=wall((wall>0 & bld>0) | (wall>2 & bld==0));
   fai(j)=sum(wall)/((lx*ly)/scale);

   subplot(2,2,4)
   imagesc(buildfromground)
   pbaspect([1 1 1])

   % pai and zHground
   bld=bld(bld>0); %building vector
   pai(j)=length(bld)/(lx*ly); %percent of pixels higher than base elevation, pseudo bldgs.
   zHground(j)=sum(bld)/length(bld); %average pseudo bldg height

   %zHsea
   bld=buildfromsea(dY,dX); %building array
   bld=bld(bld>0); %building vector
   zHsea(j)=sum(bld)/length(bld); %average pseudo bldg height

   % ground heights
```

```
    gro=ground(dY,dX);%
    zgnd(j)=mean(gro);

    fprintf(fn,'%9.3f',angle, zgnd(j), zHground(j),zHsea(j), pai(j), fai(j));
    fprintf(fn,'\r\n');
    j=j+1;
    pause(0.1)
end

fclose(fn);

%Plotting
iangle=(0:dtheta:360)*(pi/180);
figure('Name','Frontal Area Index' ,'Numbertitle','off')
polar(iangle,[fai fai(1)],'r')
set(gca,'YDir','reverse','FontSize',8,'View',[270 90],'XTickLabel','')
figure('Name','Plan Area Index' ,'Numbertitle','off')
polar(iangle,[pai pai(1)],'r')
set(gca,'YDir','reverse','FontSize',8,'View',[270 90],'XTickLabel','')
figure('Name','Average Building Height from ground' ,'Numbertitle','off')
polar(iangle,[zHground zHground(1)],'r')
set(gca,'YDir','reverse','FontSize',8,'View',[270 90],'XTickLabel','')
figure('Name','Average Building Height from sealevel' ,'Numbertitle','off')
polar(iangle,[zHsea zHsea(1)],'r')
set(gca,'YDir','reverse','FontSize',8,'View',[270 90],'XTickLabel','')
figure('Name','Average Ground Height' ,'Numbertitle','off')
polar(iangle,[zgnd zgnd(1)],'r')
set(gca,'YDir','reverse','FontSize',8,'View',[270 90],'XTickLabel','')
```

```
% FPR_Main
% This is the main program for deriving roughness parameters using a footprint area
% Fredrik Lindberg 2011-01-20
% adapted to daily processing, Simone Kotthaus 14/02/2011
% delete DIR rotation to BDG north because that is already done in eddy covariance
% processing, Simone Kotthaus 23/08/2011
% KSSW added, Alex Bjorkegren 21/10/2015

clear; close('all')
% state level of iteration (=level of input FPR_file)
IT=1;

% should results be plotted (as contour lines)?
doPLOT='FALSE';

% which site to run for
site='KSS';
if strcmp(site,'KSS') ; col=1454; row=1021;
elseif strcmp(site, 'KSSW') ; col=1446; row=1026;
elseif strcmp(site,'KSK') ; col=1457; row=1036; end

% time settings
year='2012';

% prepare building and ground dem
if 1
[b,scale,~,~,~,sizey,sizex]=Solweig_10_loaddem_V2('/home/micromet/Roofprograms/Footprint/
DEM/lidar_builddem_4m.asc');
s
=Solweig_10_loaddem_V2('/home/micromet/Roofprograms/Footprint/DEM/lidar_grounddem_4
m.asc');
b(b<0)=0;              % delete pixels with negative height
b(b==-9999)=0;
b=single(b);
s=single(s);
end
year

  for d=1:31
    if d<10 ; DOY=sprintf('00%u',d);
    elseif d<100 ; DOY=sprintf('0%u',d);
    else DOY=sprintf('%u',d);
    end

% wind direction from L2 ECFluxes
ECF = ['/data/its-
tier2/micromet/data/',year,'/London/L2/',site,'/DAY/',DOY,'/CSAT3_ECpack_',site,'_',year,DOY,'
_30min.nc'];
if exist(ECF)
    [time_EC,DIR(1:48)] = READ_dir_ECFluxes(ECF);
    DIR=double(round(DIR));
    % footprint estimate of previous level
    FPR = ['/data/its-
tier2/micromet/data/',year,'/London/L',num2str(IT),'/',site,'/DAY/',DOY,'/FPR_AB_',site,'_',year,D
OY,'_30min.nc']
    if exist(FPR,'file')
    [time_fp,PHI] = READ_fpr_KormanMeixner(FPR);

    if strcmp(doPLOT,'TRUE')
        % calculate contour lines
        t = size(time_fp,1);
        cnt(1:t,1:9)=NaN;
```

```
        for i=1:t
            desc = PHI{i};
            desc = sort(desc(desc>0),'descend');
            for c=1:9 ;
                selC=find(cumsum(desc)>(1-0.1*c),1);
                if selC>0; cnt(i,c)=desc(selC); end
            end
        end
    end

    % resize dem
    dom=size(PHI{1},1);
    nsub=floor(dom/2);
    if col<nsub||col+nsub>sizex||row<nsub||row+nsub>sizey
        error('Image too small for specified center and subset')
    end
    builddem =b(row-nsub:row+nsub,col-nsub:col+nsub);
    grounddem=s(row-nsub:row+nsub,col-nsub:col+nsub);

    % allocate output
    grd(1:48)= NaN;
    zH(1:48) = NaN;
    pai(1:48)= NaN;
    fai(1:48)= NaN;
    cai(1:48)= NaN;
    % write textfile
    outD=['/data/its-tier2/micromet/data/',year,'/London/L',num2str(IT+1),'/',site,'/DAY/',DOY];
    if ~exist(outD,'dir')
        mkdir(outD)
    end
    fn=fopen([outD,'/MORPH_AB_',site,'_',year,DOY,'.txt'],'w');
    fprintf(fn,'%19s','YYYY-mm-dd HH:MM:SS');
    fprintf(fn,'%9s','zG','zH','PAI','FAI','CAI'); fprintf(fn,'\r\n');

    for h=1:48
        index=find(time_fp==time_EC(h));
        if(any(index))

[grd(h),zH(h),pai(h),fai(h),cai(h)]=ImageMorphometricParmsFPR_V2(builddem,grounddem,scal
e,DIR(h),PHI{index});
            if strcmp(doPLOT,'TRUE')
              valid=find(~isnan(cnt(index,:)));
              valid1=find(~isnan(cntu(index,:)));
              figure('name',num2str(h));image(builddem);
              hold on; contour(PHI{index},cnt(index,valid),'col','white');
              hold on; contour(PHI{index},cnt(index,5),'col','red');
              hold on; contour(PHIu{index},cntu(index,5),'col','green');
              hold on; contour(PHI2{index},cnt2(index,5),'col','cyan');
            end
        end
        fprintf(fn,'%19s',datestr(time_EC(h),'YYYY-mm-dd HH:MM:SS'));
        fprintf(fn,'%9.3f',grd(h),zH(h),pai(h),fai(h),cai(h)); fprintf(fn,'\r\n');
    end
    fclose(fn);
    close('all')
    clear PHI DIR time_fp timr_EC builddem grounddem
end
end
end
exit
```

```
#/bin/bash
# merge hourly files to daily file
# KCLmicromet
# 22/02/2010 simone kotthaus

year=12
begin=1
end=31
level=2
site=KSS
works=/net/glusterfs/micromet/users/micromet/works/20${year}/London/
here=/export/cloud/micromet/data/20${year}/London/

for DOY in $(seq $begin $end) ; do

Dplus=`expr $DOY + 1`
Yplus=`expr $year + 1`
if [ $DOY -lt '100' ] ; then
  DOY=0$DOY
  if [ $DOY -lt '10' ] ; then DOY=0$DOY ; fi
fi
if [ $Dplus -lt '100' ] ; then
  Dplus=0$Dplus
  if [ $Dplus -lt '10' ] ; then Dplus=0$Dplus ; fi
fi

mkdir -p ${here}/L${level}/${site}/DAY/${DOY}/
cd ${here}/L${level}/${site}/DAY/${DOY}/
pwd

mv ${works}Level_${level}/FPR/${DOY}/FPR_AB_${site}_20${year}${DOY}_0030.nc .
for hh in $(seq 1 9) ; do
mv ${works}Level_${level}/FPR/${DOY}/FPR_AB_${site}_20${year}${DOY}_0${hh}?0.nc .
done
mv ${works}Level_${level}/FPR/${DOY}/FPR_AB_${site}_20${year}${DOY}_1??0.nc .
mv ${works}Level_${level}/FPR/${DOY}/FPR_AB_${site}_20${year}${DOY}_2??0.nc .
if [ $DOY -eq '365' ] ; then
mv ${works}Level_${level}/FPR/${DOY}/FPR_AB_${site}_20${Yplus}001_0000.nc .
else
mv ${works}Level_${level}/FPR/${DOY}/FPR_AB_${site}_20${year}${Dplus}_0000.nc .
fi
rm -rf FPR_AB_${site}_20${year}${DOY}_30min.nc
/opt/tools/cdo/bin/cdo mergetime FPR_AB_${site}*
FPR_AB_${site}_20${year}${DOY}_30min.nc
rm -rf FPR_AB_${site}_20?????_????.nc

done # DOY
```

Appendix 7.B: Comparison of flux footprints calculated using the 'original' IDL and the author's R translation of the Kormann and Meixner (2001) flux footprint model

Visual inspection of the average flux footprint for one half hourly period (00:00 – 00:30, 2nd January, 2012) calculated for KSS by the Kotthaus (IDL) implementation of the Kormann and Meixner (2001) footprint model, and the author's (R) translation suggest very good agreement between the two. Despite different image rotation (*rot* vs. *rotate_xy*, Barthelme, 2015) and root finding (*fx_root* vs. *uniroot,* R Development Core Team, 2013) functions the size and orientation of the plotted (Figure 7.B.1) flux footprints are almost identical in appearance.

More quantitative comparison of the output from the two sets of programs (Table 7.B.1) shows R^2 values for the regression of the R program output on the IDL program output of greater than 0.98 for all variables and a much higher (R^2>0.99) agreement for the phi (source area weighting or footprint) values. Given the slight dissimilarity of the input data due to improvements in data processing between the calculation of the original (IDL) and the R program footprint, it is suggested that these results validate the accuracy of the R translation.

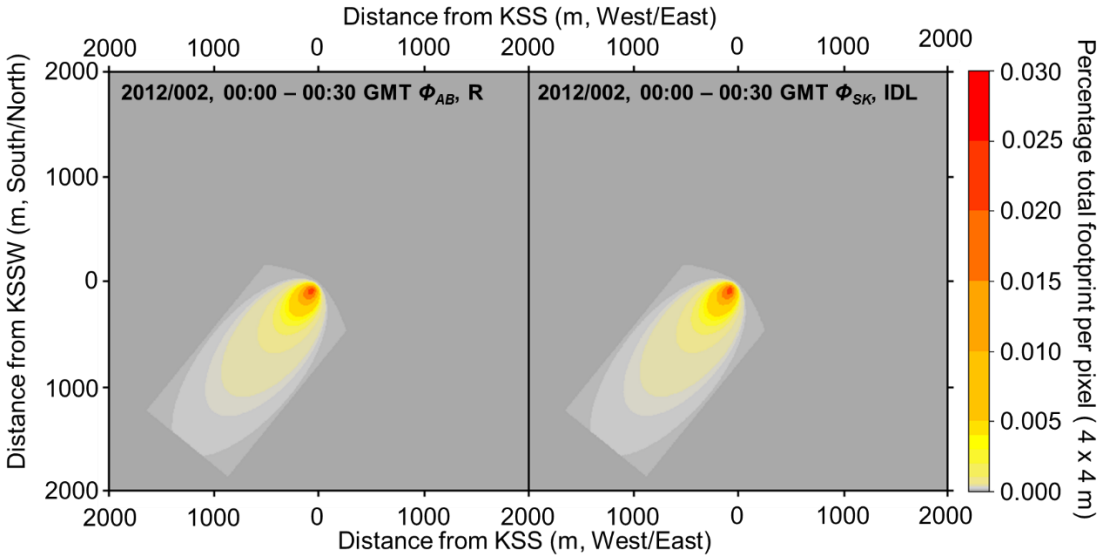

Figure 7.B.1: Average flux footprint calculated for 00:00 – 00:30 GMT on the 2nd January, 2012 by (left) author's R translation of (right) the Kotthaus modification of the IDL implementation of the Kormann and Meixner (2001) model provided by Christen.

Table 7.B.1: Results of the comparison of footprint inputs and outputs as calculated by the R translation and the IDL modification of the footprint program for January, 2012. Left is the regression of the source area weighting or Φ values from the R (Φ_{AB}) onto the IDL program (Φ_{SK}), right are the coefficients for the same regression of all other input (blue) and output (purple) variables. Differences between the input variables are due to improved processing of the data between the time of the original (IDL) and 2015 (R) calculation of the flux footprint.

Components of linear regression of Φ_{AB} on Φ_{SK}	
Intercept	0.000
Slope	0.977
Root Mean Squared Error	0.000
Degrees of Freedom	3.103×10^4
Multiple R2	0.997

Input and output variables	Units	R^2
Pixel size of the DEM	m	1.00000
Surface roughness length	m	0.98991
Effective measurement height of flux system (z')	m	0.99843
Obukhov length (L)	m	0.99991
Standard deviation of lateral wind component	$m\ s^{-1}$	0.99999
Longitudinal wind velocity component (U)	$m\ s^{-1}$	0.99998
Friction velocity (u^*)	$m\ s^{-1}$	0.99994
Wind direction	°	1.00000
Exponent of the wind velocity power law (M)	NA	0.98468
Exponent of the eddy diffusivity power law (N)	NA	0.99989
Constant in power-law profile of the wind velocity	$m^{(1-M)}\ s^{-1}$	0.99874
Constant in power-law profile of the eddy diffusivity	$m^{(2-N)}\ s^{-1}$	0.99992
Flux length scale	m	0.99875
Distance of footprint maximum from flux measurement site (X_{max})	m	0.99766

Appendix 7.C: Variation of the flux source area with changing wind speed and atmospheric stability

Comparison of periods with similar wind speed and direction conditions but different atmospheric stability conditions (Figure 7.C.1) suggests that the flux source area (95% of the flux) is most elongated under neutral (-0.01 ≤ z'/L < 0.01) conditions, followed by stable (z'/L > 0.01), near neutral unstable (-0.1 ≤ z'/L < -0.01) and unstable (-1 ≤ z'/L < -0.1), as expected.

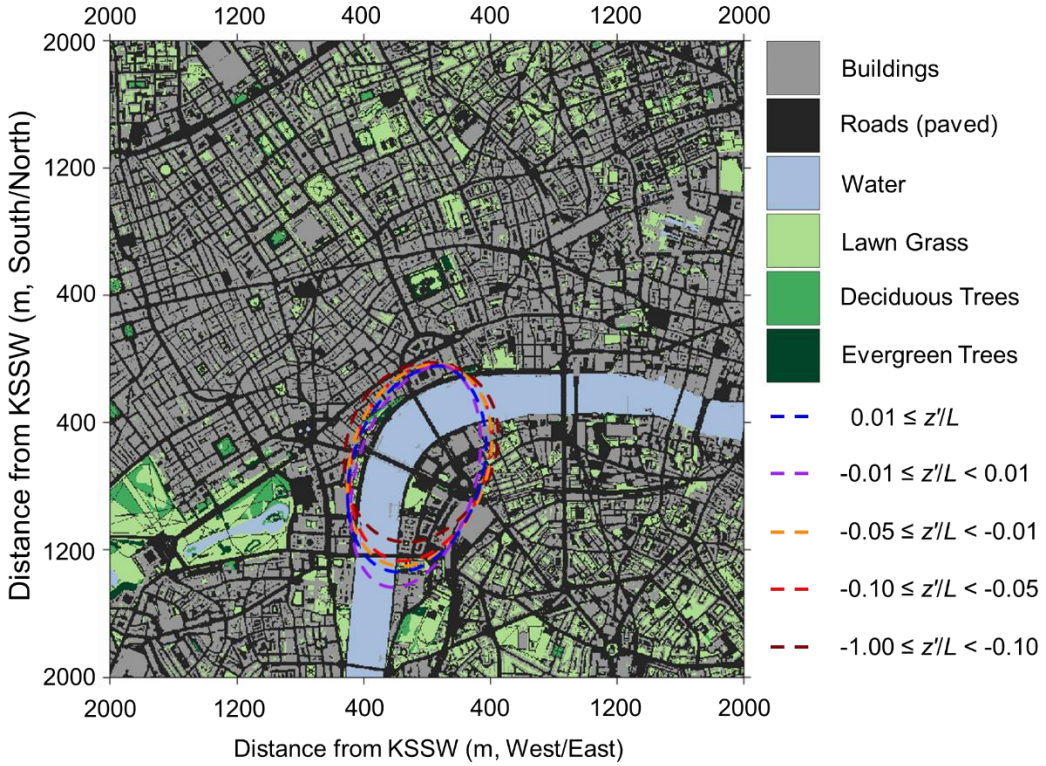

Figure 7.C.1: Flux source area (95%) for five half hourly periods with mean wind speed 3.6 to 3.8 m s^{-1} and mean wind direction 192 to 194º. z'/L values range from -0.21 to 0.04 and the half hourly periods for high (positive) to low (negative) z'/L values are (time-ending) 2013/364 22:00, 2014/016 06:30, 2013/359 07:30, 2014/047 20:00, 2014/44 06:30. All times given in GMT.

The effect of wind speed on source area is not as clear (Figure 7.C.2). The highest wind speed has the least elongated source area of those plotted; however, the second highest wind speed has the most elongated source area, along with the slowest. Although there is a general trend of increasing distance between the flux tower and the point at which the flux footprint function reaches a maximum (X_{max}) (Figure 7.C.3), the correlation is low.

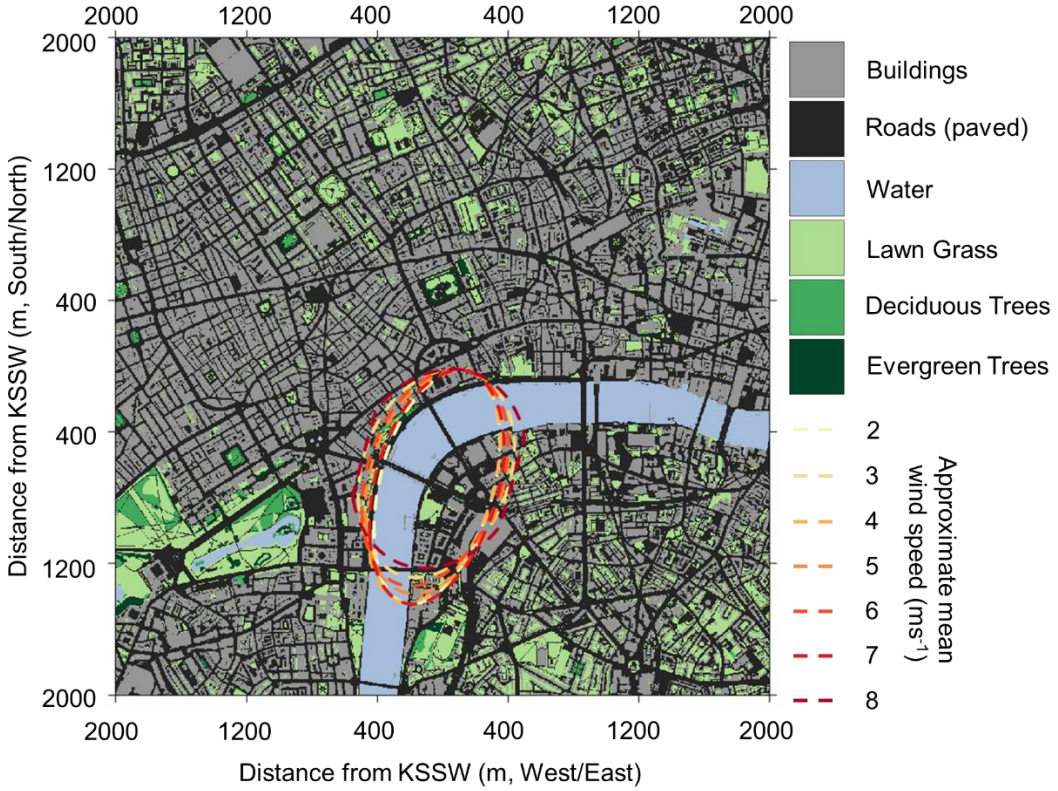

Figure 7.C.2: Flux source area (95%) for seven half hourly periods with mean wind direction 192 to 194º and z'/L values from -0.05 to 0.02. Wind speeds range from 1.97 ms^{-1} to 7.91 ms^{-1} and the half hourly periods for low to high wind speeds are (time-ending) 2014/047 21:30, 2014/272 18:30, 2014/049 09:30, 2014/365 17:00, 2013/250 15:00, 2014/035 13:30, 2013/104 11:00. All times given in GMT.

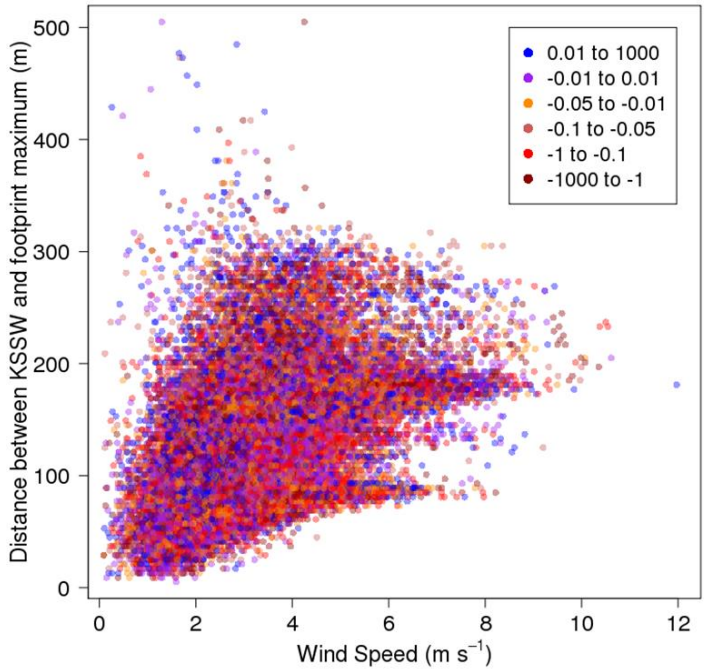

Figure 7.C.3: Distance of the maximum in the footprint function, i.e., the area which contributes the most to the overall flux, from the KSSW tower with wind speed and stability (z'/L, key upper right) measured at height A, KSSW.

Appendix 7.D: Derivation of CO_2 efflux from water samples

This section details the process and problems with calculating the CO_2 released by Thames river water using data collected from the Thames Royal National Lifeboat Institution (TLI, Figure 2.1b) as described in Section 2.2.4. Measurements were made of the uptake or loss of CO_2 from river water (Section 2.2.4), distilled (deionised) water and water that had been chilled, incubated, and/or stored in a vial rather than the sample bag in order to evaluate the effect of heating, cooling, a time lag between sample acquisition and measurement, sample storage conditions and injection procedure on results. All measurements are summarised in Table 7.D.1.

The uptake or emission of CO_2 was calculated as the difference between the concentrations of CO_2 in the air flowing from the reference cell and the sample cell. Despite matching of the two IRGAs, an offset between the two gas analysers before injection of the water sample was common. This offset was calculated as the mean difference between the two gas analysers for the 70 to 10 seconds prior to the injection of the sample and was subtracted from the calculated difference between concentrations in the sample and reference cells for all results plotted in Figure 7.D.1 to Figure 7.D.3.

Table 7.D.1: Measurements of CO_2 exchange over water made by LI6400 as described in Section *2.2.4.*

Class	*Date*	*ID number*	*Description*
Deionised water	10th July 2013	1	Deionised water, standard container
		2	
	17th January 2014	1	Deionised water, 1L container
Effect of temperature, lag and storage vessel	24th July 2013	1	River water sample (R24_1) added to sample chamber direct from sample bag.
		2	R24_1 decanted to vial prior to measurement.
		3	R24_1 refrigerated in a vial prior to measurement.
		4	R24_1 refrigerated in sample bag prior to measurement.
		5	R24_1 incubated at 30 °C in a vial prior to measurement.
		6	R24_1 stored at room temperature in a vial prior to measurement.
		7	R24_1 stored in sample bag prior to measurement.
	31st July 2013	1	F25_6 stored in a vial and refrigerated.
		2	F25_2 stored in a vial and refrigerated.
Flood tide (water level rising with time)	25th July 2013	F25_1	Sample taken at low tide.
		F25_2	Sample taken 70 minutes after low tide.
		F25_3	Sample taken 140 minutes after low tide.
		F25_4	Sample taken 205 minutes after low tide.
		F25_5	Sample taken 275 minutes after low tide (65 minutes before high tide).
		F25_6	Sample taken 10 minutes after high tide.
Ebb tide (water level falling with time)	31st July 2013	E31_1	Sample taken at high tide.
		E31_2	Sample taken 60 minutes after high tide.
		E31_3	Sample taken 120 minutes after high tide.
		E31_4	Sample taken 195 minutes after high tide.
		E31_5	Sample taken 275 minutes after high tide (80 minutes before low tide).

A low *[CO_2]* benchmark was set using de-ionised water, i.e., samples which should not contain very little dissolved CO_2 and no organic matter which might generate emissions. Figure 7.D.1 shows the reaction of de-ionised water with time to air with ambient (13_07_10_run 3 and run4: 413 ppm; 14_01_17_1L: 450 ppm) CO_2 concentrations. For most of the time series the difference between the air flow from the sample and reference cells is positive, indicating that the distilled water was absorbing CO_2 relative to the reference cell (dry Perspex). Despite there being no difference in CO_2 concentration, sample cell size or air temperature between 13_07_10_run 3 and run4, there is a difference of about 1.5 ppm. This suggests that the repeatability of this experiment is low. The surface area of the water samples measured on the 10 July 2013 was 48 cm^2 and the total water value was 50 cm^3. The water sample measured on the 17 January 2014 had a total volume of 1000 cm^3 and a surface area of 123 cm^2. The larger surface area may explain the greater rate of exchange ($[CO_2]_{Sample}$ - $[CO_2]_{Ref}$ = 5 ppm), and the larger volume may explain the slower change in the rate of exchange with time compared to the other two distilled water samples. The initial peak in the time series for water sample 14_01_17_1L is due to the method by which the sample was introduced to the sample cell – unlike all other water samples it was too large for injection and had to be poured into the sample cell whilst the sample cell was open, allowing air from the surroundings into the cell and causing a brief peak in $[CO_2]_{Sample}$ before the cell was closed once more. Injection of distilled water into the sample cell (13_07_10_run3 and 4) resulted in an immediate drop in $[CO_2]_{Sample}$ relative to $[CO_2]_{Ref}$, visible as a trough at time=0 on Figure 7.D.1. This supports the assertion that injection of the sample does not introduce atmospheric CO_2 into the sample cell.

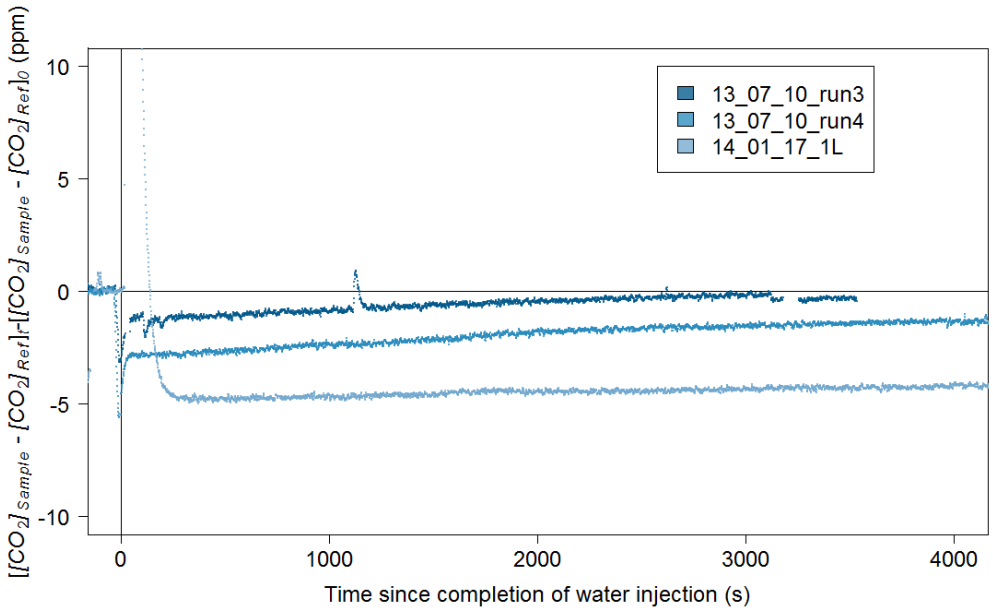

Figure 7.D.1: Change in the difference between the CO_2 concentrations measured in the airflow from the reference cell ($[CO_2]_{Ref}$) and the sample cell ($[CO_2]_{Sample}$) at time, t, compared to that measured prior to injection of the water sample (t=0) for three distilled water samples.

This assertion is important as measurements of all samples presented in Figure 7.D.2 and Figure 7.D.3 showed an initial peak in the difference between the sample and reference cell CO2 concentrations. The experiments presented in Figure 7.D.1 show that this peak is due to release of CO_2 from the sample, rather than CO_2 introduced as an air bubble in the syringe or

due to a leaky seal. It is hypothesised that this release is due to the greater surface area of the stream of water droplets exchange as the sample is rapidly injected into the cell compared to the final sample 'pool', and that this larger surface area enables more gas exchange with the air within the chamber (the secondary peak on 13_07_24_run5 coincides with changing the LI6400 battery and is not considered to reflect actual sample cell concentrations). Some tendency towards lower emissions/greater absorption was observed for incubated (red) and room temperature (orange, purple) relative to refrigerated samples (blue); however, the greatest absorption was for a sample that had been stored for 6 days in a refrigerated vial (13_07_31_testrun2). This was significantly lower than the other sample kept under the same conditions (13_07_31_testrun1). The original samples from which they had been derived (13_07_25_run2 and run6 respectively) had a similar separation of about 3 ppm, albeit the other way round, with 13_07_25_run6 (13_07_31_testrun1) absorbing less CO_2 than 13_07_25_run2 (13_07_31_testrun2). As both were stored in the same manner, this again raises doubts as the repeatability of this experiment and the value of the results. Measurements taken as soon as the sample was collected (13_07_24_run1, 13_07_24_run2) were lower than the majority of the other samples, which had been stored in the sample bag or vial for at least one hour, suggesting that the water might absorb CO_2 during storage; although given the variation observed between two identical samples (Figure 7.D.1), the significance of this observation is questionable.

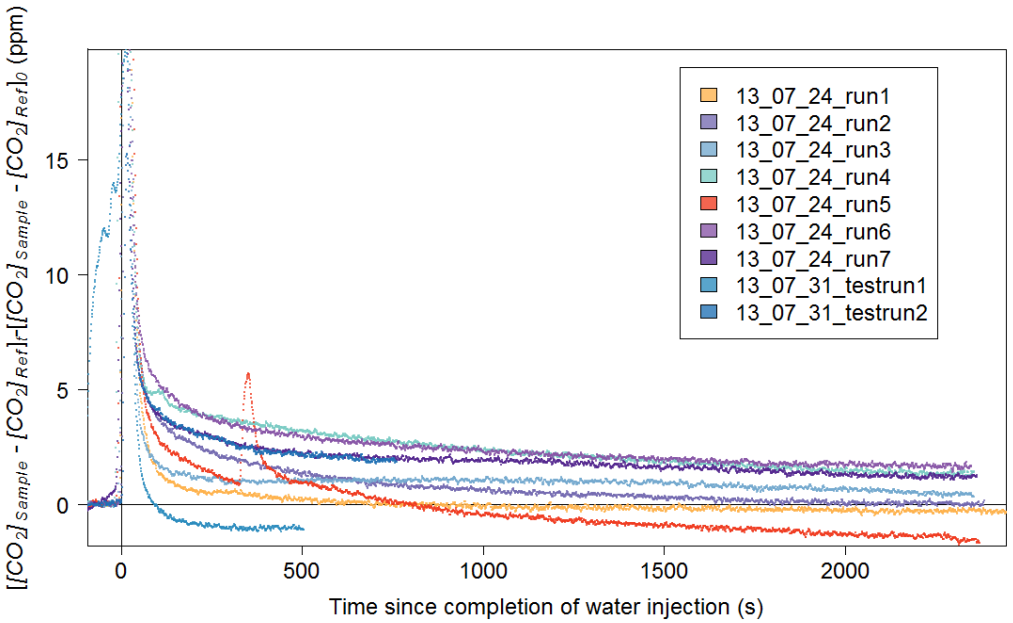

Figure 7.D.2: Change in the difference between the CO_2 concentrations measured in the airflow from the reference cell ($[CO_2]_{Ref}$) and the sample cell ($[CO_2]_{Sample}$) at time, t, compared to that measured prior to injection of the water sample (t=0) for nine river water samples which have been stored in a sample bag, or a vial, a room temperature, above room temperature or refrigerated for periods ranging from 0 hours to 6 days.

Samples of Thames water were collected from TLI over two six hour periods in July, 2013. Due to safety concerns (visibility) samples were only collected when there was sufficient daylight and the sun was high above the horizon. Samples taken during the flow tide (purple, Figure 7.D.3), when the water was travelling from the estuary up river, tended to absorb more CO_2 than those taken during the ebb tide. Due to the aforementioned release of CO_2 during the

injection period, these values cannot be converted to CO_2 fluxes as the amount of CO_2 dissolved in the water post-injection is likely to be much lower than pre-injection. Therefore, whilst these results suggest interesting avenues for future research into CO_2 fluxes from urban bodies of water, they are not used further in this study.

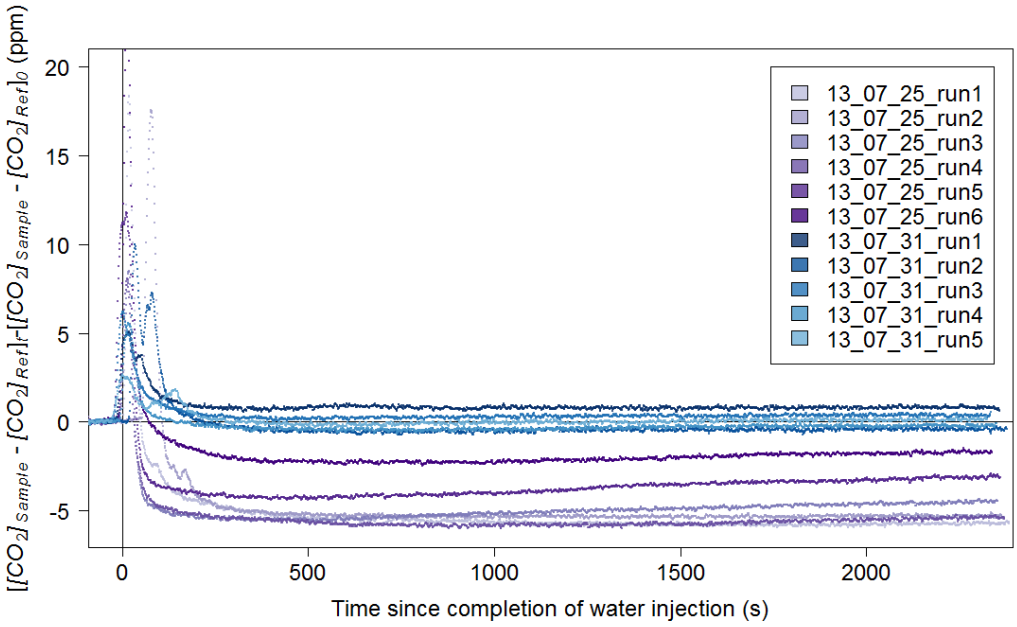

Figure 7.D.3: Change in the difference between the CO_2 concentrations measured in the airflow from the reference cell ($[CO_2]_{Ref}$) and the sample cell ($[CO_2]_{Sample}$) at time, t, compared to that measured prior to injection of the water sample (t=0) for eleven river water samples measured immediately after collection from the Thames. Points are coloured according to river depth; darker colours = deeper water/higher tide. Samples are numbered in chronological order, so purple samples were taken when the tide was coming in and blue samples when the tide was going out.

Chapter 8: Conclusions and contributions

8.1 Key findings

This study contributes to the understanding of net carbon dioxide (CO_2) exchange between the densely urbanised land surface and the urban atmospheric boundary layer. The examination of methods to measure net emissions, and data analysed, are relevant to both researchers and policymakers involved with the characterisation and control of CO_2 emissions in urban areas at time scales from the sub-hourly to the multi-annual, and spatial scales from a single street to regional.

The main conclusions are:

- Central London's local scale monthly mean CO_2 concentrations ($[CO_2]$) increased every year and were almost always above global background levels. Central London is a source of CO_2, particularly in winter.
- Local and micro scale $[CO_2]$ varied at daily, hebdomadal and seasonal time scales, driven by both human and natural factors. These include (in approximate descending order of importance): (i) emissions from vehicles, (ii) the depth of the mixing layer, (iii) emissions from combustion for building heating, (iv) emissions from human respiration, (v) atmospheric stability, and (vi) carbon dioxide uptake by vegetation.
- The magnitude and sign of the CO_2 stored within the street canyon airspace varies in a similar manner to the $[CO_2]$, and with the spacing and time resolution of the vertical profile measurements from which it is calculated. The temporal resolution of measurements was found to be more important than the spatial density, provided $[CO_2]$ data are recorded at the local scale plus at least one lower height. The lower measurements should be made at close to the height of the local roughness elements, or half the height of the local scale measurements.
- $[CO_2]$ varies with land cover. It tends to be higher in areas with medium building density and lowest in areas with low surface roughness, such as rivers and railways. The variation in $[CO_2]$ within land categories is greater than between land categories, suggesting that in greater London other factors have a larger impact on $[CO_2]$ at street level than land cover or use.
- 49.84 to 51.43 kg m^{-2} of CO_2 is emitted per year in central London. Annual emissions determined from micrometeorological and inventory methods agree to within 3%. When annual emissions are based only on the vertical flux (F_{CO2}) the two methods still agree to within 6%, i.e., net CO_2 emissions determined solely with vertical flux measurements at ca. 2.2 times the local roughness element height are viable for high density urban environments like central London.

8.2 Key contributions

The key contributions of this research are the assessment of net ecosystem exchange (NEE) or emissions of CO_2 from a densely urbanised environment, and of the methods to calculate these emissions.

Combustion for building heating plays a major role in determining $[CO_2]$, particularly during periods with low temperatures (e.g., December to February) and the response of a building heating system to lower temperatures is building use (e.g., commercial, academic) specific. An increase in traffic flow of 100 Veh h^{-1} (ca. 7% of work day traffic flow) was increase $[CO_2]$ by 2 – 5 ppm within the Strand street canyon. The impact of human respiration was smaller: a 20% increase in population density raises $[CO_2]$ within the street canyon by 1 ppm. Changes in human behaviour during the London Olympics resulted in lower $[CO_2]$ but suspension of Sunday trading laws increased $[CO_2]$ by approximately 2 ppm. An increase in mixing layer depth of 100 m was associated with a decrease in $[CO_2]$ of 1.4 ppm, but linear regression of $[CO_2]$ on mixing layer depth had a very low coefficient of determination and the significance of this result is questionable. Anthropogenic factors have a far greater effect on $[CO_2]$ in central London than natural (biological or meteorological) ones. $[CO_2]$ tended to be higher in areas with higher height to width ratios, and more buildings or roads relative to open areas with parks or the river; however, horizontal $[CO_2]$ gradients did not vary consistently with land cover. The vertical $[CO_2]$ profile can be characterised as a series of internally homogenous zones reflecting the geometry of the surrounding buildings, very different to reported rural profiles.

The $[CO_2]$ data from which the change in CO_2 stored within an airspace (CO_2 storage, ΔC_S) is calculated often do not fulfil the theoretical requirements of continuity in time and space (Aubinet *et al.*, 2005). Interpolation of $[CO_2]$ data in time is unnecessary, but it is recommended that $[CO_2]$ are linearly interpolated in space or span-weighted to the nearest physically induced point of change in the vertical profile (e.g. canopy height). The calculation of ΔC_S from $[CO_2]$ measured at one location (ΔC_{SS}) is not recommended; at least one other location is required (ΔC_{SP}). ΔC_S magnitude decreased predictably with under-sampling of $[CO_2]$ in time. The effect slow sensor response time was less correctable; it is recommended that instruments for measuring $[CO_2]$ have a response time of 0.1 s or faster. ΔC_S spectra suggest a -2/3 power law with frequency in the 0.1 - 5 Hz (0.2 to 10 s) range which may be used to assess the quality of data.

ΔC_{SP} is much smaller than ΔC_{SS}, but has more pronounced seasonal and diurnal variation. ΔC_{SS} data were heavily negatively skewed, suggesting intermittent large losses of CO_2 from the street canyon. A method to detect venting was developed using wavelet analysis. Quadrant analysis confirmed that the venting events are unlikely to be linked to coherent structures, rather they are thermally induced release of ‘bursts’ of air from the street canyon.

The relations between ΔC_S and meteorological or other factors were not strong enough for a predictive model. Missing data for all micrometeorological components of the NEE may be gap-filled with values averaged over time of day, day of week, month of year and (in the case of A_z

and A_{xy}, wind direction). This method was capable of gap-filling time series with data availabilities as low as 30% (70% missing) with <1% change, on average, in total monthly emissions (Section 3.2.2).

Calculated net CO_2 emissions for central London for June 2012 to May 2013 (inclusive) were 49.84 (inventory) to 51.43 kg CO_2 m^{-2} yr^{-1} (micrometeorological). The vertical flux was 2.6% larger than the annual total calculated by the micrometeorological method and was the largest component. The assumption that net emissions in high density city centres such as central London may be assessed solely F_{CO2} measurements is reasonable; ΔC_S and A_z are negligible. However, the full horizontal advection component was not calculable at this site and may be significant.

Despite the considerable uncertainty associated with the inventory method it has the benefit of apportioning net exchange of CO_2 by land cover types and the associated processes. The majority of CO_2 emissions in Central London are due to vehicles, followed by combustion for space heating and human respiration. Reduction of net emissions by increasing the vegetation fraction is unfeasible; halving the built fraction in the KS flux footprint (81.4% to 40.7%), with the difference given over entirely to vegetation, would reduce emissions by 22.26 kgCO_2 m^{-2} yr^{-1}, of which only 4.4% would be due to increased uptake by the vegetated surface.

This study helps rationalise the methodology of measuring net emissions in an urban area. All results reported in this study are strictly applicable only to central London and do not necessarily reflect other urban areas, or other neighbourhoods of London itself. $[CO_2]$ in different parts of London are more distinct from each other than $[CO_2]$ within different land categories in the same part of London (section 6.4). Further research is required, and suggestions for future work are the topic of the following section.

8.3 Future research

Rising urban populations and urban land area raise the importance of the processes governing CO_2 emissions in cities with regard to the global CO_2 balance and climate change. Although this study contributes to the understanding of these processes, there are a number of related areas which could benefit from further research.

CO_2 emissions from traffic were the inventory method component with the greatest associated uncertainty. This could be reduced through improved monitoring of total traffic volumes, particularly if the data distinguishes between different vehicle classes.

The micrometeorological component with the largest uncertainty is horizontal advection. The ability of cross-canyon winds to generate within-canyon helical motions may transport CO_2 emitted at street level into or out of the volume of interest normal to the axis of the street canyon. Cross-canyon $[CO_2]$ measurements are needed to resolve this issue.

A few (e.g., Christen & Vogt (2004): Basel, Switzerland; Coutts *et al*. (2007): Melbourne, Australia; Christen et al. (2011), Vancouver, Canada) studies have measured $[CO_2]$ and/or F_{CO2} in multiple locations in the same urban area, but none have attempted to evaluate all micrometeorological components of NEE over multiple neighbourhood types (e.g., city centre, suburban, industrial). Whilst net emissions may be calculated entirely from the turbulent vertical flux in a densely built city centre, the same method may not be applicable to a less intensely built suburb where stable atmospheric conditions may be more common, and storage or advection more significant.

Rivers may be a source of CO_2, particularly if connected to the sewerage system. Their low roughness length relative to the surrounding buildings facilitates transport relatively low $[CO_2]$ air into the city centre. The surface height of tidal rivers may vary by several metres, changing the displacement height and flux footprint. Cities built around a large, potentially tidal river are under-represented in the literature and the role of urban rivers on urban CO_2 concentrations has yet to be fully explored.

Calculation of emissions from an urban environment requires measurements of all components which are likely to make a significant contribution to the net total. The current understanding of the processes operating in urban areas suggests that these components are likely to be (for the inventory method) emissions from traffic, space heating, and human respiration and (for the micrometeorological method) the turbulent vertical flux. Given the large observed differences between the processes governing CO_2 exchange in urban and rural environments, examination of the validity of applying methods of measuring CO_2 exchange developed in rural areas to urban areas is required. To ensure confidence in published estimate of net emissions from urban areas, it must be clear that no CO_2 exchanges, storage or transport which would significantly affect the net total have been omitted. This is challenging in an environment as heterogeneous at the local scale as a typical urban area – assumptions or methods evaluated over a deep street canyon may not be applicable over the urban park 50 m away. Assumptions about atmospheric mixing and stability developed in colder climates, where street canyons may be relatively warm due to heat released by vehicles, may not be appropriate in areas where shading from intense insolation results in street canyons which are relatively cool. Whilst this study advances our understanding of CO_2 exchanges in a densely built city in a temperate, maritime climate, a great deal more research is needed to assess whether the results are more widely applicable to cities with differing geometries and geographies.

References

Aber, J., Melillo, J.M. (2001) Terrestrial Ecosystems, Glossary [Online] http://www.tereco.sr.unh.edu/definitions.html#n [Accessed online 30/08/2015]

Adler, D. (2005) Violplot package, R [Online] https://cran.r-project.org/web/packages/vioplot/index.html [Accessed online 07/01/2016]

Agueron, E., McPherson, E.G. (2011) Comparison of Methods for Estimating Carbon Dioxide Storage by Sacramento's Urban Forest. In *Carbon Sequestration in Urban Ecosystems*, Springer

Algesten, G., Sobek, S., Bergström, A. K., Ågren, A., Tranvik, L. J., Jansson, M. (2004) Role of lakes for organic carbon cycling in the boreal zone. *Global Change Biol*ogy, 10, 141 – 147

American Meteorological Society (AMS) (2011) glossary of meteorology [Online] http://glossary.ametsoc.org/wiki/Main_Page [Accessed online 04/02/2016]

Araujo, A.C., Dolman, A.J., Waterloo, M.J., Gash, J.H.C., Kruijt, B., Zanchi, F.B., de Lange, J.M.E., Stoevelaar, R., Manzi, A.O., Nobre, A.D., Lootens, R.N., Backer, J. (2010) The spatial variability of CO_2 storage and the interpretation of eddy covariance fluxes in central Amazonia. *Agricultural and Forest Meteorology,* 150, 226 – 237

Attié, J. L., Durand, P. (2003) Conditional wavelet technique applied to aircraft data measured in the thermal internal boundary layer during sea-breeze events. *Boundary-layer meteorology*, *106*(3), 359-382

Aubinet, M., Heinesch, B., Yernaux, M. (2003) Horizontal and vertical CO_2 advection in a sloping forest. *Boundary-Layer Meteorology,* 108, 397-417

Aubinet, M., Berbigier, P., Bernhofer, C., Cescatti, A., Feigenwinter, C., Granier, A., Grünwald, T., Havrankova, K., Heinesch, B., Longdoz, B., Marcolla, B., Montagnani, L., Sedlak, P. (2005) Comparing CO_2 storage and advection conditions at night at different Carboeuroflux sites. *Boundary-Layer Meteorology,* 116, 63-93

Bakwin, P. S., Tans, P. P., Zhao, C., Ussler, W., Quesnell, E. (1995) Measurements of carbon dioxide on a very tall tower. *Tellus B*, *47*(5), 535-549

Baldocchi, D. (1997) Measuring and modelling carbon dioxide and water vapour exchange over a temperate broad-leaved forest during the 1995 summer drought. *Plant, Cell and Environment*, 20, 1108-1122

Baldocchi, D. (2003) Assessing the eddy covariance technique for evaluating carbon dioxide exchange rates of ecosystems: past, present and future. *Global Change Biology,* 9, 479-492

Bartelink, H. H. (1997) Allometric relationships for biomass and leaf area of beech (Fagus sylvatica L). *Annales des Sciences Forestieres*, 54(1), 39-50

Barthelme, S. (2015) Imager package, R [Online] https://cran.r-project.org/web/packages/imager/index.html [Accessed online 22/02/2016]

Berry, R.D., Colls, J.J. (1990) Atmospheric Carbon Dioxide and Sulphur Dioxide on an Urban/Rural Transect-II. Measurements along the Transect. *Atmospheric Environment*, 24A(10), 2689-2694

Björkegren, A.B., Grimmond, C.S.B., Kotthaus, S., Malamud, B.D. (2015) CO_2 emission estimation in the urban environment: Measurement of the CO_2 storage term. *Atmospheric Environment*, 122, 775-790.

Bond-Lamberty, B., Thomson, A. (2010). A global database of soil respiration data. *Biogeosciences*, *7*(6), 1915-1926. Data [online] https://github.com/bpbond/srdb [Accessed online 09/02/2016]

Borchers, H.W. (2015) Pracma package, R [Online] https://cran.r-project.org/web/packages/pracma/index.html [Accessed online 30/08/2015]

Brandini, P., Tabacchi, G. (1996). Biomass and volume equations for holm oak and strawberry tree in coppice stands in southern Sardinia. *ISAFA Comunicazioni di Ricerca dell'Istituto Sperimentale per l'Assestamento Forestale e per l'Alpicoltura*, (96/1), 59-69.

Buchanan, C. (2011) *Seven Day Traffic Counts in the City of Westminster*. London.

Buffam, I., Turner, M.G., Desai, A.R., Hanson, P.C., Rusak, J.A., Lottig, N.R., Stanley, E.H. and Carpenter, S.R. (2011) Integrating aquatic and terrestrial components to construct a complete carbon budget for a north temperate lake district. *Global Change Biology*, 17(2), 1193-1211.

Bunce, R.G.H. 1968. Biomass and production of trees in a mixed deciduous woodland. I. Girth and height as parameters for the estimation of tree dry weight. *Journal of Ecology*, 56, 759–775.

Burba, G., & Anderson, D. (2010) *A brief practical guide to eddy covariance flux measurements: principles and workflow examples for scientific and industrial applications*. Li-Cor Biosciences.

Burri, S., Frey, C., Parlow, E., Vogt, R. (2009) *CO_2 fluxes and concentrations over an urban surface in Cairo, Egypt*. Paper presented at the Seventh International Conference on Urban Climate organised by the IAUC, Yokohama, 29 June–3 July

Byrne, O. (2014) *Building heating over vacation periods* [Email] Message to: Bjorkegren, A. 05/06/2014.

Cai, X., Chen, J., Desjardins, R.L. (2010) Flux footprints in the convective boundary layer: large-eddy simulation and lagrangian stochastic modelling. *Boundary Layer Meteorology*, 137, 31–47

Cairns, M.A., Brown, S., Helmer, E., Baumgardner, G.A. (1997) Root biomass allocation in the world's upland forests. *Oecologia*, 111(1), 1-11.

Canadell, J.G., Ciais, P., Dhakal, S., Le Quéré, C., Patwardhan, A., Raupach, M.R. (2009) The global carbon cycle 2 - the human perturbation of the carbon cycle. Paris, France: UNESCO-SCOPE-UNEP Policy Briefs, No.10

Casper, P., Maberly, S. C., Hall, G. H., Finlay, B. J. (2000) Fluxes of methane and carbon dioxide from a small productive lake to the atmosphere. *Biogeochemistry*, *49*(1), 1-19.

Caton, F., Britter, R.E., Dalziel, S (2003) Dispersion mechanisms in a street canyon. *Atmospheric Environment,* 37, 693-702

Christen, A., Vogt, R. (2004) Energy and radiation balance of a central European city. *International Journal of Climatology*, 24(11), 1395-1421.

Christen, A., van Gorsel, E., Vogt, R. (2007) Coherent structures in urban roughness sublayer turbulence. *International journal of Climatology*, 27(14), 1955-1968.

Christen, A., Coops, N.C., Crawford, B.R., Kellett, R., Liss, K.N., Olchovski, I., Tooke, T.R., Van Der Laan, M., Voogt, J.A. (2011) Validation of modeled carbon-dioxide emissions from an urban neighborhood with direct eddy-covariance measurements. *Atmospheric Environment*, 45(33), 6057-6069.

CityPopulation.de (2009a) *The population of the cantons of Switzerland according to census results and latest official estimates*. *Basel, 2000.* [Online] http://citypopulation.de/Switzerland-Cities.html [Accessed online 09/02/2016]

CityPopulation.de (2009b) *The population of the Italian regions according to census results and latest official estimates* [Online] http://www.citypopulation.de/Italy-Cities.html [Accessed online 09/02/2016]

Clark, D. A., Brown, S., Kicklighter, D. W., Chambers, J. Q., Thomlinson, J. R., Ni, J. (2001) Measuring net primary production in forests: concepts and field methods. *Ecological applications*, 11(2), 356-370.

Coutts, A. M., Beringer, J., Tapper, N. J. (2007) Characteristics influencing the variability of urban CO_2 fluxes in Melbourne, Australia. *Atmospheric Environment*, *41*(1), 51-62.

Crawford, B., Grimmond, C. S. B., Christen, A. (2011) Five years of carbon dioxide fluxes measurements in a highly vegetated suburban area. *Atmospheric Environment*, *45*(4), 896-905.

Crawford, B., Christen, A. (2014) Spatial variability of carbon dioxide in the urban canopy layer and implications for flux measurements. *Atmospheric Environment,* 98, 302-322.

Crawford, B., Christen, A. (2015). Spatial source attribution of measured urban eddy covariance CO_2 fluxes. *Theoretical and Applied Climatology*, *119*(3-4), 733-755.

CUFR Tree Carbon Calculator (2008) [Online] http://www.fs.usda.gov/ccrc/tools/cufr-tree-carbon-calculator-ctcc [Accessed online 09/02/2016]

Daubechies, I. (1990) The wavelet transform, time-frequency localization and signal analysis. *IEEE Transactions on Information Theory*, *36*(5), 961-1005.

Department of Energy and Climate Change (DECC) (2011) *Sub-national electricity and gas consumption statistics: analysis tool 2005 to 2013* [Online] https://www.gov.uk/government/publications/sub-national-electricity-and-gas-consumption-statistics-analysis-tool-2005-to-2009 [Accessed online 09/02/2016]

Department for Transport (DfT) (2014) Traffic counts by Local Authority [Online] http://www.dft.gov.uk/traffic-counts/cp.php [Accessed online 04/02/2016]

Denmead, O.T., Harper, L.A., Freney, J.R., Griffith, D.W.T., Leuning, R., Sharpe, R.R. (1998) A mass balance method for non-intrusive measurements of surface-air trace gas exchange. *Atmospheric Environment,* 32, 3679–3688.

Department for Environment Food and Rural Affairs (DEFRA) (2013) *UK Government conversion factors for Company Reporting* [Online] http://www.ukconversionfactorscarbonsmart.co.uk/Filter.aspx?year=27 [Accessed online 09/02/2016]

de Waele, S., Van Dijk, A., Broersen, P., Duynkerke, P. G., (2002) *Estimation of the integral time scale with time series models*. Poster P3.11, poster session 3 at the 15th Conference on Boundary Layer and Turbulence, organised by the AMS, Wageningen, 14th – 19th July.

Durrans, J. (2012) Mobile measurements of CO_2 in London from a bicycle mounted platform. *Unpublished Master's Thesis*, King's College London, London, UK

The City of Edinburgh Council (Edinburgh Council) (2004) *2011 Census – Key Trends Planning Committee Report no PC/068/03-04/CD.* The City of Edinburgh Council. [Online] http://www.edinburgh.gov.uk/download/meetings/id/2112/2001_census_-_key_trends [Accessed online 09/02/2016]

Emeis, S., Jahn, C., Münkel, C., Münsterer, C., Schäfer, K. (2007) Multiple atmospheric layering and mixing-layer height in the Inn valley observed by remote sensing. *Meteorologische Zeitschrift*, 16(4), 415-424.

European Union (2011a) *Mapping Guide for a European Urban Atlas* in uk001l_london.zip [Online] www.eea.europa.eu/data-and-maps/data/urban-atlas/ [Accessed online 09/02/2016]

European Union (2011b) *Urban Atlas – LUZ delivery report* in uk001l_london.zip [Online] www.eea.europa.eu/data-and-maps/data/urban-atlas/ [Accessed online 09/02/2016]

Farge, M. (1992) Wavelet transforms and their applications to turbulence. *Annual Review of Fluid Mechanics,* 24, 395-45

Feigenwinter, C., Vogt, R. (2005) Detection and analysis of coherent structures in urban turbulence. *Theoretical and Applied Climatology*, 81(3-4), 219-230

Feigenwinter, C., Bernhofer, C., Eichelmann, U., Heinesch,B., Hertel, M., Janous, D., Kolle, O., Lagergren, F., Lindroth, A., Minerbi, S., Moderow, U., Mölder, M., Montagnani, L., Queck, R., Rebmann, C., Vestin, P., Yernaux, M., Zeri, M., Ziegler, W., Aubinet, M. (2008) Comparison of horizontal and vertical advective CO_2 fluxes at three forest sites. *Agricultural and Forest Meteorology*, 148(1), 12-24

Feigenwinter, C., Vogt, R., Christen, A. (2012) Eddy covariance measurements over urban areas. In *Eddy Covariance*, 377-397. Springer.

Finnigan J. (2006) The storage term in eddy flux calculations. *Agricultural and Forest Meteorology*, 136, 108-113

FLIR Systems (2014) Extech Instruments User's guide [Online] http://www.extech.com/instruments/resources/manuals/CO210_UM.pdf [Accessed online 02/09/2015]

FLUXNET (2015) Distribution of tower sites within the global network of networks [Online] http://fluxnet.ornl.gov/sites/default/files/FluxnetNetwork4-2014.png [Accessed 09/12/2015]

Fox, J., Weisberg, S. (2010). *An R companion to applied regression*. Sage.

Galmarini, S., Attié, J. L. (2000) Turbulent Transport at the Thermal Internal Boundary-Layer top: Wavelet Analysis of Aircraft Measurements. *Boundary-layer meteorology*, 94(2), 175-196

GeodSolve (2015) Online geodesic calculations using the GeodSolve utility [Online] http://geographiclib.sourceforge.net/cgi-bin/GeodSolve [Accessed online 02/09/2015]

Gioli, B., Toscano, P., Lugato, E., Matese, A., Miglietta, F., Zaldei, A., Vaccari, F. P. (2012) Methane and carbon dioxide fluxes and source partitioning in urban areas: The case study of Florence, Italy. *Environmental Pollution*, 164, 125-131.

Google, Bluesky (2014) Strand campus, King's College London, UK. 51.511946, -0.116481. [Online] https://www.google.co.uk/maps/place/51%C2%B030%2743.0%22N+0%C2%B006%2759.3%22W/@51.5099573,-0.1159196,1179m/data=!3m1!1e3!4m2!3m1!1s0x0:0x0 [Accessed online 30/08/2015]

Google (2016) Strand campus, King's College London, UK. 51.511946, -0.116481. [Online] https://www.google.co.uk/maps/place/51%C2%B030'43.0%22N+0%C2%B006'59.3%22W/@51.5099573,-0.1159196,16.2z/data=!4m2!3m1!1s0x0:0x0 [Accessed online 31/01/2016]

Goulden, M.L., Munger, J.W., Fan, S.-M., Daube, B.C., Wofsy, S.C. (1996) Measurements of carbon sequestration by long-term eddy covariance: methods and a critical evaluation of accuracy. *Global Change Biology* 2, 169-182

Graps, A. (1995) An Introduction to Wavelets. *IEEE Computational Science and Engineering*, 2(2), 50-61

Greater London Authority (GLA) (2012) London View Management Framework Supplementary Planning Guidance [Online] https://www.london.gov.uk/sites/default/files/archives/LVMF%20low%20res%20part%201.pdf [Accessed online: 11/06/2015]

Greater London Authority (GLA) Opinion Research and Statistics (2013) Daytime Population, Borough [Online] http://data.london.gov.uk/dataset/daytime-population-borough [Accessed 30/08/2015]

Greater London Authority (GLA) Economics (2014a) 2013 Borough Projections [Online] http://data.london.gov.uk/dataset/gla-employment-projections [Accessed 30/08/2015]

Greater London Authority (GLA) (2014b) Daytime Population, Borough [Online] http://data.london.gov.uk/dataset/daytime-population-borough [Accessed 23/01/2016]

Greenspace Information for Greater London (GiGL) (2015) Key London Figures [Online] http://www.gigl.org.uk/our-data-holdings/keyfigures/ [Accessed online 02/09/2015]

Grier, C. C., Lee, K. M., Archibald, R. M. (1984) Effect of urea fertilization on allometric relations in young Douglas-fir trees. *Canadian Journal of Forest Research*, 14(6), 900-904.

Grimmond, C. S. B., Oke, T. R. (1991) An evapotranspiration-interception model for urban areas. *Water Resources Research*, 27(7), 1739-1755.

Grimmond CSB, Oke TR (1999a) Heat storage in urban areas: Local-scale observations and evaluation of a simple model. *Journal of Applied Meteorology,* 38: 922–940

Grimmond, C.S.B., Oke, T.R. (1999b): Aerodynamic properties of urban areas derived from analysis of surface form. *Journal of Applied Meteorology*, 38, 1262–1292

Grimmond, C.S.B., King, T.S., Cropley, F.D., Nowak, D.J., Souch, C. (2002) Local-scale fluxes of carbon dioxide in urban environments: methodological challenges and results from Chicago. *Environmental Pollution,* 116(1), 243-254

Grimmond, C.S.B., Salmond, J.A., Oke, T.R., Offerle, B., Lemonsu, A. (2004) Flux and turbulence measurements at a densely built-up site in Marseille: Heat, mass (water and carbon dioxide), and momentum. *Journal of Geophysical Research,* (109) D24101

Grimmond, C.S.B, Christen, A., (2012) Flux measurements in urban ecosystems. *FluxLetter,* 5(1), 1-8

Haiduc, I., Beldean-Galea, M.S. (2011) *Variation of Greenhouse Gases in Urban Areas-Case Study: CO_2, CO and CH_4 in Three Romanian Cities*. INTECH Open Access Publisher.

Hanna, S.R. (1981) Lagrangian and Eulerian Time-Scale Relations in the Daytime Boundary Layer. *Journal of Applied Meteorology*, 20(3), 242-249.

Hartley, A. (2006) "Fuel Poverty". West Midlands Public Health Observatory. Birmingham, UK: West Midlands Public Health Observatory.[online] Accessed at: http://www.wmpho.org.uk/resources/Fuel_Poverty_Short.pdf [Accessed 12/04/2013]

Haszpra, L., Barcza, Z., Bakwin, P. S., Berger, B. W., Davis, K. J., Weidinger, T. (2001) Biosphere/atmosphere exchange of carbon dioxide. *Journal of Geophysical Research*, 106(D3), 3057-3069.

HC Deb (2001-02) 379 col. *1113W*

Helfter, C., Famulari, D., Phillips, G.J., Barlow, J.F., Wood, C., Grimmond, C.S.B., Nemitz, E. (2011) Controls of carbon dioxide concentrations and fluxes above central London. *Atmospheric Chemistry and Physics,* 11 (5) 1913-1928.

Henninger, S.and Kuttler, W. (2007) Methodology for mobile measurements of carbon dioxide within the urban canopy layer. *Climate Research,* 34 (2), 161-167.

Henninger, S., Kuttler, W. (2010) Near surface carbon dioxide within the urban area of Essen, Germany. *Physics and Chemistry of the Earth*, 35, 76–84.

Hirano, T., Sugawara, H., Murayama, S., Kondo, H. (2015) Diurnal Variation of CO_2 Flux in an Urban Area of Tokyo. *Scientific Online Letters on the Atmosphere*, 11, 100-103.

Hong, J., Kim, J., Lee, D., Lim, J. H. (2008) Estimation of the storage and advection effects on H_2O and CO_2 exchanges in a hilly KoFlux forest catchment*. Water resources research*, 44(1), W01426.

Huotari, J., Ojala, A., Peltomaa, E., Nordbo, A., Launiainen, S., Pumpanen, J., Rasilo, T., Hari, P. and Vesala, T. (2011) Long-term direct CO_2 flux measurements over a boreal lake: Five years of eddy covariance data. *Geophysical Research Letters*, 38(18).

Husch B, Miller CI, Beers TW (1982) *Forest mensuration*. Wiley, New York

Hutyra, L.R., Munger, J.W., Hammond Pyle, E., Saleska, S.R., Restrepo-Coupe, Daube, B.C., de Camargo, P.B., Wofsy, S.C. (2008) resolving systematic errors in estimates of net ecosystem exchange of CO_2 and ecosystem respiration in a tropical forest biome. *Agricultural and Forest Meteorology,* 148, 1266-1279

Iamarino, M., Beevers, S., Grimmond, C.S.B. (2012) High-resolution (space, time) anthropogenic heat emissions: London 1970–2025. *International Journal of Climatology*, 32(11), 1754-1767.

Idso, C.D., Idso, S.B., Balling, R.C., Jr. (2001) An intensive two-week study of an urban CO_2 dome in Phoenix, Arizona, USA. *Atmospheric Environment,* 35 (6), 995-1000

Imhoff, M. L., Tucker, C. J., Lawrence, W. T., Stutzer, D. C. (2000) The use of multisource satellite and geospatial data to study the effect of urbanization on primary productivity in the United States. *IEEE Transactions on Geoscience and Remote Sensing,* 38(6), 2549-2556.

Intergovernmental Panel on Climate Change (1997) Revised 1996 IPCC Guidelines for National Greenhouse Gas Inventories, IPCC/OECD/IEA, Paris

Intergovernmental Panel on Climate Change (IPCC) (2014) *Climate Change 2013: The Physical Science Basis. Technical Summary.* [Online] http://www.ipcc.ch/report/ar5/wg1/ [Accessed online 09/02/2016]

Iwata, H., Yadvinder, M., van Randow, C. (2005) Gap-filling measurements of carbon dioxide storage in tropical rainforest canopy airspace. *Agricultural and Forest Meteorology,* 132, 305-314.

Järvi, L., Mammarella, I., Eugster, W., Ibrom, A., Siivola, E., Dellwik, E., Keronen, P., Burba, G., Vesala, T. (2009) Comparison of net CO_2 fluxes measured with open-and closed-path infrared gas analyzers in an urban complex environment. *Boreal Environment Research*, 14, 499-514.

Järvi, L., Nordbo, A., Junninen, H., Riikonen, A., Moilanen, J., Nikinmaa, E., Vesala, T. (2012). Seasonal and annual variation of carbon dioxide surface fluxes in Helsinki, Finland, in 2006–2010. *Atmospheric Chemistry and Physics*, 12(18), 8475-8489.

Jarvis, P.G., Massheder, J.M., Hale, S.E., Moncrieff, J.B., Rayment, M., Scott, S.L. (1997) Seasonal variation of carbon dioxide, water vapour, and energy exchanges of a boreal black spruce forest. *Journal of Geophysical Research: Atmospheres,* 102(D24), 28953-28966.

Jenkins, J. C., Chojnacky, D. C., Heath, L. S., Birdsey, R. A. (2003). National-scale biomass estimators for United States tree species. *Forest Science*, 49(1), 12-35.

Kaimal, J. C., Finnigan, J. J. (1994). Atmospheric boundary layer flows: their structure and measurement.

Kaimal, J. C., Wyngaard, J. C., Haugen, D. A., Coté, O. R., Izumi, Y., Caughey, S. J., Readings, C. J. (1976) Turbulence structure in the convective boundary layer. *Journal of the Atmospheric Sciences*, *33*(11), 2152-2169.

Kaiser., G. (1994). *A friendly guide to wavelets*. Springer Science & Business Media.

Kaiser, G. (2011). *A friendly guide to wavelets*. Springer Science & Business Media.

Karney, C. F. (2013) Algorithms for geodesics. *Journal of Geodesy*, *87*(1), 43-55

Katul, G., Poggi, D., Cava, D., Finnigan, J. (2006). The relative importance of ejections and sweeps to momentum transfer in the atmospheric boundary layer. *Boundary-Layer Meteorology*, *120*(3), 367-375.

Kirschbaum, M.U.F., Mueller, R. (2001) Net Ecosystem Exchange. Cooperative Research Centre for Greenhouse Accounting.[Online] Accessed at: http://www.kirschbaum.id.au/NEE_Workshop_Proceedings.pdf [Accessed 08/11/14]

Kljun, N., Rotach, M. W., Schmid, H. P. (2002) A 3D Backward Lagrangian Footprint Model for a Wide Range of Boundary Layer Stratifications. *Boundary-Layer Meteorology*, 103, 205-226.

Koehler, B., Landelius, T., Weyhenmeyer, G. A., Machida, N., Tranvik, L. J. (2014) Sunlight-induced carbon dioxide emissions from inland waters. *Global Biogeochemical Cycles*, 28(7), 696-711.

Koerner, B., Klopatek, J. (2002). Anthropogenic and natural CO 2 emission sources in an arid urban environment. *Environmental Pollution*, *116*, S45-S51.

Kormann, R., Meixner, F. X. (2001). An analytical footprint model for non-neutral stratification. *Boundary-Layer Meteorology*, 99(2), 207-224.

Kotthaus, S., Grimmond, C.S.B. (2012) Identification of Micro-scale Anthropogenic CO_2, Heat and Moisture Sources – Processing Eddy Covariance Fluxes for a Dense Urban Environment. *Atmospheric Environment,* 57, 301-316.

Kotthaus (2014) Implications of the Dense City Centre to Surface-Atmosphere Exchanges. *Unpublished Doctoral Thesis*, King's College London, London, UK.

Kotthaus, S., Grimmond, C. S. B. (2014a) Energy exchange in a dense urban environment– Part I: Temporal variability of long-term observations in central London. *Urban Climate*, *10*, 261-280.

Kotthaus, S., Grimmond, C. S. B. (2014b) Energy exchange in a dense urban environment– Part II: Impact of spatial heterogeneity of the surface. *Urban Climate*, *10*, 281-307.

Kotthaus, S., Stockdale, C., Charlton- Perez, C., O'Connor, E., Grimmond, C.S.B. (2015) Mixing height over London: spatio-temporal characteristics observed by Ceilometer networks. Presentated at the 9th Internation Conference on Urban Climate, organised by the IAUC, Toulouse, 20th – 24th July.

Kowalski, A.S. (2012) Exact Averaging of Atmospheric State and Flow Variables. *Journal of the Atmospheric Sciences*, 69, 1750–1757

Lee, X. (1998) On micrometeorological observations of surface-air exchange over tall vegetation. *Agricultural and Forest Meteorology,* 91, 39-49

Leuning, R. (2007). The correct form of the Webb, Pearman and Leuning equation for eddy fluxes of trace gases in steady and non-steady state, horizontally homogeneous flows. *Boundary-layer meteorology*, *123*(2), 263-267.

LI-COR (2003) LI7500 manual [Online] http://www.esrl.noaa.gov/psd/data/obs/instruments/GasAnalyzer.pdf [Accessed online 08/11/2014]

Lieth, H. (1975) Modeling the primary productivity of the world. In *Primary productivity of the biosphere* (pp. 237-263). Springer Berlin Heidelberg.

Lietzke, B., Vogt, R. (2013) Variability of CO_2 concentrations and fluxes in and above an urban street canyon. *Atmospheric environment*, 74, 60-72.

Lim, M.T., Cousens, J.E. (1986) The internal transfer of nutrients in a Scots pine stand I. Biomass components, current growth and their nutrient content. *Forestry*, 59(1), 1-16.

Lindberg, F., Grimmond, C.S.B. (2011) Nature of vegetation and building morphology characteristics across a city: Influence on shadow patterns and mean radiant temperatures in London. *Urban Ecosystems,* 14, 617-634

Lindberg, F., Grimmond, C. S. B., Martilli, A. (2015) Sunlit fractions on urban facets–Impact of spatial resolution and approach. *Urban Climate*, 12, 65-84.

Liu, H. Z., Feng, J. W., Järvi, L., Vesala, T. (2012) Four-year (2006–2009) eddy covariance measurements of CO_2 flux over an urban area in Beijing. *Atmospheric Chemistry and Physics*, 12(17), 7881-7892.

Lu, S. S., Willmarth, W. W. (1973) Measurements of the structure of the Reynolds stress in a turbulent boundary layer. *Journal of Fluid Mechanics*, *60*(03), 481-511.

Macdonald, R. W., Griffiths, R. F., Hall, D. J. (1998) An improved method for the estimation of surface roughness of obstacle arrays. *Atmospheric Environment*, 32(11), 1857-1864.

Marland, G. (2008). Uncertainties in accounting for CO2 from fossil fuels. *Journal of Industrial Ecology* 12(2), 136–139.

Matese, A., Gioli, B., Vaccari, F. P., Zaldei, A., Miglietta, F. (2009) Carbon dioxide emissions of the city center of Firenze, Italy: measurement, evaluation, and source partitioning. *Journal of Applied Meteorology and Climatology*, *48*(9), 1940-1947.

McIntyre, K. (2013) *Strand building heating* [Email] Message to: Bjorkegren, A. 17/07/2013.

McPherson, E. G., Xiao, Q., Aguaron, E. (2013) A new approach to quantify and map carbon stored, sequestered and emissions avoided by urban forests. *Landscape and Urban Planning*, 120, 70-84.

Mölder, M., Lindroth, A., Halldin, S. (2000) Water Vapour, CO_2, and Temperature Profiles in and above a Forest—Accuracy Assessment of an Unattended Measurement System. *Journal of Atmospheric and Oceanic Technology,* 17, 417–425.

Moriwaki, R., Kanda, M. (2004). Seasonal and diurnal fluxes of radiation, heat, water vapor, and carbon dioxide over a suburban area. *Journal of Applied Meteorology*, 43(11), 1700-1710.

Moriwaki, R., Kanda, M. (2006) Local and global similarity in turbulent transfer of heat, water vapour, and CO_2 in the dynamic convective sublayer over a suburban area. *Boundary-layer meteorology*, *120*(1), 163-179

Moriwaki, R., Kanda, M., Nitta, H. (2006) Carbon dioxide build-up within a suburban canopy layer in winter night. *Atmospheric Environment*, *40*(8), 1394-1407.

National Atmospheric Emissions Inventory (NAEI) (2010) *Fleet Weighted Road Transport Emission Factor 2010* [Online] http://naei.defra.gov.uk/data/ef-transport

National Oceanic & Atmospheric Administration (NOAA) (2014) Monthly mean atmospheric carbon dioxide at Mauna Loa Observatory, Hawaii [Online] Accessed at: http://www.esrl.noaa.gov/gmd/ccgg/trends/ [Accessed 25/02/2015]

Nemitz , E., Hargreaves, K.J., McDonald, A.G., Dorsey, J.R., Fowler, D. (2002) Micrometeorological Measurements of the Urban Heat Budget and CO_2 Emissions on a City Scale. *Environmental Science and Technology,* 36 (14), 3139-3146

Newcastle City Council guidance (2011) *Design and Construction of Roads and Accesses to Adoptable Standards. Developer Guidance.* Newcastle City Council. [Online]

https://www.newcastle.gov.uk/wwwfileroot/legacy/regen/plantrans/DesignAndConstructionOfRoadsAndAccessesToAdoptableStandardsMarch2011.pdf [Accessed online 09/02/2016]

NGVA Europe (2015) *Comparison of energy contents and CO_2 emissions from different fuels* in *Fact Sheet: NG/biomethane used as vehicle fuel*. [Online] http://www.ngva.eu/downloads/fact-sheets/NG-Biomethane-as-a-vehicle-fuel.pdf [Accessed online 09/02/2016]

Nomis (2011) KS101EW - Usual resident population [Online] http://www.nomisweb.co.uk/census/2011/KS101EW/view/2013265927?cols=measures [Accessed online 30/08/2015]

Oke, T.R. (1987) Boundary Layer Climates. 2nd Ed., London: Routledge

Office of National Statistics (ONS) (2011) Standard Area Measurements (SAM) for 2011 Local Authority Districts [Online] https://geoportal.statistics.gov.uk/Docs/Products/Standard_area_measurement_(SAM)_for_2011_local_authority_districts.zip [Accessed 23/01/2016]

Office of National Statistics (ONS) (2013) 2011 Census Analysis - Comparing Rural and Urban Areas of England and Wales [Online] http://www.ons.gov.uk/ons/rel/census/2011-census-analysis/rural-urban-analysis/comparing-rural-and-urban-areas-of-england-and-wales.html [Accessed online 30/08/2015]

Office for National Statistics (ONS) (2014) ONS 2013 mid-year population estimates [Online] https://www.london.gov.uk/sites/default/files/update-09-2014-2013-mye.pdf [Accessed online: 11/06/2015]

Office for National Statistics (ONS) (2015)a Key Figures for 2011 Census: Key Statistics, Area: Swindon (Local Authority) [Online] http://neighbourhood.statistics.gov.uk/dissemination/LeadKeyFigures.do?a=7&b=6275271&c=Swindon&d=13&e=62&g=6393411&i=1001x1003x1032x1004&m=0&r=1&enc=1 [Accessed online: 09/12/2015]

Office for National Statistics (ONS) (2015)b Glossary [Online] http://www.ons.gov.uk/ons/guide-method/geography/beginner-s-guide/glossary/glossary-i.html [Accessed online: 06/05/2015]

Oikawa, S., Meng, Y. (1995) Turbulence characteristics and organized motion in a suburban roughness sublayer. *Boundary Layer Meteorology*, 74(3), 289-312.

Papale, D., Reichstein, M., Aubinet, M., Canfora, E., Bernhofer, C., Kutsch, W., Longdoz, B., Rambal, S., Valentini, R., Vesala, T., Yakir, D. (2006) Towards a standardized processing of Net Ecosystem Exchange measured with eddy covariance technique: algorithms and uncertainty estimation. *Biogeosciences,* (3), 571-583.

Pawlak, W., Fortuniak, K., Siedlecki, M. (2011) Carbon dioxide flux in the centre of Łódź, Poland—analysis of a 2-year eddy covariance measurement data set. *International Journal of Climatology*, 31(2), 232-243.

Potter, C., Klooster, S., Hiatt, S., Fladeland, M., Genovese, V., Gross, P. (2007). Satellite-derived estimates of potential carbon sequestration through afforestation of agricultural lands in the United States. *Climatic Change*, *80*(3-4), 323-336.

Press, W.H., Rybicki, G.B. (1988) Fast algorithm for spectral analysis of unevenly sampled data. *The Astrophysical Journal,* 338, 277-280.

Press, W.H., Teukolsky, S.A., Vetterling, W.T., Flannery, B.P. (2007) *Numerical Recipes: The Art of Scientific Computing*, Third Edition, New York: Cambridge University Press.

Price, D.T., Black, T.A. (1990) Effects of short term variation in weather on diurnal canopy CO_2 flux and evapotranspiration of a juvenile Douglas-fir stand. *Agricultural and Forest Meteorology,* 50, 139-158.

Rannik, Ü., Aubinet, M., Kurbanmuradov, O., Sabelfeld, K. K., Markkanen, T., Vesala, T. (2000) Footprint analysis for measurements over a heterogeneous forest. *Boundary-Layer Meteorology*, 97(1), 137-166.

Rannik, Ü., Sogachev, A., Foken, T., Göckede, M., Kljun, N., Leclerc, M. Y., Vesala, T. (2012) Footprint analysis. In *Eddy Covariance*. Netherlands: Springer.

Rantakari, M., Kortelainen, P. (2005) Interannual variation and climatic regulation of the CO_2 emission from large boreal lakes. *Global Change Biology*, 11(8), 1368-1380.

Raupach, M. R., Antonia, R. A., Rajagopalan, S. (1991) Rough-wall turbulent boundary layers. *Applied Mechanics Reviews*, 44(1), 1-25.

Raupach, M. R., Thom, A. S. (1981) Turbulence in and above plant canopies. *Annual Review of Fluid Mechanics*, 13(1), 97-129.

R Development Core Team (2013).R: A language and environment for statistical computing. R Foundation for Statistical Computing, Vienna, Austria.

Reba, M. L., Link, T. E., Marks, D., Pomeroy, J. (2009) An assessment of corrections for eddy covariance measured turbulent fluxes over snow in mountain environments. *Water Resources Research*, 45(4).

Readings, C. J., Haugen, D. A., Kaimal, J. C. (1974). The 1973 Minnesota atmospheric boundary layer experiment. *Weather*, 29(8), 309-312.

Reid K.H., Steyn D.G. (1997) Diurnal variations of boundary-layer carbon dioxide in a coastal city--observations and comparison with model results. *Atmospheric Environment,* 31(18), 3101-3114

Rotach, M. W., Fisher, B., Pringer, M. (2002) COST 715 Workshop on urban boundary layer parameterizations. *Bulletin of the American Meteorological Society*, *83*(10), 1501.

Rotach, M.W.L., Vogt, R., Bernhofer, C., Batchvarova, E., Christen, A., Clappier, A., Feddersen, B., Gryning, S.E., Martucci, G., Mayer, H., Mitev, V., Oke, T.R., Parlow, E., Richner, H., Roth, M., Roulet, Y.A., Ruffieux, D., Salmond, J.A., Schatzmann, M., Voogt, J.A. (2005) BUBBLE - An urban boundary layer meteorology project. *Theoretical and Applied Climatology,* 81(3-4), 231-261

Roth, M. (2000) Review of atmospheric turbulence over cities. *Quarterly Journal Royal Meteorological Society,* 126, 941-990

Roth, M., Oke, T. R. (1993) Turbulent transfer relationships over an urban surface. I. Spectral characteristics. *Quarterly Journal of the Royal Meteorological Society*, *119*(513), 1071-1104.

Salmond, J.A., Oke, T.R., Grimmond, C.S.B., Roberts, S., Offerle, B. (2005) Venting of heat and carbon dioxide from urban canyons at night. *Journal of Applied Meteorology,* 44, 1180-1194

Satterthwaite, D. (2008) Cities' contribution to global warming: notes on the allocation of greenhouse gas emissions. *Environment and Urbanization,* 20 (2), 539-549

Schuepp, P. H., Leclerc, M. Y., MacPherson, J. I., Desjardins, R. L. (1990) Footprint prediction of scalar fluxes from analytical solutions of the diffusion equation. *Boundary-Layer Meteorology*, 50(1-4), 355-373.

Schmid, H.P., Cleugh, H.A., Grimmond, C.S.B., Oke, T.R. (1991) Spatial variability of energy fluxes in suburban terrain. *Boundary-Layer Meteorology,* 54, 249-276

Schmid, H. P. (1994) Source areas for scalars and scalar fluxes. *Boundary-Layer Meteorology*, *67*(3), 293-318.

Schmid, H. P. (2002) Footprint modeling for vegetation atmosphere exchange studies: a review and perspective. *Agricultural and Forest Meteorology*, *113*(1), 159-183.

Schmidt, A., Wrzesinsky, T. Klemm, O. (2008) Gap filling and quality assessment of CO2 and water vapour fluxes above an urban area with radial basis function neural networks. *Boundary-Layer Meteorology*, *126*(3), 389-413.

Sellers, P., Hesslein, R. H., Kelly, C. A. K. (1995). Continuous measurement of CO_2 for estimation of air-water fluxes in lakes: An in situ technique. *Limnology and Oceanography*, 40(3), 575-581.

Shaw, R.H., Tavangar, J., Ward, D.P. (1983) Structure of the Reynolds Stress in a Canopy Layer. *Journal of Climate and Applied Meteorology*, 22(11), 1922-1931

Singapore Department of Statistics (2015) *Population & Land Area* [Online] http://www.singstat.gov.sg/statistics/latest-data#1 [Accessed online 09/02/2016]

Siebicke, L., Steinfeld, G., Foken, T. (2010) CO_2-gradient measurements using a parallel multi-analyzer setup. *Atmospheric Measurement Techniques,* 4(3), 4383–4421

Simpson, I.J., Thurtell, G.W., Neumann, H.H., Den Hartog, G., Edwards, G.C. (1998) The validity of similarity theory in the roughness sublayer above forests. *Boundary-Layer Meteorology,* 87, 69–99.

Smale, W. (2012). Olympics 'hits London retailers as shoppers stay away'. *BBC News*. [Online] Available at: http://www.bbc.co.uk/news/business-19059880 [Accessed 09/02/2016].

Soegaard, H., Møller-Jensen, L. (2003) Towards a spatial CO_2 budget of a metropolitan region based on textural image classification and flux measurements. *Remote Sensing of Environment*, 87, 283–294

Sogachev, A., Panferov, O. (2006) Modification of two-equation models to account for plant drag. *Boundary-Layer Meteorology*, *121*(2), 229-266.

Sotis, G. (2007) Envisat-1 Products Specifications, Volume 15: Sciamachy Products Specifications [Online] Avaliable at https://earth.esa.int/c/document_library/get_file?folderId=13020&name=DLFE-625.pdf [Accessed 04/07/2015]

Sparks, N., Toumi, R. (2010) Remote sampling of a CO_2 point source in an urban setting. *Atmospheric Environment*, 44, 5287-5294

Stephenson, N.L., Das, A.J., Condit, R., Russo, S.E., Baker, P.J., Beckman, N.G., Coomes, D.A., Lines, E.R., Morris, W.K., Rüger, N., Álvarez, E. (2014) Rate of tree carbon accumulation increases continuously with tree size. *Nature*, 507(7490), 90-93.

Stull, R. B. (1988). *An introduction to boundary layer meteorology* (Vol. 13). Springer Science & Business Media.

Sun, X. M., Zhu, Z. L., Wen, X. F., Yuan, G. F., Yu, G. R. (2006) The impact of averaging period on eddy fluxes observed at ChinaFLUX sites. *Agricultural and Forest Meteorology*, *137*(3), 188-193

Sunday Trading Act (1994). London: HMSO.

Sunday Trading (London Olympic Games and Paralympic Games) Act (2012). London: HMSO.

Tans, P. (2009). An Accounting of the Observed Increase in Oceanic and Atmospheric CO_2 and the Outlook for the Future. *Oceanography*.

Thomas, S. C., Martin, A. R. (2012) Carbon content of tree tissues: a synthesis. *Forests*, 3(2), 332-352.

Torrence, C., Compo, G.P. (1998) A practical guide to wavelet analysis. *Bulletin of The American Meteorological Society,* 79(1), 61-78.

Transport for London (TfL) (2007) *London Travel report 2007*.[Online] Transport for London. Available at http://www.tfl.gov.uk/assets/downloads/London-Travel-Report-2007-final.pdf [Accessed 02/08/2012].

Transport for London (2010) Travel in London report 3 (data) [Online] https://tfl.gov.uk/corporate/publications-and-reports/travel-in-london-reports; https://www.tfl.gov.uk/cdn/static/cms/documents/travel-in-london-report-data-3.xlsx [Accessed online 30/08/2015]

Transport for London (TfL) (2012) Vehicles entering c-charge zone by month. [Online] London datastore. Available at <http://data.london.gov.uk/datastore/package/vehicles-entering-c-charge-zone-month> [Accessed 02/08/2012].

Transport for London (TfL) (2013a) *Fleet Street from 2010*. [Attachment in email response to Freedom of Information request] Message to Bjorkegren, A. 25/11/ 2013.

Transport for London (TfL) (2013b) *Olympic Legacy Monitoring: Adaptations to deliveries by businesses and freight operators during the Games. Travel in London Supplementary Report* [Online] Available at http://www.tfl.gov.uk/cdn/static/cms/documents/olympic-legacy-freight-report.pdf [Accessed 27/02/2015].

United Nations (UN) (2007) *World Urbanization Prospects. The 2007 Revision.* Department of Economic and Social Affairs, Population Division

Union Gas (2015) *Chemical Composition of Natural Gas* [Online] https://www.uniongas.com/about-us/about-natural-gas/Chemical-Composition-of-Natural-Gas [Accessed online 09/02/2016]

van Gorsel, E., Leuning, R., Cleugh, H.A., Keith, H., Suni, T. (2007) Nocturnal carbon efflux: reconciliation of eddy covariance and chamber measurements using an alternative to the u_*-threshold filtering technique. *Tellus, B* 59, 397-403

Vardoulakis, S., Fisher, B.E., Pericleous, K., Gonzalez-Flesca, N. (2003) Modelling air quality in street canyons: a review. *Atmospheric Environment*, 37(2), 155-182.

Velasco, E., Pressley, S., Allwine, E., Westberg, H., Lamb, B. (2005) Measurements of CO_2 fluxes from the Mexico City urban landscape. *Atmospheric Environment*, 39(38), 7433-7446

Velasco, E., Pressley, S., Grivicke, R., Allwine, E., Coons, T., Foster, W., Jobson, B.T., Westberg, H., Ramos, R., Hernández, F., Molina, L.T., Lamb, B. (2009) Eddy covariance flux measurements of pollutant gases in urban Mexico City. *Atmospheric Chemistry and Physics,* 9, 7325-7342

Velasco, E., Roth, M. (2010) Cities as Net Sources of CO_2: Review of Atmospheric CO_2 Exchange in Urban Environments Measured by Eddy Covariance Technique. *Geography Compass,* 4/9, 1238-1259

Velasco, E., Roth, M., Tan, S. H., Quak, M., Nabarro, S. D. A., Norford, L. (2013) The role of vegetation in the CO_2 flux from a tropical urban neighbourhood. *Atmospheric Chemistry and Physics*, 13, 10185-10202.

Velasco, E., Perrusquia, R., Jiménez, E., Hernández, F., Camacho, P., Rodríguez, S., Retama, A. and Molina, L.T., (2014) Sources and sinks of carbon dioxide in a neighborhood of Mexico City. *Atmospheric Environment*, 97, 226-238.

Vermettern, A.W.M, Ganzeveld, L., Jeuken, A., Hofschreuder, P., Mohren, G.M.J. (1994) CO_2 uptake by a stand of Douglas fir: flux measurements compared with model calculations. *Agricultural and Forest Meteorology,* 72, 57-80

Vesala, T., Kljun, N., Rannik, Ü., Rinne, J., Sogachev, A., Markkanen, T., Sabelfeld, K., Foken, T., Leclerc, M.Y. (2008) Flux and concentration footprint modelling: State of the art. *Environmental Pollution,* 152, 653-666

Vogt, R., Christen, A., Rotach, M.W., Roth M., Satyanarayana, A.N.V. (2006) Temporal dynamics of CO_2 fluxes and profiles over a Central European city. *Theoretical and Applied Climatology,* 84, 117–126

Wallace, J. M., Eckelmann, H., Brodkey, R. S. (1972) The wall region in turbulent shear flow. *Journal of Fluid Mechanics*, *54*(01), 39-48

Ward, H. C., Evans, J. G., Grimmond, C. S. B. (2013) Multi-season eddy covariance observations of energy, water and carbon fluxes over a suburban area in Swindon, UK. *Atmospheric Chemistry and Physics*, 13(9), 4645-4666.

Ward, H.C, Kotthaus, S.K, Iamarino, M. (2014) *Fuel for conversion from building heat flux to CO_2* [Email] Messages to: Ward, H.C, Kotthaus, S.K, Iamarino, M. 07/05/2014 to 21/05/2014. Messages forwarded to: Alex Bjorkegren 23/11/2015

Ward, H.C., Kotthaus, S., Grimmond, C.S.B., Bjorkegren, A., Wilkinson, M., Morrison, W.T.J., Evans, J.G., Morison, J.I.L., Iamarino, M. (2015) Effects of urban density on carbon dioxide exchanges: Observations of dense urban, suburban and woodland areas of southern England. *Environmental Pollution*, 198, 186-200

Webb, E.K, Pearman, G.I., Leuning, R. (1980) Correction of the flux measurements for density effects due to heat and water vapour transfer. *Quarterly Journal of the Royal Meteorological Society*, 106(447), 85-100

Wenger, K. F. (1984) *Forestry handbook*. New York: John Wiley & Sons.

White, J. (1998) *Forestry Commission Information Note 12. Estimating the Age of Large and Veteran Trees in Britain*. Forestry Practice. [Online] http://www.forestry.gov.uk/pdf/fcin12.pdf [Accessed online 09/02/2016]

Wofsy, S.C., Goulden, M.L., Munger, J.W., Fan, S.–M., Bakwin, P.S., Daube, B.C., Bassow, S.L., Bazzazz, F.A. (1993) Net exchange of CO_2 in a mid-latitude forest. *Science,* 260(5112), 1314-1317

Woodwell, G.M., Houghton, R.A., Tempel, N.R. (1973) Atmospheric CO_2 at Brookhaven, Long Island, New York: Patterns of variation up to 125 meters. *Journal of Geophysical Research*, 78(6), 932-940

Worden, H.M., Cheng, Y., Pfister, G., Carmichael, G.R., Zhang, Q., Streets, D.G., Deeter, M., Edwards, D.P., Gille, J.C., Worden, J.R. (2012) Satellite-based estimates of reduced CO and CO2 emissions due to traffic restrictions during the 2008 Beijing Olympics. *Geophysical Research Letters*, 39(14), L14812

Workplace (Health, Safety and Welfare) Regulations (1992). London: HMSO

Xu, L-K., Matista, A., Hsiao, T.C. (1999) A technique for measuring CO_2 and water vapour profiles within and above plant canopies over short periods. *Agricultural and Forest Meteorology,* 94, 1-12

Yang, B., Hanson, P.J., Riggs, J.S., Pallardy, S.G., Heuer, M., Hosman, K.P., Meyers, T.P., Wullschleger, S.D., Gu, L.-H. (2007) Biases of CO_2 storage in eddy flux measurements in a forest pertinent to vertical configurations of a profile system and CO_2 density averaging. *Journal of Geophysical Research*, 112, D20

Zhao, C.L., Bakwin, P.S., Tans, P.P. (1997) A Design for Unattended Monitoring of Carbon Dioxide on a Very Tall Tower. *Journal of Atmospheric and Oceanic Technology,* 4,1139-1145